CRANFIELD UNIVERSITY

SADAF SAAD ANJUM

FABRICATION OF SMART INTERCALATED POLYMER – SMA NANOCOMPOSITE

SCHOOL OF AEROSPACE, TRANSPORT AND MANUFACTURING

PHD THESIS
Academic Years: 2011- 2014

SUPERVISORS:
PROF JOHN NICHOLLS, DR JEFF RAO

16th March 2015

Cranfield University

SCHOOL OF AEROSPACE, TRANSPORT AND MANUFACTURING

PhD Thesis

Academic Years: 2011- 2014

Sadaf Saad Anjum

Fabrication of Smart Intercalated Polymer – SMA Nanocomposite

Supervisors: Prof John Nicholls, Dr Jeff Rao

16th March 2015

This report is submitted in partial fulfilment of the requirements for Ph.D.

ABSTRACT

Mimicking nature gives rise to many important facets of biomaterials. This study is inspired by nature and reports on the fabrication of an intercalated polymer-NiTi nanocomposite that mimics the structural order of urethral tissue performing micturition. PTFE is chosen due to its hydrophobicity, low surface energy, and thermal and chemical stability. NiTi has been selected as a prime candidate for this research due to its excellent mechanical stability, corrosion resistance, energy absorbance, shape memory and biocompatibility. Nanoscale engineering of intercalated nanocomposites is done by PVD sputtering PTFE and NiTi. FTIR spectroscopy confirms that PTFE reforms as polymer chains after sputtering. Suitable PVD sputtering parameters were selected by investigating their influence on deposition rates, microstructure and properties of PTFE and NiTi thin films.

PTFE forms stable nanocomposite coatings with NiTi and displays favourable surface interactions, known as 'intercalation'. Intercalated PTFE-NiTi films were fabricated as layered and co-sputtered thin films. Co-sputtered nanocomposites contained nearly one-third vacant sites within its internal microstructure because of intercalation while intercalation introduced minute pits in fibrous NiTi columns of layered nanocomposites. These pits allow PTFE to extend their chains and crosslinks, resulting in microstructural and functional changes in the thin films. Intercalated PTFE-NiTi nanocomposites offer a close match to the natural tissue in terms of responding to the fluid contact (wetting angle modifications), and allow the soft and hard matter to incorporate in one framework without any chemical reactions (intercalation). An intercalated microstructure in co-sputtered and layered nanocomposites was verified by EDS-SEM and EDS-TEM techniques. The functional responses were witnessed by changes in water contact angle (WCA) and coefficient of friction (CoF) values measured on the film surface. The WCA (99°) and CoF (0.1 – 0.2) of the intercalated nanocomposite (sample PNT12) were different to the NiTi (top layer). WCA and CoF indicate the internal microstructural interactions because of intercalation.

Although the pseudoelastic behaviour of NiTi can provide additional fluid response but the difficulty is an absence of crystallinity in as-deposited NiTi, and the heat treatment that melts PTFE. However, DSC and XRD techniques were employed to find the optimum NiTi composition and transition temperatures for phase transformation related to pseudoelasticity. This study provides the basis to incorporate the shape memory (pseudoelasticity or thermal shape memory effect (shape memory effect)) features of NiTi into the intercalated nanocomposite in future. The intercalated PTFE-NiTi nanocomposite reveals a fascinating research precinct, having the response generating characteristics similar to that of natural tissue.

KEYWORDS

Intercalated nanocomposite, intercalated thin films, PVD magnetron sputtering, thin films, nanocomposites, nanomaterial, PTFE-NiTi, PVD-NiTi, PVD-PTFE, PVD manufacturing parameters.

In the name of Allah, the Most Gracious, the Most Merciful

Affectionately dedicated to my grandparents

Mr. and Mrs. Abdul-ur-Rahim

ACKNOWLEDGEMENTS

Firstly, I thank my supervisors Professor J. R. Nicholls and Dr J. Rao (Cranfield University) for their support and guidance throughout this work. I am also thankful for the Cranfield University staff especially Tracey Roberts, Sharon McGuire, Xianwei Liu, Mark Craig, Christene Chalk, Tony Gray, and Christine Kimpton for their help and assistance in all situations.

I am grateful to my wonderful family especially my brother Noman, and all my friends for their love, never ending patience and support. A special appreciation for my grandparents Mr. and Mrs Abdul Ur Rahim, who have always been my motivation ad courage. Without their care and prayers, my studies and this Ph.D. would have been impossible.

TABLE OF CONTENTS

LIST OF FIGURES

LIST OF TABLES

LIST OF EQUATIONS

LIST OF ABBREVIATIONS

A	Austenite phase
A_f	Austenite finish temperature
A_s	Austenite start temperature
AFM	Atomic Force Microscopy
ASH	Average step height
CA	Contact angle
CoF	Coefficient of friction
DC	Direct current
EDS	Elemental; detection spectroscopy
FTIR	Fourier transforms infrared
HA-PEEK	Hydroxyapatite – polyetheretherketone
IR	Infrared
M	Martensitic phase
M_f	Martensitic finish temperature
M_s	Martensitic start temperature
NiTi	Nickel titanium (shape memory alloy)
PET	Polyethylene terephthalate
PI	Polyimide
PU	Polyurethane
PMMA	Polymethylmethacrylate
PTFE	Polytetrafluoroethylene
PVD	Physical vapour deposition
Raman	Regional Atmospheric Measurement and Analysis Network
RF	Radio frequency
SD	Standard deviation
SEM	Scanning electron microscopy
SMA	Shape memory alloy
SME	Shape memory effect

TEM	Transmission electron microscopy
WCA	Water contact angle
XPS	X - ray photoelectron spectroscopy
XRD	X-ray diffraction

1 AIMS AND OBJECTIVES

The aim of the project is PVD sputtered[1] manufacturing of an intercalated[2] PTFE-NiTi nanocomposite[3], by mimicking[4] the micturition[5].

Intercalation would offer a collective control of microstructure, wetting and lubricity in a similar way as micturition. This research also addresses the critical thin film production issues for better understanding and the deposition control of PVD manufacturing process.

---

[1] **PVD sputtering** involves the ejection of particles from the surface of a solid target material by bombardment of heavy inert gaseous ions having high K.E (>10 eV), which generates the plasma, and condenses the target material onto a substrate to form the thin films [52; 53].

[2] **Intercalation** is the inclusion of the guest particles within the interplanner voids of a material's lamellar layers, forming a hybrid network [1].

[3] **Nanocomposites** are the materials that consist of dissimilar substances forming the major and minor phases called matrix and fillers respectively, and combine the favourable characteristics of both phase-components at a nanoscale, realising new functionalities [33; 43].

[4] **Biomimicking** is an approach adopted to produce devices and materials that imitate the nature [2]. In this project, the structural order of a physiological function, micturition, is mimicked.

[5] **Micturition** is a urethral function that relaxes the urethra voluntarily, when it senses that the bladder is full.

The following objectives are slated to accomplish the aims.

1. PVD magnetron sputtering deposits PTFE and NiTi thin films at various process conditions. PTFE and NiTi coatings are characterised and compared to the existing literature for establishing a standard data, and to evaluate if they behave as expected. The coatings were analysed by SEM (surface morphology), AFM (for surface topography and average step height), EDS (for elemental composition), WCA (for hydrophobicity), and scratch testing (for lubricity).
2. Deposition rates, microstructure, composition, surface properties and hydrophobicity of PTFE and NiTi thin films are investigated for a range of deposition parameters including pressure, power and coating thickness. The control of working conditions is crucial because PVD films properties are significantly dependent upon them, and slight changes can lead to substantial deviations in film properties.
3. PVD sputtered PTFE thin films reform as intact polymer chains, like their bulk form, which can be characterised by FTIR spectroscopy to report on chemical structure and polymerised content within the coatings.
4. Tailoring the NiTi composition to attain the SMA's transformation (transition temperature) relating to pseudoelasticity at the body temperature. NiTi thin films are analysed by DSC (phase transformations and associated enthalpies) and XRD (crystal structure and composition).
5. The preparation of PTFE-NiTi nanocomposite coatings followed by AFM, SEM, EDS, WCA, scratch testing and TEM analysis.
6. Finally, an intercalated PTFE-NiTi nanocomposite model will be manufactured by modifying the sputtering conditions, layer thickness and composition. Controlled wetting is intended to be perceived by alterations in the wetting angles while maintaining the lubricity of the thin films.

2 INTRODUCTION

The inclusions of one type of particles within the interplanner voids of another material's lamellar layers, forming a hybrid network, are named as intercalation [1]. In this project, PTFE-NiTi nanocomposite will be manufactured by inclusion of NiTi and PTFE into the thin layers of each other forming an intercalated structure. The aim is to use intercalation as an advantageous function to allow the interaction between both materials, enabling the control of the wettability. PVD manufacturing of PTFE-NiTi nanocomposites in both matrix based and multilayer nanocomposite settings will be attempted. Filler content and layer thickness can be varied to study the behaviour of novel material with diverse compositional-assembly.

Biomimicking is a method of fabricating the devices and materials that imitate nature. Hydrophobic and super-adhesive glues (inspired by lotus leaf, gecko feet, rose petals and beehives), and anti-fogging and anti-reflection coatings (inspired by mosquito eyes) are examples of the applications that have been inspired by nature [2]. Biomimicry of phospholipid bilayer membrane is used in several devices for controlling the flow of fluids. These devices have exceptional mechanical characteristics (strength and flexibility) and narrow size dispersal of the vesicles having a shape control mechanism. The shape control mechanism activates in response to the alterations in pH, light intensity, temperature or chemical reactions.[3]

The structure, properties and functions of natural tissue have been mimicked in the past, according to the needs of the application. For example, lubricated systems have low frictions, adhesives require high frictions and some applications even demand precise and adjustable frictional surfaces [4]. Thus, employing biomimicked systems for such applications can be used to tailor the frictional characteristics, and other properties depending on their functions. The range of biomimicry applications is widespread, and the matching requirements for natural tissue are complex. For this reason, no materials could be considered as ideal biomaterials [5]. Although the materials used in biomimicry applications (polymers, metals, ceramics, composites)

encompass different advantageous properties; however, all those materials have their drawbacks too [2].

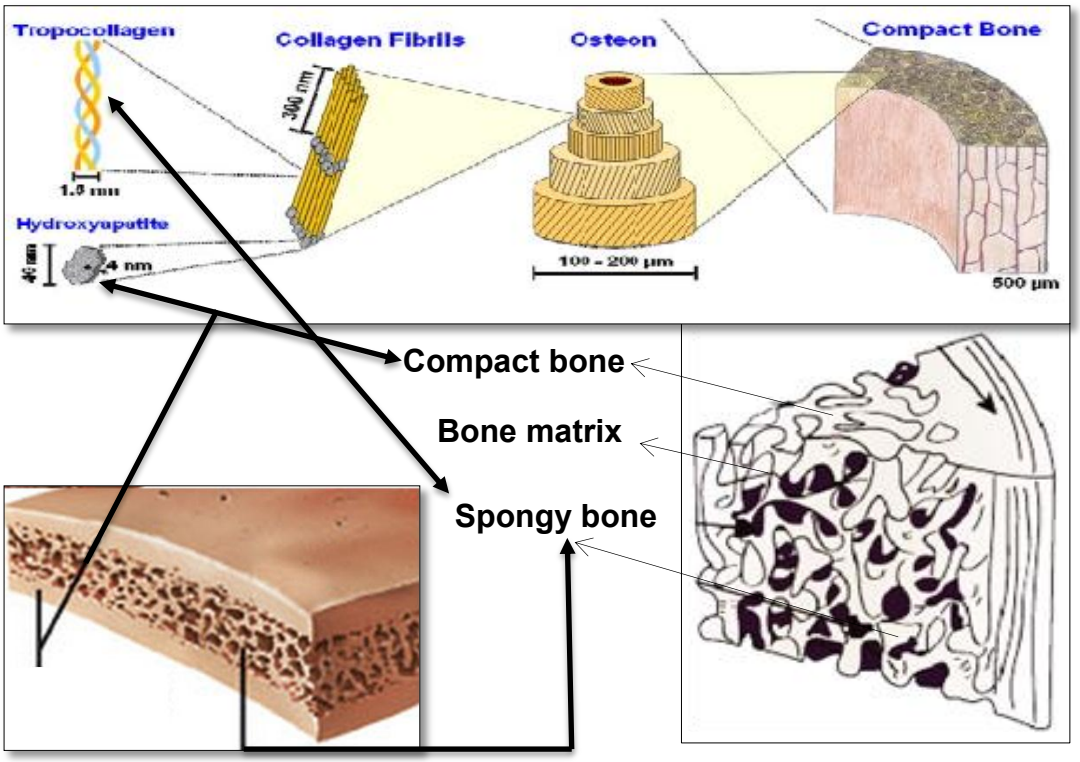

Figure 1: The natural tissue structure, representing a structural combination of hard and soft tissue [6; 7].

The manufacturing of PTFE-NiTi nanocomposite follows the idea of biomimicking where the material composition varies in a similar way as the structural formulation of the natural tissue. Natural tissue is made of hard and soft tissue material such as tropocollagen and hydroxyapatite respectively (Figure 1). The relative composition of soft and hard materials in natural tissue varies according to tissue type and function. The soft material has elastomer and provides cushion to the tissue while the hard material is responsible strength and load bearing. The combination hard and soft tissue formulate compact lamellae that can perform as a strong, flexible, load bearing, lubricious and wear resistant material. In our study, the hard and soft components of the natural tissue are mimicked by PTFE and NiTi respectively. The reasons for the selection of these two materials and the properties these two materials would inherit to the potential nanocomposite are described in section 2.1.

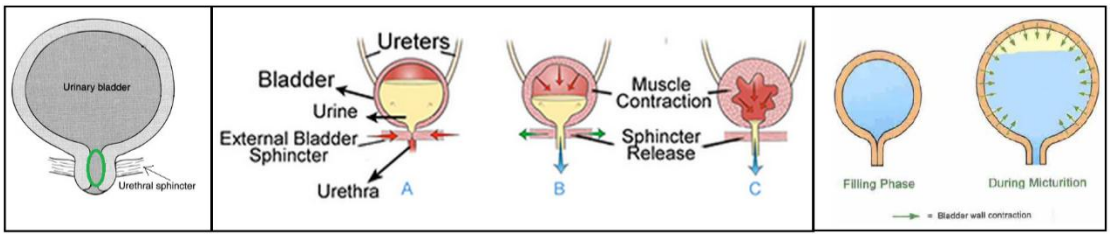

Figure 2: Urinary system of a female [8; 9].

A physiological function, micturition, provides further functional explanation of the biomimicking approach adopted for this project (Figure 2). In females, micturition is a physiological urethral function only that relaxes the urethra voluntarily at sensing that the bladder is full. The approach, of mimicking the structural properties of urethra performing micturition, is adapted to aid the manufacturing path and to simplify the functional demonstration of smart-intercalated nanocomposite. A tubular structure of the urethra executes micturition, which involves the liquid flow. Natural tissues involving fluid flow have WCA values matching to their functional requirements. Wetting angles below 90° favour capillary action and keep the surface wet by providing excess fluids. Contrastingly, the WCA above 90° deter the hydrophilic substances and maintain a contamination free surface for longer. Although urinary flow is mainly controlled by sphincter muscles working in response to the messages received by the nervous system. This study does not mimic the role of the nervous system to control the micturition, but the eventual micturition function is mimicked by controlling the liquid flow. The control of fluid flow is proposed by formulating a mechanism to adjust following four thin film features in one system.

- Microstructure
- Wetting angles
- Lubricity
- Pseudoelasticity[6]

[6] Pseudoelasticity is the ability of SMAs to display a loading-unloading cycle by rearranging their atomic lattice at specific temperatures. Pseudoelastic

A combination of the above four properties in one system would award a flow control in a similar way as micturition. It is aimed to find a way to fine-tune microstructure, wetting angles and lubricity by intercalation. Solid-solid intercalation in PVD sputtered thin films without involving chemical reactions is a novel phenomenon in thin film engineering. Although shape memory can allow mimicking the function of sphincter muscles additionally; however, the difficulty is the lack of crystallinity for as-deposited NiTi in nanocomposites. Crystallinity in NiTi can be achieved by heat treatment procedure during the manufacturing process or by post-sputter heat treatment. In either case, it requires a temperature above the melting point of PTFE, making it challenging to accommodate this additional feature. For this reason, the scope of the project is limited to intercalation, which would regulate the first three features listed above.

Nevertheless, some additional research is intended to explore an opportunity to accommodate shape memory effect (particularly pseudoelasticity) in intercalated PTFE-NiTi nanocomposite. It is envisioned that the nanocomposite would maintain NiTi's pseudoelastic behaviour within the intercalated settings. Above the body temperature, the nanocomposite would be responsive to the stress-induction of fluid loads by expanding and relaxing the intercalated lattices. NiTi SMA allows stress-induced shape memory and has a low wetting angle (hydrophilic). Hence, the fluid flow on NiTi film surface is a self-driven phenomenon. PTFE deters water particles away from the surface generating a contrary lethargy of water particles to their surface. The aim of this research is producing an intercalated nanocomposite, alongside that the additional investigation is conducted on NiTi transformations and the optimisation of pseudoelastic isothermal temperature, which provides a baseline data to continue the future research. As a consequence, the modified intercalated PTFE-NiTi nanocomposite displaying a controlled flow would lead to micturition-like microfluidics applications.

SMAs exhibit large elastic strains and accommodate recoverable inelastic deformations.[11; 22; 27; 136; 137]

This research is the first effort to assemble and intercalate polymer (PTFE) and SMAs (NiTi) by PVD magnetron sputtering for manufacturing a nanocomposite. The deposition of PTFE and NiTi by sputtering at suitable conditions would devise a stable and lubricious nanocomposite, having responsive surface to the fluids. Hybrid assemblies of PTFE-NiTi mimic the structural arrangement and the functioning of the tissue involved in micturition and achieve various tissue properties within one framework. The wetting of the thin films would alter with changing composition and intercalated structure. Table 1 simplifies the features that would be biomimicked in the intercalated nanocomposite.

Table 1: Characteristics of micturition mimicked within smart nanocomposite.

PTFE-NiTi nanocomposite	**Micturition**
NiTi mimics the tough fibres and mineral phase while PTFE imitates the soft constituents of the tissue. Those soft components contribute to natural lubrication mechanism of the biological structures.	The composition of natural tissue is mimicked, where the tissue structure is made of the collagen type I, and the strength varies by altering the content of hard and soft collagen ratio within the tissue composition.
The material will have intercalated arrangement of PTFE and NiTi for controlling the surface free energy; thus, altering the WCA. Consequently, the film surface would offer a potentially controlled response to the fluid.	The surface made of different tissue types include smooth muscles, epithelial muscles and glands, which coordinate with each other to allow an apposite response to wetting. The interaction of glands and epithelial muscles is of particular importance during micturition.
Pseudoelasticity in NiTi would be explored additionally, which may allow relaxation and expansion of the application of load. NiTi changes from the austenitic phase (B2) to deformed martensitic phase (B19′), which is recoverable on removal of load above austenitic finish (A_f).	Muscles receive signals from the brain to produce voluntary response by relaxing and expanding to allow excretion. Sphincter muscles control the micturition by autonomic and somatic nervous systems.

2.1 Material selection for the potential nanocomposite

The strategy for preparing the aimed nanocomposite is intercalating hierarchical assemblies of PTFE and NiTi while taking the advantages of the distinct materials within one framework. Along with that the combination of both materials would influence the wetting capacity of the coating surface. Two types of materials (a polymer and SMA) potentially offer distinctive properties within the nanocomposite structure. In principal functionality of the nanocomposite, PTFE would provide self-lubrication and hydrophobicity while NiTi can explicate material matrix having mechanical strength and possibly the stress-induced austenite-martensitic phase transformations as well. Biocompatibility is the most important pre-requisite to mimic natural tissue for the majority of applications. Biocompatibility is the ability of a material to be accepted by the tissue without inducing a toxic or inflammatory response to implantation and during healing and regeneration processes [5; 10; 11]. PTFE and NiTi are biocompatible and thermally stable above 300°C [12].

PTFE does not have a complex structure like most polymers, and it is made of simple linear chains of $-CF_2-$ repeat units. Deposition of PTFE by PVD sputtering has been reported previously, and the linear CF_2 chains reformed as thin film coating, despite PVD being a destructive process [13-16]. PTFE is a lubricious material with extremely low friction coefficients ~ 0.05 - 0.2 under various loading rates, which are independent of load and film thickness [13-15]. PTFE has been chosen to enhance the hydrophobicity of the nanocomposite because sputtered NiTi has very low wetting angle. PVD-PTFE thin films have low surface energy and surface tension and consequently high wetting angles [15; 17]. Sputtered PTFE films are non-wetting and highly hydrophobic with WCA ranging from 112° to 170° depending on sputtering conditions [14; 15]. Low surface energy is desired to decrease the possibility of corrosion and side reactions at the time of interaction with natural tissue and wet environment for a longer lifetime if the biomaterial. Hydrophobic nature also inhibits the moist from initiating any unwanted chemical changes such as oxidation [18]. PTFE has an extreme chemical inertness and thermal resistance to allow resistance to spreading of

infection [15; 17]. Chemical inertness is because of carbon–fluorine bond strength, meaning PTFE cannot be cross-linked like an elastomer, resulting in long and linear chains. The drawbacks of PTFE sputtered thin films include lack of strength, deformation over time and heat treatment of substrate or thin films affecting the lifetime of the coatings [15; 18; 19]. Poor adhesion and reduced abrasive wear resistance are also the downsides that arise with an increase in deposition thickness of the coatings [15; 18; 19]. PVD-PTFE thin films have been extensively used in numerous applications such as surface modifications, optical coatings and protective electronic films [18-20]. The properties related to these applications include long-term biocompatibility, ease of processing and fabrication, low surface energy to achieve durable stability and chemical resistance [18-20]. PTFE is a recipe of mechanical, dielectric, tribological and lubricious thin film applications [13; 14; 20]. PTFE is a prime candidate for many implant applications such as artificial ligaments in musco-skeletal system, acetabular cup, catheters construction, facial reconstructive, GORE VIABAHAN®, endoprosthetic stent graft, sutures, and flexible metallic tubular device lined with PTFE for improving the blood flow in blocked femoral artery and vascular grafts [17].

The reported advantages of NiTi in composite are high specific force generation, capability of direct and angular movements at microscopic level, noiseless operation, robust, production of the compact and flexible devices to allow easy access to difficult areas, and an ability to work with variable and harsh environment [21]. Bulk NiTi has excellent durability, ductility, fatigue resistance and mechanical stability. The material exhibits shape memory and pseudoelasticity characteristics, with the ability to transform between martensite and austenite. Due to its pseudoelastic behaviour, NiTi displays constant restoration stress and working output. The martensitic transformations are force generators in NiTi [11; 22]. NiTi-based thin films have been used in microfluidic applications (bio-MEMS actuators), for example, microvalves, microwrappers, micropumps, and stents for neurovascular blood vessels [23-25]. These applications comprise of freestanding NiTi thin films that enable production of large strains and work output up to about 10 J/cm^3 [25].

NiTi based SMA's are most potent materials for actuation, and for that reason have long been used to develop micro-electromechanical systems, which require large forces for long displacements. NiTi SMAs produce up to 105/cm^3 work output. NiTi exhibits high ductility that enables its use as actuators and microsensors in form of thin films. Recoverable stress up to 50MPa, transformation temperatures above 32°C, and hysteresis between 5 and 13°C have been reported features for Ni-Ti-Cu SMA films. Microvalves with NiTi ligaments serving as the actuator were developed based on the same principal. A membrane-based gas microvalve of NiTi endured more than two million cycles. SMA actuators are dedicated to multiactuator systems like arrays for particle transport or cooperating microgrippers in the field of microassembly.[25-27]

An example of NiTi thermal deployment is the 'Simon Vena Cava' filter used to filter large symbolised blood clots in the vena cava vein. As the blood returns from lower body to the heart, the clots trap in the device and dissolve over time. The device is preloaded into a catheter while in the martensitic state. Streaming of the chilled saline solution through the catheter retains the filter at the deployment position (M_s). When catheter is released followed by the discontinued flow of chilled saline, the change in surrounding blood temperature enables the device to recover to its pre-defined shape. Stents have an A_f temperature slightly above room temperature; thus, they are pseudoelastic at M_s Stents do not adopt their expanded shape at room temperature, but as the temperature increases due to body temperature, the stents typically expand by 3–8 times the catheter diameter.[11]

Within the nanocomposite thin film, the force required for the expansion and relaxation device can be provided by NiTi, which is generated while resisting the martensite to austenite deformation. The functioning of a smart nanocomposite can be understood by the example of T4 virus, which exhibits similar behaviour, where NiTi-like martensitic phase transformations occur in nature at a nano-scale. An interesting hypothesis put forward is the outer tail sheath of the T4-virus undergoes a phase transformation. The protein crystal within lattice exhibits a uniaxial contraction via atomic rearrangement.

Contraction provides the force necessary to drive the inner tail tube through the cell membrane of host cell and permits the transmittance of foreign DNA [28-30].

Researchers have given a prime value to the composites in recent decades due to the advanced combination of desired characteristics matching with natural tissue in one system while overcoming the disadvantages in combination. Glass-polypropylene, glass-polyepoxies and HA-PEEK are engineered biomaterial composites for various applications including adhesives and dental resins, where glass and polymer together provide anticipated features from both materials [2; 31]. Type I collagen found in different tissue exhibit diverse properties. For example, bone matrix and tendon elastomers both have type I collagen in their composition, but their structure and properties vary because of their compositional ratio [2]. Both bone matrix and tendon elastomers endure a composite-type composition having hard and soft collagen materials, which maintain the tissue functionality. The structural properties bone matrix and tendon elastomers vary depending upon the proportion of hard and soft collagen material. In contrast to other composite materials, SMA thin film composites can provide deflections on a smaller scale, very similar to a complete gripper system [25]. Winzek et al. [25] suggested that compared to NiTi freestanding thin films, NiTi composites prepared by a simple manufacturing method are preferred for bio-MEMS actuators. Polymer-metal thin films have been used for protective coatings, electrical shielding, electrical conductance, optical filters, reduced permeability, tailored biodegradability, self-passivation, electrostatic discharge, remote shape recovery, and ablation resistance [12; 32]. Multi-layered thin films have been used for wear resistance and optical applications including heat mirrors and band-pass filters. Polymer and oxide multi-layered coatings provide oxygen and moisture permeation barrier.[33]

2.2 Selection of the manufacturing method - PVD magnetron sputtering

PVD sputter deposition is a simple, environmental friendly, and time-saving process [34]. It has been used extensively in the past to deposit metals, intermetallics, polymers and composites. Plasma-based production methods such as PVD sputtering produce smooth and homogeneous thin films [35]. PVD sputtered thin films have better substrate adhesion compared to the coatings prepared by other deposition methods. Although evaporation has higher deposition rates than sputtering, however, sputtering has an advantage of higher deposition volume (deposition over a large area) than evaporation [36]. No container contamination occurs during PVD sputtering, which is critical for purity of nanoscale manufacturing [34]. The sputtering apparatus is selected according to the substrate size and shape, material type, process temperature, material resistance to plasma irradiation, film thickness, coating lifetime, and cost [37]. Along with those features, the choice of single or multilayer coating design also matters [37]. The benefits of magnetron sputtering include efficient deposition rates, an upright control of uniformity of the film thickness over a large area, and an ability to retain the maximum parent material's properties in the thin films [36; 37]. Alongside those benefits, this thin film manufacturing method facilitates the production of thin film with various morphological and crystal structures [38].

PVD sputtering is selected in this project for depositing PTFE and NiTi. This is because the evaporation caused by sputtering has lower deposition rate than chemical methods; therefore, it allows achieving better atomic level control for the composition of nanostructures [27; 38; 39]. As the deposition rate increases, the control on the thin film characteristics deteriorates, that is why it is important to have controlled deposition rate for achieving the desired nanocomposite composition and thickness. In this project, modified sputtering technique named as PVD unbalanced magnetron sputtering enables to overcome the difficulty in degree of confinement of plasma [40]. PVD is the only type of coating fabrication methods that allows deposition of both NiTi and PTFE, with precisely controlled deposition rate [41]. PVD sputtering also

gives a choice of different power supplies depending on material characteristics such as conductors or insulators [34]. In this project, the pulsed DC power supply is used to deposit NiTi coatings (conductive) while RF power supply has been chosen to prepare PTFE thin films (insulators).

Sputtering allows the deposition of alloys (NiTi in this project), where the resulting film retains the properties of the parent target material, with the compositional control during deposition. Practically only sputter deposition has succeeded to produce perfect shape memory effect, similar to bulk materials [23]. The main issue with NiTi deposition is Ti hastily reacting with oxygen, nitrogen and water vapour, and for that reason the high purity inert gas (argon) is used to generate the plasma.

The most conventional approaches to prepare the ‘polymer-metal composite coatings’ include physical vapour deposition (PVD), thermal evaporation, simultaneous plasma etching, high-energy ball milling, sol-gel, hydrothermal synthesis, chemical vapour deposition (CVD), and polymerization [32; 42-44]. This research only reviews the nanocomposites manufactured by PVD magnetron sputtering in polymer-metal combinations. The advantages of using this manufacturing method include better step exposure of layers within the nanocomposite in comparison to other vacuum evaporation methods. This method also provides uniform films, excellent adhesion to the most substrates, and enhanced control over compositional mechanism and metal filling factor of nanocomposites [32; 43]. The evaporation caused by sputtering has lower deposition rate to allow achieving the atomic level control [27; 39]. Deposition methods other than sputtering, used for the preparation of polymer-metal nanocomposites, have a small amount of metal clusters. The clusters have approximately 100 nm in size (ranging from a few atoms to islands), which are dispersed within a polymer matrix. In some other direct mixing methods such as CVD and sol-gel, the polymer-metal mixing only takes place at micrometric scale or above. However, PVD sputtering allows direct mixing of polymer and metallic phases on a nanometre scale, with a broad range of compositional configurations.[12]

2.3 Benefits of the project

Engineering of novel polymer-SMA nanocomposite is a pioneering effort in the multidisciplinary research of thin films. PTFE-NiTi coatings will be the first to intercalate the polymer and NiTi within a nanocomposite, offering a control of internal microstructure. Mimicking micturition would fabricate potential intercalated-nanocomposite films that would enable influencing the wetting capacity of the coating surface. The combination of polymer and NiTi forms a new composite material, structurally different from the original constituents without involving a chemical reaction. Composites allow taking advantages of the individual characteristics of both materials in combination, along with added benefit of their assemblage in intercalated setting. This would edify the researchers about this type of innovative polymer-SMA interactions in thin film manufacturing. The nanocomposite would demonstrate additional significantly distinct characteristics compared to the constituent materials.

As a nano-fabrication method, PVD sputtering is complex at the atomic level, and slight deviations have a substantial influence on a film's structure and properties. This builds the prerequisite for further understanding of the complex nanoscale deposition. Comparative study of polymer and intermetallic deposition conditions and characterising them is very beneficial for thin film manufacturing industry. The knowledge of working parameters for polymer and SMA deposition allows better control during the deposition process. Fundamental manufacturing aspects of PVD sputtered thin film are also investigated to understand the engineering parameters in greater detail, which would enable acquiring a superior manufacturing process for the deposition of thin films.

Appetiser of the novel nanocomposite uncovers innovative ground for the multidisciplinary research of thin film active surfaces and offers potential for fluid flow applications, controlled by stress-induced contraction. Some additional advantages of this novel research are also proposed in chapter 6.6, which are beyond the scope of this research project, but the innovative nanomaterial can be a prime aspirant for further studies and applications.

3 LITERATURE REVIEW

This chapter comprehends a critical analysis and background research associated with the scope of the project. Relevant theories, previous findings and experimental evidences provide the baseline to build the further research upon the existing gaps and contribute to the innovative multidisciplinary engineering. The first section of this chapter demonstrates the fundamental concepts of thin films engineering, and the provisions of PVD magnetron sputtering, which is the manufacturing method for thin films in this project. The steps and the structural patterns of thin films growth are also discussed in relation to their characteristics evaluated in the previous studies. This follows the comprehensive reviews sections of the existing studies relating to PTFE, NiTi and PTFE-based nanocomposite thin films manufactured by PVD sputtering. The results of various existing studies are contrasted, compared and critically analysed to identify the gaps in the literature. Subsequent to this, previous studies relating to the intercalating within thin films are discussed to apprehend the effect of this structural feature on the functioning of the material. Finally, a detailed scheme for this project is provided based on the requisite of re-establishing the existing experimental data, and further experimental outline is proposed to fill the gaps found in the literature. Depending upon the results yielded by the initial stages of PTFE and NiTi thin films, an innovative idea is provided to engineer the intercalated PTFE-NiTi nanocomposite thin films.

3.1 Thin film engineering

Thin films are three-dimensional condensed matter with one dimension much smaller than the dimensions (nanometric scale) in the other perpendicular directions [45]. Thin films deposition methods divide into two categories namely physical and chemical. Chemical techniques involve chemical reactions, and these methods are economical, but the film quality is not right enough for many applications [46]. Physical deposition techniques involve the evaporation or ejection of material from the target source producing reliable and reproducible films, but these methods involve high cost compared to chemical approaches [46; 47]. Most of the thin film manufacturing procedures involve following steps [45].

1. Substrate preparation.
2. Choice of deposition material, which can be a solid target, solution, molten, or vapourised substances.
3. Selection of suitable control parameters to attain required thin film microstructure and morphology.
4. Phase transformation and adherence of the deposition material from fluid or vapours on the substrate surface, which are usually present in space directly above or below the substrate.
5. Condensation and growth into crystalline or amorphous thin films.

PVD magnetron sputtering is commonly used to fabricate thin films with advanced thermal, mechanical and chemical properties for many industrial applications including corrosion resistant coatings for aerospace, hard ceramic coatings for wear resistance, and microelectronic thin films [37; 39; 40]. This section narrates the PVD magnetron sputtering, plasma generation during the process, power supplies and thin film growth, together with resulting structure and properties of the thin films.

3.1.1 Physical vapour deposition (PVD)

Physical vapour deposition (PVD) involves physically generated energetic vapours from target material depositing atom by atom onto the substrate at low temperature by condensation under high vacuum with significantly low base pressure (10^{-4} – 10^{-7} mbar) [48; 49]. Basic apparatuses of PVD systems include gas delivery system, high purity source material and a substrate mounting assembly [49]. Commonly used PVD processes are thermal evaporation, activated reactive evaporation, glow discharge / ion beam plating, glow discharge / ion beam sputtering [50].

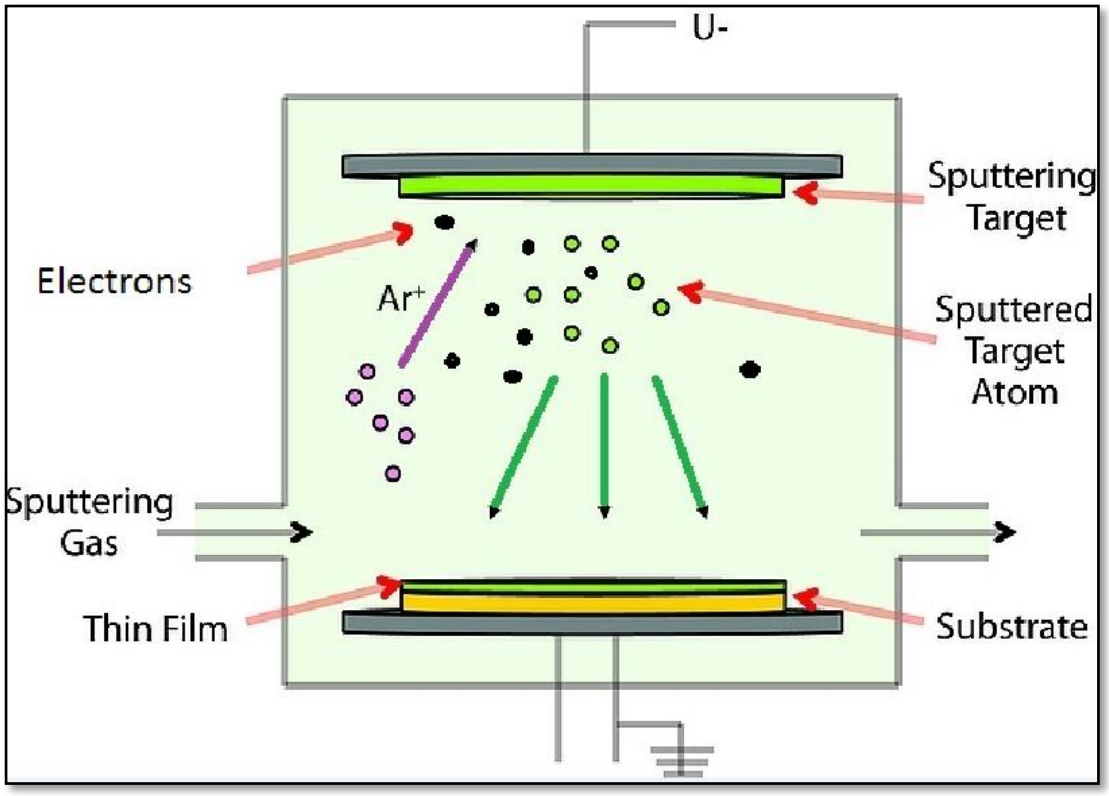

Figure 3: Schematic representation of PVD sputtering [51].

PVD sputtering involves the ejection (evaporation) of particles from a surface of a solid target material by the bombardment of heavy inert gas ions typically argon with high kinetic energy (greater than 10 eV), which generate a cold plasma and condenses target material onto a substrate to form thin film [52; 53]. Sputtering is the most common vapour deposition technique, which operates on the physical phenomenon of momentum transfer resulting from the impact of highly energetic particles [52].

Figure 3 schematically shows the PVD vacuum chamber with a typical substrate-target layout during the sputtering process. Kinetic energy is transformed into internal vibrational energy (more than the bond energy) during sputtering, which ionises the argon gas. The ionisation of argon gas sputter the target material and stimulate the positive ions, which accelerate towards the substrate following a collision cascade to generate plasma / flux of thin film [40; 53]. The substrate, positioned in front of the target consequently meets the ionic flux / plasma of sputtered atoms [50].

Plasma is the fourth state of matter, as it was first described as an assembly of ionised gases, by Irving Langmuir and his co-workers in 1929. A plasma consists of quasineutral sub-systems of particles including electrons, ions and other neutral gas particles, where the mass of an electron is negligible compared to other particles such as ions and neutral gaseous particles. Thermal equilibrium is attained and maintained when electron temperature (T_e), ion temperature (T_i) and gas particles temperature (T_{gas}) are the same [53]. Two types of plasma are known depending upon temperature and pressure of particles as shown in Table 2.[53]

Table 2: The description of plasma types [53].

Thermal plasma (Atmospheric plasma)	**Cold plasma (Low-pressure plasma)**
$T_e \sim T_i \sim T_{gas}$	$T_e >> T_i / \sim T_{gas}$
At local thermodynamic equilibrium	Not at local thermodynamic equilibrium
Temperature ranges around few thousand kelvins.	$T_i \sim T_{gas} \sim RT$ $T_e \sim 10^4 – 10^5$ (1–10 eV)

During PVD sputtering, the cold plasma particles, not being in thermal equilibrium are excited by high electric fields (DC, RF or MW). Electrons being the most energetic and accelerated particles, import their kinetic energy to other particles in the plasma by collisions on relaxation (de-excitation). If the gas pressure is kept at 100 mbar or lower, the temperature of all particles congregates to a similar value, which produces plasma comprised of sub-systems of those particles. Collisions of electrons with heavier particles, to generate plasma, are initially elastic followed by inelastic collisions. Elastic collisions between electrons and other particles occur initially. Over time, the rate of collisions and the energy transfer from electrons to the heavier particles reduce, leading to a greater temperature difference between the electrons and the heavy particles. A higher temperature difference is observed with a larger number of collisions. The particles gain energy to overcome the temperature difference until it is sufficient to do inelastic collisions by exciting and ionising those particles and fragmenting the molecules. Electrons with high kinetic energies produce greater ionisations until they maintain plasma.[50; 53]

During sputtering, heterogeneous reactions take place, which are mostly physical reactions that occur on a solid substrate surface due to the presence of high-energy electrons and electromagnetic radiations within plasma, which originate from the substrate surface. Electromagnetic radiations produce glow within plasma. Heterogeneous physical reactions are referred to the Equation 1 below, where A and B are molecules sputter-deposit at a substrate surface S, in gaseous (g) and solid (s) states [53].

Equation 1: Heterogeneous physical changes while sputtering the reaction.

$$S + B_{(s)} + A^{+}_{(g)} \rightarrow S^{+} + B_{(g)} + A_{(g)}$$

Magnetron sputtering is a modification of conventional PVD sputtering system to increase the sputtering yield[7]. Magnets are used on the backside of the target to confine electrons near the target surface, thereby enhancing the sputtering yield. Use of the magnetron leads to a higher rate, and efficiency of ion bombardment and better coating structure [36; 40]. Kusmuto et al. [54] investigated the erosion of magnetron targets, and concluded that the erosion profile of the target became narrower and tapered at low-pressure of 1 x 10^{-2} mbar and higher magnetic field intensities (B_T = 0.11).

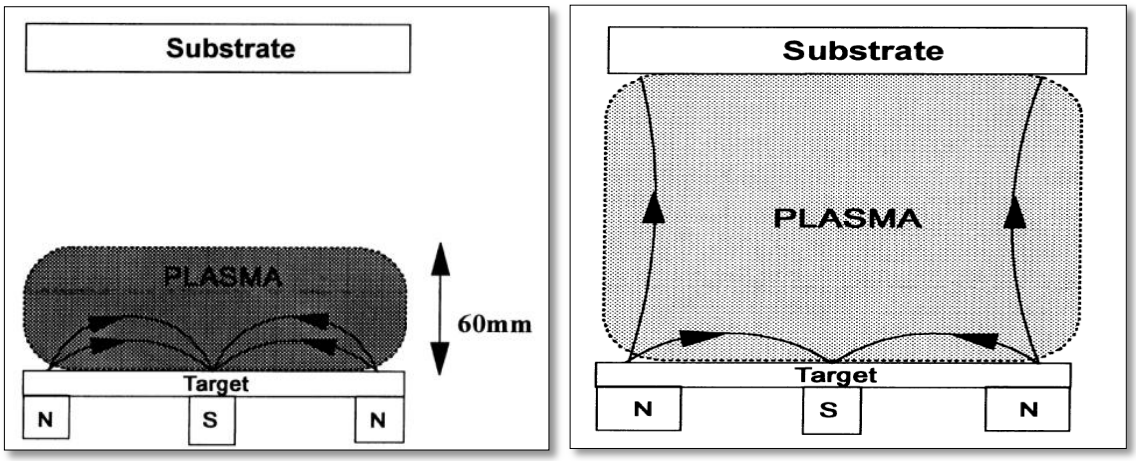

Figure 4: Unbalanced magnetron (right) and conventional magnetron (left) used for PVD sputtering [40].

PVD magnetron sputtering offers enhanced ionisation efficiency by trapping electrons near the target while reducing the plasma loss. This results in higher deposition rates, reduced substrate heating, better surface coverage and the ability to work at reduced pressures when required. The drawbacks of magnetron sputtering include the need for efficient target cooling and low utilisation of sputtering targets due to preferred erosion area associated with the magnetron plasma enhancement. In a conventional magnetron, the dense plasma strappingly narrows to the area extending about 60 mm in front of the target. Film growth on the substrate located in this area enhances the thickness of the coating and enhances the structure. Therefore, the film growth on a substrate placed outside the dense plasma region encounters an

[7] Sputtering yield: “The number of atoms ejected from a target surface per incident energetic particle” [36].

insufficient ion bombardment, and modifies the microstructure of the growing film by not producing fully dense, high-quality coatings on large and multifaceted substrates.[37; 40]

Power supplies typically employed during PVD sputtering include direct current (DC), pulsed DC, radio frequency (RF), microwave (MW) or electron cyclotron resonance (ECR) [53]. The choice of power supply depends upon the deposition material [55]. Table 3 summarises the characteristics of RF and DC power supplies, which are commonly used for insulators and conductors respectively.

Table 3: Characteristics of cold plasma power supplies [53].

Power supplies	**Coupling of the electric power**	**Ionisation degree**	**Ion density (cm^{-3})**
DC	Internal and conductive electrodes	<<0.1%	$<10^{10}$
RF	Internal and external electrodes, (conductive/ non-conductive)	<<0.1%	$\sim10^{10}$

DC sputtering is limited to the deposition of conducting materials. However, the introduction of RF supplies in 1970s allowed a broader variety of materials to be deposited by PVD sputtering [20; 27; 56; 57]. Common RF sputtered materials include insulators (ceramics or polymers) and dielectrics. Polymer coatings are not sputtered efficiently by DC sputtering because of the charge build-up on the target surface [41]. NiTi thin films having both shape memory and pseudoelastic properties have been successfully deposited using RF power [27; 58].

PVD sputtering is carried out by delivering RF power of 13.56 MHz to the magnetron electrode via a matchbox [20]. RF sputtering is considered too slow and complex arc process for large-scale commercial applications [59]. Kinetic energy of ions hitting the substrate is very high (100 – 600 eV) [53].

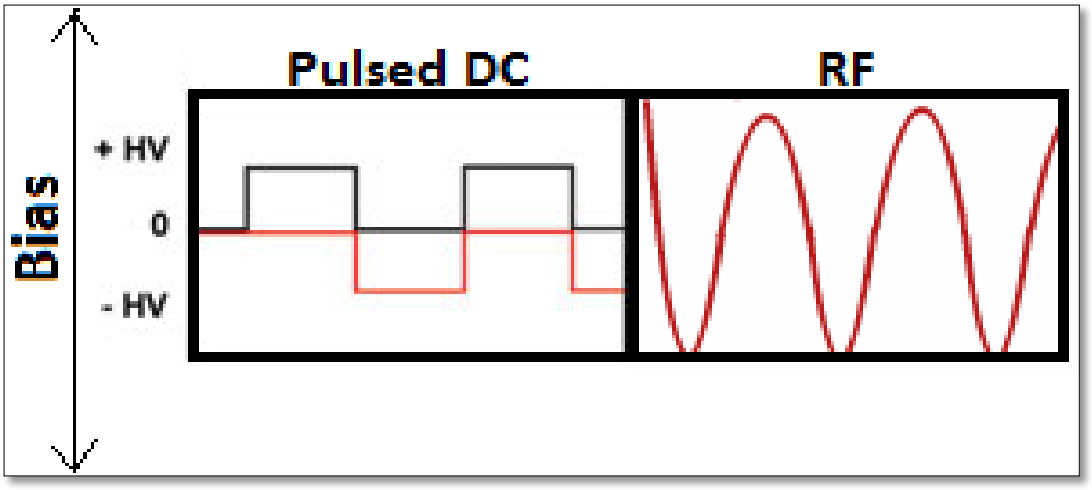

Figure 5: Pulsed DC and RF waveform bias profiles.

PVD sputtering of NiTi is commonly carried out by pulsed DC [27; 60]. Kelly et al. [59] reported that pulsed DC system generates five times greater deposition rate compared to RF sputtering, for the metallic substances (alumina). Kinetic energy of ions hitting the substrate is controlled by a negative bias. Pulsed DC power supply provides more deposition control parameters including power, frequency, and voltage [53; 59].

3.1.2 Thin film growth

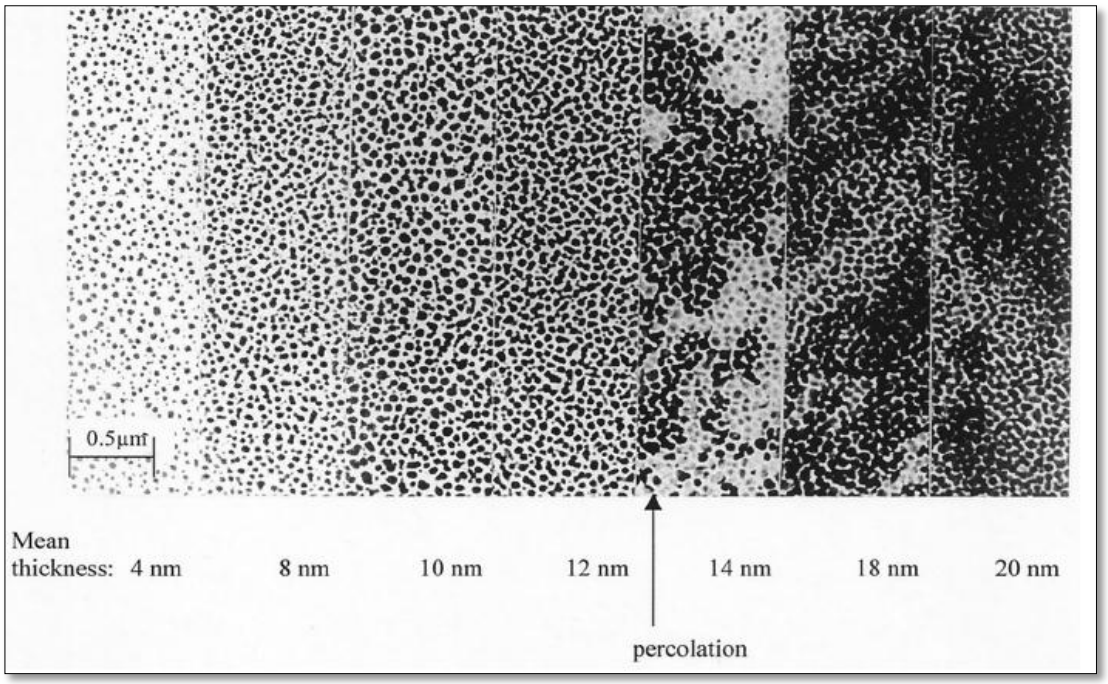

Figure 6: TEM image of the development of Sb film (nucleation, nuclei growth leading to coalescence, ultimately forming the homogenous film. An amorphous to crystalline phase transition takes place at percolation [61].

Thin film growth takes place in three dimensions by kinetic absorption and diffusion of the individual particles in three steps, namely nucleation, coalescence and film growth [61]. The nucleation occurs when the initial adatoms (surface atoms) arrive on the substrate (Figure 7.ii) and begin the condensation of adatom vapours on the substrate surface. This leads to nucleation resulting in the formation of small clusters, which appear as a new phase within the matrix of the mother phase [45; 61; 62]. The free energy of the cluster determines the thermodynamic stability of the cluster, which is the difference in free energy between the cluster and the equivalent free-energy of the matrix and is also related to the cluster size. Up to a certain cluster-size, the free energy remains positive so that the creation of the cluster is unfavourable [45]. In the early stage of nucleation, the clusters are small, and their concentration is low resulting in a low surface coverage [45; 63]. The nucleation process is well defined by the mean-field nucleation theory. Nucleation is a non-equilibrium process taking place at supersaturation, and is

affected by the concentration of vapour pressures, type of the deposited and substrate materials, temperature, and molecular weight of the deposit materials [61]. Initially, the nucleation is random, and as it continues more nuclei start to grow, capturing atoms from the supersaturated adatom phase. When the supersaturation reduces significantly, the nucleation process ceases [64]. In other words, nucleation continues if the probability of diffusing adatoms is much higher than that for it to form a juncture with a second adatom belonging to the new cluster nuclei [63].

The early stage of growth transitions between nucleation and the late stage growth regime (Figure 6iiia). During the early stage growth, the development of the cluster morphology depends primarily on the deposition rate. All impinging adatoms on the substrate are captured by the existing clusters to formulate two-dimensional clusters [62]. This follows a distinguished lateral growth stage where the diffusing adatoms adsorb into the two-dimensional clusters to enhance the surface coverage and decrease the travelling distance of adatoms to reach the substrate. Clusters continue to grow, but other processes dominate, such as ripening, i.e., growth of larger clusters at the expense of smaller clusters that dissolve and execute coalescence. While ripening, a small cluster size causes the cluster to travel along the substrate and seam with other clusters. A fast lateral growth stage results in loss of cluster shapes due to lack of equilibrium and polygonal shaped clusters are formed. If the deposition continues during the early stages of cluster growth, the system asymptotically approaches a coalescence stage, which is kinetically slower than the lateral growth.[63; 64]

Coalescence is the growth of islands until they touch one another to form a continuous network of channel type structure producing continuous layers [61; 62]. An island is an object on the surface disconnected to another object grown as single crystal rather than an extension of the neighbouring object [65]. The grown clusters at high concentration during nucleation could intrude upon the neighbouring clusters and coalesce forming larger clusters [45]. Coalescence regulates the eventual grain structure in a continuous film [63]. The coalescence of clusters corresponds to multistep transitions of the cluster size [45]. Coalescence can be following two types [61]:

- Solid-like coalescence: This occurs when two islands join in a fashion that the grain boundary remains between them.
- Liquid-like coalescence: In this type of Coalescence the grain boundaries may fuse together to form a new, larger and boundary-free island.

The clusters now in close contact with each other reach a transition point where the mean cluster diameter is approximately the same as an average correlation distance between the two clusters [63]. Any uncovered surface still follows the lateral growth mechanism, ultimately resulting in a continuous film, and this phenomenon is named as coarsening. Polop et al. [65] highlighted those uncovered surfaces forming holes during the initial island growth (Figure 7.i.b). Kaune et al. [63] reported a minimum of 9 nm film thickness for a totally covered gold thin film having polygonal shape of the clusters. Figure 7.i. also shows the STM topographs of the Ag film growth presented by Polop et al. [65] who reported a film thickness below 0.8 nm for the nucleation and island growth stage, followed by the coalescence forming the thin films having thickness up to 10 nm. A fully covered thin film formed during coalescence continues to grow vertically by adsorption resulting in the cluster height equal to the film thickness. A lateral stage of coarsening occurs by motion of the cluster boundaries instead of the entire clusters resulting in defined grains and grain boundaries. The vapour deposited film growth by coarsening eventually fabricates a continues polycrystalline grain structure having a macroscopic network of the clusters.[63]

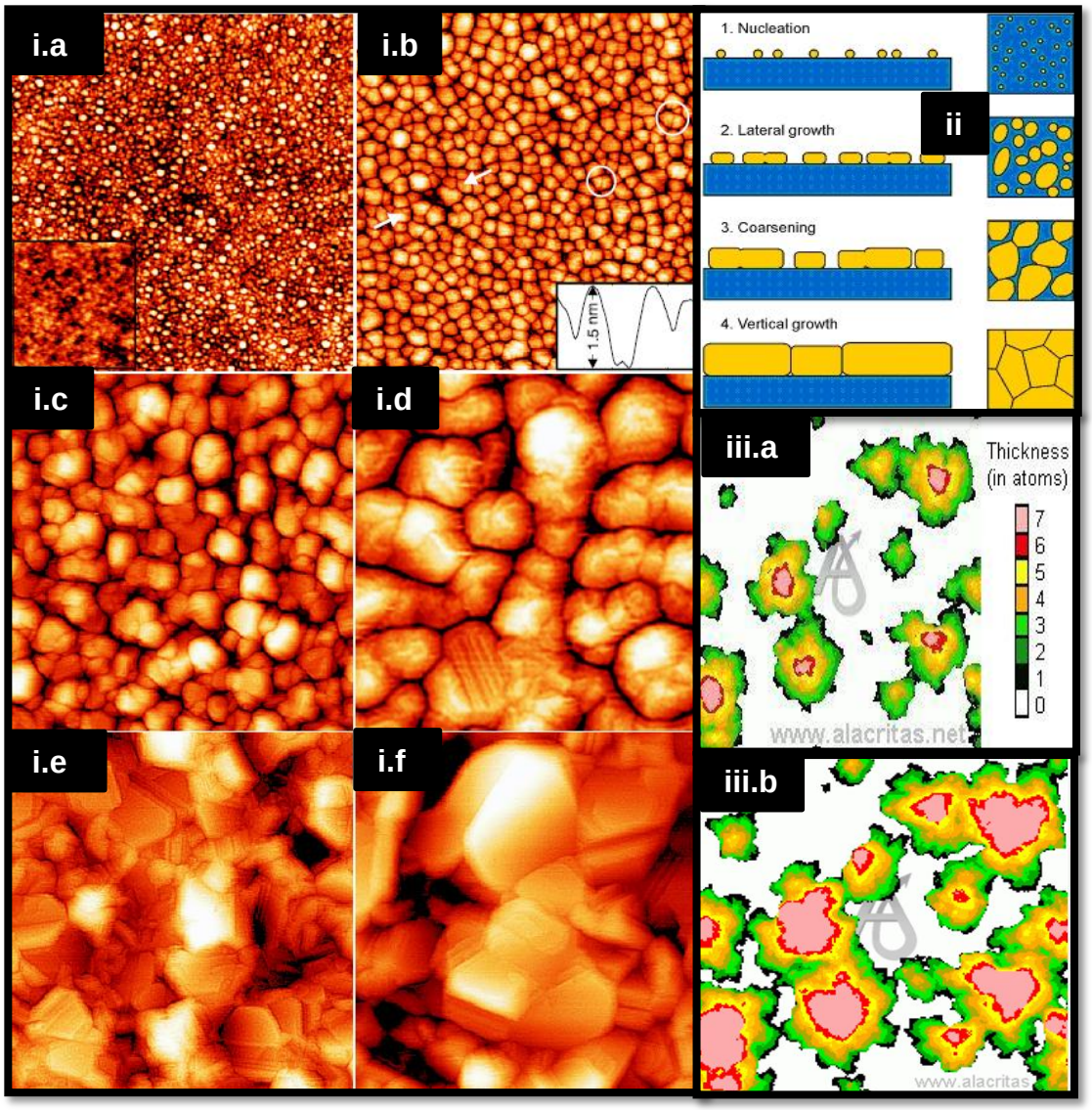

Figure 7: (i) STM topographs of Ag films deposited at 27°C with thicknesses of (a) 0.3 nm, (b) 1.0 nm, (c) 2.7 nm, (d) 8.5 nm, (e) 15.9 nm and (f) 30.0 nm. Image size = 160 nm×160 nm. The inset in (a) shows an STM image (60 nm x 60 nm) of the amorphous substrate, and in (b), a line scan between the arrows in the topograph, which reaches down to the substrate [65].

(ii) A schematic drawing showing the growth of Au cluster. [63].

(iii) Growth of thin films showing (a) island growth, (b) island assembly [66].

The evolution of sequestered islands to a continuous macroscopic network can be characterised by a percolation threshold thickness. To percolate, means to pass or to cause to pass through the porous material. At percolation thickness, coalescence creates a continuous path of electrons through the coating, and conductivity rises steeply by several orders of magnitude. A phase transition takes place at the percolation threshold, with optical properties of the film changing exponentially [61]. The values for the minimum thickness of a continuous film vary depending on deposition materials and process parameters. A constant supply of incoming particles, provided by a plasma flux leads to the three dimensional growth of clusters [62]. Most films have percolation thickness in the range of 1 – 20 nm, typically between 5 and 15 nm [61; 66]. Further material deposition does not directly increase the percolation thickness [61]. Polop et al. [65] also reported the same percolation thickness range (5 – 15 nm) for polycrystalline Ag thin films. 50 nm thick PVD continuous coatings exhibit four stages of continuous film development [67].

- Island stage (0-20 nm)
- Network stage (20-35 nm)
- Hole stage (35-45 nm)
- Continuous film (50 nm and more)

Figure 7.i.e presents the crystalline island growth (3D) of the single crystal on an amorphous substrate [65]. The absolute structure of coatings is determined by shadowing, surface diffusion, bulk diffusion and recrystallization. Shadowing is the interaction arising from the geometric constraint imposed by surface roughness of the growing film and the arriving particles. This effect is dominant at low substrate temperatures (Ts) values matching to zone 1 of structure zone models. Surface diffusion occurs due to the mobility of particles at the near surface region and grain boundaries interfaces, and is dominant at medium substrate temperatures (Ts) values corresponding to zone 2. Bulk diffusion takes place because of the mobility of particles in the volume of grains. During recrystallization (desorption), a transition occurs because of a complete change in crystal orientation. Recrystallization is dominant at and above percolation thickness. Bulk diffusion and recrystallization are dominant

at high substrate temperatures (Ts), and for this reason assimilate in zone 3 of structure zone models.[53; 61] The growth of thin films occurs by formation of nuclei by one of the three film-growth modes depending on interaction energies of substrate atoms and film atoms. Three primary growth modes named as Frank – Vander Merwe, Volmer – Weber and Stranski – Krastanov, which are summarised in Table 4.

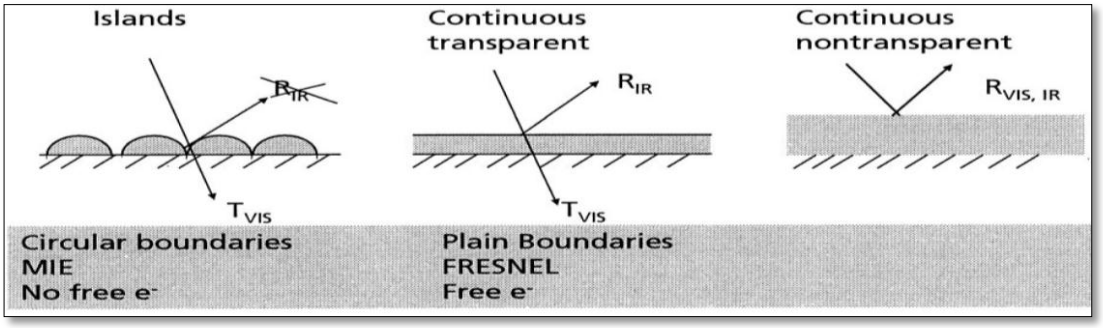

Figure 8: Growth of the metal film, starting from islands to continuous transparent to non-transparent films [61].

The microstructure of polycrystalline thin films is dependent on control of nucleation and growth processes [45]. A Stranski– Krastanov growth mode was reported prior to the appearance of the film growth by 3D island mode for the polycrystalline Ag thin films on a Si substrate [65]. PVD gold films also grow by 3D-islands rather than monolayer-by-monolayer mode [63]. Kumomi et al. [45] also reported the evolution of island growth of crystallites like Volmer-Weber or Stranski-Krastanov modes for polycrystalline thin films, and the grain boundaries developing where the adjacent islands meet. The metal coatings initially grow in the form of islands following the Volmer – Weber mechanism, as shown in Figure 8. The Islands are transparent to visible and IR radiation. Percolation thickness reforms the metal film into a continuous structure, and it is now only transparent to visible light while it reflects IR radiation [61]. If the thickness increases any further (above ~20nm) all radiations, reflect [61]. The structure of metallic coatings strongly influences their adhesion to the substrate surface, which also influences the durability of the coating [68]. The crystalline grains of NiTi nucleate first at the free surface and then grow rapidly in the lateral direction until impingement occurs. The further growth of those grains happens inwards resulting in columnar

structure. The crystallisation process completes itself in the columnar grains near the centre of the film. The incubation times for the nucleation increases with decreasing the deposition temperature. A lateral growth step is very fast initially and slows down as it proceeds.[69]

Table 4: Growth modes of thin films - Initial states of film growth (Θ = substrate coverage in monolayers (ML)) [61]

Growth mode	Definition	Surface energy requisite
2D Layer by layer **Frank – Vander Merwe**	In 2D mode, one layer grows onto another one. Interaction between substrate and film particles is more than between neighbouring particles.	φ > 0 It requires that $\gamma_B < \gamma^* + \gamma_A$
Θ < 1ML 	**1ML < Θ < 2ML** 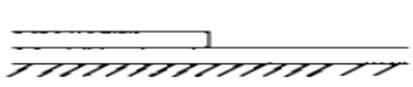	Θ > 2ML 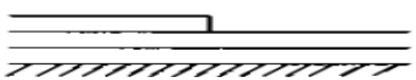
3 D Island **Volmer – Weber**	In the Volmer – Weber mode, 2D separate islands form on the substrate surface. Interaction between films particles is greater than between adjacent film and substrate particles.	φ = 0 It requires that $\gamma_B > \gamma^* + \gamma_A$
Θ < 1ML 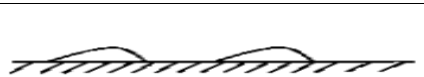	1ML < Θ < 2ML 	**Θ > 2ML** 
Layer plus island **Stranski - Krastanov**	In the Stranski – Krastanov mode, formation of the island leads to the formation of one or two monolayers.	γ increases with film thickness; a layer on the top of the substrate is strained to fit the substrate.
Θ < 1ML 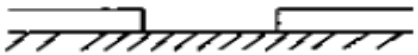	1ML < Θ < 2ML 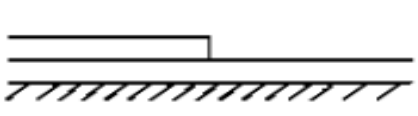	**Θ > 2ML** 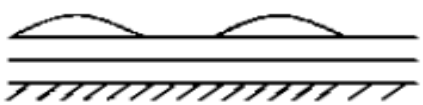

The growth modes are controlled by interface energies and supersaturation during the surface and bulk diffusion, and can be distinguished based on the bonding strength between depositing atoms and substrate atoms [49; 61]. Growth tends to shift from island to layer as supersaturation increases [61]. These structures are often thermodynamically favoured over uniform films containing the three-dimensional structures (clusters) and two-dimensional structures (islands) [64]. The growth modes are calculated by the wetting angle (φ) of a liquid nucleus on a substrate, and they are classified using Young's equation of surface energies as given below in Equation 2 [61].

Equation 2: Young's equation of surface energies.

$$\boldsymbol{\gamma B = \gamma * + \gamma A \cos\varphi}$$

γ_B = Surface energy of the substrate

γ_A = Surface energy of film materials

γ * = Interface energy of the film – substrate

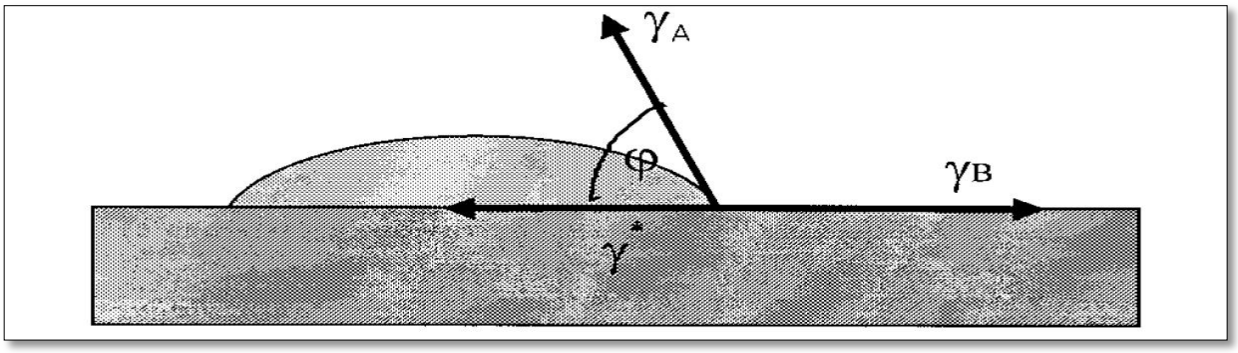

Figure 9: Parameters to calculate wetting angle φ and hence growth modes of a liquid nucleus on a substrate by Young's equation [61].

PVD thin films have a columnar grain structure with crystallites about 0.1 tetrameter in diameter, which produce a basic structure comprising of two surfaces and an intermediate bulk among them. Unless the thin film is freestanding, it touches another adjacent layer(s) as a substrate, with one surface becoming the interface. The atoms that compose the film and the chemical bonds between them make up the nanostructure. The energetic particle bombardment affects the morphology of PVD deposited thin films during sputtering. The incorporated atoms (incident atoms becoming bonded to adatoms) reach their equilibrium positions in the lattice by bulk

diffusive motion. The resultant coatings are denser and have a more homogenous structure [45; 53]. The control features of thin film polycrystalline microstructure include grain size, size distribution of the grains and the grain locations [45]. Furthermore, the nucleation steps and growth mechanisms of PVD films determine the microstructure and morphology of the deposited materials, which ultimately determine the physical properties of PVD films [45; 49]. These properties include microhardness, residual stresses, surface roughness, mass density, and reflectivity. [45; 49]. The microstructure-property relationship of PVD thin films is discussed in detail in section 3.1.4.

3.1.3 Structural zone models PVD of thin film

Movchan and Demchishin proposed a structural zone model in 1969 for the microstructure of metal and oxide films produced by electron beam evaporation, describing the morphology of PVD films as a function of normalized growth temperature Ts/Tm [49; 53]. Ts/Tm is the ratio between the absolute substrate temperature and the absolute melting point of the deposited material (condensate) [49]. Ts/Tm relates the thin film structure to zones of the structural model (Table 5). Movechan and Demchishin analysed the film structure by high-resolution TEM and identified three temperature zones according to Ts/Tm that formed characteristic film morphologies, as tabulated in Table 5 [53].

Table 5: Thin film structural zones [61].

Zone	Ts/Tm	Real structure	Description
I	T_s/T_m <0.3	Fine, grained and porous	Low mobility, particles stick where they land
II	0.3<T_s/T_m <0.5	Columnar	Surface diffusion occurs with activation energies of 0.1–0.3eV
III	T_s/T_m >0.5	Rough equiaxed grains	Bulk diffusion occurs with activation energies above 0.3eV

Thin film microstructures produced at low deposition temperatures (Ts/Tm < 0.3) corresponds to zone 1, where the grains appear as the tapered crystallites. The tapered crystallites with domed tops are poorly defined, separated by open voided boundaries and dislocations. Each grain may extend through the thickness of the film, which consist of textured and fibrous grains. The film contains very fine (20nm in diameter) equiaxed grains, i.e., grains of equal extent in all three dimensions, composed of bundles of approximately the same orientation. Grain size increases with increasing Ts/Tm [36; 49; 53].

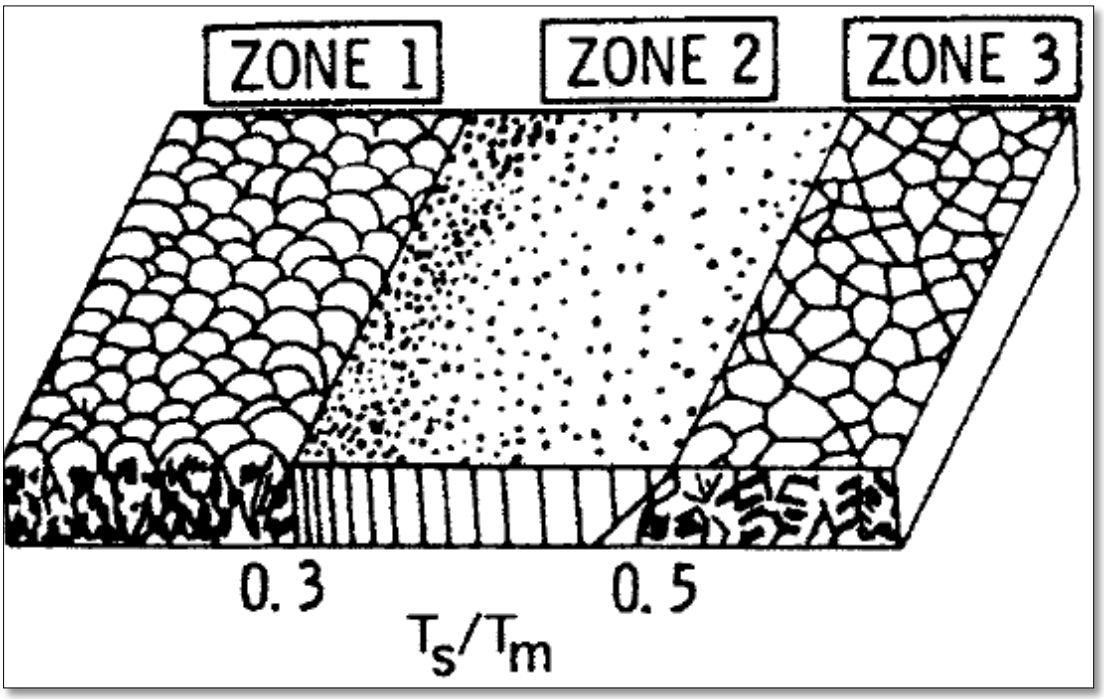

Figure 10: Zone model by Movechan and Demchishin for metal and insulating thin films manufactured by thermal evaporation (1969) [49; 61].

In zone 2, (0.3 < Ts/Tm < 0.5), columnar grains (relatively smoother than zone 1) are separated by dense intercrystalline boundaries with some dislocations appearing because of the surface diffusion controlled growth. As the substrate temperature increases, the columnar diameter also increases and porosity decreases [49; 53]. In zone 3, (0.5 < Ts/Tm < 1), the films consist of recrystallized and uniform columnar grains with diameters exceeding the film thickness. The surface of the deposited material is smooth and shiny for metal films. The film growth is bulk diffusion controlled, giving rise to an equiaxed recrystallized grain structure [49; 53]. The adatoms in zone 1 have a limited mobility of only 1 to 3 atomic positions, which is lower than the crystal size (nanocrystalline). The adatoms belonging to zone 2 or 3 having Ts/Tm ration above 0.3 have higher adatom mobility, resulting in microcrystalline (zone 2) or macrocrystalline (zone 3) because the adatoms have enough surface mobilities to formulate well-ordered arrays of atomic units at larger scale.[36]

J. A. Thornton [70] extended Movchan and Demchishin work by presenting a homologous structural zone models for PVD magnetron sputtered metallic films. Thornton analysed the Ti, Cr, Fe, Cu, Mo and Al films with thicknesses up to 250 µm deposited at 5 – 2000 $nm.min^{-1}$ on metal and glass by DC power supply. Thornton investigated the effects of working gas pressure on the growth of film during sputtering and introduced an additional axis in the Movchan and Demchishin zone model. It is reported in Thornton zone model that the normalized growth temperature at which the zone boundaries occur increases with increasing gas pressure. The sputtering gas pressure affects the microstructure of PVD sputtered films via an array of indirect mechanisms, resulting in an additional zone T. Poorly defined crystals and voids appear in zone 1, and columnar grain with cavities on the boundary have a dense array of fibrous grains without voids. [49; 61; 70]

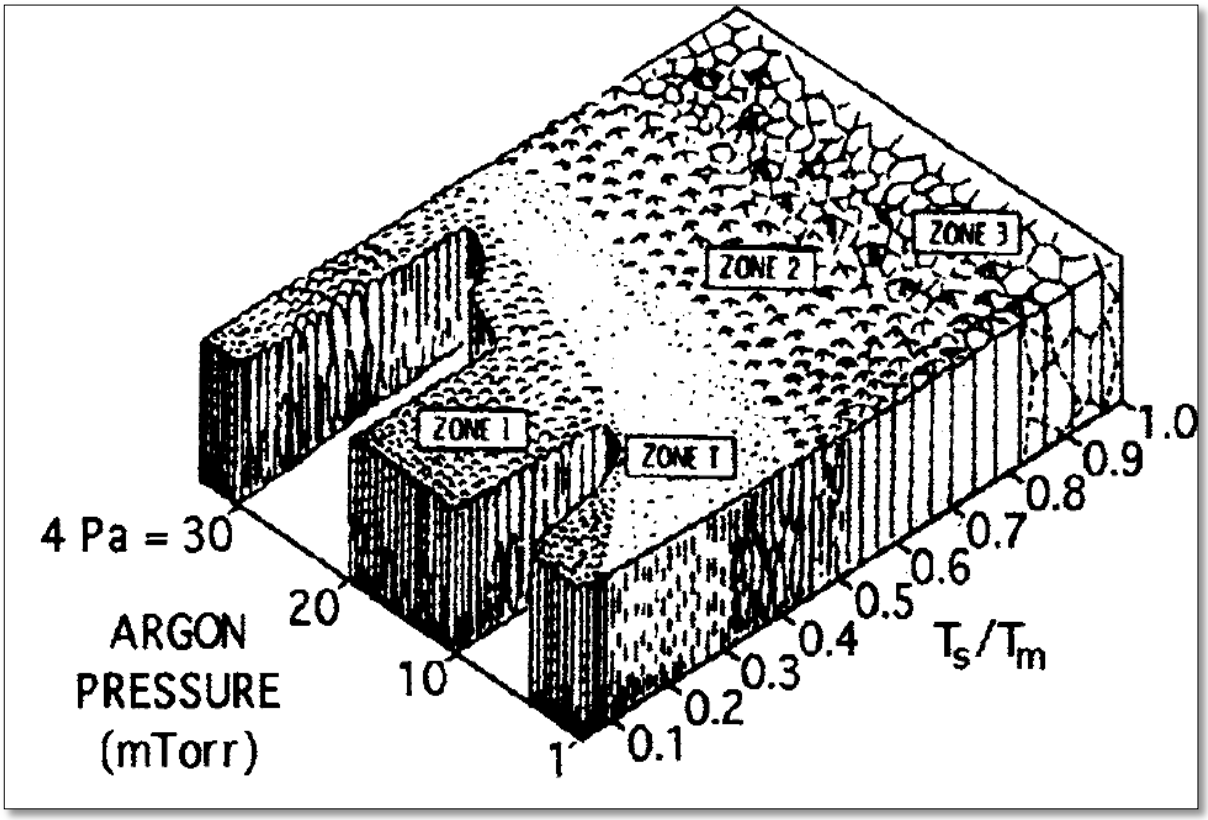

Figure 11: Structural zone model of thin films proposed by Thornton (1974) [49; 61].

Zone T (densely packed fibrous grains) appears in the Thornton structure-zone diagram between zones 1 and 2 (Figure 11). The microstructure consists of a dense array of poorly defined fibrous grains, and surface of the films in zone T is relatively smoother than that of films corresponding to the zone 1. The grains that form first

play a significant role in controlling the final grain structure of films. Higher substrate temperatures are required for granular epitaxy (grains ordered arrangement) to occur if the deposition rate of films is very high [49]. The pressure of sputtering gas influences the film structure substantially for Ts/Tm less than 0.5 (i.e. Zones 1, T and 2), while this effect becomes insignificant for the higher temperature ranges [70]. The film morphology belonging to zone T is influenced most significantly by the working gas pressure. With an increase in gas pressure, the mean free path for elastic collisions between sputtered (evaporated) species and the sputtering gas (residual gas) atoms decrease down to the source or target-substrate distance. As a result, the sputtered particles condense on the substrate increases and films with a more open voided microstructure corresponding to zone 1. Furthermore, a decrease in sputtering gas pressure during deposition results in larger mean free paths of particles; therefore, the kinetic energy of species impinging on the substrate surface increases. Sputter-deposited films produced under low sputtering gas pressures exhibit relatively dense microstructures. The morphological features (roughness) of the film surface are approximately in the range of 2 to 20 μm in size for Zone 1 (cauliflower). Zone T in thin films contains granular structures having relatively smaller diameter; consequently, zone T has a smoother surface.[36; 49]

The shadowing effect produces imitation of substrate morphology within the films, which retains all scratches, bumps and surface imperfections of the coatings. Bulk diffusion is responsible for the shadowing effect in zone 1 and zone T. In zone 2, the shadowing is faint, but does not disappear entirely. In zone 3, the deposition temperature is higher, and for that reason, the surface and bulk diffusion are greater than zone 2, and recrystallization along with grain growth may occur. Lowering of the working gas pressure can slightly reduce the shadowing effect especially in zone T and zone 2.[70]

In 1978, Lardon et al. [53] extended the structure zone scheme through the bias potential (Ubias) parameter by taking into account the influence of energetic particle bombardment on the condensate morphology. Bombardment of energetic particles leads to the displacement of coating atoms and generate the lattice defects, which increase the mobility of the adatoms, resulting in denser and more homogenous thin films. The bombardment of the energetic ions on the substrate surface causes local heating, which increases the mobility of the atoms in the impact zone. Ultimately, the

energetic particle bombardment influences the morphology of the coating by shifting the boundaries in the zone corresponding to a lower Ts/Tm range.[53]

The zone models for ion-assisted deposition were also elaborated by Messier et al. [36; 61] and Grovenor et al. [36; 61], who explained the effect of substrate morphology on thin films zone models, but that discussion is beyond the scope of this project.

3.1.4 Microstructure – property relationship of PVD thin films

The theoretical structure of solids proposes that they can be either crystalline or entirely amorphous [61]. However, the real structure of PVD thin films is polycrystalline, and it always differs from the ideal structure described in the theoretical structural models [71]. The extent of the difference depends on deposition parameters during all stages of film growth, and small variations in those parameters result in significant changes in microstructure [61]. The deposition parameters are type of working gas, pressure, power, working distance and temperature [14; 45; 61; 71]. The critical process parameters, affecting the early stages of growth, include the source and substrate materials purity, composition, crystallographic orientation of substrate surface, deposition rate, substrate temperature, pressure, and K.E of the species arriving at the film surface [49]. Deposition power, process pressure and substrate temperature are the most influencing parameters for composition, microstructure and deposition rate of the resulting film [23; 45; 49; 71].

Temperature defines the structural zones within Thornton model [72]. Substrate temperature and kinetic energy of the particles condensing on the surface influence the diffusion parameters such as mobility of particles over the surface and atomic rearrangements within deposited material's lattice. The kinetics of diffusion processes is thermally activated; therefore, these diffusion parameters determine the adatom surface mobility and the bulk diffusion rates. An increase in substrate temperature and K.E increases the bulk diffusion rate, resulting in enhanced condensation and higher density within the columnar grains of thin film microstructure (Figure 12). Smooth substrate surfaces lead to more uniform fine-grained microstructures. Rough surfaces with various defects (peaks, valleys) exhibit preferred adsorption, nucleation, and growth sites, leading to shadowing effects of the adatoms, and more columnar open voided microstructures can be expected. However, at relatively high substrate temperatures, the kinetics of surface diffusion processes is sufficiently fast to overcome topological effects and resulting thin films have relatively smooth surfaces.[49]

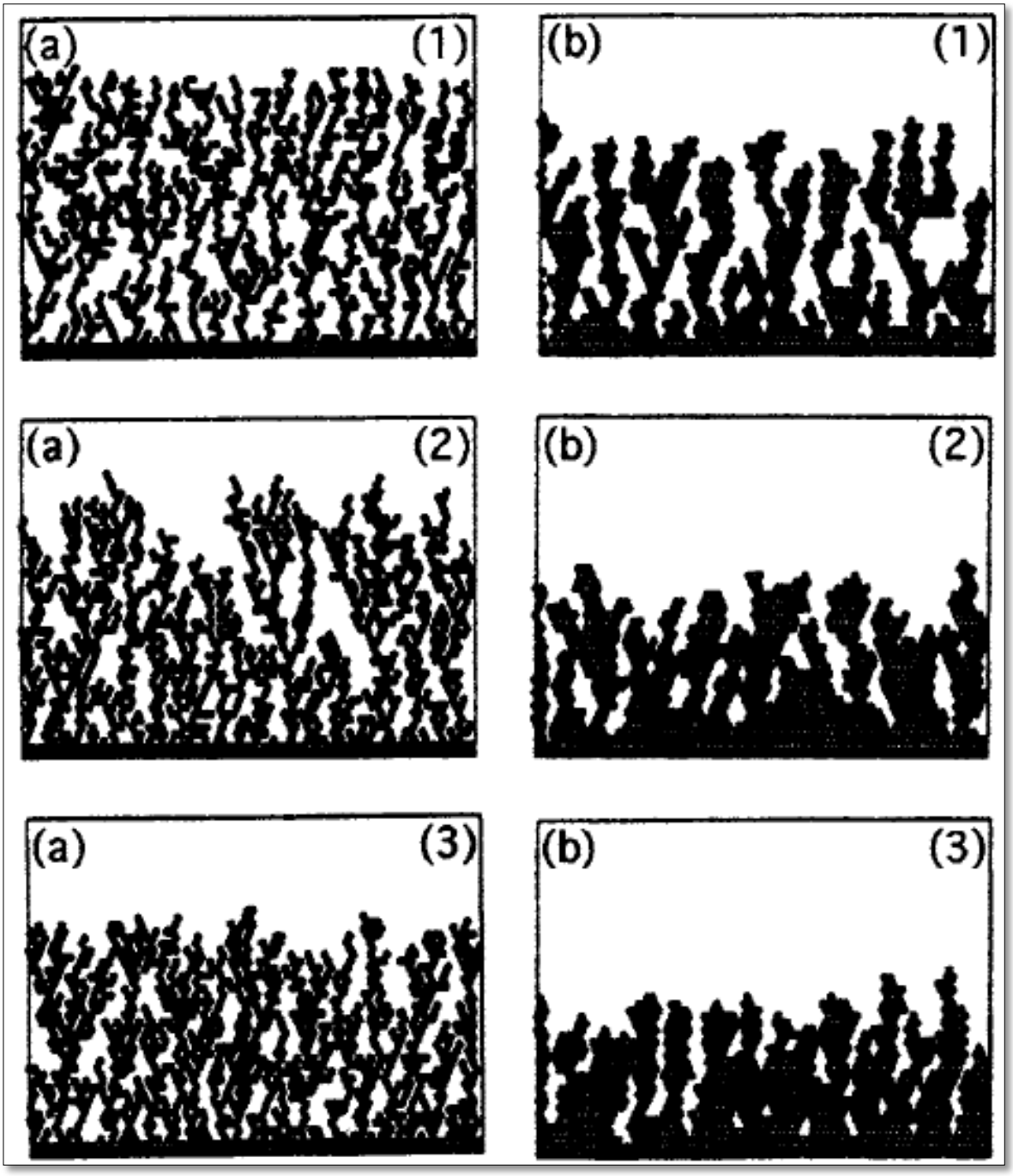

Figure 12: Simulation results of thin film growth at a substrate temperature of (a) 573°C, (b) 673°C with a KE of condensing Ni (1) 0.1 eV, (2) 1 eV, and (3) 2eV [49].

The transition temperatures in structure-zone diagrams are dependent on the deposition rate and the impurity concentration on the surface of growing films. The packing density of the films increases with increasing incident kinetic energy. PVD sputtered thin films have an incident kinetic energy “i” higher than 0.5 εo as shown in Figure 13. Therefore, the voided microstructure and the porosity of PVD films are clearly related to low particle impact mobility. Gas pressure effect the kinetic energy

of particles. The particles with particular kinetic energies can either supplement to the growth of films by adsorbing on the substrate or reflect from the substrate and return to the gaseous phase via elastic collisions. Kinetic energy is large for the particles falling in the temperature range of microstructural zone T, which allows surface diffusion at energetically favourable sites before the arrival of the additional condensing particles.[49]

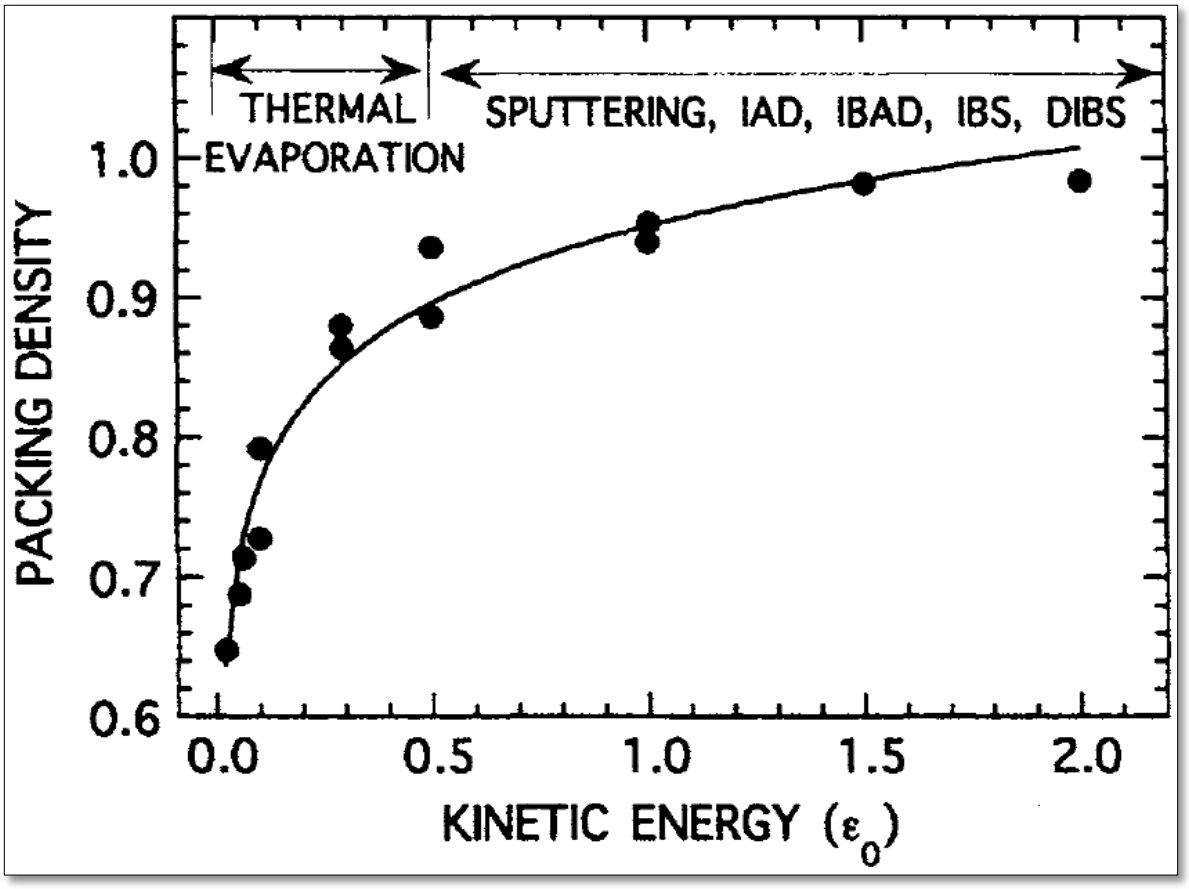

Figure 13: Packing density vs. incident KE of the adatoms [49].

Typical carrier gases are nitrogen and the noble gases [53]. Argon gas is used as a carrier gas in this project because nitrogen and titanium would immediately react and form titanium nitrides. Ar gas pressure would influence the nanocomposite film structure and the shape memory effect of NiTi thin films [23]. Substrate type also influences the microstructure, residual stress and morphology of the thin films. Substrates types can be a single crystal, polycrystalline or amorphous. Majority of PVD thin films are deposited onto non-epitaxial substrates, i.e., the substrate is amorphous or polycrystalline and may be covered with an adsorbed film of impurities providing weak bonds to the adatoms. This type of substrate is likely to induce an

island mode of growth with no crystallographic relationship between the orientation of the islands (if crystalline) and the substrate, which means the islands are not epitaxial with the substrate. The defects in the atomic structure such as vacancies, interstitial atoms, impurities, broken bonds, deformed bonds, and the surface roughness depreciate the film properties. The chain or group of these defects include voids, stacking faults, spatial fluctuation of the atomic composition, segregation of the impurities, dislocations and twin boundaries in crystalline films, surface undulation and spatial variation of the film thickness, and these features contribute to the ultimate microstructure of the PVD films in combination. Imperfect smoothness of the substrate surface directly causes the interfacial roughness or becomes the origin of the defects that could propagate in the deposited film.[45][49] Kaiser et al. [61] demonstrated this phenomenon very well in Figure 15, which shows a metastable ideal single crystal state, which is far different to the energetic minimum. As soon as enough energy becomes available, the real structure also changes. The anticipated structure is acquired by controlling the grain size, orientation and defect density, which are governed by altering deposition parameters. The real microstructure and chemical composition of thin films determine their morphological, physical, and mechanical properties. Stoichiometry can tailor the desired properties, grain size and grain size distribution of the thin films [61; 73]. These features are controlled by deposition parameters, which influence the bonding structure, residual strain, impurities, voids and surface roughness and determine the interaction between growth mechanism and the coating surface [45; 71].

Impurities insoluble in the lattice segregate to grain boundaries and onto the growing surface. At a critical impurity concentration, a fixed passivation layer forms, upon which secondary nucleation takes place. Hence, undiluted impurities concentrate at interfaces. Structural zones shift along the T_s/T_m axis toward a fine, crystalline and porous structure. Barnal and Adamik [61] elaborated the basic structure zone model, starting with a simple, impurity-free thin film increasing in the number of impurities as shown in Figure 14.

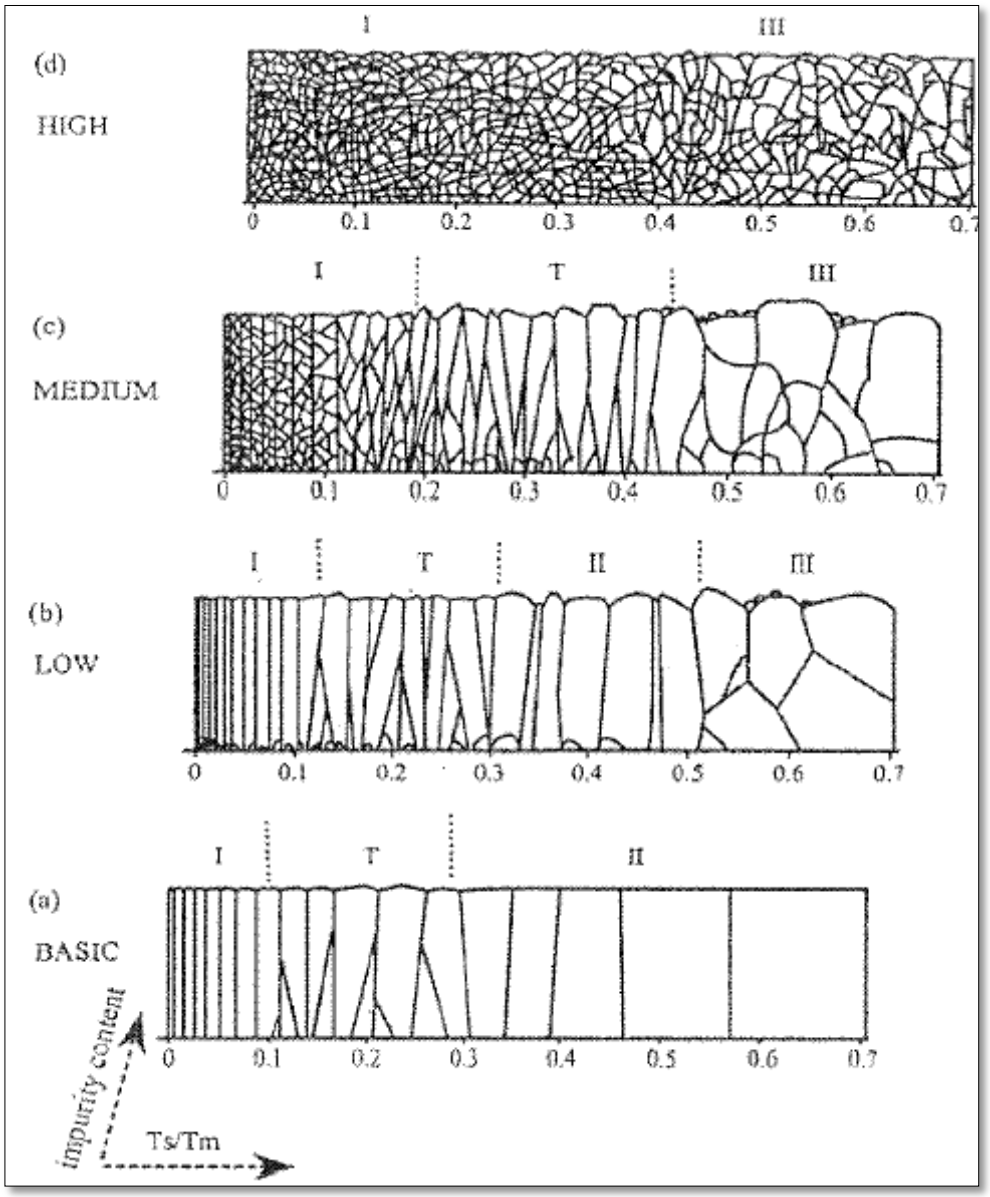

Figure 14: Basic and real structural zone models for low, medium and high impurity concentrations in thin films [61].

In polycrystalline thin films, the crystallographic orientations of the granular structures vary in size and geometry. These structures are related to the mechanical, chemical, electrical, optical properties and spatial uniformity of the thin films. In other words, the properties or the uniformity is limited by their microstructure. For instance, the point defects and the dislocations in the epitaxial thin films always limit their performance. Polycrystalline thin films deposited on an insulating amorphous substrate can be melted and recrystallized by sweeping a stripe heater over the thin films, which is known as zone melting technique.[45]

PVD deposition rate is directly proportional to the concentration of chemically reactive species in the plasma that attach to the substrate surface. The sputtering rates and the energy distribution within the target are influenced by the particles emitted from target surface and the ion flux generated by the ionisation of Ar. At an optimum pressure of a few Pa, the highest ionization efficiency and plasma-density (corresponding to the high argon density) are observed because of an increase in collisions. Increasing the argon pressure decreases the ionisation possibility due to decline in average free path of the electrons. The mean ion energy within the plasma reduces with an increase in argon pressure with a constant power supply and target-substrate distance, resulting in less polymeric target fragmentation and emission. This might inhibit some of the reactive species required for thin film growth reaching the substrate leading to a decline in deposition rate.[74]

The growth mechanism of NiTi thin films can be affected by the deposition method, the substrate material, optional seed layers and the variation of the annealing treatment. Anisotropic grain growth provides superior properties such as deposition of high purity films [25]. Sputtered metallic thin films are made from a flux impending the substrate from particular directions and forming columnar grains. At room temperature, a columnar growth-structure distinct by voided boundaries overlays the intrinsic grain structure of thin films. The anisotropic character of NiTi thin films effects the films properties, and the voided growth defect appear due to atomic shadowing. The shadowing occurs because of the alterations in deposition parameters including working geometry, argon pressure and surface roughness of the substrate. The diagonal constituent of the flux enriches by an increase in argon pressure forming less dense NiTi films and further gas scattering causes an enhanced shadowing effect to occur.[23]

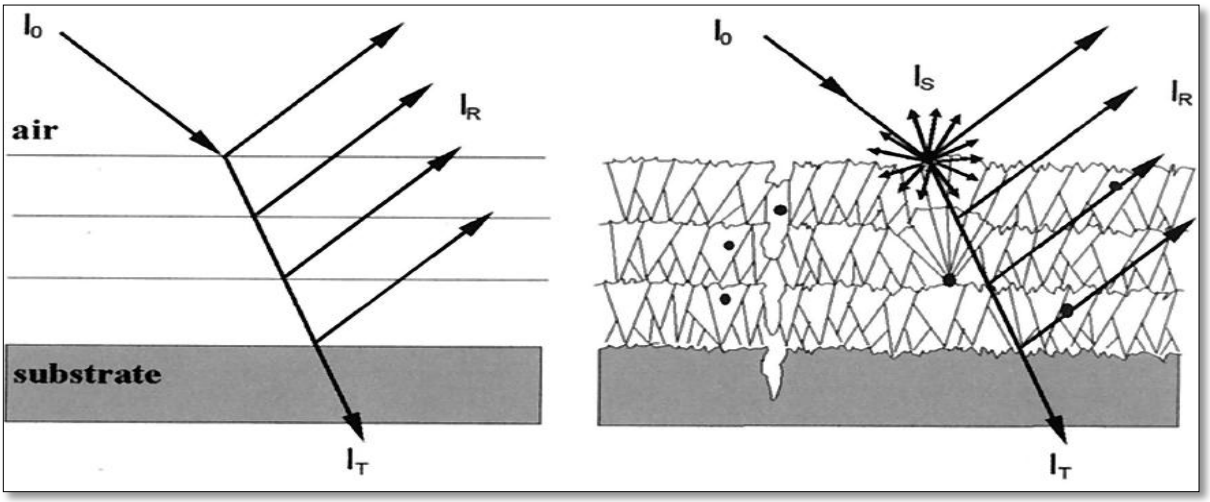

Figure 15: Left: ideal single crystalline substrate coated with ideal single-crystalline films. Incoming light with intensity I_O is split into reflected and transmitted parts I_R and I_T, respectively. Conservation of energy is given by $I = I_R + I_T$. Right: the real substrate, with a real coating. Part of the incoming intensity, I, is absorbed (I_A) or scattered (I_S). Conservation of energy is given by $I_O = I_R + I_T + I_A + I_S$ [61].

Some characteristics of thin films are significantly different from their bulk materials, for example, surface energies. Contrastingly some other properties of the bulk materials are inherent in PVD sputtered thin films, for instance, the functional groups. Chemical structure and morphology of the films determine the surface energy and wettability of the films [14; 61]. However, the chemical composition and morphology of thin films are dependent on film microstructure, and films can grow in various dimensions from isolated clusters to a continuous microscopic network [61]. Physical features of the resulting films such as microstructure, grain size, morphology and texture are directly dependent on the deposition parameters, particularly substrate temperature and process pressure. The substrate temperature and process parameters affect the kinetic energy of species and in turn change the substrate or film surface during the deposition process [49]. Incident species including molecules, radicals, atoms, ions can be either condensed and incorporated in the film lattice or just reflected at the film surface (Figure 14) [49]. Good contact between the wetting phase and the substrate, and the absence of weak boundary layers improves adhesion of the coatings [68]. PVD Thin films characteristics vary significantly from their properties in bulk form, which can be further modified by altering deposition conditions during sputtering. Those thin film characteristics such as the complete

dimensions of the thin films and the shape and size of clusters are studied by various spectroscopic and diffraction techniques, for example, Raman spectroscopy and XRD. Raman spectroscopy provides an average size of crystalline clusters as well as other structural information such as strain or stress. This method by itself could not always provide the absolute dimensions, without relying on the empirical conversion from the Raman spectra to the average size of clusters. XRD estimates the average size of crystallites at each crystallographic orientation while neglecting the influence of the random stress. Most of the spectroscopic or diffraction methods consider that crystalline region has a single crystallinity; thus, the cluster groups containing imperfections, such as stacking faults and twin boundaries cannot be examined accurately. Two and three-dimensional high-resolution microscopy can produce the real images to allow observing the imperfections. Although, the high-resolution microscopy permits to conduct a detailed examination of the atomic images of the coating structures, but it does not provide the precise count of all the particulates included in a cluster, unless the clusters are two-dimensional islands with uniform layered thickness of monomers.[45]

Range of thin film characterisation methods used in this research project are briefed in section 5.3, and the significance of their results is evaluated. Sections 3.2, 0 and 3.4 provide a comprehensive range of experiment based studies, which analyse PTFE, NiTi and nanocomposite thin films respectively. Detailed microstructure, material properties and the influence of PVD sputtering parameters are also discussed in the sections mentioned above.

3.1.5 Adhesion, interface and thin film fractures

The grains size and material composition of polymer-metal thin films are strongly influenced by the adhesion between polymer and metal layers [68]. In addition, PVD thin films must adhere tightly to the substrate surfaces for the most applications unless the application demands freestanding thin films. Defects and delamination at the film-substrate interfaces lead to poor performance and destruction of the devices. The broadening of the substrate – coating interfaces results in a better adhesion of the coating but mainly lead to stress accumulation at the interfaces [45; 53]. Stress in PVD films develops if the film is firmly bonded to a substrate that is much thicker than the film. This results in broad interface, and any change in the length along the film plane, that do not match exactly to an equal change in length of the substrate, leads to the development of stress in thin films [49].

Practically, all PVD coatings are under stress, and excessive residual stresses in thin films may cause mechanical damage (fracture) and adhesion failures along with defect formation in the substrate. Thermal stress, intrinsic stress and extrinsic stress are the constituents of overall residual stresses in thin films at a given temperature. Thermal stress arises from the difference in thermal expansion coefficients of film and substrate. Another cause of thermal stress is the difference between the substrate temperature (Ts) and the temperature of samples (Tr) during the determination of stresses, which is commonly equal to the room temperature. The intrinsic stress in thin films is introduced during the PVD process, and the intrinsic stress is not directly related to the thermal mismatch between the deposited material and the substrate. This type of stress originates from incomplete structural assembly occurring because of the accumulating effect of the crystallographic flaws during the film deposition. The extent of the intrinsic stress is related to the morphology and microstructure, which depend on the process parameters. Extrinsic stress relates to the external factors such as the interactions between deposited material and surroundings that are generated after the PVD sputtering process. For example, when the porous films exposed to the atmosphere, the water vapour adsorption can lead to the development of intrinsic stress instantly after the deposition process. The interactions between adsorbed species and films may be responsible for any changes in composition and volume of the deposited material, resulting in a slow and progressive variation of the extrinsic stress observed as a function of the aging time

of adsorbed species within coatings. Any changes in the geometry of the sputtering apparatus also vary the state of stress in thin films significantly [49; 75].

PVD sputtering is a non-equilibrium process that produces intrinsic and extrinsic defects that are around five orders of magnitude greater than in the bulk. Single crystal films have many intrinsic and extrinsic defects. The intrinsic defects have stoichiometry, as long as the atoms do not alter their arrangement post-deposition; however, non-stoichiometry takes place in extrinsic defects. Intrinsic and extrinsic defects have a substantial impact on the film growth. It takes about 1 second to form a monolayer of residual gas particles on a substrate surface at a pressure of 10^{-6} mbar. The monolayer forms because of supersaturation by comparatively greater impurity concentrations during sputtering. Due to intrinsic and extrinsic defects, the properties of thin films differ considerably from bulk materials and polycrystalline films contain defect-rich crystalline grains separated by impurity-enriched grain boundaries.[61]

The effect of the changes in dimensions and geometry of the PVD sputter coater on the variance in stress related film properties is beyond the scope of this research. For this reason, the maintenance of a constant internal geometry of the sputter coater is a prerequisite in this research. This would allow minimising the possibility of any changes in film properties including the alterations in the stress state owing to any geometrical changes. The film-substrate adhesion should be able to withstand the force applied to the residual stress (mainly intrinsic), which increases with the increasing film thickness [75]. Thicker films result in stress cracking, bulking and poor adhesion during the adhesion test. The forces, between the thin films and substrates and within the layers of thin films, are categorised as cohesive and adhesive forces. The adhesive or cohesive nature of the coating failure is determined by the moment of failure, which is calculated by estimating the critical load for the thin films. An adhesive failure removes the film from the substrate as large flakes or finely cracked debris exposing the substrate and demonstrating a weak interface between the coating and substrate. If the film is thick with a layered structure, the first layer from the top comes off from the substrate followed by the weakening of interlayers bonding strength. Cohesive failure occurs because of the fragile bulk coherence within thin films, and it is not influenced by the interfacial interactions. During cohesive failure, the coatings do not crack at the interface, but

cracks in a parallel direction to the substrate. Oxidation, manufacturing faults, contamination and internal stresses take place because of this type of failure.[49; 76; 77]

In continuous thin films, an average magnitude of the residual stresses is independent of the film thickness.[49][49; 49; 61]. Large stresses can affect optical, electrical, and magnetic properties of the thin films. The elimination and the release of intrinsic stresses by bulk diffusion lead to the undesirable formation of hillocks, whiskers, and holes in PVD thin films made of soft materials such as polymers. The bulk diffusion increases with increasing Ts/Tm. The process of relaxation (release in stress) is called recovery or recrystallization in metallic thin films, and it produces vacancies, interstitial defects, and dislocations in zone 1 of the thin films. At higher Ts/Tm ratio, the stress accumulation decreases. The intrinsic stresses accumulate in the film structure and dominate over thermal stress in hard coatings materials such as metals, which generate stress cracking and buckling. Usually, the control of residual stresses is a critical point in a given PVD process to produce reliable thin films. The need to understand the origin of the residual stresses is vital for the efficient PVD manufacturing resulting in the high-quality thin films, which would also be suitable for an extensive range of applications. These applications potentially include protective films, active and passive electronic devices, and the layered composite structures. If the film growth is interrupted, the tensile stress significantly upsurges in a few seconds during the film growth, which follows the launch of compressive stress for any further film growth taking place.[49; 75]

This research involves the deposition of metals and polymer substances configured in a filler matrix arrangement by co-sputtering or sputtered layered arrangement. The two types of materials influence the metallic film morphology during nucleation and the initial film growth. Kaune et al. [63] provided a schematic representing the stages of metallic thin film growth (gold) on a polymer substrate, as shown in Figure 7.ii. According to their study, a gold atom impinges on the substrate during nucleation, followed by an absorption and lateral diffusion processes occurring along the substrate surface. A small condensation coefficient (below 1) results in a weak adhesive bond at the polymer-metal interface, and the adatoms desorb easily. The formation of the stable nuclei forming by the conjuncture of the two adatoms operates in competition with the desorption process, which leads to the development

of small clusters. The clusters at the polymer-metal interface modify themselves into spherical or ellipsoidal shapes having a magnitude of the cluster height that is multiple of the film thicknesses (3D-growth). The kinetic growth process at the metal and polymer interface, and the correlation of structural features (including cluster size, shape and spatial distribution of the metal amount) are the crucial control parameters for thin film adhesion and for the band alignment of metal-polymer interfaces.[63; 65]

3.1.6 Summary

PVD magnetron sputtering is a suitable method to manufacture reliable and reproducible thin films. RF and DC power supplies efficiently deposit PTFE (insulating) and NiTi (conducting) by PVD sputtering. The deposition process involves the condensation of plasma by heterogeneous physical reactions taking place on a substrate. Magnetrons installed in the sputtering apparatus enhance the sputtering yield because of higher deposition rates and efficient ion bombardment. The ability of magnetron sputtering to work at reduced pressures when required is an additional feature that allows better control over the deposition process.

Thin film growth takes place in three steps, namely nucleation, coalescence and film growth. Nucleation involves the arrival followed by condensation of the adatom vapours occurring on the substrate surface. Nucleation is a nonequilibrium process that takes place at supersaturation and is affected by the concentration of vapour pressures, the deposited and substrate materials, molecular weight of the deposit materials and the temperature. Nucleation trails an early stage growth during which all impinging adatoms on the substrate are captured by the existing clusters to formulate two-dimensional clusters. This follows a fast transitional growth regime called lateral growth stage where the diffusing adatoms adsorb on the pre-deposited two-dimensional clusters. The adsorption of adatoms happens along with enhancement of the surface coverage, and the travelling distance of adatoms to reach the substrate decreases, ultimately leading to coalescence. Coalescence is growth of islands until the islands touch one another to form a continuous network of channel type structure producing continuous layers. Coalescence regulates the eventual grain structure in a continuous film after which a totally covered thin film forms, for which a vertical growth of clusters by adsorption can occur. Ultimately a continues polycrystalline grain structure formulas having a macroscopic network of the clusters, named as a ‘thin film’.

There are four stages of continuous film development of PVD coatings in terms of the percolation thickness, named as, island stage (0 – 20 nm), network stage (20 – 35 nm), hole stage (35 – 45 nm) and continuous film (50 nm and more). The growth of thin films occurs by formation of nuclei by one of the three film-growth modes named as Frank – Vander Merwe, Volmer – Weber and Stranski – Krastanov. The

absolute structure of coatings is determined by shadowing, surface diffusion, bulk diffusion and recrystallization. Volmer-Weber or Stranski-Krastanov modes are the commonly reported growth modes for polycrystalline thin films, which are controlled by the interface energies and supersaturation during the surface and bulk diffusion. These two growth modes can be distinguished by the strength of bonding between the depositing atoms and substrate atoms. As the supersaturation increases, PVD thin film growth tends to shift from island to layer, resulting in a columnar grain structure. The control features of the polycrystalline coatings microstructure include grain size, size distribution of the grains and grain locations.

Movchan and Demchishin provided a structural zone model for thin films produced by electron beam evaporation. Zone 1 ($Ts/Tm < 0.3$) of the zone model contains poorly defined tapered crystallites with domed tops, separated by open voided boundaries and dislocations. Grain size increases with increasing Ts/Tm, therefore, as the substrate temperature increases, the columnar diameter also increases and the porosity decreases. Zone 2 ($0.3 < Ts/Tm < 0.5$) has columnar grains (relatively smoother than zone 1) that are separated by dense intercrystalline boundaries with some dislocations, which appears because of the surface diffusion during controlled growth. In zone 3, ($0.5 < Ts/Tm < 1$), the films consist of recrystallized and uniform columnar grains with diameters exceeding the film thickness. Later, Thornton et al. investigated the effects of working gas pressure on the film growth during sputtering, and they introduced an additional axis in previous zone model. According to Thornton zone model, pressure of the sputtering gas affects the microstructure of PVD films via an array of indirect mechanisms, and therefore produces an additional zone T (densely packed fibrous grains) between zones 1 and 2.

The real structure of PVD thin films is polycrystalline and has various disparities compared to the ideal structure. The extent of the difference depends on deposition parameters during all stages of film growth, and small variations in those parameters result in significant changes in the microstructure of the film. Deposition parameters include the type of working gas, pressure, power, working distance, substrate type and temperature. The defects in the atomic structure such as vacancies, interstitial atoms, impurities, broken bonds deformed bonds and surface roughness depreciate the film properties. Virtually, all PVD coatings are under stress, and the excessive residual stresses (thermal stress, intrinsic stress and extrinsic stress) in thin films

may cause a mechanical damage and the adhesion failures along with defect formation in the substrate. Thicker films are less adhesive, and the defects and delamination at the film-substrate interface lead to poor performance and destruction of devices. Due to intrinsic and extrinsic defects, the properties of the thin films differ considerably from bulk materials and polycrystalline films contains defect rich crystalline grains separated by impurity-enriched grain boundaries. Any changes in the geometry of the sputtering apparatus also significantly vary the state of stress in thin films.

3.2 Polytetrafluoroethylene (PTFE) thin films

Polytetrafluoroethylene (PTFE) is a synthetic thermoplastic polymer, commonly known as Teflon, with a melting point of 600 K (327°C) and Young modulus of 0.5 GPa. Physical vapour magnetron sputtering has been used as a method for depositing the fluoropolymers since 1970, allowing controlled deposition rates and efficient target consumption, and to make uniform coatings over large areas [13; 40; 78]. PVD sputtering is an extremely energetic process, which dissociates the polymeric chain into smaller chain fragments and monomers. It is essential that the elementary PTFE structure (Figure 16) successfully reform as polymeric chains within the sputter-deposited thin films by sputtering.

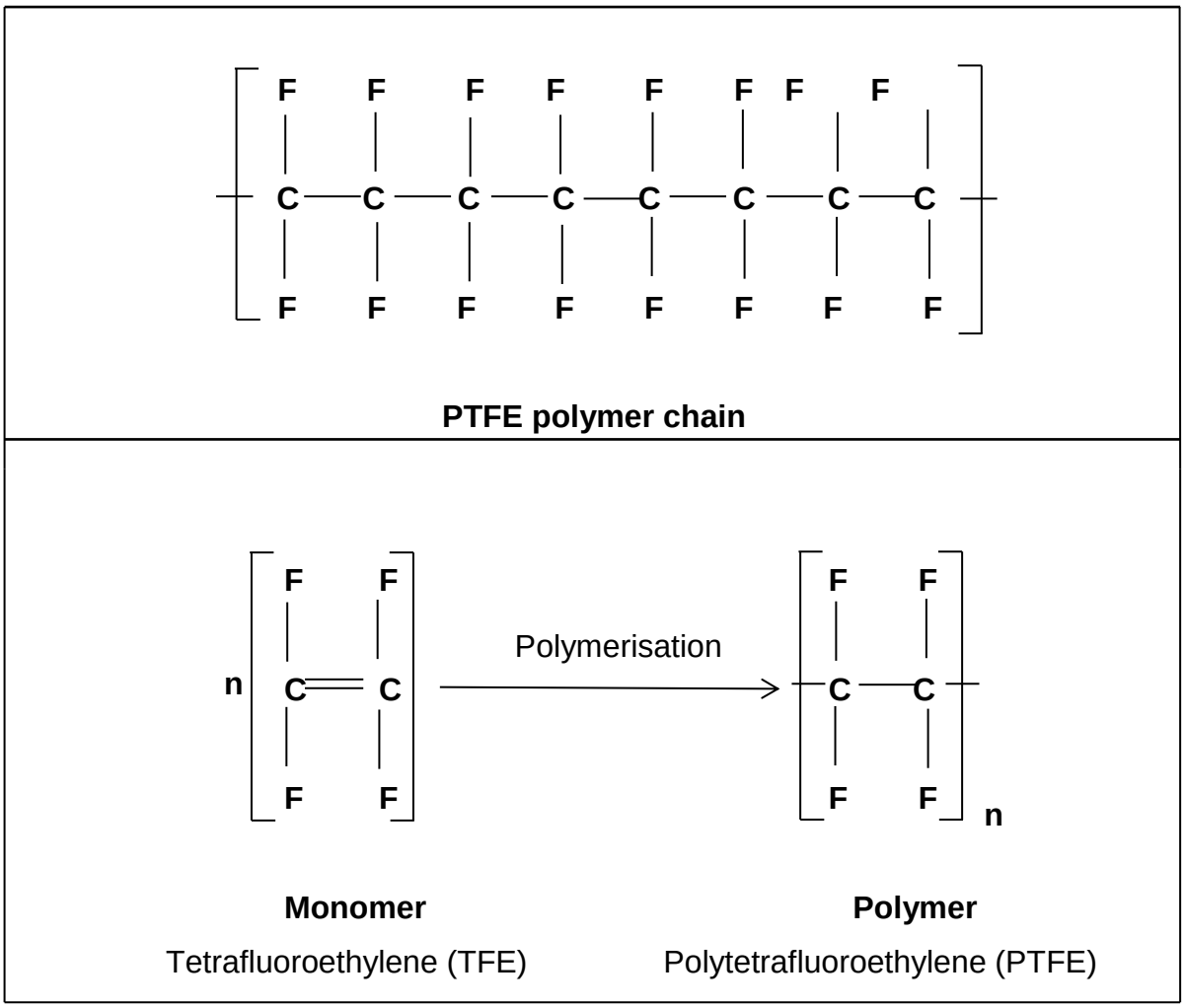

Figure 16: PTFE polymerisation from its monomers.

PTFE thin films are conventionally prepared by RF-PVD magnetron sputtering at low argon pressure. The films appear to be slightly yellowish in colour similar to their bulk material [79; 80]. Biederman et al. [81] reports that the PVD sputtered PTFE films are compact, continuous and smooth above room temperature. During PVD sputtering, the PTFE target undergoes ion bombardment causing the polymer chains to break into shorter CF fragments and single atoms clusters [82]. The fragments and clusters condense and repolymerise onto a substrate forming a PTFE thin film. The tetrafluoroethylene (C_2F_4) monomers re-join to form polytetrafluoroethylene (PTFE) by polymer free-radical polymerization. Mass spectroscopy (MS), EDS, FTIR spectroscopy and Raman spectroscopy are the standard techniques to study the chemistry of PTFE and other polymers. They chemical data include compositional structure, functional groups and fragments present in the polymer chains. Figure 17 shows a standard IR (upper trace) and Raman (lower trace) spectra of bulk PTFE with various possible configurations of functional groups their alignments (e.g. stretched, deformed, symmetric stretched, scissoring, bending, twisting, wagging and rocking) [83]. Table 6 shows the functional groups of PTFE identified by wavenumbers and bonding movement's data, which was obtained from the findings reported by Mihaly et al. [83] (Figure 17) and other studies including Yamda et al. [84] (Figure 18), Bodas et al. [85] (Figure 23A), Li et al. [86] (Figure 23B), Biederman et al. [74] (Figure 29) and Drabik et al. [14] (Figure 33). Table 6 and the spectra provided in Figure 17 will be used as the standard data in this project for comparing the chemical structure of PTFE thin films with their bulk form.

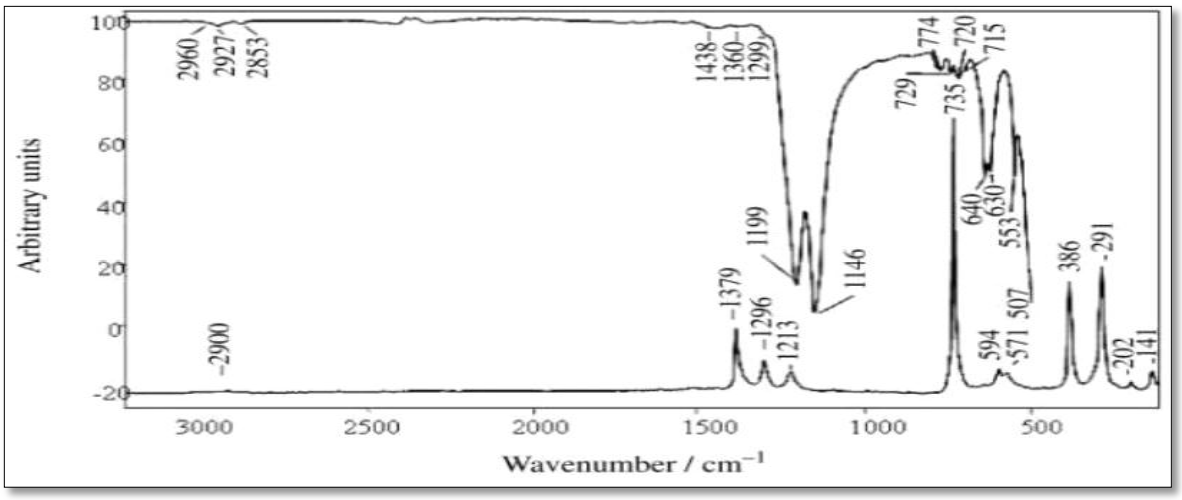

Figure 17: Infrared (upper trace) and Raman (lower trace) spectra of bulk PTFE.[83]

Table 6: IR band assignments of PTFE [14; 74; 83-86].

IR wavenumber bands (cm^{-1})	Description
2400 – 2927	CH_2, CH_3 stretching
1720 – 1730	$C=CF_2$
1600 – 1640	- CF_2CO_2
1600 – 1660	C = C
1541 – 1548	CH_2, CH_3 deformation
1360	NO^{3-}
1199 – 1258	C – C stretching (Major)
1186 – 1456	CF_x (x = 1, 2 and 3) stretching
1146 – 1282	CF_2 asymmetric stretching (Major)
1050 – 1146	CF_2 symmetric stretching (Major)
732 – 1103	CF_3 deformation and amorphous PTFE
729 – 734	CF_2 scissoring (wagging)
635 – 640	CF deformation
625 – 630	CF_2 deformation
550 – 600	CF_2 bending
502 – 510	CF_2 twisting

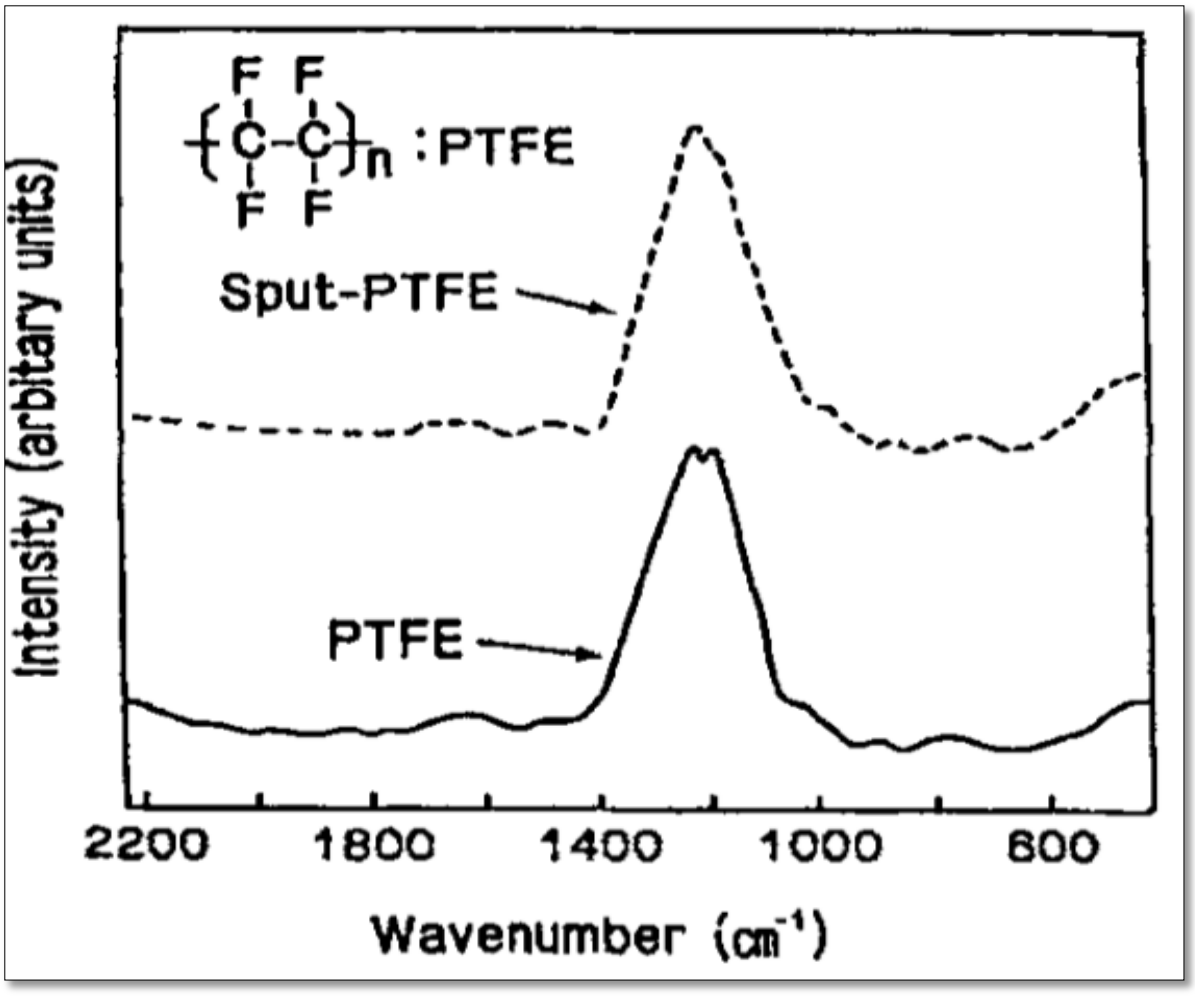

Figure 18: Infrared spectra of bulk PTFE and PVD sputtered PTFE [84].

Figure 18 shows the FTIR spectra of bulk PTFE and a PVD-PTFE thin film deposited at 1.33 x 10^{-2} mbar. PTFE has a simple polymer chain structure, and it is sputtered in larger molecular units resulting in easier re-polymerisation after PVD process. FTIR spectra of the bulk and sputtered PTFE are identical to each other. The most relevant area of an FTIR spectrum of PTFE is between 600 and 1400 cm^{-1}. The maximal stretching doublets representing C – F and C – C spectral bands are the most prominent peaks relating to PTFE. These peaks appear within the chemical band ranges of 1199 – 1258 cm^{-1} for C – C vibrations, 1146 – 1282 cm^{-1} for CF_2 asymmetrical stretching and 1050 – 1146 cm^{-1} for CF_2 symmetrical stretching [74; 87]. C – C vibrations and CF_2 symmetrical stretch peaks overlay each other occasionally and appear as one peak [74; 86]. In the FTIR spectrum of sputtered PTFE thin films, the major CF_2 stretching peaks represent the symmetric and asymmetric stretches from the bulk PTFE, which merge together resulting in a strong

CFx (x = 1, 2 and 3) peak appearing at the same position, as shown in Figure 18. This phenomenon can also be observed by comparing the bulk and sputtered PTFE spectra in Figure 23B, where peaks appearing at 1146 cm^{-1} and 1202 cm^{-1} in bulk PTFE combine and reappear in the form of string CFx peak at 1186 cm^{-1} [86]. Similar peak appears at 1263 cm^{-1} in Figure 23A as well [85]. In bulk PTFE, the strong absorption peaks at 502 – 510 cm^{-1}, 550 – 600 cm^{-1} and 625 – 630 cm^{-1} are due to twisting, bending and deformation vibrations of CF_2 groups and an additional peak at 635 – 640 cm^{-1} appears because of CF deformation, as shown in Figure 17. The additional peak sometimes disappears in PVD sputtered thin films because of the presence of CF instead of CF_2 resulting in irregular films [74; 87]. Thus, the CF deformation band is partially replaced by CF deformation stretching in the range of 635 – 640 cm^{-1}.

CF_2 scissoring generates small peaks in the chemical range of 729 – 734 cm^{-1}. CF_2 scissoring peaks are more prominent in the FTIR spectrum of sputtered PTFE (Figure 23B) as compared to the bulk PTFE spectrum (Figure 17). The reason for the enhancement of CF_2 scissoring after PVD sputtering is the formation of CF_3 fragments and amorphous PTFE content within the polymer material. CF_3 fragments and amorphous PTFE correspond to the peaks at 732 – 1103 cm^{-1} [86]. The strength of these peaks in sputtered PTFE thin films reflects the extent of polymerisation. The stronger this peak is, the more amorphous the polymer becomes and contains more crosslinks within its structure. CF_3 produces a deformation peak at 740 – 741 cm^{-1}, as shown in Figure 23B (bulk PTFE) and Figure 29a (sputtered PTFE) [74; 87]. The peak responsible for the graphitic (slippery) films appears in the chemical band of 1720 – 1730 cm^{-1}, which is a characteristic feature of C – CF_2 fragments. Drabik et al. [14] observed a low-intensity C = C peak and a high-intensity perfluoroalkyl group (CF_2CO_2) stretch between 1600 – 1640 cm^{-1}, for PTFE films deposited with argon used as a working gas.

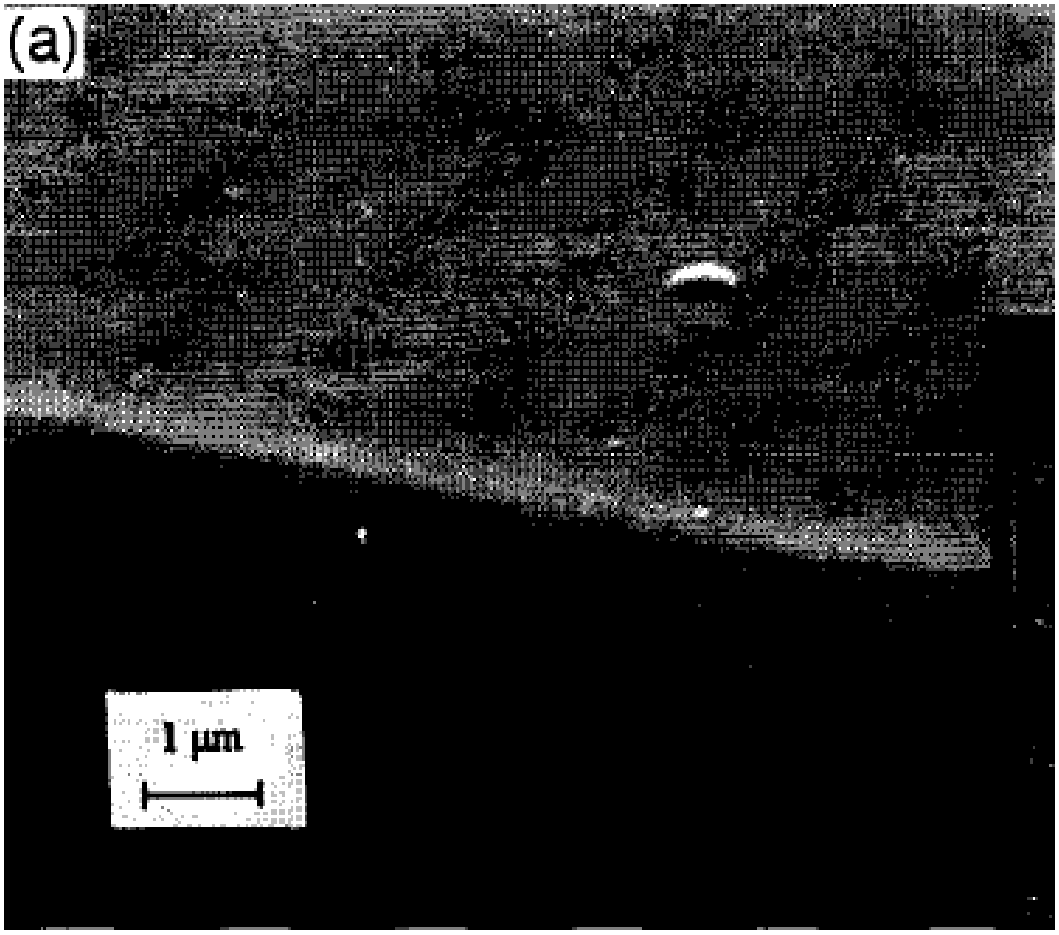

Figure 19: self-sputtered PTFE film at 250W [87].

In SEM image shown in Figure 19, some dense fibres are observed in a perpendicular direction to the substrate [87]. Biederman et al. [20] derived a hypothetical model of PVD sputtered PTFE thin film on glass substrates (precoated by Al) after considering the structure scheme of wavenumber shifts within FTIR spectrum (Figure 18) and the SEM image presented in Figure 19.

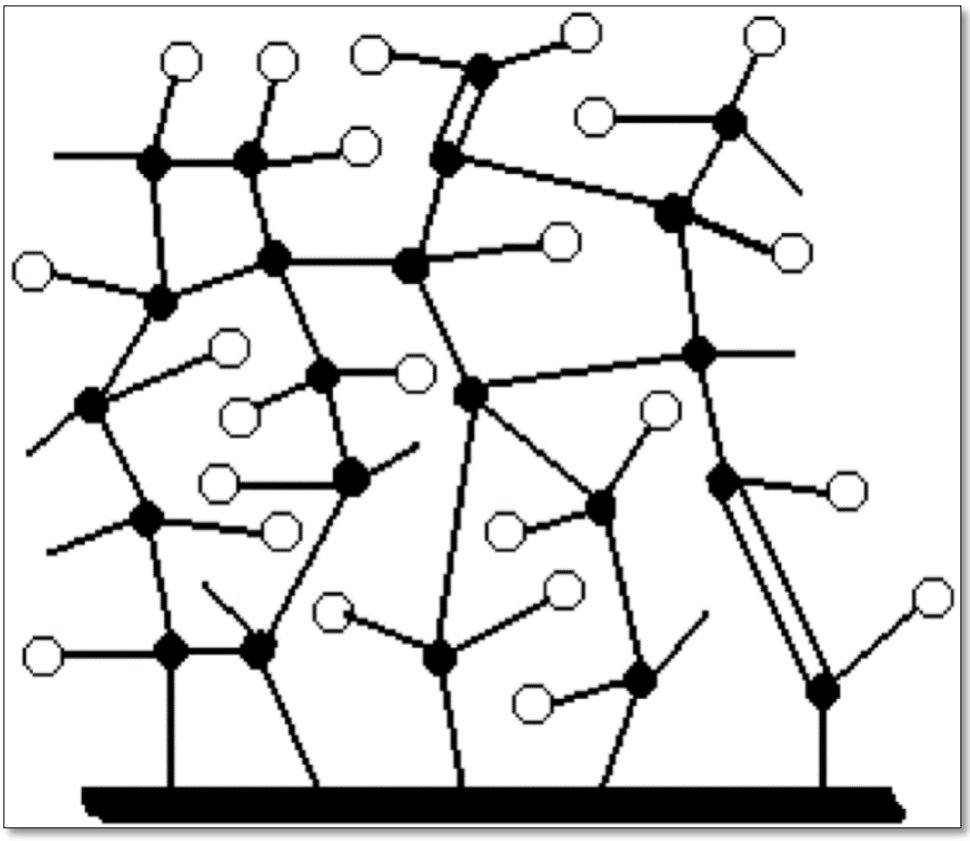

Figure 20: Model of a fluorocarbon plasma polymer obtained by PTFE sputtering (○ *Fluorine* ● *Carbon)* [20].

The hypothetical model represented in Figure 20 symbolizes a simple zero-order structure of a film that was retained under a constant vacuum for a long deposition period; therefore, the model does not include any free radicals [87]. The model illustrates that the PVD-PTFE consists of a central linear chain of C – C bonds and fluorine atoms on one or both sides of the carbon chain [81]. Linear carbon chains are arranged perpendicular to the substrate, with numerous irregular crosslinks along with several double bonds within the structure, whereas the C – F bonds are oriented parallel to the sample plane [81; 87]. The greater the number of crosslinks, the more amorphous the structure becomes because of the deficiency of long chain lengths [87]. CF, C_2F_2, CF_3, C_2F_4 and CF_4 were detected by mass spectroscopy as building fragments of RF - PVD thin film of PTFE structure [20].

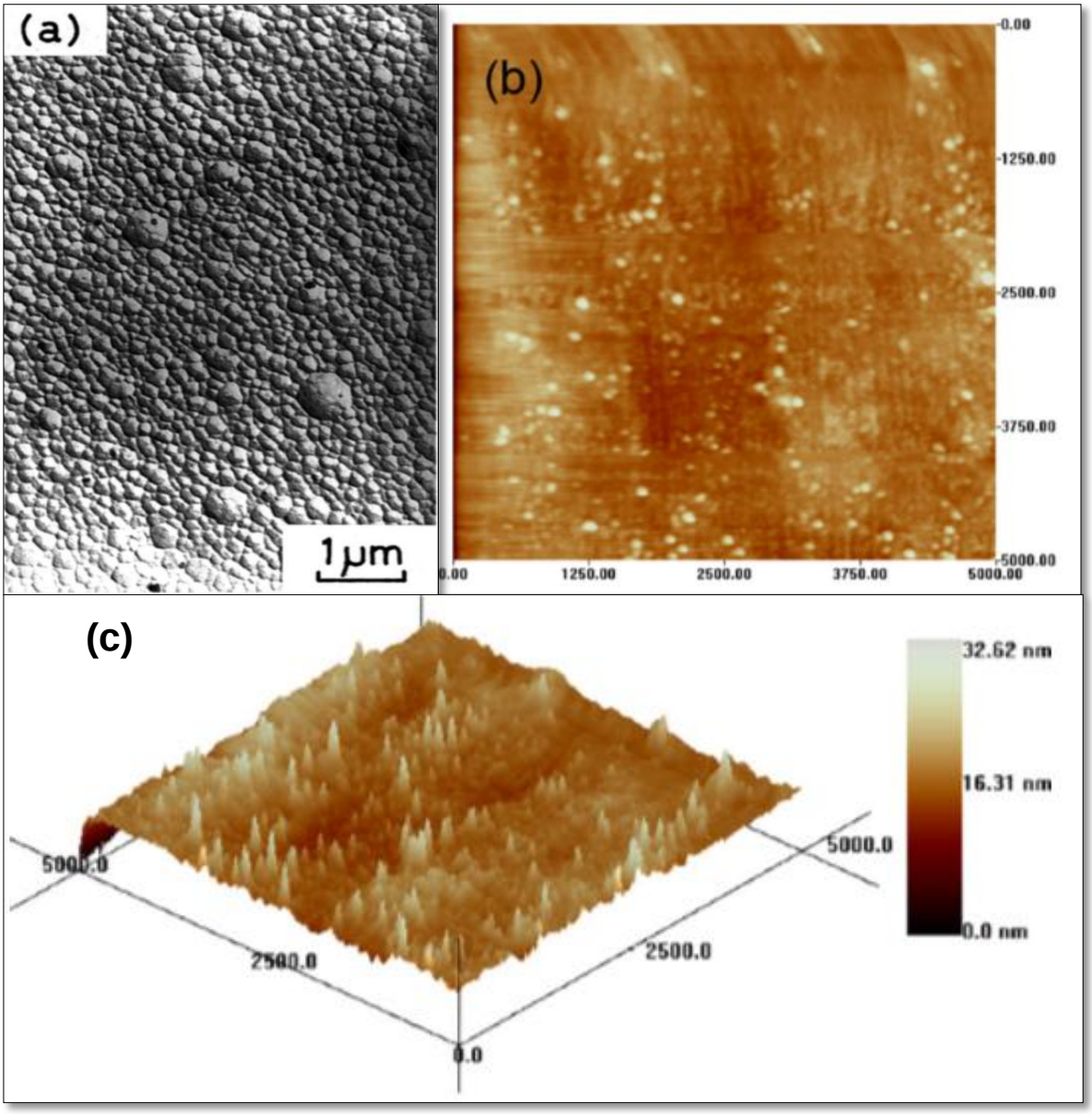

Figure 21: (a) TEM micrographs of PTFE sputtered coatings (1 µm thick) [20; 84]. *(b-c) Surface morphology of PTFE coating prepared at 105 W RF, Ar flux 6.0 sccm, process pressure 0.8 x 10^{-2} mbar, 2D and 3D images* [86].

Figure 21a represents a TEM micrograph of 1µm PTFE film acquired by Yadma et al. [84], which displays an aggregation of small particles forming smooth, homogenous and pinhole free surface. Li et al. [86] reported a surface roughness of 7.418 nm for PTFE thin film, sputtered at 105 W, 0.8 x 10^{-2} mbar and Ar flux of 6.0 sccm on NiTi substrate (Figure 21b and Figure 21c).

PVD sputtering modifies the thin film characteristics of PTFE from its bulk form. Deposition parameters of PVD sputtering influence the structure significantly and

properties of PVD sputtered thin films. Liu et al. [88] conducted a study to investigate the change in PTFE composition and microstructure by altering the process conditions, and they stated that the variance in process parameters control the film compositions and the surface structure. The influences of sputtering parameters on PTFE thin films structure and the associated coating properties are discussed below.

3.2.1 Impact of variance in deposition power

Biederman et al. [89] conducted PVD sputtering of PTFE on Si substrate for 15 min at 0.03 mbar N_2 and RF magnitudes of 150 and 200 W. The deposition rate increased steeply in first 6 minutes followed by a slow decrease in the deposition rate. The deposition rate declines due to increasing target temperature. A higher deposition rate was reported at 200W as compared to the rate observed at a lower deposition power of 150W. The magnitude of deposition power not only influences the deposition rates, but also affects the growth mechanism, morphology and chemical properties.

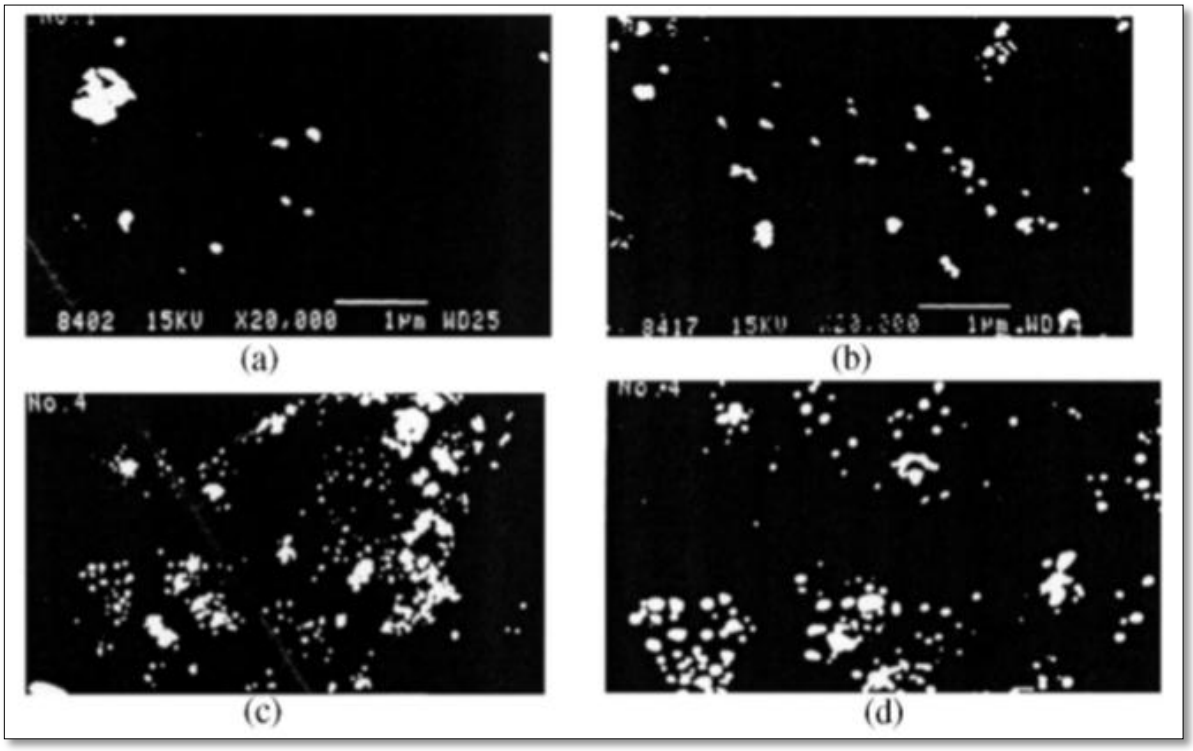

Figure 22: SEM images of PTFE films (x20,000) deposited for 5 min at (a) 200 W, (b) 500 W, (c) 800 W and (d) 1000 W [34].

Qi et al. [34] carried out a detailed investigation of the growth patterns during the nucleation and early growth for PTFE thin films, when deposited at varied deposition power. SEM studies (Figure 22) provided by Qi et al. demonstrate that an increase in deposition powers results in more uniform, finer, more round and closer segregated-grains of PTFE, and the critical size of the grains declines.

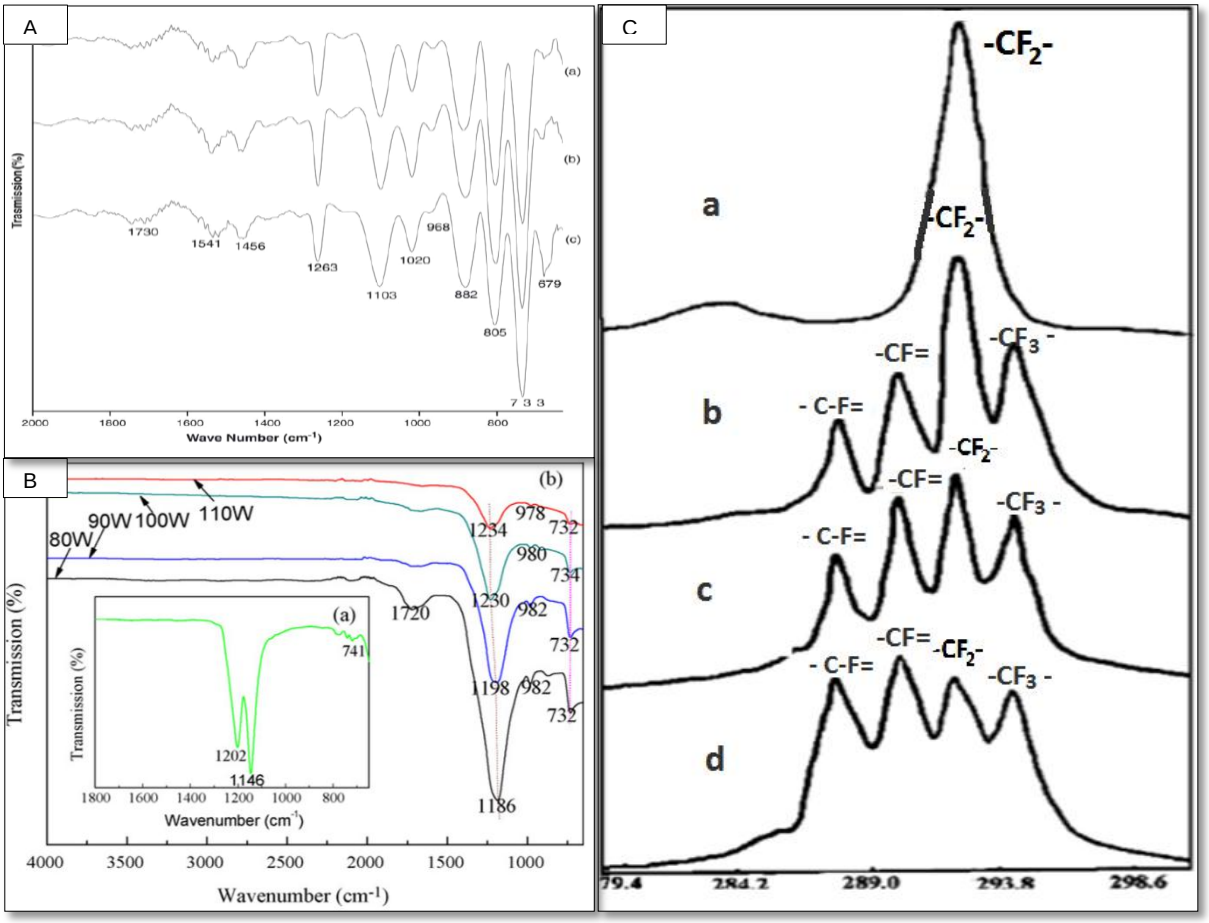

Figure 23: (A) FTIR spectra for RF-PTFE deposited for 60 min at (a) 100W, (b) 150W, (c) 200W [85]*. (B) (a) FTIR spectrum of PTFE target; (b) FTIR spectra of PTFE film, at a constant deposition time of 55 min at RF of 80, 90, 100 and 110 W* [86]*. (C) XPS spectra of (a) pristine PTFE coatings, and sputtered PTFE for 1 hour at (b) 50W RF power (c) 100W RF Power (d) 150W RF power* [44]*.*

Mandale et al. [85] and Li et al. [86] described the effect of varying the PVD deposition power on FTIR spectra of PTFE, as shown in Figure 23A and Figure 23B. According to Mandale et al. [85] the functional groups and peak positions of all films were similar when deposited at 100, 150, and 200 W. Li et al. also reported about the analogous chemical peaks of all thin films deposited at 80, 90, 100 and 110 W. Overall, the results of the both studies establish that the deposition power of PTFE thin films alters the film transparency without changing the functional groups and chemical structure of PTFE thin films [85; 86].

For a coating deposited at 80W, the peak at 1720 cm^{-1} represents C = CF_2 stretch with an ability to form complex cross-linked chains during concurrent etching and deposition [86]. With the increase in the sputtering power, this peak loses its strength, as shown in Figure 23B. Figure 23A represents the spectra belonging to higher power depositions; therefore, a minor peak of C = CF_2 appears at 1730 cm^{-1}. The major CF_x peak at 1186 cm^{-1} in Figure 23B relates to the polymerised content of the polymer within the chain, which decreases in strength with an increase in power from 80W to 100W. The PTFE film deposited at higher powers ranging 100 – 200 W show even smaller CF_x peaks in Figure 23A. Correspondingly, the CF_3 deformation and amorphous PTFE peaks in the region of 732 – 1103 cm^{-1} are stronger in Figure 23A, and the peaks strength decrease with decreasing the deposition power (Figure 23B). Combining the two sets of results in Figure 23, allows establishing that the extent of polymerisation decreases with an increase in deposition power. However, the differences between the spectra of the two studies show discrete trends of %T at various deposition powers. With increasing RF, the transmittance of the PVD films decreases in Figure 23A while it increases in Figure 23B. The deposition times for the both deposition processes are 60 and 5 minutes respectively; thus, the change in transmittance behaviour is related to the film thickness [85; 86]. The thicker the coating, the less the transmittance it demonstrates. To understand the above differences, the trend of deposition rate against RF needs a detailed investigation and understanding.

Liu et al. [44] investigated the effects of deposition power on PTFE film compositions, as shown in Figure 23C. The XPS spectra show that the main –CF– (292 eV) peak of pristine PTFE, shrinks with the increasing power, while the intensities of the –C–CFs (287.7 eV) and –CF–(290 eV) rise considerably. The –CF– (294.0 eV) peak present in the sputtered PTFE remains unchanged with the increasing deposition power. The fluorine to carbon ratio in deposited thin films was calculated by relative peak intensities in the XPS spectra and the fluorine to carbon ratio in PVD sputtered thin films was found to be lower than that in bulk PTFE target material. As the RF power increases (50, 100 and 150 W), the fluorine to carbon ratio decreases (1.75, 1.69 and 1.58 respectively). During sputtering, PTFE decomposes into fragments by RF power supply.[44]

Combining the results presented in Figure 23 establishes that altering the deposition power does not change the functional groups, but the morphology and the proportion of different polymeric fragments vary. %T observed by FTIR spectroscopy indicates the changes in morphological properties i.e. the cluster arrangement within the thin film. The alteration in carbon to fluorine ratio within the polymer, observed by XPS study represent variances in the polymerization ratio after PVD sputtering. No further studies were found to investigate the polymerised content in PVD sputtered PTFE films; thus, it will be attempted in the current study.

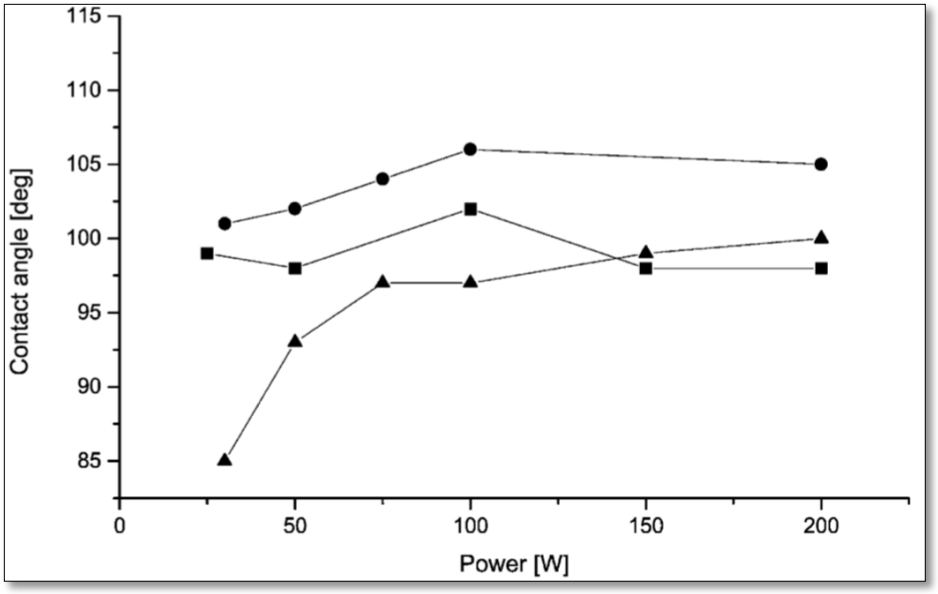

Figure 24: The dependence of static WCA on RF, for PTFE films sputtered at a process pressure of 0.03 mbar and flow rate 7 sccm/min, in Ar the film thickness was 400 nm (-● -), in N_2 the film thickness was 250 nm (-■ -), and in wet N_2 the film thickness was 350 nm (-▲ -) [89].

The influence of varying the RF magnitude on the wetting angle of PVD-PTFE was investigated by Biederman et al. [89], who conducted the magnetron sputtering at 0.03 mbar, and 7 sccm/min flow rate of the working gases (argon and nitrogen). Figure 24 shows that the static WCA increases with increasing RF power from 25 to 100 W. Further increase in deposition power only changes the WCA slightly. A similar trend was reported in the same study for CFx fragment detection by mass spectroscopy, where the RF varies similarly with the amount of CFx fragments. This can be explained by the fact that the greater incorporation of CF and CFx fragments occurs on the film surface resulting in compact structure with higher hydrophobicity

at higher power magnitudes. In the overall trend of RF power against WCA (Figure 24), the use of Ar as a working gas produces more hydrophobic PTFE thin films showing less variance in WCA with changing power. The use of dry nitrogen as a working gas incorporates up to 11 at.% nitrogen and 5 at.% surface oxygen resulting in decreased hydrophobicity. The wetting angle drops further when wet nitrogen is used as sputtering atmosphere. This is due to the integration of additional polar species within the polymer chain during the sputtering process.

3.2.2 Influence of variance in deposition pressure

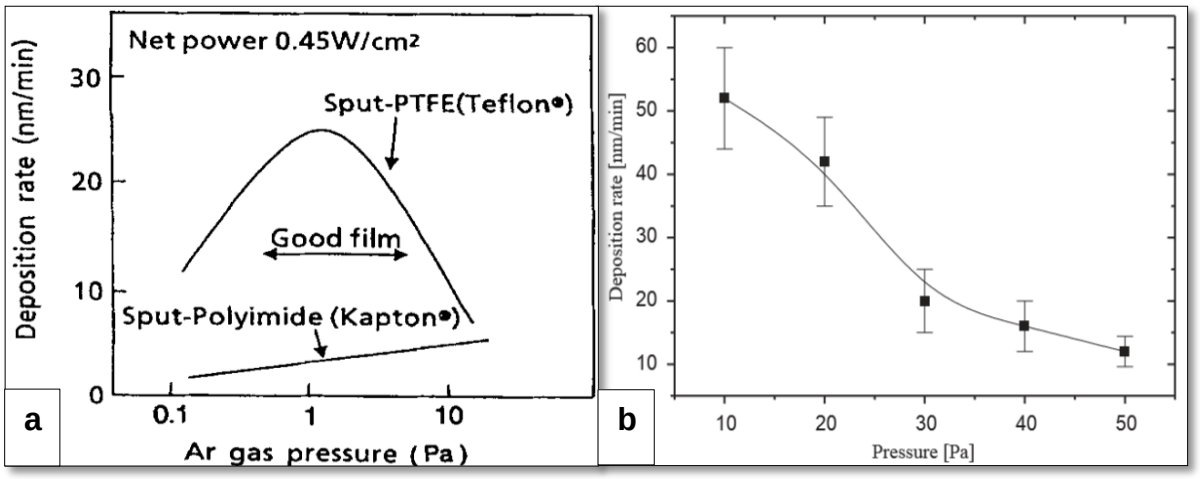

Figure 25: (a) Deposition rate of PTFE coatings, RF-sputtered at 120 – 300 W at Ar pressure of 0.133 x 10^{-2} – 13.3 x 10^{-2} mbar (0.133 – 13.3 Pa), and 40 mm target substrate distance [80]*. (b) Deposition rate of PTFE films as a function of process pressure during deposition; 200W R and 80 mm target substrate distance, Ar flow rate 26 sccm* [74]*.*

Working gas pressure is the most influencing factor on the chemical composition and structure of thin film [74]. Kitoh et al. [84] sputtered the PTFE and polyimide (PI) films at 120 – 300 W (net power: 0.45 W/cm^2) and 0.133 x 10^{-2} – 13.3 x 10^{-2} mbar Ar pressure, while maintaining the target substrate distance at 40mm (Figure 25a). The deposition rate of PTFE was greater than that of PI. They revealed an obvious difference in the trend of deposition rate against deposition pressure for the two polymers. The deposition rate of PI increases with increasing argon gas pressure but for PTFE, an increase in deposition rate was observed following a decrease continuous decrease [84]. This difference in trend of different polymers appears because PTFE has much simpler polymer chain structure, and it is sputtered in larger molecular units resulting in higher deposition rates.

As the argon pressure increases to 1 x 10^{-2} mbar, the breakdown of the PTFE polymer chain due to destructive sputtering process also increases. Therefore, it takes longer to re-polymerise in the form of deposited clusters on the surface of the substrate, resulting in the declining deposition rate [80]. Biederman et al. [87] conducted another study to investigate the influence of variance in pressure on PTFE deposition rate. They observed the deposition rate of PTFE at higher

deposition pressure conditions (0.1 – 0.5 mbar / 10 – 50 Pa). During 40 minutes sputtering process, the PTFE deposition rate declined by approximately 30%. To investigate the reason for this decline Biederman et al. [20] calculated the F:C for PTFE target by ECSA after sputtering in another study. They reported that the fluorine to carbon ratio of the target's erosion track was 0.7:1 and C:F in the target centre was 1.3:1. The target material develops a carbon-enriched layer on the target material during deposition, which takes longer to sputter compared to the fluorocarbon. Therefore, the deposition rate of PTFE declines with increasing the pressure due to carbon enriched altered layer on the target material.[20; 87]

The decline in deposition rate of PTFE is elucidated further by its relationship to the concentration of chemically reactive species in the plasma that attach to the substrate surface. At low argon pressure, the ionisation efficiency and the plasma density increase, ultimately leading to more collisions. Increasing the argon pressure decreases the ionisation possibility due to declining average free path of the electrons, resulting in less polymeric target fragmentation and emission. This also inhibits some of the reactive species required for thin film growth reaching the substrate and leading to a decline in deposition rate.[74]

It is noteworthy that there is a significant difference between the PTFE deposition rates of the two studies, which were both conducted by sputtering at 0.1 mbar. The deposition rate reported by Biederman et al. [74] is 52 nm/min at 0.1 mbar, which is approximately five times greater than that of Kitoh et al.'s [80] value, despite larger target substrate distance in the first study. This substantial dissimilarity is because Kitoh et al. [80] used conventional PVD sputtering apparatus with no magnetrons, while Biederman et al. [74] employed magnetron sputtering having more efficient target utilisation.

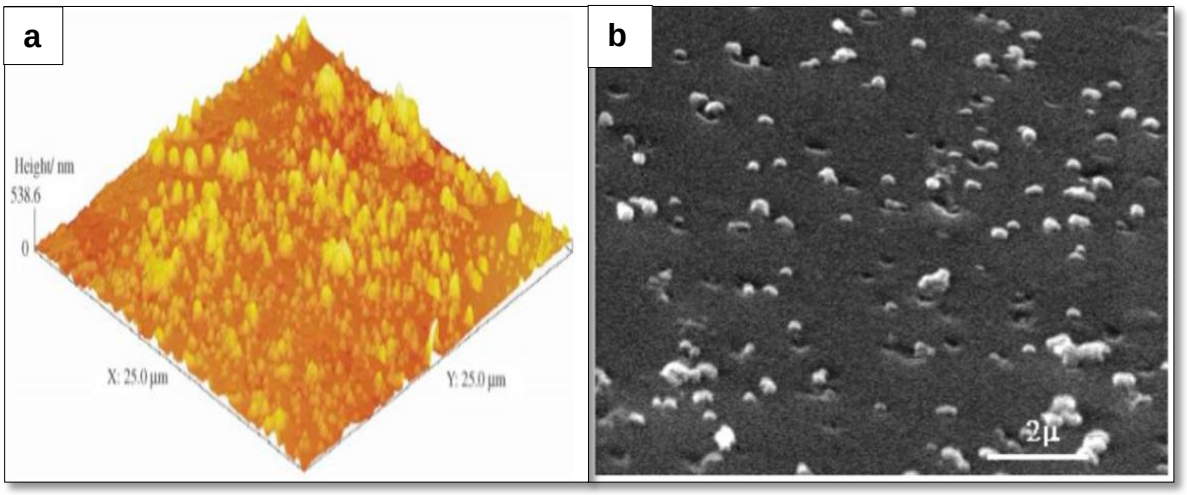

Figure 26: (a) AFM image of PTFE coating sputtered at Ar pressure of 0.1 mbar. (b) SEM image of PTFE deposited at 0.7 mbar Ar pressure, magnification x10000 [74].

Compared to the surface roughness of 7.418 nm reported by Li et al. [86] (Figure 21c), Biederman et al. [74] reported a lower surface roughness of approximately 3 nm, for the thin films deposited in the range of 0.1 – 0.5 mbar at 200W, and at Ar flux of 26 sccm (Figure 26a). The surface roughness increases to 40 nm when the pressure is increased to 0.7 mbar, and flakes-like structures appear on the film surface. The small variance in the roughness values at low deposition pressure occurs due to the differences in other deposition parameters including deposition power, substrate type and the argon flux. The flakes on the film surface appear during the plasma polymerization process involving various fragments ejecting from the surface of the PTFE target.

After combining observations of the above studies, it is determined that the PVD sputtered thin film of PTFE demonstrates a columnar structure along with three-dimensional island growth mode, and the structure contains semi-continuous sub-layers consisting of 100 nm silk worm-like islands connecting to each other. During the deposition of initial layers, few clusters of sub-layers also start to grow. The sub – layers cover the initial layer by 50 – 70 % and then the growth of sub-layer stops. The films have wider columns at higher pressure, and this observation corresponds to the description by Thornton zone models, which were originally illustrated by metallic thin film growth. [34; 74]

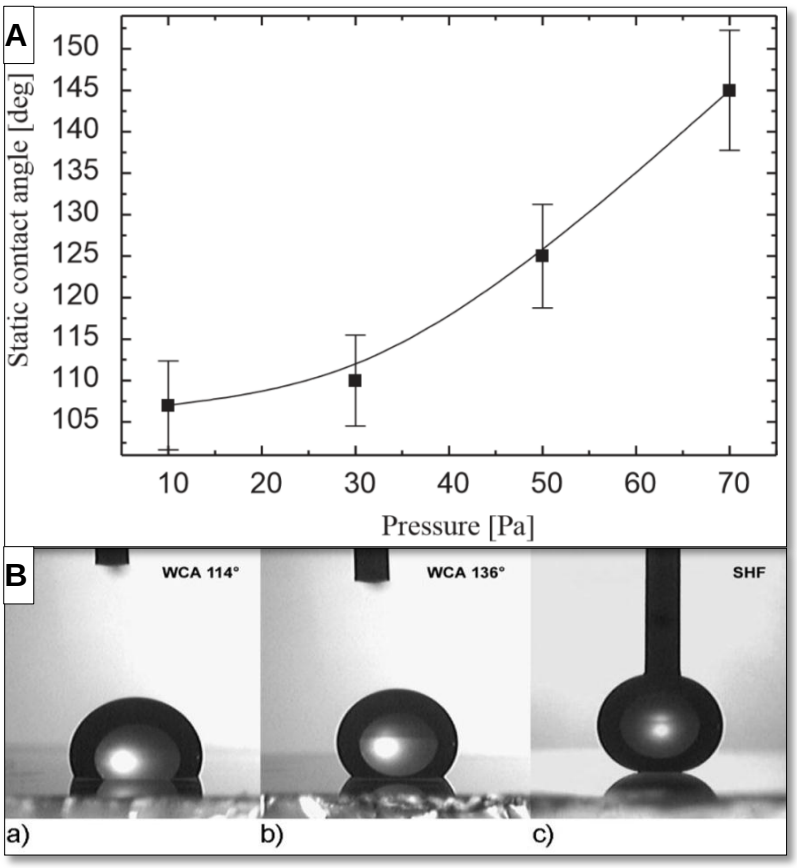

Figure 27: (A) Static WCA as a function of Ar pressure (0.1 – 0.7 mbar / 10 – 70 Pa) at 200 W, flow rate of 26 sccm [74]*. (B) Shape of a water droplet on PTFE surface deposited at a target-substrate distance of 25 cm from the magnetron and a process pressure of (a) 0.05 mbar (b) 0.25 mbar (c) 0.5 mbar. The droplet for 'c' is held by a syringe tip to avoid rolling away from the surface immediately* [14]*.*

Along with varying the deposition rate and film morphology, the deposition pressure also alters the properties of PTFE thin films. For example, Stelmashuk et al. [74] reported that an increase in argon pressure during PVD process decreases the wettability of PTFE films as presented in Figure 27A. A working distance of 5 cm was maintained because at a working distance around 18 cm and 0.2 – 1.0 mbar process pressure, the clusters of PTFE appeared on the substrate that were grown from CF_2 precursor. The depositions of the films at 0.7 mbar and 5 cm working distance were super-hydrophobic (146°), slippery and appropriate for industrial use. Drabik et al. [14] conducted another study on PTFE thin films deposited at 0.05, 0.25 and 0.5 mbar and target substrate distance of 25 cm. They observed that with an increase in

deposition pressure from 0.05 to 0.5 mbar, the WCA increases sharply from 113° to above 170° as shown in Figure 27B.

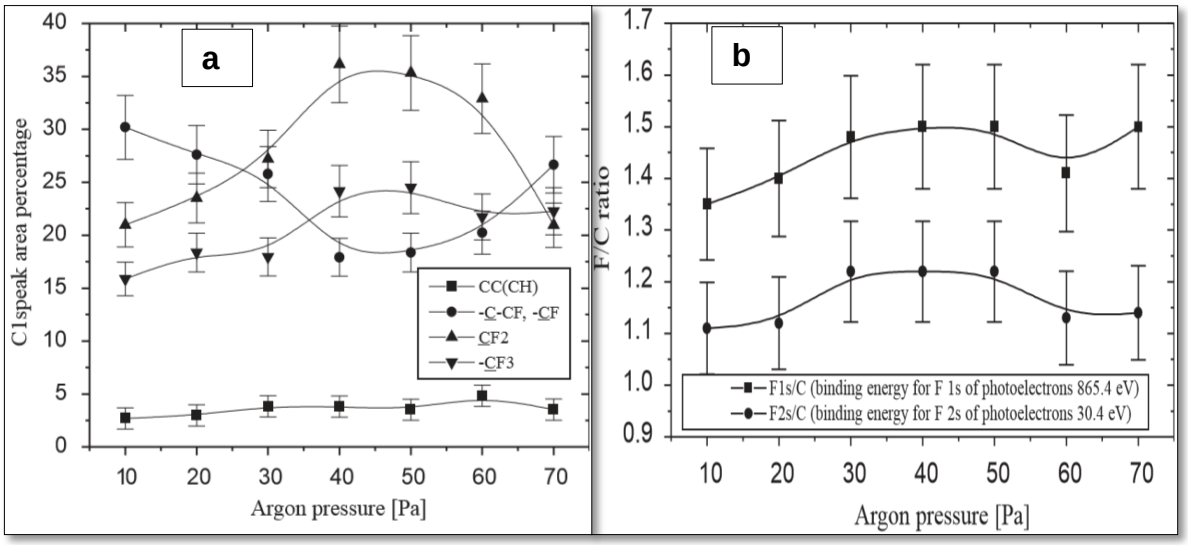

Figure 28: (a) *The contents of various structural groups in PTFE deposited at various Argon pressures (0.1 – 0.7 mbar / 10 – 70 Pa), which are shown in C1s XPS spectra. (b) F/C ratio as a function of Ar pressure (0.1 – 0.7 mbar / 10 – 70 Pa) calculated from C1s, F1s and F2s photoelectron spectra.*[74]

Stelmashuk et al. [74] further investigated the results presented in Figure 27 andthey suggested that the increased roughness is not the direct cause of a rise in the hydrophobicity of the thin films but the hydrophobicity rose by the alteration in chemical composition. Liu et al. [88] argued that the surface roughness alter the WCA of PTFE thin films while Stelmashuk et al. explained this by XPS studies presenting a change in the chemical structure with a rise in working gas pressure. XPS showed that the extent of PTFE degradation of PTFE is higher at lower pressures because of high-energy cations bombarding the target surface. As the working gas pressure increases, the amount of CF_2 fragments increases; thus, the chemical structure starts to resemble the chemical structure of bulk PTFE. At pressures above 0.4 mbar, the amount of CF_3 fragments increases while CF fragments decrease. At argon pressures above 0.5 mbar, the substrate surface and the chemical reactions within the plasma change resulting in an increase in CF and a decrease in CF_2 fragments. The surface of PTFE thin films is fluorine enriched due to the presence of CF_3 fragments resulting in higher WCA.[74]

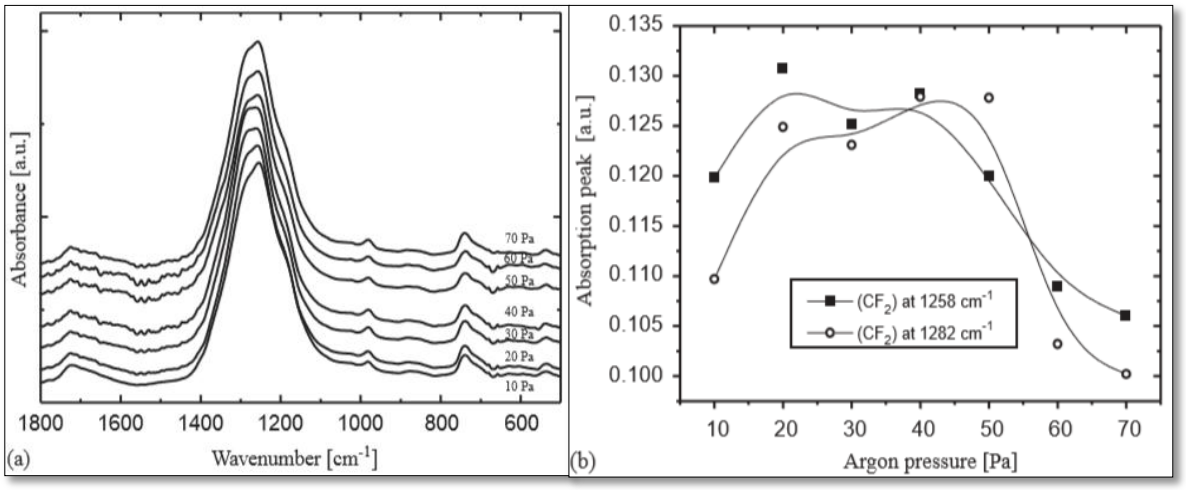

Figure 29: (a) The FTIR absorbance axis holds for the curve for 0.1 mbar / 10 Pa while other curves are shifted for clarity. (b) FTIR absorption peaks at 1258 cm^{-1} and 1282 cm^{-1} as a function of Ar pressure (0.1 – 0.7 mbar / 10 – 70 Pa) [74].

Figure 29A shows the FTIR spectra of PTFE deposited by PVD sputtering at various pressure in the range of 0.1 – 0.7 mbar, where the absorbance axis holds for the curve for 0.1 mbar while other curves are shifted for clarity. The absorption peaks CF_2 appearing at 1258 and 1282 cm^{-1} were plotted as a function of Ar pressure in Figure 29B. Figure 29B shows that the absorption CF_2 peaks shifts upwards with increasing pressure followed by a decline in absorbance. A small shoulder at 1600 cm^{-1} corresponding to $–CF_2CO_2$ becomes prominent for high working gas pressure.[74]

3.2.3 Influence of variance in working distance

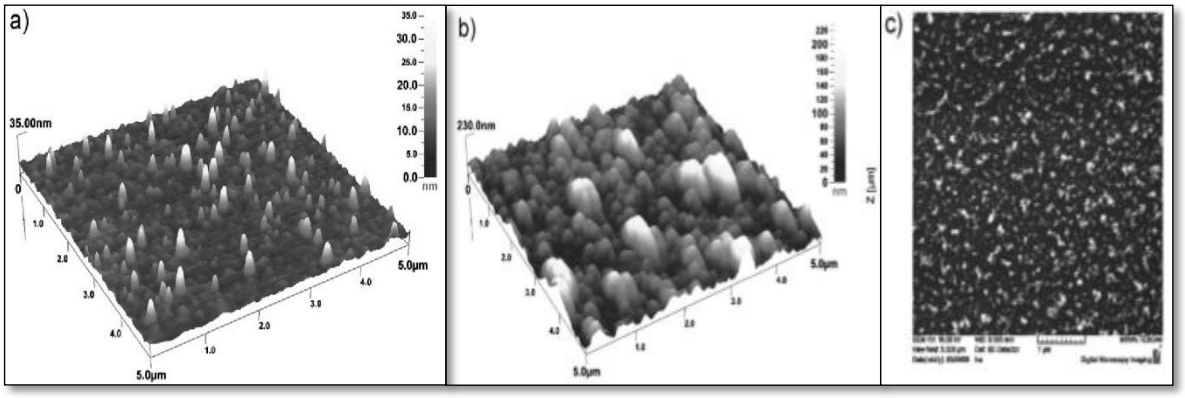

Figure 30: AFM images (5 x 5mm area) of PTFE films with thicknesses of about 70 nm deposited at a working gas pressure of 0.5 mbar and at a different distance from target: (a) 14 cm, (b) 25 cm, and (c) SEM micrograph of sample from b.[14]

Drabik et al. [14] investigated the influence of working distance on the PVD sputtered PTFE thin film properties. 70 nm thick PTFE films were sputtered at 0.5 mbar and variable working distances in the range of 14 – 25 cm. They investigated the surface roughness, chemical characteristics and the wetting angles of the PTFE thin films at 14 – 25 cm working distances. An increase in working distance from 14 – 25 cm increases the roughness of thin films, as shown in Figure 30. PTFE thin film deposited at 14 cm working distance has a surface roughness of 35 nm as represented in Figure 30a, which increase to 230 nm for the thin film deposited at 25 cm working distance, as shown in Figure 30b. Therefore, the higher the working distance, the rougher the PVD-PTFE coatings are.

Water contact angle for PTFE deposited at 0.5 mbar and distances of 14 cm and 25 cm was also reported by Drabik et al. [14] at variant pressures as shown in Figure 31. Figure 31a represents the influence of changing working distance on hydrophobicity of PVD-PTFE coatings. At a target-substrate distance greater than 20 cm, the water contact angle increases steeply. At 14 cm, the WCA is constant around 115° but a steep variation of WCA occurs at 25 cm. WCA changes from 113° at 0.05 mbar to ~ 170° at 0.4 mbar.[14]

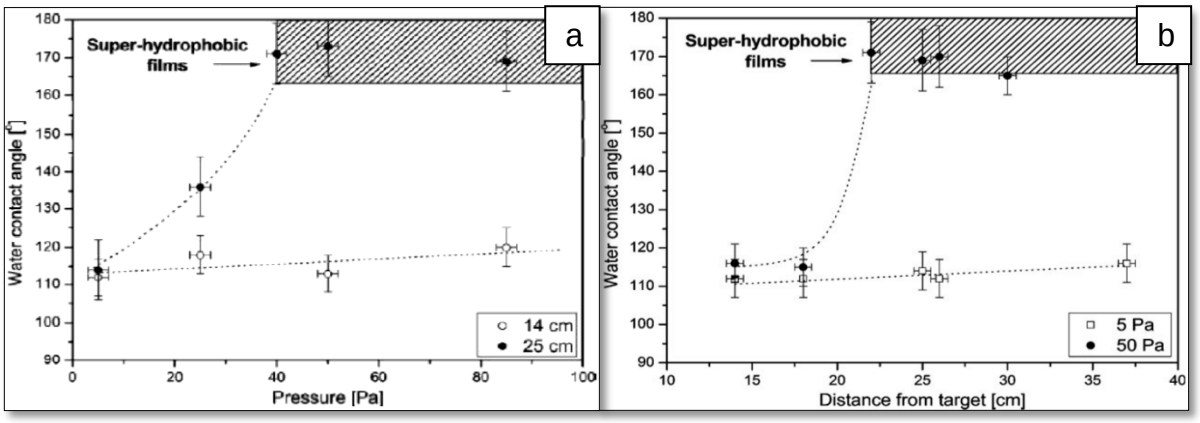

Figure 31: (a) Dependence of static water contact angle of PTFE deposited at 0.5 mbar and distances of 14 cm and 25 cm for coating thickness of 70 nm. (b) Variation in the static water contact angle of PTFE films with the substrate-target distance. Film thicknesses are about 70 nm.[14]

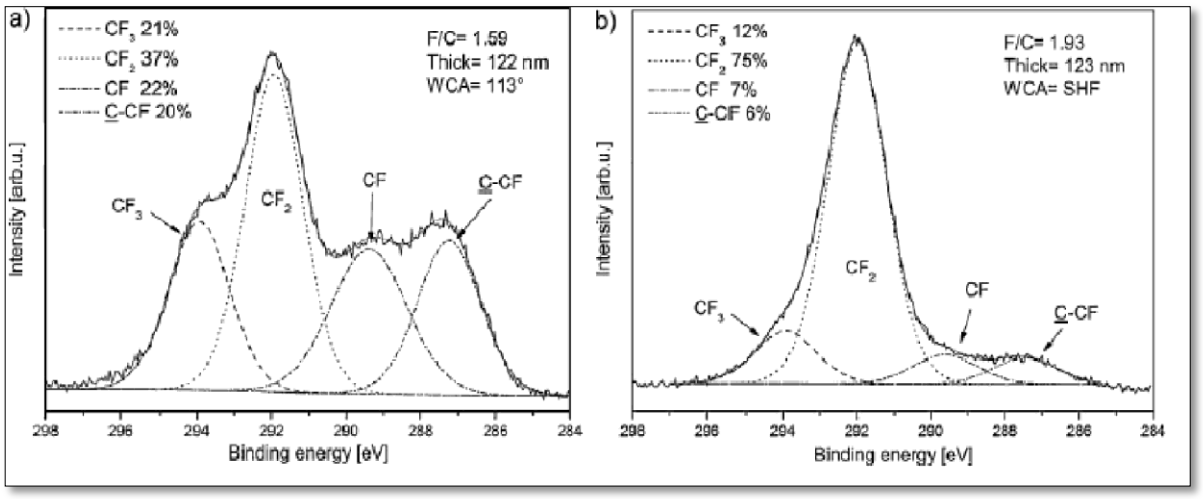

Figure 32: C_{1s} XPS spectra of PTFE deposited at 0.5 mbar at working distances of (a) 14 cm (b) 25 cm [14]*.*

To investigate the effect of variance in working distance on PTFE thin film characteristics further, Debrik et al. [14] carried out an XPS study of PTFE films as shown in Figure 32a and Figure 32b. The abundances of XPS peaks determine that the fluorine content within films increases with an increase in working distance and the wetting angle of the film increases. At 14cm, the F/C ration increases from 1.38 to 1.59 with an increase in pressure from 0.05 mbar to 0.5 mbar, whereas a much-pronounced increase of F/C was observed at higher working distances. When the working distance is increased from 14 – 25 cm, the F/C ratio increases from 1.59 to

1.93, and the PTFE films become superhydrophobic. Immediately after deposition, the surface energy of these films seem to be comparable to the conventional PTFE, as apparent from WCA measurements, but these films are much more prone to ageing, and lose their hydrophobic character when exposed to the atmosphere.[14]

After a combined examination of the surface roughness study shown in Figure 30 and the WCA results provided in Figure 32, it can be deduced that the rougher the surface the higher surface energy it has, resulting in an increase in hydrophobicity.

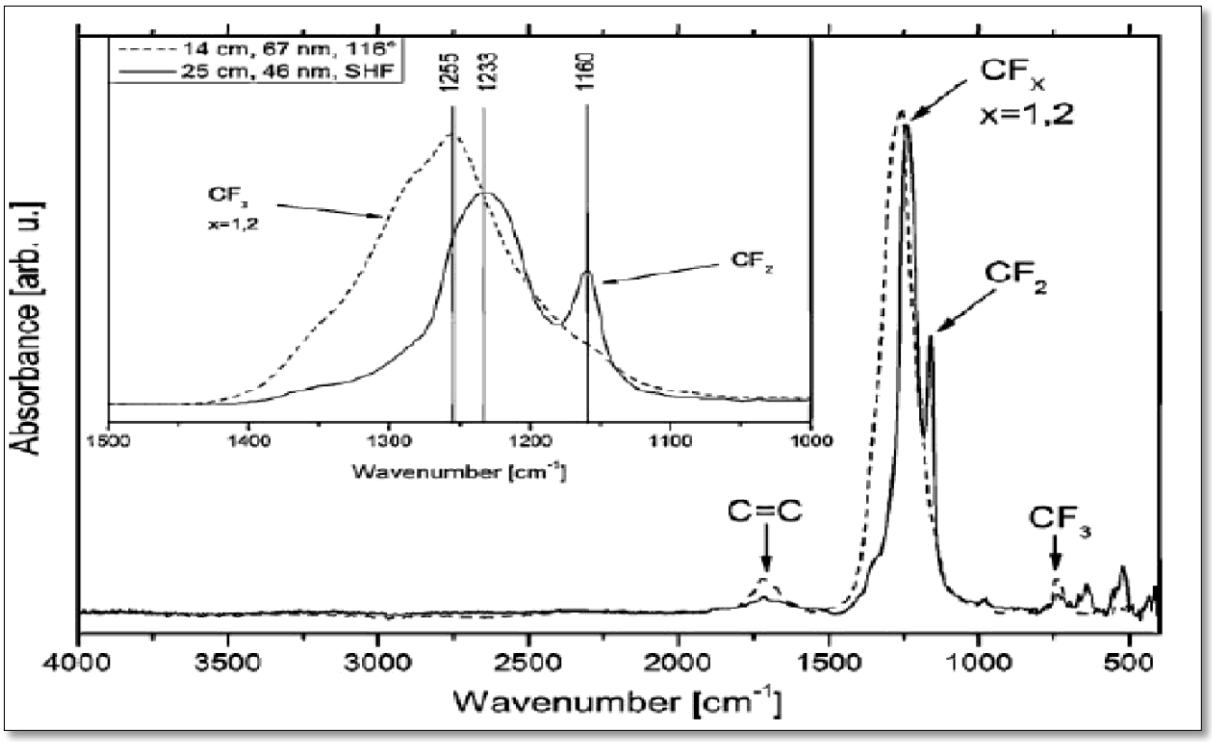

Figure 33: FTIR spectra of PTFE coatings deposited at 0.5 mbar and distances of 14 cm and 25 cm [14].

High-resolution FTIR absorbance spectra of PVD sputtered PTFE at 14 and 25 cm working distances were compared to each other, as shown in Figure 33. For the PVD sputtered film of PTFE at 14 cm, the absorption maxima at 1255 cm^{-1} corresponds to CF_x peak, which shifts to 1233 cm^{-1} for the superhydrophobic film deposited at 25 cm working distance. A new absorption peak representing symmetric CF_2 stretching vibration also appears at 1160 cm^{-1}, when the working distance was increased from 14 cm to 25 cm [14]. The alteration in peak position and appearance of a new peak are associated phenomena to an increase in F/C ratio; thus, the FTIR results verify the results of XPS study provided in Figure 32a and b.

3.2.4 Target and substrate temperature, and the plasma treatment

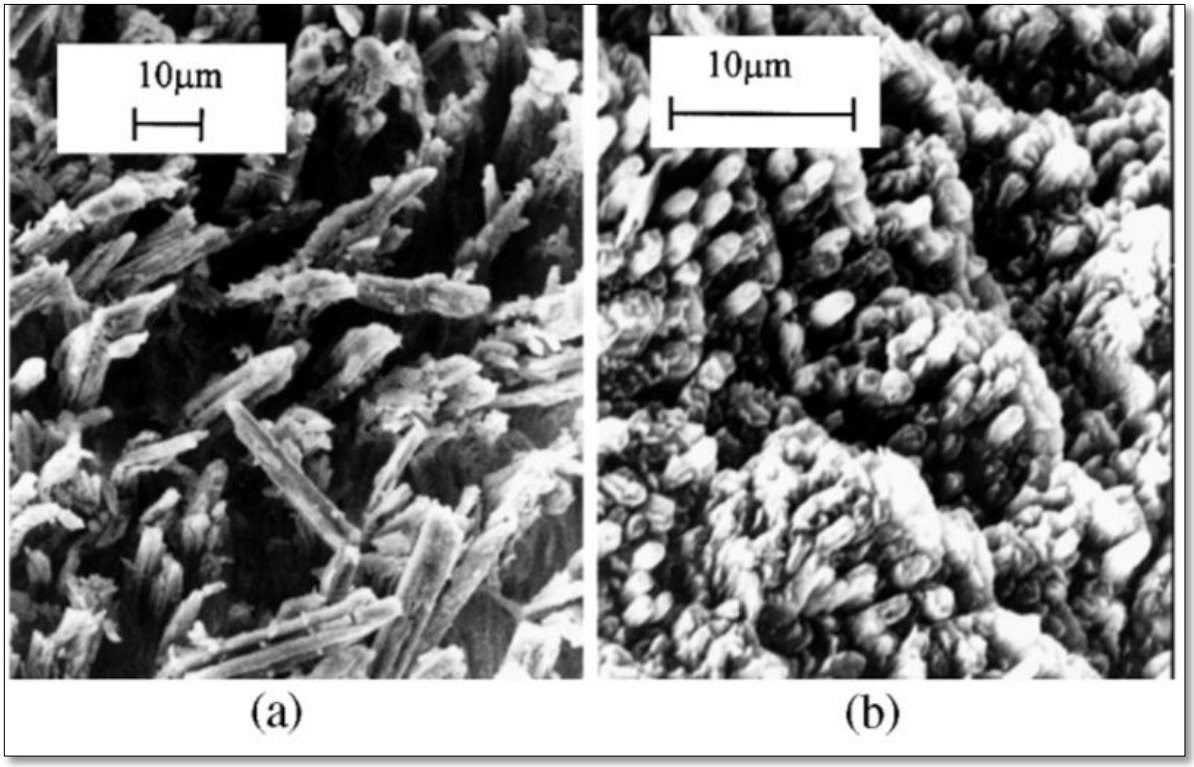

Figure 34: SEM image of PTFE target surface several hours after PVD sputtering (a) 1000x in the center (b) x 3000 in the erosion zone [89].

Biederman et al. [89] investigated the influence of changing PTFE target temperature during the magnetron sputtering process. They reported that the target temperature always remains below 300°C, which is lower than the M.P of PTFE. For instance, a set of their deposition conditions was self-sputtering at pressure ranging from approximately 0.001 to 0.034 mbar and 125W RF for 10 min. Target temperatures were recorded in the range of 150 – 250°C with changing deposition pressure. On repeating the experiments with similar sputtering conditions but nitrogen as the working gas, the target temperature falls in the range of 50 – 175°C. Biederman et al. [89] observed the surface morphology of the PTFE target after the PVD magnetron sputtering for few hours. Figure 34 images the PTFE target at the center and the erosion track. Although the target temperature does not exceed the PTFE's M.T (327°C); however, the most of energy intemperate at the erosion track due to magnetron installation causing the surface damage and melting. Thermal evaporation does not take place from the target material, but some tapered cones were observed on the erosion track. The surface morphology of the magnetron

sputtered target center containing cone-like structure appeared due to preferential sputtering, matches the PTFE target surface seen by sputtering without the induction of the magnetic field (Figure 34). A strong influence of target temperature on the deposition rate was described as follows. A steep increase in the target temperature was observed along with high deposition rates during the initial sputtering process (6 min). After that, an altered carbon enriched layer develops on the target surface. Thus, the sputtering rate decreases between 6 to 11 min of the deposition, and the target temperature does not rise as steeply as it rises during the initial PVD deposition.

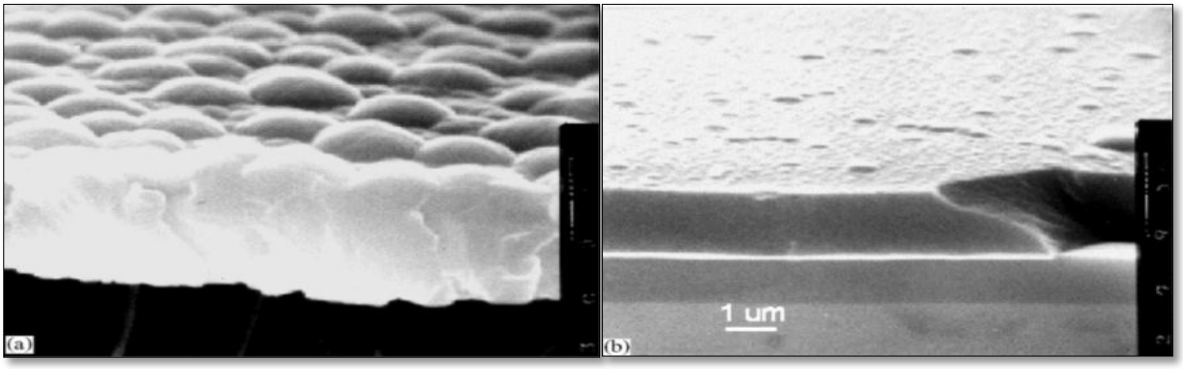

Figure 35: The cross section of the film deposited on Si at 85 W, self – sputtering (a) -15°C (b) + 38°C [20].

The surface morphology of PVD thin films changes with changing deposition temperatures, as stated previously in 3.1.3. Low-temperature deposition in zone 1 produces a thin film microstructure with tapered crystallites having equiaxed grains, separated by open voided boundaries. Slight increase in temperature results in zone T type columnar grains followed by an appearance of zone 2 at further rise of the temperature. The temperature change takes place due to variance in sputtering conditions such as deposition power or pressure [89]. High-temperature zone 3 corresponds to an equiaxed recrystallised grain structure formed as a result of bulk diffusion and recrystallisation [49; 53]. Figure 35 can verify the explanation of the zone models, which shows a cross-sectional SEM morphology of PVD-PTFE thin film on Si, produced by Biederman et al. [20] at 220W using RF at 85 W. The thin films exhibit a columnar surface within the negative temperature range (-15°C), which transform into the fibrous structure at room temperature but an amorphous continuous film appears at high deposition temperature of +38°C. Biederman et al.

[89] also reported the formation of a compact and amorphous PTFE thin film at approximately 40°C (zone 3). At lower temperature of 0°C, a columnar structure was observed that matches to the zone 2 of the structural zone models. Further decreasing the substrate temperature to -23°C produces a 5 µm thin film of PTFE having a microstructure matching to zone T, which contains the microcolumns of 3 µm diameter.[20; 89]

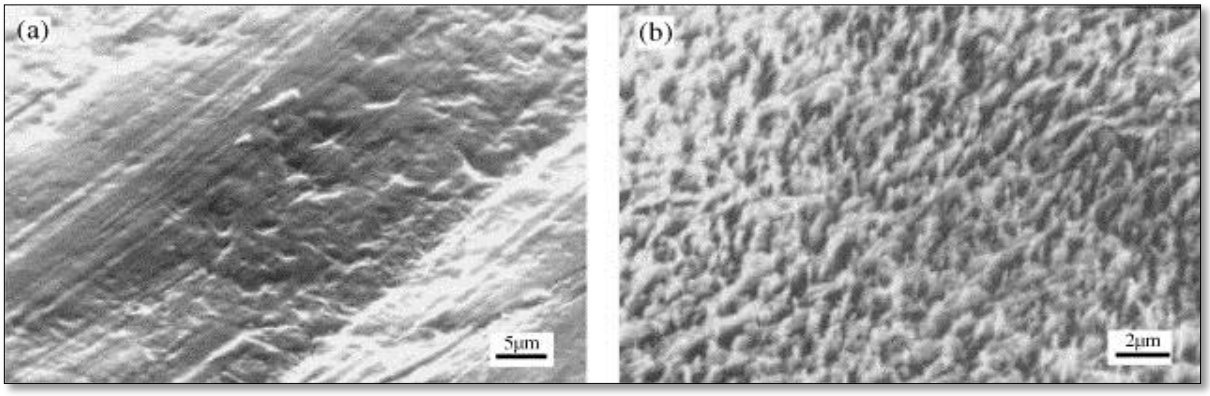

Figure 36: SEM micrographs of PTFE, (a) before (b) after the plasma treatment (500 W, 2 min, Argon pressure of 1.7×10^{-3} mbar) [15].

Liu et al. [90] treated the PTFE surface with an argon plasma at 4.5 x 10^{-3} mbar and 500 W for 2 minutes to observe the surface morphology. They reported that the PTFE surface becomes polar and rougher due to etching caused by heat produced at high RF as shown in Figure 36. This type of surface morphology enhances mechanical interlocking of incoming adatoms to the thin film during further deposition process.[90]

3.2.5 Influence of deposition thickness

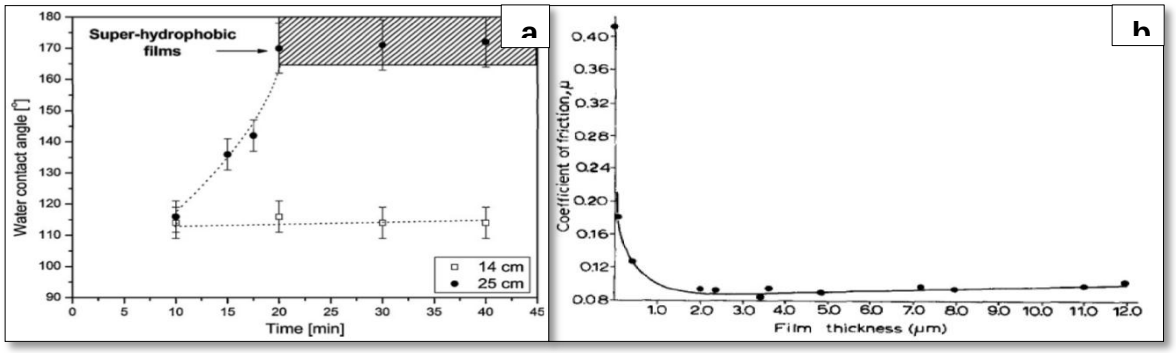

Figure 37: (a) WCA of PVD-PTFE as a function of the deposition time. Coatings deposited at a working gas pressure of 0.5 mbar [14]*. (b) Friction coefficient vs. coating thickness for PTFE* [91]*.*

PTFE film thickness does not change its polymeric makeup. Increasing the thickness affects surface roughness, and as a result the hydrophobicity increases, as seen in Figure 37a [14]. Drabik et al. [14] reported that the film deposited for a longer period is more hydrophobic and therefore contains higher surface energy. The hydrophobicity as a function of deposition time was observed at 0.5 mbar in the range of 14 to 25 cm working distances. The increase in wetting angle was steeper for the film deposited at 25 cm working distance compared to the film deposited at a working distance of 14 cm.

Harrop et al. [91] also reported their findings of the influence of coating thickness on friction coefficient (CoF), investigated by scratch testing of PTFE thin films, as shown in Figure 37b. The CoF of PTFE thin films remains constant in the range of 0.08 – 0.09 for film thickness above 2 µm; hence, the friction coefficient becomes independent of the coating thickness. PTFE Films with less than 1µm thickness have a noteworthy increase in the CoF from 0.08 to 0.15. Scratch testing results are also related to the scratch depth. Therefore, the greater the scratch depth, the greater the volume is required to move the stylus, needing more tangential forces resulting in the higher coefficient of friction. The conclusion drawn by Harrop et al. about the influence of film thickness on CoF was also supported by Yamada et al. Yamada et al. [84] described that the friction coefficient of 1 µm thin films was higher than that of the polymer target because the sputtered thin films exhibit higher surface energy than the target material.

3.2.6 Friction of PVD sputtered PTFE thin films

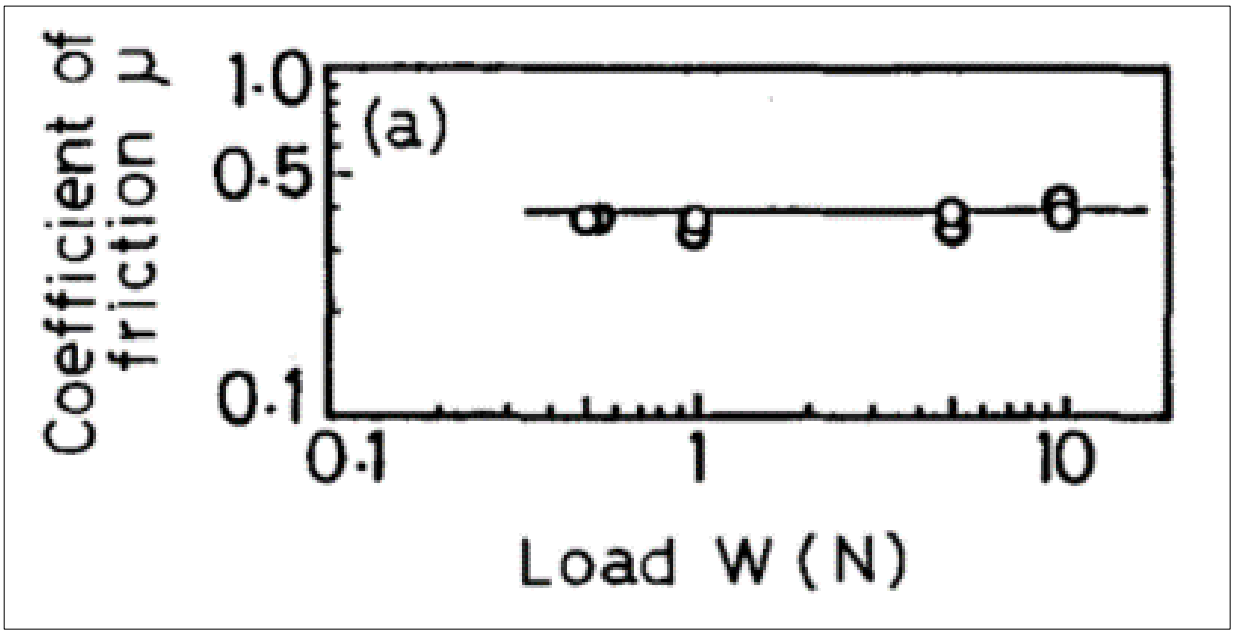

Figure 38: Friction coefficient as a function of load for PTFE (coating thickness, 1 μm; V = 0.04 cms^{-1} [84].

Yamda et al. [84] measured the frictional force of PTFE against a sliding steel ball and observed that the friction coefficient was approximately 0.3 under a 5N load. It was found that the friction coefficient was independent of the film thickness. Figure 39 shows the fluctuation of frictional force observed against number of passes while maintaining a constant load in a sliding ball scratch testing study of thin films. The PVD deposited PTFE sustain the film stability for the first 14 passes with CoF ranging from 0.2 to 0.3. Past 14 passes, the CoF fluctuates severely because of the damaged coating on the sliding track and consequently PTFE film plastically deforms, and 25th pass removes most of it. It was also reported that the heat treatment increases the durability of PTFE coatings.[84]

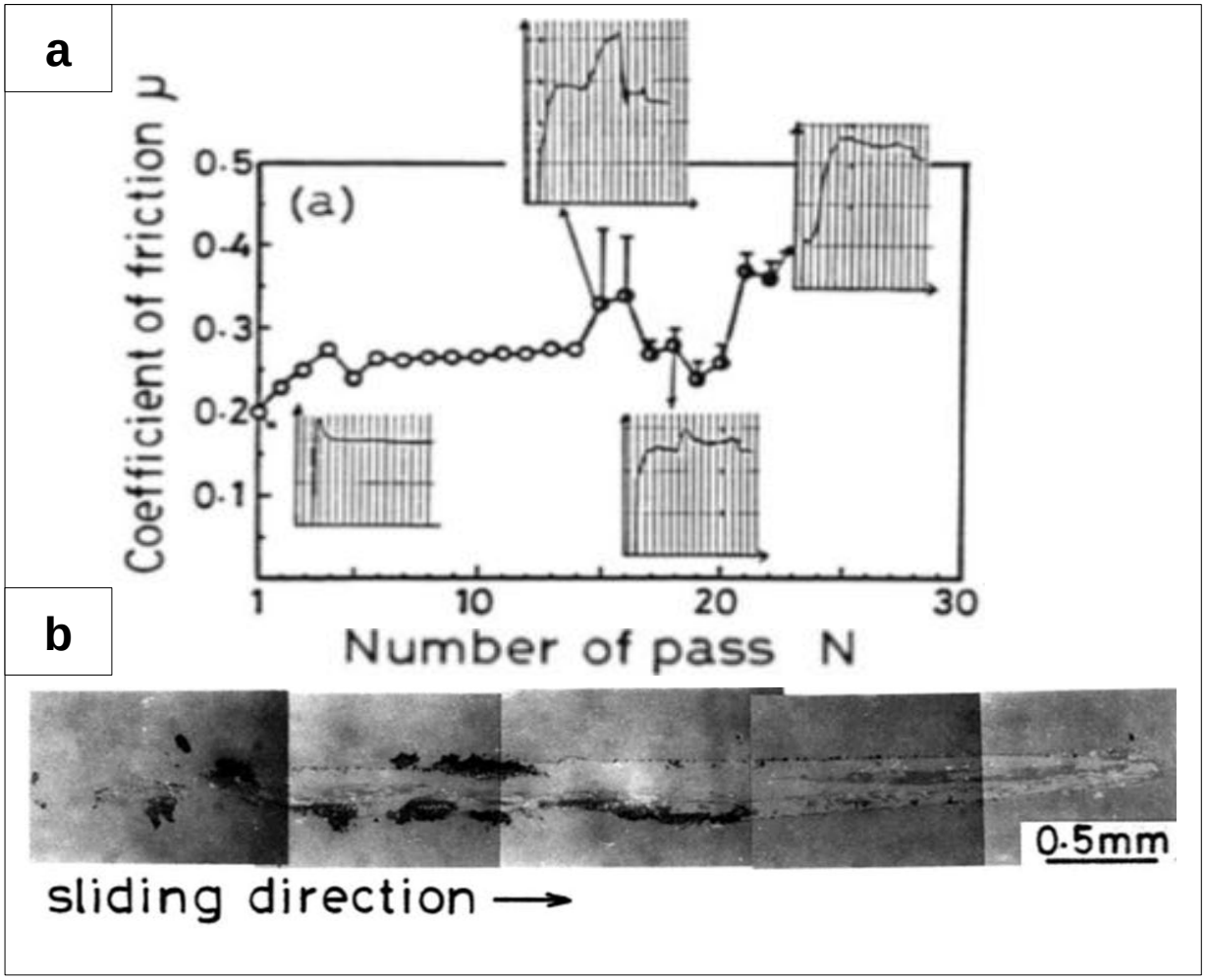

Figure 39: (a) Friction coefficient as a function of number of passes (W = 5N; V = 0.05 cm.s^{-1}). (b) Frictional tracks damaged by repeated linear siding (W = 5N; V = 0.05 cm.s^{-1}) [84].

3.2.7 Summary

PVD sputtering is an energetic process, which dissociates the polymeric chain. Although PTFE has been successfully deposited as polymer (polymer-reformations) by PVD sputtering, as reported by various research-based studies in the past but the extent of polymerization has not been quantified so far. The influence of deposition parameters on the amount of polymerised content with the polymer chain also needs to be investigated in detail. PTFE has much simpler polymer chain structure than the most of other polymers, and it is sputtered in larger molecular units resulting in higher deposition rates. The FTIR spectra of bulk and sputtered PTFE are identical to each other. Superhydrophobic PVD-PTFE films are prone to ageing and lose their hydrophobic character when exposed to the atmosphere. The rougher the surface, the higher surface energy it has, therefore, the hydrophobicity of thin films increases.

PVD-PTFE is observed as dense fibres in a perpendicular direction to the substrate. A 1µm PTFE film shows aggregation of small particles having smooth, homogenous and pinhole free surface. PTFE demonstrates a columnar structure along with three-dimensional island growth mode, and the structure contains semi-continuous sub-layers consisting of 100 nm silk worm-like islands connecting to each other. The hypothetical model illustrates that the PVD-PTFE consists of a central linear chain of C – C bonds and fluorine atoms on one or both sides of the carbon chain. Linear carbon chains are arranged perpendicular to the substrate, with numerous irregular crosslinks along with several double bonds within the structure, whereas the C – F bonds are oriented parallel to the sample plane. The greater the number of crosslinks, the more amorphous the structure becomes because of the deficiency of long chain lengths [87][87; 89].

The existing literature provides data on the influence of process conditions such as power, pressure, working distance, working gas, and temperature on PTFE film morphology, chemical structure, hydrophobicity, and deposition rates. Slight variance in those deposition conditions significantly changes the deposited microstructure and properties. Therefore, it is important to choose the process conditions cautiously and ensure that the independent variable do not alter during the experiments. The deposition power not only affects the deposition rates, but also the growth mechanism, morphology and chemical properties are affected by varying the RF.

- The segregated grains of PTFE film become more, uniform, finer, round, and closer by increasing the power, and critical size of the grains declines. The deposition power of PTFE thin films alters the film transparency morphology and the proportion of different polymeric fragments without changing the functional groups and chemical structure of PTFE thin films. As the RF power increases, the fluorine to carbon ratio decreases. The static WCA increases with increasing RF power for the first few minutes of deposition. Further increase in power only changes the WCA slightly. A compact structure forms with higher hydrophobicity at higher power magnitudes.
- Working gas pressure is the most influencing factor on the chemical composition and structure of thin film. As the argon pressure rises, the breakdown of the PTFE polymer chain due to destructive sputtering process enhanced. Consequently, it takes longer to re-polymerise in the form of deposited clusters on the surface of the substrate, resulting in the declining deposition rate. Another reason for the decrease in deposition rate of PTFE with increasing the pressure is the formation of carbon enriched altered layer on the target material. An increase in argon pressure during PVD process decreases the wettability of the PTFE films. With an increase in deposition pressure, the WCA also increases promptly, which makes it possible to use deposition pressure as control tool to obtain superhydrophobic PTFE thin films. WCA changes from 113° at 0.05 mbar to ~ 170° at 0.4 mbar.
- An increase in working distance increases the roughness of thin films. At a target-substrate distance greater than 20 cm, the water contact angle increases steeply. At 14 cm, the WCA is constant around 115° but a steep variation of WCA occurs at 25 cm.
- The surface morphology of PVD thin films changes with changing target temperatures. Low-temperature deposition in zone 1 produces a thin film microstructure with tapered crystallites having equiaxed grains, separated by open voided boundaries. Slight increase in temperature results in zone T type columnar grains followed by an appearance of zone 2 at further rise of the temperature. The temperature change takes place due to variance in sputtering conditions such as deposition power or pressure. High-temperature

zone 3 corresponds to an equiaxed recrystallised grain structure formed as a result of bulk diffusion and recrystallisation.

- Increasing the PTFE film thickness does not alter its polymeric makeup but increase the surface roughness, which results in a rise of WCA.
- The CoF of PTFE thin films remains constant in the range of 0.08 – 0.09 for film thickness above 2 µm; hence, the friction coefficient becomes independent of coating thickness. PTFE Films with less than 1µm thickness have a noteworthy increase in the CoF from 0.08 to 0.15.

The control on PTFE WCA is an essential prerequisite for this research project; therefore, the study conducted by Biederman et al. [89] provides assistance for determining the type of working gas. Argon is selected to manufacture RF-sputtered PTFE thin films because of the film purity and a straightforward trend of RF against WCA (Figure 24). PVD-PTFE thin films will be sputtered at several of magnitudes in the range of 75 – 150 W. The upper limit of this investigative range (150W) is selected to avoid the target melting during sputtering. RF below 75W can also result in significantly low deposition rates. Previous studies reported in Section 3.2.1 also sputtered PTFE at similar deposition powers. The influence of deposition pressure on PTFE film will also be investigated across a wide pressure range (0.05 – 0.25 mbar) to find more about the impact of varying pressure on deposition rates, surface properties, hydrophobicity and associated film properties. A pressure value below 0.05 mbar would lead to more destructive sputtering process leading to a low polymerisation content, and it will make it difficult to get a stable plasma at such a small magnitude of Ar pressure. As the process pressure increases, the possibility to introduce oxygen and other impurities in the residual atmosphere within the sputtering chamber also increases resulting in impure films. There was no existing literature found to back this up quantitatively. Therefore, it is essential to determine the optimum process conditions for PTFE and NiTi such as Ar pressure and deposition power, which would permit to achieve the reasonable deposition rates and desired properties of PTFE and NiTi for the fabrication of nanocomposite.

3.3 PVD sputtered NiTi thin films

Au-Cd were the first shape memory alloys discovered by a Swedish researcher Arne Ölander in 1932 [92]. Later, Greninger and Mooradian observed that a martensitic phase forms and disappears in Cu- Zn according to temperature [92]. W. J. Buehler and F. Wang discovered shape memory properties of NiTi during their research at the US Laboratory in 1962, when they were trying to develop a heat and corrosion resistant alloy. Nitinol is named after its composition and place of discovery, (**N**ickel **T**itanium **N**aval **O**rdnance **L**aboratory) [11; 92; 93]. NiTi is an example of a shape memory alloy (SMA) that can retain its original shape (crystallographic orientation) even after plastic deformation [22; 27; 30; 94]. NiTi SMA exists in defined stoichiometric combination of nickel and titanium partaking following crystal orientations:

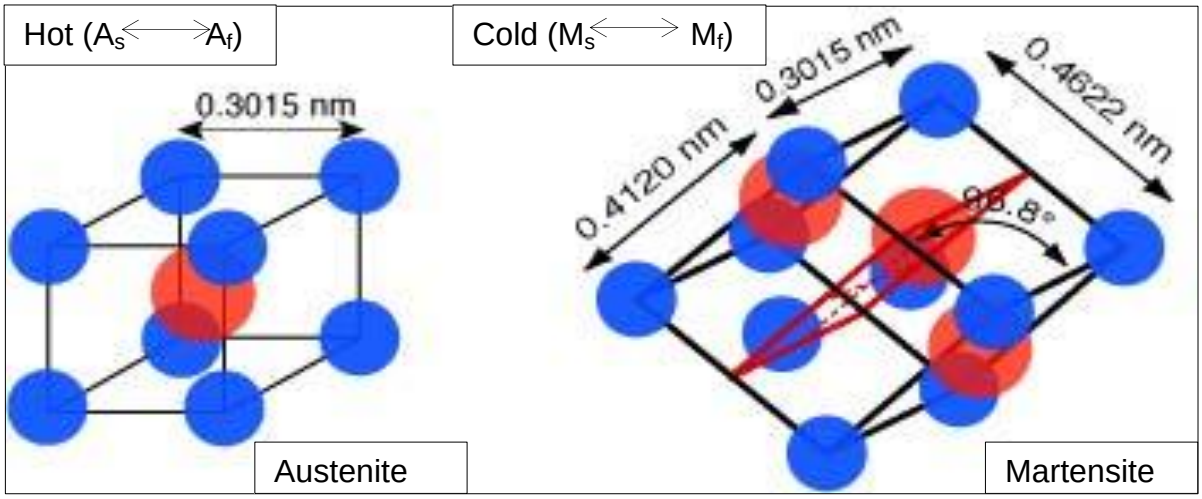

Figure 40: Austenite and martensitic crystal structures of NiTi [95].

- Austenite (A) or B2 is less stressed parent phase of NiTi at high temperature, comprising of interpenetrating primitive cubic (B2') crystals of mild or high symmetry [22; 96].
- Martensite (M) or B19' is highly stressed daughter phase of NiTi at low-temperature, comprising of a monoclinic (B19') crystal of low symmetry. [22; 96] SMA can be bent and deformed easily in this phase producing internal stresses [96].
- Rhombohedral (R) phase is an intermediate phase with a trigonal crystal structure that can appear between the A and M phases. Two-step phase

transformation occurs in the presence of R-phase. A high-temperature austenite phase transforms via the R-phase into the martensite phase at low temperature. R-phase appears during heat treatment in a particular temperature range depending on NiTi composition and thermal history.[97-99]

Austenite NiTi crystal structures can perform solid–solid phase transformations to a martensitic phase at some lower temperature, which can instantaneously reversible without long-range diffusion [22]. Reversible phase transformations can occur due to internal molecular restructuring and are more likely when the convention plane between both phases is consistent along with symmetrical parent phase [22]. Due to a reversible austenite and martensitic transformation NiTi can exhibit solid-state strains that can be recovered by following [22; 30; 94; 100]:

- Thermal shape memory effect (heating / cooling)
- Pseudoelasticity (removing the load / stress within specific temperature range)

Shape memory effect and the pseudoelasticity and discussed in detail in section 3.3.5.

PVD sputtering has deposited NiTi since 1990, and currently is the most common method to deposit NiTi thin films with a thickness less than 2 µm [25; 58]. This method allows depositing the pure NiTi thin films with controlled composition and deposition rate. The reasons for the selection of PVD magnetron sputtering to deposit NiTi thin films are discussed in detail in section 2.2. NiTi thin films are prepared conventionally by PVD magnetron sputtering connected to pulsed DC power supply in low argon pressure. Most of the previous studies selected DC as the power supply for the sputtering process of NiTi due to its conductive property. Most of the previous studies have attained a high vacuum (below 1×10^{-7} mbar pressure) to ensure the film purity, which becomes particularly concerning for NiTi thin films due to high-Ti affinity for oxygen and nitrogen [25; 27; 101; 102]. As-sputtered NiTi thin films are amorphous [25; 27; 103]. Heat treatment of PVD sputtered NiTi is conducted to introduce crystallinity and prevent titanium oxidation as titanium oxidises over time due to its high affinity for atmospheric oxygen [27]. A detailed account of heat treatment methods and previous studies relating to the influence of heat treatment methods on thin film microstructure is provided in section 3.3.2.

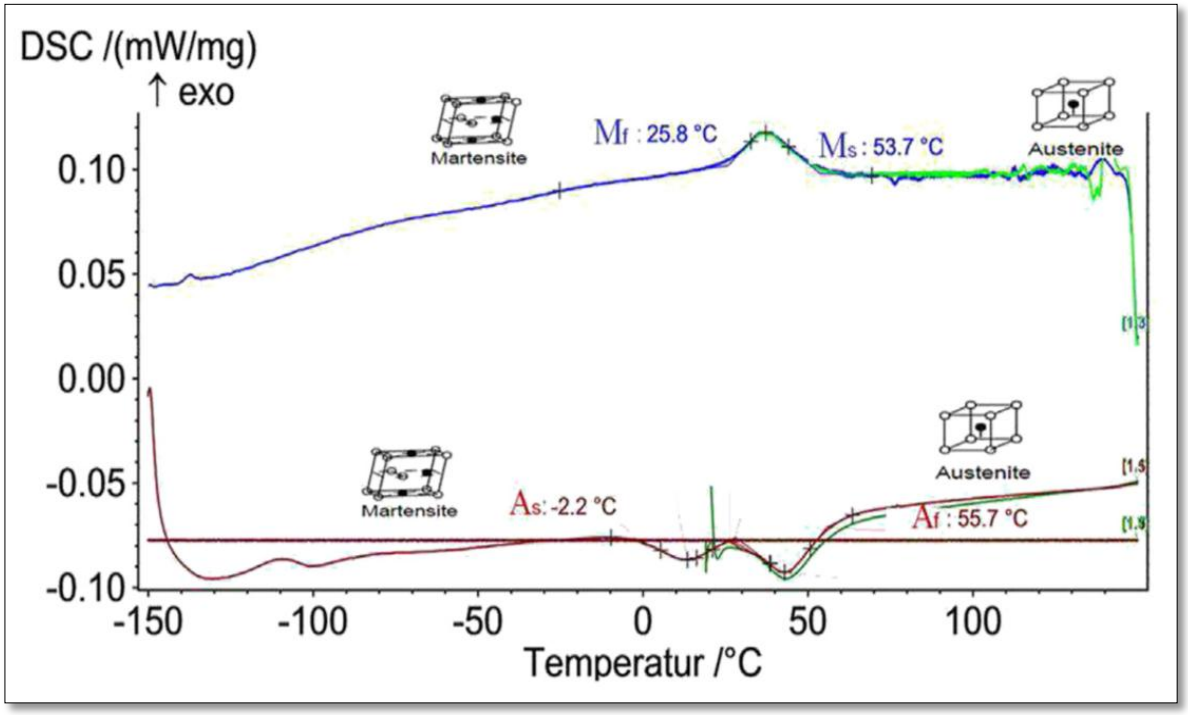

Figure 41: DSC spectra of $Ni_{48.18}Ti_{51.82}$ thin film [104].

The M – A phase transformation happens in a particular temperature interval in crystalline NiTi ([105]. Within that temperature range, heating the martensite alloy initiates the austenite at A_s and finish the transformation at A_f. While cooling, the austenite-martensite starts at M_s and transformation, and completes at M_f [22]. Four transition states (A_s, A_f, M_s and M_f) define the reversible, and hysteretic M ↔ A transformation and vary depending mainly upon the composition of NiTi [105; 106]. These transition temperatures are determined by the onset and offset points of DSC thermograms, as shown in a typical DSC thermogram presented in Figure 41 [100]. Hysteresis defines the transformation behaviour of NiTi by its width, called the hysteresis loop (A_f – M_s). Hysteresis specifies the rapidity of the transformation, which alters by alloying or thermomechanical processing [22]. DSC thermogram of an as-sputtered amorphous NiTi thin film display no thermal events (transition states during hysteresis) [103][25; 27; 103].

Figure 42 is a binary equilibrium phase diagram showing different compositions of belonging to various phase-field regions [107; 108]. The equilibrium phase diagram explains the temperature and composition where NiTi is in thermodynamic equilibrium, and it reveals that NiTi is stable at temperatures above 630°C [22; 107; 108][108].

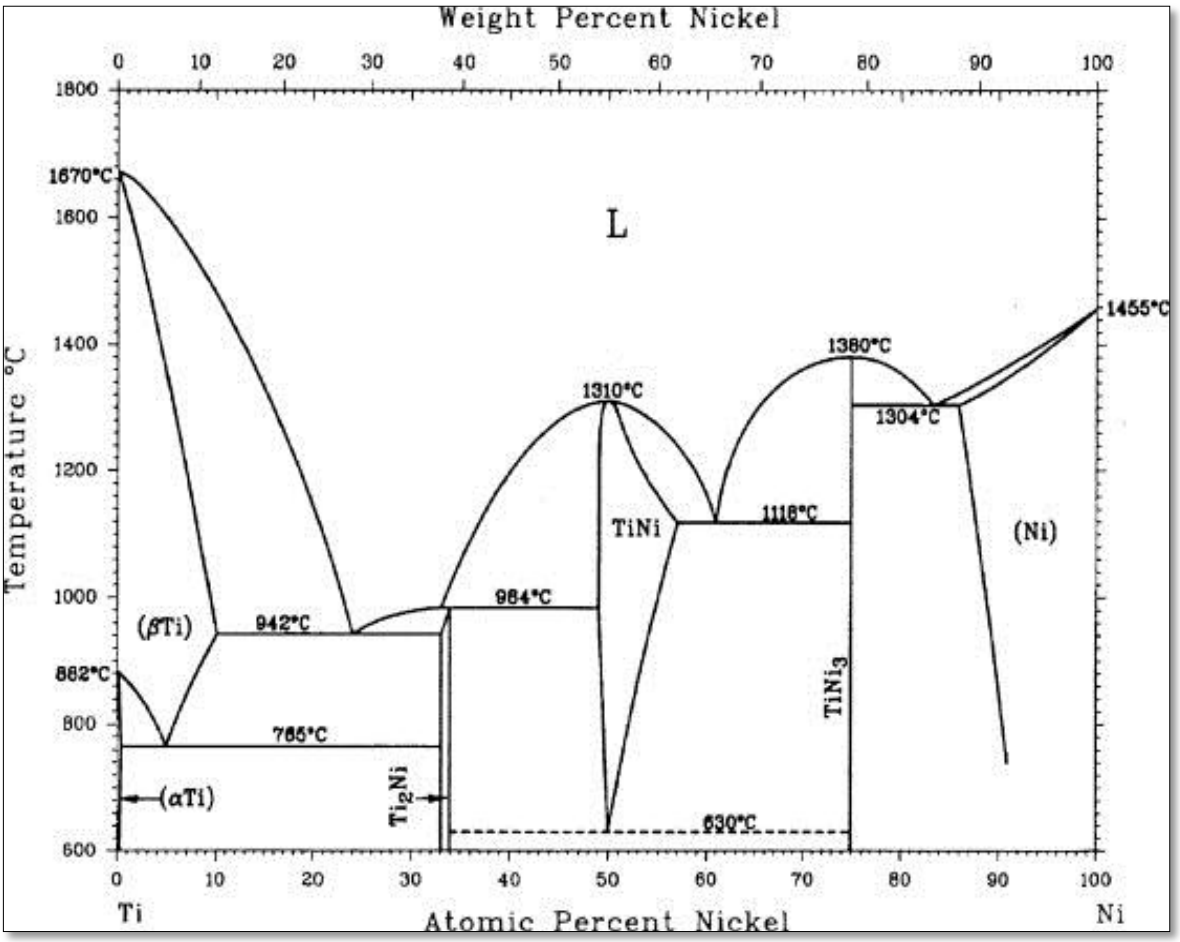

Figure 42: Phase equilibrium diagram of NiTi [107; 108].

3.3.1 Control on NiTi film composition

The compositions of the sputtered films are always titanium deficient with respect to the target (by 2 – 4 at. %) [23; 23]. The sputtering yield of titanium is lower than Ni; therefore, an equiatomic NiTi target deposits a Ti-rich thin film of NiTi [104]. Rumpf et al. [109] documented the Ti loss rates of 4.3 at.% in Ti-rich targets, whereas 0.5 – 1.5 at.% for the Ni-rich sputtering targets. The Ti content also varies during sputtering depending on various sputtering parameters such as process pressure, sputtering power, type of power supply and titanium content within the target [27]. The geometry of the sputtering chamber also influences the NiTi stoichiometry. This was explained by Surbled et al. [102], who reported that the percentage of titanium changes with the radial position of substrate with respect to the target, owing to a faster thermalisation of the nickel at various angular distributions. The control of composition uniformity is necessary, requiring appropriate deposition geometry (e.g. inclining the axis of the targets, and optimizing the substrate-target distance, and the size and shape of the targets) [23]. In current study, the substrate holder will be placed at a suitable fixed position within the sputtering chamber during all experiments involving stationary mode of PVD sputtering. During co-sputtering, a constant target-substrate distance will be maintained in all experiments. The above steps would allow minimising the influence of radial positions and angular distributions within the sputtering chamber on the film composition. Following are some methods to control the Ti content in PVD sputtered NiTi thin films that were adopted by various researchers in the past.

The conventional way to solve the stoichiometric issues in PVD-NiTi thin films is to place pure titanium pieces on the racetrack region of the target, which would allow attaining the desired film stoichiometry [23; 24; 27; 104]. Target modification requires trial and error approach to producing the correct film composition. The compositional adjustment using Ti or Ni pieces requires control of various parameters including geometry, size and position, and any subsequent changes of the deposition parameters require re-adjustment.[23] The stoichiometric issues of NiTi can also be resolved by using an alloy target enriched in titanium [23; 101]. An example is Tillmann et al.'s [104] study who obtained a $Ni_{50}Ti_{50}$ SMA by using a target atomic composition of $Ni_{48.18}Ti_{51.82}$.

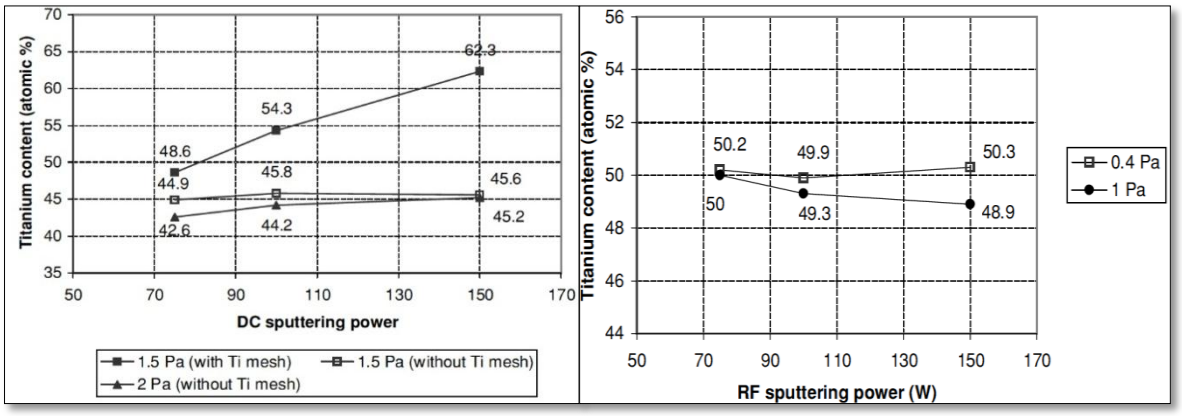

Figure 43: (a) At.% of titanium vs. DC sputtering power for various Ar pressures [27]*. (b) At.% titanium versus RF sputtering power at Ar pressures of 0.4 Pa (4 x 10^{-3} mbar) and 1 Pa (1 x 10^{-3} mbar)* [27].

Another approach to controlling the Ti content in NiTi thin films is by adjusting the process parameters. The control of film composition from the separate targets, by adjusting the power ratio, which is more flexible than the use of additional Ti pieces [23]. Kumar et al. [38] adjusted the films composition by sputtering power. Sanjabi.et al. [23] suggested controlling the film composition via target power when using separate Ni and Ti targets. Zhang et al. [110] controlled the composition of NiTi films by changing the Ti target DC power (between 188 and 204 W), along with fixed power magnitude (800 W) of a $Ni_{50}Ti_{50}$ target. Wibowo et al. [27] also investigated the influence of power and pressure on the film composition, as shown in Figure 43. Figure 43 describes an increase in titanium atomic percent of DC sputtered NiTi film with the increases in power; however, it also increases slightly with a decrease in pressure. The titanium content changes marginally with the increasing power during RF deposition at 4 x 10^{-3} mbar; however, when pressure is increased to 1 x 10^{-3} mbar, the Ti content decreases promptly with a rise in power. The titanium content in NiTi thin films increases with DC or RF sputtering power because the titanium's strong affinity for oxygen creates a thin layer of TiO_x on the surface of sputtering target. Sputtering of TiO_x requires higher energies than sputtering metallic Ti. The increase in sputtering power increases the energy of argon ions, which in turn increases the rate of sputtering TiO_x. As a result, higher titanium content is formed in the NiTi coatings [27].

Wibowo et al. [24; 27] suggested the deposition of NiTi at low DC power because increasing the sputtering power has significant implications on coating properties such as residual stress. The stoichiometric problems of NiTi thin films can be solved by varying the working gas pressure in the chamber. The shape memory effect deteriorates with an increase in argon pressure, despite controlling the alloy composition [23]. Another problem is that the films become brittle at high pressures, and the structure declines [23].

In this research project, the NiTi stoichiometric composition will be adjusted by adding Ti pieces on the racetrack of equiatomic NiTi target. EDX will be used to monitor the film composition after each deposition run; therefore, adjusted Ti content will be adjusted by a trial and error approach. This selection is made because the choice of sputtering parameters also depends upon PTFE deposition and the intercalation during the nanocomposite fabrication. Therefore, any changes in sputtering conditions for adjusting the NiTi film composition, would alter the nanocomposite properties. The manufacturing process would involve sputtering from PTFE and NiTi targets. Thus, the use of additional Ti pieces excludes the need for the third Ti target to adjust the Ti content.

3.3.2 Heat treatment and crystallisation of PVD sputtered NiTi thin films

Sanjabi et al. [23] heated equiatomic NiTi thin films up to 600°C, at a constant heating and cooling rate of 10°C/min, to investigate the crystallisation temperature of PVD sputtered NiTi thin films. By plotting the heat flow against temperature, a crystallisation temperature at 472°C was measured (Figure 44), associated with an enthalpy change of 28 J/g. Zhang et al. [111] also determined by DSC analysis that the crystallisation temperature of PVD sputtered NiTi thin films lies within the range of 470 – 500 °C. Vestel et al. [69; 112] recommended that a thick-freestanding amorphous NiTi films need annealing at least 400°C to become crystalline. Yang et al. [113] observed an exothermic crystallization peak at 497°C and informed that the film was still amorphous at 450°C but crystallized at 500°C. Overall, the above observations suggest 500°C to be enough temperature for the annealing of NiTi.

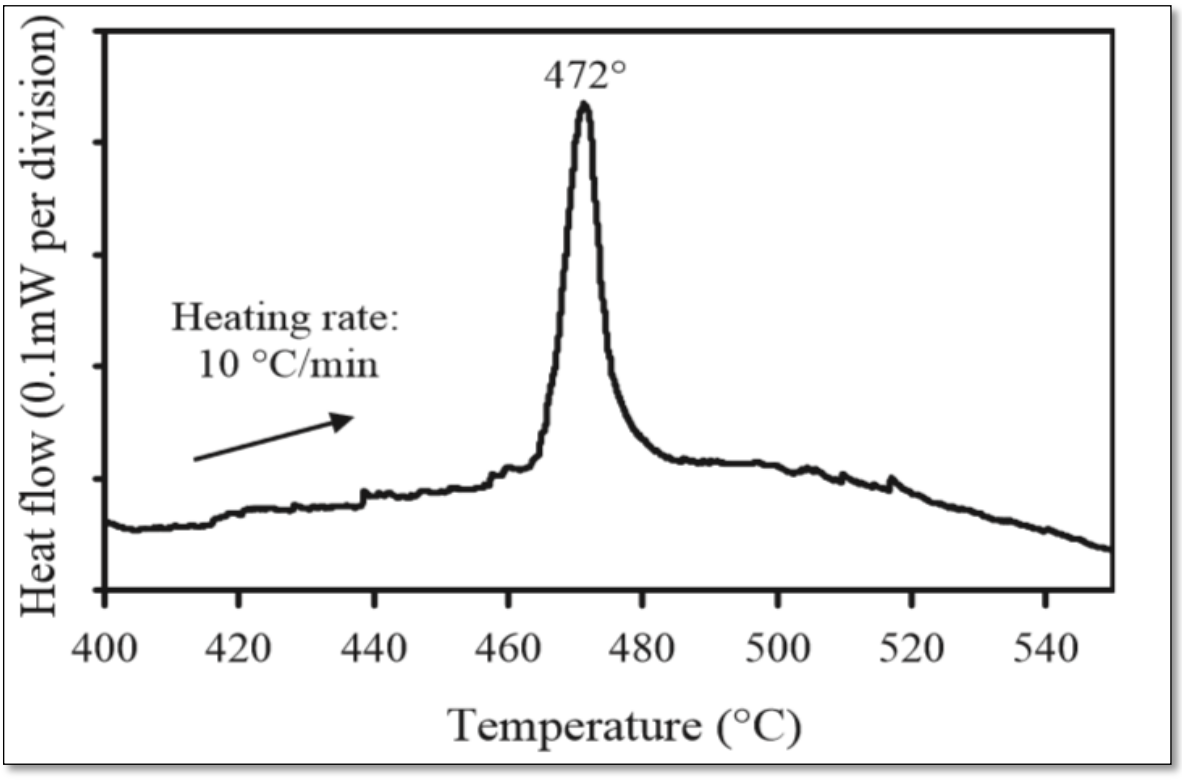

Figure 44: DSC trace of crystallisation temperature of as-deposited near equiatomic thin films [23].

The heat treatment not only improves the as-deposited thin film features by crystallization but also introduces some new structural features within coatings [45]. Those structural characteristics include varied crystalline orientation of NiTi and Ni-rich and Ti-rich precipitates at the grain boundaries. Heat treatment of as-deposited amorphous thin films results in the lesser amount of NiTi in film undergoing the phase transformation compared to that of NiTi target. This was investigated by Wibowo et al. [27] who reported that the outcome of the enthalpy change in heating and cooling is 1.8 Jmg^{-1} from PVD sputtered NiTi thin films, which is lower than that of sputtering target enthalpy change (5 Jmg^{-1}). Nomura et al. [114] suggested quenching the NiTi films after heat treatment, but Wibowo et al. [27] recommended no quenching because large surface area to volume ratio of thin films leads to faster cooling. Cooling is critical to ensure no further reactions; particularly precipitation takes place after crystallisation of NiTi thin films. Substrate heat treatment and post sputter heat treatment (solution heat treatment) are two ways to crystallise NiTi coatings as explained below.

During substrate heat treatment, the substrate temperature is maintained in the range of 350 – 460 °C during deposition. Wang et al. [115] reported that only a few areas exhibit crystalline structure at 320°C, while the thin film becomes fully crystallized when the substrate temperature was increased to 370°C. Tillmann et al. [104] also prepared crystalline Ni-rich thin films of austenite NiTi having Ni-rich precipitates by maintaining the substrate temperature at 425°C. Wibowo et al. [27] suggested the substrate annealing at 550°C, above the crystallisation temperature of NiTi alloy. The surface of the films that were substrate heat-treated at 550°C appeared to be foggy because of large grain size ~ 600 nm diameter as shown in Figure 46c. The larger grain size appears because of high substrate temperature annealing. The grains appearance matches to the structure described by Movchan and Demchisin zonal model. According to Movchan and Demchisin zone model, sputter-deposited coatings should have three-dimensional large grains [27]. Annealing a Ti-rich film at a lower temperature of 500°C, results in transformation below room temperature because of the early stage precipitation known as Guinier–Preston (GP) zones formation [23]. Annealing at temperatures above 600°C can resolve this matter [23].

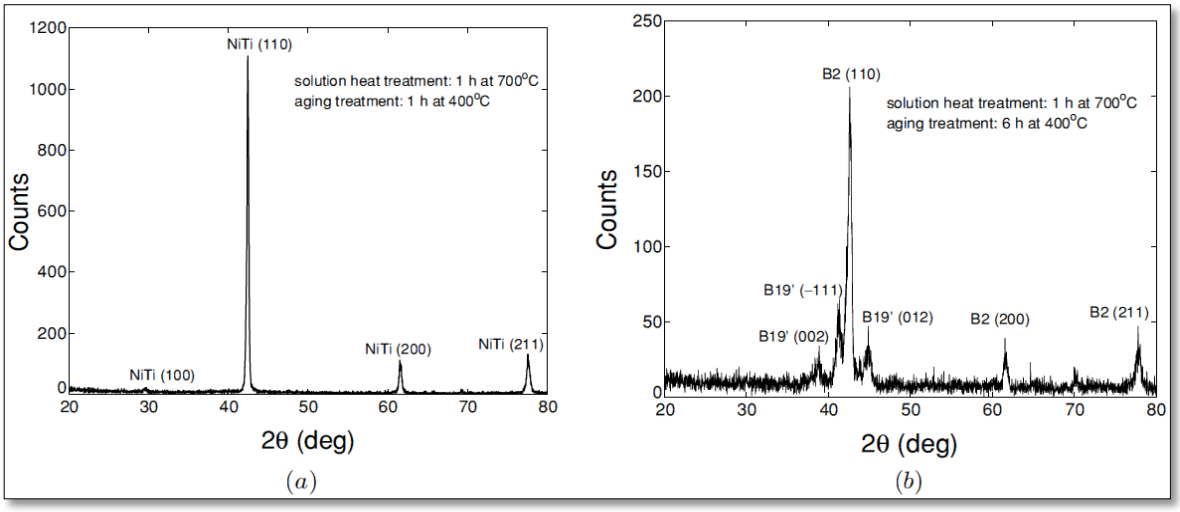

Figure 45: XRD profiles of (a) 1h aged film (b) 6h aged film (aging at 400°C) [27].

Wibowo et al. [27] conducted post-sputter heat treatment of PVD-NiTi thin films in a vacuum, after depositing the films at room temperature. Post-sputter solution heat treatment was completed at 700°C for 1 hour, and the films cooled down to room temperature in a vacuum chamber. NiTi films were then aged (precipitated) at 400°C, for 1 hour and 6 hours to introduce precipitates so that the precipitates such as Ti_3Ni_4 or Ti_2Ni start to disperse as fine particles above 400°C, as presented in the phase diagram (Figure 42a). XRD patterns in Figure 45 display that the film aged at 1h (Ni 51 at% Ti) shows B2 phase while the film aged at 6h (Ni 50.7 at% Ti) appears as a mixture of austenite (B2) and martensite phase (B19). Comparison of films aged at 1h and aged at 6h show that the film aged at 6h has higher enthalpy change (ΔH), equivalent to that of sputtering target (Jg^{-1}). It suggests more amount of NiTi in the film undergoing phase transformation.[27]

Kumar et al. [116] suggested taking an advantage of both substrate heat-treatment and post-sputter heat treatment. They deposited two sets of Ti-rich NiTi films by PVD sputtering at the substrate temperature of 300°C and 400°C, and found both film sets having amorphous structure. To introduce the crystallinity in as-deposited NiTi films, an annealing was conducted at 600°C for 4 hours, which resulted in martensitic thin films having Ti_2Ni precipitates. The reasons for these conditions for heat treatment are not explained in their study. The possible advantage of performing both types of heat treatments for PVD-NiTi can be explained as follows. If only post-sputter heat treatment was conducted, the thin films would have required aging before annealing step requiring higher thermal energy along with more precipitation formation.

Heating rate during the post-sputtering annealing heat treatment is an influential factor for the phase transformation of SMA. Liu et al. [117] investigated the onset temperature, the peak temperature and exothermic enthalpy released on crystallisation for the $Ni_{50.5}Ti_{49.6}$ thin films at various heating rates. The onset temperature increased from 529°C to 556 °C by increasing the heating rate from 5 to 50 K/min, and the transformation peak also alters from 535°C to 657 °C, while the enthalpy changes from 24.8 to 45.7 J/g. Therefore, the onset temperature and the transformation peak temperature increases with the increasing heating rate, whereas the reaction becomes more exothermic.

Substrate heat treatment and post-sputter heat treatment methods have their individual benefits and drawbacks. Substrate heat treatment eliminates the need for an additional post-sputter annealing process [104; 115]. Other advantages of substrate heat treatment in comparison to post sputter heat treatment include higher reliability, prevention of surface oxidation, inhibition of polymeric crystallisation and a lower prospect for the film substrate reactions [101]. Post-sputter heat treatment undesirably influences the morphological features, microstructure and shape memory properties of NiTi thin films due to higher temperature, which can be avoided by substrate heat treatment while sputtering [38; 101]. Thus, the substrate heat treatment also reduces the thermal processing budget due to lesser heating needs [101].

Although the crystallisation temperature of NiTi thin films has always been found ranging from 470°C to 500°C, but the post-sputtered heat treatment is performed at or above 600°C while the substrate heat treatment is conducted at 300 – 450 °C [101][115]. The transformational temperature deviates from its original value because of precipitates formation during the heat treatment. Different precipitated species influence the crystal structures differently resulting in an increase or decrease in the transformational temperature. For example, Elahinia et al. [108] investigated the precipitation in a Ni-rich SMA (NiTi and $Ni_{14}Ti_{11}$) after subjecting the alloy to 300 – 500 °C aging treatment. During the precipitation reaction, the migration of Ni atom to the precipitate ($Ni_{14}Ti_{11}$) takes place, which causes diffusion of Ti atoms into the $Ni_{50}Ti_{50}$ matrix. If the aging temperature increases further to 500°C, the precipitates dissolve and Ni atoms diffuse into the matrix. This increases the overall

diffusion rate of SMA resulting in a decrease in the transformation temperature, and the transformation time decreases [108].

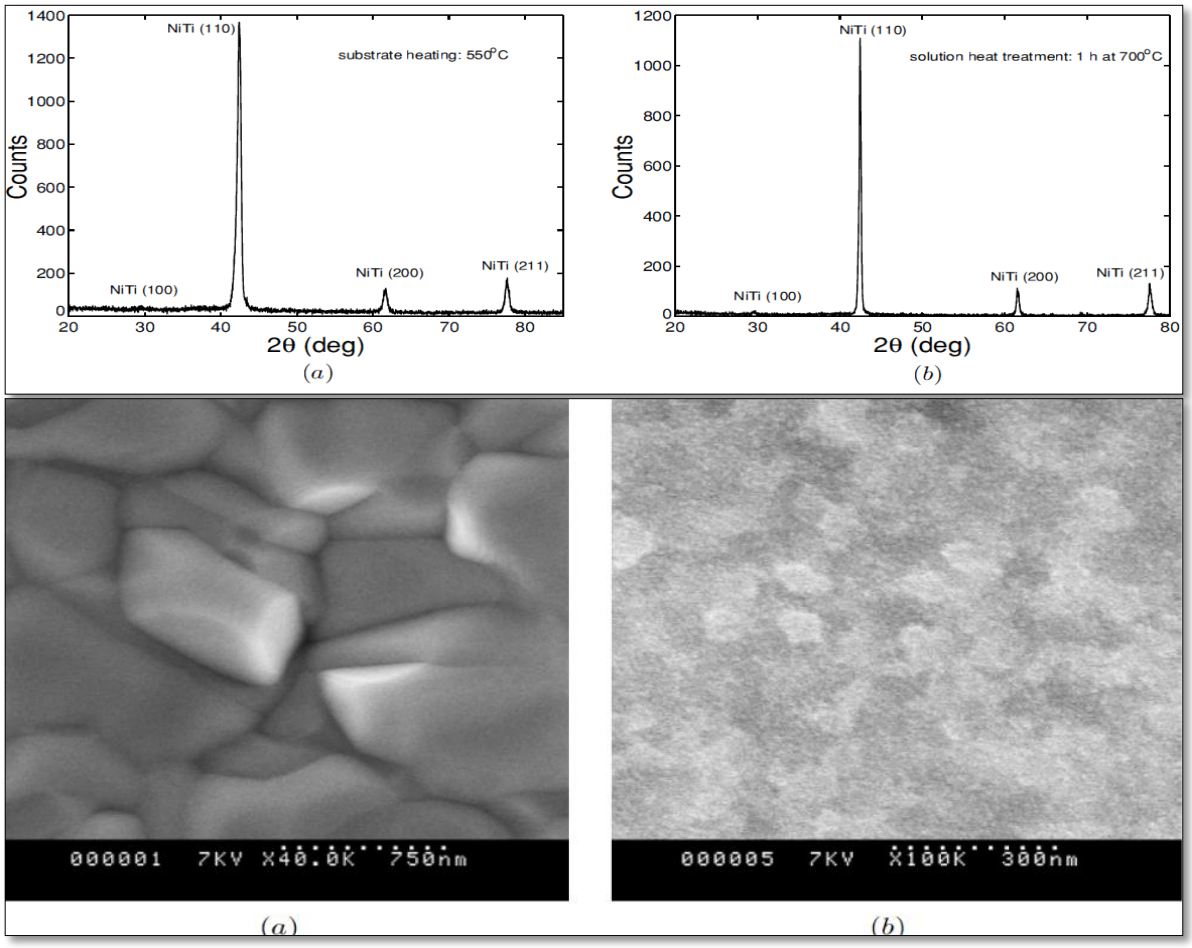

Figure 46: XRD profiles of (a) a substrate – heated NiTi film (Ni – 47.3 at% Ti) and (b) a post-sputter heat treated NiTi film (Ni – 51.6 at% Ti). FE-SEM images of the grains (100kx) for (c) Substrate heated NiTi film at 500°C (magnitude of 40kx). (d) Solution heat treated NiTi film at 700°C for 1h and aged at 400°C for 6h.[27]

Wibowo et al. [27] also compared the characteristic XRD peaks of NiTi crystals, which were obtained in the films subjected to substrate and post-sputter heat treatments. The XRD patterns shown in Figure 46 show that there are no differences in the crystal structures of NiTi subjected to each of those heat treatment methods. It was noted that the NiTi films for each heat treatments method have different composition, i.e. Ni – 47.3 at.% Ti for substrate heat treatment and Ni – 51.6 at% Ti for solution heat treatment. The enthalpy change of post-sputter heat-treated aged films (ΔH_{rev} = 5.44 Jg^{-1} and ΔH_{fwd} = -5.37Jg^{-1}) was much higher compared to those of only substrate treated films (ΔH_{rev} = 1.81Jg^{-1} and ΔH_{fwd} = -1.89Jg^{-1}). A greater portion

of NiTi film undergoes the phase transformation by post-sputter solution heat treatment followed by aging in comparison to substrate heat treatment. The grain size of post-sputter heat treated thin films is much smaller than substrate heat-treated thin film grain size, while the shape is similar, as shown in Figure 46. The smaller grains would require less activation energy corresponding to higher content enduring a phase transformation. Therefore, post-sputter heat treatment is better than substrate heating because of more part undergoing phase transformation, means more energy is available for NiTi film to return to their original shape during reverse transformations. Post-sputter annealing heat treatment is chosen for this project because the higher transformed content of thin film in post-sputter heat treated and aged for a longer time leads to a successful transformation.

3.3.3 Morphology, precipitation and microstructure of PVD-NiTi

SEM analysis shows that the PVD-thin films have smooth and free from pinhole like surface defects [103; 114]. The surface roughness of the as-deposited thin films can be reduced by etching or polishing techniques, but these processes bring some defects into the thin films [45]. The SEM images of 2 µm thick freestanding NiTi films prepared by PVD sputtering at a deposition temperature of 450°C are presented in Figure 47. The images specify a dense crystallised microstructure matching to the high-temperature zone 3 of the thin film models. This type of structure results from an extensive volume diffusion. A ductile deformation apparently produced the triangular shaped structures in the material emerging in the lower part of Figure 10a during the fabrication.[118]

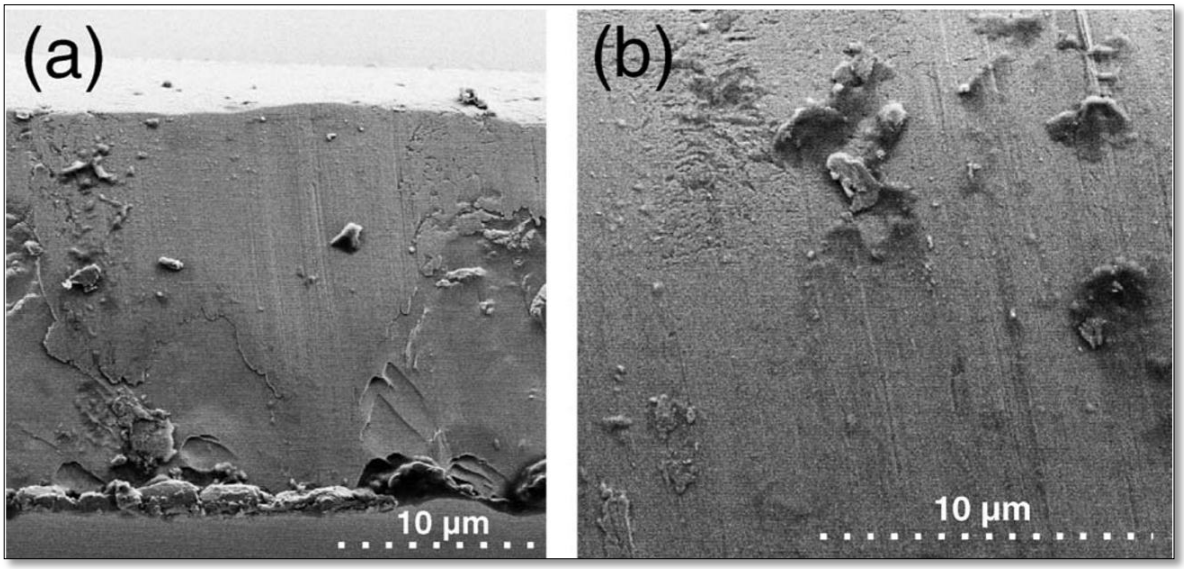

Figure 47: SEM images of freestanding NiTi (21m in thickness) indicate a dense microstructure. The triangular shaped structures in the material, which emerge in the lower part of (a), were supposedly caused by a ductile deformation of the NiTi because of the fabrication method.[118]

The microstructure and transformation temperature of PVD sputtered NiTi thin film are significantly affected by precipitation during heat treatment [25; 27]. These precipitates are related directly to the film composition. Sanjabi et al. [23] explained the relationship between the NiTi film composition with the microstructure and precipitation. Two sets of XRD spectra of three thin films (Ti-rich ($Ni_{47.2}Ti_{52.8}$), near-equiatomic ($Ni_{49.4}Ti_{50.6}$) and Ni-rich ($Ni_{51.2}Ti_{48.8}$) film) are given in Figure 48 to explain

this relationship, which were deposited at room temperature followed by annealing at 500°C. One set of XRD trace was obtained at RT while the second set was examined at 100°C. The results obtained by Figure 48 along with the results of other studies are summarised below to understand the effect of NiTi stoichiometric composition on the microstructure mainly precipitation.

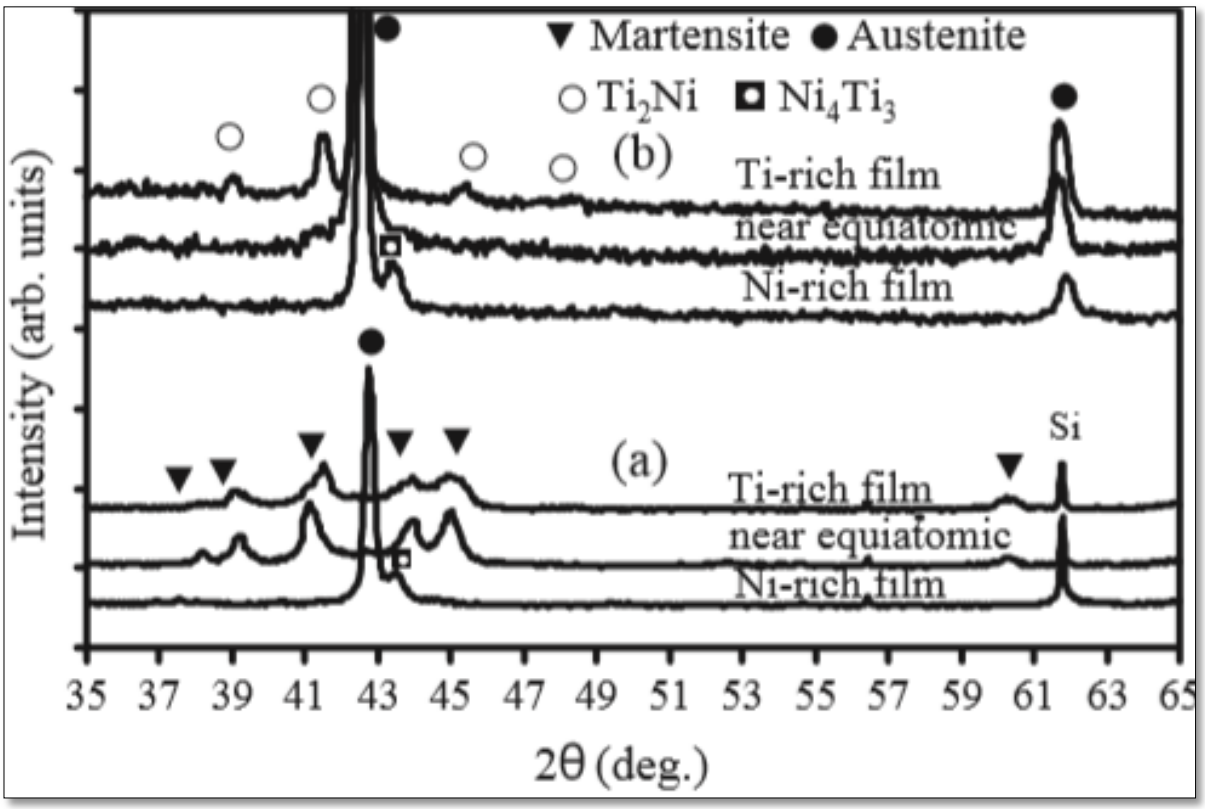

Figure 48: XRD profiles of Ti-rich ($Ni_{47.2}Ti_{52.8}$), near-equiatomic ($Ni_{49.4}Ti_{50.6}$) and Ni-rich ($Ni_{51.2}Ti_{48.8}$) films annealed at 500°C (a) RT (b) 100 °C [23].

No precipitation is observed in **equiatomic** NiTi films, but the precipitates form in both Ni-rich and Ti-rich, coatings. The equiatomic SMA thin films at room temperature display monocline structure and prime martensite (B19') 2Θ diffraction peaks are observed at 38.2 {110}, 39.1 {002}, 41.3 {111}, 44.05 {020}, 45.1 {012} and 60.2 {022}. Those martensitic peaks disappear after heating at 100°C, and the 2Θ austenite peaks appear at 42.7 {110) and 62 {200}.[23]

In **Ti-rich** NiTi thin films, Ti_2Ni precipitates nucleate and grow along with grain boundaries of the austenite phase [23]. In the XRD spectra presented in Figure 48, the Ti-rich NiTi thin films show similar XRD traces as the equiatomic NiTi with additional precipitation peaks for Ti_2Ni at room temperature. The Ti_2Ni peaks have a

similar position as martensite traces at room temperature (2Θ: 37° to 47°). A distinct peak of Ti_2Ni can be observed near austenite peak (2Θ = 42.7°) at temperatures above 100°C, which does not alter its position on any further heating. The traces associated to Ti_2Ni include 2Θ = 38.9 {422}, 2Θ = 41.4 {511}, 2Θ = 45.3 {440}, and 2Θ = 47.5 {531}. Vestel et al. [69] reported that the Ti_2Ni precipitates begin to nucleate near to the end of the crystallisation process at the columnar / plate grain interfaces having maximum density. A high titanium concentration at crystalline / amorphous interfaces and high precipitation at the columnar/plate grain interfaces was observed because the excess titanium slides into the amorphous region at those interfaces. The amorphous–crystalline interfaces are ostensibly flat, which make it easier for Ti atoms to drive in during crystallisation.[69]

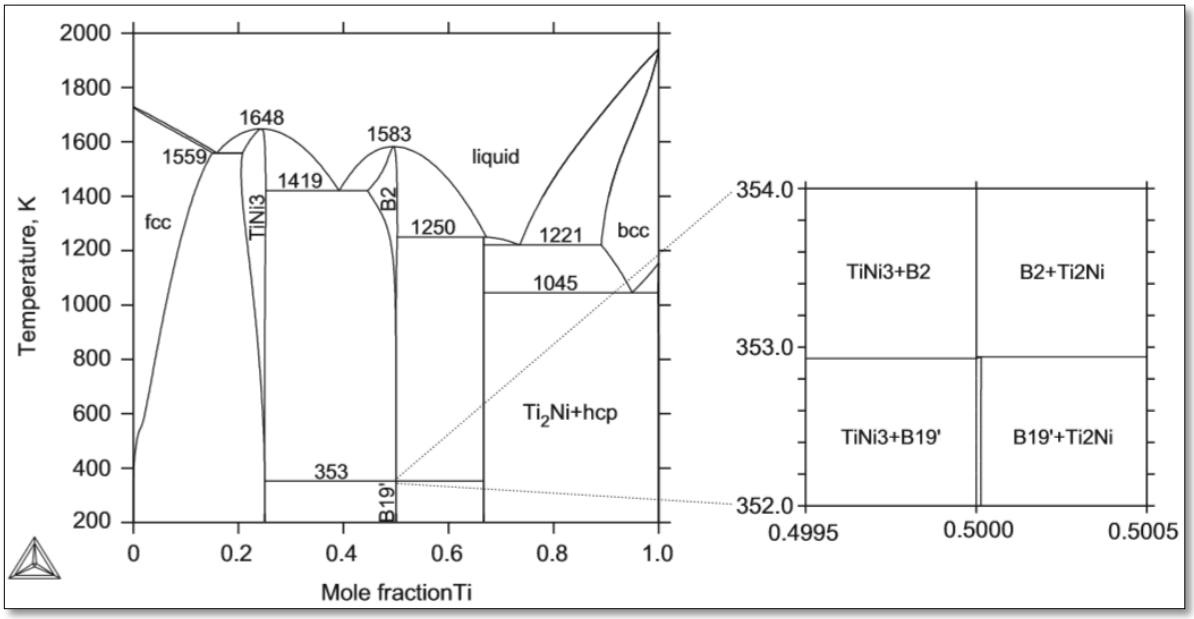

Figure 49: Equilibrium phase diagram calculated for NiTi system [119].

Ni-rich NiTi thin films at room temperature exhibit austenite (B2) CsCl type structure, and display a large XRD peak at 2Θ = 42.7° {110} and a small peak at 2Θ = 61.2° {200} [23]. Ti_4Ni_3 peak is observed at 2Θ = 43.4° {122} at room temperature and at 100 °C, which forms within the matrix of Ni-rich, thin films [23]. Miyazaki et al. and Tillmann et al. [101; 104] also observed non-equilibrium precipitation reactions (relating to Ni_4Ti_3 precipitates) during sputtering of Ni-rich NiTi thin films, resulting in a weak and broad peak at 2Θ = 37.8 in the XRD profile. The inset of Figure 49 shows the presence of the line compounds of the metastable phase of Ni-rich NiTi include Ti_3Ni_4 and Ti_2Ni_3, which form during aging [119]. Gong et al. [120] also fabricated the Ni-rich thin films ($Ni_{51.2}Ti_{48.8}$) by PVD sputtering at 160W DC power supply and 5 x 10^{-3} mbar working gas pressure, followed by annealing and characterising. Mainly austenite crystal phase was observed along with Ni_4Ti_3 precipitates, which are typical for PVD-sputtered Ni-rich thin films of NiTi.

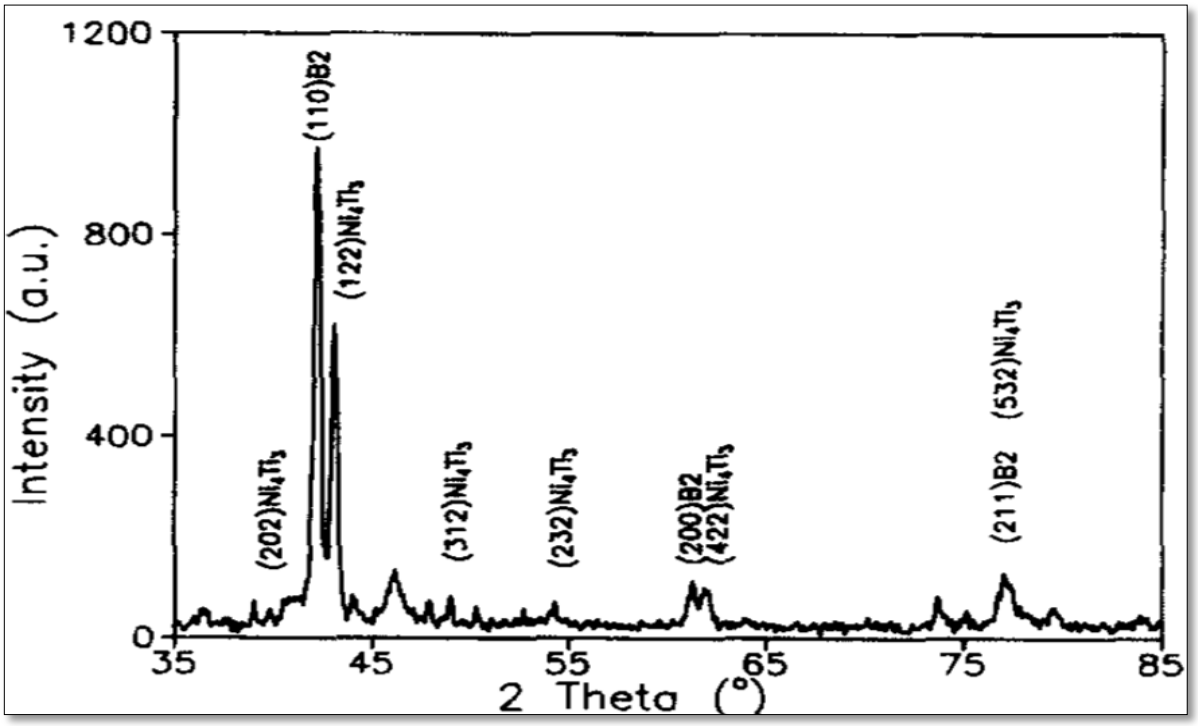

Figure 50: XRD pattern of $Ni_{51.2}Ti_{48.8}$ coatings [120].

Surface roughness delayed the onset of surface nucleation. For very smooth surfaces, crystallization of columnar grains nucleated quickly, but after lateral impingement, inward growth was more sluggish. Martensitic phase has a rougher film surface than its parent phase. Martensitic phase having multidirectional laminar microstructures forms, when the grains perform the bulk nucleation in the interior of the NiTi thin films. This process should remain independent of the surface nucleation of the columnar grains, previously occurred or happening simultaneously. This process yields the stratified crystalline regions with relatively shallow and wider grains. The microstructure of martensite in the sputter deposited $Ni_{48.9}Ti_{51.1}$ thin films changes with increasing size and amount of Guinier – Preston (GP) zones. The GP zones are the coherent plate precipitates with a few atomic layers thickness that affect the twinning modes of the B19 phase for the sputter-deposited NiTi thin films. A few GP zones are observed in equiatomic NiTi thin films.[38; 69; 112; 121]

The microstructure of PVD sputtered NiTi thin film is considerably vulnerable to stoichiometric disruption by minor changes to the process conditions [25; 27]. Sanjabi et al. [23] investigated the influence of process pressure on film composition, microstructure and transformation temperatures. They compared the XRD spectra of two as-deposited NiTi thin films sputtered at different process pressures. $Ni_{48.8}Ti_{51.2}$ thin film deposited at 1.2 x 10^{-2} mbar and $Ni_{50.6}Ti_{49.4}$ film deposited at 6 x 10^{-3} mbar. Although, the same target material was used to deposit both films, but the NiTi films vary in composition due to a different process pressures. The films deposited at various argon gas pressures exhibit different crystalline structures after annealing at 500°C for 1 hour. $Ni_{48.8}Ti_{51.2}$ film deposited at 1.2 x 10^{-2} mbar present a complete austenite crystalline structure with peaks at $2\Theta = 42.7°$ {110} and $2\Theta = 62°$ {200}, and display transformation below room temperature (one unclear transformation type peak was also observed around 40°C, which was unexplained in the study). $Ni_{50.6}Ti_{49.4}$ film deposited at 6 x 10^{-3} mbar shows a martensitic structure at room temperature that indicates that the phase transformation above the room temperature.

Another example of the influence of process conditions on NiTi film properties is the effect of substrate temperature on the film thickness and the microstructure. PVD-NiTi coating thickness increases from 2.2 to 2.5 µm by increasing the substrate heat

treatment temperature from 350°C to 650°C [38]. Tillmann et al. [101] reported a similar trend, as they reported that the film thickness also shows a 20% increase by increasing the temperature from 80°C to 305°C, which is due to the fact that the nucleation and growth zones are more active at higher temperature. No significant changes were reported for increasing the temperature from 305 to 425°C. Further increasing the temperature to 505°C decreases the film thickness by 12% because the higher volume diffusion results in a more conventional and denser microstructure. NiTi thin film sputtered at 425°C substrate temperature exhibit R-phase resulting in a two-step transformation. Increasing the substrate temperature to 525°C only displays one-step transformation [101]. Ni_4Ti_3 precipitates have also been reported as another reason for the two-step transformation, which dissolves at higher temperature [101; 108].

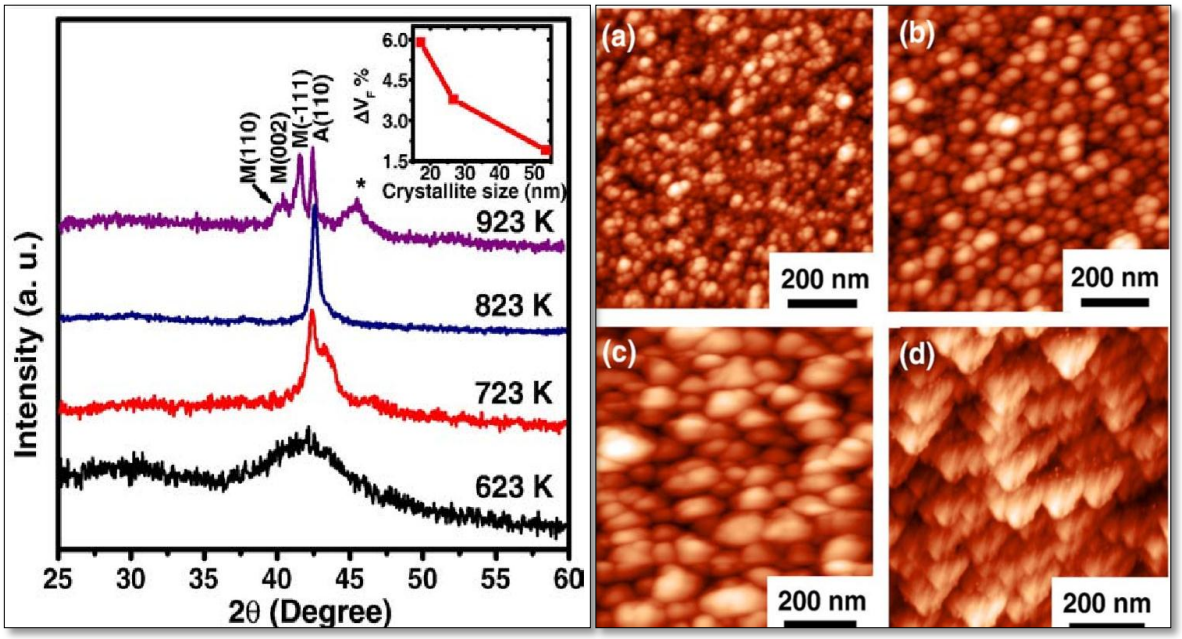

Figure 51: XRD profiles of NiTi films prepared at Ts of 350°C, 450°C, 550°C and 650°C (left image). AFM topographs of NiTi sputtered at Ts of (a) 350°C, (b) 450°C, (c) 550°C and (d) 650°C (right) [38].

The grain size and the crystallisation extent increase with an increase in the substrate temperature. Kumar et al. [38] explained this by setting the substrate temperatures at 350, 450, 550 and 650°C, and examining the peak sizes provided in XRD profile given in Figure 51. An amorphous film was deposited at 350°C followed by an austenite phase *at* 450°C and 550°C. Further increasing the temperature to 650°C displays fewer intensity peaks of the monoclinic martensitic structure along with B2 phase. The rapid crystallization from 350°C to 550°C restrains the atoms as the crystallized grains of a tiny size. This occurs due to an energetic process involving the migration of absorbed atoms on the surface to the favourable energy positions generating a strong {110} plane texture. At a further higher temperature such as 650°C, the small grains aggregate and grow into broader grains. The estimated average crystal sizes in the films deposited at 450, 550 and 650°C were 17.2, 26.7 and 53.4 nm respectively, which were calculated by the broadening of the XRD lines of austenite peaks and using the Sherrer's formula. AFM images in Figure 51 demonstrate a smooth structure for 350°C followed by an average roughness of 6.75 and 8.12 nm for the facets containing thin films deposited at 450°C and 550°C respectively. Martensitic plate facets with preferential in-plane orientation of martensitic phase are seen at 650°C substrate temperature. A higher surface roughness for the films deposited at 650°C confirmed the martensite crystals. As the crystallite size increases, the volume of the grain boundaries decreases, but the grain boundaries increase in quantity [38]. Similar observations are found in Figure 46 for the SEM images provided by Wibowo et al. [27], where the grain size is, and the grain boundaries are proportional to each other. Table 7 summarises the grain sizes of PVD-NiTi estimated by Kumar et al. [38] who employed various characterization techniques to determine the grain size.

Table 7: Various parameters of NiTi films deposited at Ts of 350°C, 450°C, 550°C and 650°C [38].

Sample number	Substrate temperature (T_s)	Grain size (nm)				Avg. roughness (nm)	EDAX at. wt.% Ti: Ni
		XRD along (110) peak	FESEM	TEM	AFM		
1.	623 K	–	21.7	20.1	22.2	3.87	49.7:50.3
2.	723 K	17.2	38.3	33.6	39.6	6.75	49.9:50.1
3.	823 K	26.7	77.7	67.0	80.0	8.12	50.2:49.8
4.	923 K	53.4	108.2	98.2	112.5	23.4	50.6:49.4

Wang et al. [115] and Kumar et al. [38] investigated the influence of temperature on the grain size of substrate heat-treated thin films. Wang et al. [115] found similar results as Kumar et al. [38] that increasing the substrate temperature increase the grain size. Lack of crystallinity was reported at a deposition temperature of 320°C because a fully crystallised thin films from at 370°C having grain size of approximately 70 nm. Further increasing the temperature increased the grain size up to the micron scale.

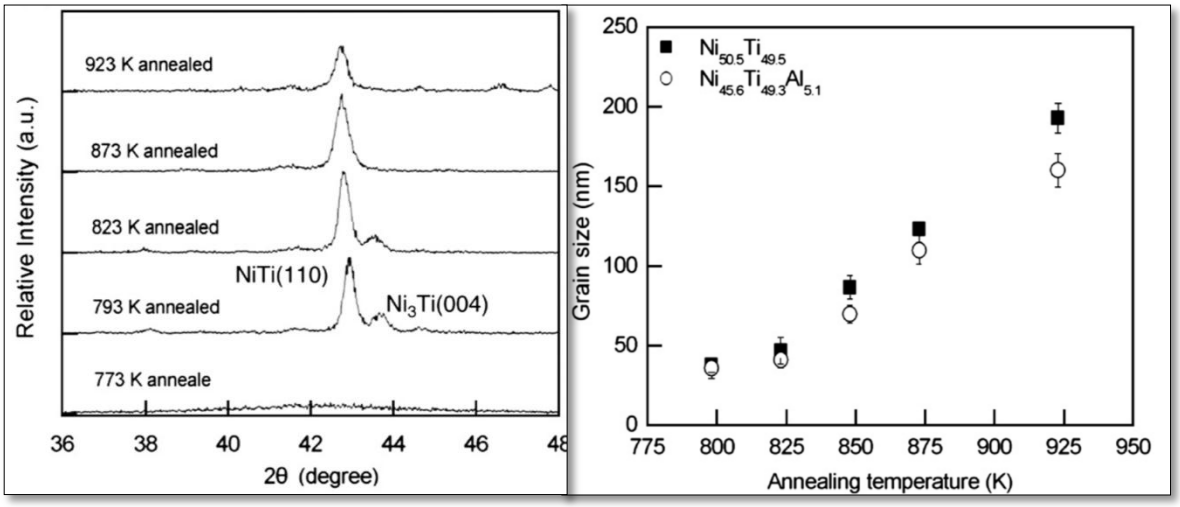

Figure 52: XRD patterns at several annealing temperatures from 773 K (500°C) to 923 K (650°C) for $Ni_{50.5}Ti_{49.5}$ thin films (left). Grain size of annealed thin films at different annealing temperatures from 773 K (500°C) to 923 K (650°C) for $Ni_{50.5}Ti_{49.5}$ and $Ni_{45.6}Ti_{49.3}Al_{5.1}$ (right).[117]

Liu et al. [117] also examined the effect of post sputter heat treatment temperature on the grain size of $Ni_{50.5}Ti_{49.5}$ thin films deposited on a silicon substrate (Figure 52). The thin films were annealed at 500, 525, 550, 600, and 650°C at DSC heating and cooling cycle of 5 – 50 K/min. An amorphous structure is observed for the films heat-treated at 500°C. Above 525°C, the consistent NiTi {110} and Ni_3Ti {004} phases were found, matching to the binary NiTi phase diagram for Ni-rich alloys. 500°C was the most suitable temperature because Ni_3Ti peak disappears. The grain size of annealed $Ni_{50.5}Ti_{49.5}$ was calculated by Scherrer's formula, for which NiTi {110} peak was considered. Figure 52 shows that as the annealing temperature increases, the grain size also increased. By combining the results in Figure 51 and Figure 52, it can be deduced that the heat treatment method does not affect the trend of grain size against the heat treatment temperatures. As the annealing temperature increases, the grain size also increases for both substrate treated and solution heat-treated NiTi thin films.

3.3.4 The relationship between 'NiTi film composition and heat treatment method' with thermal events during hysteresis

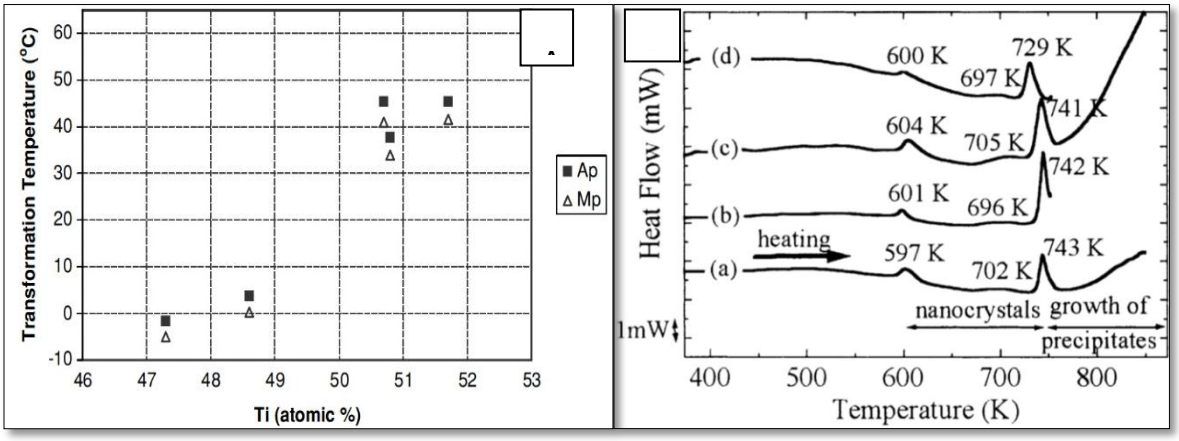

Figure 53: (A) The disparity of transformation temperatures with Ti content.[27] *(B) DSC thermograms crystallization of several Ti Ni thin films: (a) 48.0; (b) 48.7; (c) 49.7 and (d) 51.3 at.% Ti* [102].

Compositional control of NiTi thin film and determining the martensitic and austenitic transformation temperatures are crucial to adjust the working temperature of the microdevices [24; 103]. The transformational temperatures depend significantly upon the heat treatment parameters and the film compositions [102]. Minor variations in atomic composition of the alloy composition significantly alter transition temperatures of PVD sputtered NiTi thin films, even below the room temperature. These prompt alterations in transformation temperatures deteriorate the practical control on the film quality, making their use challenging for many applications such as microactuators [27; 111; 122]. This problem becomes more challenging because of inhomogeneous distribution of Ni within the PVD sputtered NiTi thin film material [111]. Only 1 at.% variation of composition can cause 100°C shift in transformation temperature [23; 108; 111]. As the titanium content increases, the transformation temperature also increases, as shown in Figure 53. Excess of nickel content decreases the transformation temperatures drastically below room temperature with an approximate deterioration rate of 25°C per 0.2 at.% Ni increase [27; 107]. Zhang et al. [111] observed a similar transformation change (100°C) while the film composition varied from $Ni_{50}Ti_{50}$ to $Ni_{51}Ti_{49}$.

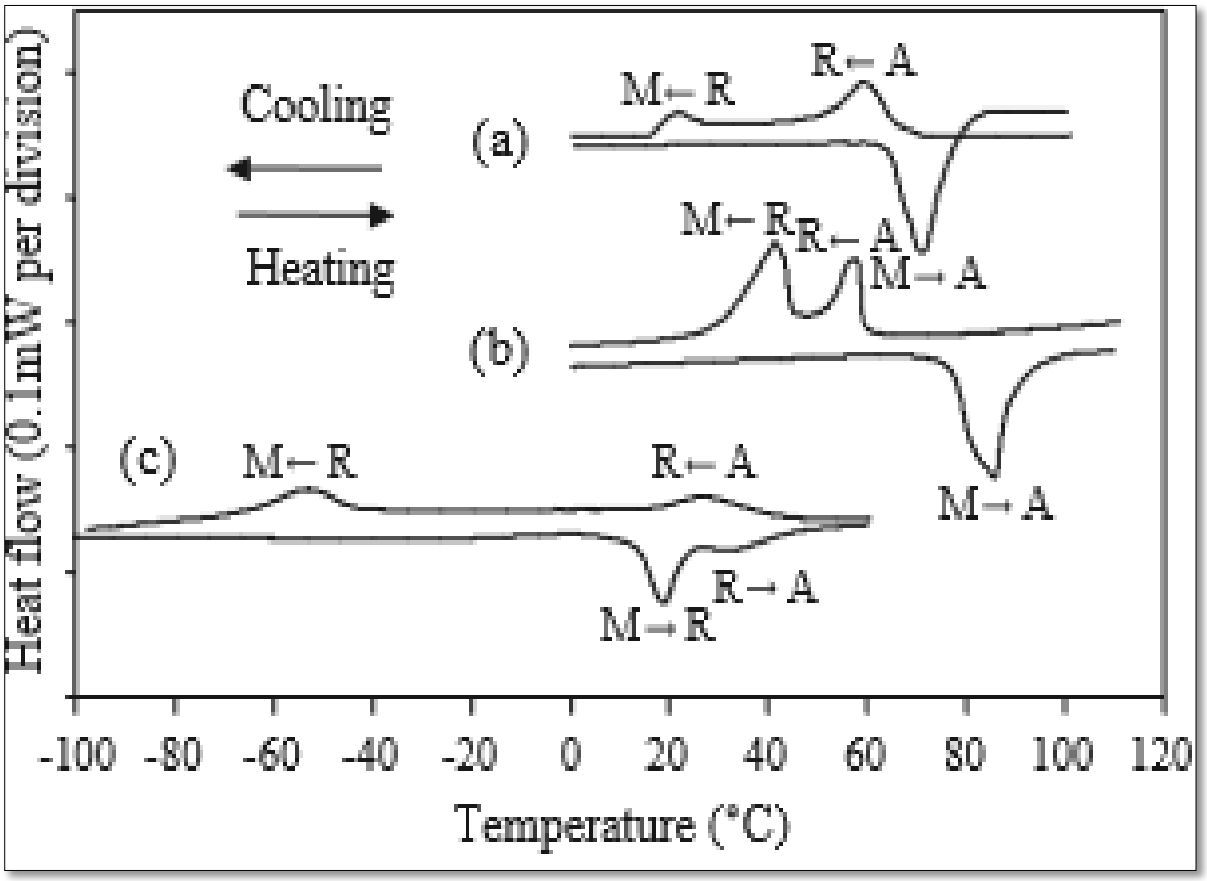

Figure 54: DSC curves of (a) Ti – rich ($Ni_{47.2}Ti_{52.8}$) (b) near-equiatomic ($Ni_{49.4}Ti_{50.6}$) (c) Ni – rich ($Ni_{51.2}Ti_{48.8}$) films annealed at 500°C [23].

Commercial NiTi alloys have transformation temperatures in the range of 70 – 130 °C depending on the compositional ratio [22]. $Ni_{47.2}Ti_{52.8}$ (Ti-rich), $Ni_{49.4}Ti_{50.}6$ (near-equiatomic) and $Ni_{51.2}Ti_{48.8}$ (Ni-rich) NiTi thin films were deposited by PVD sputtering at 6 x 10^{-3} mbar Ar pressure, and annealed at 500°C for 1 hour (Figure 54). The equiatomic and Ti-rich thin films transform above the room temperature, but nickel-rich films have low transformation temperatures [23], which is a similar outcome as reported in the studies conducted by Haung et al. [100], Porter et al. [123] and Surlbled et al. [102].

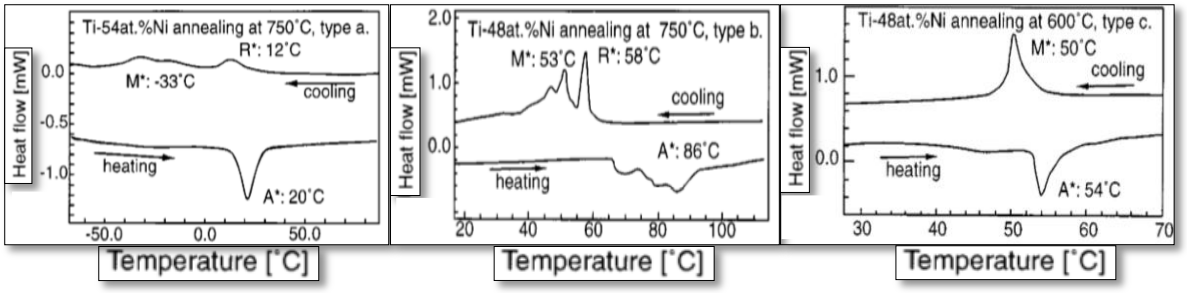

Figure 55: DSC thermograms show the transformation temperatures (M and A*) for (a) $Ni_{46}Ti_{54}$ (b) $Ni_{52}Ti_{48}$ (c) $Ni_{52}Ti_{48}$. The first peak in the cooling process of type a and b shows R phase* [124].

Takeuchi et al. [124] performed an investigation of the austenite and martensite transition temperatures for sputtered and annealed NiTi thin films, having the stoichiometric compositions of $Ni_{54}Ti_{46}$ and $Ni_{48}Ti_{52}$. The martensite transformation temperature of $Ni_{48}Ti_{52}$ is higher than that of $Ni_{54}Ti_{46}$, as shown in Figure 55. M_s of Ni-rich film exceeds the room temperature due to the presence of ductility within thin films. $Ni_{48}Ti_{52}$ was annealed at two different temperatures (600 and 750 °C). Two-step transformation was observed after higher temperature annealing due to the presence of R-phase (750°C), which was absent in the thermogram of the thin film annealed at a low temperature (600°C).

The significant parameters of thermal hysteresis of PVD sputtered NiTi films having various stoichiometric compositions were summarised in Table 8. Table 8 provides a summary of the transition states and reversible enthalpies along with the heat treatment conditions reported in various literature studies of a range of NiTi atomic compositions. The heat treatment temperatures used in all research studies are above the crystallisation temperature, which ranges from 470 – 500 °C (section 3.3.2). Only few researchers [104; 118; 125; 126] have used a substrate heat treatment temperature above 470°C, which is typical for substrate heat treated specimen. This is because the low pressure during sputtering reduces the crystallisation temperature, and the precipitation during nucleation changes the transition temperatures. This has been already discussed in detail in section 3.3.2.

Another observation about post-sputter heat treatment from Table 8 is that relatively higher heat treatment temperature was selected for the Ni-rich thin films as compared to Ti-rich or equiatomic thin films. This excludes the Takeuchi et al. [124]

and Sanjabi et al. [23] studies because they investigated the transformation behaviours of Ni-rich, Ti-rich and equiatomic thin films at the constant annealing temperature; thus, conducted their studies with using the transformation temperatures as independent variable. The transformation temperatures decrease with decreasing the annealing temperature [102]. Surbled et al. [102] also reported that the transformation temperatures of Ti-rich thin films are influenced more by heat treatment conditions in comparison to the Ni-rich thin films. This was probably the reason for using a lower annealing temperature for Ti-rich thin films so that the precipitation and fluctuation in transformation temperatures can be avoided.

Table 8: Summary of the significant parameters of PVD sputtered NiTi films having various stoichiometric compositions and transition temperatures. (Colour key: Annealing was not require, not measured / reported in the literature studies)

Heat treatment	NiTi	M (cooling) (M_f – M_s) °C	ΔH_{fwd} J/g	A (heating) (A_s – A_f) °C	ΔH_{rev} J/g	Heat treatment		Annealing		Ref
						°C	Time	°C	Time	
Substrate	$Ni_{47.3}$ $Ti_{52.7}$	0.3	- 1.89	3.7	1.806	550				[27]
	$Ni_{50.22}Ti_{49.78}$	(26 – 54)		(-2 – 56)		425				[104]
	$Ni_{49}Ti_{51}$	(11 – 39)		(23 – 40)		450				[126]
	NiTi	(-42 – -13)	-7.1	(25 –)	20.6	430				[125]
	$Ni_{51}Ti_{49}$			A = 33 (18 –)		450				[118]
Post sputter	$Ni_{47.5}$ $Ti_{52.5}$			(80 – 102)		600	0.5			[103]
	$Ni_{49.6}$ $Ti_{50.4}$			(60 – 68)		600	0.5			[103]
	Ni_{50} Ti_{50}	(58 – 70)		(90 – 110)		500	0.1			[127]
	Ni $_{50}Ti_{50}$	(52 – 67)		(75 – 102)						[128]
	Ni $_{50}Ti_{50}$	(-32 – -54)		(8 – 32)		500	3.6			[129]
	Ni_{48} Ti_{52}	(-73 – -40)		(37 – 52)						[130]
	Ni_{48} Ti_{52}	(-33 – 60)		(39 – 48)		500	3.6			[129]
	Ni_{49} Ti_{51}	(-65)		(87 – 55)		600	1			[131]
	Ni $_{51}Ti_{49}$	(-38 – -59)		(3 – 27)		600	1			[131]
	$Ni_{51.3}$ $Ti_{48.7}$	24	- 1.37	27.03	1.048	700	1	400	1	[27]
	$Ni_{51.6}$ $Ti_{48.4}$	41	- 5.37	45	5.441	700	1	400	6	[27]
	$Ni_{51.7}Ti_{48.3}$		- 4.33	~ 38	4.014					[27]
	$Ni_{50.7}$ $Ti_{49.3}$		- 5.37	~ 38	5.44					[27]
	$Ni_{50.8}$ $Ti_{48.2}$		- 2.68	~ 38	4.609					[27]
	$Ni_{48.6}$ $Ti_{51.4}$		- 1.89		1.806					[27]
	$Ni_{47.3}$ $Ti_{52.7}$		- 0.53		4.6					[27]
	Ni_{46} Ti_{54}	-33 (R = 12)		20		750		400	9	[124]
	Ni_{52} Ti_{48}	53 (R = 58)		86		750		400	9	[124]
	Ni_{52} Ti_{48}	50		54		600				[124]

	$Ni_{47.2}$ $Ti_{52.8}$	(11 – 27)	4.5	(64 – 78)	17.3	700	1	400	6	[23]
	$Ni_{49.4}$ $Ti_{50.6}$	(26 – 44)	14.3	(71 – 86)	22.3	700	1	400	6	[23]
	$Ni_{51.2}$ $Ti_{48.8}$	(-71 – - 42)	5.9	(27 – 44)	1.4	700	1	400	6	[23]
	$Ni_{53.1}Ti_{46.9}$	(-35 – 38)	-4.4	(33 - 40)	-15.3	600	1	400	1	[109]
	$Ni_{48.3}Ti_{51.7}$	(– 57)		(– 97)						[132]
Substrate followed by Post-sputter	$Ni_{48.9}Ti_{51.1}$	(43 – 70)		(78 – 98)		150 (substrate)	1	550		[133]

Table 9: The relationship of Ti at.% with martensitic and austenitic peaks (°C) for the substrate heat treated and post-sputter heat treated NiTi thin films.

Heat treatment	Ti at.% in NiTi	M (cooling) °C	A (heating) °C
Substrate	52.7	0.3	3.7
	49.78	80	-29
	51	25	32
	49		33
Post sputter	52.5		91
	50.4		64
	50	64	100
	50	60	89
	50	-43	20
	52	-57	45
	52	47	44
	51	-50	71
	49	-49	15
	48.7	24	27
	48.4	41	45
	48.3		38
	49.3		38
	48.2		38
	54	-33	20
	48	53	86
	48	50	54
	52.8	19	71
	50.6	70	79
	48.8	57	36
	46.9	-36	37
	51.7	-45	80

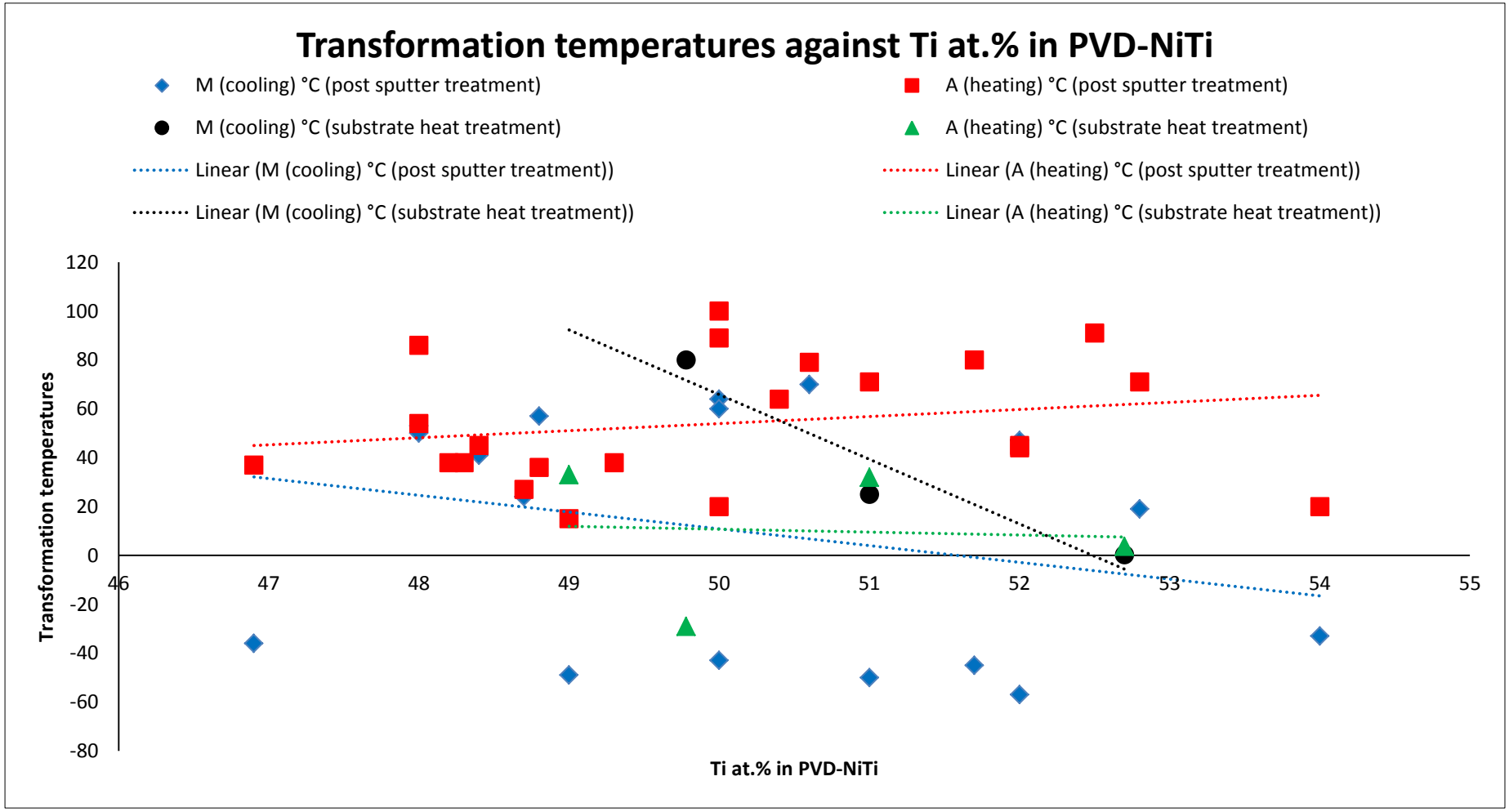

Figure 56: The relationship between Ti at.% with martensitic and austenitic peaks (°C) for the substrate heat treated and post-sputter heat treated NiTi thin films.

The data in Table 9 was extracted from Table 8, and Table 9 data was plotted to obtain a relationship between Ti at.% and M↔A transformation peaks (°C) (Figure 56) for the substrate heat treated and post-sputter heat treated NiTi thin films. Some studies did not provide the M and A peaks, but M_s, M_f, A_s and A_f temperatures were given, which were used to estimate the A and M peaks. A middle point of A_s and A_f was taken as the austenitic peaks while the central point of M_f and M_s was considered to be a martensitic peak. Although, Figure 56 confirms the previous discussion that minor variations in the atomic composition of NiTi can vary the transformation temperatures dramatically, however, the trends presented in Figure 53 do not match the results shown in Figure 56. Figure 53 explains that as the titanium content increases, the transformation temperature also increases. The results presented in Figure 53 have already been previously discussed in detail; however, the difference of trend in Figure 56 and Figure 53 needs to be further investigated. Unlike Figure 53, Figure 56 shows random trends of transformation temperatures against Ti content. The martensitic peaks decrease with increasing Ti content for both substrate and post-sputter heat treatment. The influence of Ti increasing Ti content is less for the austenitic transformation temperatures. Alongside the above dissimilarities, it is also important to consider that the same relationship between Ti at.% and the transformation temperature has been reported consistently by many researchers [23; 24; 27; 102; 103; 107; 108; 111; 123; 124]. However when the results of those studies were combined, the similar trend of Ti content against transformation temperatures does not follow, even when the heat treatment temperatures also fall in the same range as most of the above-mentioned studies relating to PVD sputtered NiTi. This explains the fact that other factors such as process conditions during sputtering, substrate type, sputter coater geometry and the film purity should also be further investigated to understand the disparities in the above observations.

Table 10: The relationship of Ti at.% with reversible enthalpies (J/g).

Ti at.% in NiTi	ΔH_{fwd} (J/g)	ΔH_{rev} (J/g)
48.7	- 1.37	1.048
48.4	- 5.37	5.441
48.3	- 4.33	4.014
49.3	- 5.37	5.44
48.2	- 2.68	4.609
51.4	- 1.89	1.806
52.7	- 0.53	4.6
52.8	4.5	17.3
50.6	14.3	22.3
48.8	5.9	1.4
46.9	-4.4	-15.3

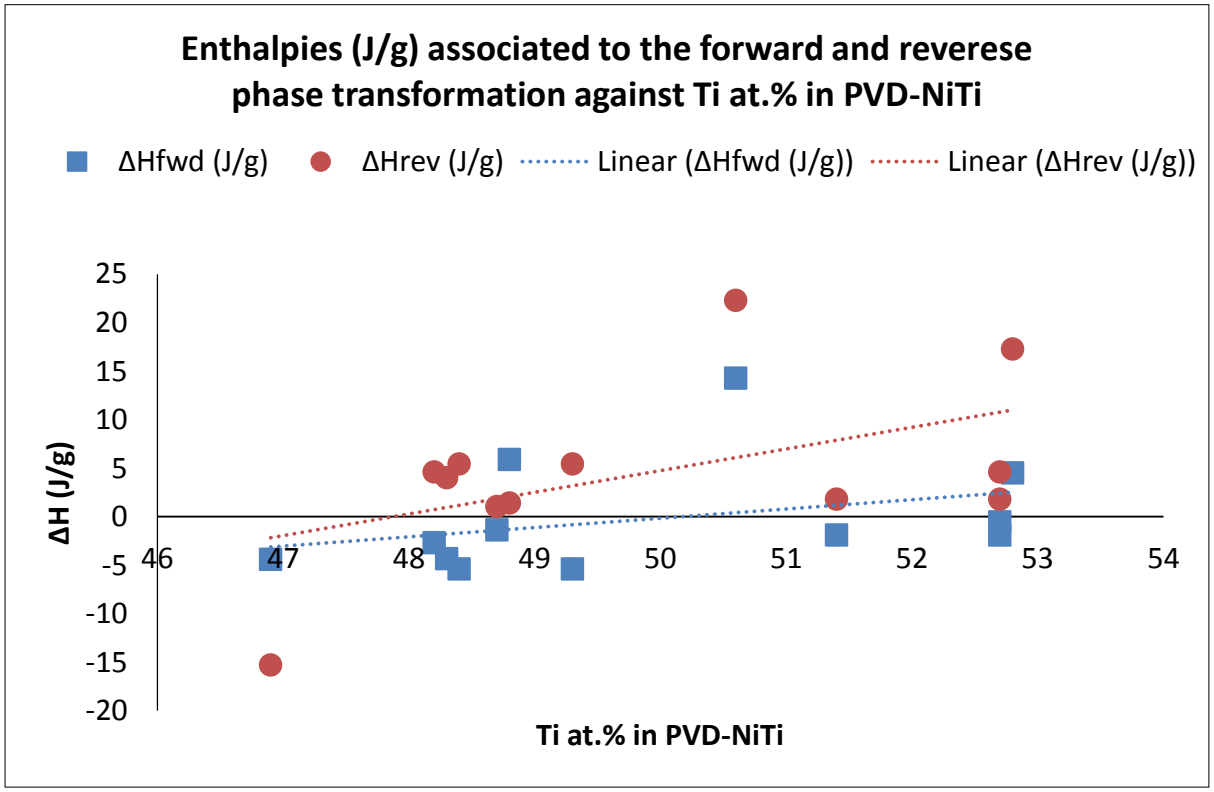

Figure 57: The relationship of Ti at.% with reversible enthalpies (J/g).

The data provided in Table 10 and Figure 57 have been taken from Table 8, which provide the relationship of Ti at.% with reversible enthalpies (J/g) during martensitic and austenitic phase transformations. The enthalpy values increase with increasing Ti content; thus, the phase transformations of Ti-rich thin films yield greater exothermic and endothermic enthalpies than Ni-rich thin films. This is because the precipitates forming in Ni-rich thin films (Ni_4Ti_3) probably hinder the transformations more than the precipitates of Ti-rich thin films hindering the phase transformations.

Table 11: The thermal hysteresis in relation to the reversible transformation enthalpies for nearly equiatomic, Ti-rich and Ni-rich thin films.

NiTi	**Hysteresis °C**	**ΔH_{fwd} J/g**	**ΔH_{rev} J/g**
$Ni_{(49.5–50.5)}Ti_{(49.5–50.5)}$	60	14.3	22.3
	75	-7.1	20.6
Ti-rich	3.4	- 1.89	1.806
	67	4.5	17.3
Ni-rich	3.4	- 1.37	1.048
	4.4	- 5.37	5.441
	115	5.9	1.4
	5.3	-4.4	-15.3

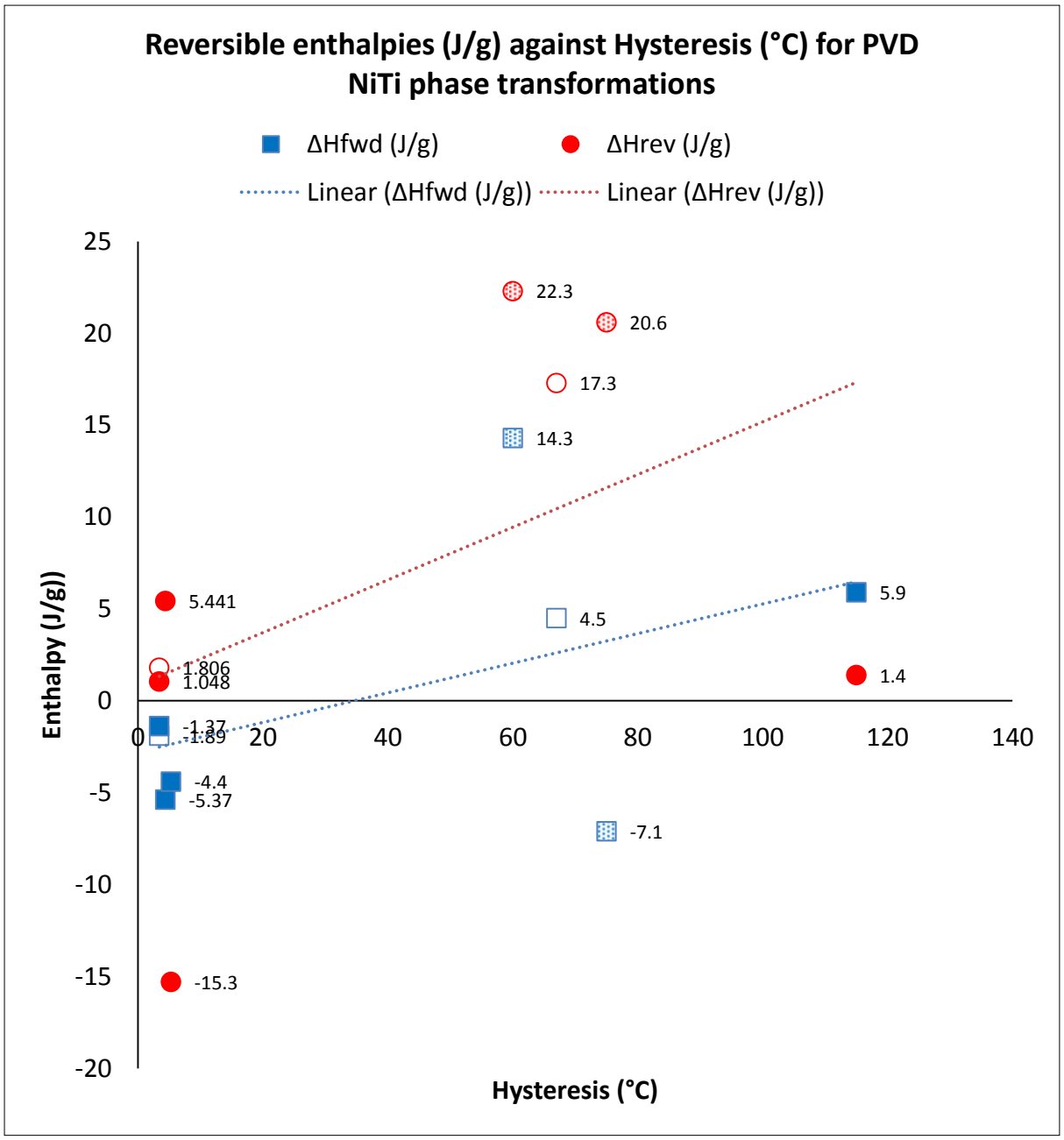

Figure 58: Reversible enthalpies (J/g) against Hysteresis (°C) for PVD NiTi phase transformations (Pattern filled data points are for equiatomic, unfilled data points for Ti-rich, and filled data points represent Ni-rich thin films.

The data provided in Table 8 was used to acquire Table 11 and Figure 58, which offer an understanding of the thermal hysteresis in relation to the reversible transformation enthalpies for nearly equiatomic, Ti-rich and Ni-rich thin films. The equiatomic NiTi films have a greater hysteresis than Ti-rich and Ni-rich thin films resulting in the higher enthalpy values, which means that more amount of NiTi in the film undergoes the phase transformation. This is expected because it is explained in

section 3.3.2 that equiatomic thin films lack precipitation; thus, the grain boundaries do not have restricted rotation requiring less energy for the phase changes of the crystals.

The only exception was an exceptionally wide hysteresis loop (115°C) for a Ni-rich thin film ($Ni_{51.2}Ti_{48.8}$), which was deposited by Sanjabi et al. [23]. Despite a wide hysteresis, the enthalpy values are comparable to those of other Ni-rich and Ti-rich thin films, due to the restricted grain rotation by Ni4Ti3. There was no explanation found for this broad thermal hysteresis of this film and needs further investigation. Sanjabi et al. [23] used the same sputtering and annealing conditions for equiatomic and Ti-rich thin films, but the hysteresis of those films fall in line with their respective trends. Other research studies involving the sputtering of Ni-rich thin films have reported annealing of Ni-rich thin films without aging, but Sanjabi et al. aged all NiTi films for 6 hours before annealing. For this reason, aging or some other sputtering condition may have resulted in this outlier, which is yet unexplained in the literature. Overall, a wider hysteresis relates more endothermic and to more exothermic enthalpies, meaning a larger amount of film material performing phase transformation.

Surbled et al. [102] reported that a small hysteresis is particularly useful for the MEMs applications requiring a fast frequency response and that the hysteresis decreases with decreasing annealing temperature. NiTi stoichiometry and the annealing temperature have a significant influence on the transformation temperature, shape memory and the pseudoelastic ability of NiTi. Small changes to the stoichiometric ratio and the annealing temperature lead to substantial variance in the SMA properties and the crystal orientation; therefore, the properties of NiTi also change. This can be used as an advantage also to tailor-make the SMA in accordance with the manufacturing desires.

3.3.5 Shape memory effect (thermal SME and pseudoelasticity)

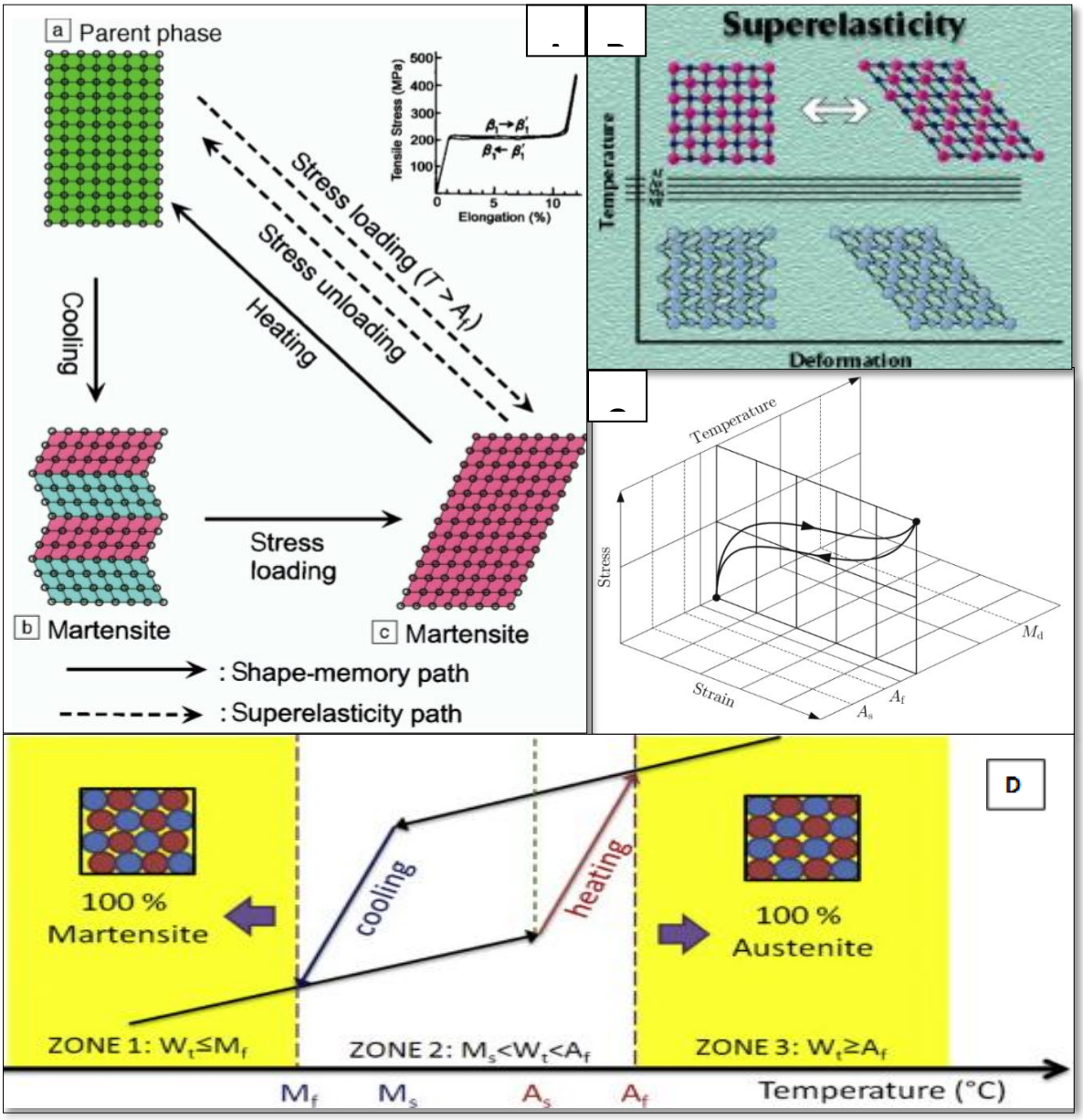

Figure 59: (A) a – c: Schematic illustration of the mechanism of the shape memory effect and pseudoelasticity, in which solid lines represent the shape-memory path, and dotted lines represent the pseudoelasticity path [134]*. (B) Pseudoelasticity involves the stress-induced transformation of A to M* [107]*. (C) Stress-strain-temperature diagram of pseudoelasticity, where the SMA is deformed at constant temperature* [105]*. (D) Stress–strain curve for NiTi* [135]*.*

NiTi SMA exhibits shape memory effect due to a reversible austenite and martensitic transformation, which can be induced thermally (thermal shape memory effect) or mechanically (pseudoelasticity) [105]. Materials that undergo martensitic

transformations do not always exhibit shape memory effect, and the pseudoelasticity [22]. Shape memory effect and the pseudoelasticity are discussed below in further detail. This research project takes advantage of the pseudoelasticity effect of NiTi.

Shape memory effect is thermoelastic and crystallographic reversible phase transformation from high-temperature phase (B2) to a low-temperature phase (B19), where the material can be deformed at a low temperature and recover its original undeformed shape by heating above a given transformation temperature [22; 99]. In other words, SMA undergoes thermoelastic transformations by induction of strain below A_s, to deform the martensitic phase to a maximum strain through the movement of twin phase boundaries, and accommodation of M phase variants in the microstructure [22; 27; 30]. When heated above A_f (that is above transformation temperature) the alloy's atomic lattice displays, a coordinated "shear like" distortion and hence recovers to its original undeformed austenitic state [22; 27; 30]. Volume of the alloy remains constant in both contracted (heated) and relaxed (cooled) phase [96]. Recoverable strain limit establishes the position where martensitic variants become dominant, and ahead of that point, some permanent unrecoverable strain acts by slipping [22].

Spontaneous plastic deformation of martensitic phase occurs by induced twinning at stresses below the stresses needed to nucleate and move dislocations. Twining can cause a rearrangement of atomic planes without slipping or permanent deformation while facing bulk strains of about 6 – 8 %, which turns the martensitic phase without inducing permanent deformation [22]. Essential twins can be readily present in NiTi microstructure without requiring nucleation. Deformation occurs by the growth of those twins, which are aligned with the principal shear component and shrinkage; therefore, ultimate exclusion of those twins occurs with significantly negative constituent. As long as dislocation slip does not happen, and deformation of martensite is only through twinning, the orientation of the parent phase on heating will stay unaffected [22]. Shape memory behaviour takes place by directional reorientation or detwinning and has been classified as one-way and two-way memory effect. In one-way SEM, only austenite phase can be recovered but two-way shape memory means a martensitic phase can also attain stabilised configuration via irreversible slip [104]. Two-way shape memory allows the shape memory of both parent and daughter crystals by exothermic and endothermic phase changes [123].

Pseudoelasticity is an ability of an SMAs to exhibit large elastic strains at the absolute temperatures by demonstrating an unloading cycle of rearranging their atomic lattice [11; 22; 27; 136; 137]. Pseudoelasticity is related to a reversible microstructural deformation mechanism, known as stress-induced martensitic transformation [99]. Above $A_{f,}$ a non-linear recoverable deformation behaviour results in forward and reverse transformations [108]. The application of stress forms martensite arrangement at narrow temperature range, above M_s and the SMA return to its undeformed austenite shape upon unloading, when stress drops below a particular value, without needing a temperature change [11; 27; 100; 107; 136]. Only the variant parallel to the direction of the applied stress transforms during an isothermal stress-induced M-phase; hence, the stress causes the phase transformation [107].

NiTi exhibits enormous elasticity of 10 - 20 times than ordinary alloy such as stainless steel [11; 27; 136]. To make the use of pseudoelasticity, a tensile test is carried out between A_f and T_f. T_f is the highest temperature for stress-induced martensitic transformation. A – M transformation between A_f – T_d results in a stress plateau in the stress-strain curve, which can be recovered upon unloading [100; 105]. The materials have an M-phase below T_d, whereas A-phase is observed above T_d [100]. Zampooni et al. [126] conducted a tensile testing experiment on freestanding $Ni_{49}Ti_{51}$ thin films having film thickness of 10 µm, deposited by PVD magnetron sputtering on Si {100} substrate at substrate heat treatment temperature of 450°C. The transformation temperatures of the thin film were A_s = 23°C, A_f = 40°C, M_s = 39°C, M_f = 11°C. The specimen was tested at 36°C and 24°C. More stresses were accommodated at 36°C, demonstrating the pseudoelastic property in a closed-loop hysteresis having 6 % strain. Frick et al. [30] used nanoindentation to study M – A events during stress-induced martensitic transformations and reported an inherent link between the martensitic phase transformation behaviour and the local martensitic structure. Their study has put forward the evidence of stress-induced transformations at the nanometre scale and provided an opportunity for the use of nano-actuators in future.[30]

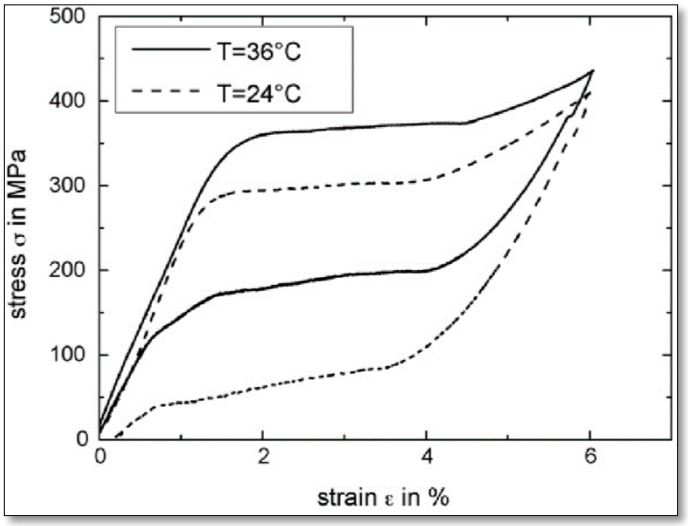

Figure 60: Tensile testing experiments were conducted on freestanding as-deposited NiTi films. Pseudoelasticity was realized at and below 36°C [126].

Along with a recovery of 10% strain, bulk NiTi SMAs can recover the stress up to 400 MPa, generating a "spring back effect" [11; 103; 111; 123]. Approximately 4 – 8 % strain recovery is observed in equiatomic NiTi thin films [22; 137]. In NiTi thin films, one-way and two-way shape memory can successfully be generated, but 10% of pseudoelastic strain from bulk crystals is very rare [25]. Ishida et al. [25; 138] reported only 6% pseudoelastic strain, but NiTi thin films are still being investigated to retain maximum pseudoelasticity from bulk NiTi into coatings. Rumpf et al. [109] reported the highest strain of 11.5% along with 1180 MPa tensile strength for freestanding PVD sputtered thin films of $Ni_{51}Ti_{49}$, which are pseudoelastic at 37°C and have an austenite peak at 33°C (A_s = 18°C). Miyazaki et al. [58] also successfully prepared pseudoelastic thin films having similar stress-strain properties to those of the bulk materials.

Orientation of thin films distinctly influences the elastic properties of NiTi, which vary the percentage of elastic recovery [25]. B2-NiTi {111} single crystals exhibit the pseudoelastic strain of 9.8%, which is greater than 2.7% along the {001} B2 direction. Therefore, the single crystal NiTi thin films having {111} orientation exceed the percentage recovery value of polycrystalline film, which are fabricated typically during PVD sputtering [25; 139]. High strains of the single crystals within the NiTi thin film can be used as an advantage because those strains direct the thin films to grow epitaxial with a significant anisotropy [25]. Factors affecting the pseudoelastic

properties of NiTi thin films include temperature, annealing condition, grain size, stress mode, and microstructure (particularly the material's texture) [108]. This is because the above factors introduce the lattice defects, internal stress-strain field and precipitates that affect the martensitic interface mobility, and ultimately influence the shape memory [108]. The pseudoelastic hysteresis of NiTi reduces the energy storage efficiency, i.e. a device requiring 5 J for deformation may only return 2 J of mechanical energy upon unloading, and this was considered a drawback in the past. NiTi offers a dynamic outward force of small magnitude having high radial resistance. A_f temperature should be as high as possible but still below the body temperature. A_f temperature above body temperature would always keep NiTi in martensitic phase as a biomaterial.[11]

Martensitic transformation accompanies quite a strong force, which requires deformation pressure of 10,000 to 20,000 psi (69 to 138 MPa) because of the movement at a molecular level, taking place without breaking the bonds**.** This kind of deformation is called twinning. Spontaneous plastic deformation of martensitic phase can occur by induced twinning at stresses, below the stresses needed to nucleate and move dislocations. Twining can cause a rearrangement of atomic planes without causing slip or permanent deformation, while facing bulky strains of about 6 - 8%, which turns the martensitic phase without inducing permanent deformation. Essential twins are readily present in the microstructure of NiTi, which do not require nucleation. Deformation occurs by growth of those twins aligned with the principal shear component and shrinkage, therefore, ultimate exclusion of those twins with the significant negative constituent. As long as dislocation slip does not happen, and only deformation of martensite is through deformation twinning, orientation of the parent phase on heating will stay unaffected.[22]

Zhang et al. [132] suggested the use of pseudoelastic NiTi thin films as interlayers between the metal substrate and the hard coatings deposited on them due to their tribological properties and rubber-like mechanical behaviour of PVD-NiTi. These features would allow the use of NiTi interlayers as a metallic glue between the two surfaces by enhancing the adhesion while providing the surface protection against the plastic deformation [112]. Similar advantages are employed from NiTi thin films in the current research project for preparing PTFE-NiTi nanocomposite having contact deformation by phase transformation.

3.3.6 The dependence of shape memory properties of PVD-NiTi on composition and heat treatment conditions

The shape memory properties of NiTi thin films are subtle to the heat treatment temperature and duration [38]. According to Frick et al. [30], equiatomic NiTi has a relatively weak shape-memory property compared to Ni-rich NiTi containing second phase precipitates. Elahinnia et al. [108] reported that the typical temperature of pseudoelastic $Ni_{50.8}Ti_{49.2}$ is approximately 8°C. Habijan et al. [140] also reported similar results, according to which Ni-rich thin films $Ni_{50-\varepsilon}Ti_{50-\varepsilon}$ (ε~0.7) demonstrate pseudoelasticity at approximately 37°C; however, the shape memory deteriorates beyond the stated range of NiTi thin film composition because of the appearance of TiN_3 precipitates. If the Ni content is increased any further by about 0.5 wt.%, the shape memory property is lost fully in PVD-NiTi films [123]. At low Ni content, only Ni_4Ti_3 precipitates coherent with the austenite matrix are present in Ni-rich thin films, which do not deteriorate the shape memory effect of the thin films annealed at relatively low temperature and duration [141]. If the annealing time and temperature is increased, Ni_4Ti_3 precipitates grow and become more coherent deterring the shape memory effect. This leads to thermal etching, hindered grain boundaries, and stressed pitches [141].

Titanium-rich coatings are potential candidates for biomaterials due to their transformation temperature, resulting in pseudoelastic features operating at the body temperature [27]. Implant applications of bulk NiTi reportedly exhibit an austenite finish between 0 – 100 °C and a thermal hysteresis of 25 – 40 °C [108]. Haung et al. [100] investigated the influence of annealing temperature on pseudoelasticity and transformation temperature of bulk NiTi. They reported that an increase in annealing temperature also increases the strain of the forward stress-induced transformation. Maximum 9 % strain by extensometer was reported in their study, which was obtained by annealing at 600°C, and the plateau stress was minimum at these conditions. The lowest plateau strain was observed by annealing at 400°C while the highest R_f and A_s temperatures were documented in association with the lowest plateau strain.

The thermal shape memory effect observed in NiTi thin films is influenced by the annealing conditions, unlike bulk NiTi. Ishida et al. [138] annealed Ti-rich thin films

of NiTi, at 599, 600 and 700 °C, for 1, 10 and 100 hours. As the temperature and time for heat treatment increases, reverse and forward martensite transformations take place at higher temperature. The higher the annealing temperature and time, the more possibility there is for one-way shape memory to be observed with an absence of R – phase.[138]

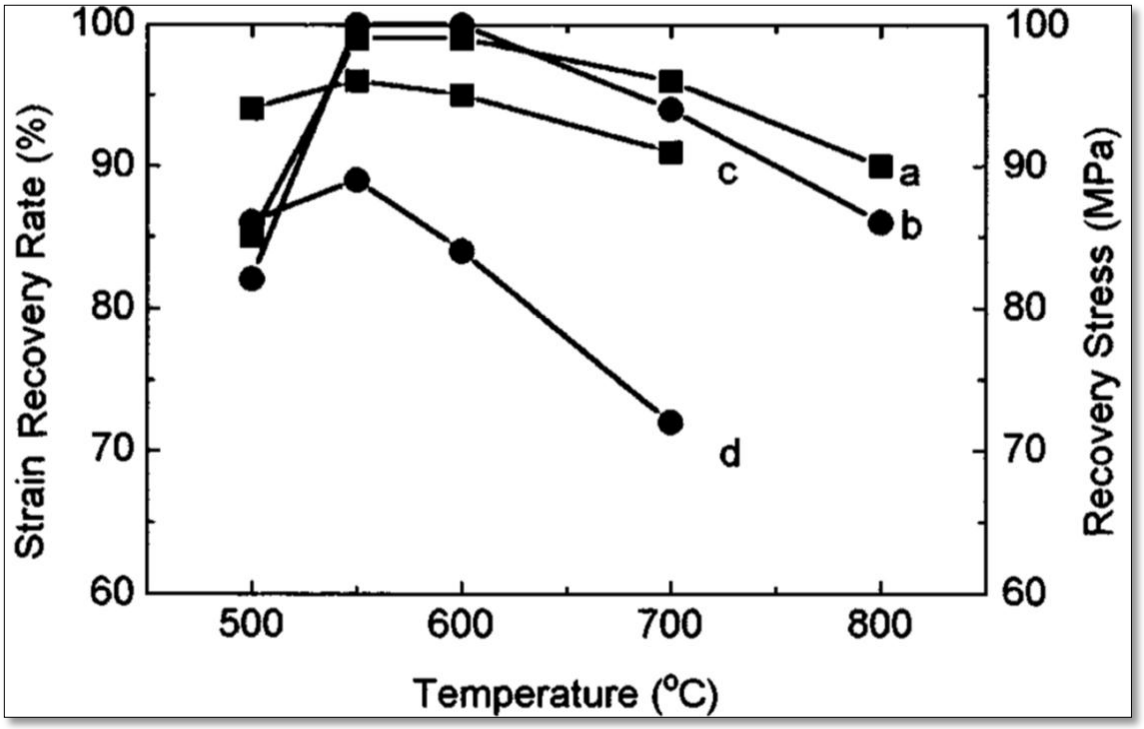

Figure 61: Annealing temperature dependence of the strain recovery rate (■) and the recovery stress (●) of the films annealed (a) and (b) for 0.5 h, and (c) and (d) for 2 h [141].

Gong et al. [141] measured the influence of annealing temperature on the shape memory effect of the thin films prepared by PVD sputtering. Ni_4Ti_3 precipitates were observed because the films were slightly Ni-rich, which did not hinder the phase transformations. The thin films demonstrated a shape memory effect after annealing at 700°C despite having a brittle nature (Figure 61). NiTi thin films cracked upon bending after being annealed at 850°C. The shape memory behaviour deteriorates further upon increasing the annealing temperature any further. This deterioration is related to Ni_3Ti_2 precipitates rather than the coherent Ni_4Ti_3 precipitates. Therefore, the recommended annealing conditions are of 550 – 700 °C for 0.5 h. To obtain good shape memory effect, a smooth film surface is desired after the annealing treatment.

Zhang et al. [110] also investigated the stress-induced martensitic transformations of NiTi thin films by tensile testing. Ti-rich films were deposited by magnetron sputtering at 273°C for two hours followed by annealing at 600°C for 1 hour. In Ti-rich NiTi films, GP zones along with a homogeneous dispersal of Ti_2N precipitates vary the shape memory effect properties as compared to the bulk materials. In such thin films, a larger transformational strain is observed but the recovery becomes difficult because of Ti_2N precipitates hinder the growth of the martensite plates. Contrastingly, if the GP zones deform elastically during M transformation, a large shape recovery strain can still be obtained from Ti-rich thin films.

After selecting a suitable composition of NiTi, the transformation temperature is adjusted by varying the heat treatment conditions. The transformation temperatures of T-rich NiTi decrease with decreasing the annealing temperature [124]. Annealing NiTi at 600°C for additional 20 min caused the austenite peak to drop from 86°C to 54°C and the martensitic transformation temperature to decline from 53°C and 50°C (Figure 55c) [124]. The actuation temperature can be further decreased to biologically safe temperature i.e. body temperature, by decreasing the annealing below 600°C and annealing for a shorter period as described in section 3.3.4.

3.3.7 Oxygen and other impurities within NiTi thin films

The impurities particularly oxygen significantly influence the characteristics of NiTi thin films, affecting ductility, the most important parameter that influences the pseudoelasticity of NiTi thin films [25; 142]. Oxygen contamination and impurities from precipitation change the matrix stoichiometry resulting in brittle NiTi films and the phase transformations also vary their magnitudes [25; 143]. There are two primary sources of oxygen contamination during PVD sputtering process; the oxygen from the residual atmosphere and the oxygen trapped in substrate or target material.

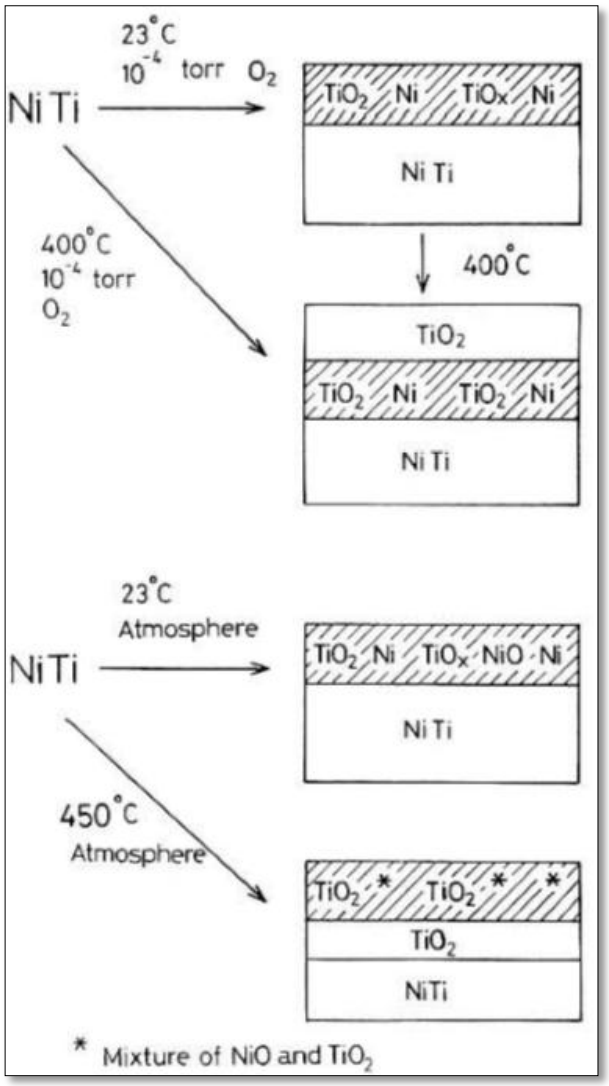

Figure 62: A schematic diagram showing oxidation at various oxygen exposure levels and temperatures [144].

Chan et al. [144] provided the mechanism for the formation of oxides in NiTi thin films, who oxidised $Ni_{50}Ti_{50}$ thin films under high vacuum (10^{-4} torr) at RT for 40 minutes of the exposure time. The thin films were exposed to oxygen at 23°C followed by 400°C or a direct exposure at 400°C, and 450°C was performed (Figure 62). Ti reaction was favourable producing TiO_x (x = 2, 3) compounds on the film surface and just underneath the surface while Ni remained unreacted on the surface. For the low-temperature reaction, NiO also forms on or just underneath the surface, after the first minute.

This research involves the deposition of polymer and SMA. The presence of oxygen at the film substrate interface, and at the interfaces, within the polymer-metal layers, can influence the film properties. If the present at the interfaces, oxygen affects the adhesion between metal and polymer for which minimal oxygen content is essential. The oxygen content in coatings plays a significant role in the microstructure and influences nucleation and growth of metal layers by acting as a preferential site for nucleation, leads to the formation of oxides, and produces stress concentration. High oxygen contamination results in compressive stress while low oxygen content generates tensile stress. Stress concentration increases with decrease in adhesion, and with increasing oxygen content in residual atmosphere. The presence of higher stress within the coating, and at the metal-polymer and film substrate interfaces could ultimately decrease the deposition rate and cause disbonding.[68][68; 112]

“Thin film effect” is another impurity defect reported for the NiTi thin films, which means the martensitic transformation always start from thicker area followed by its propagation towards the thinner area [145]. ‘Thin film effect’ ultimately suppresses the transformational behaviour of NiTi on reducing the film thickness to approximately 50 nm [145]. This is because, at this film thickness, the interfacial layer (~15 nm) and surface oxide layer constitute the most volume fraction of the film material, which hinders the B19’ transformations [145]. A large amount and size of GP zones leading to twinning is also considered as an internal defect of the thin films. The amount and size of the GP zones increase with the increasing annealing temperature and time; thus, the likelihood of the formation of {111} twinning also increases.[121]

Some problems concerning NiTi thin film impurities and their suggested solutions have been disused as follows. Target materials are a source of impurities in NiTi thin films. Conventional casting and powder metallurgy are conventional manufacturing methods for NiTi alloy targets, which have the required compositions but may contain impurities such as oxygen and pre-alloyed powder impurities. In order to obtain homogeneous sputtered films, powder metallurgical targets must consist of relatively small but well-mixed powders of elements [23]. The problem with these conventional methods is high impurities presence in resulting thin films due to the large surface contribution of the targets. The solution of this problem is the production of cast-melted targets, which are reliable in terms of achieving lower levels of oxygen impurities; however, their deposition requires high vacuum conditions [23]. Winzek et al. [25] also suggested targets manufacturing by vacuum cast-melting process rather than powder metallurgy. Another approach for avoiding any oxygen influence during alloying process of NiTi target manufacturing is using pure nickel and titanium targets. The plastic deformation in NiTi thin films due to impurities can also be reduced by annealing treatments [25; 146].

During the nucleation growth of PVD sputtered NiTi films, the potential barrier is reported to be smaller, resulting in rapid crystallisation process during heat treatment, which leads to favourable precipitation [113]. Atomic reordering and grain realignment takes place within the microstructure, and the internal stress develops in PVD sputtered NiTi thin films because of quickly accumulated defects by impurities and precipitation [113]. For this reason, the crystals display lower transition temperatures than their parent materials, and less amount of film material undergoes the phase transformation [147]. For example, Yang et al. [113] reported that the M_s of PVD thin film was 50°C lower than its parent material. Wibowo et al. [27] reported that the outcome of the enthalpy change in heating and cooling is 1.8 Jmg^{-1} for PVD sputtered NiTi thin films, which is lower than that of sputtering target enthalpy change (5 $J.mg^{-1}$). The martensitic phase growth constraints arise at the grain boundaries, which restrain the transformed segment of the film material in the nanocrystals [38]. The B19’ growth that nucleates with the grain structure is hindered and ultimately stop when reaches the grain boundary. The grains at the boundary plates have to exert stress to stimulate the growth process [38].

3.3.8 Mechanical properties and stressed in PVD-NiTi thin films

NiTi has good mechanical stability, biased stiffness, fatigue resistance, lightweight material compared to the most of other metallic substances and display constant restraint to the uploading stresses [11; 99]. Due to an excellent mechanical stability, bulk NiTi displays 50 – 60 % elongation before fracture and tensile strength ~ 1000 MPa [27; 134]. Martensite is a ductile phase, and austenite is reported as a stiffer austenite phase of NiTi [69]. The amorphous NiTi deposited films have compressive, and the recrystallized films exhibit high tensile strength in the range of 500 – 600 MPa. Residual stress is a common problem that influences the performance of NiTi thin films. It can arise due to the following reasons. With an increased sputtering power, the higher deposition rates induce residual stress, resulting in low-density films. This effect is more for tensile stress while less for compressive stress producing more tensile and less compressive NiTi coatings. After solution heat treatment, the stress modifies from compressive to tensile because of microstructural changes from amorphous to crystalline. Another cause of residual stress in the NiTi films is the thermal expansion coefficient difference with the substrate. The thermal expansion coefficient of NiTi is 11 x 10^{-6} °C^{-1} for austenite NiTi and 6 x 10^{-6} °C^{-1} for martensitic NiTi while it is 2.5 × 10^{-6} °C^{-1} for the Si substrate.[27]

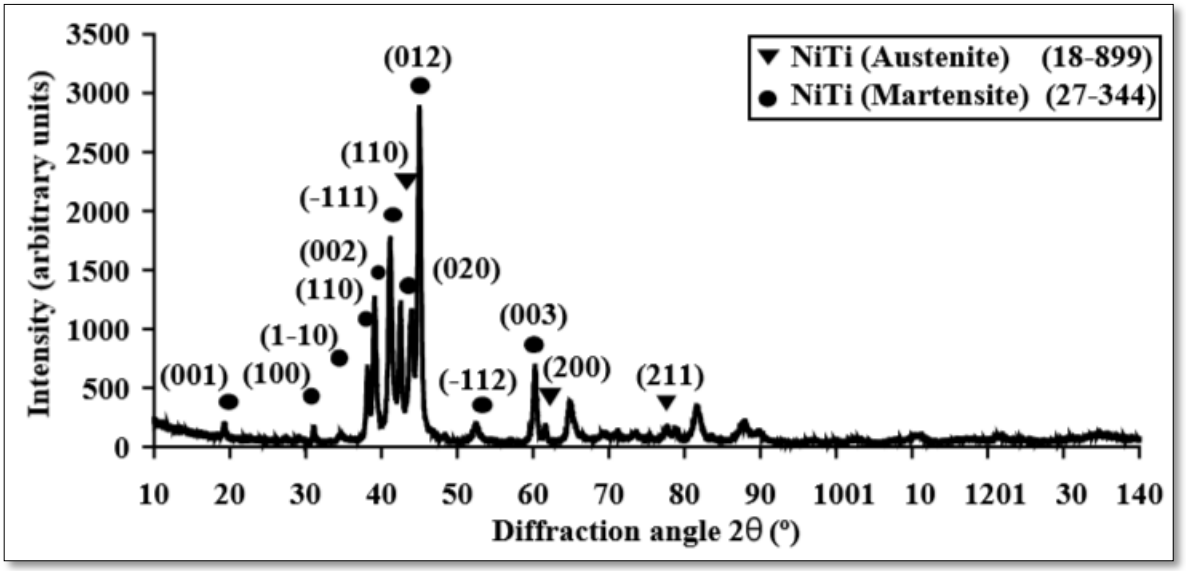

Figure 63: XRD obtained from NiTi coatings after the heat treatment [103].

Botterill et al. [103] measured the residual stress of NiTi coatings by measuring the angular shift in the XRD diffractogram peaks. Prior to the XRD analysis, the samples

were cooled down to –10°C and brought back to ambient temperature in order to observe a predominantly martensitic structure as shown in Figure 63. A polycrystalline structure is found in the presence of martensitic phase varying along with low-intensity reflections of some austenite crystals retained within thin films. Fewer austenite crystals were retained because of the constraints in the interfacial region appearing during the high-temperature post-deposition heat treatment. The presence of austenite can be enhanced by cooling below M_s and $M_{f,}$ and a low-temperature martensitic phase transformation is obtained. Comparison between the residual stresses measured from the angular shift in the XRD peaks and an unstressed powder diffraction standard allowed the author to measure a stress between 200 – 700 MPa in the films. The only explanations of a broad range of stress values provided by the author are likelihood of measurement inaccurately or the absence of considerable stresses present in the source the onset of stress-induced martensitic transformations. Nevertheless, previously mentioned Wibowo et al. [27] tensile strength values (500 – 600 MPa) for PVD thin films fall within the range of Botterill et al. [103] measurements (200 – 700 MPa).

Kumar et al. [116] investigated the influence of film compositions and heat treatment temperatures on the film hardness and the elastic modulus. At a constant substrate temperature and various film compositions, the elastic modulus and hardness of an amorphous NiTi thin film remains constant. Nevertheless, the elastic modulus and hardness of an amorphous NiTi thin film change with changing film compositions, at a constant substrate temperature. The elastic modulus and hardness of a Ti-rich thin film remain similar to the amorphous NiTi thin film even after annealing. Increasing the annealing temperature also increased the elastic modulus and hardness of NiTi thin films.

Wibowo et al. [27] carried out nanoindentation studies for measuring the Young modulus of the martensitic and austenite phases for 3 µm thick PVD-NiTi films deposited on silicon. The measured the Young’s modulus of the martensite phase of about 14 GPa while 56 GPa was reported for the austenite phase. According to Cripps, a Young’s modulus of a thin film of a substrate is an extrapolated value of bulk material’s Young modulus where the penetration depth is close to zero [27; 148]. The Young modulus of NiTi films increased as the penetration depth increased.

While estimating Young's modulus, the nanoindentation results are only indicative if the indentation penetration depth is close to the surface (10% of NiTi film thickness). This is because NiTi films re-orient to particular martensitic variants on exertion of an external force below the transformation temperature, resulting in changes in their mechanical properties. Above their phase transformation temperature, the nanoindenter may record inaccurate values of the Young's modulus in the martensitic state because NiTi films experience stress-induced pseudoelasticity at that temperature.[27; 149]

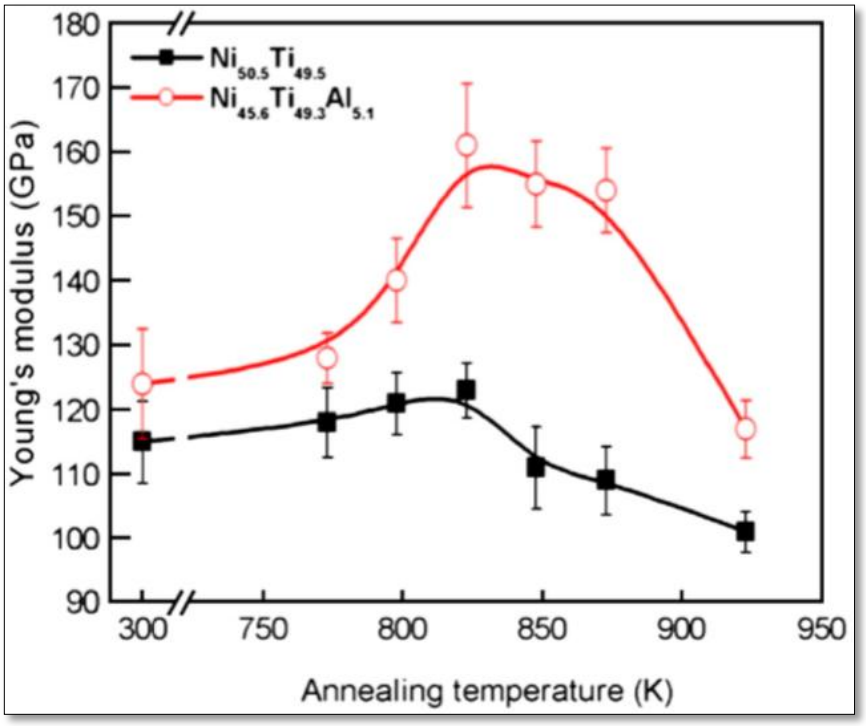

Figure 64: (a) Hardness (b) Young's modulus with different annealing temperatures from 773 K (500°C) to 923 K(650°C) for $Ni_{50.5}Ti_{49.5}$ and $Ni_{45.6}Ti_{49.3}Al_{5.1}$ [117].

Liu et al. [117] reported a hardness of 8.8 GPa for the PVD sputtered $Ni_{50.5}Ti_{49.5}$ thin films deposited on a silicon substrate and annealed by post sputter heat treatment. They also indicated the trend of Young modulus against annealing temperature, as shown in Figure 64. The Young modulus increases with increasing the annealing temperature (300 – 825 °C) followed by a decrease, observed after further increasing the annealing temperature. (825 – 923 °C). Maximum Young modulus of 155 GPa was recorded for at approximately 825°C. The Young modulus estimated by Wibowo et al. [27] is 56 GPa, which is much lower than the Young modulus reported by Liu et al. [117]. One reason for this difference is found Figure 64, where the annealing

conditions can be witnessed as significantly influential factor in the determination of Young modulus of NiTi thin film. Other factors, that influence the mechanical properties of PVD, sputtered NiTi thin films are film compositions, annealing, aging temperature and sputtering conditions, which affect the nucleation and growth process resulting in changes in microstructure and mechanical properties [117]. Surbled et al. [102] also recommended lower annealing temperatures (<467°C) for the development of SMA microactuators by PVD sputtering to minimise the thermal, and mechanical stresses.

3.3.9 Biomaterial aptitude of NiTi

The human body is an isothermal environment; therefore, the body temperature is impeccably pitched for pseudoelastic applications of NiTi, which do not require cryogenic alloys for coupling and fasteners or high M_s for actuators. Conventional materials such as stainless steel and titanium are very stiff and exert an unnecessary degree of pressure on surrounding tissue as biomaterial implants. NiTi shows extraordinary physiological and mechanical similarity to the natural tissue (Figure 65) and makes itself suitable for use as stents in the body. Healing occurs by the encouragement of bone in-growth by sharing loads with the surrounding tissue. Ti has exceptional biocompatibility and chemical resistance, due to the creation of a passive titanium oxide (TiO_2) layer, and thermodynamic data verifies the preferential free energy of formation of TiO_2 over other nickel or titanium oxides. TiO_2 oxide layer increases the stability of the surface layers by protecting the bulk material from corrosion and forms a physio-chemical barrier against Nickel oxidation by modifying its oxidation pathways.[11; 99]

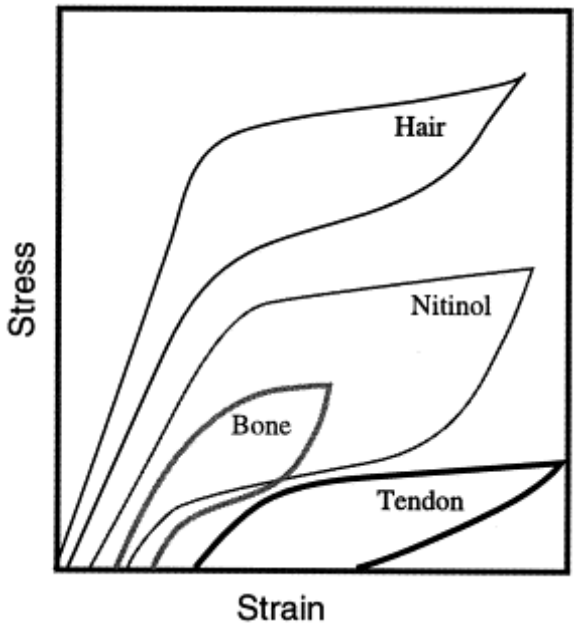

Figure 65: The stress–strain curves of numerous natural materials overlaid on NiTi's curve. The resemblance of NiTi to natural tissue is apparent [11].

NiTi excludes the need for aggressive medical procedures, capable of microtubing and laser cut tubing with high precision. In simulated physiological solutions, NiTi is more resistant to chemical failure than 316L stainless steel but less than Ti–6Al–4V. In the course of the in-vitro dissolution studies, Barret et al. and Bishara et al. [11; 150] found that NiTi appliances released an average of 13.05 μg day−1 Ni, which is considerably below the projected average dietary intake of 200–300 μg day−1. Nickel concentration level increases significantly over time in the blood of orthodontic patients with NiTi implants.[11; 150; 151]

NiTi scripts adaptive and hybrid (smart) composites and has excellent biocompatibility and bone contact and flexibility. NiTi is widely used in biological and biomedical applications, and it is a potential candidate for many more devices as described below. Metals and alloys have excellent mechanical properties, but they do not satisfy the arduous demands of biomaterials as they need to be decidedly biocompatible and biofunctional. Metals such as Ti and its alloys, cobalt – Chromium alloys (FeCrNi, CoCr and TiAlV) and stainless steel are commonly accepted metallic implant substances, but the best consideration is given to NiTi SMA due to its pseudoelastic features.[21; 27; 134]

3.3.10 Summary

NiTi is an SMA that can retain its original crystallographic orientation even after plastic deformation by reversible solid-solid A↔M transformations due to thermally or mechanically induced shape memory effect (thermal shape memory effect and the pseudoelasticity). DC magnetron sputtering under high vacuum allows deposition of NiTi thin films having shape memory properties that are comparable to their bulk materials. As-sputtered NiTi thin films are amorphous, and heat treatment is conducted to introduce crystallinity. Substrate heat treatment and post sputter heat treatment are two ways to crystallise NiTi coatings. Substrate heat treatment eliminates the need for an additional post-sputter annealing process. NiTi thin films subjected to substrate and post-sputter heat treatments show no differences in the crystal structures. Post-sputter annealing heat treatment is chosen for this project because the higher transformed content of thin film in post-sputter heat treated and aged for a longer time leads to a successful transformation. Various researchers determined the crystallisation temperature of PVD-NiTi thin films deposited on different sputtering conditions within the range of 470 – 500 °C by DSC analysis; therefore, 500°C is optimum for annealing temperature for crystallisation. At 500°C, Ti-rich films result in GP zones formation, which can be addressed by annealing at temperatures greater than 600°C. During post-sputter heat treatment, the films aged for a longer time yield more amount of NiTi in the film undergoing phase transformation. The transformational temperature deviates from its original value because of precipitates formation in Ti-rich and Ni-rich thin films during the heat treatment.

PVD-thin films have smooth and free from pinhole like surface defects with a dense crystallised microstructure matching to the high-temperature zone 3 of the thin film models. The microstructure and transformation temperature of PVD sputtered NiTi thin films are significantly affected by precipitation during heat treatment. The microstructure of PVD sputtered NiTi thin film is considerably vulnerable to stoichiometric disruption by minor changes to the process conditions. The substrate temperature also affects the on the film thickness and the microstructure. The grain size and the crystallisation extent increase with an increase in substrate temperature. NiTi has an excellent mechanical stability and displays constant

restraint to the uploading stresses. Martensite is a ductile phase, and austenite is reported as a stiffer austenite phase of NiTi.

The compositions of the sputtered films are always titanium deficient with respect to the target (by 2 – 4 at.%). The stoichiometric issues in PVD-NiTi thin films will be solved in the current study by placing pure titanium pieces on the racetrack region of the target. The transformational temperatures of NiTi thin films depend significantly upon the heat treatment parameters and the film compositions. As the titanium content increases, the transformation temperature also increases. A higher heat treatment temperature was required for the Ni-rich thin films as compared to Ti-rich or equiatomic thin films. The transformation enthalpy values increase with increasing Ti content. Thus, the phase transformation of Ti-rich thin films result in greater exothermic and endothermic enthalpies than Ni-rich thin films. The equiatomic NiTi films have a larger hysteresis than Ti-rich and Ni-rich thin films resulting in the higher enthalpy values, which means that more amount of NiTi in the film undergoes the phase transformation due to lack precipitation. NiTi stoichiometry and the annealing temperature have a significant influence on the transformation temperature, shape memory and the pseudoelastic ability of NiTi. Small changes to the stoichiometric ratio and the annealing temperature lead to substantial variance in the SMA properties and the crystal orientation; therefore, the properties of NiTi also change. This can be used as an advantage to tailor-make the SMA in accordance with the manufacturing desires.

The impurities particularly oxygen significantly influence the characteristics of NiTi thin films, affecting ductility and transformations temperatures, and result in brittle films. High oxygen contamination leads to compressive stress while low oxygen content generates tensile stress. Decrease in adhesion and increase in oxygen content in residual atmosphere increase the stress concentration in NiTi films. Ti reacts favourably with oxygen producing TiO_x (x = 2, 3) compounds on the film surface and just underneath the surface while Ni remains unreacted on the surface. For the low-temperature reaction, NiO also forms on or just underneath the surface, during the initial phase of oxidation. Oxygen content in coatings plays a significant role for the microstructure and influences nucleation and growth of the metal layers by acting as a preferential site for nucleation, leads to the formation of oxides, and

produces stress concentration. This research involves the deposition of polymer and SMA, and the presence of oxygen at the film substrate interface, and at the interface of the polymer-metal layers can influence the film properties. If present at interfaces, it affects the adhesion between metal and polymer for which the minimal oxygen content is essential. The presence of higher stress within the coating, and high stress at the metal-polymer and film substrate interfaces could ultimately decrease the deposition rate and cause disbonding [11; 68; 99]. The use of cast-melted targets and high vacuum conditions are suggested for achieving low levels of oxygen impurities.

The human body is an isothermal environment; therefore, the body temperature is immaculately pitched for pseudoelastic applications of NiTi. NiTi has been a candidate for various biomaterials applications in the past as well. NiTi exhibits enormous elasticity of 10 - 20 times than that of ordinary alloy such as stainless steel. In NiTi thin films, one-way and two-way shape memories have successfully been generated in the past. The highest strain of 11.5% along with 1180 MPa tensile strength has been reported, which was achieved with freestanding PVD sputtered thin films ($Ni_{51}Ti_{49}$) that are pseudoelastic at 37°C. Factors affecting the pseudoelastic properties of NiTi thin films include temperature, annealing condition, grain size, stress mode, and microstructure. These factors introduce the lattice defects, internal stress-strain, precipitates formation that affect the martensitic interface mobility, and ultimately influence the shape memory. To take an advantage of pseudoelasticity the NiTi thin films should be slightly Ni-rich, and the A_f temperature should be as high as possible but still below body temperature. Pseudoelastic NiTi has potential use as interlayers between the substrate and coatings of other materials due to their tribological ability of acting as a metallic glue between the two surfaces by enhancing the adhesion. This feature would be advantageous for better adhesion between NiTi and PTFE layers within PTFE-NiTi nanocomposite.

3.4 Polymer-based (PTFE) or metal-based (NiTi) PVD sputtered nanocomposites

Nanocomposite means dissimilar substances combined within one material framework, where major and minor phases are called matrix and fillers respectively [33]. A nanocomposite combines the favourable characteristics of the both components at a nanoscale and realises new functionalities [43]. Matrix is the larger constituent of the composites having the filler particles dispersed within the matrix. The control parameters for nanocomposite thin film manufacturing and structure determination are the spatial distribution, composition of filler particles, size and shape of fillers and the filling factor [152; 153]. Nanocomposite thin films have attracted a prime prominence in the recent decade because of the advanced combination of desired characteristics from dissimilar materials that matches well to the necessities of the application, and overcomes the shortcomings in combination.

PVD thin film composites can be multi-layered, engineered by alternative deposition of individual materials or dispersed-phase coatings are co-sputtered to scatter the fillers within matrix [33]. In PVD sputtering, magnetrons ensure homogenous filler dispersion by plasma deposition because of the reduced plasma loss and better surface coverage [12; 20; 32; 37; 40]. Dispersed-phase co-deposited thin films can result in the reaction between two phases. For example, co-deposition of nickel and titanium produces a dispersed phased composite of nickel and titanium oxide, where the titanium oxide forms because Ti exhibits high oxygen affinity. Phase dispersed nanocomposite coatings have better load bearing ability than multilayer thin films [154].

PVD sputtered polymer-metal nanocomposites have been successfully deposited in the past, consisting of either polymer or metallic matrix. Biederman et al. first prepared RF-sputtered polymer-metal nanocomposite films in 1983 [42]. The matrix-filler configuration of polymer-metal nanocomposites relates to the mechanism of metal cluster formation on the polymer surface. During the deposition process involving initial growth of the nanocomposite matrix, the energetic metallic filler intrudes onto the polymeric surface by a random walk, diffusion or desorption. The initial growth by nucleation follows an ultimately stable growth involving clusters

coalescing, which forms continuous nanocomposite thin films. During the initial diffusion process, if the metallic fillers come across each other, surface defects develop within the thin films. Two factors that determine the metal filling factor of the nanocomposite are condensation coefficient of metal particles and metal - polymer desorption ratio. Like other vapour-based techniques, PVD sputtering provides an excellent control on both of the above factors. Several previous methods employed to integrate the metallic fillers into the polymeric matrix for fabricating the nanocomposites include ball milling, sputtering, the metal salt, and co-evaporation of a metal and an organic component. PVD sputtering produces polymer-metal nanocomposites with higher sputtering rates and reduced stresses, unlike wet chemical approaches where the control on metal filling factor is compromised.[43; 152]

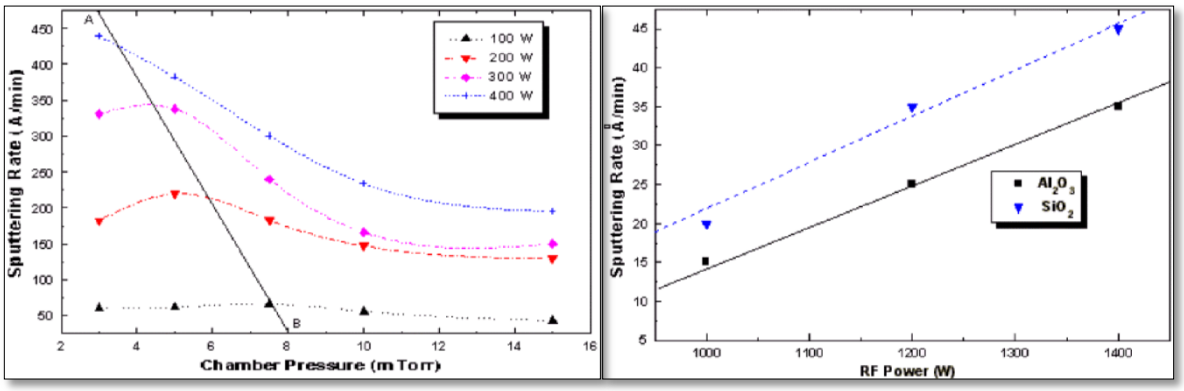

Figure 66: The optimized chamber pressure (3 – 15 mtorr / 4 x 10^{-3} – 2 x 10^{-2} mbar) for PVD sputtering at various powers, (b) PVD deposition rates of SiO_2 and Al_2O_3 against RF power [155].

Farooq et al. [155] studied the optimization of the PVD sputtering process for fabricating the composite thin films by altering the process parameters such as pressure, voltage and current at various RF powers. The deposition rates of metals including Al, Ni and V, and the dielectrics including SiO_2 and Al_2O_3 were investigated at different process conditions. Changes to those conditions altered the growth rates and the volume fractions of the thin film nanocomposites because of the variance in film composition and deposition thickness. The author reported the sensitivity of those process conditions for the sputtering process, as minor changes could lead to substantial deviations in the film properties. Farooq et al. [155] observed the correlation of sputtering power and pressure with the sputtering rate, as shown in

Figure 66. High process pressure and low deposition power resulted in charged particles accumulating on the substrate surface because of the reduction in energy. At a constant deposition power of 100W, the process pressure varied in the range of $4 \times 10^{-3} - 2 \times 10^{-2}$ mbar. With an increase in process pressure, the ion density increases resulting in an increase in deposition rates. Further increasing the pressure decreases the deposition rate due to back diffusion and collisions with the working gas (Ar). Increasing deposition power within the range of 100 – 400 W increases the deposition rate because of more available energy ionising and sputtering more number of particles, and more collisions with Ar particles. The decline in deposition rate against pressure is steeper at high power values, which accounts for the current density increasing with increasing power. Alongside that the temperature also increases by the sputtered flux of incident ionic species and reflected ions from the cathode surface. The increase in temperature reduces the gas density near the cathode. The gas density in the rest of the deposition chamber does not change. The gas density near the cathode also decreases if the target-sputtering yield or the working gas mass declines. Lower sputtering yield of polymers as compared to metal would have resulted in even lower deposition rates. Cooling of the target was recommended to prevent the target damage.[155]

In contrast to other composite materials, SMA composites can provide deflections, which have the same magnitude as the dimensions of the complete gripper system. Winzek et al. [25] reported that compared to freestanding NiTi, composites are preferred for bio-MEMS actuators if the work output is set aside while employing a simple manufacturing method. Krulevitch et al. [25; 26] introduced microgripper made of composite of TiNiCu/Mo thin film actuators on silicon substrates. Use of those microgrippers, e.g. grippers with fine end-effectors like tweezers, is for microassembly devices, which need tools like microgrippers to handle micro-parts, due to their ability to provide appropriate forces. The large deflections of the actuators demonstrate the uniqueness of SMA thin film composites. SMA thin film actuators are superior to other micro-electromechanical mechanisms if there is not sufficient space for large comb structures or large piezo stacks.[25]

The SMA-polymer nanocomposites endure an advanced mechanical performance and have an ability to work under thermomechanical loading. The mechanical

properties of SMA-based composites relate to the filler and matrix dispersal mechanism. The polymer having small elastic strain can take advantage from 6 – 11 % transformation strain of SMA in a polymer-matrix-based nanocomposite. Polymer-matrix based SMA nanocomposite would also provide the strength of the matrix [156]. The incorporation of NiTi with polymer in a nanocomposite has not been done before by PVD sputtering. Few more studies mentioned below fabricate NiTi-polymer nanocomposites by other manufacturing methods. Tihari et al. [157; 158] and Winzek et al. [157; 159] augmented the functionality of an SMA actuator by uniting the NiTi with a polymer and exploiting the difference between phase transition temperature of SMA and the glass transition temperature of the polymer. As-sputtered NiTi is amorphous, and its crystallisation temperature (500°C) is above the melting point (350°C) of PTFE. The difficulty with using shape memory behaviours is the inability to heat the nanocomposite during or after fabrication at a high temperature or for a long time, in order to protect the polymer structure. Excellent adhesion between polymer and NiTi in a nanocomposite is a pre-requisite for most of the potential applications discussed in section [157]. Neuking et al. [157; 160] and Smith et al. [161] acquainted the SMA with silane coupling agents by injection moulding to enhance the adhesion between the NiTi and polymer (polyamide); thus, influenced the physical, chemical and mechanical properties of the material. The composite wires having a polymer matrix and NiTi display nearly 100% improvements in the adhesion properties [161]. Improved tensile behaviour, fatigue resistance and damping properties were achieved using various shapes of SMA in variety of matrix materials [161].

3.4.1 PVD sputtered manufacturing of PTFE-metal nanocomposites

The lubricity of fluoropolymer is remarkable, but the downside is their inferior load bearing capacity as compared to other polymers and metallic substances because of easy slip planes. The inferior load bearing of bulk PTFE results in a short life span of the applications based on their use. In metallic-matrix nanocomposite thin films, PTFE chains are drawn-out on the metallic framework, resulting in lower shear conductance and low CoF of the material; therefore, a longer life span is expected**.** Contrastingly, the addition of metal fillers in the polymer matrix also enhances the load carrying capacity of the substance because of the higher mechanical strength of metals. The poor thermal conductivity of fluoropolymers limits their discrete use as insulators only, whereas the addition of the metallic phase in nanocomposites may enable the material to display the conductivity. The addition of lubricious polymeric fillers to the metallic matrix would lower the friction coefficient; thus, the tribology of thin films improves, and the wear rate reduces. In space applications, PTFE based self-lubricating composite coatings have been used. For example, PTFE-MoS_2 for bearing cages and gears, and PTFE-bronze thin films have been used for bushings and rotating nuts. These coatings provide excellent tribological properties such as lubrication, dynamic stress and tangential stress confrontation and prevention of catastrophic failure.[154]

Preparation of PTFE-NiTi nanocomposite in current research project is the first study to combine PTFE and an SMA by PVD sputtering; however, previous studies report about the incorporation of other metallic filler substances in PVD nanocomposites. Filler substances used in the previous studeis include silver, gold, titanium, molybdenum, aluminium, copper, platinum, rhodium, and zinc in PTFE matrix [20; 32; 35; 42; 43; 78; 152; 162-165]. Target cross contamination was observed by for PVD magnetron co-sputtering of polymer and metals. Some studies reporting this manufacturing issue are discussed below. Beiderman et al. [20] produced composites and performed co-sputtering of PTFE with range of metals including Au, Cu and Pt-10%Rh. Those composites have metal concentrations ranging 1 – 40 %. Target cross – contamination results in small sputtering rate and resputtering, and affects the substrate surface. Roy et al. [12] also explored the target's cross contamination, who co-sputtered PTFE and metal thin films (PTFE – Pt -10%Rh,

PTFE-Au, PTFE-Cu) by RF in 6.7 x 10^{-3} – 100 x 10^{-3} mbar Ar pressure, 25 – 100 W power, and at a working distance of 20 – 80 mm. They placed a 5 cm metal foil on one side of the PTFE target. Both metal and polymer were present in the coatings, but they observed limited deposition process because of target cross-contamination after some depositing time depending on the target diameter. Target cross-contamination occurs during re-sputtering due to the formation of negatively charged the fluorine or other molecular ions containing fluorine. Those ions are highly electronegative with a low ionization potential, which accelerate from the target and attack the substrate as a very energetic beam of neutral particles. The negative ion re-sputtering leads the PTFE-metal nanocomposite to result in a columnar structure. To avoid the impact of re-sputtering for PTFE-metal PVD sputtering a change in the target geometry with separate and independently controlled RF power supply units for PTFE and metal targets are suggested.

PTFE-metal nanocomposites have been used for magnetic, antibacterial and optical applications. For example, Greve et al. [166] prepared PVD co-sputtered PTFE-(Fe–Ni–Co) and took an advantage from the magnetic properties of Fe–Ni–Co. The nanocomposite thin films have polymer matrix with Fe–Ni–Co clusters forming a closed magnetic core within the structure. A multi-layered PVD sputtered nanocomposites of PTFE-$Fe_{54}Ni_{27}Co_{19}$ was manufactured with various layer thicknesses. PTFE-$Fe_{54}Ni_{27}Co_{19}$ thin films are promising candidates in mobile communication electronics because of their ferromagnetic resonance frequencies and high-frequency permeability. Takele et al. [162] suggested manufacturing an efficient Bragg reflector comprising of four co-sputtered PTFE-Ag nanocomposite layers, where PTFE deposits in between every two layers of PTFE-Ag nanocomposite. The absorption wavelength range is 350 – 420 nm for the nanocomposite with small filling factor. Above the percolation threshold, the small compositional changes in the filling factors shift the wavelength range from 405 nm to 500 nm. Near the percolation threshold, a rise in the metallic fillers content decreases the gaps between single clusters, resulting in coalescence, which in turn changes the shape and size of the clusters.[163]

Use of metals as fillers is advantageous for antibacterial applications because of exceptional dispersal of metallic particles on PTFE thin films, which prepare an enormous operational surface for the release of metal ions [152; 167].

Zaporojtchenko et al. [152; 167] co-sputtered PTFE with silver and other noble metals to manufacture the antibacterial thin films, and analysed physiochemical and antibacterial properties of the thin films. 100 nm thick nanocomposite thin films were prepared to have a filling factor (f) of 0.15, which release silver ions of approximately 5 $\times 10^{15}$ cm^{-2}/day from 1 cm^2 film area. Silver ion-release accelerated with the deposition of an additional small amount of gold and silver (< 1 $mg.m^{-2}$ of the film) on the surface of PTFE-Ag nanocomposite. The increase in magnitude order is because of galvanisation of silver and gold coupled nanoparticles. Enhanced silver ion formation occurs because Ag is more dynamic than Au in the galvanic pair. Another set of co-sputtered Ag/Au-PTFE nanocomposite (10% - 40% metal fillers) was also an efficient system for metallic ion release. They incorporated Ag/Au metals by dispersing them only within the surface layer (100 – 300 nm) as nanoparticles. The antimicrobial efficiency of the thin films contrary to different bacteria was verified by very minute metal consumption (gold: ~1 mgm^{-2}, silver: ~0.1 gm^{-2}). Ag/Au-PTFE nanocomposite displayed higher antibacterial ability than PTFE-Ag nanocomposite. Alissawi et al. [168] also prepared antibacterial coatings of PTFE-Ag nanocomposite. They deposited a PTFE coating by PVD sputtering and then deposited silver nanoparticles by thermal evaporation, followed by a top PTFE layer deposition by sputtering. The top porous layer of PTFE ensures the control of silver ion release. The PTFE layer acts as a barrier that alleviates the morphology.

PVD sputtering allows homogeneous dispersion of metallic fillers within in the PTFE matrix, which is essential for obtaining excellent physical and mechanical properties [169]. The magnitude of DC power acts as a control parameter to adjust the metal content with the polymer matrix, and this method for controlling the filler content provides an excellent reproducibility [32]. Schürmann et al. [163] proposed a measurement method of filling factor (f) for PTFE-Ag nanocomposite that involves following relationship between the polymeric matrix density (ρp), the metallic filler density (ρm), and the volume (V) and mass (m) of the thin films, as shown in Equation 3. The volume of the nanocomposite film was calculated by the coatings thickness and sample area. The density of sputtered PTFE is 2.1 gcm^{-3} gravimetrically.

Equation 3: Schürmann et al. equation to determine .the filling factor (f).

$$f = \frac{\frac{m}{v} - \rho p}{\rho m - \rho p}$$

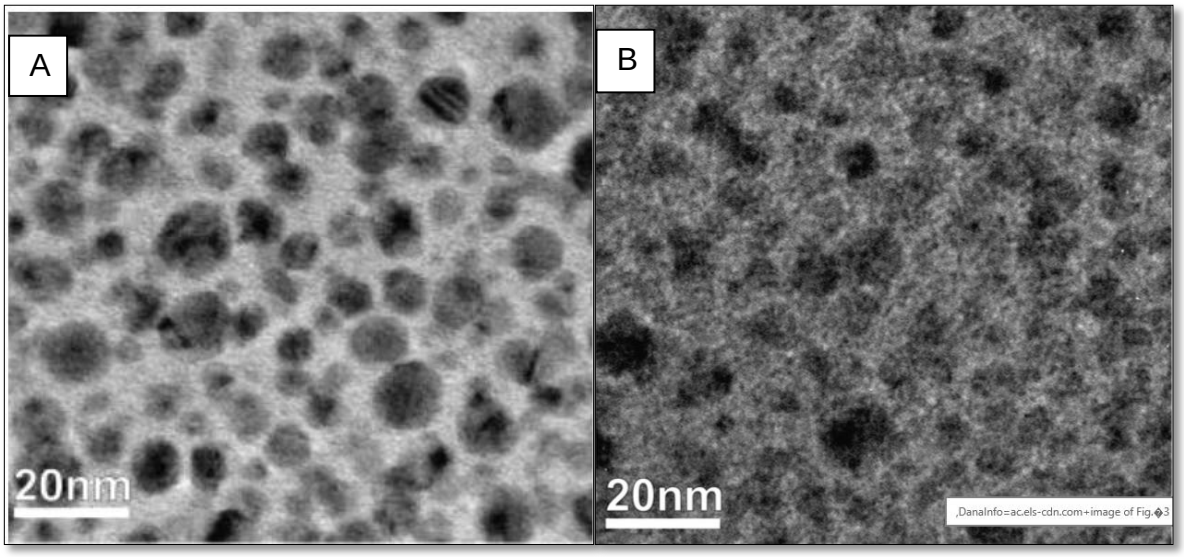

Figure 67: TEM images of Ag–PTFE nanocomposite sputtered with different silver filling factors: (A) 20%, (B) 25% [32].

EDX - TEM is another way to determine the filling factor as suggested by Schürmann et al. [163], which involves estimating the individual material content by EDX at different areas on the thin films, and matching EDX results to the pictorial filler distribution obtained by TEM. Figure 67 shows TEM micrographs of a PTFE-Ag nanocomposite film with 20 and 25 % filler content, where the dark sphericals represent four metallic filler spots of 15 nm in size, entrenched within the polymeric matrix. The AFM topographs of the same films described atomically smooth surface with roughness parameters of Ra = 0.36 and Ra = 0.3 nm respectively [32]. Figure 68 illustrates a characteristic filler distribution of PTFE-Ag nanocomposite determined by EDX-TEM having gradient change of filler content for homogenous PTFE-metal nanocomposite prepared by co-sputtering. PVD co-sputtering allows a simultaneous deposition of polymer and metal during the manufacturing process.

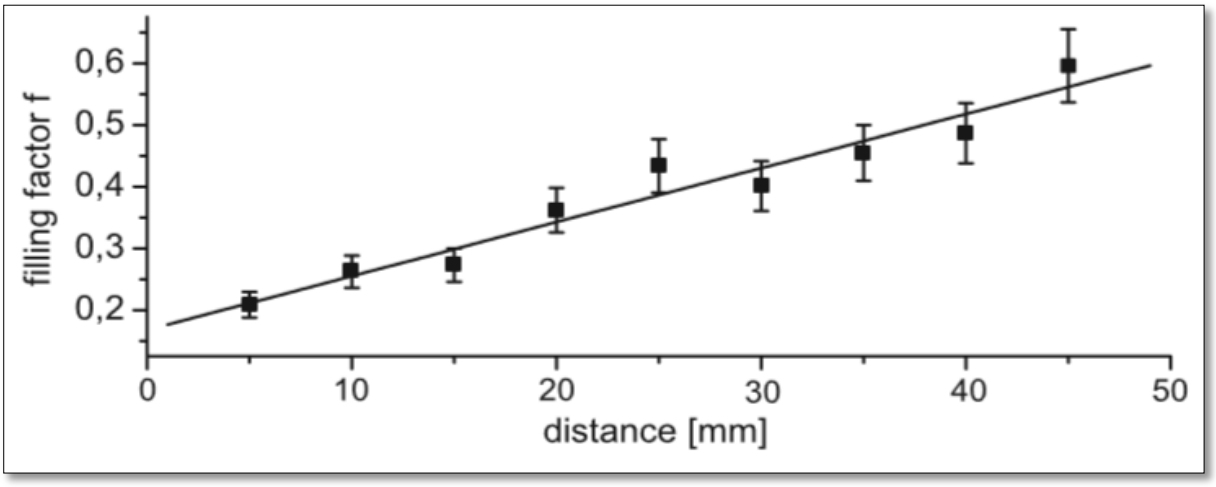

Figure 68: Typical metal distribution in a PTFE-metal nanocomposite having gradient change of filler content (sample length 50 mm; thickness, 100 – 500 nm), and a sketch of a slice through a sample of the nanocomposite [163].

Another method was presented by Farooq et al. [155] to control the filler volume in polymer-metal nanocomposites, who used following equation to determine the volume fraction (V_f) of the composite films, where the sputtering rates of the metal and insulator are represented by A and B respectively.

Equation 4: The relationship to calculate volume fraction of PVD sputtered nanocomposite.

$$\boldsymbol{Vf = \frac{A}{A + B}}$$

The advantages of previously described numerical approaches over EDX-TEM technique are more accurate filler factor measurements and finding a quantitative trend to predict the metallic filling factor at a given distance and power magnitude. For the filling factor above 0.1, a high EDX measurement error (approximately 10%) was found (Figure 68). Unknown layers thickness of unknown or spherical clusters is the main difficulty in determining the filling factor by TEM analysis. Contrastingly, EDX and TEM techniques permit the determination of the filling factor by monitoring the filler size and the filler dispersal patterns along with observing the changes in filling factor. The influence of filler factor on electrical and optical properties of PTFE-Ag nanocomposite is described below.

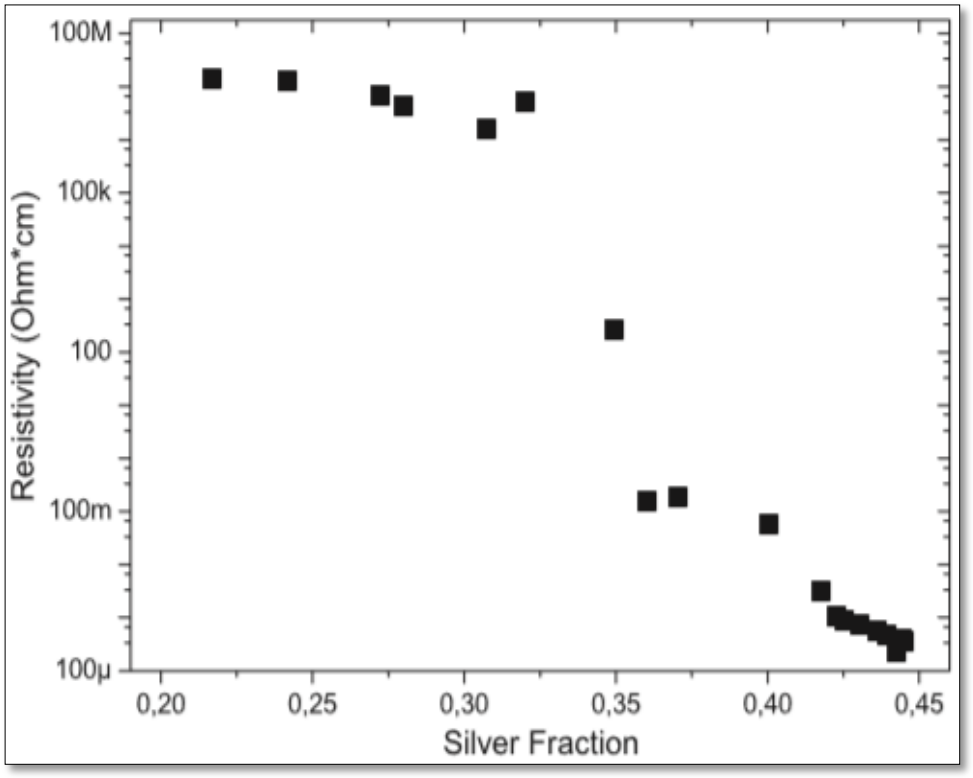

Figure 69: Variance in electrical resistivity of the increasing filling factor of PTFE-Ag nanocomposite deposited by PVD sputtering [162; 163].

Ag is a conductor while PTFE is an insulating material. Like other properties, their combination influences the conductance and resistance of PTFE-metal nanocomposites, which vary significantly with small changes in metal filler content. Small filler concentrations have isolated metal clusters dispersed in the polymer matrix producing an insulating nanocomposite. Figure 69 also shows that the percolation occurs between a filling factor of 0.35 and 0.29. Near the percolation threshold, the electrical characteristics alter severely from insulating to conductive. This means increasing metallic filler amount by few percent in the polymer matrix also increases electron tunnelling between neighbouring metal clusters, and in turn, the magnitude of resistivity decreases by 12 orders, from about 10^{6} Ωcm to 10^{-6} Ωcm.[35; 162; 163; 170]

Similarly, Miyake et al. [171] fabricated RF-sputtered PTFE-Au multilayer nanocomposites. Ten times higher sputtering rate was observed for gold compared to that of PTFE due to lower sputtering yield of the polymer. The polymeric materials fragmentize into smaller units due to physically destructive sputtering process, followed by repolymerisation. For this reason, PVD polymers have lower deposition

rates than metals. Uniform PTFE layer increases the electrical resistivity and lowers the surface roughness, for which the reason is that the uniform surface only forms above the percolation thickness of the thin film, requiring a higher amount of PTFE, which is an insulator. The nanocomposite combination with higher gold content than PTFE has a lower electrical resistivity of 0.02 Ω cm due to metal conductance and a lower CoF (0.05) because of the synergic effect. Increasing the fluorocarbon content at low power results in a higher wetting angle (130°) and reduced surface energy of 29 mN/m. High power deposition procedures are more durable and rougher coatings. This study describes the relationship between deposition power with WCA and surface roughness does not correlate with Zalman et al. [89] findings, which reported that the WCA increases with an increase in deposition power (Figure 24). The rougher surface has a lower surface energy and higher WCA. For this reason, surface roughness may be the result of PTFE incorporation in the composite structure leading to rough and hydrophobic surfaces. The author suggested that the multilayer Au-PTFE thin film with around 80 at.% Au is electroconductive, durable, lubricious and have low surface energy.

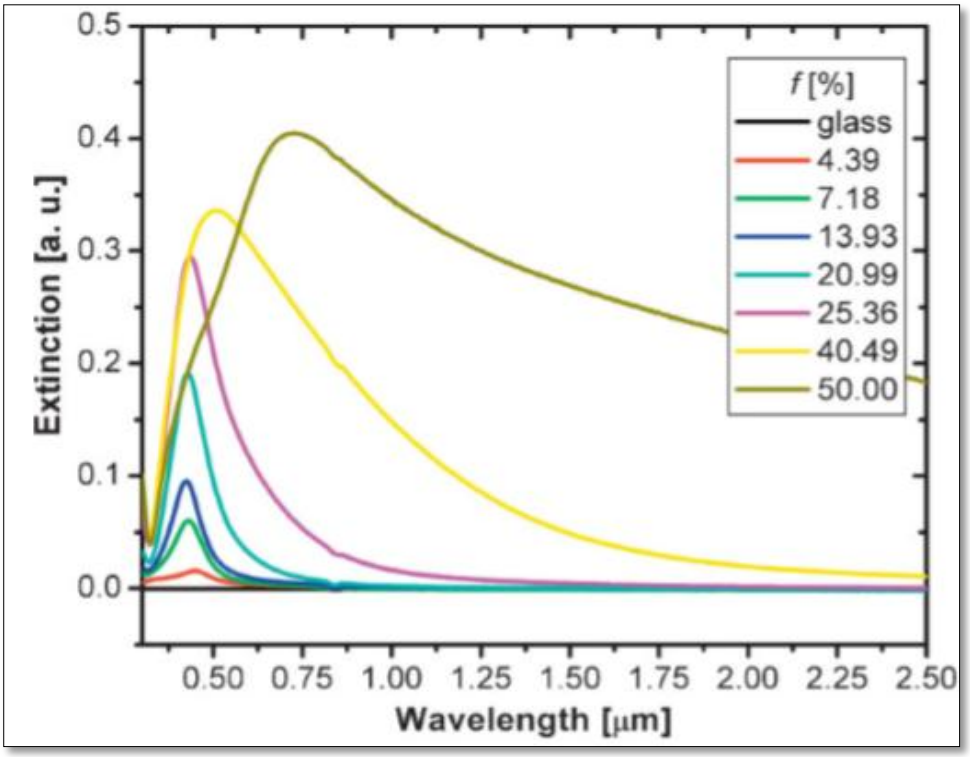

Figure 70: Normalized extinction UV–vis spectra of Au-PTFE nanocomposites at various volume fractions of gold in nanocomposites [43].

The filler content also affects the filler properties of PTFE-metal thin films. For example, Figure 70 shows UV-Vis spectrum of the PVD sputtered Au-PTFE nanocomposite in which fillers were co-deposited with the matrix by Faupel et al. [43]. The noble nature of gold prevents the reaction between matrix and filler during sputtering. The scattering declines and the nanocomposites become transparent since the size of nanoparticles is smaller than the wavelength of light. The increase in transparency with the smaller sized nanoparticles applies to high as well as low filler concentrations because the interaction between the nanoparticles becomes negligible at low filling factors. A rise in filler factor leads to peak broadening, causing a shift towards maximum possible absorption wavelength and enhanced particle interaction [43; 163].

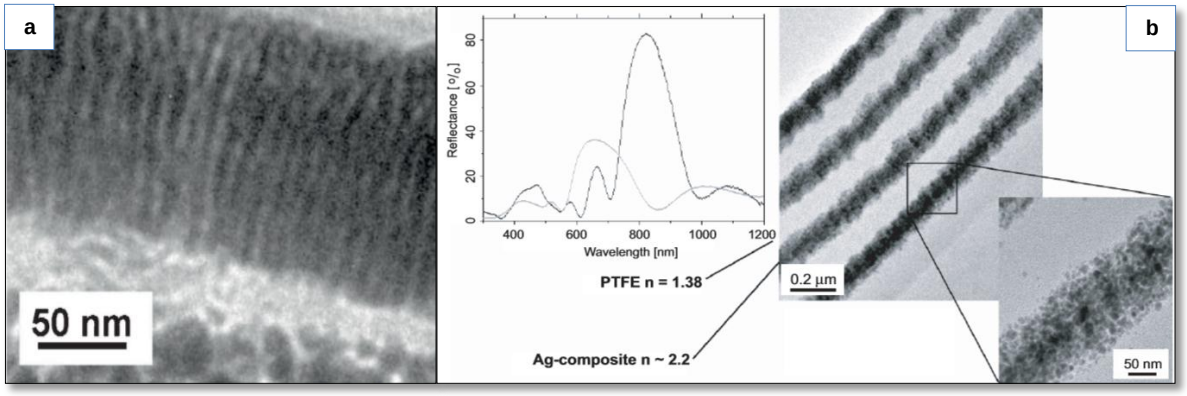

Figure 71: (a) TEM image of Fe-Ni-Co nanorods on top of a layer of Ag clusters in an evaporated PTFE (TAF) matrix [43]*. (b) Spectra of a simple Bragg reflector containing only four composite layers together with cross-sectional TEM of a multilayer structure* [152]*.*

Another study of Faupel et al. [152] also reports the relationship between optical properties and filler volume fraction in PVD sputtered PTFE-Ag nanocomposite having alternative Ag and PTFE layers (Figure 71). The author suggested the use of multi-layered PTFE-Au nanocomposites to build Bragg reflectors. The filling factor and the type of filler were used to adjust refraction index, which was monitored by UV spectrum. For example, the refraction index increases from 1.38 for PTFE to approximately 2.2 for PTFE-Ag nanocomposite at the UV wavelength of 633 nm. Multi-Layered nanocomposite manufacturing is intended in this project along with the co-sputtered nanocomposite fabrication. In multi-Layered nanocomposite

manufacturing the two materials would intercalate each other at the layers interface to compliment the functional properties of each other in one system.

Table 12: XPS data showing the elemental composition of Ag-PTFE. [164].

Samples	Sputtering time (s)	Elemental composition (at.%)			
		Ag	O	F	C
As-sputtered	20	11.7	2.8	37.3	48.2
	100	28.7	8.5	7.9	54.8
	200	29.9	15.3	-	54.8
Relaxed	20	11.0	6.6	30.1	52.3
	100	23.6	6.0	21.1	49.3
	200	25.0	10.2	2.0	62.8
Annealed	20	-	-	66.0	34.0
	100	2.5	0.9	57.7	39.0
	200	4.4	0.7	59.6	35.3

Polívková et al. [164] conducted an XPS study on PVD sputtered PTFE-Ag nanocomposites, prepared by depositing silver nanolayers sputtered on PTFE substrates. The XPS study provides elemental composition limited to 8 to 10 atomic layers as presented in Table 12. In PTFE, the carbon to fluorine ratio is 1:2. Discrete nanoislands appear subsequent to the thermal annealing of silver nanolayers. Over silver deposition span of up to 200s, an increase in silver content and a decrease in fluorine content is detected because of the masking effect of silver on the surface of PTFE. Once the silver film becomes homogenous and continuous, the fluorine is not detected any longer. The masking effect dissipates with the emergence of cracks, discrete islands form, and fluorine is detected again. With the disappearance of fluorine content, a high carbon amount was still detected (54 at.%), which relates to hydrocarbons and other C-rich compounds contamination from the ambient atmosphere. Substantial change in nanocomposite composition happens after 14 days when the specimen had relaxed configuration. A gradual decrease in silver content decreases the surface energy at the interface of polymeric and metallic substances due to oxygen containing groups reorienting themselves towards polymer material; therefore, introducing cracks within the film structure. The cracks expose the PTFE phases so that the fluorine is detected on the surface. A significant

decline is observed in nanocomposite surface composition after the annealing because of intensive coalescence of silver atoms into the islands-like formations. Annealing leads to the oxygen desorption, and the fluorine content increases on the surface because of the exposure of PTFE to post annealing treatment.

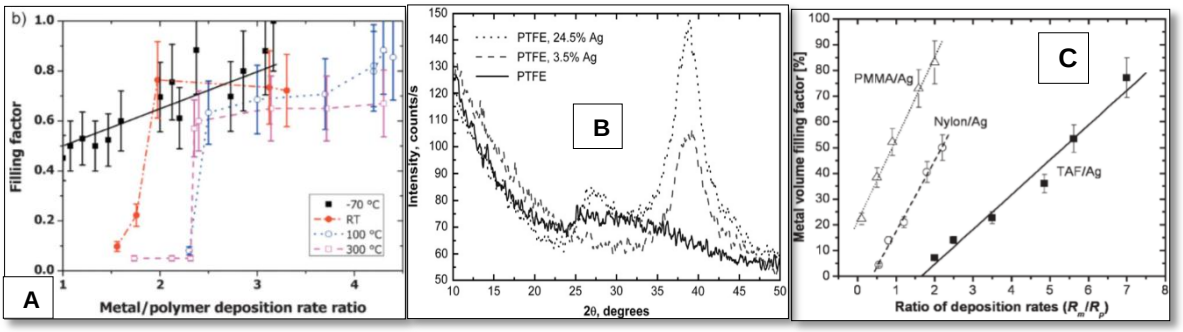

Figure 72: (a) Metal filling factor versus metal organic deposition rates at various temperatures [43]*. (b) XRD pattern of Ag/sputtered PTFE films with different metal filling factors: pure PTFE (solid line), 3.5% Ag (dashed line) and 24.5% Ag (dotted line)* [32]*. (c) Ag filling factor in nanocomposites versus ratio of evaporation rates Rm / Rp of Ag to PTFE (TAF), nylon and PMMA* [43]*.*

The substrate temperature also plays a significant role in configuration of PTFE-metal nanocomposites. Figure 72a shows that no cluster formation happens at low temperatures. Therefore, the substrate and annealing temperature significantly influence the morphology and chemical composition of the nanocomposites similar to the results presented in Table 12. Metallic substances require high temperature for annealing while polymers deteriorate and melt at high temperatures. If the temperature is below the melting point of the polymer, the structure and morphology of the nanocomposite are still affected. Amorphous PTFE deposits by sputtering as shown in XRD patterns presented in Figure 72b, whereas crystalline {111} silver peak appears from nanocomposite on addition of silver in PTFE matrix. The Ag crystalline peak at 2Θ = 40° increases with increasing filler content. The 2Θ = 27° peak corresponds to Si {111} sample holder.[32]

Zaporojtchenko et al. [32] manufactured PTFE-Ag nanocomposite thin films having 800 – 1100 nm thickness. RF and DC powers were used to sputter PTFE and silver respectively, during the PVD magnetron sputtering process. A constant rotation of 10 – 20 revolutions per minute obtains uniform coating composition having 3.5 – 24.5 volume fractions of silver in the polymeric matrix. Figure 72c shows that the filling

factor of PTFE and other polymers increase with increasing deposition rates. Figure 72c also demonstrates that PTFE has a sputtering yield that is two orders of magnitude greater than nylon and PMMA. Sputtered PTFE has more cross-linking than less chain scission due to higher sputtering rate. However, as compared to other sputtered polymers, PTFE has less crosslinking because of higher sputtering rate and advanced lubricity. Therefore, PTFE has twice-sputtering yield and fewer internal stresses. The residual stress of PTFE-Ag nanocomposites was in the range of 6.24 to 12.2 MPa depending on the matrix-filler composition. Pure PTFE films were under a tensile stress, which become increasingly more compressive upon increasing the filling factor of metallic nanoparticles. The Young modulus of pure PTFE was 3.75 GPa, which changed to 7.7 and 22.0 GPa for 3.5 and 20.9 % Ag concentrations respectively in the nanocomposite.[43; 152]

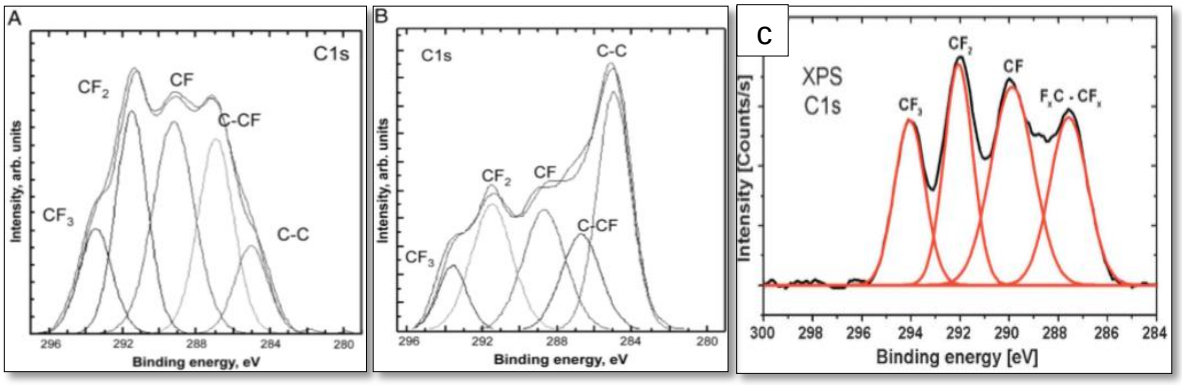

Figure 73: C1s XPS spectra of (A) sputtered PTFE and (B) Ag / sputtered PTFE (24.5 % Ag) [32]*. (C) XPS C1s spectra of Ag-coated PTFE showing cross-links* [43]*.*

Figure 73 shows the XPS spectra of PTFE-Ag nanocomposites from two different studies in which various cross-linking peaks can be observed, indicating an interaction between two materials. Pure PTFE generates a single peak of CF_2 at 290.0 eV. With an addition of PTFE fillers, more peaks appear (Figure 73b) for CF (28.1 % Ag content at 290.2 eV), CF_2 (31.7 % Ag content at 290.0 eV), CF_3 (22.6 % Ag content at 293.9 eV) and C – CF (17.6 % Ag content at 287.9 eV). The author also verified this observation by IR spectroscopy. The cross-linking of PTFE observed by these results verifies the outcome relating to Figure 73c. The crosslinking in polymer-metal nanocomposite can improve the mechanical strength of the resulting materials as compared to bulk PTFE.[32; 43]

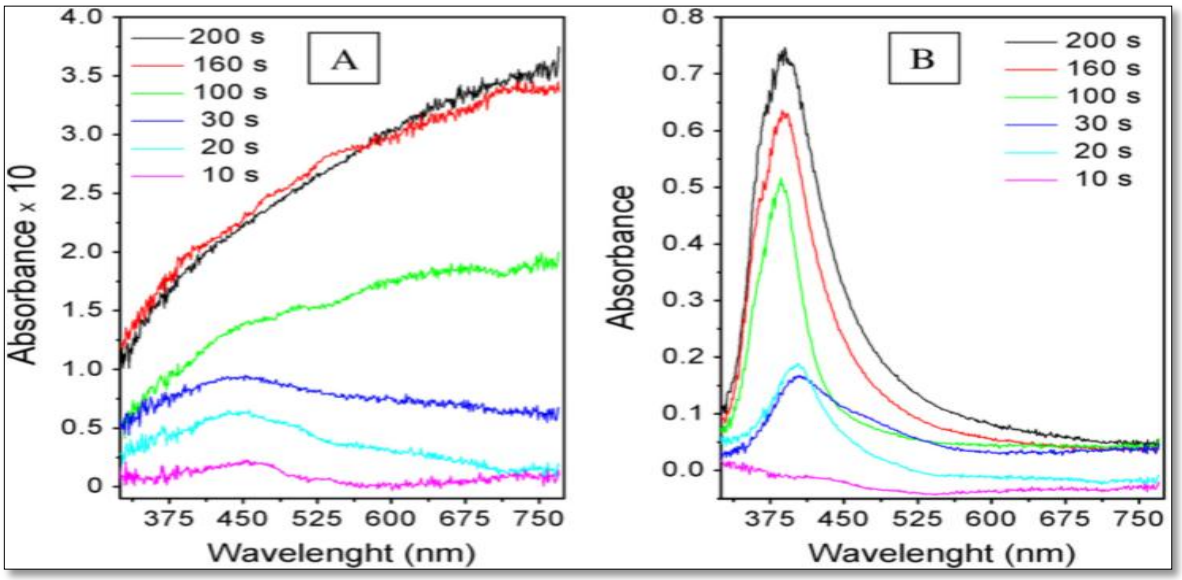

Figure 74: UV-Vis absorption spectra of Ag-coated PTFE, sputtered for various times, (A) as deposited, (B) annealed [164].

Polívková et al. [164] studied the morphology, and the surface properties of PVD sputtered PTFE-Ag thin films. The surface roughness of the thin films increases during the initial film growth subsequent to a constant decrease over sputtering time. Layer growth mechanism is observed firstly with some distinct Ag islands, followed by the formation of interconnections between clusters, and the nanocomposite layers transform into uniform, homogenous and smooth surfaces. Annealing alters the surface morphology of nanocomposite thin films by developing hummock-like coalescence, which appears because of accelerated diffusion of the silver nanoparticles at higher temperatures changing the smooth surface into island assemblies. Nanosized metallic clusters melt at 300°C to 400°C lower temperature in nanocomposite materials compared to their bulk form, depending on their size and shape. The formation of these island assemblies occurs because of solid-state dewetting, which decomposes the dense layers into islets and clusters having reduced surface energies. The sputtering span also influences the optical properties of PTFE-Ag thin films. The absorbance increases with increased silver sputtering span, as shown in Figure 74. A distinct and narrow absorption peak appears around 400 nm. An increase in metallic filler density shifts the absorption band bounded plasma resonance to the higher wavelengths. The thicker silver layers broaden the absorption band because of the wider distribution of the particulates size. For the

30s deposition span, the UV peak remains weak, widespread and hardly identifiable, because of insufficient clusters distinction within the initial growth.[164]

Zhang et al. [165] also reported the effect of deposition time on UV absorbance by PTFE-ZnO thin films. PTFE-ZnO thin films were prepared by PVD sputtering with the use of argon and oxygen as working gases. A growth mode expansion observed in nanocomposite thin film fabrication means that the zinc oxide deposits on the top surface first, followed by depositing all around and growing within PTFE internal structure. The UV absorbance of nanocomposite films was same as sputtered-PTFE thin films after 2 minutes deposition of zinc, but the UV absorbance increases significantly within first 5 minutes of sputtering. Multi-enhanced UV absorbance was found because of nanoparticle-pore reflection and absorbance of nano-ZnO. Multi-enhanced UV absorbance means PTFE-ZnO nanohybrids form a π-conjugated molecular structure, which increase the UV absorbance in thin films more than the total absorbance of PTFE and ZnO individual UV absorption. This occurs because of exceptional reflection property of porous PTFE and Nanosized effect of ZnO.

Liu et al. [44] successfully fabricated PVD sputtered PTFE-Ti multilayer nanocomposite films having excellent adhesion and tribological properties. The thin films deposited on stainless steel have a PTFE rich surface, and the films exhibit a composition gradient, meaning the Ti content gradually decreases in every consecutive layer. In other words, the composition of nanocomposite thin films progressively changes from titanium to an intermediate Ti-TiC-PTFE, followed by fluorocarbon layers on the top surface. The coating compositions were varied by altering PTFE and titanium power during sputtering. The XPS studies report that the nanocomposite having an initial titanium matrix follows an intermediate phase having oligomeric agglomerates of CFx and titanium carbide. During the co-sputtering, some titanium and PTFE-carbon react to form titanium carbide, leaving PTFE with excess fluorination. TiC phase only appears in thin films having higher fluorocarbon ratio within the nanocomposite combination. A dense nanocomposite yields with a combination of titanium matrix having 6.7% fluorocarbon, where 0.1 - 0.5 mm clusters entrench within the PTFE-Ti structure.

Enhanced tribological properties and reduction in stress within layers are observed with increasing PTFE content and gradual variance in PTFE and metal composition

of the layers. The film thickness, interfacial structure and compositions, and the elastic and thermal disparity influence the adhesion of PTFE-Ti nanocomposite. The thermal stresses between the coating and substrate reduce because of the gradual changes in the composition. PTFE films have high interfacial stress with stainless steel substrate, which significantly declines by co-sputtering with titanium. Greater interfacial stresses correlate with higher thermal expansion coefficient ratio, and no interfacial stress is observed for two adjacent layers when the layers have same thermal expansion coefficients. The tribological properties of PTFE-based nanocomposite depend upon the sliding distance / time and the sputtering parameters. The CoF decreases initially followed by an increase that remains at a steady state, under the normal load of 3 N and the sliding speed of 3.14 $m.min^{-1}$ of the hardened steel ball having 6.35 mm diameter. Following the steady state, a further slow or a steep increase in CoF was also observed for some PTFE-Ti specimens. Overall, the CoF remains within the range of 0.1 – 0.3. An increase in the PTFE content decreases the CoF during the initial wear process but is not influential during the later wear stages because the following wear processes are mainly subjective to the coating removal. The multilayer nanocomposites display a better tribological performance because of two layers acting as two single coatings; therefore, demonstrating the desirable synergetic effect. The titanium matrix within the nanocomposite provides an enhanced mechanical strength to PTFE while the PTFE-based lubricious coating have a longer life.[44]

The above study suggests that successful interfacial adhesion is possible between the layers of PTFE and Ti, which is encouraging to hope that NiTi SMA (Ti in its structure) would also incorporate PTFE within its layers for the production of nanocomposite. Presuming the successful deposition of stable PTFE-NiTi coatings, it will still be challenging to observe novel intercalated function for the nanocomposite structure. The study also provides a useful background knowledge to predict PTFE-NiTi tribological and adhesive properties.

The chemical composition and the surface morphology directly influence the surface properties, such as wettability. Shimizu et al. [172] also controlled the wetting angles of RF-co-sputtered nanocomposite by altering the chemical composition, structure and design. SEM spectroscopy found no cracks and defects in hydrophobic thin

films. The thin films conserve the hydrophobic nature of the PTFE and the high transparency of TiO_2 simultaneously. PTFE-Ti combinations formed thick structures that are rod-like and have a smooth surface, while PTFE-TiO_2 have sea-island surface consisting of small round structures. The crystalline peak appeared in the thin films without any heat treatment. PVD sputtered Ti endures needle-like structures covered by PTFE and PTFE-TiO_2 during deposition. Wetting angles of the thin films were 168° and 111° – 116° for PTFE-Ti and PTFE-TiO_2 regions respectively within the nanocomposite thin films.

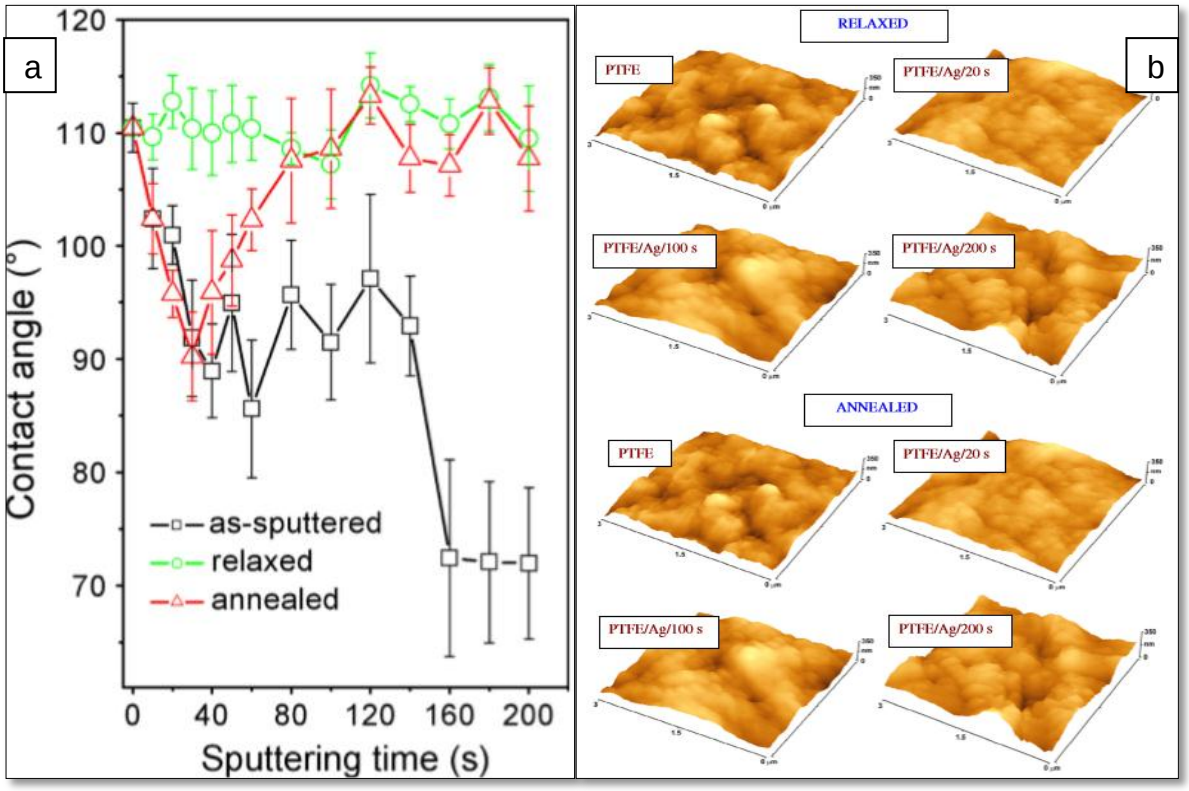

Figure 75: (a) Dependence of WCA on deposition time for pristine PTFE (deposition time 0s) and Ag-coated PTFE. WCA was measured immediately after Ag coating (as-sputtered), after 14 days from the Ag deposition (relaxed), and on annealed and relaxed sections (annealed). (b) AFM topographs of pristine and Ag-coated PTFE (20, 100 and 200 s) for relaxed and annealed samples.[164]

Polívková et al. [164] also recorded the WCA of as-deposited PTFE-Ag thin films for the deposition times ranging 10 – 200 s. The WCA of PTFE-Ag was recorded immediately after deposition (as-deposited), after 14 days of deposition (relaxed configurations) and after annealing of the relaxed specimen. The wetting angle of pristine PTFE (110° +/- 2°) reduces after silver deposition resulting in an increase in

wettability. In as-deposited nanocomposites, three eminent regions are observed at the range of sputtering times. In the first region of 10 – 40 s sputtering, the WCA decreases over deposition time. In the second region, from 40 to 140 s the wettability increases again to 92° followed by a subsequent decrease to 72° in the third area. The wetting properties of PTFE-NiTi will also be analysed and adjusted by intercalation. For the annealed nanocomposite samples, the WCA slightly decreases from 10 – 30 s sputtering time. After the 30s, the wettability decreases significantly and gradually, and ultimately the surface shows similar hydrophobicity to PTFE. This increase in WCA becomes nearly constant after this rise in hydrophobicity, which indicates that the annealing causes the coalescence of the silver particles in the distinct islands, which expose the PTFE surface. During the deposition, the initial drop of hydrophobicity occurs due to petite silver particulates reacting with atmospheric oxygen to cause oxygen enrichment within the structure.[164] It is important to realise from the above-mentioned PTFE-Ag study that the deposition time (deposition rate) needs to be controlled or kept constant in all experiments, because the wetting angle of PTFE-Ag nanocomposite varies for thin films deposited for various sputtering times. Changing sputtering rate or sputtering time can influence the surface properties mainly wetting angle of PTFE-NiTi nanocomposite rather than wetting angle being controlled by intercalation.

3.4.2 Summary

Lubricious, hydrophobic and insulting PTFE material can successfully deposit with range of conductive metals having good mechanical strength, by PVD magnetron sputtering in the form of co-sputtered and multi-layered thin films. NiTi-polymer combination by PVD sputtering was not found in existing literature so far. Target cross contamination is a potential difficulty to perform co-sputter deposition of PTFE-metal nanocomposites, as it reduces the deposition rates significantly. The general trends of deposition pressure and deposition powers vs. deposition rates of the metals were found in the literature; nevertheless, a similar quantitative study to understand the same for polymer deposition lacks in the literature. Increasing deposition power increases the deposition rates while increasing the deposition pressure also increases the deposition rates followed by a decline. The deposition rate increases followed by a decrease because the rising ion density increases resulting in an increase in deposition rates followed by the back diffusion and collisions with the working gas (Ar) decreasing the deposition rate. The polymers might not provide a similar process conditions vs. sputtering rates at all powers and pressure due to fragmentation and repolymerisation during sputtering. It is also essential to understand that complex polymers chains cannot be successfully deposited by PVD sputtering, and various polymers would vary their deposition rates at given process conditions for nanocomposite manufacturing. It will be interesting to compare the deposition rates vs. process conditions behaviours of polymers and metals because they influence the film properties significantly.

The existing applications of PTFE-metal nanocomposite include optical antibacterial and magnetic applications so far. The filler volume is controlled by numerical methods and EDS-TEM analysis. The recompenses of using the numerical methods over EDX-TEM procedure are accurate filler factor measurement, finding a quantitative inclination to predict the metallic filling factor at a given distance and power, and smaller measurement error. The trouble with the filling factor determination by TEM is unknown layers thickness in case of unknown or spherical clusters. Contrastingly, the determination of filling the factor by EDX and TEM techniques permit monitoring the filler size and the filler dispersal patterns along with observing the filling factor.

The substrate temperature plays a significant role in configuration of PTFE-metal nanocomposites. The substrate and annealing temperature significantly influence the morphology and chemical composition of the nanocomposites. The crosslinking in polymer-metal nanocomposite improved the mechanical strength of the resulting materials as compared to bulk PTFE. Ten times higher sputtering rate was observed for gold compared to PTFE in multilayer PTFE-Au nanocomposite, which was lubricious (CoF: 0.05), hydrophobic (WCA: 130°), having good optical properties and less conductive than a polymer. Approximately 80 at.% Au in multilayer Au-PTFE produces thin films that are electroconductive, durable, lubricious and have low surface energy. The noble nature of gold prevents the reaction between matrix and filler during sputtering.

For PTFE-Ag nanocomposite, the small filler concentrations have isolated metal clusters dispersed in the polymer matrix producing an insulating material. Near the percolation threshold, the electrical characteristics alter severely from insulating to conductive. The refraction index increases from 1.38 for PTFE to approximately 2.2 for PTFE-Ag nanocomposite at the UV wavelength of 633 nm. A significant decline is observed in nanocomposite surface composition after the annealing because of intensive coalescence of silver atoms into the islands-like formations. Annealing leads to the oxygen desorption, and the fluorine content increases on the surface because of the exposure of PTFE to post annealing treatment. Amorphous PTFE deposits by sputtering, whereas crystalline silver peak (111) appears from nanocomposite on addition of silver in PTFE matrix. The filling factor of PTFE and other polymers in PTFE-Ag nanocomposites increase with increasing deposition rates. The residual stress of PTFE-Ag nanocomposites was in the range of 6.24 to 12.2 MPa depending on the matrix-filler composition. Pure PTFE films were under tensile stresses, which become increasingly more compressive upon increasing the filling factor of metallic nanoparticles. The Young modulus of pure PTFE was 3.75 GPa, which changed to 7.7 and 22.0 GPa for 3.5 and 20.9 % Ag concentrations respectively in the nanocomposite. Layer growth mechanism is observed firstly with some distinct Ag islands, followed by the formation of interconnections between clusters, and the nanocomposite layers transform into uniform, homogenous and smooth surfaces. During the deposition, a drop of hydrophobicity occurs due to petite

silver particulates reacting with atmospheric oxygen to cause oxygen enrichment within the structure.

PVD sputtered PTFE-Ti multilayer nanocomposite films have outstanding adhesion and enhanced tribological properties. The composition of nanocomposite thin films progressively changes from titanium to an intermediate Ti-TiC-PTFE followed by fluorocarbon layers on the top surface producing a dense nanocomposite with a combination of titanium matrix having 6.7% fluorocarbon, where 0.1 - 0.5 mm clusters entrench within the PTFE-Ti structure. Increasing the PTFE content and the gradual variance in PTFE and metal composition of the nanocomposite layers resulted in enhanced tribological properties and reduced in stress within layers. The film thickness, interfacial structure and compositions, and the elastic and thermal disparity influence the adhesion of PTFE-Ti nanocomposite. The thermal stresses between the coating and substrate reduce because of the gradual change in compositions. SEM spectroscopy found no cracks and defects in thin films of PTFE-TiO_2. The thin films conserve the hydrophobic nature of the PTFE and the high transparency simultaneously. PTFE-Ti combinations formed thick structures that are rod-like and have a smooth surface, while PTFE-TiO_2 have sea-island surface consisting of small round structures. PVD sputtered Ti has a needle-like structure covered with PTFE and PTFE-TiO_2. Wetting angles of the thin films were 168° and 111° – 116° for PTFE-Ti and PTFE-TiO_2 regions respectively within the nanocomposite films.

A study reporting about PTFE-Ti nanocomposite suggests that a successful interfacial adhesion between the layers of PTFE and Ti, which is encouraging to hope for NiTi SMA (having Ti in its structure) to incorporate with PTFE producing a nanocomposite. Presuming the successful deposition of stable PTFE-NiTi coatings, it will still be challenging to observe novel intercalated function for the nanocomposite structure. The deposition time (deposition rate) needs to be controlled or kept constant in all experiments because the wetting angle of nanocomposite varies at thin films deposited for various sputtering times and conditions. Changing sputtering rate or sputtering conditions would influence the surface properties mainly WCA of PTFE-NiTi nanocomposite, rather than wetting angle being controlled by intercalation as proposed in this project.

3.5 Intercalated nanomaterials

Intercalation is the inclusion of guest species in the accessible unoccupied-interplanner voids of another solid's layers (host); thus, expanding the van der Waals gap between the molecules / layers to form a hybrid network [1; 173]. Intercalation is explicated as a topochemical diffusion-reaction requiring energy for the enhancement of bidimensional van der Waal gaps [1]. The integrity and stability of the host material are retained after intercalation process. The internal primary bonding of the host material's matrix should be strong enough that the material should expand the van der Waal gaps in the interplanner voids by guest species without compromising its structure. Intercalation involves changes in bonding and composition because of the insertion of guest species introducing van der Waal gaps, which influence the material's structural properties and the functional behaviour. The structural modifications produce materials with low defect concentration and steric restrictions. Small defect concentration and steric restrictions of the interlayer-intercalation can errand particular cluster geometry at layer-interfaces. Subsequently, this may influence the granular configurations in amorphous nanocomposite films. There is a possibility that too low temperature during the manufacturing process inhibits the interaction because of the lack of sufficient activation energy for the diffusion of guest particles.[174]

Atomic scale intercalation (nano-intercalation) has been observed previously between the host materials such as fullerenes and the guest particles, for example, peroxides and mercury. Although a nanoscale intercalation of PTFE-NiTi nanocomposite is aimed; however, the above-described materials partake the solid-liquid interaction rather than potential solid-solid intercalation for the nanocomposite manufacturing in the current project. Solid-solid intercalated structural features have been reported for the interconnected cavities and tunnels of some 3D structures and between the lamellar transition metal chalcogenides and graphite. Intercalation in those materials resulted in empty octahedra, tetrahedra or trigonal prisms between the host materials lamellar layers, depending on the stacking mode of the atoms. [173]

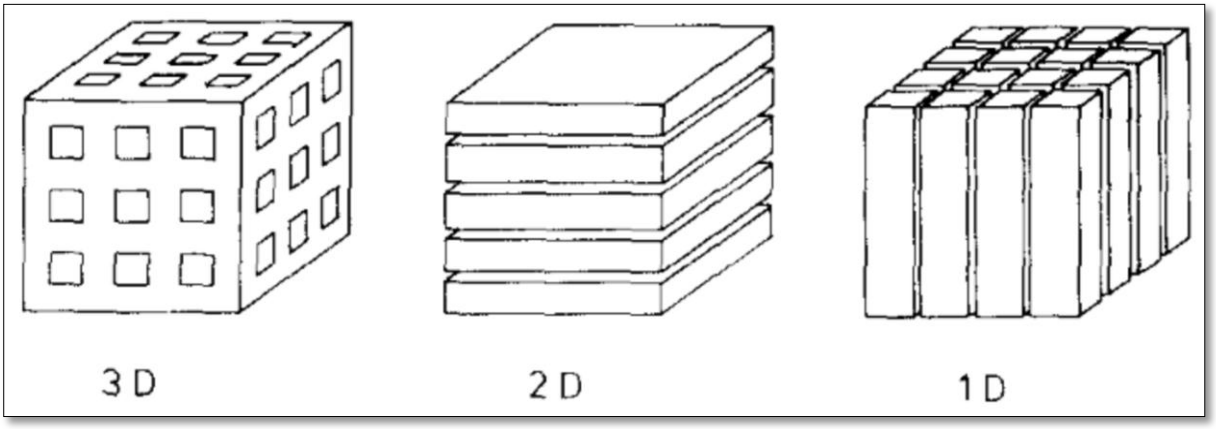

Figure 76: Scheme of basic host lattice types [174].

The structures of the host lattices are schematically described as one-dimensional, two-dimensional and three-dimensional system as shown in Figure 76. One-dimensional host lattice systems have van der Waal gaps located in the lattice vacancies of chain-type units bound together. Two-dimensional host lattice systems have van der Waal gaps between the interlayer-voids of the neutral matrix-based layers. Three-dimensional host lattice systems have unoccupied voids in polyhedral channels of a matrix framework. The potential PTFE-NiTi nanocomposite will be manufactured in the form of thin films. Thin films are defined as two-dimensional structures, which can be deposited as a layered material by sputtering the alternative layers of PTFE and NiTi from discrete targets. Thus, the prospective PTFE-NiTi nanocomposite thin films would be intercalated structures formed of Two-dimensional host lattice systems. Weak interactions between the matrix-layers of 2D host lattice systems allow accommodating large guest species during intercalation without declining its stability and integrity, and moderate dimensional restrictions (Figure 77).[174]

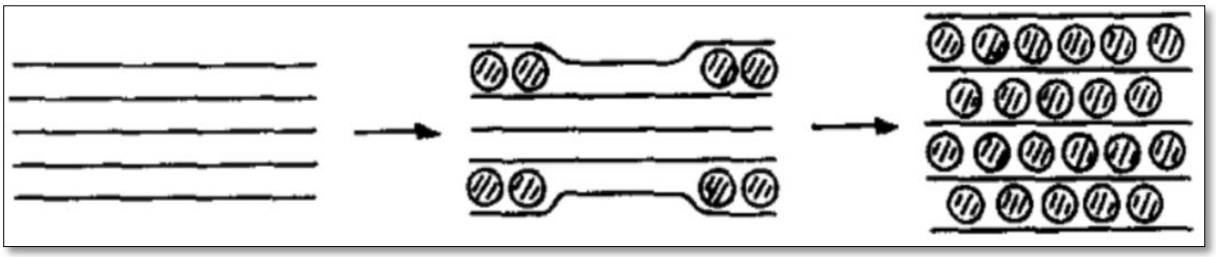

Figure 77: A schematic of the basic mechanism of formation of layered intercalation compounds [174].

Co-sputtered manufacturing of potential PTFE-NiTi material is intended to investigate the possibility of intercalation in filler-matrix type nanocomposites rather than layered structures. Similar filler-matrix type settings are reported in epoxy nanocomposites by LeBaron et al. [175] as shown in Figure 78. The epoxy clay-polymer nanocomposites intercalate by reinforced exfoliation and homogenous dispersion of the clay nanolayers in a polymeric matrix. These types of intercalated nanocomposites have advanced structural properties because of repeating nanolayer-stacking pattern having a consistent gallery height between the stacks. For example, the elastomeric polymer network crosslinking of PU display a modified stress-strain behaviour. Thus, the intercalated nanocomposite exhibits a tougher and stronger polymer matrix as compared to the pristine polymer. Similar interaction property was acquired for organoclay-PP nanocomposites also.[175]

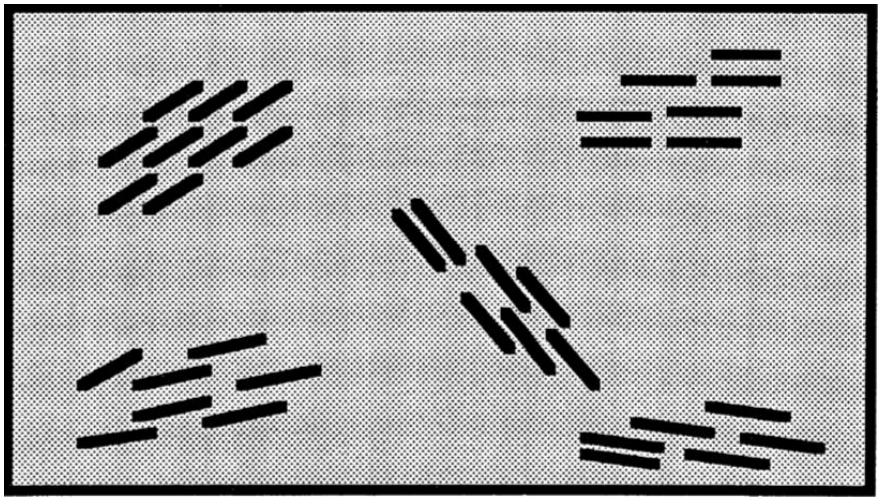

Figure 78: Schematic illustrations of an intercalated. The clay interlayer spacing is fixed in an intercalated nanocomposite [175].

The literature describes a successful solid-solid intercalation mechanism of polymeric guest species in CNT-polymer composites of buckypoymers. Porous carbon-nanotube (CNT) buckypolymers intercalate polymeric binding agents into their internal structure, fabricating the reinforced nanotube with superior mechanical properties mainly loading performance [176]. Colman et al. [177] improved the tensile strength and Young modulus of the SWNT buckypolymers by intercalating PVA into their structure, by 3 and 9 times respectively. Intercalating polyurethane (PU) into PEG functionalised nanotubes also resulted in a nanocomposite having 800 times higher Young modulus. Solid-solid intercalation in the above structures

improved the mechanical properties in the above studies, involving polymer wrapping around the nanotube. The wrapping in the intercalated structure occurs by π-π stacking of polymer onto nanotube and van der Waal interactions. Intercalation through wrapping changes the geometry of the nanomaterial; thus minimise the energy and improve the mechanical properties.[176] The above-described examples of intercalation in nanomaterials involve various manufacturing methods; however, the scope of this project is limited to PVD manufacturing of thin films. Only a few studies were few found that report intercalation in nanocomposites prepared by PVD magnetron sputtering, which are briefed below.[178][43; 178]

Liao et al. [178] deposited lithium-cobalt-oxide ($LiCoO_2$) nanorods by RF magnetron sputtering, in which intercalation / deintercalation of lithium ion (Li^+) takes place in layer structure. Figueroa et al. [179] investigated the dependence of the process parameters on RF sputtered thin films of WO_3 intercalated with Li^+ [180][165; 180]. Brousse et al. [180] also prepared $LiCoO_2$ and $Li_{4/3}Ti_{5/3}O_4$ thin films by RF magnetron sputtering to examine the interaction capacity of Li^+ with PVD thin film structures. Miyazaki et al. [181] evaluated the reversible intercalation and deintercalation mechanism of [175][172; 175]. RF-sputtered vanadium oxide (V_2O_5) films deposited by reactive RF magnetron sputtering. Thißen et al. [182] characterised the chemical properties of Li^+ intercalation and deintercalation in lithium ion batteries. Punitha et al. [183] prepared WO_3 films intercalated to H^+ ions by cycling into sulphuric acid (H_2SO_4). All of the above studies involve electrochemical reactions involving charged ions as guest species, and commonly a solid-liquid intercalation takes place. The details of the findings of above studies are beyond the scope of this research because the electrochemical intercalation mechanism is utterly different from potential solid-solid intercalation between a metal and polymer in this project. Primary bonding in polymer and SMA is covalent and metallic respectively unlike ionic electrochemical reactions. PVD sputtered solid-solid intercalation involving polymer and metal (SMA) has not been observed so far in 2D host lattice systems or filler-matrix type nanocomposites. An example of solid-solid intercalation is Selinder et al. [184] performance assessment of cemented carbide tools superlattice coated by TiN/TaN and TiN/NbN for stainless steel machining. The intercalation was realised by ion plating of TiN and reactive sputtering of NbN and TaN. TiN/NbN lamellar coating on the microscopic superlattice B2 structure exhibit a Vickers

microhardness (HV0.5N) ranging 32 – 39 GPa and substantially lower residual stress. High hardness values along with a restrained amount of intrinsic compressive stresses lead to extraordinary wear resistance too. Intercalation has been explained as a topochemical reaction requiring energy for the insertion of guest species in the host material and for the enhancement of van der Waal gaps [1]. During solid-solid interaction by physical vapour deposition (sputtering), the energy is provided by the energetic sputtering process and topological-intercalation is aimed by physical means rather than a chemical reaction.

4 PROPOSAL FOR PTFE-NiTi NANOCOMPOSITES MANUFACTURING BY PVD MAGNETRON SPUTTERING

"In the proposed intercalated PTFE-NiTi nanocomposite, PTFE and NiTi would be structurally associated with each other and form nano interlayer hybrids due to intermolecular forces realignment. Structural properties should influence the functional characteristics of the material such as wetting behaviour and lubricity. It is crucial that the intercalated nanocomposites have PTFE and NiTi configured as guest and host configuration instead of conventional composite arrangement. In conventional composites, the filler dispersion is not limited to intermolecular interactions only; instead, the chemical reactions or modified physical bonding controls the structural features and properties of those materials. Thus, both constituent materials would maintain their discrete properties to some extent while the composition and intercalated structure at constituent materials interfaces would determine the nanocomposites' responsive wetting behaviour of the thin films."

Biomimicry would accede some of the structural and functional features of urethral tissue into the proposed intercalated PTFE-NiTi nanocomposite. The advantage of using the biomimicry framework to construct project proposal provides manufacturing reliability, efficient conceptual control on the engineering process [185]. A miniaturisation approach of cells forming tissue inherits from nature, along with the idea of forming hybrid grading in the nanocomposites matching to that of natural tissue structure. Hybrid features provide enhanced resistance against multidimensional wear loads by improving the nanoscale design [41]. The compositional ratio of PTFE and NiTi in nanocomposites would be varied to investigate the influence of change in composition and structure on properties and functionality of the thin films. This idea emanates from the fact that the hard and soft material composition in natural tissue according to the functional need of that tissue. For example, the bone needs to be strong and load bearing; for this reason, a greater amount of tough collagen and hydroxyapatite is present with some elastomer material. Contrastingly, tendons and epithelial muscles contain higher soft tissue elastomer content than tough collagen fibers because of their requisite of flexibility.

Pseudoelasticity of NiTi can be an additional benefit for the intended material, which would provide additional functionality feature and expand the scope of application. A physiological function, micturition, provides further functional explanation of the biomimicking approach adopted in this project. In females, micturition is a physiological urethral function only that relaxes the urethra voluntarily at sensing that the bladder is full. The approach of mimicking the micturition is adapted to aid the manufacturing path and to simplify the functional demonstration of smart-intercalated nanocomposite. Although the aim of this research is producing an intercalated nanocomposite; however, some additional research will be conducted on NiTi transformations relating to adjusting pseudoelastic isothermal temperature, which would provide the baseline data to conduct further research on this subject in future. Thus, intercalated PTFE-NiTi nanocomposite would further modify as a device displaying a controlled flow, leading to micturition-like microfluidics applications.

As a nano-fabrication method, PVD manufacturing is complex at the atomic level, and slight deviations have a substantial influence on a film's structure and properties. Thus, This research also addresses following critical thin films manufacturing issues for better understanding and deposition control of PVD sputtering process. It is crucial to monitor the working parameters because PVD thin-films properties are significantly dependent upon deposition parameters, and slight changes can lead to substantial deviations in film properties. A comprehensive study to find out the influence of deposition power and process pressure on deposition rates of PTFE and NiTi thin films is required. These results not only allow better understanding of the PVD manufacturing process of polymer and SMA, but also enable the selection of the suitable working parameters for the desired nanocomposite production along with controlling the filler content in PTFE-NiTi. Comparative study of polymer and intermetallic deposition conditions and characteristics would also be performed. The knowledge of relative working parameters of polymer and SMA deposition allows better control during the deposition process. SEM images, along with other results related to the deposition conditions will be explored and compared to the existing literature, with the purpose of remarking on thin film growth and zone-models of PTFE, NiTi, and PTFE-NiTi thin films.

A comprehensive analysis of NiTi thin films by DSC (phase transformations and associated enthalpies) and XRD (crystal structure and composition) is intended. DSC method will be used to explore various post-sputter heat treatment conditions for NiTi, and the influence of film composition and heat treatment conditions on transition temperatures and compositional properties of NiTi will be studied. Tailoring the NiTi composition would lead to achieving the SMA's pseudoelastic behaviour at body temperature. Post-sputter annealing heat treatment is chosen for this project because the higher transformed content of thin film in post-sputter heat treated and aged for a longer time leads to a successful transformation. Impurities and defects leading to oxidation, precipitation and stress accumulation in thin films will be analysed. The impurities particularly oxygen significantly influence the characteristics of NiTi thin films, affecting ductility, resulting in brittle NiTi films, and the phase transformations temperatures also vary. High oxygen contamination leads to compressive stress while low oxygen content generates tensile stress. This research involves the deposition of polymer and SMA, the presence of oxygen at the film substrate interface, and at the interfaces within the polymer-metal layers can influence the film properties. If the present at interfaces, oxygen affects the adhesion between metal and polymer for which optimum minimal oxygen content is essential. The presence of higher stress within the coating, and at the metal-polymer and film substrate interfaces could ultimately decrease the deposition rate and cause disbonding.[68][68; 174]

PVD sputtering is an energetic process involving physical reactions, which lead to destructive fragmentation of polymers such as PTFE. A detailed investigation will be performed to ensure that PTFE thin films reform as intact polymer chains, which can be characterised by FTIR spectroscopy. PTFE has much simpler polymer chain structure than most of the other polymers, and it is sputtered in larger molecular units resulting in higher deposition rates. Although PTFE has been successfully deposited as polymer (polymer-reformations) by PVD sputtering, as reported by various research-based studies in the past but the extent of repolymerisation has not been quantified so far. The influence of deposition parameters on the amount of polymerised content with the polymer chain also needs to be investigated in detail. The chemical structure and polymerised content of PTFE within the coatings at

various deposition conditions requisite for an investigation and the results will correlate to the surface morphology and wetting angles.

Nanocomposite thin-films are fascinating functional materials because of the advanced combination of desired characteristics from dissimilar materials, matching well to the needs of the application while together overcoming the disadvantages of individual material. Literature review suggests that PVD sputtered nanocomposite manufacturing is possible in both matrix-based and layered structures by co-sputtering and deposition from alternative targets. Both types of nanocomposite materials may have intercalation perspective depending on the materials characteristics and combinations. The solid-solid intercalation for metal-polymer nanocomposite combination of thin films manufactured by PVD magnetron sputtering is not reported previously. Therefore, it is proposed to manufacture PTFE-NiTi nanocomposite in both matrix-based and layered structures, and to investigate their functional features of PTFE and NiTi such as hydrophobicity and lubricity.

Co-sputtered PTFE-NiTi nanocomposite having a PTFE matrix would potentially form a cross-linked and lubricious film structure with potential applications as elastomeric biomaterials. NiTi filler dispersed in PTFE matrix would enhance the mechanical properties, and a possibility of stress-induced transformation would improve the stress-strain behaviour and accumulation of stress in thin films. The co-sputtered PTFE-NiTi nanocomposite thin films would have a NiTi matrix, which may provide the mechanical strength and a possibility of introducing the pseudoelasticity and generating the appropriate force for the expansion and relaxation of the nanocomposite surface by stress-induced transformations. Small amount of incorporated PTFE in the NiTi matrix would act as lubricant filler and permit adjusting the tribological properties and the wetting angles.

The layered arrangement of PTFE-NiTi nanocomposites is another manufacturing approach in this project. The thin films are expected to act as the self-lubricating material with an ability to minimise the wear and friction, which is intended to realise by introducing intercalation. Hydrophobicity and layer thickness relationship should equate to regulate the fluid interaction with the coating, and gear the wetting properties of the film surface. The NiTi SMA layer would also inherit the wetting and tribological properties from the polymer layer underneath. In addition, assuming the

formulation of a crystalline pseudoelastic PTFE-NiTi nanocomposite would let its pseudoelastic nature take better control of nanocomposite function by stress-induced relaxation and expansion.

PTFE-NiTi thin films would be initially examined by wetting angles, EDS micrographs, and SEM and TEM images, which would explain if PTFE and NiTi successfully integrate with the nanocomposite structure. Depending on the results obtained by SEM and WCA, the nanocomposite composition and configuration would need optimisation to fabricate an exemplary model of ensuing intercalated PTFE-NiTi nanocomposite films. As a final point, the prospective characteristics of PTFE-NiTi nanocomposite are listed below.

- TEM and / or SEM images of PTFE-NiTi demonstrating that PTFE and NiTi are structurally associated with each other and form nano-hybrids due to intermolecular forces realignment at the discrete materials-interfaces.
- Structural properties that verify intercalation should also correlate to the functional characteristics such as optimised wetting behaviour and lubricity, validating the fabrication of a newly-fangled intercalated nanocomposite.
- Wetting angles and lubricity of the intercalated thin films should not only be a representative of the material deposited on the top layer but the intercalation within the thin films would have altered the surface energy and tribology of the material on the surface; thus, the WCA and CoF should indicate the two materials (PTFE and NiTi) integrated to each other by intercalation and formulating a collective wetting and tribological response. Hence, the WCAs are expected to be in between PTFE and NiTi contact angles, and should vary in a controlled manner with changes in the composition or intercalated configuration of the nanocomposite.
- SEM images would show that PTFE-NiTi nanocomposite form stable thin films having nearly defect-free surfaces and have appropriate adhesion to the substrate.

5 METHODOLOGY AND MANUFACTURING

5.1 Research plan and methodology

The experimental plan tabulated in Table 13 presents an overview of the manufacturing and characterisation steps for the fabrication and modification of intercalated PTFE-NiTi nanocomposite. Prior to attempting the nanocomposite manufacturing, it is important to investigate the deposition rates, structure, composition and sustainable sputtering conditions for both PTFE and NiTi thin films. The sputtering conditions that were examined and controlled in this project include power, pressure and the working location within the coater. The reasons for the selection of particular deposition conditions for PTFE and NiTi are explained in the description of the Table 14. Table 13 provides a summary of the data type obtained from the chosen characterisation methods, which were selected to evaluate the structure and properties of PTFE, NiTi and PTFE-NiTi thin films. The project employs SEM, AFM and TEM techniques to understand the surface morphology, whereas FTIR and EDS provide the information about the chemical properties of the thin films. The NiTi phase transformations and crystal structures are studied by DSC thermogram followed by XRD. The intercalated performance of the nanocomposite will be examined by WCA measurements, scratch testing and TEM analysis. The reasons for the selection and the operational procedures of each of the above-mentioned characterisation methods are discussed in detail in section 5.3.

Table 13: Research plans to prepare and characterise the PTFE and NiTi thin films.

<table>
<tr><td>Manufacturing Apparatus</td><td colspan="3">1. Physical vapour deposition (PVD) sputter coater
2. Radio frequency (RF) and DC power supplies</td></tr>
<tr><td>Experiment</td><td colspan="3">Sputtering PTFE and NiTi at range of working conditions scoping sputtering parameters.</td></tr>
<tr><td>Objective</td><td colspan="3">Investigation of appropriate process parameters for PTFE and NiTi thin films, verifying the PTFE polymerisation, and performing NiTi heat treatments and crystallised phase transformations.</td></tr>
<tr><td>Optimised features</td><td colspan="3">• Layer thickness, working distance, power, pressure
• Repolymerised PTFE content in thin films
• Ti / Ni content in SMA and transformation temperatures before and after sputtering were explored and optimised.</td></tr>
<tr><td>Experiment</td><td colspan="3">Sputtering PTFE and NiTi at selected working conditions
a. In layers
b. Co-sputtering</td></tr>
<tr><td>Objective</td><td colspan="3">Designing and optimising intercalated PTFE-NiTi nanocomposite thin films.</td></tr>
<tr><td>Optimised features</td><td colspan="3">• Intercalation
• Wettability
• Lubricity</td></tr>
<tr><td rowspan="6">Characterisation</td><td>DSC</td><td>Quantitative</td><td>• Post sputter heat treatment
• Transition temperatures during transformations</td></tr>
<tr><td>FTIR</td><td>Qualitative</td><td>• Validation of the chemical structure
• To establish % polymerisation</td></tr>
<tr><td rowspan="2">EDS-SEM</td><td>Quantitative</td><td rowspan="2">• Thin film composition
• Surface morphology
• Intercalation</td></tr>
<tr><td>Qualitative</td></tr>
<tr><td>WCA</td><td>Quantitative</td><td>Wettability of the thin films</td></tr>
<tr><td>XRD</td><td>Quantitative</td><td>Crystallinity of the thin films</td></tr>
<tr><td>Scratch test</td><td>Quantitative</td><td>Tribology of the thin films</td></tr>
</table>

	Mapping sputter coater	Quantitative	• To control deposition parameters • To estimate the deposition rate at a particular location within the coater
	AFM	Quantitative	• ASH • Surface topography
	TEM	Qualitative	Intercalated microstructure

5.2 Thin films manufacturing by PVD sputtering

5.2.1 Manufacturing apparatus

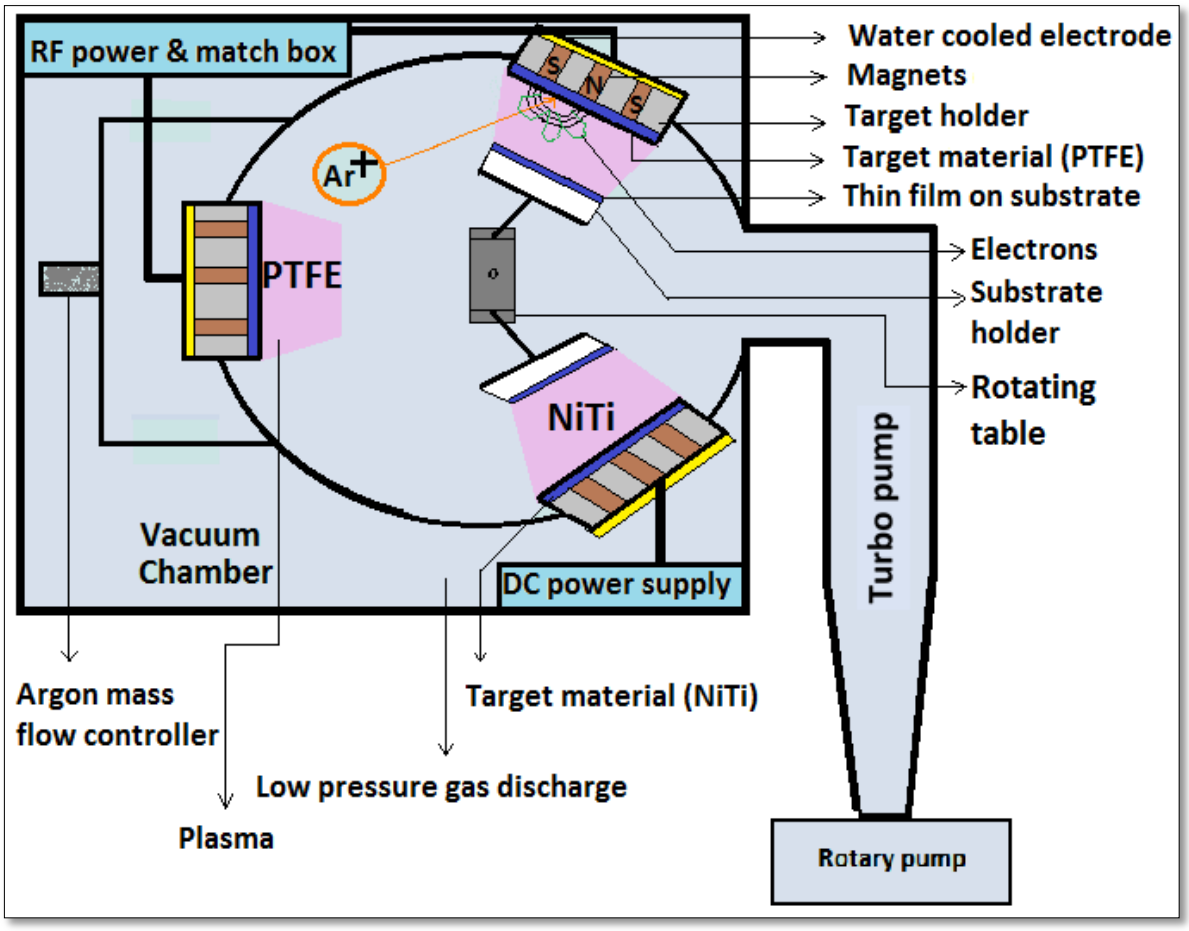

Figure 79: Schematic of Leybold L560 PVD magnetron sputter coater.

All coatings were prepared in a Leybold 560 PVD sputter coater (Figure 79), equipped with following components.

- Three magnetrons equipped with conventional circular cathodes were placed around cylindrical chamber walls in a triangular arrangement.
- Three 3-inch targets holders connected to magnetrons with a water cooling system. Two target holders were used to allow simultaneous deposition from different materials taking place for the manufacturing of thin films (co-sputtering) or the fabrication of multi-layered coatings in same deposition run (Layered nanocomposites production). The water cooling system prevents the metallic target from cracking and the polymer target from degrading and melting due to the temperature difference between magnetrons connected to DC power supply and residual atmosphere during the sputtering process. Water cooling system maintains the temperature of the polymeric target below 327°C, which is the melting point of PTFE.
- Before each run, the system is turbo-pumped to approximately 1 x 10^{-6} mbar base pressure. Vacuum chamber can pump down from atmospheric pressure to 1 x 10^{-4} mbar in ten minutes. Rapid pumping down of the sputtering chamber permits more than one deposition per day to save the time.
- A baratron measures the process pressures of the working gas. Argon gas was selected because of its inertness.
- PTFE was deposited using 13.56MHz RF power supply. NiTi was coated using an Advanced Energy® Pulsed DC power supply (f = 200 kHz; rate = 1.6µs) [20]. The frequency values and the rate of power supply are similar to those described in the literature review (section 3.1).
- A getter having Ti core was connected to the argon gas lines, and the temperature was raised to 700°C prior to the deposition process. The process is used to purify the gas coming into the sputtering system.

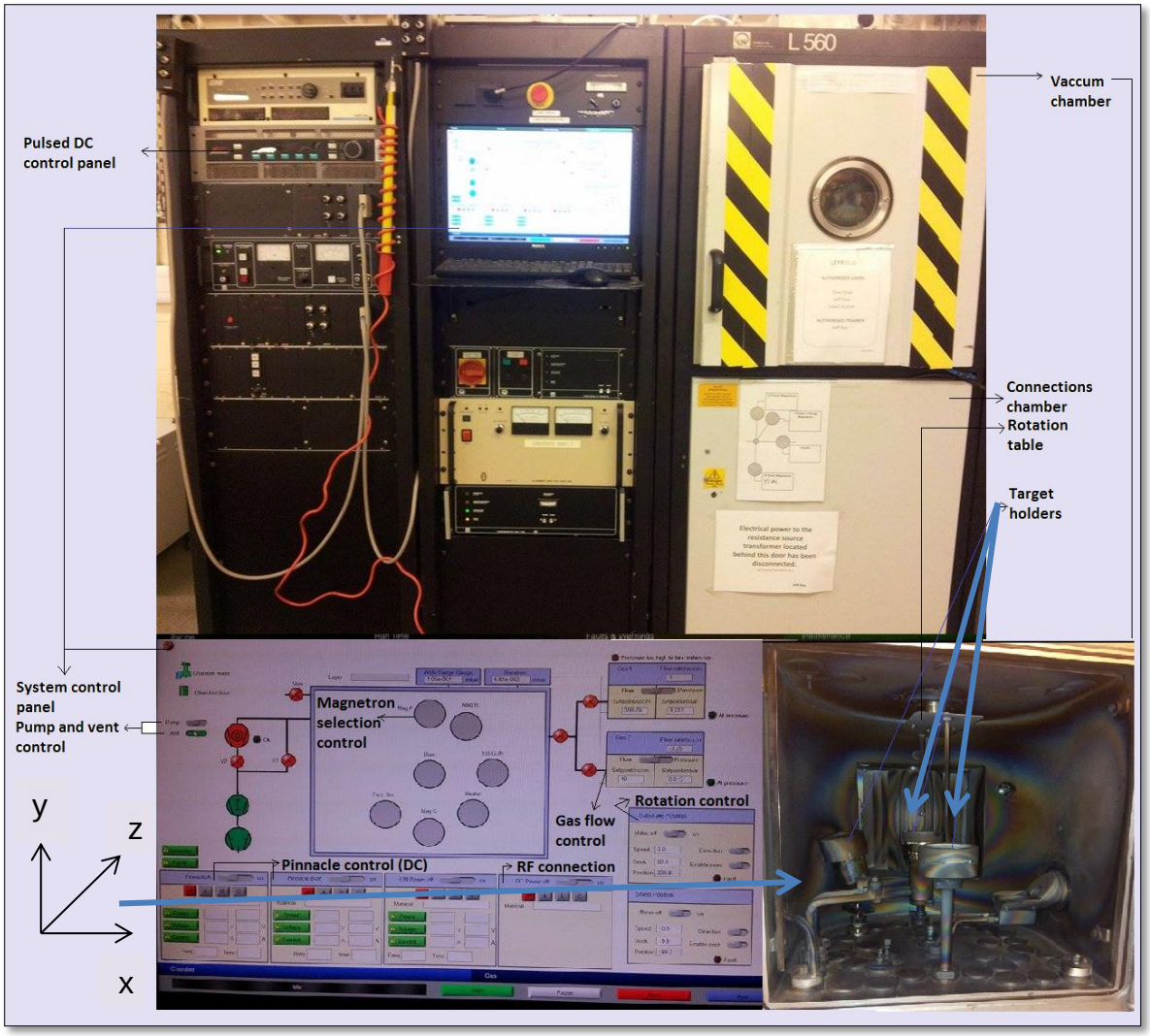

Figure 80: Leybold L560 PVD magnetron sputter coater.

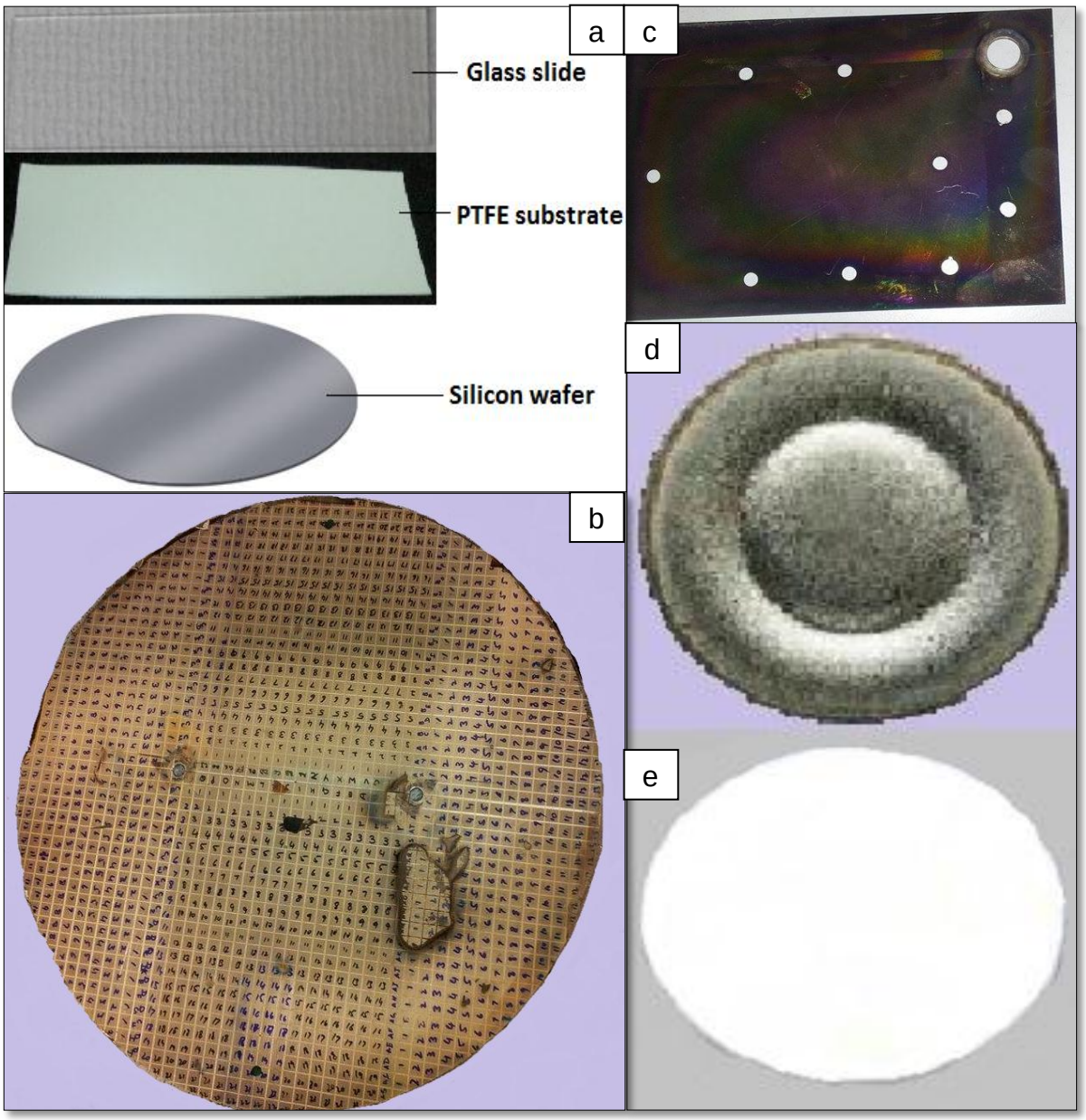

Figure 81: (a) Substrates including glass slide, PTFE substrate and silicon wafer. (b) Substrate holder. (c) Mapping substrate holder. (d) NiTi target. (e) PTFE target.

Glass, Si wafers and PTFE were used as substrates to prepare the thin films because most of the characterization can be performed on them. (Figure 81a). Two types of substrate holders were used to coat the flat substrates. A large circular mapping frame was used to find a suitable location within the vacuum chamber for deposition (Figure 81b). Following to this, a small horizontal stainless steel disc was used in all experiments for preparing the thin films at the chosen location within the coater (Figure 81c). 3-inch in diameter, 3 mm thick PTFE and $Ni_{50}Ti_{50}$ targets were used for thin film deposition (Figure 81d and e). Two different PTFE substrate thicknesses (0.5 mm and 2.5 µm) were used during deposition. 0.025 mm thick PTFE substrate was used only to prepare the final nanocomposite model because PTFE is one of the substances used in thin film compositions; therefore, it would be considered as a middle layer within the nanocomposite structure.

Appropriate surface cleaning of the substrate and thin film is vital to surface engineering at the nanoscale. All substrates and dismountable parts of sputtering equipment were cleaned with isopropanol at ambient temperature. IPA was used to clean the surface and to remove the contamination and oxidation scale. Target materials were also sputter cleaned prior to the deposition to remove initial impure atomic layer. Grit-blast cleaning was used to clean the substrate holder and target holders and dismountable parts of the deposition chamber. The targets were sputter-cleaned (pre-sputtering) for five minutes before every sputtering run. Pre-sputtering was done to remove the impurities layer on the target surface if found and get a fresh target surface, and to ascertain the same target state at the start of every sputtering run.

Individual PTFE, NiTi and nanocomposite thin films were prepared in Leybold 560 sputter coater under stationary and rotatory modes, which are described as follows. In stationary mode, the substrate is placed in a fixed position in front of the target, with given horizontal and vertical distance from specific targets within the vacuum chamber. In the stationary mode, multilayer coatings can be manufactured by depositing one material and then moving the substrate holder to another target material located at the second target station. For this reason, layered nanocomposites were prepared in a number of repeated cycles above each target, and the coatings with predetermined layer thickness and desired number of

deposited layers were produced. In rotation mode, the substrates are continuously rotated, and PTFE and NiTi were co-sputtered. In constant rotation, the vertical target substrate distance was same as the stationary mode. The advantage of rotatory deposition mode is that the time spent in front of each target is equal. Therefore, this method permits uniform deposition of both materials types simultaneously providing the same microstructure throughout on the thin film surface.

5.2.2 Mapping sputter coater

The first step of PVD sputtered film manufacturing is to find a suitable deposition location within the sputter coater. Minor variations of sample locations lead to substantial changes in thin film composition and properties. The sputter coater was mapped to find a suitable deposition location with respect to x and y-axis within the coater while the working distance (z-axis) remained constant at 10 cm. A substrate holder of 47 cm in diameter and 0.4 cm thickness (Figure 81B and Figure 82) was placed in the sputter coater. The substrate holder that mapped the sputter coater was made of Al and covered by stainless steel layer marked at specific measuring points. After PTFE deposition at 25 x 10^{-3} mbar and 100W, the thicknesses (ASH) of coating at various marked locations on the substrate holder were determined (Figure 82). The variation of deposition rate at different places within a vacuum chamber would produce different nanocomposite thicknesses and compositions, affecting properties such as morphology, hydrophobicity, surface roughness, lubricity, and chemical and mechanical properties.

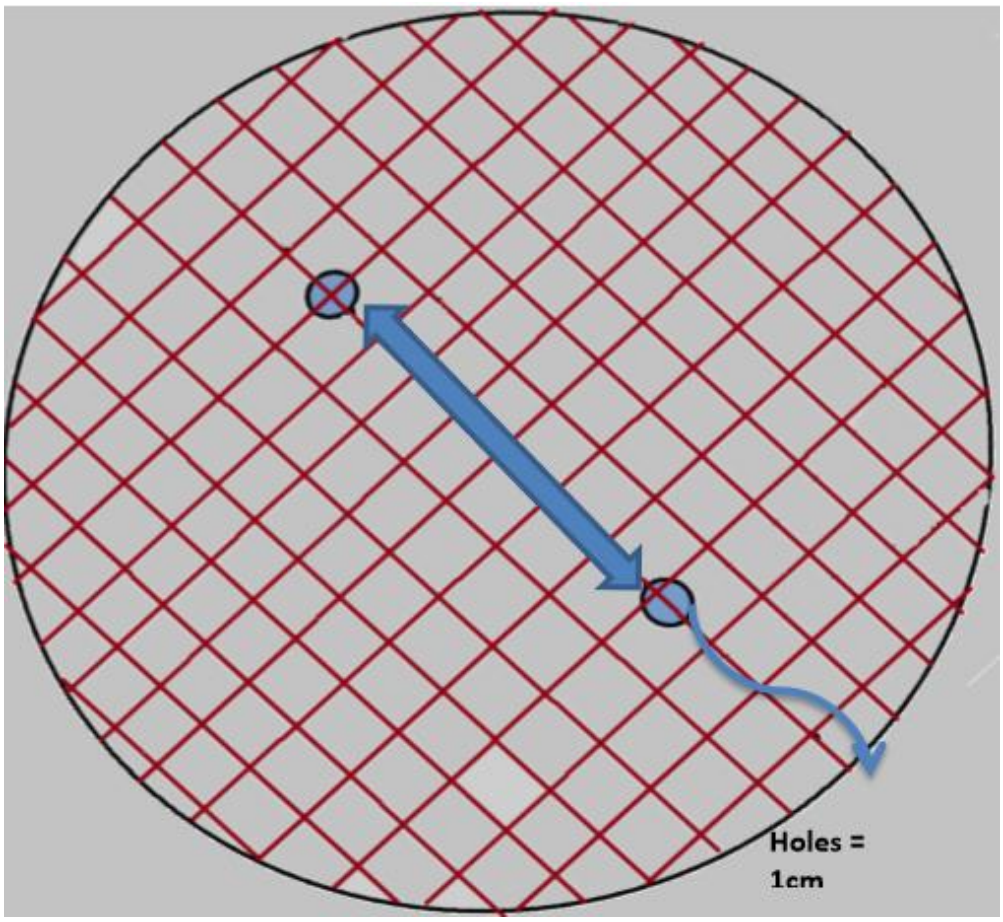

Figure 82: Layout of the substrate holder to map the sputter coater.

5.2.3 Process parameters of PTFE and NiTi thin films fabrication

Argon was selected as working gas during the process because of its common use in most of the studies discussed in the literature review and its ability to participate in the sputtering process as an inert gas. To study the structure and composition of the thin films with respect to the deposition rates and suitable sputtering conditions, PTFE and NiTi were deposited at range of process conditions. Power and pressure are the sputtering conditions that were investigated and controlled during the manufacturing process. Table 14 shows the process conditions of pressure and power for PTFE and NiTi deposition.

The selected ranges of deposition powers are 75 – 150 W RF for PTFE and 25 – 100 W DC for NiTi deposition. Relatively higher deposition powers were chosen for PTFE deposition in comparison to NiTi deposition power because of the significantly lower deposition rate of PTFE than that of metals. The deposition rates of polymers are lower than metals because of lower sputtering yield. Maximum sputtering power for the polymer target was kept at 150W, to prevent the target from melting or degrading. 25W was the minimum DC power for sputtering in this project because this was the lowest power at which a stable plasma was obtained to conduct the sputtering process.

The deposition rates were investigated for the process pressure ranging 5×10^{-3} – 25×10^{-3} mbar, and this range lowers the process pressure ranges selected by most of the previous studies that are discussed in the literature review. This would enable comparing the results with existing literature and outline any disparities found in the comparison of the results of various studies along with filling in the gaps in the present-day literature. The deposition pressure below 5×10^{-3} mbar is not sufficient to generate plasma or sustain a stable plasma during sputtering; while the deposition process conducted above 25×10^{-3} mbar pressure have higher vulnerability for the moist, oxygen and other impurities that may add to the residual atmosphere within the sputtering chamber with the working gas supply.

Table 14: Working parameters for PTFE and NiTi thin films.

Process pressure (x 10^{-3} mbar)	**PTFE deposition power – RF (W)**	**NiTi deposition power – DC (W)**
25	150	100
	125	75
	100	50
	75	25
20	150	100
	125	75
	100	50
	75	25
15	150	100
	125	75
	100	50
	75	25
10	150	100
	125	75
	100	50
	75	25
05	150	100
	125	75
	100	50
	75	25

5.2.4 PTFE-NiTi intercalated nanocomposite production

Leybold L560 sputter coater prepared layered, and co-sputtered PTFE-NiTi samples at constant target-substrate distance of 10 cm. The volume fractions of PTFE and NiTi in nanocomposites samples are given in Table 15. PTFE target was connected to RF power supply while pulsed DC NiTi power supply was used to sputter NiTi because of their insulating and conducting properties respectively. In each deposition run, three substrates including glass, silicon wafer and 0.5 mm PTFE were placed on the substrates holder. Total film thickness, thickness of individual layers and volume fraction of PTFE and NiTi were controlled by selecting various sputtering conditions (power and pressure) as provided in Table 15. The volume fractions were calculated and controlled by the individual PTFE and NiTi deposition rates at various power and pressure conditions. PTFE and NiTi deposition rates at different power and pressure conditions were obtained from the results of the experiments described previously. The selected deposition conditions will be used to achieve the desired volume fraction of the nanocomposites, after the results of deposition rates against power and pressure for PTFE and NiTi are reported.

Co-sputtered samples were prepared by depositing from PTFE and NiTi targets simultaneously. To prepare the layered samples the sample holder was placed at fixed positions above PTFE and NiTi targets alternatively, and at a time, the power supply of only one target was turned on. Figure 83 shows the schematic plan of all samples where the depositions of PTFE and NiTi on substrate are illustrated in pink and blue colours respectively. Co-sputtering needs the rotatory table to be moving continuously in order to deposit evenly distributed composition of PTFE and NiTi. Co-sputtering is a time-consuming process, and it was found that co-sputtering associated with approximately 3.5 times lower deposition rates as compared to the time consumed by stationary mode sputtering for depositing the same film thickness. Therefore, 3.5-times longer time was allowed for depositing of the co-sputtered thin films as compared to the deposited layered nanocomposites of the same deposition thickness. The deposition rates of PTFE and NiTi may reduce further by target cross-contamination as reported by the literature in section 3.4.1. An aluminium foil having 2 mm thickness was placed in the sputter coater to separate the target plasma and to avoid the target cross-contamination.

The PTFE-NiTi samples prepared according to the deposition conditions described in Table 15 were characterised by AFM, scratch tester, SEM-EDS, FIB-TEM and WCA (section 5.3). The characterisation results for nanocomposites thin film samples were used to modify the nanocomposite structure and to achieve the desired properties such as intercalation, lubricity, fluidity control and stability of the films.

Table 15: Deposition conditions for PTFE-NiTi fabrication by PVD sputtering (the deposition rates correspond to stationary mode PVD sputtering where the rotatory table is placed in a fixed position above a particular target).

Schematic Layout	**Co-sputtered**			**Layered**		
Sample ID	PNK1	PNA2	PNF3	PNS6	PND7	PNL8
Volume fraction (PTFE:NiTi)	35:65	54:46	60:40	50:50	75:25	25:75
Film thickness (µm)	0.5	0.5	0.5	1	0.75	0.75
Pressure (x 10^{-3} mbar)	10	5	20	10	10	10
RF power - the PTFE deposition (W)	150	150	100	150	150	150
DC power - NiTi deposition (W)	50	25	25	50	50	50
Deposition rate - PTFE (nm/h)	24	49	69	24	24	24
Deposition rate - NiTi (nm/h)	45	42	52	45	45	45
Co-sputtering time (h)	30	30	30			
Number of Layers				20	10	10
PTFE layer thickness (nm)				50	100	25
NiTi layer thickness (nm)				50	25	100
Deposition time for 1 PTFE layer (h)				2	4	1
Deposition time for 1 NiTi layer (h)				1	0.5	2

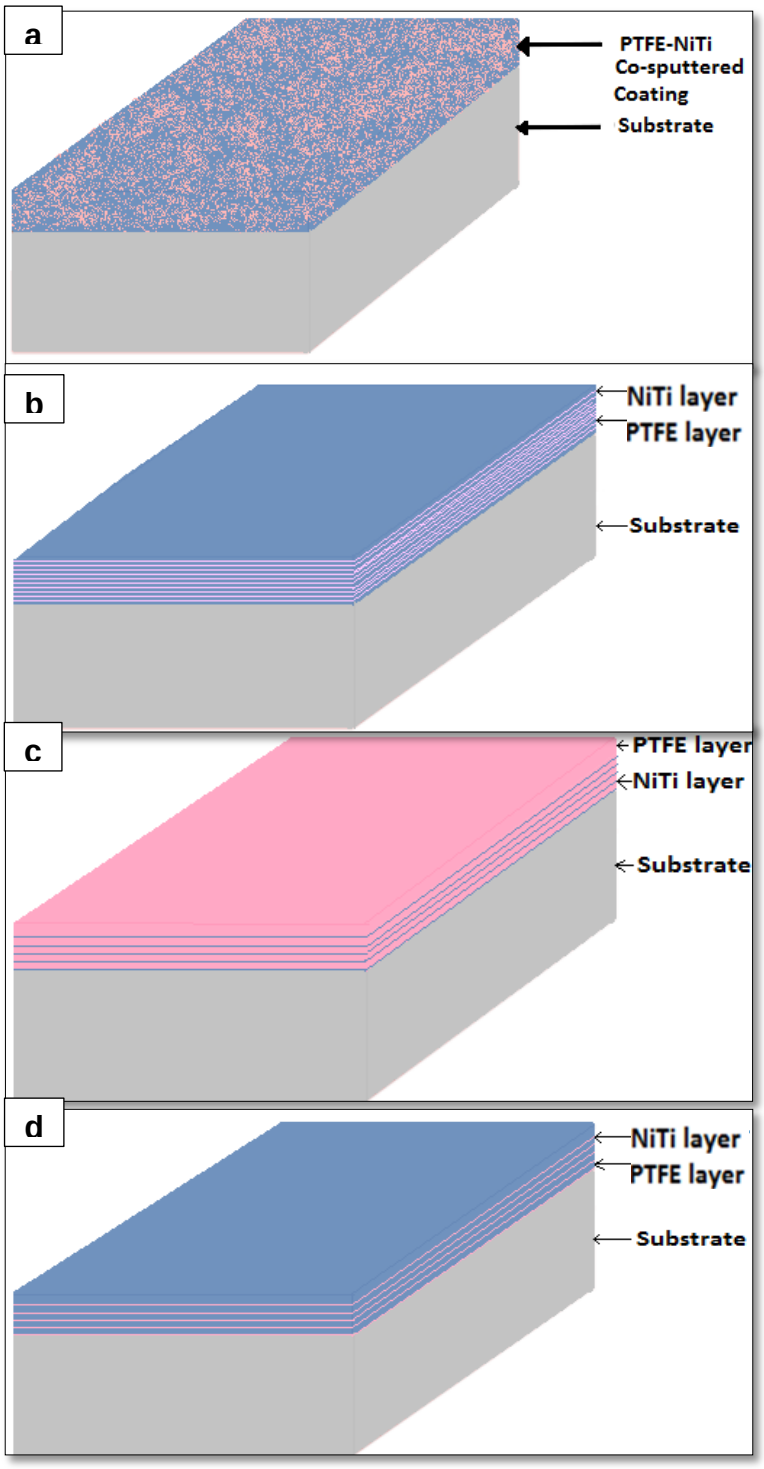

Figure 83: Schematic illustrations of PTFE-NiTi coatings: (a) PNK1, PNA2 and PNF3: co-sputtered coatings of PTFE and NiTi with vol. fraction ratios of 50:50, 25:75 and 60:40 respectively, (b) PNS6: 50:50 vol. fraction of PTFE and NiTi in 20 alternative layers. (c) PND7: 25:75 vol. fraction of PTFE and NiTi in 10 alternative layers. (8) PNL2: 75:25 vol. fraction of PTFE and NiTi in 10 alternative layers.

5.3 Characterisation of the thin films

After depositing PTFE and NiTi thin films at various deposition conditions, the thin films were characterised by their structure and properties by employing a range of characterisation techniques. Depending on the results, the scheme for the manufacturing of intercalated PTFE-NiTi nanocomposite was crafted. The characterisation of the nanocomposite informs about the structural and functional properties of the material, which allow optimising the nanocomposite for obtaining the desired modifications followed by monitoring those modifications. The characterisation methods selected to assess the structure and properties of PTFE, NiTi and PTFE-NiTi thin films are described in this section, along with their working procedures, and the reasons for choice of each characterisation methods are described. The above characterisation techniques were selected in accordance with the designated characterisation methods in the literature studies for the examination of similar material properties.

5.3.1 Atomic force microscopy (AFM)

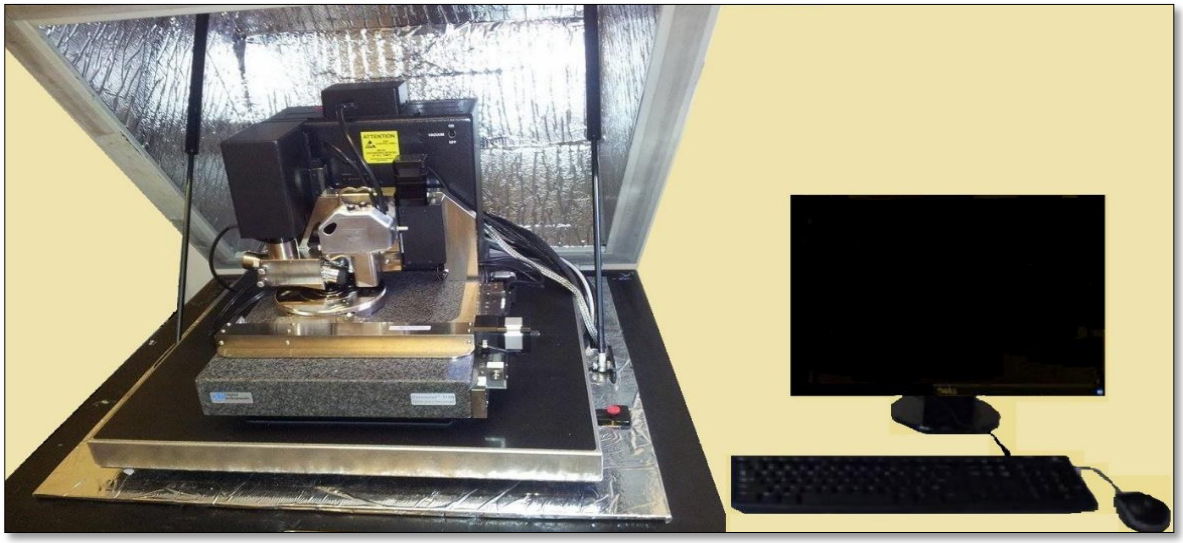

Figure 84: Veeco dimension V AFM equipment at Cranfield University.

AFM technique provides high-resolution surface topographic images. Surface morphology of a thin film depends upon its chemical structure and physical properties (surface hardness) while affecting the film's lubricity, adhesion and strength. In tapping mode, AFM image provides morphology and nano-scale features within thin films. Vertical and lateral forces between a sharp tip and the surface provide average step height measurements (ASH). ASH is used to estimate the film thickness; therefore, the deposition rate of the thin films can be adjusted from the known deposition thickness and time.

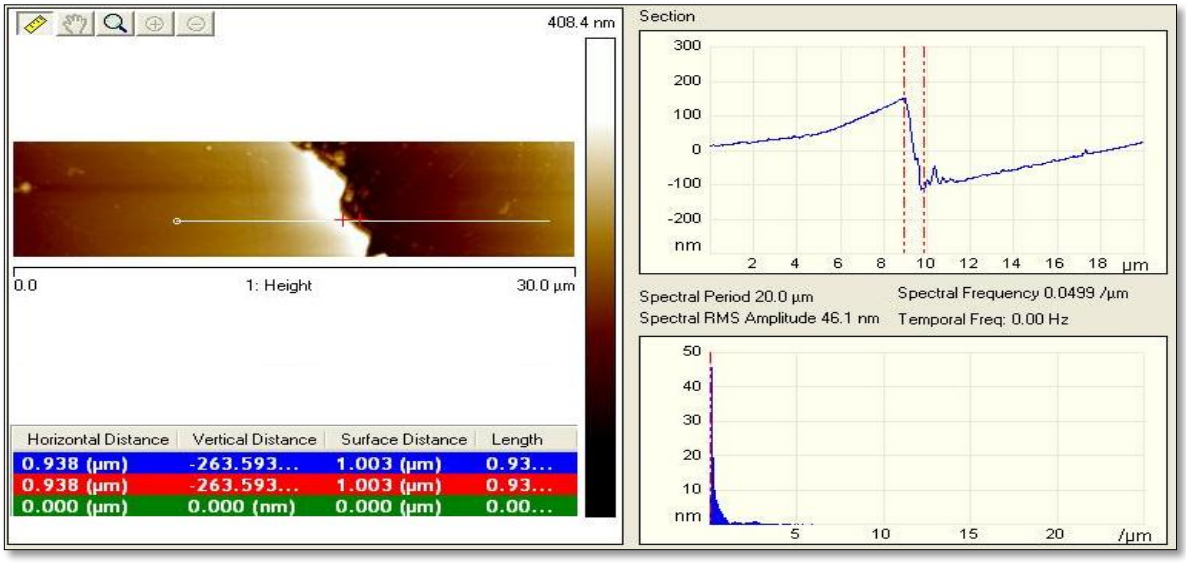

Figure 85: Veeco DimensionTM 3100 V atomic force microscope.

A Veeco Dimension^{TM} 3100 V atomic force microscope was used to examine the average step height (ASH), surface morphology, polymeric and metallic material distribution of thin films. The substrates were masked at borders by high-temperature resistant adhesive tape to determine the ASH. The Nanoscope Realtime1 software, in tapping-in-air mode, was operated at scan rate of 0.5 Hz and scan velocity of 30 µm/s. Live real-time full-offset data was recorded at scale of 200 nm. The schematic and working procedure of AFM technique are given below.

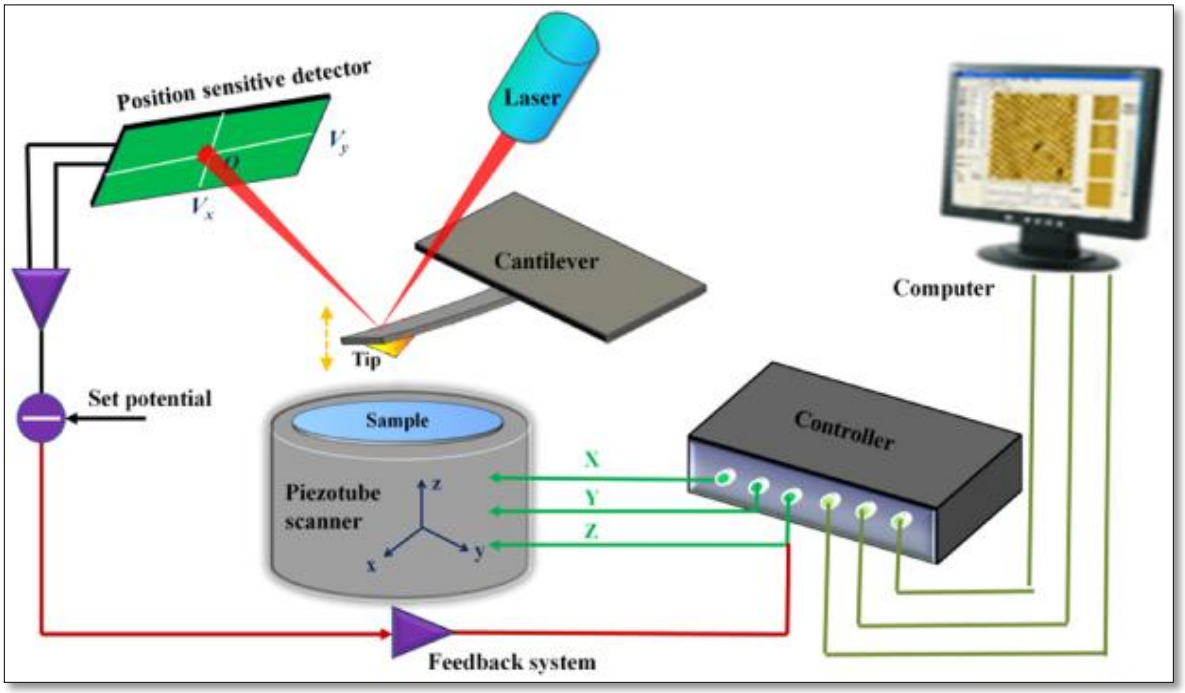

Figure 86: Schematic diagram of the basic working principle of AFM [186].

A scanning probe tip usually made of Si, is placed on a flexible cantilever, which uses a piezoelectric scanner associated with nanoscale three-dimensional movements of the sample [187]. The tip meets the sample surface or a voltage and magnetic field prevents the physical contact keeping the tip very close to the sample, and producing a raster-scan, which deflects the cantilever by topographic variation and reflects the laser beam [174]. A photodetector detects these changes in topography and reflectivity and transmits the data to generate the surface profile image. The AFM detector has four diodes, which collect the topographic data and respond to the friction created by cantilever changes.[186; 188]

5.3.2 FTIR analysis of PTFE

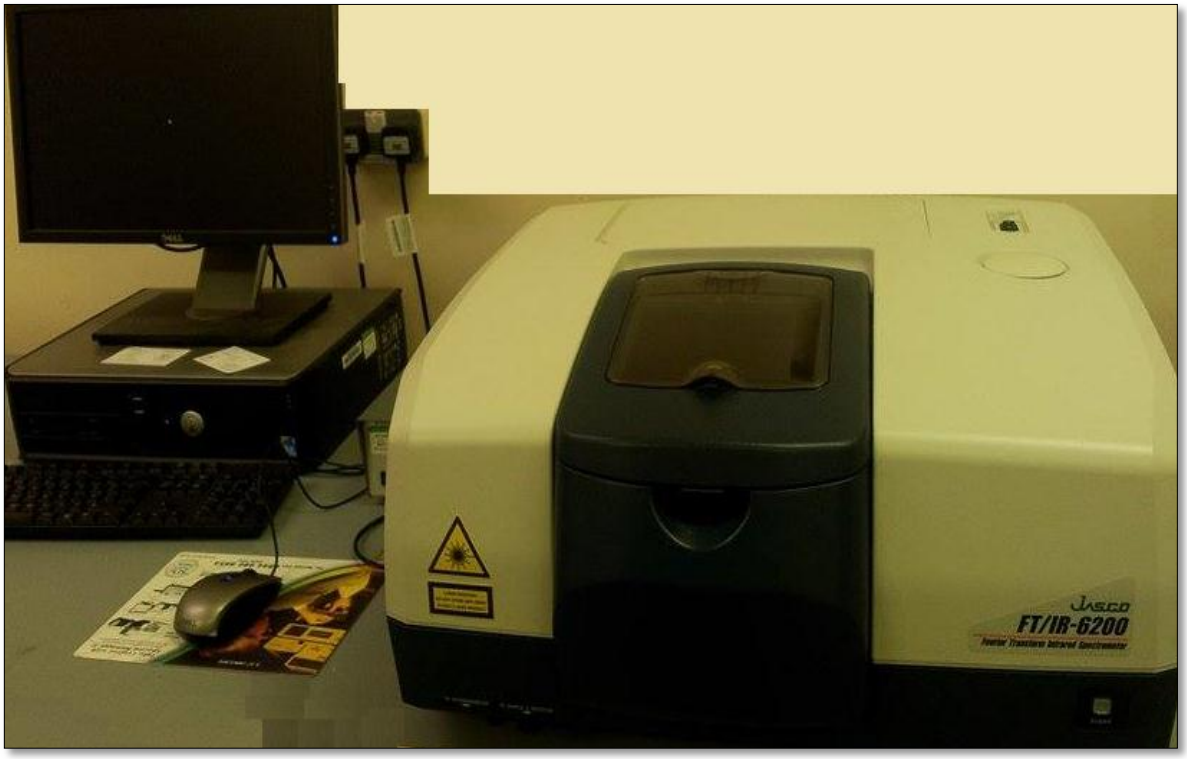

Figure 87: A JASCO FTIR 6200 – A spectrometer at Cranfield University.

Fourier Transmission Infrared Spectroscopy (FTIR) is an absorption technique that relates the IR frequency to the bonding vibrations of different functional groups. Chemical identity of a substance is determined by matching the infrared wavenumbers to existing databases [189; 190]. Therefore, FTIR spectroscopy identifies the unknown substances and determines the materials quality and quantity. The peak size indicates the material amount within the sample [191]. PVD sputtering involves the bombardment of high-energy inert gas particles onto the polymeric target material (PTFE), which decompose the polymer chains in small fragments, ions and monomers. At the deposition, PTFE is expected to re-polymerise similar to its bulk target material, which is tested by examining the presence of polymer functional groups using FTIR spectroscopy.

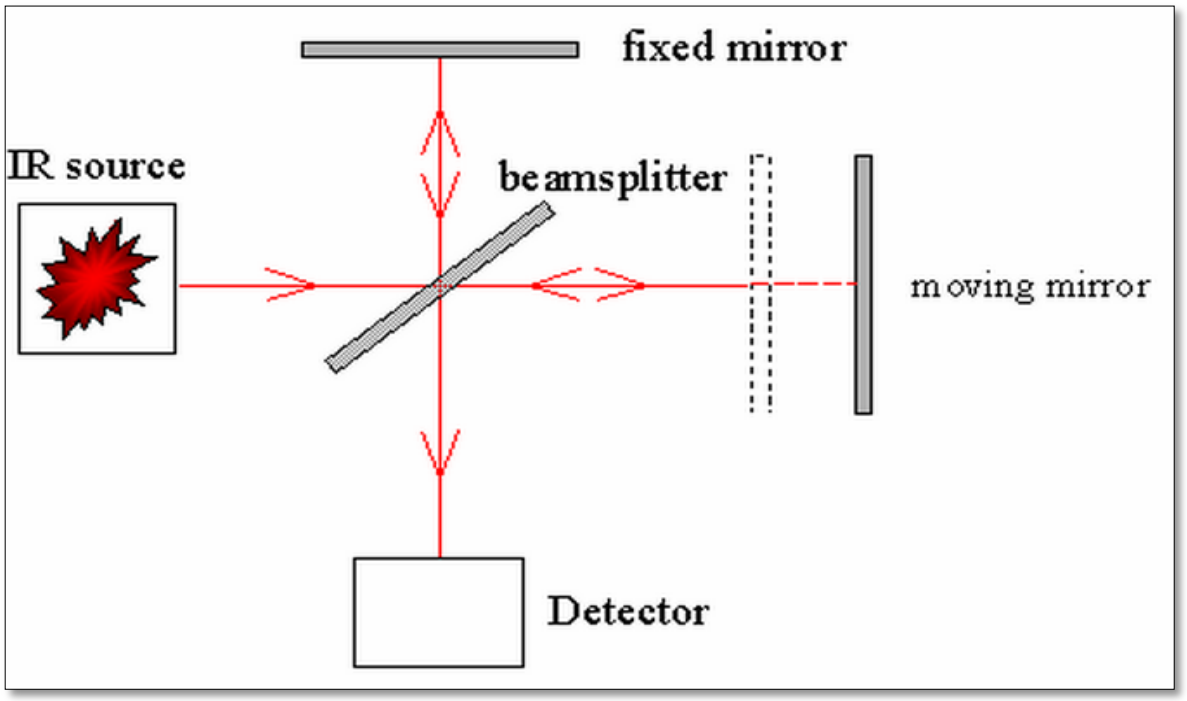

Figure 88: Schematic illustration of FTIR spectroscopy.[189]

FTIR spectroscopy was undertaken to observe the chemical structure of PTFE thin films using a JASCO – FTIR 6200 type - Sensor Nite. The spectra were also used to establish the degree of polymerisation. Absorption mode was chosen because of transparent thin films and reflection mode was selected for the non-transparent PTFE target materials. The resolution was set at 4 cm^{-1} for an accumulation of 128, with a standard TGG detector (thermogravimetry detector). Characteristic chemical band of 400 – 4000 cm^{-1} in single scan range was selected to ensure that all peaks associated with PTFE can be observed. The operational procedure of FTIR spectroscopy is described below [189-191].

A blackbody source emits IR radiations that pass through the aperture. The aperture regulates the amount of energy transferred to the sample and the detector. The IR radiation then reaches the interferometer for the spectral encoding. FTIR spectroscopy relies on interference of the IR waves, which strike a beam splitter and partially reflect in either a stationary mirror or a moving mirror. The light recombines after reflection from one of these mirrors, which then directs towards the specimen. The quanta of infrared electromagnetic radiation interact with the particles of the specimen, which leads to energy absorbance and bond vibrations. IR absorption only occurs if the quantum has sufficient energy to transmit to the next vibrational

energy state, at the time of dipole alteration. At this stage, either transmittance or the reflectance takes place depending on the type of selected analysis. After absorption by the sample, the detector detects the light energy and unusual pattern appears, called an interferogram, which measures the particular interferogram signal. Constructive interference occurs most, when the moving and stationary mirrors are at the same distances. The signal is then digitised and converted into a spectrum by Fourier Transformation software in computer. The absorption or transmission spectrum exhibits a unique specimen fingerprint. Two different molecular structures cannot generate the same IR fingerprints. A background spectrum (without sample in the path of the beam) is initially run to obtain a relative measurement for the absorbance or transmittance intensity. The background spectrum is compared to the sample measurements that produce the resulting percentage absorbance or transmittance spectrum [189-191].

5.3.3 Differential scanning calorimetry (DSC)

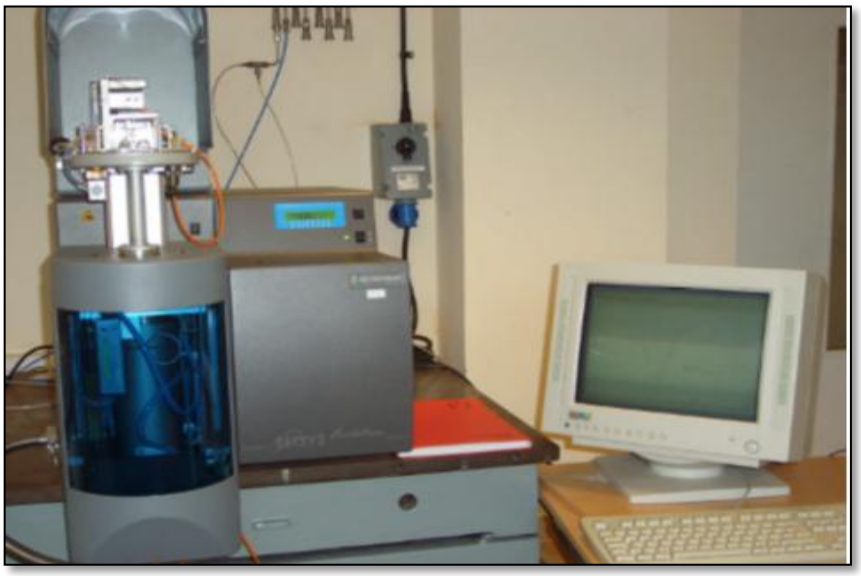

Figure 89: Setaram Setsys Evolution 16/18 DSC apparatus at Cranfield University.

Differential scanning calorimetry (DSC) is a heat-induced macromolecular transitional measure of the variance in physical characteristics of a substance, against temperature as a time function, and permits to identify the transition phases that are not detectable by simple calorimetric analysis. A heat energy amount is absorbed or radiated (endothermic or exothermic) in the process, depending on the temperature difference between the sample and the reference material [192]. Those physical characteristics include glass transition, crystallization, specific heat capacity, state changes, thermal curing, thermal history and purity.

The M↔A transformation temperatures of NiTi are determined by DSC [100]. DSC apparatus allows carrying out the post sputtering heat treatment of the thin films followed by determination of enthalpy values in heat cycles as a function of time. Prior to heat treatment, the PVD sputtered NiTi thin films are amorphous. The latent heat of SMA phase transformation is presented by the area under the peak in a DSC curve. The heat treatment prepares the thin films for XRD analysis to study crystal structures and phase changes that match to enthalpy measurements. Any changes in crystal structures and grain orientation (position, sharpness and shape of clusters) would influence the DSC results.[192; 193]

NiTi films having various Ni – Ti atomic compositions, were analysed for M↔A transformation temperatures by DSC thermal analysis, in an argon atmosphere, at a heating / cooling rate of 20°C min^{-1} (Table 16). Setaram Setsys Evolution 16/18 DSC apparatus, with Setsoft 2000 software was used to carry out the annealing heat treatment and heating cycles. Temperature calibration is performed first using pure materials of known melting temperature within the required temperature range. All NiTi films were peeled from substrates by a 'stainless steel scalpel blade' so that the transformation temperatures can be measured under no stress. The mass of the NiTi films under thermal analysis was recorded (Table 16) and provided to the Setsoft 2000 software to enable enthalpy determination by the system. The steps of heat treatment and thermal cycling are explained below.

High vacuum DSC chamber was surged with Ar gas, once a low-pressure Ar atmosphere (~2.5 x 10^{-7} mbar) was maintained in the chamber, after which the argon supply was disconnected. A constant supply of Ar gas was avoided to prevent the NiTi films from reacting with residual impurities particularly oxygen. Titanium promptly reacts to any moist and impurities present in working gas to form nitrides and oxides during heat treatment. Freestanding NiTi thin films were aged at 1100ºC for half an hour followed by annealing at 550ºC for 2.5 hours. Another set of freestanding NiTi films was aged at 850ºC for half an hour followed by annealing at 550ºC for 2.5 hours. NiTi alloy was subjected to thermal cycles after heat treatment within the temperature ranges provided in Table 16. Enthalpy changes are associated with the differential thermocouple in the reference cell and the sample holder, which display the data in the form of differential temperature curve against temperature or time. The heating rate lowers during endothermic reactions due to heat absorption and results in a negative heat-flow (μV) between the reference and the specimen. Contrastingly, the heating rate increases during an exothermic reaction profile resulting in a positive heat-flow (μV). The operational steps of DSC apparatus are given underneath.

Table 16: DSC conditions for various NiTi compositions.

ID	At. Composition		Mass (mg)	Temperature range(°C)	Heat treatment		Annealing	
	Element	%			hours	°C	hours	°C
E	Ni	48.3	3.31	20 - 400	1	1100	6	550
	Ti	48.6						
	O	2.7						
	N	0.4						
L	Ni	41.9	1.69	20 - 400	2.5	850	0.5	550
	Ti	58.1						
	O	0						
AE	Ni	46.7	1.84	20 - 400	1	1100	6	550
	Ti	52.1						
	O	1.2						
R	Ni	45.3	1.61	20 - 400	1	1100	6	550
	Ti	52.4						
	O	2.3						
J	Ni	49	2.57	20 - 400	1	1100	6	550
	Ti	48.8						
	O	2.1						
K	Ni	43.5	3.01	20 - 400	1	1100	6	550
	Ti	56.5						
	O	0						
O	Ni	47.2	1.51	20 - 400	2.5	850	0.5	550
	Ti	44.3						
	O	8.5						
J2	Ni	49	3.36	(-60 - 260)	2.5	850	0.5	550
	Ti	48.8						
	O	2.1						
R2	Ni	45.3	8.27	(-60 - 260)	2.5	850	0.5	550
	Ti	52.4						
	O	2.3						
AE2	Ni	52.5	4.35	(-60 - 260)	2.5	850	0.5	550
	Ti	47.1						
	O	0.4						
DD	Ni	53.5	6.37	(-60 - 260)	2.5	850	0.5	550
	Ti	46.5						
	O	0						

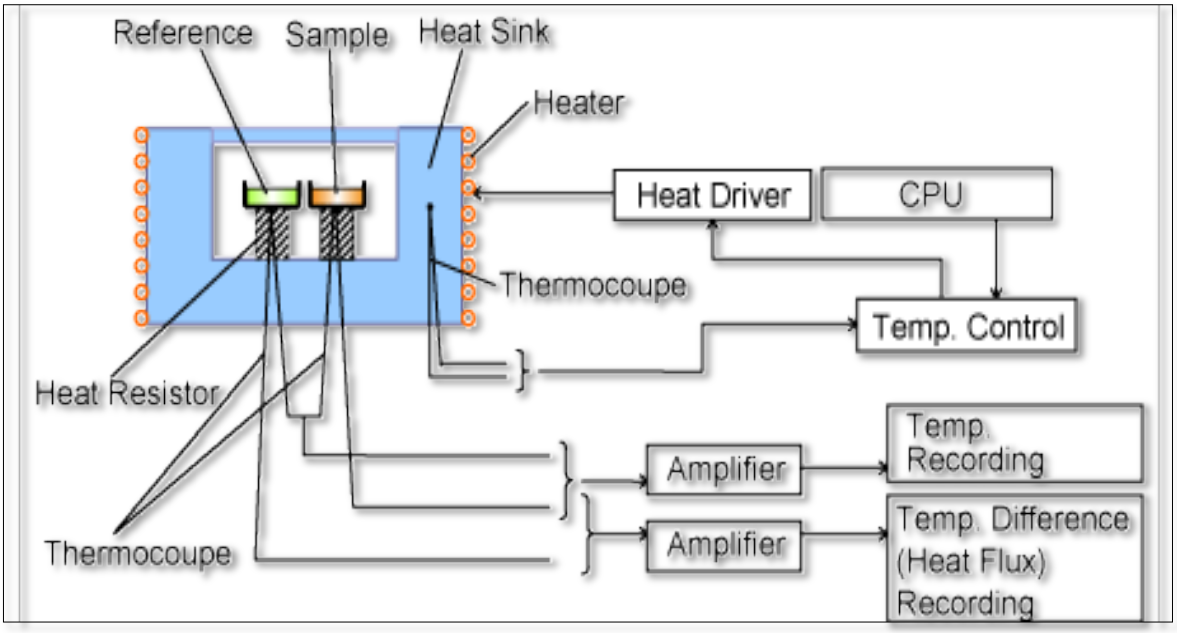

Figure 90: Schematic illustration of heat flux DSC [193].

Heat Flux DSC includes the heating resistor, heat sink, heater, and the sample and reference containers. The sample pan and the reference pan are positioned on a thermoelectric disc (heat sink) enclosed in a furnace heater. The Heater provides heat flow to the sample pan, and an empty reference pan through the heat sink and resistor at a linear heating rate. The heat flow is relational to the heat difference between the heat sink and containers. Heat sink has the higher heat capacity than the sample, to perform the exothermic reactions. A constant temperature difference between the reference and sample creates a steady difference of heat energy between them. The area thermocouples monitored the temperature over time and recorded on a computer, from where the heat flow is regulated, and the physical changes are recorded and displayed in the form of selected output data.[192-194]

5.3.4 X – Ray diffractometer (XRD)

Figure 91: Seimens D5005 X- Ray Diffractometer at Cranfield University.

X – Rays are short wave electromagnetic radiations, which are generated in XRD because of the deceleration of the electrically charged energised particles. In an X-ray tube fitted with copper targets, the X-rays radiate in all directions due to influence of high voltage across the electrodes. Upon meeting a crystal lattice the incident X – rays scatter in all specific directions. Along with that the incident X-rays eliminate themselves by distractive interference and an enhanced constructive interference of the reflected waves results in the diffraction, which distinguishes the atomic planes at designated crystal phases. The following Bragg equation relates the diffraction of X-rays within a crystal structure.[195]

Equation 5: Bragg's equation.

$$2d(sin\theta) = \lambda_{\circ}$$

d = Lattice interplanner spacing of the crystal

Θ = X – ray incidence angle (Braggs angle)

λ = Wavelength of the characteristics X - rays

Crystal structure of pre-heat treated NiTi films was analysed with a Siemens X-ray diffractometer D5005 and a DIFFRACTplus XRD Commander Software. The copper (Cu) target generates X-rays at 40kV and 30mA with a speed of 1° min^{-1} and a wavelength of 1.541838Å, in the 2θ ranging 20° – 90° degrees. XRD monitor is used before each run to ensure that there are no X-ray leaks from the instrument.

X-ray diffraction is the fundamental technique to witnesses the degree of crystallinity and determines the existence of NiTi crystalline blends in thin films at various PVD sputtering parameters and heat treatments conditions. X – Ray diffraction data can be used to ascertain the dimension of the unit cell. The angular positions plotted against the intensities of the diffraction peaks generate a characteristic pattern of the material and phase analysis can be carried out. JCPDS database is used to identify the peaks of unknown substances. Following Scherrer's formula is used to calculate the crystal / grain size, which can be estimated from the full width at half-maximum of the intense diffraction line of the peak.

Equation 6: Scherrer's formula.

$$D = \frac{k\lambda}{\beta \cos \theta}$$

D = Crystal size

K = Constant value varies from 0.89 to 1.39. (0.9 in present study)

λ = Wavelength of the characteristics X – rays (1.541838 Å)

β = Full width at half maximum (FWHM) in radians

Θ = X – ray incidence angle (Braggs angle)

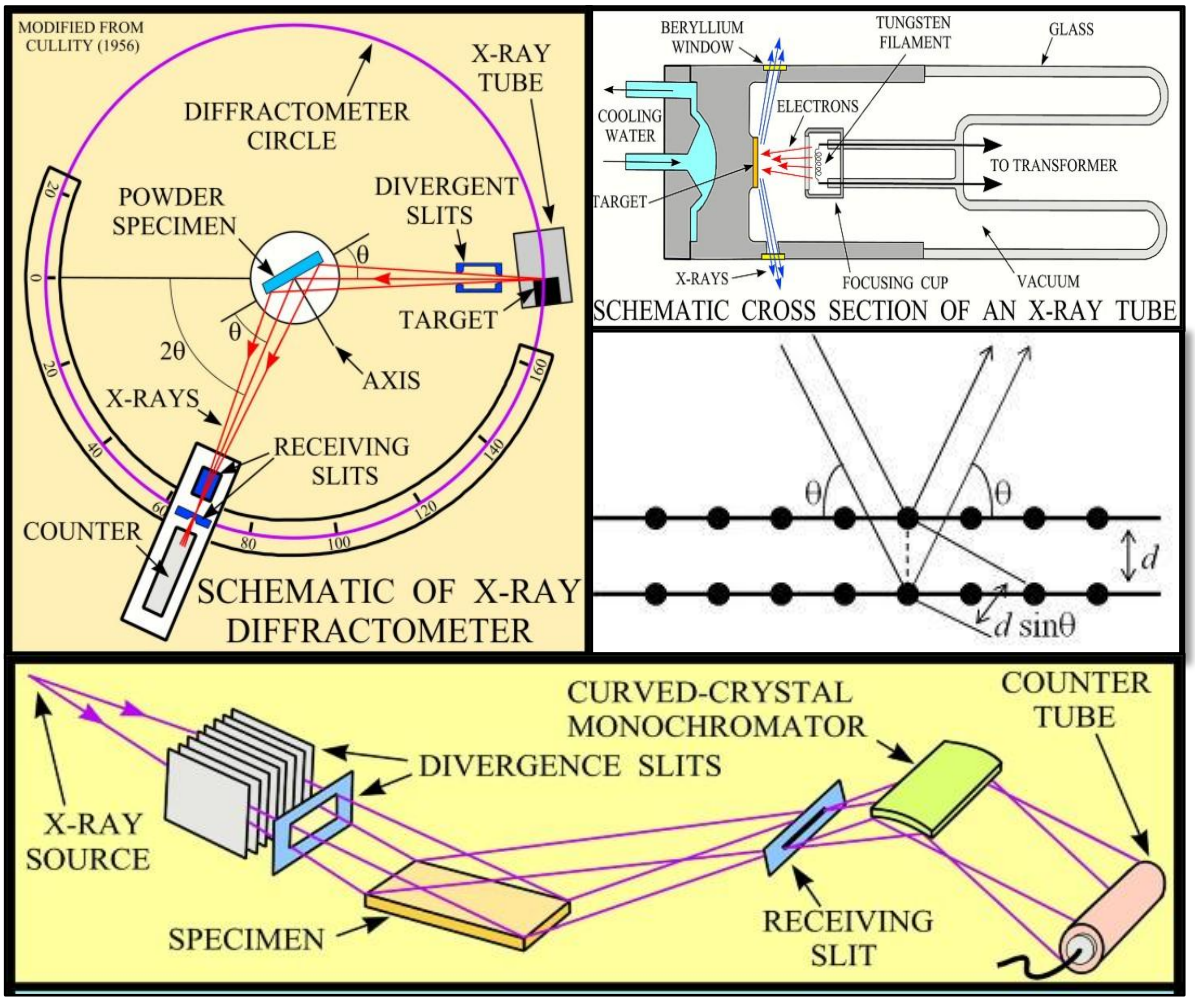

Figure 92: XRD Schematic illustration [195].

The main components of an X-ray diffractometer include a source of a curved monochromator with a graphite crystal, a detector, a sample stage located on the circular circumference, a divergent slit situated between the source and sample, and another slit between the sample and the detector. The divergent slits reduce the non-diffracted radiation and the background noise. A goniometer is mechanically connected to the detector and sample holder to control the rotation of the detector and the specimen. The detector uses the pulse-height analysis to filter the signals and scale them to calculable magnitudes, which are converted into a continuous current by a linear ratemeter, and computer-based devices produce the output.[195]

5.3.5 Scratch testing

Figure 93: Scratch test equipment – Bruker UMT at Cranfield University.

Scratch test is a mechanical testing method to evaluate adhesion, friction coefficient, fractures toughness, coating hardness, and surface fatigue of 0.1 to 20 µm thick films [196-201]. Scratch testing is significantly dependent upon the material type, structure, surface roughness, effect on frictional forces, and the type of the scratch test with applied size and shape of the stylus [196; 202]. Scratch testing examines the tribological factors such as adhesion and lubricity of PVD thin films, which have a direct relationship with the film composition and morphology and influence the nanocomposite behaviour. The load versus friction curve defines the friction coefficient using coulombs equation and characterises the surface behaviour of thin films. Further characteristics can also be determined by of an optical microscope, which include the normal load for coating failure, adhesion strength and mechanisms of various failure categories. The friction coefficient, the failure mechanism and failure thin film are affected by film thickness and substrate hardness. Less than 1µm

films display good adhesion to the substrate, but partial failing of the coatings start to appear in the form of cohesive flakes in thicker films. With an increasing film thickness, a continuous adhesion failure occurs, creating fragments and flakes due to the hardness (approximately above 600 HV).[203]

A Bruker UMT scratch tester was used to perform scratch tests for exploring the friction coefficient and coating durability. Unidirectional sliding was carried out by a tungsten carbide ball of 6 mm a diameter under a “single pass with continuously progressive load increase” mode on a scratch length of 10 mm. The load rose by 1 to 100 N at a loading rate of 100 N/min with maximum friction force of 50 N. The working scheme of a typical scratch tester is given below.

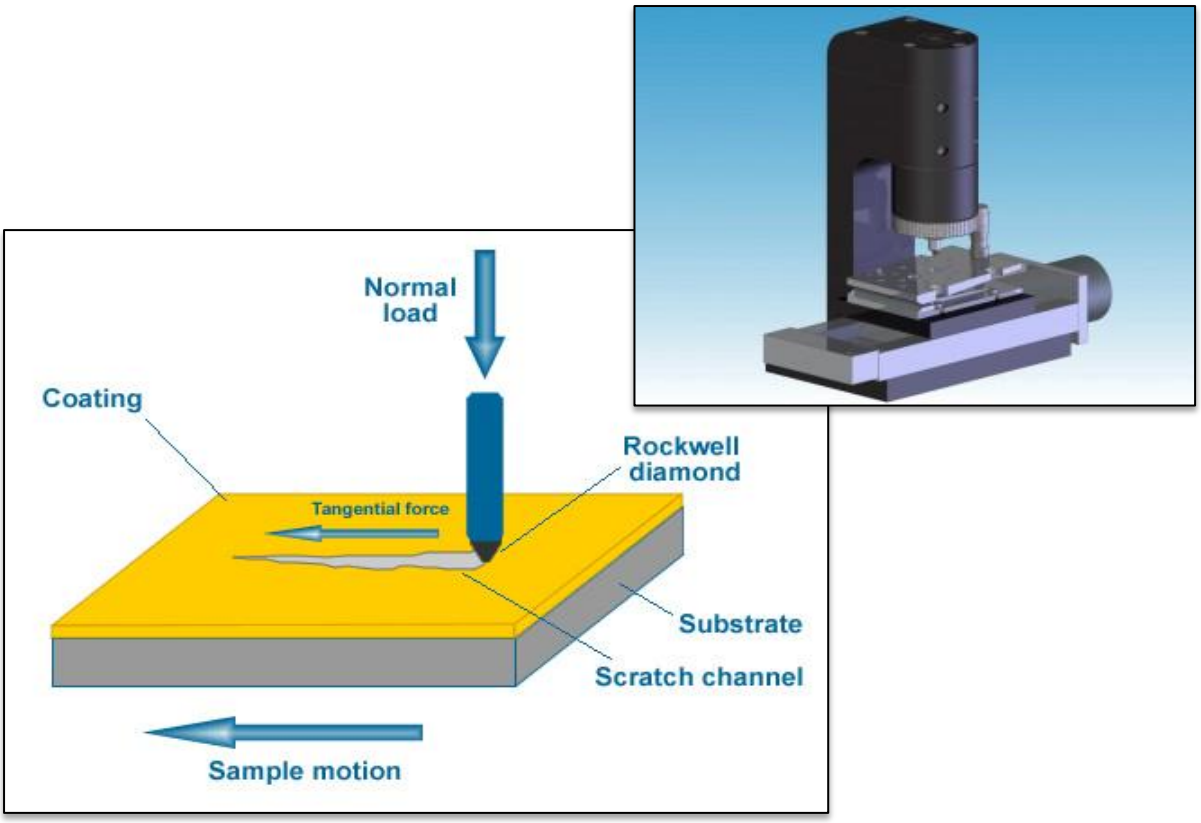

Figure 94: Schematic representation of scratch tester [204].

The scratch testing equipment has a metallic or diamond stylus with a Rockwell tip of ~ 200µm radius. The shape and size of the stylus depend upon the coating and substrate material and the purpose of examination. While the stylus tip moves with a steady speed because of normal loading force, a tangential frictional force tries to overcome the load. A detector associated with the stylus records both forces, and the plot for the load versus friction generates. Scratch mark study also considers various stress forces and the frictional forces between the sliding tip and the film surface. The delamination occurs within the thin film – substrate structure at the surface and interface because of the stress induced by moving tip, which leads to coating failure at critical loading. The compressive stress generates from the push of forward-facing indenter and tension occurs because of the backward pull.[196; 203-205]

Large radius indenters are suitable for the harder coatings, for which loads per surface contact area must be of small magnitude, in order to resist the tip penetration. The adhesion of hard thin film is measured conveniently by the deposition hardness exceeding 54 HRC. Small radius indenters are suitable for the soft coatings, for which loads per surface contact area is of smaller for rapid cutting and expositing the substrate during the scratch test. For this reason, the substrate then becomes the test surface. If the stylus radius exceeds the diameter of 6 mm for a soft film, the indenter’s tip slides on the surface while examining the coating tribology.[202-204]

5.3.6 Water contact angle (WCA)

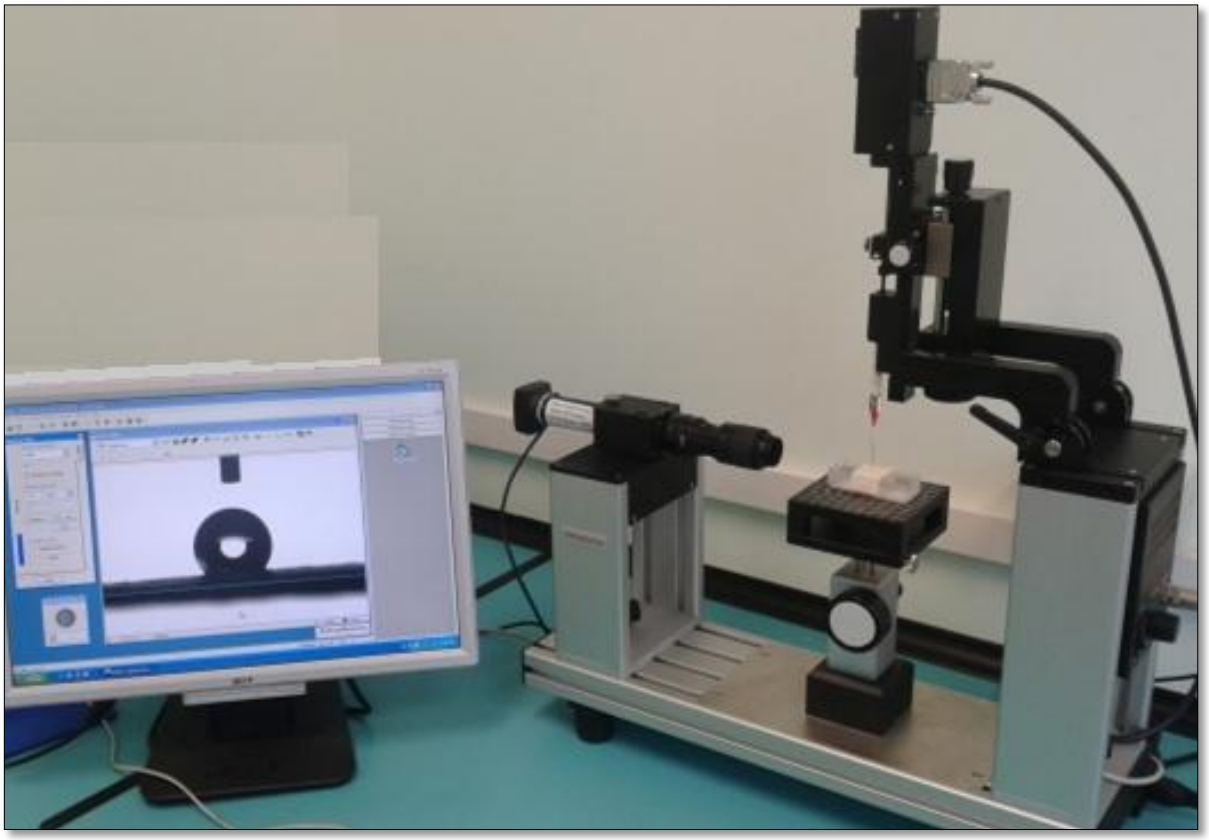

Figure 95: Dataphysics OCA20 contact angle instrument at Loughborough University.

Static water contact angles of PTFE, NiTi and nanocomposite thin films were measured by sessile droplet method. To start the analysis the sample was placed on stage, and a syringe raised and then filled with deionised water. The cold light source was adjusted, depending on surface reflectivity fo the sample, using illumination. The instrument uses an SCA20 software to capture images and then calculate the contact angle. Sessile droplet type was selected, and the water droplets were dispensed with a dosing volume of 1.0 µl at 2.0 µl/s dosing rate. The baseline was adjusted for uneven substrates, and the contact angles were recorded along with corresponding images. The wetting angles of the thin films relate to the surface energy and surface roughness. A higher surface energy or surface roughness leads to enhanced hydrophobicity of the thin film material giving rise to the WCA.

5.3.7 Autonomic sputter coater

Conductive coatings do not charge up by accumulating electrons on the surface, therefore, produce clear microscopic images without any sample preparation. In contrast to that, the insulators are coated by sputter coater with a thin layer of a conductive substance, using an electric field and argon gas. During sample preparation, the sample should not be wet because the water vapours can contaminate the vacuum.[206]

Figure 96: Agar Autonomic sputter coater at Cranfield University.

Before characterising them by SEM and FIB, an Agar B7341 Autonomic sputter coater was used to deposit 10 nm gold layer on the thin film specimens of PTFE or those containing a higher percentage of PTFE. The autonomic sputter coater was fitted with Pfieffer Rotary Vane vacuum pump. Non-conductive thin films were coated so that the gold layer allow imaging without accumulating the charge build up on the film surface during scans.

5.3.8 Focused ion beam (FIB)

Figure 97: Focused ion beam equipment (Fei FIB 200) at Cranfield University.

Cross – sections of PTFE-NiTi nanocomposite were prepared by Fei FIB200 and further investigated by a high-resolution scanning electron microscope and transmission electron microscope. The FIB instrument has an integrated dual beam of SEM within the chamber to observe the sample during sputter etching. On a small-area, a thin platinum layer was coated to protect the surface of the specimen. The thin film is tilted at 45° after etching and then trenched by following the process.

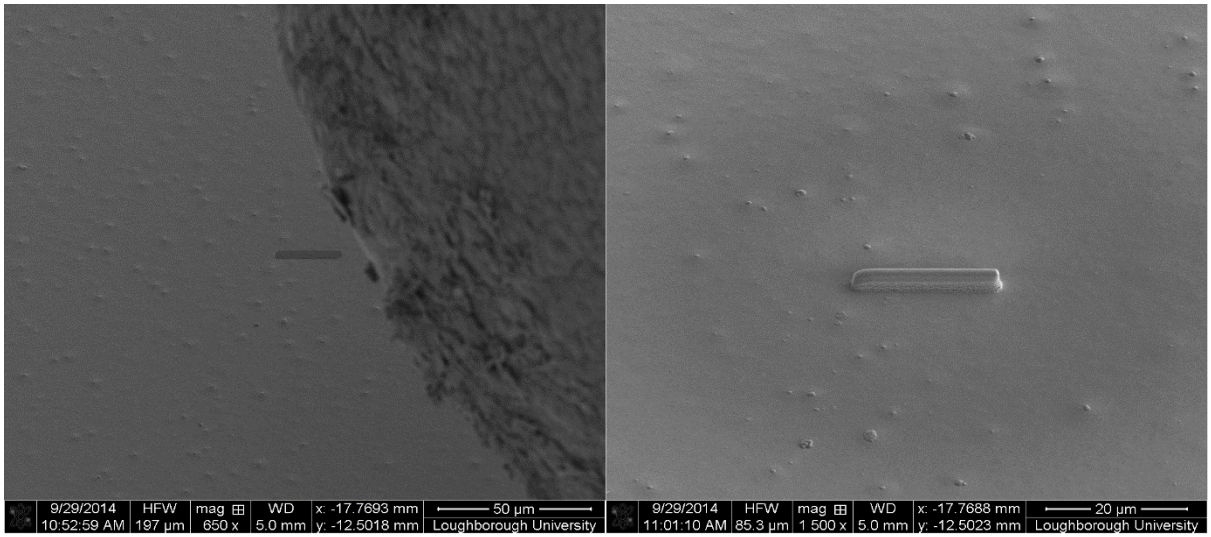

Figure 98: Deposition of the platinum layer on the selected area.

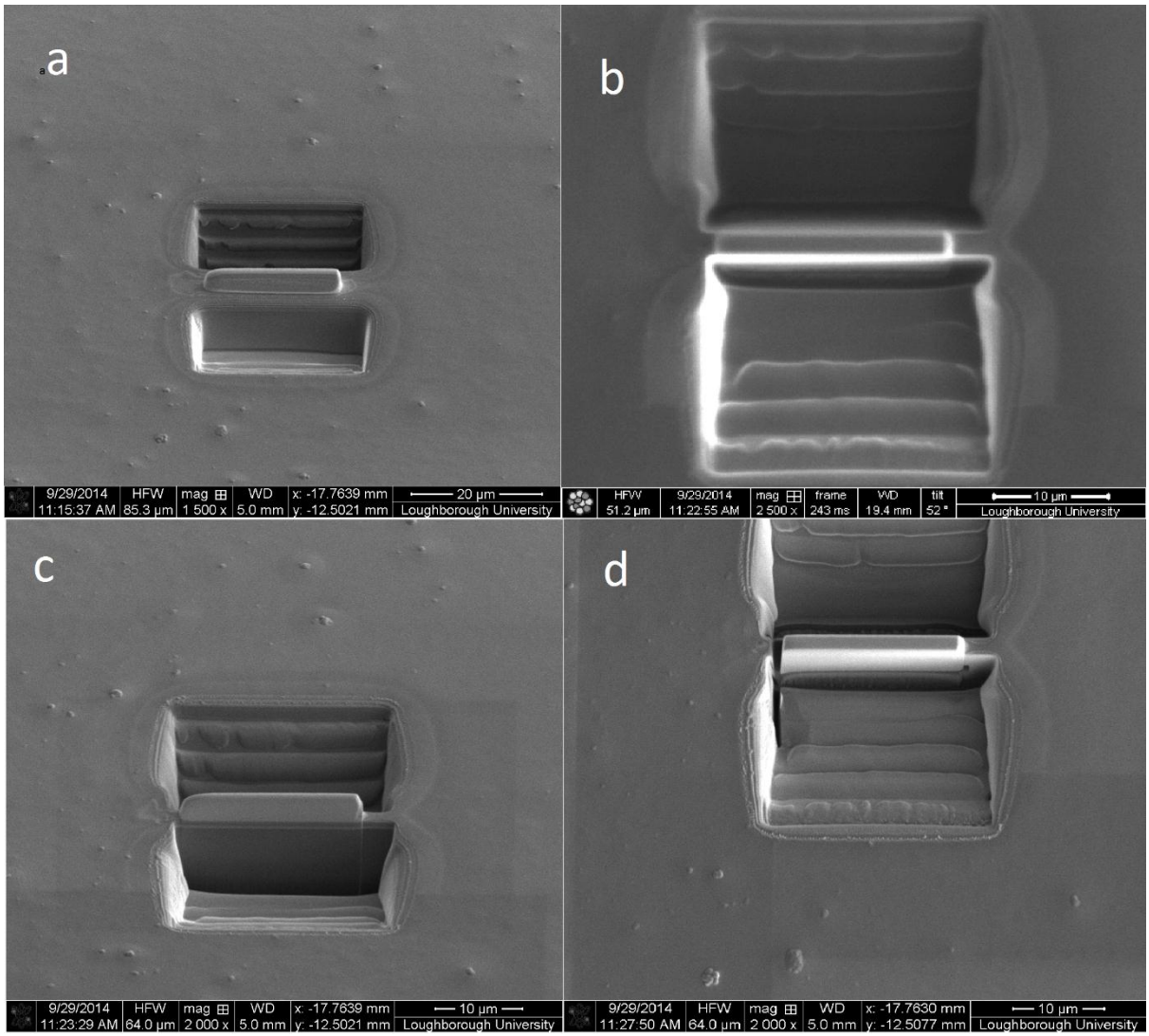

Figure 99: (a) A gallium ion trench at 45° in thin film (b) Closer view of an Ion trench at 45° in thin film (c) Clean up after milling (d) Shape cut of the trench.

Platinum coated small-area of thin film is sputtered by a finely focused primary gallium ions (Ga^{+}) beam with small current that hit the film surface and leave as secondary or neutral ions, while generating the secondary electrons. The sputtered particles form an image by the signals collected by scanning of the primary beam on the surface. An electromagnetic aperture located subsequent to the ion gun permit the selection of beam current ranging 1 – 11500 pA. Lower current (1 – 70 pA), images the specimen while sputter ion etching and higher current mills the substrate energetically. The milling depth is controlled by changing the current. Increasing the current above 70 pA may damage the polymeric layers in PTFE-NiTi specimen. For that reason, lower current values were chosen along with longer milling time to prepare the specimen. Although increasing milling current would reduce the milling

time, but thermally affected area would be larger around the milling zone. Milling zone appears as a staircase shaped trench. Then the sample is extracted from the surface by bonding it to a platinum needle and then placed on the specimen holder. The last step is to carry out a stepwise thinning of the sample, which makes it sufficiently thin at the front edge to conduct transmittance during TEM analysis.

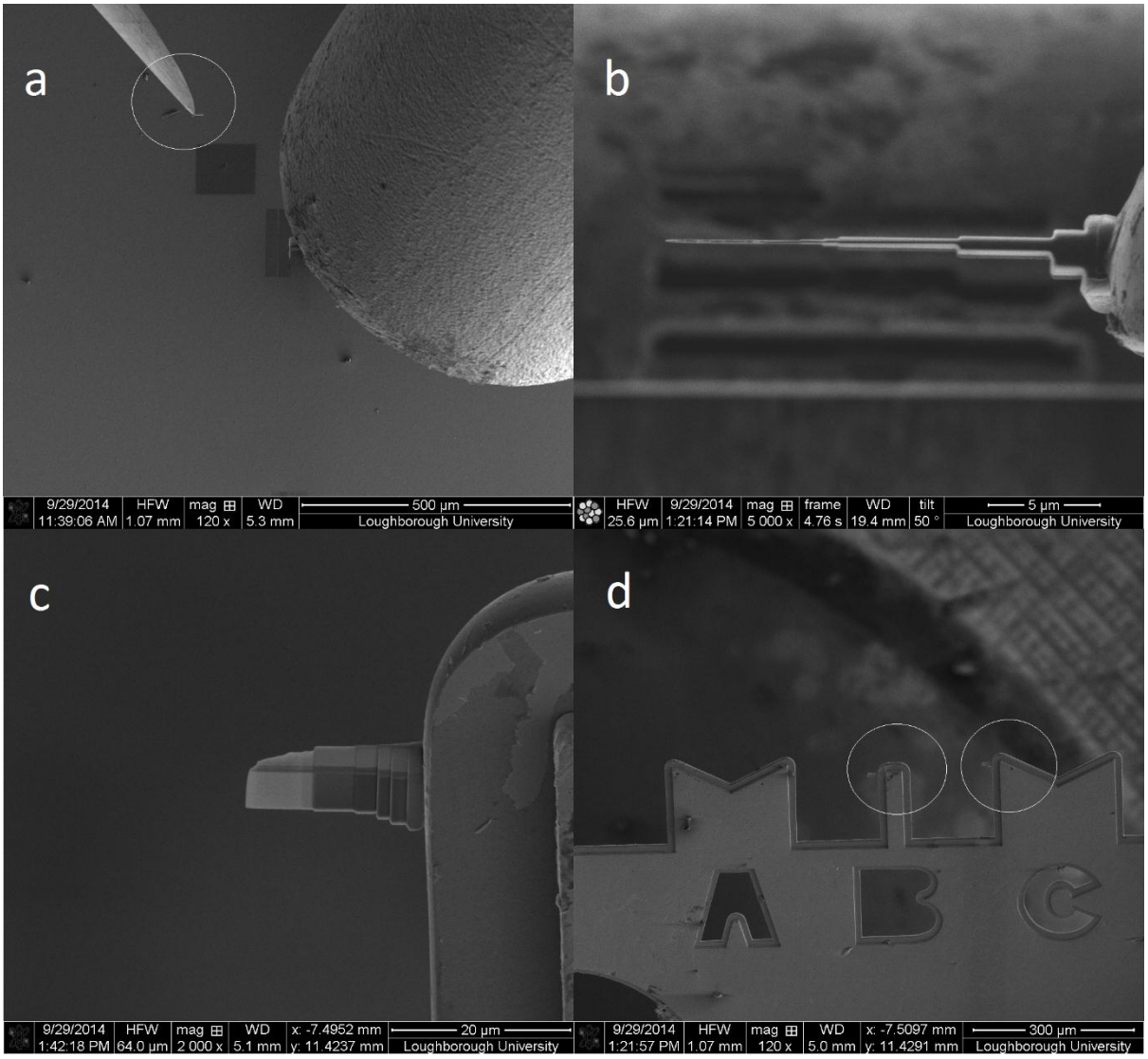

Figure 100: (a) Specimen extraction (b) Thinning of the specimen (c) Final specimen for TEM analysis (d) Specimen wedged to positions B and C of sample holder, for TEM analysis.

5.3.9 Transmission electron microscopy (TEM)

Figure 101: Transmission electron microscope (Philips CM 20 SFEG TEM) at Cranfield University.

Extremely thin specimen prepared by FIB were imaged by Philips CM 20 transmission electron microscope for imaging and elemental analysis of the layered structure. A high energy electron beam crosses through the specimen and the beam drives through a series of lenses and focuses on the screen.

Transmission electron microscopy (TEM) provides atomic resolution images of the materials showing thin film defects, diffraction patterns of crystals as well as spectroscopic data at scale up to ~ 0.2 nm. A TEM image develops by a light beam by means of the electron as an energy source, which transmit through the sample partially according to specimen density and replicates sample features. More electrons are transmitted through a porous material in comparison to a dense material, resulting in differentiation between variable densities within the internal structure of the substance. Diffraction patterns produced by TEM apprise about the crystal structure and lattice parameters. Some unscattered electrons within the beam of electrons passing through a significantly thin material utilise a fluorescent screen to generate the TEM image. Variable darkness intensities within the TEM images relates to the changes in material density.[186; 192; 207; 208][100; 188; 189; 192; 195; 206; 209]

Plan-view and cross-sectional view TEM analysis can be carried out to obtain the bright-field and dark-field images. If the clusters diameter is similar to the film thickness, the outlines of the clusters projected onto the film plane are measured. For smaller 3D clusters of thin films, the apparent cross-section of the clusters is not always equal to their maximum cross-section, and their sizes would be less estimated than they are. Usually, it is challenging to measure densely packed cluster's size. For smaller 2D clusters of the films thinner than μm, TEM measures their size and volume from the plan-view images, regardless of their shapes. It is undertaken by calculating the areas of the particulates bunch and multiplying them by the film thickness. For the polycrystalline film with randomly oriented crystallites, the dark-field TEM images distinguish the area of the crystallites with a particular crystallographic orientation from the others and measure their sizes. Although it is not easy to measure all the crystallites with various orientations but the columnar and flat, thin films having engraved ditches along the grain boundaries are analysed by TEM performed under transmission and diffraction modes with 100 KeV electrons. This allows examining the grain size within layers, calculating the volume and the number of monomers. TEM only works if the scattering of the incident electron beam inside the cluster is uniform and different from that of the grain boundaries, the places of the uniformly sized clusters are periodical, and the

locations of the grain boundaries are random with variable shape. Therefore, it is crucial to observe the shape of each cluster for measuring their sizes.[45; 68]

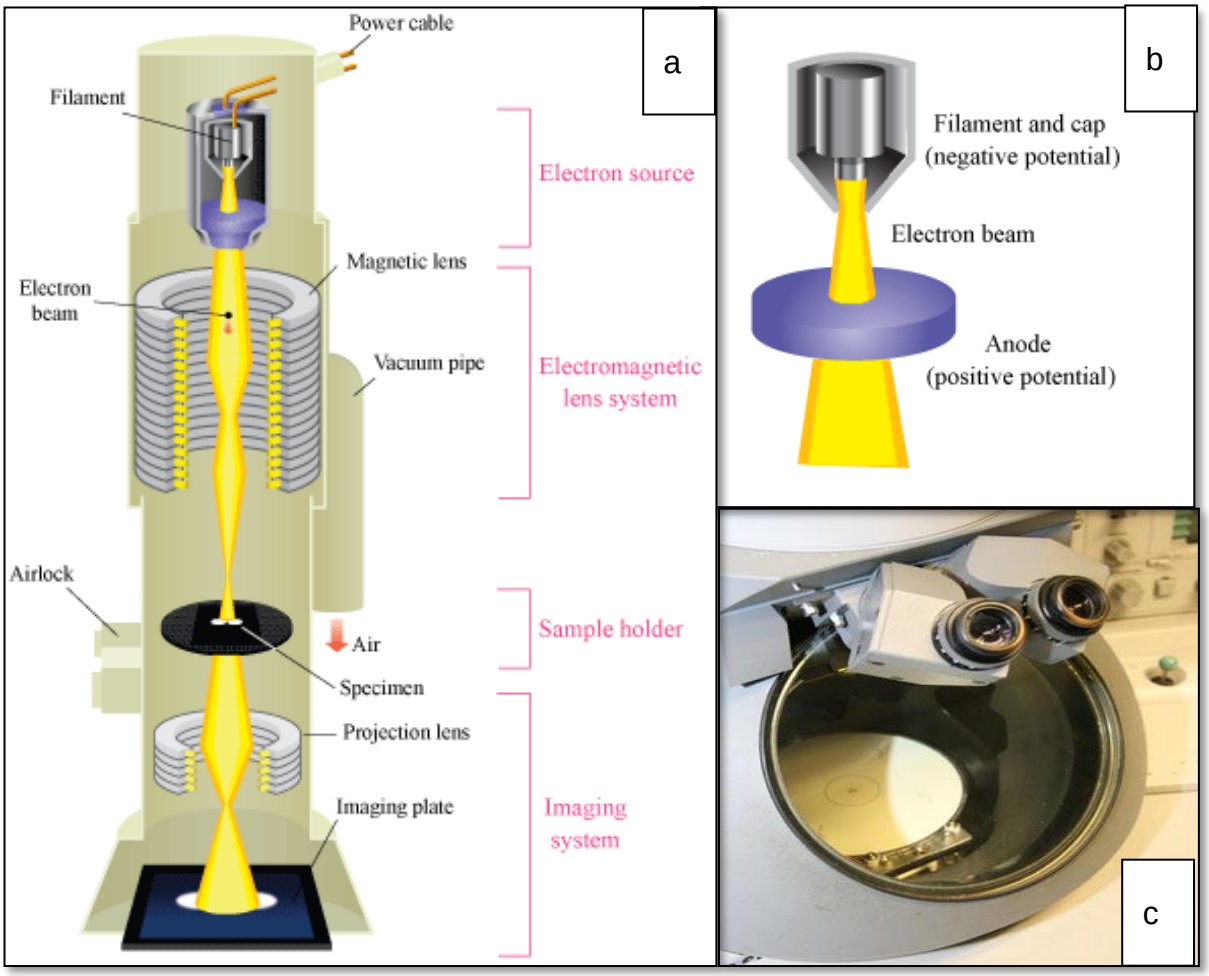

Figure 102: (a) Schematic of transmission electron microscope. (b) Electron source. (c) Imaging system.[207]

A TEM system consists of following four parts, which work together to provide a high-resolution image by an accelerated electron beam. Those four parts are named as an electron source, an electromagnetic lens system, a sample holder, and an imaging system. An electron source comprises of a cathode of the tungsten filament, and an anode. When the filament heats, it releases the electrons, which are absorbed by a negative cap within a loosely focused beam, as shown in Figure 102b. Electron beam passes through the sample while the electrons at the edge of the beam hit the anode, and the rest of the electrons pass through a small slit in anode. The electron beam transmission relies on the properties of the material. Electromagnetic lens and metal apertures then firmly focus the electron beam by

letting only a small (well-defined) energy range of electrons to transmit. Magnetic Lenses are circular electromagnets, which produce a defined circular magnetic field, which performs as an optical lens to focus the electrons. Aperture is a thin disk with a circular hole sized 2 - 100 µm, which confines the electron beam before striking the sample placed in a sample holder. A sample holder is a stage armed with a mechanical appendage for placing and monitoring the sample position. A secondary electromagnetic lens system (imaging system) consisting of two lens schemes coordinating to the screen with a phosphorescent plate. One lens scheme refocuses the image after they go to the sample while the other lens system is for the image enlargement and projection. The screen phosphorescent plate glows at encountering the electron beam.[207]

5.3.10 Energy dispersive X - ray spectroscopy (EDS) and scanning electron microscopy (SEM)

PTFE, NiTi and PTFE-NiTi thin films were examined by a high resolution scanning electron microscope (SEM) 'FEI XL30 SFEG' associated with energy dispersive X-ray spectroscopy (EDX) to study the film surface and the elemental composition. A 20 kV electron beam was employed with slow scan settings.

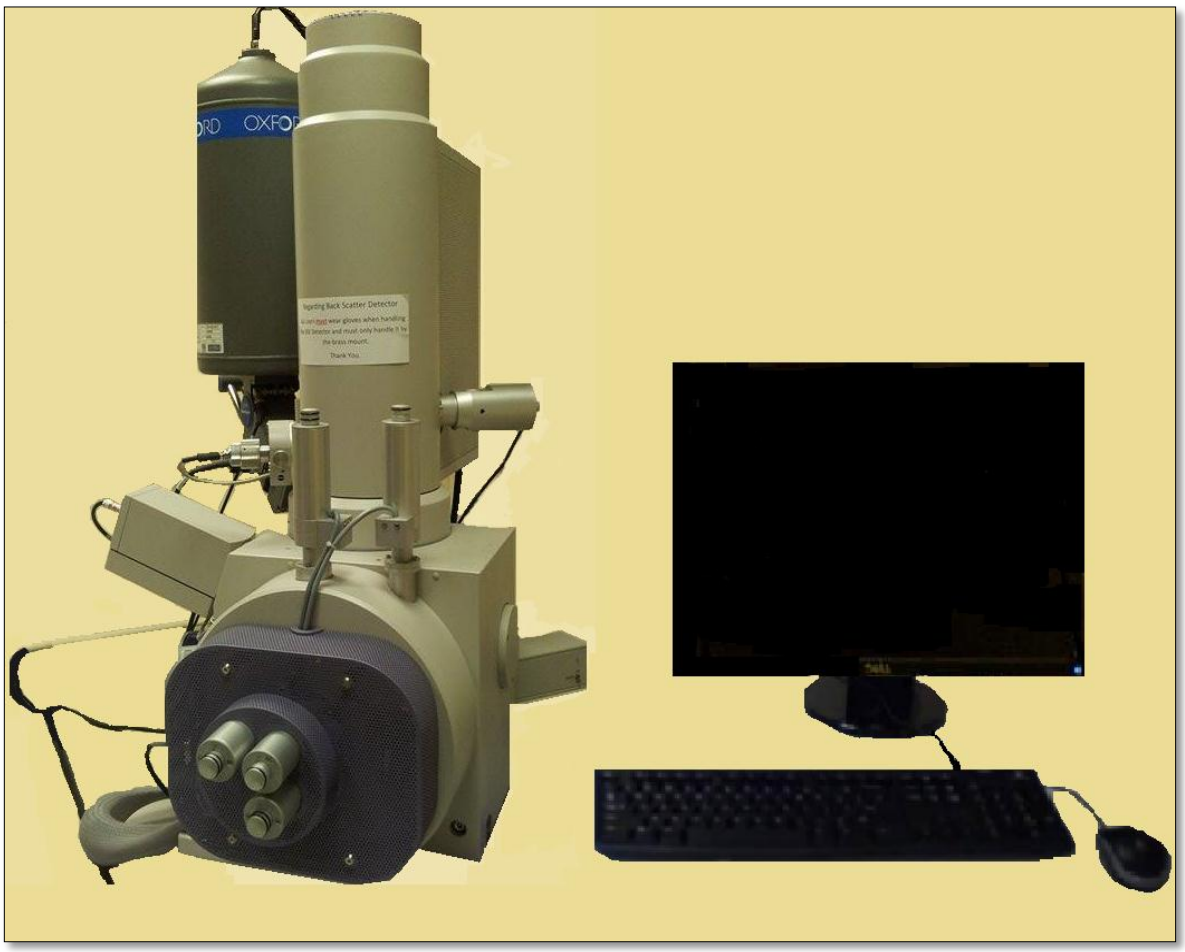

Figure 103: An FEI XL30 SFEG Scanning Electron Microscope (SEM) with Energy Dispersive X-ray Spectroscopy (EDX) at Cranfield University.

Scanning electron microscopy (SEM) is a microscopic technique that uses electrons as a substitute of light, and generates a surface image of high resolution, due to a large depth of field and magnifications of up to x 100,000 (1 µm) for closely spaced specimen. The specimen is constantly scanning it with a focused beam of electrons [206]. Energy dispersive X - ray spectroscopy (EDS / EDX) is an additional module associated with scanning electron microscopy. EDS provides a chemical

composition of the material, including the relative amounts of its constituent elements. Although EDS-SEM does not provide the complete information about the structure of the materials but it provides the composition of the constituent elements and help to be familiar with the chemistry of the coatings after PVD deposition. The penetration depth of the electron beam within the thin film depends on the material density. A typical penetration depth for Ni coatings by 20 kV electron beam is ~1.1µm. The elemental composition obtained by EDS represent the average amount of each element present in the analysed area. Thus, EDX may not determine the correct elements composition of multilayer thin film or if the elemental composition changes with the depth of the material. An EDX spectrum is a plot to show the frequency of an X-ray influx at a particular energy level and the energy level for which most X – rays were detected. The higher elemental peak in the spectrum corresponds to a higher amount of that element within the thin film.

In SEM images of flat PVD thin films, the morphology, columnar structure with engraved grain boundaries and clusters assembly can be observed. Scanning electron microscopy can be used to examine two-dimensional and three-dimensional clusters within PVD thin films. For the smaller clusters, SEM captures their plane and slanted-view images by three-dimensional clusters analysis. The sufficient focus depth allows a detailed observation of the shapes of the clusters. It is impossible to quantify all 3D shapes of the clusters in thin film, without capturing their 2D images from various directions. This is because 3D thin films have a columnar structure composed of the 2D clusters; SEM captures the images of the grain boundaries and the shapes of the clusters. The surface of the films is not flat so that the observed grain boundaries at conjunction of the two surfaces with the adjacent clusters meet at a particular contained angle.[45; 68]

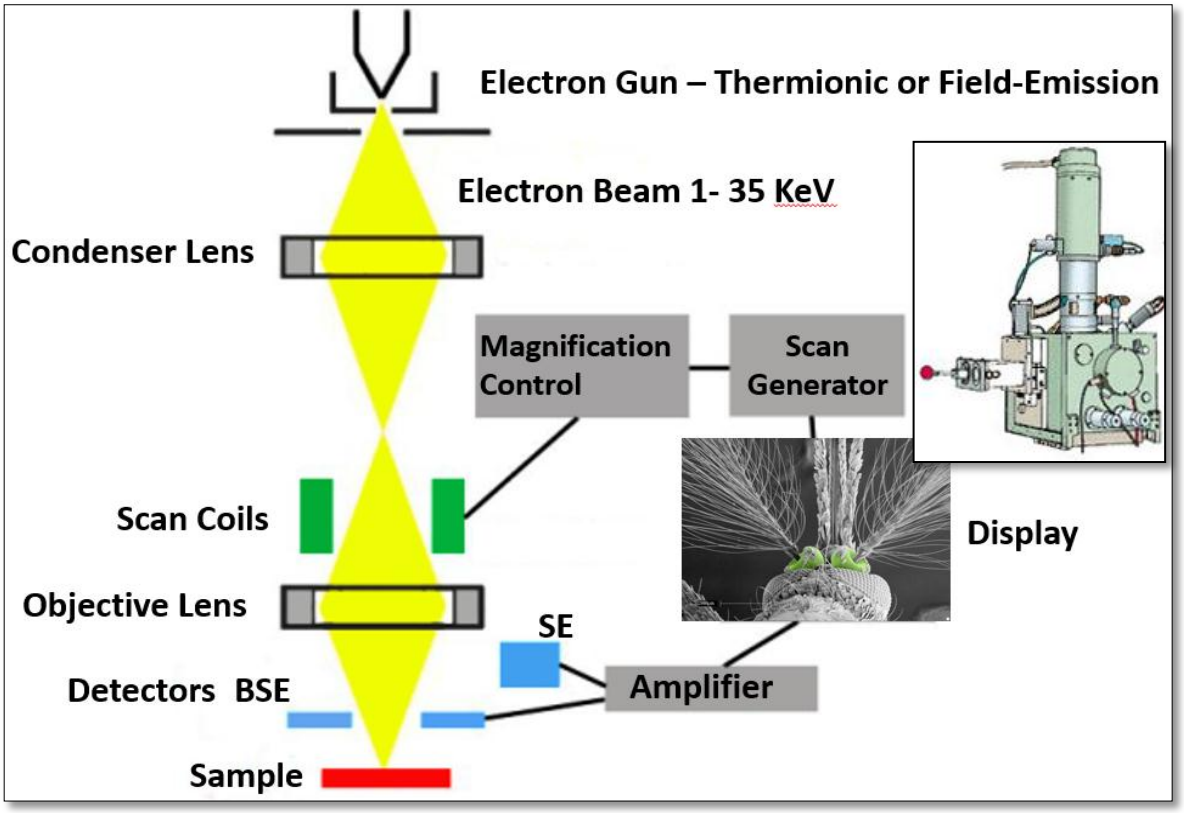

Figure 104: Schematic of scanning electron microscope [210; 211].

The electron gun provides an electron beam that is accelerated to energies in the range of 1 - 30 KeV within a column that houses an electron gun [212]. A high vacuum pumping system maintains high vacuum within the vertical track electron beam through the microscope. A system of condenser lenses with deflections adjusts the electrons on their track, and direct the electron beam to form an electron probe of approximately 1 – 10 nm in size while the electron beam carries a current of 1 – 100 pA. The SEM uses electromagnets rather than conventional lenses to allow a better control of the degree of magnification. The electron beam travels through the electromagnetic fields and SEM lenses, which focus the beam down toward the sample. Once the beam hits the specimen, electrons and X-rays are ejected from the sample surface. Secondary or back- scattered electron detectors detect the scattered electrons, which collect these X-rays, backscattered and secondary electrons, and convert them into a signal. The signal is directed to the screen, and the final image appears. All SEM components are connected to a computer, which gear its operation and processes data from electron detectors to image the specimen.[206; 212]

The operational procedure of a standard EDS spectroscopy is detailed as follows:

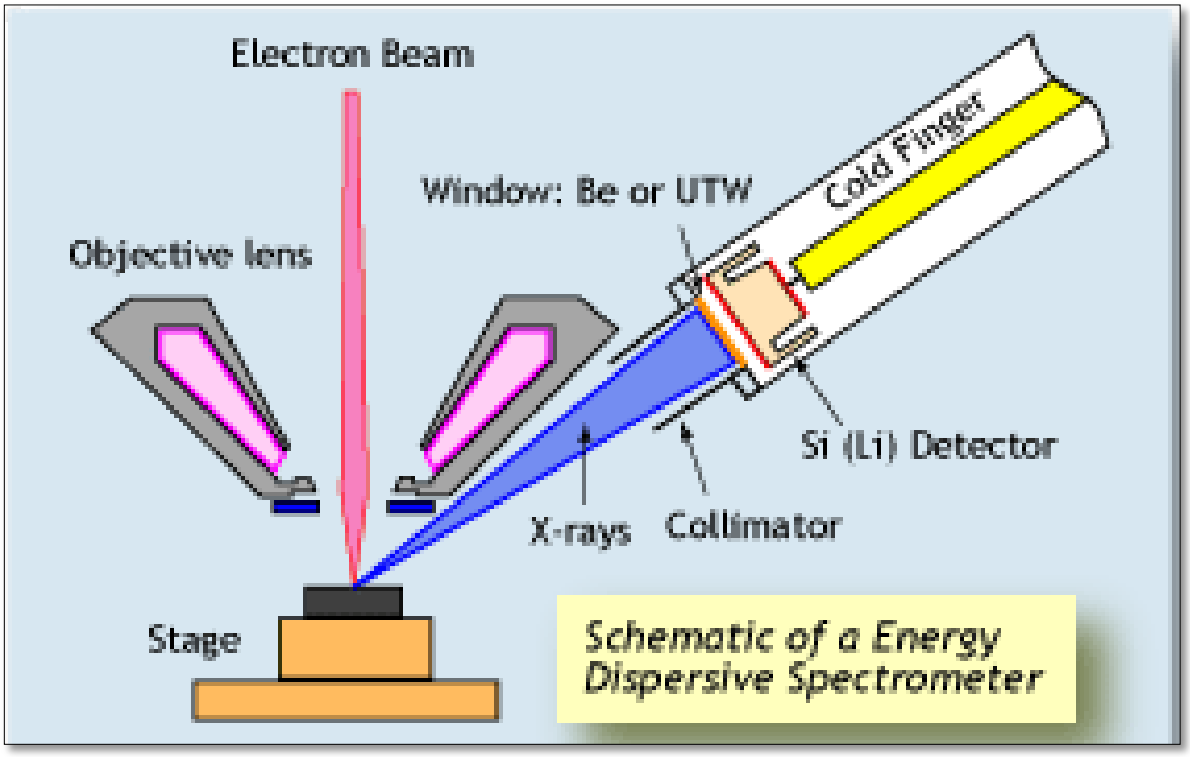

Figure 105: Schematic of energy dispersive spectrometer [213].

Characteristic X-rays are emitted from individual elements because of its unique atomic structure, which interact with the electron beam. Resulting peak positions and intensities are related to different elements and their content within the substances. X – Ray photons are detected by a solid-state detector made of a semiconductor such as Si, which produces small current and knockout the electrons from the semiconductor. These electrons absorb ~ 3.8 eV of X-ray energy; the X – ray photons of every element have distinctive starting energy and produce a specific amount of current by emitting those electrons. The magnitude of current created by each X-ray photon is measured to calculate the original energy of the X-rays of individual elements, resulting in an EDS spectrum providing the number of X-rays measured at each energy.[213]

6 RESULTS AND DISCUSSION

This chapter presents the experimental results along with the observations for the manufacturing and characterisation of thin films including PTFE, NiTi and PTFE-NiTi deposited under various process conditions. Prior to the deposition of the thin films, the sputtering chamber was mapped to find a suitable deposition location within the chamber, for which the findings are reported in section 6.1. Following to this, the results for the influence of various process conditions on deposition rates of PTFE and NiTi films are shown in section 6.2. These deposition rates results are later combined with the characterisation results to estimate the suitable deposition conditions to sputter of PTFE and NiTi for the fabrication of PTFE-NiTi nanocomposites (section 6.7).

Oxygen can poison the targets, and alter the composition and microstructure of the resulting thin films. This becomes crucial for NiTi deposition because of pointedly high titanium's affinity for oxygen. Therefore, section 6.3 shows the results of an investigation to find out the oxygen content at various base pressures and process pressures. Considering the results presented in section 6.3, the base pressure is maintained below 1 x 10^{-6} mbar and the process pressure is kept at or below 10 x 10^{-3} mbar for the rest of the depositions in order to avoid the oxygen contaminations. Section 6.4 represents the findings of composition and heat treatment procedure significantly affecting the microstructure and phase transformations demonstrating the shape memory of NiTi thin films. NiTi compositions were tailor-made to obtain thin films having potential pseudoelasticity.

PVD sputtering is an energetic process and fragmentize PTFE chain; therefore, the repolymerised content of PTFE films was investigated by areas under the FTIR peaks when the depositions were carried out at various process conditions (section 6.5). Subsequent to the above results, the surface analysis of PTFE and NiTi thin films is provided to analyse the microstructure and surface properties of the thin films that were deposited at various process conditions (section 6.6). The microstructure and surface properties are studied in terms of morphology, topography, lubricity and wettability.

Section 6.7 summarises the findings of deposition rates and characterisation, and reports about the suitable deposition conditions down-selected to sputter of PTFE and NiTi for fabricating PTFE-NiTi nanocomposites. Finally, co-sputtered and layered PTFE-NiTi nanocomposites were fabricated at selected process conditions (sections 6.8 – 6.9). PTFE-NiTi nanocomposites were characterised by EDS-SEM, TEM, WCA and CoF. Depending on the formation of stable coatings and intercalated properties, the optimum fabrication parameters are chosen to prepare the final model of intercalated PTFE-NiTi nanocomposite (PNT12) (section 6.10). For all of the above sections (6.1 – 6.10), the observations and experimental results are reported and explained followed by a detailed discussion at the end of each section. The discussion contained the scientific reasoning of those observations and results, and an understanding of the results in relation to the literature review is acquired.

6.1 Mapping the sputtering coater deposition rates

The Leybold L560 sputter coater was mapped for the PTFE deposition thickness at various locations within the deposition chamber of sputter coater. PTFE was sputtered at 100W RF power and 20 x 10^{-3} mbar process pressure. The film thickness was determined in terms of average step height (ASH) by AFM as presented in Table 17 and Figure 106.

Table 17: Deposition thickness against distance from the target in coater.

Distance from the target centre (cm)	Deposition thickness (nm)
2	3060
3	4000
4	4883
6	4500
8	4600
11	4867
15	3800
21	3500
26	2895
29	1676
30	1260
32	1200

The maximum deposition thickness was measured above the outer ring of the magnetron, which is 3 – 4 cm from the centre of the target. Figure 106 shows a steady increase in deposition thickness as the distance from the target centre increases followed by a constant decrease in deposition thickness some critical standoff distance. At a higher distance from the magnetron, the deposition thickness decreases because the power distributes, and vapour is dispersed within the coater.

To acquire a high sputtering rate, the substrate holder was placed at a constant location above the magnetron ring, approximately 3 cm from the target centre. The vertical target substrate distance was maintained at 10 cm. All deposition experiments following this first step of sputter-coater mapping were conducted at this selected position within the chamber.

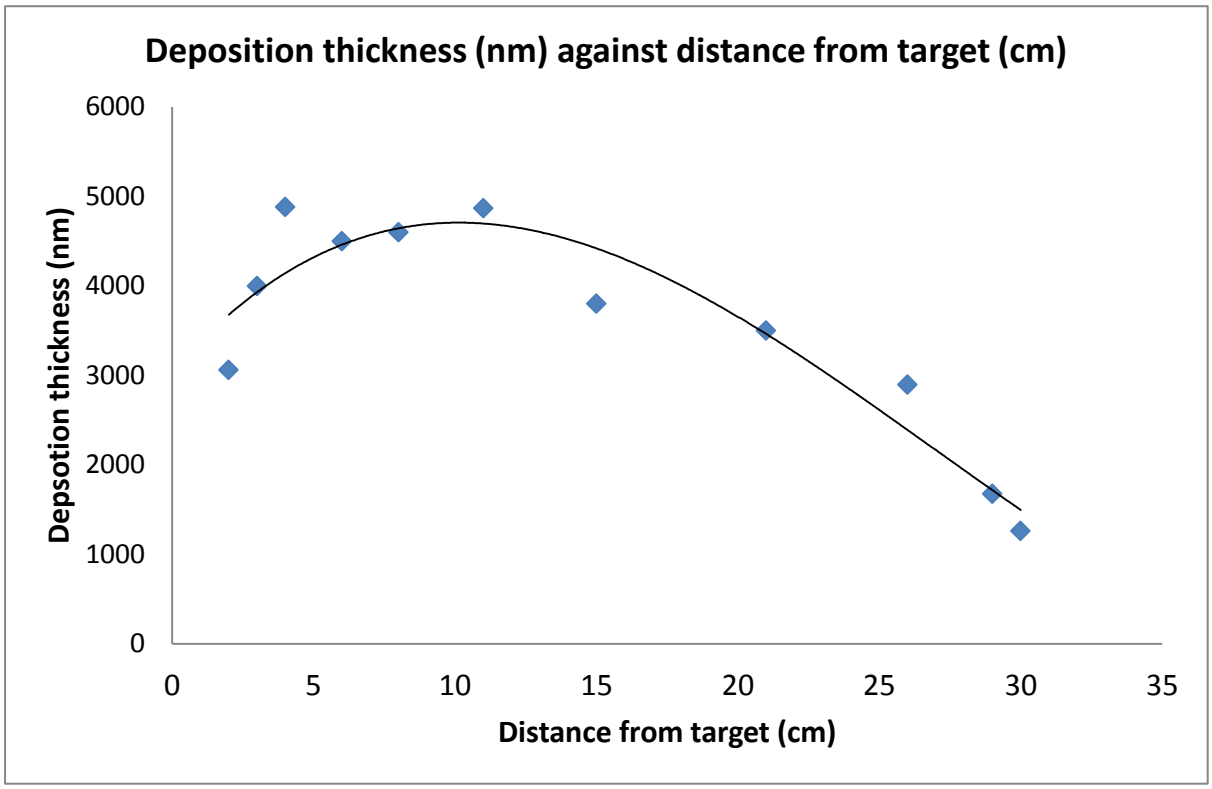

Figure 106: Deposition thickness against distance from the target in coater.

It was essential to find a suitable position within the sputter coater before starting any other deposition experiments because minor variations of sample locations lead to substantial changes in thin film composition and properties. For example, Sanjabi et al. [23] experienced '0.01 at.% / horizontal mm' deviation in NiTi composition. The geometry of the sputtering chamber would have also influenced the NiTi stoichiometry. This was explained by Surbled et al. [102], who reported that the percentage of titanium changes with the radial position of the substrate with respect to the target, owing to faster thermalisation of the nickel element at various angular distributions. Therefore, the variation of deposition rate at different location within a vacuum chamber would produce different nanocomposite thicknesses and compositions, affecting the properties such as morphology, hydrophobicity, surface roughness, lubricity and chemical and mechanical properties.

6.2 Deposition rates of PTFE and NiTi

It is essential to deposit a known volume fraction of each material within a nanocomposite coating, which is controlled by deposition rates in this project. Deposition rate directly influences the thin film structure; therefore, the properties. PTFE and NiTi deposition rates were determined over a range of power and pressure parameters by following Equation 7 as presented in Table 18.

Equation 7: Equation for deposition rates measurements.

$$\boldsymbol{Deposition\ rate} = \frac{\boldsymbol{Average\ of\ three\ ASH\ measurements}}{\boldsymbol{Deposition\ time}}$$

Table 18: Deposition rate (nm/h) of PTFE and NiTi at range of pressure (mbar) and power (W) values.

Pressure (x 10^{-3} mbar)	log pressure (mbar)	PTFE		NiTi	
		Power (W)	Rate (nm/h)	Power (W)	Rate (nm/h)
25	1.34	150	12.5	100	74.5
		125	22	75	74.0
		100	65	50	72.7
		75	45	25	49.0
20	1.30	150	16.2	100	66.3
		125	19	75	72.0
		100	69.2	50	52.0
		75	40	25	50.0
15	1.18	150	23.9	100	146.1
		125	21	75	93.0
		100	18.8	50	62.2
		75	16	25	56.0
10	1	150	23.6	100	138.1
		125	23	75	112.0
		100	16.2	50	45.4
		75	14	25	44.0
5	0.70	150	49.2	100	212.6
		125	19.4	75	190.0
		100	10.1	50	166.6
`		75	9	25	42.0

6.2.1 Deposition rates of PTFE at various process conditions

The deposition rates of PTFE at range of process parameters were obtained and from Table 18 to acquire a pattern for deposition rates against power and pressures as shown in Figure 107 and Figure 108. Figure 107 demonstrates the influence of variation in power on deposition rate of PTFE, which was investigated at process pressures ranging 5 $x10^{-3}$ – 25 $x10^{-3}$ mbar. PTFE was sputtered at 75, 100, 125 and 150 W. At the process conditions of 25 $x10^{-3}$ mbar, and 75W, the deposition rate of PTFE is 45 nm/h. For the same process pressure, the deposition rate increased to 65 nm/h by increasing the power to 100W. On increasing the RF further to 125 and 150W, the deposition rate decreased continually to 22 and 12.5 nm/h respectively. The same pattern of deposition rate against power was observed, when the process pressure was reduced to 20 $x10^{-3}$ mbar, as presented in Figure 107. The graphs in Figure 107 and Figure 108 are extrapolated to zero power and pressure because the deposition rate is theoretically zero at zero power and pressure. In Figure 108, pressure is plotted as a log scale because it is not practically possible to get a pressure of zero. Deposition rate trends depend upon the power of particular pressure, not the linear pressure; therefore, the deposition rate trends obtained at pressure log scale cause less error in the data plotted on the graphs.

At 15 $x10^{-3}$ – 5 $x10^{-3}$ mbar, the trend of deposition rate against power is different as compared to the trend obtained at 20 $x10^{-3}$ and 25 $x10^{-3}$ mbar. At 75W, the deposition rates for 15 $x10^{-3}$, 10 $x10^{-3}$ and 5 $x10^{-3}$ mbar are 16, 14 and 9 nm/h respectively, which are significantly lower than the deposition rates measured at higher process pressures. At lower deposition pressure, the deposition rate increases with an increase in RF power. The continuous increase in deposition rates against power at 5 $x10^{-3}$ mbar was steeper than that of 15 $x10^{-3}$ and 10 $x10^{-3}$ mbar. The highest deposition rate was recorded at 5 $x10^{-3}$ mbar and 150W under these low deposition pressure conditions. Another observation is that the deposition rates at 125W deposition power are not influenced by changing process pressure. All values of deposition rates, recorded at 125W for a range of process pressures are similar and seem independent of the process pressure.

The reasons for the above changes in deposition rates at various process conditions are discussed at the end of this section, which are reasoned in view of the scientific principals and literature review.

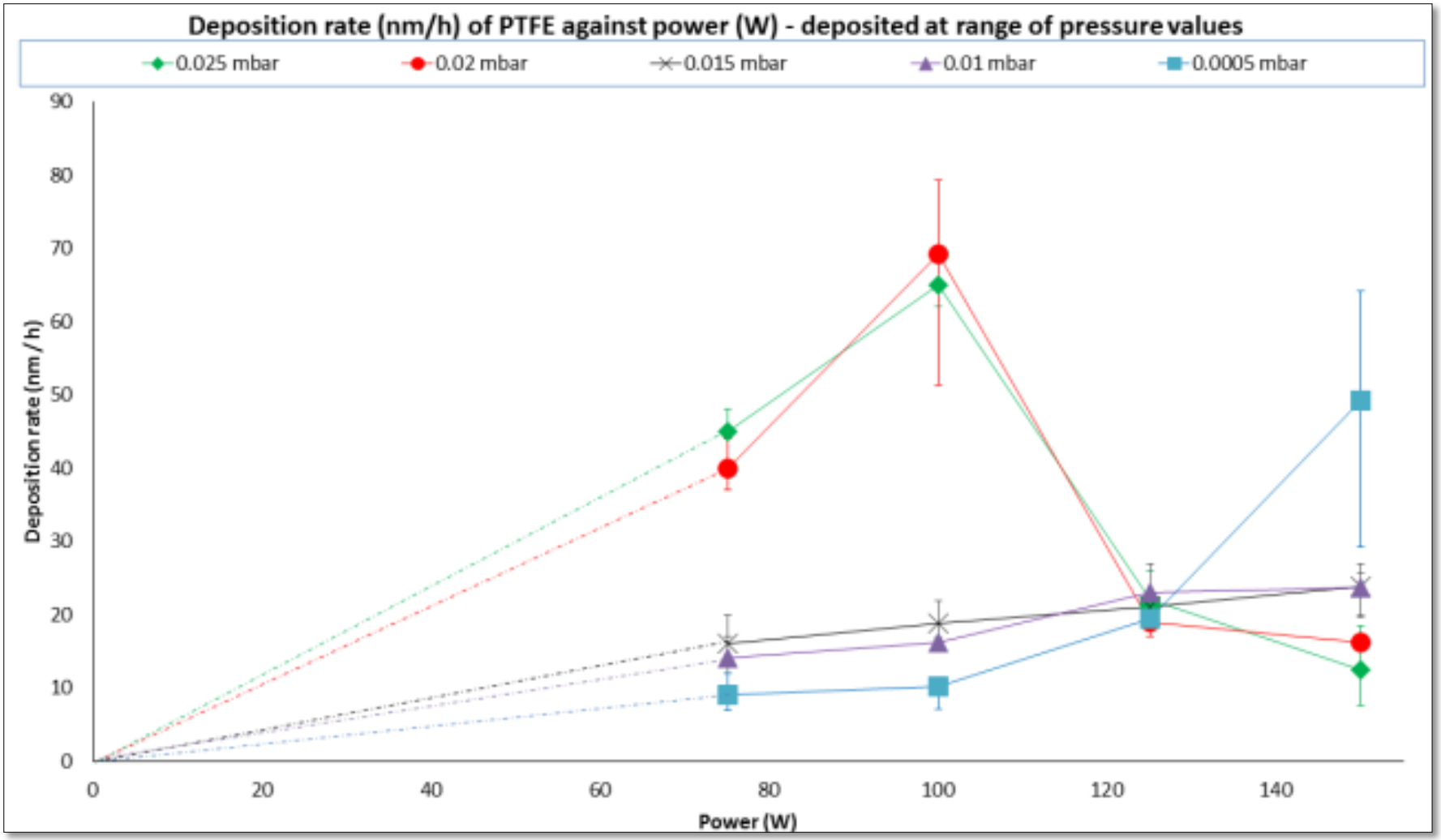

Figure 107: Deposition rate (nm/h) of PTFE against power (W) - deposited at range of pressure values.

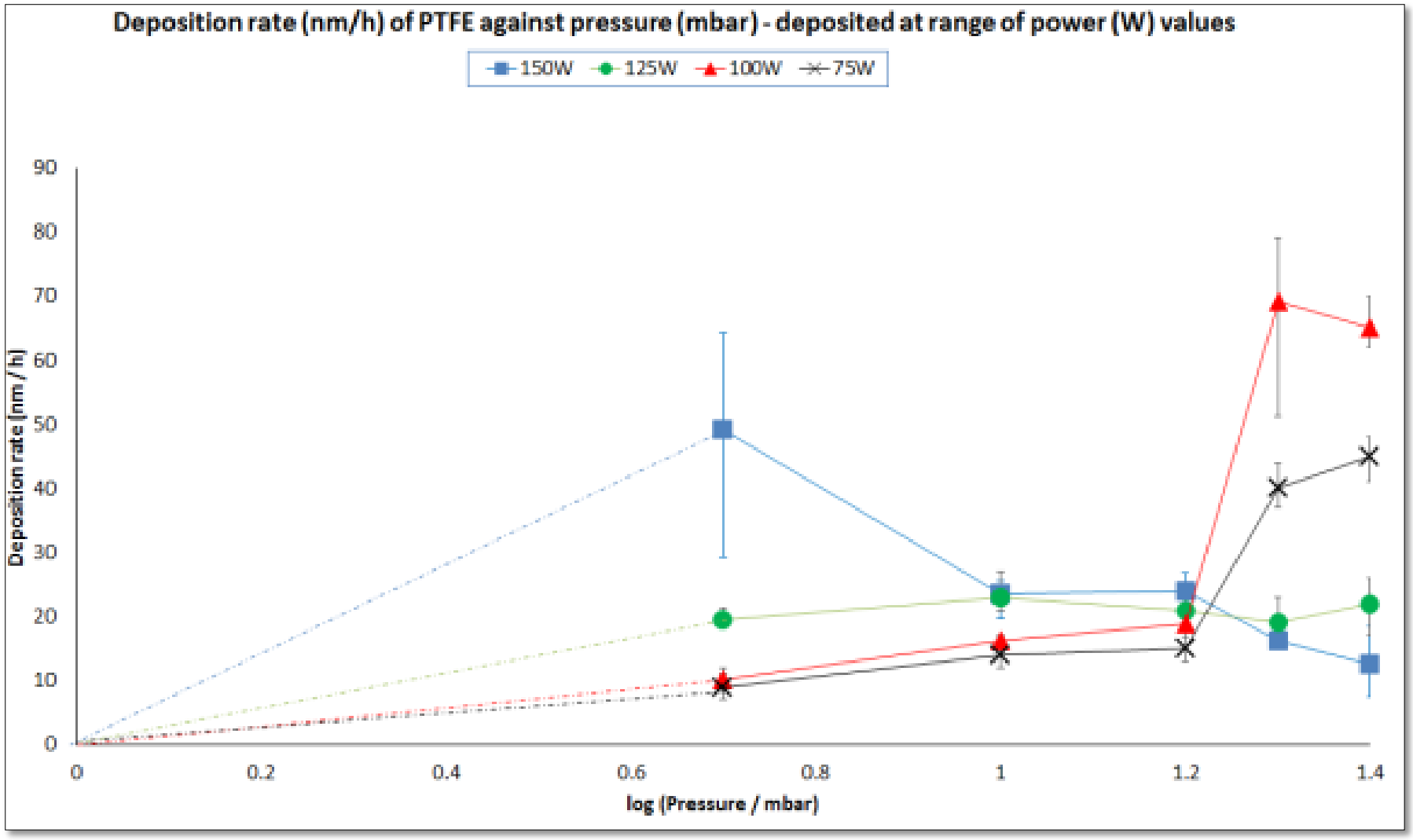

Figure 108: Deposition rate (nm/h) of PTFE against pressure (mbar) - deposited at range of power values.

Figure 108 was generated using the same data as Figure 107, from Table 17, with the purpose of further understanding of the relationship between PTFE deposition rates and PVD sputtering conditions. Figure 108 determines the influence of variation in process pressure on deposition rate of PTFE, investigated at range of power values (75 – 150W). At 150W, the deposition rate of PTFE declines with increasing pressures. The deposition rate of 49.2 nm/h was recorded at 5 $x10^{-3}$ mbar, which declines to 12.5 nm/h at 25 $x10^{-3}$ mbar. To investigate further, the RF power was reduced to 125W, and the deposition rate was studied in the same range of process pressures. The deposition rates do not alter; therefore, an approximately straight line was observed. At lower RF power of 100 and 75 W, the deposition rates increase with increasing process pressures. The highest deposition rates were obtained at low power, and high process pressures. The deposition rate against pressure trend was steeper at 100W as compared to 75W, resulting in a greater magnitude of deposition rate of 65 nm/h at process conditions of 25 $x10^{-3}$ mbar and 100W. It is interesting to observe that the deposition rate of PTFE becomes independent of power at 15 $x10^{-3}$ mbar. Increasing or decreasing the pressure from 15 $x10^{-3}$ mbar changes this pattern, and the deposition rates are greatly influenced by variance in RF power. The reasons for the above changes in deposition rates are discussed at the end of this section.

6.2.2 Deposition rates of NiTi at various process conditions

The data presented in Table 17 was used to plot the graphs in Figure 109 and Figure 110 for studying the relationship between deposition rate and the process conditions (power and pressure) for NiTi thin films. The graphs in Figure 109 and Figure 110 are extrapolated to zero power and pressure because the deposition rate is theoretically zero at zero power and pressure.

Figure 109 shows that the deposition rate of NiTi increases with an increase in power, when sputtered at range of process pressures. At high process pressures (20 $x10^{-3}$ and 25 $x10^{-3}$ mbar), there is a slow increase in deposition rate against deposition power. For example, the deposition rate of NiTi at 25W and 25 $x10^{-3}$ mbar is 49 nm/h, which increases to 74.5 nm/h at 100W, while the same pressure was maintained throughout the process. Compared to this, lowering the process pressure to 15 $x10^{-3}$ and 10 $x10^{-3}$ mbar changes the deposition rate more rapidly with increasing power. For example, the deposition rate is 56 nm/h at 25W and 15 $x10^{-3}$ mbar, which increases to 146 nm/h at 100W, while keeping the process pressure unchanged during the deposition run. A more rapid increase in deposition rate was observed with increasing deposition power, at the lowest pressure of 5 $x10^{-3}$ mbar. At 5 $x10^{-3}$ mbar, a quick rise in deposition rate was observed with increasing the deposition power from 25W to 50W where the deposition rate increases from 42 – 166 nm/h. This is followed by a relatively slower increasing trend of deposition rate against power at the same process pressure for higher deposition powers as shown by the blue line graph in Figure 109. At 25W, the deposition rates of the NiTi coincide and become independent of the variation in process pressure. Above this power, as the deposition power increases the deposition rate becomes more influenced by the process pressure.

Figure 110 was produced using the same data as Figure 109, from Table 17, with an intention to study further about the relationship between deposition rates and PVD sputtering conditions of NiTi. Figure 110 demonstrates the influence of process pressure on deposition rate at the range of power magnitudes. A small increase in deposition rate is observed with increasing process pressure at 25W, but at higher deposition powers, the deposition rate decreases steeply with increase in deposition pressure. At 5 $x10^{-3}$ mbar, the deposition rates are significantly higher for the NiTi

sample sputtered at higher powers. As the pressure increases, the deposition rate continuously declines while maintaining the same power. At 25 $x10^{-3}$ mbar, the deposition rates of NiTi accord with each other and become independent of changing power.

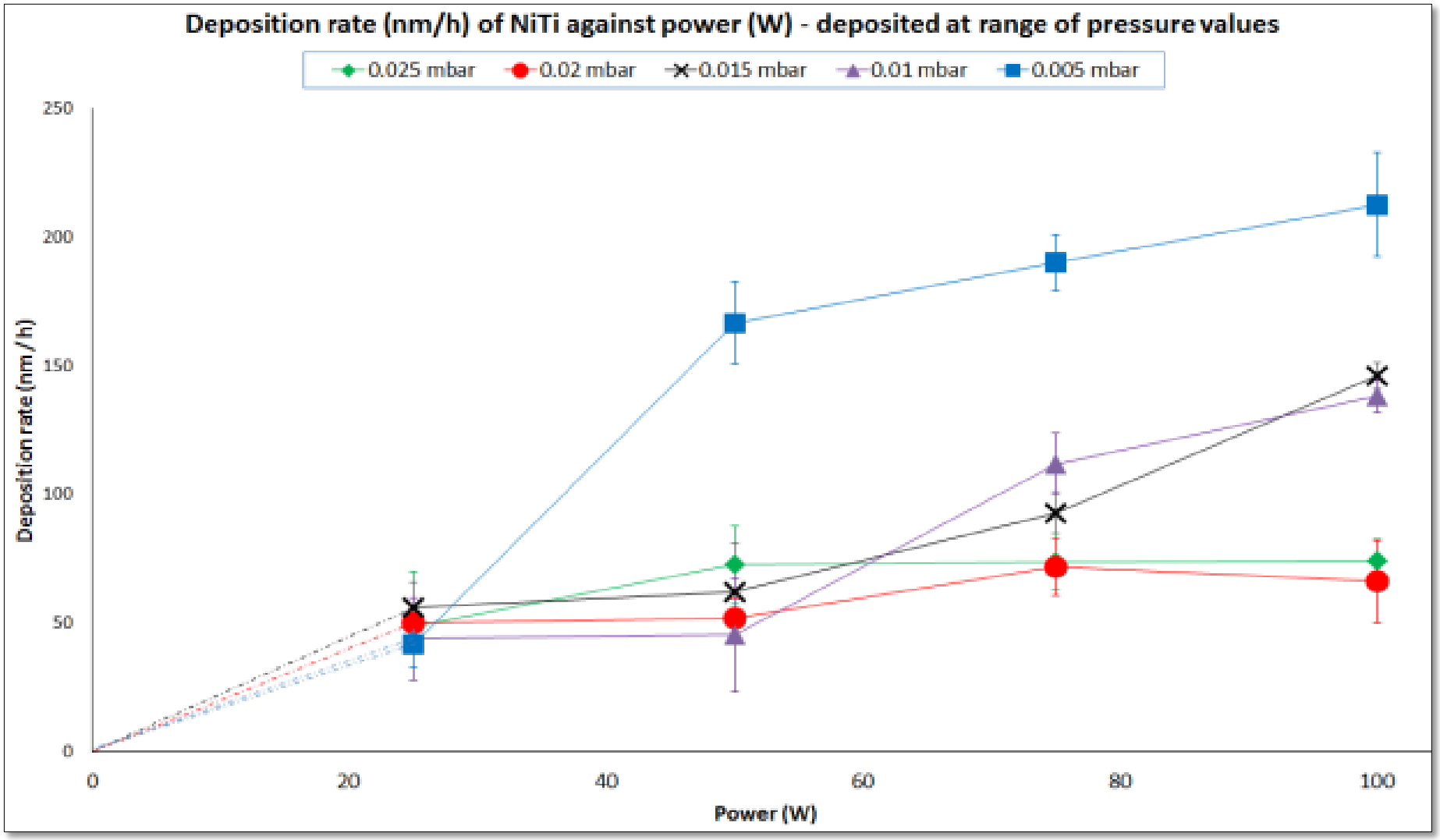

Figure 109: Deposition rate (nm/h) of NiTi against power (W) - deposited at range of pressure values.

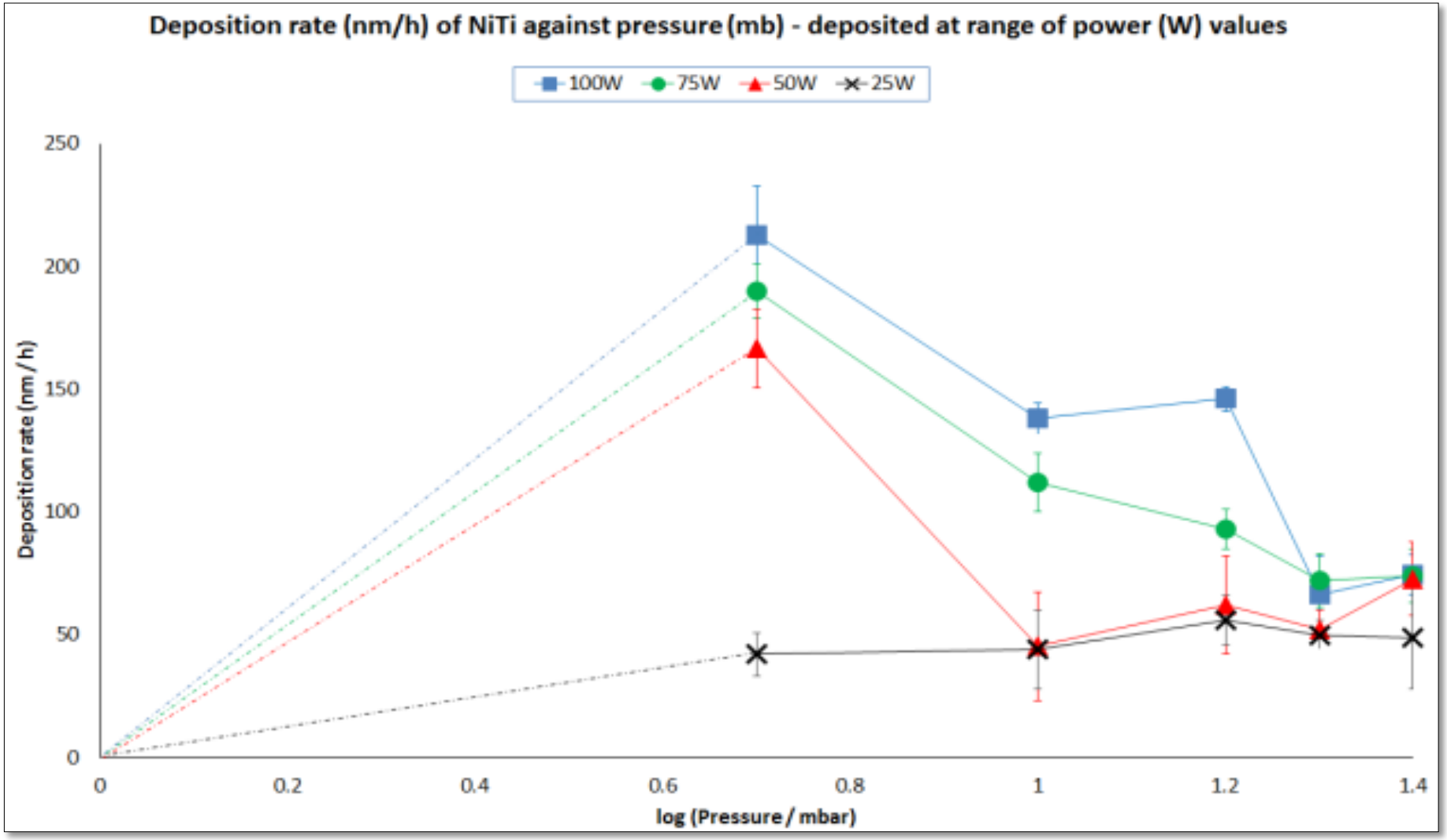

Figure 110: Deposition rate (nm/h) of NiTi against pressure (mbar) - deposited at a range of power values.

6.2.3 Comparison of PTFE and NiTi deposition rates

To control the composition of PTFE-NiTi nanocomposite, the volume fraction of PTFE and NiTi should be known. To deposit the known, and desired content of each material, the deposition rates of PTFE and NiTi were compared and contrasted in Figure 111 and Figure 112. Figure 111 combines the PTFE and NiTi results of deposition rates against power at range of process pressures as previously provided in Figure 107 and Figure 109. It can be clearly seen that NiTi has higher deposition rates compared to PTFE, at all power and pressure values. The sputtering chamber needs to be maintained at suitable pressure value for obtaining the desired deposition rates of each material during co-sputtering of PTFE and NiTi. The same process pressure value is needed for PTFE and NiTi as both targets are placed within the same sputtering chamber, and the magnetrons associated with PTFE and NiTi targets are linked to RF and DC power supply respectively. Figure 112 combines the results of Figure 108 and Figure 110 demonstrating the effect of variance in process pressure on deposition rate of PTFE and NiTi at various deposition powers. At any given pressure, the deposition rate of NiTi is higher than that of PTFE. This difference is greater at lower process pressures but lesser at higher process pressures.

Figure 111 and Figure 112 were used to estimate the volume fractions of PTFE and NiTi within the nanocomposite. This approach allows control of the composition, which regulates the properties of the nanocomposites by the process parameters. For example, to prepare a nanocomposite with nearly equal PTFE and NiTi content at 5 $x10^{-3}$ mbar, PTFE deposits at 150W RF and NiTi sputters at 25W from the DC power supply. Figure 111 shows that the both materials have similar deposition rates at those process parameters, which are 49.2 nm/h and 42.0 nm/h respectively. PTFE and NiTi are deposited at 100W to obtain nearly equal volume fractions of both materials at 25 $x10^{-3}$ mbar, because the deposition rates at those process parameters are 69 nm/h and 72.7 nm/h, which are also nearly the same.

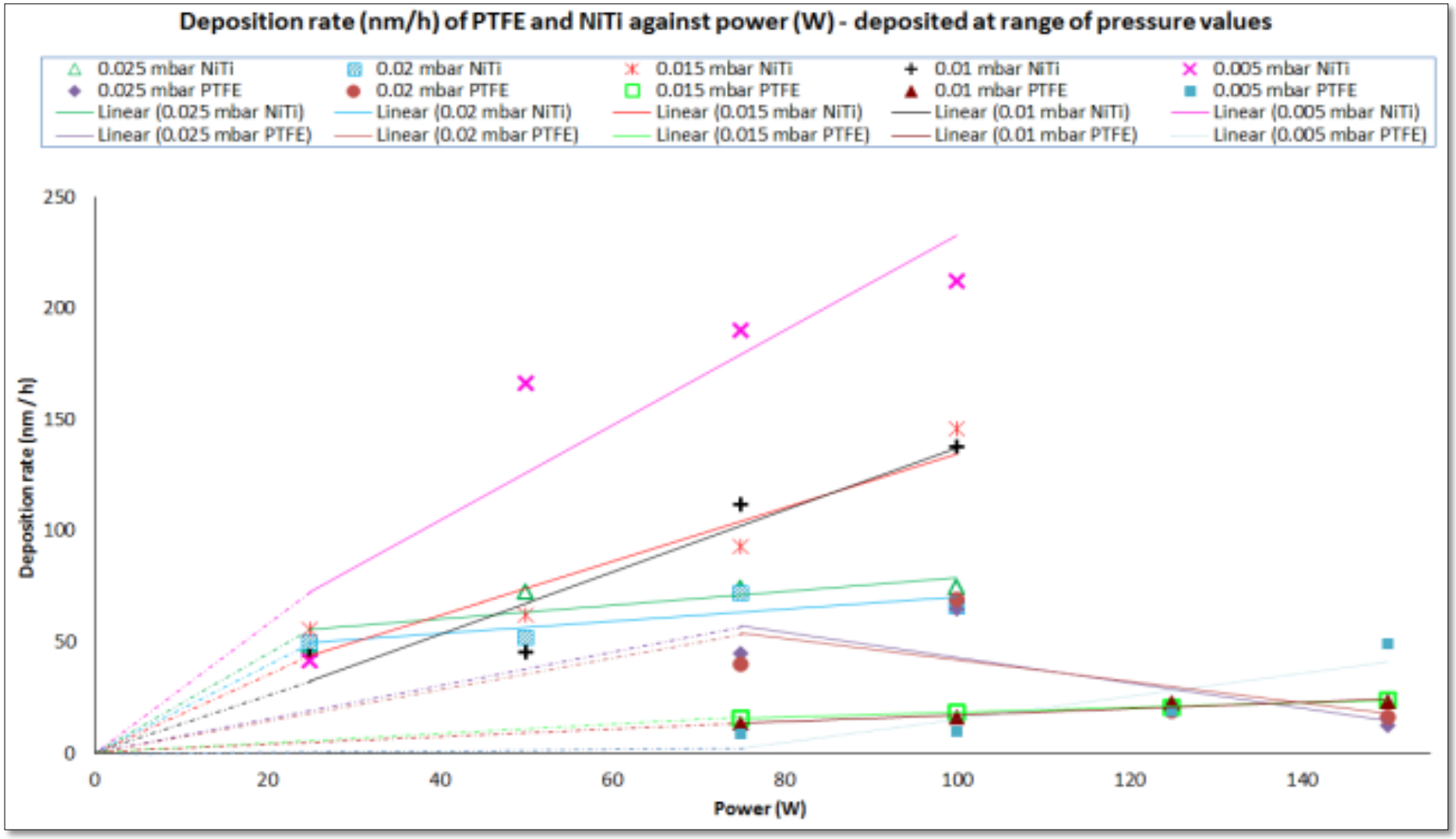

Figure 111: Deposition rates (nm/h) of PTFE and NiTi against power (W) - deposited at range of pressure values.

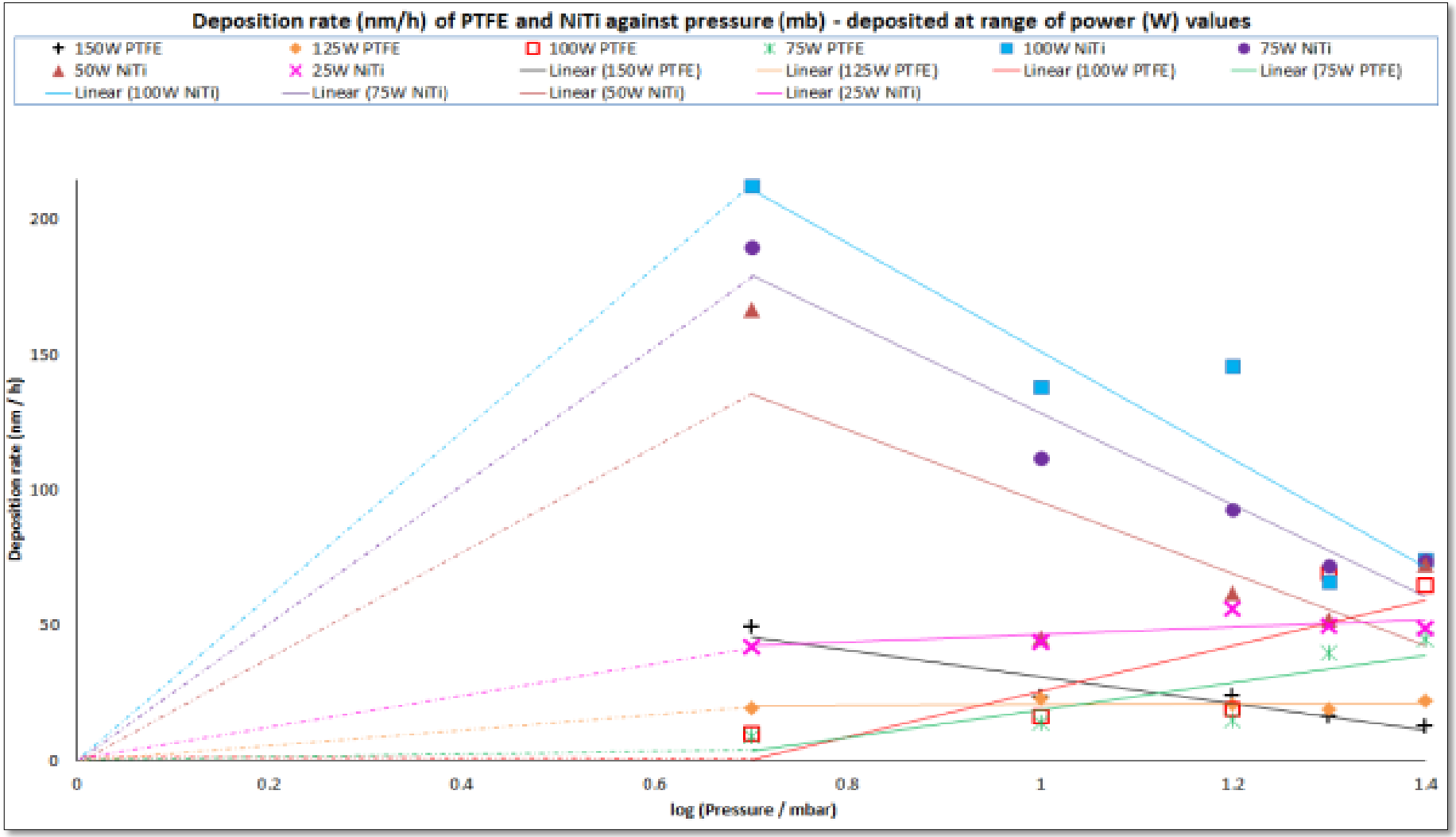

Figure 112: Deposition rates (nm/h) of PTFE and NiTi against pressure (mbar) - deposited at range of power values.

PVD sputtering is a nanoscale process and subtle to range of process conditions including temperature, deposition pressure, power, working distance, type of working gas, base pressure, cooling efficiency, and the geometrical arrangement of targets and substrate in sputtering chamber. Minute changes to any of those process parameters alter the deposition rates, chemical composition and the microstructure of the thin films. There was limited information found in the literature about the relationship between deposition rates and process parameters, which is specific to PTFE and NiTi. The deposition rates of various materials would be dissimilar due to the differences in their physical and chemical properties. For example, metals and polymers sputter at different deposition rates and by various chemical and physical mechanisms when formed as a coating and therefore result in disparate microstructure and associated properties. Polymers having different molecular weight and chain complexity resulting in various sputtering rates, microstructure and post-sputtering polymerised content with thin films. For metals, the density of particles, its atomic bonding and therefore crystal structure alter the sputtering rate. Heavier metallic particles have different elastic properties, and K.E. within the plasma compared to the lighter metallic particles, a result of atomic size effect and bonding; therefore, the deposition rates can alter significantly for various metals.

The deposition rates of PTFE at all deposition conditions were lower than NiTi (Figure 111 and Figure 112). It was expected to obtain low deposition rates of PTFE compared to NiTi due to the dissimilarities in material properties and different types of power supplies used for PTFE and NiTi. Selection of various types of power supplies for PTFE and NiTi was done because of their insulating and conducting natures respectively. RF sputtering is a slow deposition process having various chemical reactions taking place in the plasma declining the repolymerisation. For Al deposition, Kelly et al. [59] reported a five times lower deposition rate by RF power supply, as compared to DC power supply, when rest of the conditions were kept the same, i.e. depositing at the sample chamber pressure and power level. Therefore, NiTi sputtered by DC deposited was expected to be much faster than PTFE deposition by RF.

The other reason for slower deposition of PTFE by RF is the lower sputtering yield of a polymer (PTFE) as compared to NiTi. Sputtering is an extremely energetic method of depositing thin films, and it can lead to local breaking of polymer chains which can then crosslink with the creation of a complex of polymer chains associated with plasma polymerisation [50]. As a result of such atomic rearrangment during deposition, related to plasma polymerisation, polymer film growth is slow and this leads to a lower sputtering yield of polymers as compared to metals because metallic particles only involve physical condensation and adsorption of adatoms during the film growth stage. The higher PTFE fragmentation is, the longer it takes to repolymerise, reducing the sputtering yield and polymerised content of PTFE after polymerisation. To obtain a higher polymerised content, low deposition rates of PTFE were sustained as a compromise. The reason is that the higher the deposition rates, the more destructive the sputtering process is; and the rise in K.E. would lead to the monomers impacting with high energy on the substrates, resulting in a lower polymer sputtering yield.

Another reason for maintaining a low deposition rate during sputtering is that the increase the deposition rate reduces the control of the sputtering process resulting in loss of control over the thin film characteristics. As the deposition rate increases, the control on the thin film characteristics depreciates [27; 39]. The difficulty of maintaining control on the deposition rates at high deposition rates can be observed by considering the error bars on Figure 107 – Figure 110. Longer error bars appear for higher deposition rates. Therefore, it is vital to have moderate deposition rates to attain a desired composition and thickness of nanocomposite thin films, especially when co-sputtering polymers and intermetallics.

Figure 109 and Figure 110 present that NiTi yields high deposition rates at low process pressures and high power. NiTi is a conductive intermetallic material sputtered by DC power supply, leading to simpler deposition trends of increase and decrease depending on energy and power density. The higher the deposition power, the faster sputtering would occur. The rate of energy transfer is greater at high power that allows overcoming the electrostatic forces within the metallic structure faster. This explains the relationship between power and energy; therefore, the metallic particles sputter at higher rate. Higher K.E. would lead to an increased the number of elastic collisions between Ar gas and sputtered particles. An increase in K.E

increases the bulk mobility leading to a faster condensation of the metallic particles on the substrate surface, which results in higher deposition rates. In other words, increasing the deposition power increase the deposition rate because of more available energy ionising and sputtering a greater number of particles through more collisions with energetic Ar ions.

Observations in Figure 108 and Figure 110 provide a thorough analysis of deposition rates against pressure for PTFE and NiTi respectively, showing that the deposition rates of PTFE and NiTi may either decrease or stay the same approximately, with increasing process pressure. A combination of high process pressure and low deposition power results in charged particles accumulating on the substrate surface because the reduction in energy leading to lower deposition rates. Increasing the pressure decreases the deposition rate due to back diffusion and collisions with the working gas (Ar). The decline in deposition rate against pressure is steeper at higher power, which accounts for the increasing current density with increasing power. The current density increases as the deposition rate falls because of the backscattering of poorly bonded fragments during the sputtering process.

This observation can be explained further for PTFE by the fact that the low deposition powers prevent excess destruction of polymeric fragments during sputtering, thus the polymer fragments residence time increases, and repolymerisation occurs at a faster rate. Along with a simultaneous increase in power and pressure, the deposition rate decreases due to excessive fragmentation of the polymer chain, which can be pumped away as vapour, and local target melting leads to higher carbon content on the target surface. At low process pressures, the deposition rate vs. deposition power becomes relatively independent of chamber pressure, resulting in a direct relation between deposition rate and power as shown in Figure 107. This is because along with a decrease in working gas pressure, the number of elastic collisions between the working gas particles and sputtered species decreases. Thus, fewer small fragments are created that can be pumped away as vapour meaning more of the sputtered material condenses on the substrate and increase the deposition rate. The above observations can be verified further by the trends shown in Figure 108, where low pressure and low deposition power

combination, also gives rise to high deposition rates and permit the polymeric fragments to deposit faster onto the substrate.

In comparison to NiTi, PTFE is an insulating material and more sensitive to the changes in deposition parameters. Broadly, the deposition trends of PTFE can be divided into two regions in Figure 107. Figure 107 present two regions of deposition rates vs. power pattern on right and left side of 100W power. On the left side of Figure 107, increasing in deposition power increases the deposition rates under all pressure conditions, and the increase is steeper at high process pressures than the lower ones. The steepness is because of oxygen entrapping in polymer chains at high pressures. The results shown later in section 6.3 concluded that high process pressures more oxygen entraps within the thin film structure. On the right-hand side of Figure 107, when the power increases above 100W, the deposition rate becomes more sensitive to the deposition powers and pressure. Therefore, information collected from this region is considered as a separate trend. This is due to increased fragments formation and small fragments being pumped away; wltimately leading to less chance for polymerisation.

Along with a rise in pressure above 15 x 10^{-3} mbar, at low deposition power of PTFE in Figure 108, the deposition rate of PTFE increases with increasing pressure. At high pressure and low power, the mean free path for elastic collisions between sputtered species and the sputtering gas atoms decrease down to the source or target-substrate distance [49]. Thus, the sputtered particles condensing faster on the substrate increase the deposition rate. This rise in deposition rate with increasing deposition pressure, matches well to the studies conducted by Biederman et al. [74] and Kitoh et al. [80], which are previously discussed in section 3.2.2 of the literature review. Biederman et al. and Kitoh et al. sputtered PTFE at process pressures of 5 x 10^{-3} mbar and below and deposition powers of 200W and 120 – 300 W respectively. Simple and linear chain of PTFE breaks into larger molecular units at low pressure and high power during sputtering; thus, it takes less time to re-polymerise resulting in high deposition rates. As the Ar pressure increases, the chain destruction due to sputtering also increases, breaking the polymer into smaller fragments; for this reason, it takes longer to re-polymerise [80]. According to Biederman et al. [74], the deposition rate of PTFE declines by approximately 30%, within the first 40 minutes during the sputtering process with increasing process pressure, which can be

explained by its relationship to the concentration of chemically reactive species in the plasma that attach to the substrate surface. At low argon pressure, the ionisation efficiency and the plasma density increase resulting in more collisions. Therefore, at these conditions, the optimum mean free path is the lowest potential difference for the plasma formation according to the Pachen's law. Increasing the pressure decreases the ionisation ability due to a decline in average free path of the electrons, resulting in less polymeric target fragmentation and emission and inhibiting some of the reactive species required for thin film growth reaching to the substrate, which leads to a decline in deposition rate. Biederman et al. [74] explain this further by reporting on the relationship between deposition rate with F:C at the PTFE target's surface. F:C ratio at the target surface changes during sputtering resulting in a carbon-enriched layer on the surface leading to low deposition rates against pressure. Carbon enriched fluorocarbon takes longer to sputter compared to PTFE. Carbon enriched fluorocarbon indicate the formation of ringed structure rather than more or less branched chain polymer structures, which require more energy to break carbon-carbon bonds in the ring rather than dissociating carbon-fluorine bonds within the polymer chains.

The scientific knowledge from previous literature only allowed a better understanding of the decline in deposition rate with increasing process pressure at 150W for PTFE. The trends of deposition rate against process pressure at lower RF had not been reported previously in the literature. The variation in deposition patterns of PTFE and NiTi at low power is explained for the first time in this study. It is also the first attempt to compare and contrast the deposition patterns of metal and polymer. Deposition rates against process conditions for NiTi were also not found in the literature; however, the findings matched well to those reported for aluminium and alumina because reactive metals have similar deposition mechanisms.

The RF deposition of alumina (Figure 66) resulted in somewhat linear trends of deposition rates against power and pressure whereas the shape of the DC sputtered NiTi trendline changes because of the variances in deposition rates of Ni and Ti. The amount of Ni and Ti deposition is influenced by changing process parameters, resulting in changes in overall deposition rates of NiTi (Figure 43). Ni and Ti have different properties such as density, threshold power and affinity for oxygen therefore

deposit at various rates. Combining the above-mentioned results with Wibowo et al. [27] findings allow better understanding of the NiTi deposition rate patterns with respect to power and pressure. They explained that titanium content in NiTi films increases with increasing DC sputtering power, at high process pressures (125 and 150 W trendlines shown in Figure 108 (green and blue trendlines respectively)). This is because of titanium's strong affinity for oxygen creates a thin layer of TiO_x on the surface of sputtering target. Sputtering of TiO_x requires higher energies than sputtering metallic Ti. Thus, at low powers part of the NiTi target is covered with meaning Ti is more likely to be sputtered than TiO_x, with a lower deposition rate at low power. The increase in sputtering power increases the energy of argon ions, which in turn increases the rate of sputtering TiO_x. As a result, higher titanium content is formed in the NiTi coatings.

This can be explained better by Figure 109, where low process pressures of 15×10^{-3} and 10×10^{-3} result in steeper increase in deposition rate against power, accounting for a rise in Ti deposition in comparison to the deposition of TiO_x at higher powers. This rise in deposition rate against power is even steeper at further lower process pressure of 5×10^{-3}, where Ti wins its deposition composition over TiO_x at 50W and higher powers. More TiO_x produces at low powers and high-pressure values. This behaviour follows classic reactive deposition behaviour. The target is practically poisoned by oxygen or water vapour; thus, the deposition rate is a balance between sputtering 'TiO_x and NiTi' (on areas not in the racetrack) which sputters at a slower rate, and sputtering of NiTi happened from the racetrack at a much higher rate. This leads to more oxygen in the films that are sputtered at lower power and higher pressure.

6.2.4 Summary

The following conclusions about the effect of process parameters on deposition rate of PTFE and NiTi can be deduced, after analysing the results presented in Figure 107 – Figure 110.

- The magnitudes of power and process pressure significantly affect the deposition rates of PTFE and NiTi, providing different deposition rates vs. power patterns at various process pressures. This also applies to the deposition rate vs. pressure trends at range of power values.
- It is established that higher deposition rates of PTFE can be achieved by maintaining low-pressure (5×10^{-3} mbar) and high power (150W). To obtain high deposition rates at lower power values, the process pressure needs to be increased. At 125W, the deposition rate is relatively independent of changing pressure, and at 15×10^{-3} mbar, the deposition rate does not change significantly by altering the power within the range of 75 to 150W.
- Higher deposition rate for NiTi can be attained by sputtering at high power and maintaining low pressures. At 25W, the deposition rate is approximately independent of the variance in pressure, and at 25×10^{-3} mbar, the deposition rates of NiTi become independent of changing power from 25 to 100 W.
- At any specified process pressure and power, the deposition rate of NiTi is higher than that of PTFE. This difference is greater at lower pressures but lesser at higher process pressures.
- The process parameters of power and pressure allow altering the deposition rate of PTFE and NiTi. The deposition rates can be used to calculate the layer thickness of deposited material content at a given time, which would permit controlling the volume fractions of PTFE and NiTi in the nanocomposite. This approach enables adjusting the nanocomposite composition; therefore, the properties of the nanocomposites are controlled by these process parameters.
- These deposition rates results are combined with later discussed characterisation results to choose the suitable deposition conditions to sputter of PTFE and NiTi for the fabrication of PTFE-NiTi nanocomposites (section 6.7).

6.3 Oxygen content in PVD sputtered NiTi

Titanium has high affinity to react with oxygen and forming titanium oxides, or to dissolve in the material clusters within NiTi thin films. The oxygen influences the film impurities, transformation temperatures, ductility, microstructure, the nucleation process and further growth of the NiTi [25; 68]. Excess oxygen in NiTi lattice acts as a preferential site for nucleation and metals can form grains around oxygen atoms within the structure, leading to concentration of stress with the coating among metal and polymer layers and could ultimately cause disbonding [68]. In the nanocomposite deposition condition settings, the presence of oxygen at interfaces of metal and polymer induces a depletion of oxygen near to the polymeric surface, leading to the formation of weak boundary layer, and reducing the adhesion between the layers. There are two primary sources of oxygen contamination during PVD sputtering process; the oxygen from the residual atmosphere and the oxygen trapped in substrate or target material.[68]

In the project, the sputtering system was pumped down to low base pressures in the range of 1×10^{-6} mbar, for avoiding the residual oxygen from the atmosphere contaminating the NiTi thin films. Additionally, the composition of NiTi target was confirmed before the sputtering run by EDX and no oxygen content was detected. Titanium compounds can contaminate themselves by an oxide layer on the surface of NiTi targets when left in the atmospheric environment. To avoid the deposition of oxygen trapped on the target surface, the NiTi was pre-sputtered for 15 minutes before each deposition run, without facing the target to the substrate. This would have removed any existing oxygen layer from the racetrack on the target surface. Thus, a pure NiTi deposition was expected. Further to the above steps, a titanium getter was also connected to the supply lines of the working gas to purify the gas coming into the system.

A significant amount of oxygen was detected in the PVD sputtered thin films of NiTi, despite taking the above steps. To investigate this further, the relationship between oxygen atomic percent in NiTi thin films with base and process pressures was analysed, as shown in Table 19 and Figure 113.

Table 19: Oxygen content (atomic %) within PVD sputtered NiTi deposited at 100W and range of process, along with base pressure for each deposition run.

Process pressure (x 10^{-3} mbar)	**Base pressure (mbar) x10^{-6}**	**Oxygen content (atomic %) within PVD sputtered NiTi**
25	1.78	18.5
	0.63	10.9
	1.52	17.2
	0.57	15.7
	8.00	53.4
	1.68	21.1
	1.65	31.3
20	4.62	51.7
	0.63	4.3
	0.97	10.9
	0.76	12.1
15	6.52	22.4
	1.99	8.7
	1.45	2.7
	1.46	2.1
10	1.70	2.3
	1.47	4.0
	0.55	0
	5.47	34.0
5	1.42	0
	0.82	8.5
	2.29	21.4
	7.38	4.0

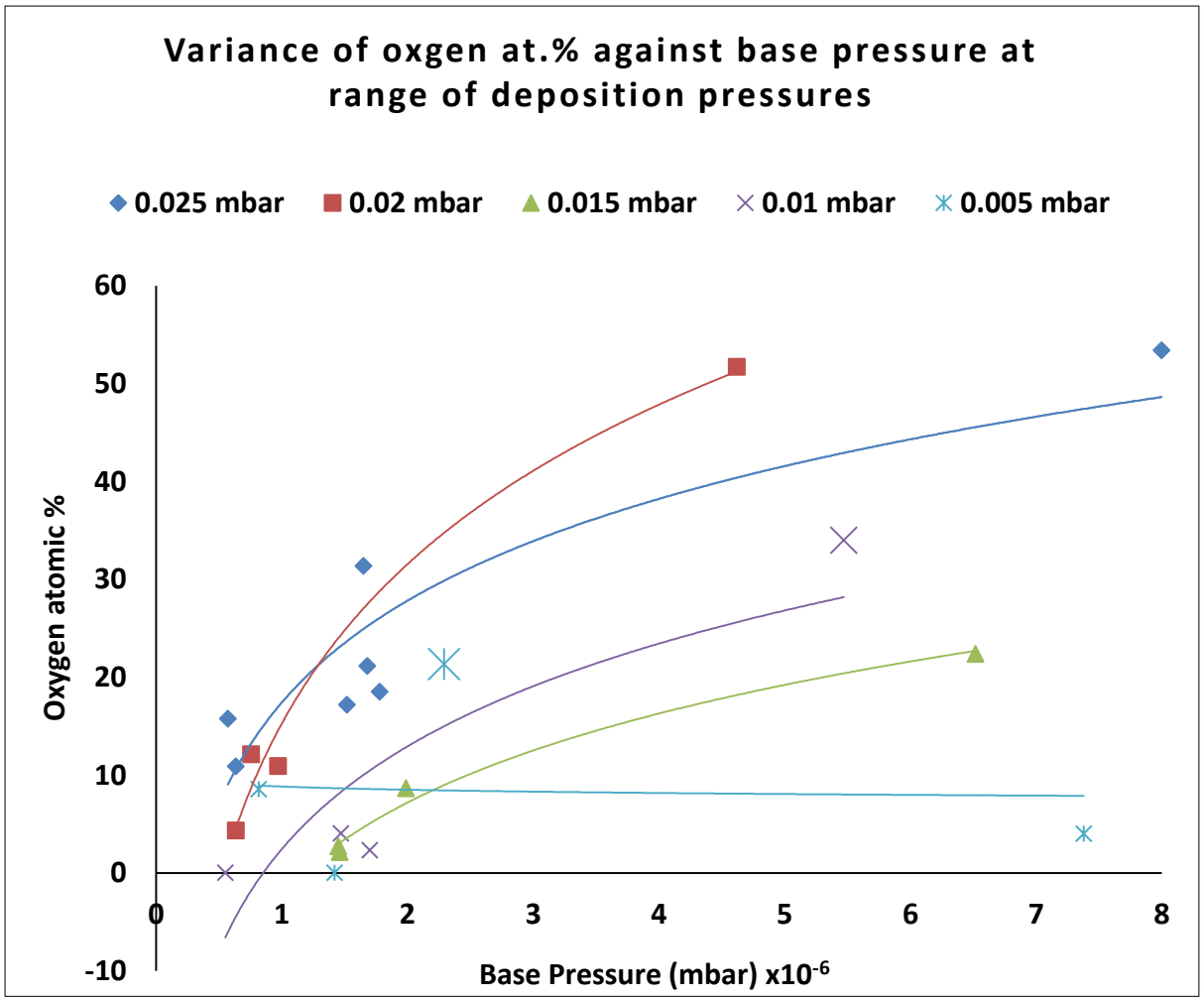

Figure 113: The atomic percent of oxygen in NiTi thin films against the base pressure at various process pressure parameters.

Figure 113 shows that the oxygen content in NiTi increased with increasing base pressure, at all process pressures ranging 10 x 10^{-3} – 25 x 10^{-3} mbar. This trend indicates the affinity of oxygen to titanium because even at low base pressures in the range of 10^{-6}, slight changes in the in the base pressures are very significant to the extent of oxygen reaction to NiTi within NiTi thin films. The combination of low base pressure and low process pressures results in low level of oxygen within the coating. The only two outliers to this trend where at process pressure of 10 x 10^{-3} mbar and base pressure of 5.47 x 10^{-6} mbar result in high oxygen content (34 at.%) and at process pressure of 5 x 10^{-3} mbar and base pressure of 2.29 x 10^{-6} mbar resulting in high oxygen content (21.4 at.%). These data points represent a slight leak in the system letting slight oxygen or water vapour remain within the pumped down sputtering chamber.

For pointedly low base pressures of 0.82 x 10^{-6} Pa and 1.42 x 10^{-6} Pa at 5 x 10^{-3} mbar, the oxygen content decreases to 0 and 8.55 at.%. Slight deviation from 0 to 8.55 % relates to the change in power, which decreased from 100 to 50 W, establishing that the deposition power has some effect on oxygen content of PVD sputtered NiTi thin films. This is related to the thermodynamics and kinetics of Ti sputtering from NiTi and titanium oxides formation. There is a direct relationship between the deposition power and rate of energy transfer. At low deposition pressures, the titanium and its oxides compete for deposition onto the substrate. The higher the deposition power, the higher the rate of energy transfer would be, and the greater the energy transfer during the sputtering process the faster atoms of titanium and the titanium oxides deposit onto the substrate. At low deposition powers, the rate of energy transfer declines, which is still sufficient for titanium sputtering from the racetrack but insufficient for titanium oxide sputtering and inhibit the titanium oxides to deposit onto the surface. This description can be further verified Wibowo et al. [27] study discussed in section 3.3.6 of the literature review, which compares the deposition of titanium and nickel content within the SMA, and reported that the titanium content in NiTi thin films increases with power because of titanium's strong affinity for oxygen that creates a thin layer of TiO_x on the surface of sputtering target. TiO_x sputtering requires higher energies than sputtering the metallic Ti. The increase in sputtering power also increases the energy of argon ions, which in turn increase the sputtering rate of titanium and TiO_x; as a result, higher titanium content is formed in the NiTi coatings. Therefore, increasing sputtering power can be used to incorporate more titanium in NiTi films, but this has significant implications for the coating properties such as residual stress.

The above explanations also aid to the further understanding of previously discussed results obtained from Figure 109 and Figure 110. The differences in trends presented in Figure 109 at various deposition pressures correspond to deposition of titanium oxides in the coatings at high process pressures and deposition of relatively pure NiTi at low process pressures. At process pressures of 5 x 10^{-3}, 10 x 10^{-3} and 15 x 10^{-3} mbar, the deposition of NiTi dominates over titanium oxides and nickel combination. Figure 110 also indicates that the sputtering rate of the pure titanium in the alloys forming at low process pressures higher than alloys containing titanium oxides being produced at higher process pressures.

To conclude the above discussion, it is recognised that relatively small magnitudes of base pressures, low process pressures and small values of deposition power are recommended to avoid the oxidation of NiTi thin films. Therefore, the above results highlight the best working parameters within the range of 5 x 10^{-3} to 10 x 10^{-3} mbar and DC power supply to 50W for future depositions of NiTi. The 50W power at 5 x 10^{-3} mbar provides a condition where NiTi with a lower oxygen content is deposited. Under this condition, the NiTi would deposit at 167 nm/h. At this pressure, the PTFE deposition rate would be 49 nm/h at 150W RF power.

6.4 Phase transformations of PVD sputtered NiTi thin films devised of various atomic compositions

As-sputtered NiTi thin films are amorphous, and DSC thermogram can observe no thermal events. To perceive phase transformations from NiTi thin films, the as-deposited coatings are subjected to heat treatment followed by annealing. The annealed NiTi SMA is crystalline and shows austenite to the martensite phase transformations during exothermic and endothermic DSC cycles. DSC thermograms are used to obtain enthalpy values associated with those phase changes. The information about transforming the crystal structures can also be obtained by XRD profiles. This section provides the results of the above experiments for a range of stoichiometric compositions of NiTi thin films. A comprehensive discussion is also provided to compare the results to the existing literature.

6.4.1 Post sputter heat treatment and phase transformations

NiTi coatings (1 μm × (3 × 6) mm^2) deposited on glass were removed and subjected to heat treatment followed by annealing. The annealed thin films were subjected to three heating and cooling cycles. DSC transformation data along with XRD profiles of the as-deposited and annealed thin films are reported in this section. A detailed description is provided below explaining the influence of atomic composition on transformation temperatures of NiTi thin films that were subjected to various heat treatment and annealing conditions.

The PVD sputtered NiTi thin films tends be approximately 2 – 5 at.% Ti deficient compared to their target material. This is because the deposition rate of Ti is different from Ni, and the extent of this difference depends on the process parameters and power supply used. Therefore, pure Ti pieces (1x1 mm^2) were placed on NiTi target's racetrack for preparing the equiatomic and Ti-rich thin films of NiTi (Table 16). Ni-rich thin films (SM/AO and SMA/A - Table 20) were prepared by sputtering from the target without addition of any additional meshes. For more Ni-rich NiTi thin film (sample SMA/DD - Table 21), two additional Ni pieces (1 x 1 mm^2) were added to the racetrack of NiTi target. This method required trial and error approach to obtain the desired compositions of NiTi.

Table 20: DSC heat treatment and annealing conditions for NiTi thin films devised for range of atomic compositions. The samples are subjected to heating and cooling cycles in the range of 20 – 400°C.

ID	At. Composition before heat treatment			Heat treatment		Annealing		At. Composition after heat treatment		
	Element %		NiTi ratio	hours	°C	hours	°C	Element %		NiTi ratio
SMA/E	Ni	46.6	47.3:52.7	1	1100	6	550	Ni	19.9	40:60
	Ti	52						Ti	28.3	
	O	1.1						O	50.8	
	N	0.3						N	1.7	
SMA/L	Ni	46.9	46.9:53.1	2.5	850	0.5	550	Ni	19.4	44:54
	Ti	53.1						Ti	22.4	
	O	0						O	58.2	
SMA/J1	Ni	49	50.1:49.9	1	1100	6	550	Ni	25.1	51:49
	Ti	48.8						Ti	24.4	
	O	2.1						O	50.5	
SMA/R1	Ni	45.3	46.4:53.6	1	1100	6	550	Ni	15.9	39:61
	Ti	52.4						Ti	25	
	O	2.3						O	59.1	
SMA/K	Ni	43.5	43.5:56.5	1	1100	6	550	Ni	18.3	40:60
	Ti	56.5						Ti	27.2	
	O	0						O	54.5	
SMA/O	Ni	47.2	51.6:48.4	2.5	850	0.5	550	Ni	23.6	61:39
	Ti	44.3						Ti	14.8	
	O	8.5						O	61.5	
SMA/AE	Ni	52.5	52.7:47.3	2.5	850	0.5	550	Ni	24.6	59:41
	Ti	47.1						Ti	17.3	
	O	0.4						O	58.1	

Sample SMA/E

A titanium-rich NiTi (sample SMA/E) was subjected to heat treatment at 1100°C for one hour followed by annealing at 550°C for 6 hours. The DSC chamber was purged followed by a low-pressure argon gas supply, before the heat treatment and annealing process. Three continuous heating and cooling cycles and visual observations reveal following results.

- An oxidation reaction was observed, as the sample changed from metallic grey to brown fluorescent substance, and it can be confirmed by EDS results. Oxygen was 2.7 % in the original sample, which increases to 51 % after the heat treatment.

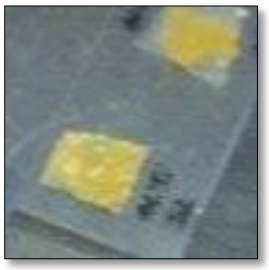

Figure 114: NiTi (sample SMA/E) changed from metallic grey to brown fluorescent substance after post sputter heat treatment at 1100°C for one hour followed by annealing at 550°C for 6 hours.

- No measurable transformation peaks were observed during heating cycles.
- EDX analysis would suggest that the titanium present in the film has oxidised forming titanium oxide, which can also seen by the formation of the fluorescent brown substance of TiO_2. Rutile TiO_2, anatase TiO_2 and the mixture of both rutile and anatase TiO_2 has been reported as fluorescent materials. However, rutile TiO_2 is known for scattering the light more competently.

Sample SMA/L

A higher heat treatment temperature (1100°C) might be resulting in additional reactions forming impurities such as precipitates, GP zones, and greater affinity to form oxides and nitrides. All those factors count towards a decreased NiTi content in the heat-treated film. Accumulation of precipitates at grain boundaries restricts the transformations as well. Although GP zones are a direct result of Ti-rich composition; however, higher temperature may contribute more K.E participating towards faster reactions and readily available activation energy enhancing the affinity for those side reactions.

The heat treatment temperature was reduced to evade any side reactions from taking place and in an attempt to prevent oxidation. A titanium-rich NiTi (sample SMA/L) was heat-treated at 800°C for one hour followed by annealing at 550°C for 6 hours. The selected heat treatment temperature is not far different from the heat treatment temperature (750°C) chosen in various literature studies, which reported successful NiTi thin films transformations (Table 8).

The DSC chamber was purged, and a low-pressure argon gas supply was associated with the chamber throughout the heat treatment and annealing process.

- Similar oxidation results were obtained as sample SMA/E. EDX analysis confirms significant oxidation of titanium, which forms TiO_2.
- No transformation peaks were observed during heating cycles as shown in Figure 115.

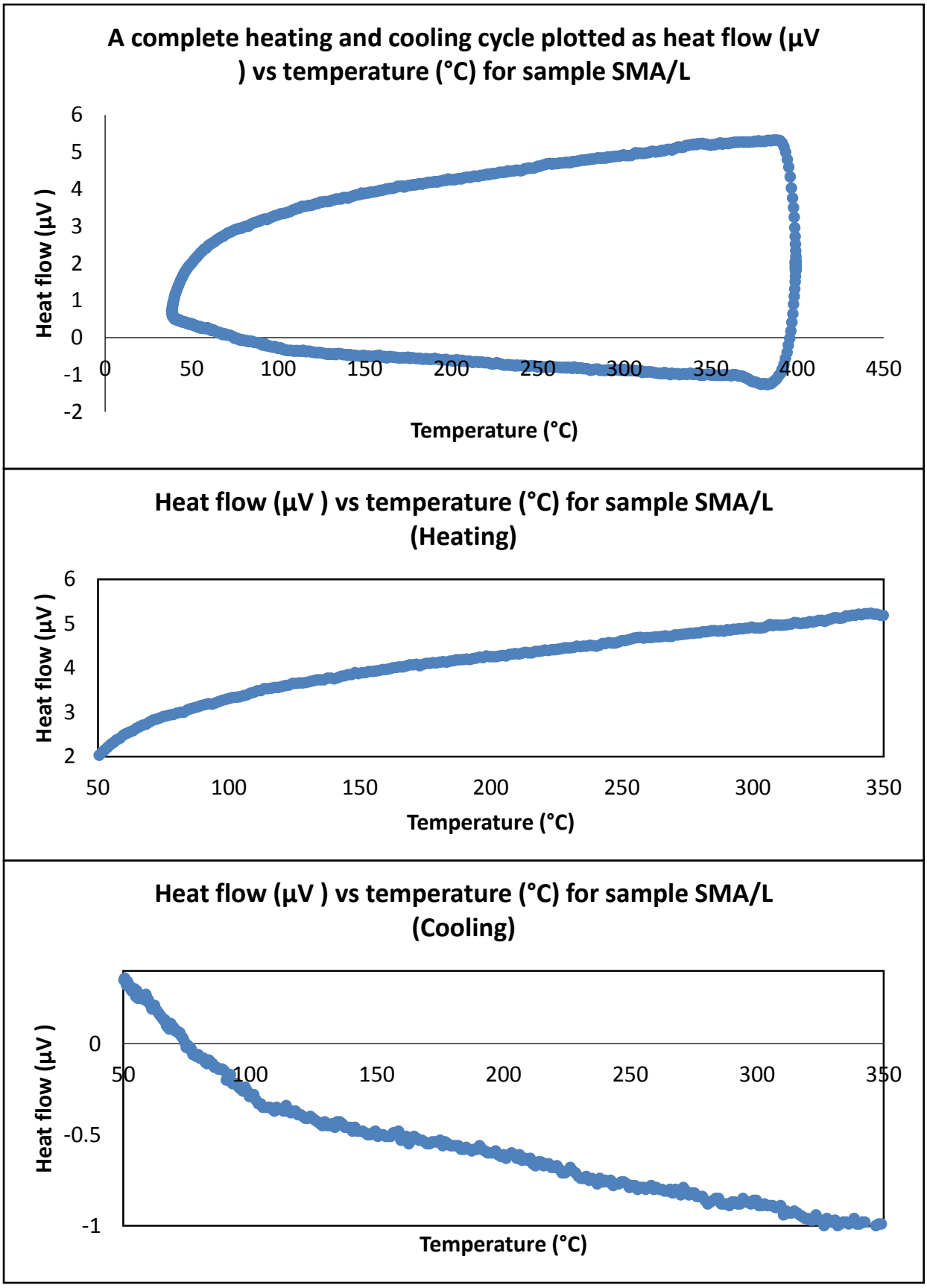

Figure 115: Heat flow (µVs/mg) vs. temperature (°C) for sample L.

Modification of the procedure of purging the DSC chamber and pumping the carrier gas

Table 20 shows that the NiTi thin films have very minute oxygen content, which increased to < 50 % during heat treatment and annealing, for the sample SMA/E and SMA/L. The samples turned colour from metallic grey to fluorescent brown. Reducing the heat treatment temperature did not inhibit the oxidation reaction. Moist in carrier gas line could be a potential reason for oxidation during heat treatment. Following steps were undertaken before starting the heat treatment to minimise the oxidation possibility.

For heat treatment of samples SMAJ1, SMAR1 and SMAK, the DSC chamber was pumped down to low base pressure followed by purging Ar at low pressure. Once the argon pressure was maintained, the argon supply was disconnected. The chamber was heated from room temperature to 1100°C at 30 °C/min, followed by maintaining the temperature at 1100°C for 1 hour. After an hour, the temperature was reduced to 500°C at 30 °C/min, and the sample was annealed at 500°C for 6 hours.

Sample SMA/J1 - equiatomic

An equiatomic sample J was subjected to 3 heating and cooling cycles in the range of 30 – 400 °C, after heat treatment and annealing. Following observations and results were obtained for sample SMA/J1.

- Martensite and austenite transformations were observed for all three cycles. The heating peaks were observed at approximately 242 °C (+/- 2) while the cooling peaks were produced at 175 °C (+/-9).
- The sample had changed colour from metallic grey to silver grey after the heat treatment. Elemental analysis still revealed more than 50 % oxygen content at the end of the three cycles the silver grey colour would suggest less, but still significant surface oxidation.

Figure 116: NiTi (sample SMA/J1) changed from metallic grey to brown fluorescent substance after post sputter heat treatment at 800°C for one hour followed by annealing at 550°C for 6 hours.

The sample maintained a grey-colour after experiencing the modified heat treatment procedure, and resulted in martensite and austenite transformation values in DSC cycle. Thus, there was a successful NiTi reaction in the sample structure. Any oxygen and / or moist presence in the chamber would have dissolved into the surface particles of the sample resulting in high oxygen content according to EDS results provided in Table 20. Comparing the above observations to the scientific description provided in Figure 62 explain further about the chemical composition of NiTi thin films. Figure 62 shows that Ti favours the formation of TiO_x (x = 2, 3) compounds on the film surface and just underneath the surface while some Ni may remain unreacted on the surface. Similar phenomena are experimented here, NiTi SMA thin films are covered by oxide layers along with atomic Ni, and the films additionally dissolve oxygen on the surface. The crystals of NiTi SMA successfully form under the oxidised surface. For this reason, successful transformations were experienced in the DSC cycle. Ni, Ti and O in the composition of SMA/J1 films with TiO_x (x = 2) compounds can be clearly seen in Table 20 after the heat treatment. TiO_2 forms along with NiTi SMA Formation when x = 2 while $NiTiO_3$ is most likely produced when x = 3.

Sample SMA/R1 and sample SMA/K – titanium-rich

Two NiTi samples having 53.6 at.% Ti (sample SMA/R1) and 56.5 at.% Ti (sample K) were tested by DSC heating and cooling cycles in the range of 30 – 400 °C after the heat treatment and annealing, and following results were recorded.

- On increasing the Ti content from 50 at.% (sample SMA/J) to 53 at.% (sample SMA/R1), the heating peak shifts further on the scale to 260 °C (+/- 3), while the cooling peak was too small.
- For Ti content 56.5 at.% (sample SMA/K), the heating peak appears at 249.6 °C (+/- 3), and the cooling peak appeared at 179 °C (+/-10).
- According to EDX samples both samples still oxidised at the end of the test (Table 20).

Sample SMA/O and SMA/AE1– nickel-rich

NiTi thin films samples having higher nickel content were also subjected to DSC heating and cooling cycles, after heat treatment and annealing, and following results were obtained.

- On increasing the Ni content from 50 at.% (sample SMAJ) to 52 at.% (sample SMA/O), the heating peak appears at 250°C (+/-3) while the cooling peak was recorded at 175°C. Further increase of nickel content shifts the peak to 203.1°C. The general trend is that the decrease in Ti content and an increase in Ni within SMA result in transformations at relatively lower temperatures.
- To avoid the excess heat leading to side reactions, the heat treatment temperature was reduced from 1100 °C to 850 °C. The NiTi transformation was still possible, as shown in Figure 117, which led to the decision that heat treatment at 850°C for 2.5 hours is sufficient for further experiments. Sanjabi et al. [23] also subjected the equiatomic NiTi thin films prepared by PVD sputtering, to 600°C at a constant rate of 10°C/min in DSC settings, and reported 500°C to be enough temperature for annealing of NiTi. This is because the standard crystallisation temperatures for NiTi is 472°C (Figure 44), associated with an enthalpy change of 28J/g.

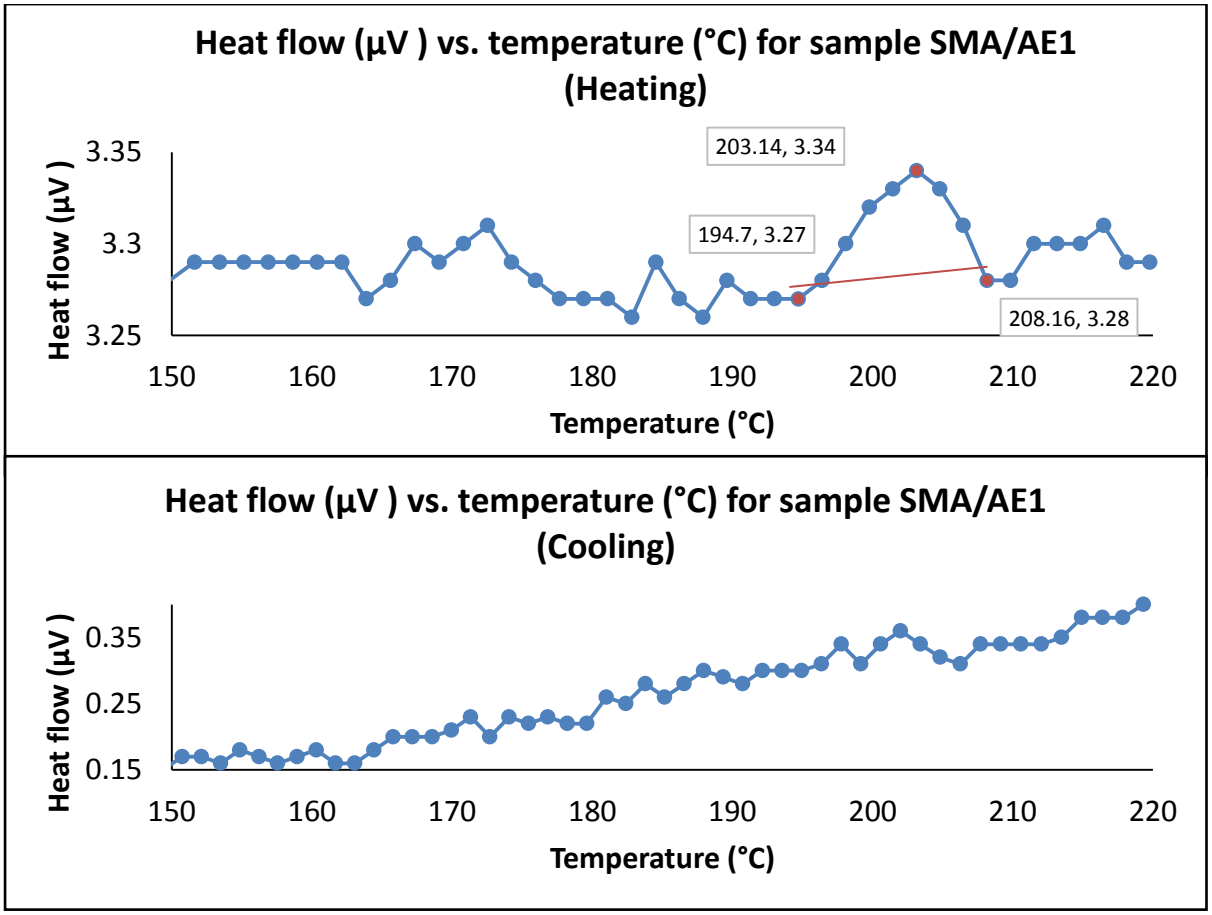

Figure 117: Heat flow (µVs/mg) vs. temperature (°C) for sample SMA/AE.

The heating and cooling transformation temperatures are plotted against the composition (Figure 119) to obtain the trends from the above results after conducting more experiments at different range of heating and cooling cycles. In the above experiments, three heating and cooling cycles were carried out to observe the transformations. The results were consistent showing similar amount of material undergoing the transformation each time disregarding the possibility of excess oxidation.

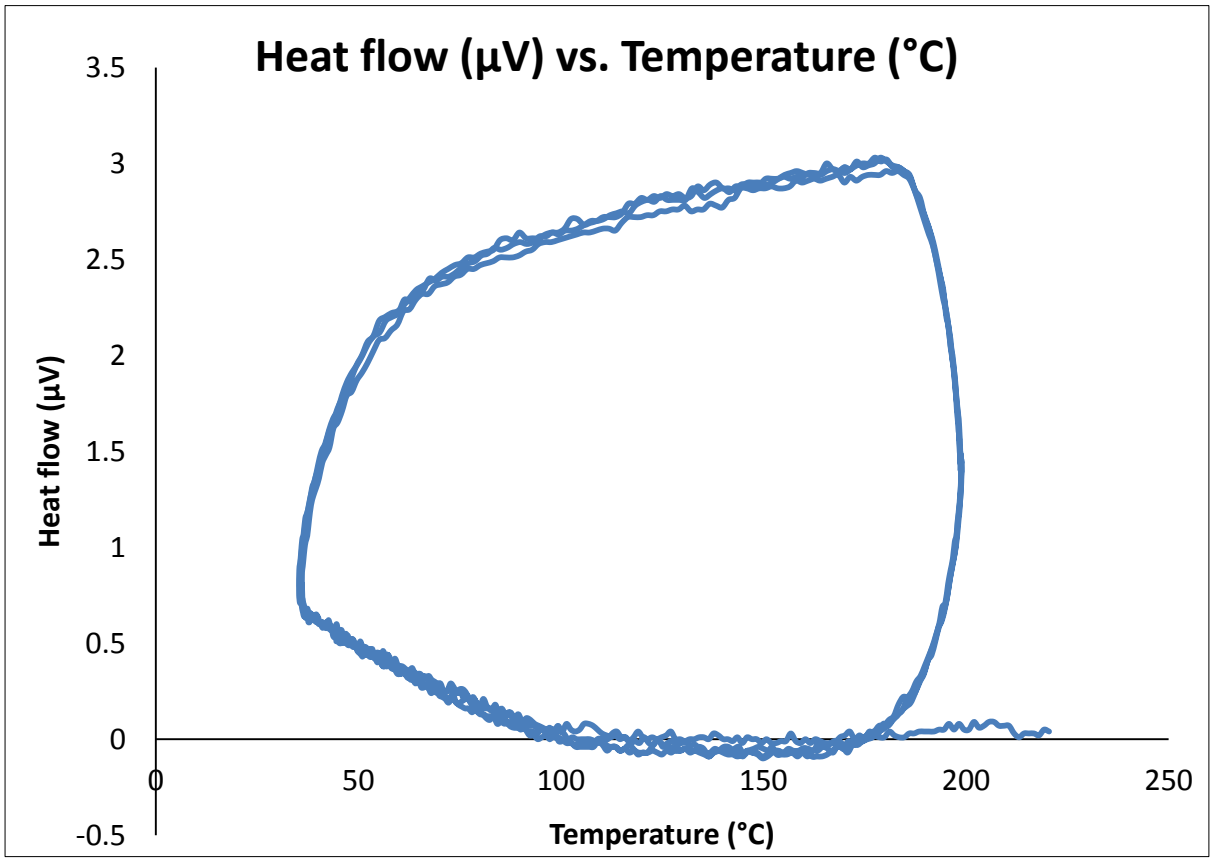

Figure 118: Three heating and cooling cycles showing heat flow (µVs/mg) vs. temperature (°C) for sample SMA/E.

Phase transformations during heating and cooling cycles operating in lower temperature range of -60 to 260°C

This project intends to take an advantage of pseudoelastic characteristics of NiTi alloy. The alloy exhibits pseudoelasticity at body temperature when its austenite finish is below the body temperature. The above transformations occur well above the required range of temperatures. The literature reports NiTi transformations can occur below the body temperatures. To investigate the lower transformations range of the NiTi samples listed in Table 16, the samples were subjected to DSC heating and cooling cycles at a lower temperature range of - 60 – 260 °C using a different DSC software named as TA universal analysis (Table 21). These are the same film materials as those previously discussed. The only difference is that these samples have been subjected to the heating and cooling cycles of a different temperature ranges, i.e. SMA/J1 and SMA/J2 are the samples from same thin film material, which are subjected to DSC heating and cooling cycles of different temperature ranges (20 to 400°C and -60 to 260°C respectively).

All NiTi samples recorded in Table 21 were also oxidised on the surface; however, the successful phase transformations in all of those samples suggest formation of NiTi-SMA crystals within the films structure and therefore much less oxidation effects. The transformation data and enthalpy values for exothermic and endothermic DSC cycles for NiTi are recorded in Table 22, where the NiTi compositions are same as those mentioned previously in Table 20 and Table 21. All NiTi samples were subjected to three heating and cooling cycles, and thermal events for every cycle were recorded. Those thermal events include austenite start (As), austenite finish (Af), martensitic start (Ms), martensitic finish (Mf) temperatures, austenitic transformation peak (Ap) and martensitic transformation peak (Ms) along with exothermic and endothermic enthalpies, as shown in Table 22. The transformation temperatures were used to calculate the enthalpy values by line transaction method. The transformation values have an accuracy of 0.5°C calculated from three heating and cooling cycles of various samples.

Table 21: The atomic compositions of NiTi thin films before and after heat treatment. All samples were DSC heat treated at 850°C for 2.5 hours and annealed at 550°C for 0.5-hour. The samples were then subject to heating and cooling cycles in the range of -60 to 260°C.

ID	At. Compositions before heat treatment			At. Compositions after heat treatment		
	Element	%	NiTi ratio	Element	%	NiTi ratio
SMA/J2	Ni	49	50.1:49.9	Ni	35.4	58.6:41.4
	Ti	48.8		Ti	24.9	
	O	2.1		O	39.6	
SMA/R2	Ni	45.3	46.4:53.6	Ni	19.5	34.9:65.1
	Ti	52.4		Ti	36.5	
	O	2.3		O	43.9	
SMA/AE2	Ni	52.5	52.7:47.3	Ni	25.2	64.5:35.5
	Ti	47.1		Ti	13.9	
	O	0.4		O	60.9	
SMA/DD	Ni	53.5	53.5:46.5	Ni	28.9	54.7:45.3
	Ti	46.5		Ti	23.9	
	O	0		O	47.2	

Table 22: Transformation peaks data and enthalpy values for exothermic and endothermic DSC cycles of NiTi at various compositions.

ID	Ni:Ti ratio	Heating (endothermic)				Cooling (exothermic)			
		As (°C)	Af (°C)	Ap (°C)	Enthalpy (J/g)	Ms (°C)	Mf (°C)	Mp (°C)	Enthalpy (J/g)
SMA/J1	50.1:49.9	221	260.1	242.8	15.5	212.1	167.1	182.2	-27.4
SMA/R1	46.4:53.6	234.3	253.6	249.6	11.9	213.7	147.5	177.9	-43.25
SMA/K	43.5:56.5	253.3	265.4	259.4	10.3	Too small cooling peak to measure			
SMA/O	52:48:00	242.5	289.3	259	40.8	225.5	178.4	194.2	-17.3
SMA/AE1	52.7:47.3	194.7	208.3	203.1	13.8	Too small cooling peak to measure			
SMA/J2	50.1:49.9	64.78	67.51	65.3	2.2	Too small cooling peak to measure			
SMA/R2	46.4:53.6	119	132.5	126.3	9.3	104	85	93.4	-8.4
SMA/AE2	52.7:47.3	32.1	38.65	35.2	8.6	-10.2	-40.2	-25.3	-16.8
SMA/DD	53.5:46.5	-32.5	-5.58	-19.24	1.6	Not found in the selected temperature range			

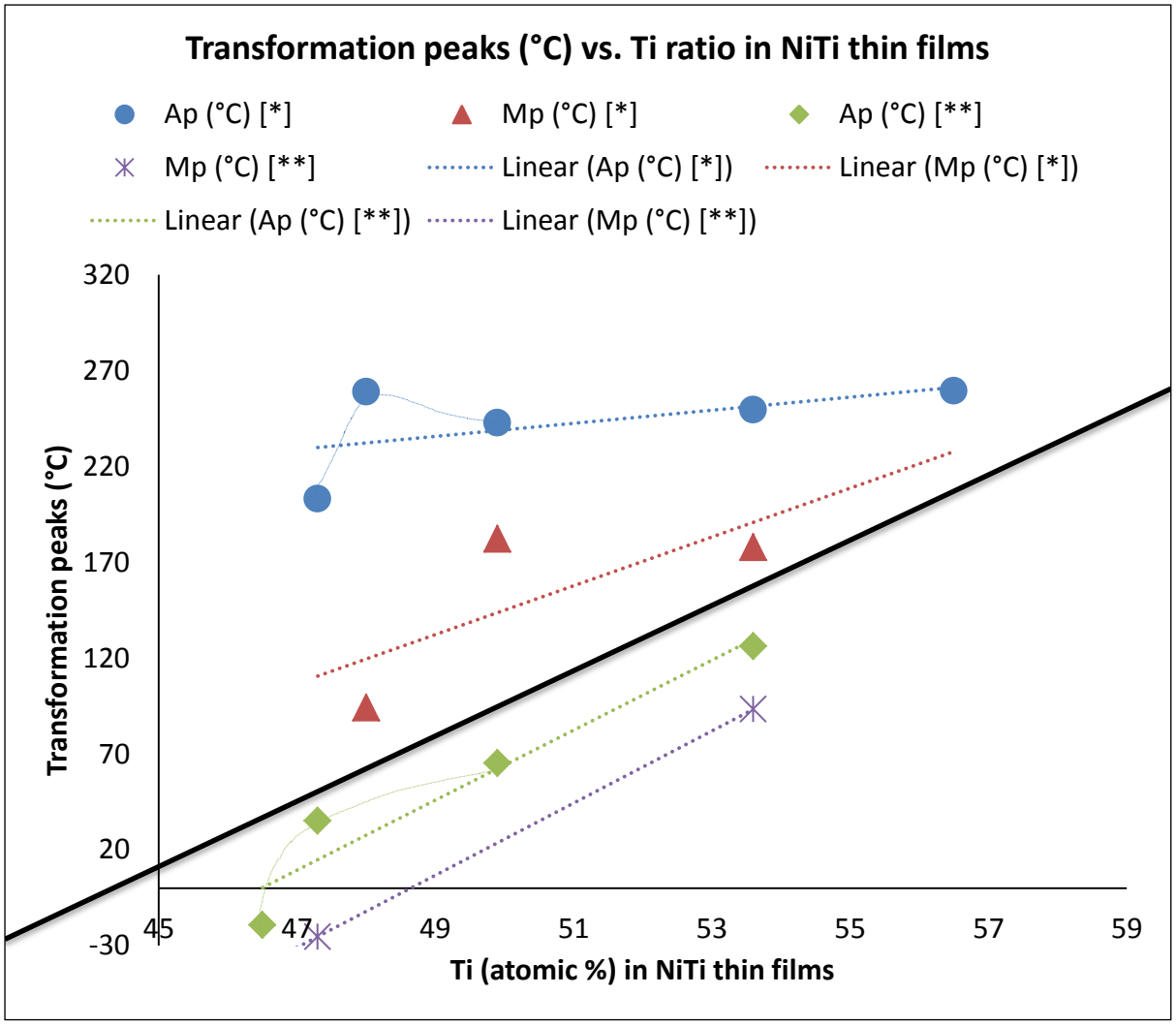

*Figure 119: NiTi phase transformation peaks vs. Ti ratio in NiTi thin films during heating and cooling cycles. (The data points marked with * in the legends relate to the NiTi samples subjected to heating and cooling cycles in the range of 20 – 400°C and the data points marked with ** in the legends relate to the NiTi samples subjected to heating and cooling cycles in the range of -60 – 260°C.*

Figure 119 elaborates a direct correlation between NiTi stoichiometric ratio and the transformation temperatures. As the Ti content in the SMA increases, the transformation temperatures also increase, which match to the previously discussed trend by Sanjabi et al. [23]. An additional attention-grabbing observation of the current study is that the NiTi SMA undergoes multiple phase transformations, and for the reason more than one hysteresis may be acquired. Equiatomic $Ni_{50.1}$:$Ti_{49.9}$ (Sample SMA/J2) produces its endothermic and exothermic transformations peaks at 242.8°C (Ap) and 182.2°C (Mp) respectively when observed for heating and

cooling cycles in the range of 20 – 400°C. To investigate the occurrence of transformations at lower temperature, the equiatomic SMA was subjected to a lower range of heating and cooling cycle at -60 – 260°C, which also resulted in successful phase transformation at 65.3°C (Ap). The similar outcome was acquired by the titanium-rich (SMA/R) and nickel-rich samples (SMA/AE) of NiTi. $Ni_{52.7}Ti_{47.3}$ (sample SMA/AE) produces endothermic austenite peak (Ap) at 35.2°C, which is slightly lower than the body temperature, ensuring the pseudoelasticity at body temperature. Ap is desired to be well below 37°C to ensure all NiTi crystals transforming and displaying pseudoelasticity at body temperature. 35°C is near to body temperature, so the Ni content in SMA was increased producing sample SMA/DD having stoichiometry of $Ni_{53.5}Ti_{46.5}$. Sample DD is more Ni-rich and lowers the Ap to -19.24°C, as shown in Figure 120. For that reason, $Ni_{53.5}Ti_{46.5}$ (sample SMA/DD) is selected for smart PTFE-NiTi nanocomposite.

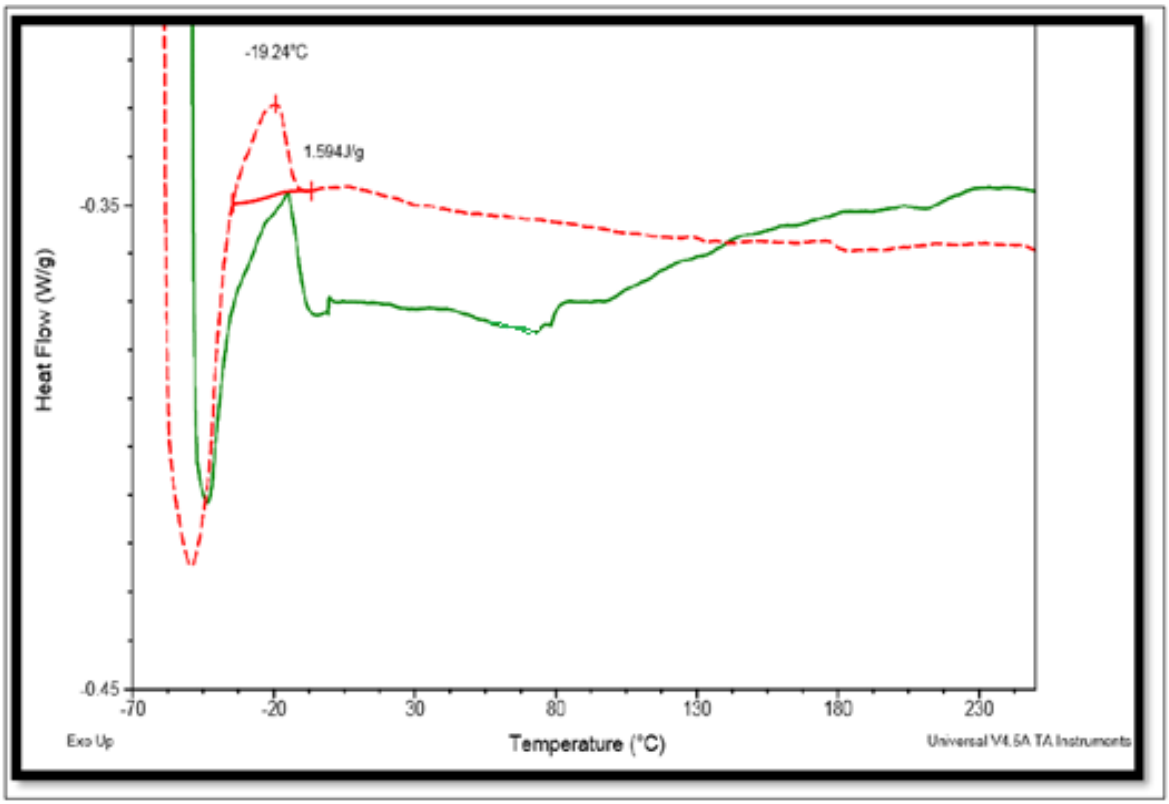

Figure 120: DSC heating cycles showing heat flow (W/g) versus temperature (°C) for sample SMA/DD.

The transformation temperatures observed during lower temperature range of heating and cooling cycle (-60 – 260°C) are more sensitive to NiTi composition, compared to heating and cooling cycle ranging 20 – 400 °C, resulting in steeper trends for the lower range cycles. Figure 119 shows that slight changes in NiTi atomic composition varies the transformation temperature largely. This shift of transformation temperatures against NiTi composition is swifter for the Ni-rich samples. For example, 0.7 at.% difference in Ni-rich NiTi samples O and AE1 lead to the variation in Ap by 56°C. An increase in Ni content by 0.8 at.% from sample SMA/AE to sample SMA/DD also lowers the Ap by 54.4°C. Sanjabi et al. [23] reported the same while affirming that only 1 at.% variation of composition can cause 100°C shift in transformation temperature. Excess of nickel content decreases the transformation temperatures significantly by about 25°C per 0.2 at.% Ni increase below room temperature [27; 107].

The phase transformations during the high-temperature heating and cooling cycle (20 – 400°C) result in higher enthalpy values and wider hysteresis compared to those at heating and cooling cycle ranging from -60 to 260°C. The higher enthalpy and the wider hysteresis indicate greater amount of SMA undergoing the phase changes. Most of the other studies conducted on PVD sputtered NiTi thin films investigated the phase changes in lower temperature range during heating and cooling cycles as summarised in Table 8. The enthalpy values reported by those studies are similar to the samples subjected to heating and cooling cycle of -60 to 260°C in this study. Therefore, this research reports the possibility to achieve much higher enthalpies at high-temperature transformations, where more material undergoes a phase change generating greater force for pseudoelastic applications.

The line that separates two data sets in Figure 119 shows that NiTi has been transformed within upper and lower range of temperature at specific NiTi compositions. This phenomenon of multiple transformations is not discussed previously in the literature. Most of the previous studies have conducted the experiments in the lower range (according to Figure 119) of heating and cooling cycles and found similar results, as shown in Figure 56.

.

In these experiments, relating to DSC heating and cooling cycles conducted at lower temperature range, the transformations occurred consuming less material in the subsequent cycles after the first one (Figure 121). The results were consistent for all the samples reported in Table 21, and the lower amount of material undergoes the transformation in second and third cycles compared to the first one, which indicates the influence of oxygen. Formation pf TiO_2 and $NiTiO_3$ reduces the amount of NiTi SMA producing and undergoing the transformation.

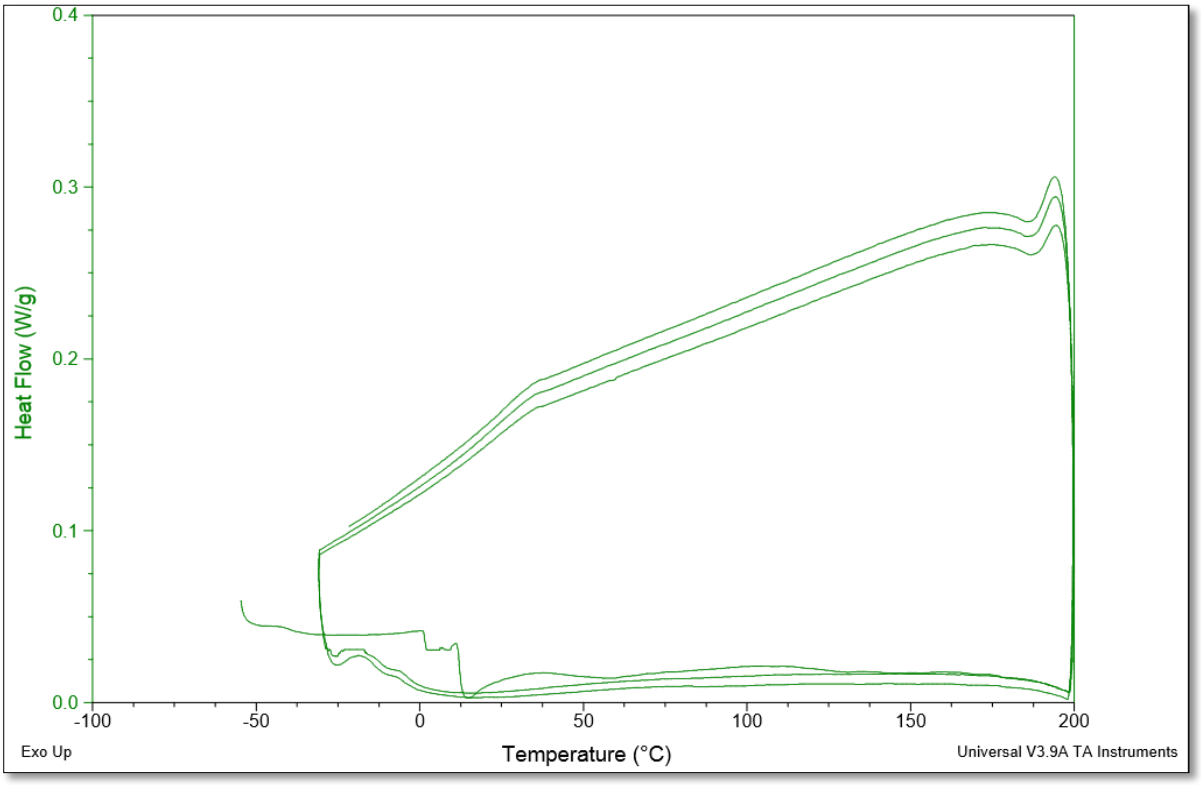

Figure 121: Three heating and cooling cycles showing heat flow (W/g) vs. temperature (°C).

6.4.2 XRD analysis for PVD-NiTi

An XRD study was conducted to identify the crystal structures associated with the phase transformations of NiTi in thin films. The XRD profile of as-deposited NiTi thin films (Figure 122) has a limited number of crystalline peaks suggesting an overall amorphous structure with some {200} nuclei. This also indicates the reason of no thermal events appearing during the heating and cooling cycles in DSC thermogram. However, the presence of some crystallinity in the as-deposited thin film is evident within an overall amorphous structure because the XRD profile shapes up in the form of a broad peak positioned at 2Θ = 42.7°, which is typical for B2 NiTi crystals {110} in austenite phase.

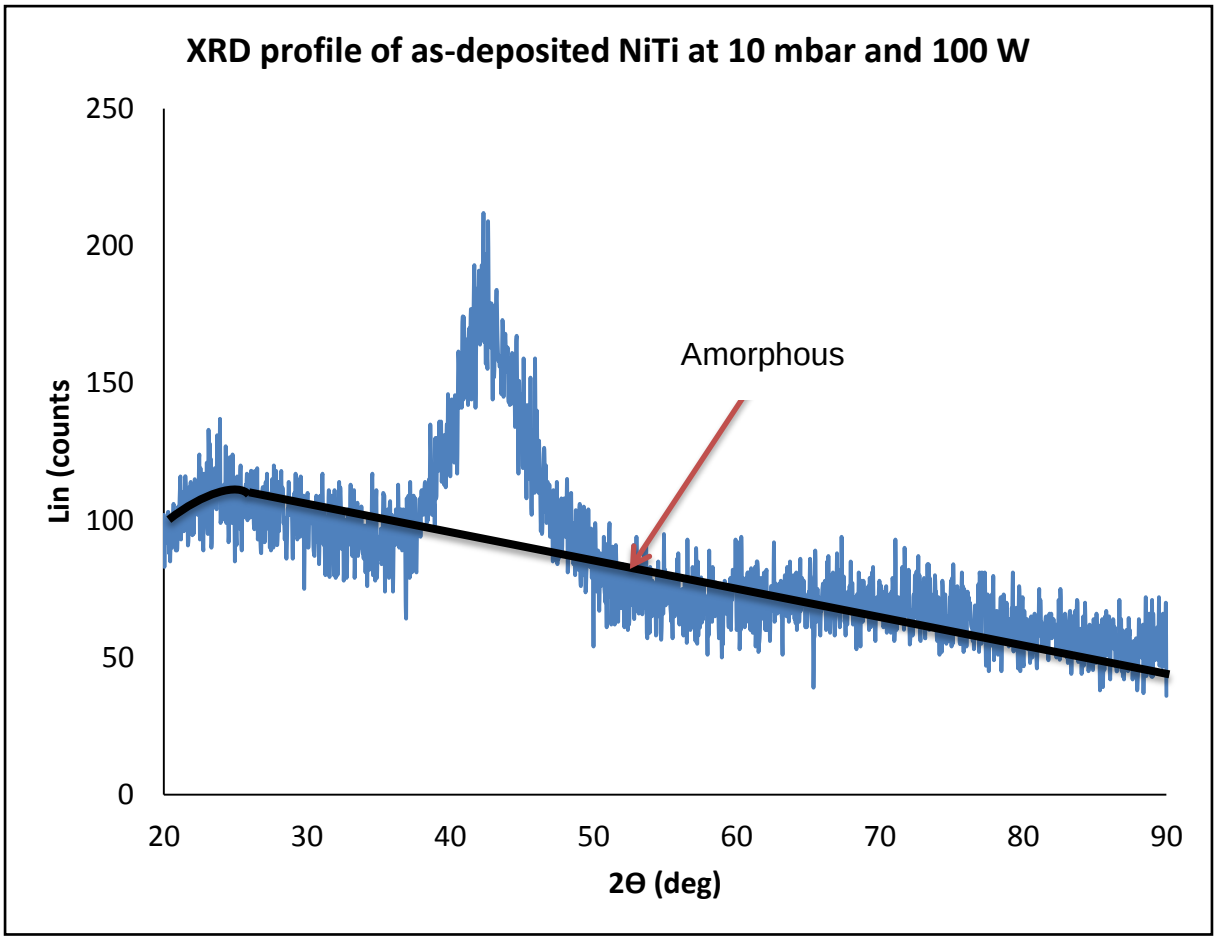

Figure 122: XRD profile of as-deposited NiTi at 10 x 10-3 mbar and 100W.

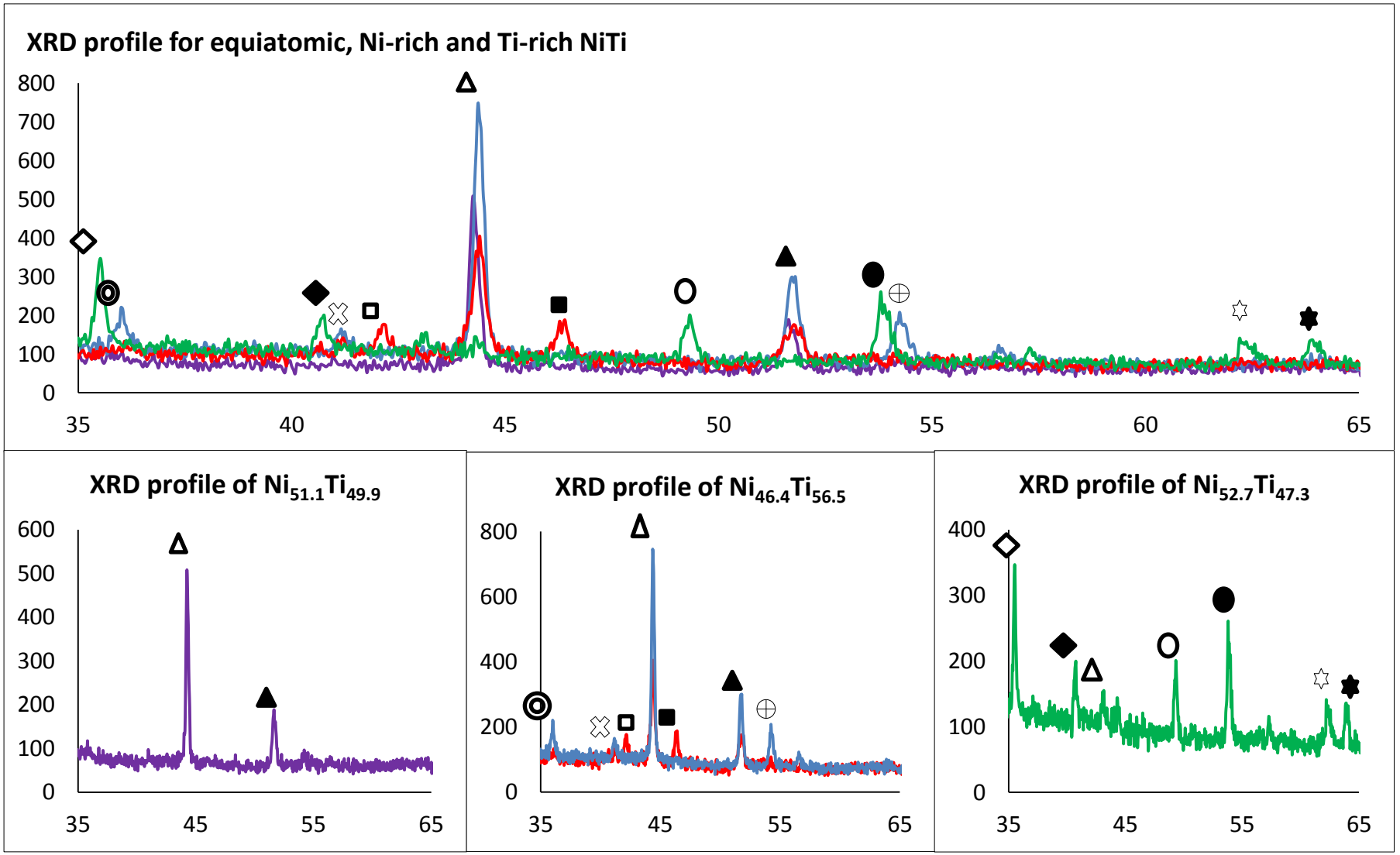

Figure 123: XRD profiles for equiatomic, Ni-rich and Ti-rich PVD-NiTi thin films.

Table 23: XRD profiles key for equiatomic, Ni-rich and Ti-rich PVD-NiTi thin films.

Mark	Peak Identity	Plane	Reference	Mark	Peak Identity	Reference
△	NiTi B19’	20	[103]	◇ ◆ ○ ●	Ni	[23; 60; 214; 215]
▲	NiTi B19’	-112	[103]	✡ ✸	Ni_3Ti	
✖	NiTi B19’	2	[103]		Ni_3Ti_2	
◎	Ti	2	[214]		Ni_4Ti_3	
▭	Ni Ti_2	115	[214]			
■	Ni Ti_2	440	[23]	⊕	$NiTiO_3$	

As-deposited NiTi films were aged an annealed to introduce further crystallinity as previously discussed in section 6.4.1. Figure 123 shows the XRD profiles for equiatomic, Ni-rich and Ti-rich samples of crystalline NiTi, formed after aging and annealing by post sputter heat treatment. XRD results demonstrate a single phase with no second phase precipitation in near-equiatomic NiTi, but further precipitation is observed in Ni-rich and Ti-rich films. An XRD profile of near-equiatomic NiTi (SMA/J) in Figure 123 reveals a martensitic crystal structure having no second phase precipitation. Two sharp peaks appearing at 2Θ = 44 and 2Θ = 52 represent B19’ crystals having {020} and {-112} planes respectively.

2 XRD profiles representing Ti-rich $Ni_{46.4}Ti_{53.6}$ in Figure 123 were heat treated at different temperatures (1100 and 800 °C). Both XRD profiles of Ti-rich $Ni_{46.4}Ti_{53.6}$ resemble to XRD profile of near equiatomic NiTi containing two sharp martensitic (B19’) peaks at 2Θ = 44° {020} and 2Θ = 52° {-112} respectively. However, some second phase precipitation of $NiTi_2$ is also observed in both Ti-rich XRD profiles. High Ti content films nucleate and grow the $NiTi_2$ precipitates along the grain boundaries of NiTi crystals. The XRD profile of Ti-rich $Ni_{46.4}Ti_{53.6}$ sample heat-treated at 850°C have peaks at 2Θ = 41.4° {511} and 2Θ = 46° {440} respectively. Heat treatment at 1100°C disperse and dissolve those $NiTi_2$ precipitates, and more peaks appear at 2Θ = 37° {002} and 2Θ = 41° {-111} representing Ti and martensitic NiTi respectively. An additional peak is observed at 2Θ = 54°. No information to define this peak was found in literature and databases. XRD peaks related to excess

titanium forming TiO_2 have either an anatase or a rutile phase, and often disappear within the background noise of the XRD profile. The peak detected at 2Θ = 54° may also belong to titanium oxide that appeared due to change in a stoichiometric ratio and the reaction between titanium and oxygen, when heat-treated at 1100°C. Ti peak at 2Θ = 37° seems to be attributable to the presence of excess Ti, which dissolves the residual oxygen from the film surface without a chemical reaction to form a TiOx phase. Alongside, high Ti content, those films nucleate and grow the Ti_2Ni precipitated crystals along the grain boundaries of austenite crystals of NiTi. Heat treatment at 1100°C leads to more material undergoing phase transformations, as indicated by higher and sharp peaks in the XRD profiles. The content of material transformation for Ti-rich NiTi heat-treated at 1100°C is comparable to near-equiatomic NiTi.

It is essential to take the titanium's reaction affinity to oxygen into account when considering the NiTi stoichiometric ratio. Some titanium content preferentially reacts with oxygen and form TiO_x (x = 1,2), which changes the original stoichiometric ratio of Ni and Ti forming the SMA. The stoichiometric ratio also changes when small amount of Ti is used up on the thin film surface to dissolve the residual oxygen without reacting chemically. The changes in SMA stoichiometry lead to changes in transformation temperatures and the amount of material undergoing the phase transformation. For example, 2.3 at.% oxygen was detected in the surface composition of $Ni_{46.4}Ti_{53.6}$ thin films. Thus, the material's stoichiometry on the film surface would be $Ni_{46.4}Ti_{51.3}TiO$ and $Ni_{46.4}Ti_{52.45}TiO_2$ in the events of TiO and TiO_2 formation respectively. Comparison of the XRD profiles of $Ni_{46.4}Ti_{53.6}$ and equiatomic NiTi (both heat-treated at 1100°C) provide further evidence of the above discussion, as there are similar peak heights representing the same martensitic planes of NiTi. This indicates similar crystallographic arrangement and the same amount of material undergoing the phase transformation despite the difference in NiTi stoichiometry. However, Ti-rich NiTi exhibits lower enthalpy values during exothermic and endothermic cycles in comparison to equiatomic NiTi as shown in Table 22. The explanation of lower enthalpy values for the Ti-rich thin films is the assembling of Ti_2Ni precipitates at columnar-grain interface of NiTi lattice and GP zones formation, hindering phase transformations.

The XRD profile of Ni-rich NiTi appears to have various other phases that may form compared to equiatomic and Ti-rich NiTi films. The concentration of atomic Ni and Ni-rich precipitates (including Ni_3Ti, Ni_3Ti_2 and Ni_4Ti_3) is pointedly high in the SMA structure. These precipitates form at the crystal boundaries deforming the NiTi martensitic lattices and resist the phase transformations. This is also evident by small enthalpy value of $Ni_{52.7}Ti_{47.3}$ (sample SMA/DD) reported in Table 22. The phase transformation temperature and the amount of material transforming for the Ni-rich samples is much more dependent on the composition, compared to the Ti-rich and equiatomic NiTi samples, and alter the enthalpy values significantly with minute changes in the stoichiometry of the SMA. The evidences of this subtlety are small XRD peaks along with pointedly low enthalpy values (Table 22) of Ni-rich $Ni_{52.7}Ti_{47.3}$ (sample SMA/DD), and this is also described in the discussion related to Table 22.

The XRD profile of Ti-rich NiTi contains $NiTiO_3$ peak, which forms as a natural blend of TiO_2 and NiO. The EDS results of heat-treated NiTi provided previously in Table 20 and Table 21 show that the approximate stoichiometry of Ni, Ti and oxygen contains 25 at.% Ti, 25 at.% Ni and 50 at.%. This stoichiometry shows the production of NiO and TiO_2, NiO and TiO_2 cannot co-exist due to the restrictions of thermodynamic stability; therefore, a naturally favourable reaction takes place between the respective oxides of Ni and Ti react to produce a naturally blended compound of $NiTiO_3$. $NiTiO_3$ is mostly generated on the top surface of NiTi films and therefore this compound is detected primarily by EDS.

6.4.3 Summary

The atomic composition is the most important factor affecting the phase transformations and crystal structures of PVD-NiTi thin films. The following conclusions can be drawn from processing and analysing the results presented in Figure 115 - Figure 123 and in Table 16 to Table 22, in accordance with the literature review.

- Heat treatment and annealing are essential for PVD sputtered NiTi thin films because the as-sputtered NiTi is mostly amorphous. A small single peak corresponding to {110} of B2 NiTi is observed the absence of any other second phase transformations. The heat treatment and annealing temperature significantly influence the phase transformations and the associated enthalpies.
- The desired atomic compositions of NiTi thin films were achieved by the addition of small Ni or Ti pieces on the racetrack of the target, and a trial and error approach was used. To prepare equiatomic thin films, additional Ti pieces were added because the sputtered thin films were Ti deficient in comparison to their equiatomic target materials.
- Excess oxidation within the SMA during the heat treatment result in the absence of any phase changes. The procedure of thermal treatment within the DSC chamber was modified by disconnecting the Ar supply after purging the chamber. This minimises the oxidation within the SMA and results in successful phase transformations during endothermic and exothermic cycles. Any residual oxygen would oxidise the material's surface and could physically dissolve the oxygen in Ti. Titanium oxides formation results in more than 50 at.% oxygen in the film. Despite this oxidation successful phase transformations and generating a Ti peak in the XRD profile of Ti-rich NiTi were observed.
- Various stoichiometric compositions of PVD – NiTi materials were subjected to the heating and cooling cycles in two different temperatures ranges of 20 – 400°C and -60 – 260 °C. Successful phase transformations were observed in both types of heating and cooling cycles. Multiple phase changes were

observed for the NiTi indicate the metastable state of NiTi below 550°C, which can be verified by the phase diagram also. The transformation temperatures and associated enthalpies for the phase changes in the lower range heating-cooling cycle are influenced more by varying the NiTi stoichiometric ratio as compared to the upper range phase transformations. The transformation temperatures and the enthalpies values of the phase transformations for the Ni-rich samples are altered more by changes in NiTi stoichiometric ratio, as compared to the equiatomic and Ti-rich thin film materials.

- The transformation peaks of NiTi decrease with an increase in Ni content. The Ni content was increased to obtain an austenite finish temperature below room temperature for acquiring a pseudoelastic material. The composition of Ni-rich $Ni_{53.5}Ti_{46.5}$ having the Ap of -19.24°C was chosen for PTFE-NiTi nanocomposite production.
- Wider hysteresis and the higher enthalpy values of the transformations occurring in the upper range heating-cooling cycle represent larger amount of material undergoing phase transformation, as compared to the phase changes in the lower temperature range heating and cooling cycles.
- As-deposited NiTi produces an XRD pattern presenting an amorphous structure with a few small B2 NiTi crystals shaping up a broad peak positioned at $2\Theta = 42.7°$ {110}. All NiTi samples including near-equiatomic, Ti-rich and Ni-rich films exhibit a martensitic structure after being processed by heat treatment and annealing followed by cooling to room temperature.
- The Ti-rich NiTi heat treated at 1100°C resembles more to the equiatomic crystal structure having less secondary precipitation and higher enthalpies associated to the phase transformations. Low-temperature heat treatment at 850°C for the same Ti-rich material contains more secondary precipitation within the SMA lattice. Excess Ti in Ti-rich samples causes nucleation and growth of $NiTi_2$ precipitates. This lead to lower enthalpy values for the thin films where the assembling of Ti_2Ni precipitates at columnar-grain interface of NiTi lattice hinder the phase transformations. Formation of titanium oxides (TiO_x) varies the SMA's stoichiometric ratio, depending on the value of x.
- The Ni-rich NiTi accrues a high concentration of Ni-rich precipitates assembling on the crystal boundaries, deforming the martensitic NiTi lattices

and resisting the phase transformations, resulting in small enthalpy values and weak XRD peaks. The phase transformation temperatures and the amount of material transforming for the Ni-rich samples are much more sensitive to the composition, compared to the Ti-rich and equiatomic NiTi samples, and alter the enthalpy values more significantly with minute changes in the stoichiometry of the SMA.

6.5 Polymerisation of PVD-RF sputtered PTFE

Sputtering is an energetic method of depositing thin films, and it can lead to the creation of complex chains of polymers leading to the polymerization during ion bombardment of the plasma [50]. To verify that the chemical composition of films remains similar to the target material after sputtering, FTIR spectroscopy of PTFE thin film was performed. PTFE was deposited at 100 W and 15 x 10^{-3} mbar at a working distance of 10 cm and Ar as the working gas. The FTIR spectrum of PTFE deposited on a glass was obtained by subtracting glass slide constituent from the spectra, as shown in Figure 124, which determines the chemical features of PTFE after RF-PVD sputtering. Significant peaks were observed between 500 cm^{-1} and 1600 cm^{-1}. This region is the most relevant part of the spectrum to study PTFE deposition. The FTIR spectrum was analysed with respect to Table 6 showing all the characteristic IR vibrations relating to PTFE [14][14; 80].

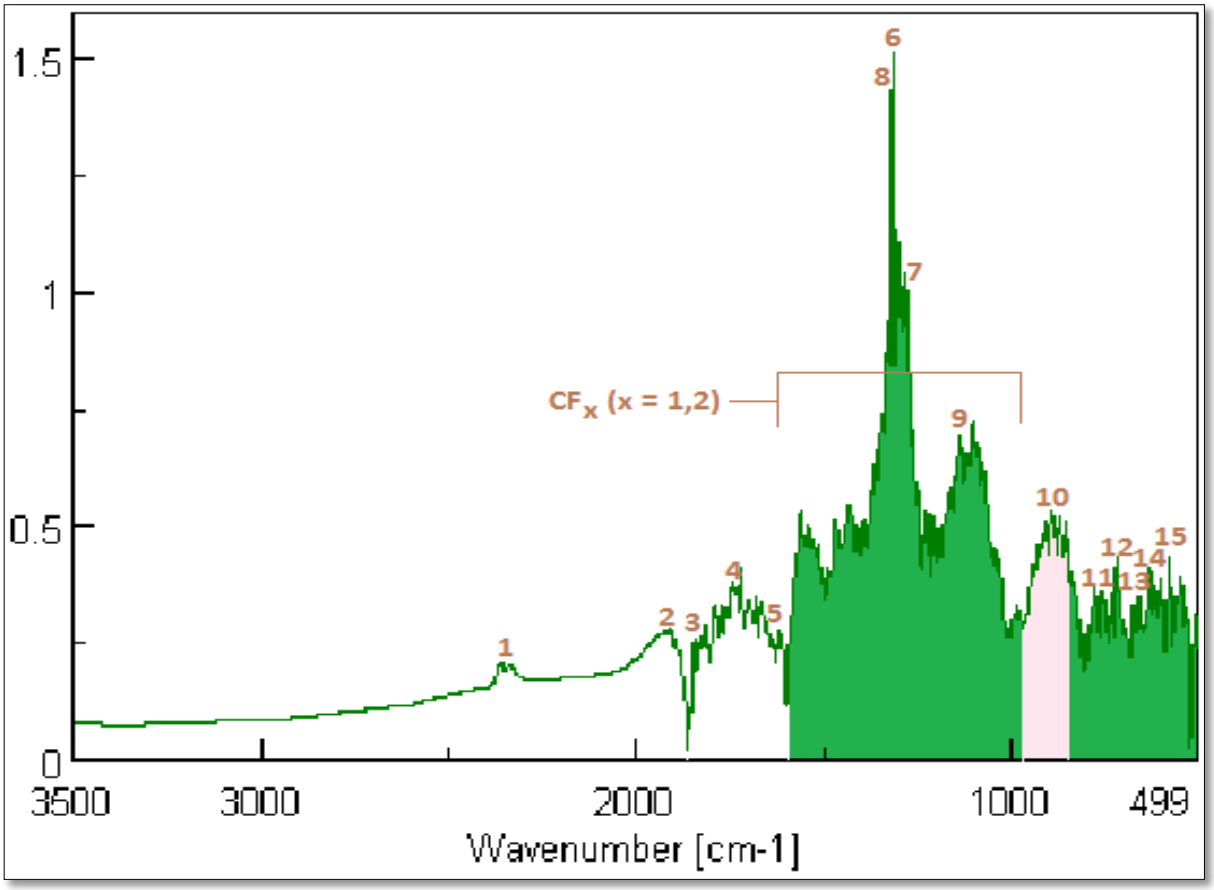

Figure 124: The resulting FTIR absorbance spectrum of a PTFE thin film after subtracting the blank glass substrate.

Table 24: Characteristic FTIR peaks description for PVD sputtered PTFE. Area under peak for CFx (x: 1, 2) & CF_3 is 50:1 (2%).

Peak	IR wavenumber (cm^{-1})	Description
1	2385	CH_2, CH_3 stretching
2	1813	$C=CF_2$
3	1698	- CF_2CO_2
4	1665	C = C
5	1597	CH_2, CH_3 deformation
6	1315	CF_x (x = 1, 2 and 3) stretching
7	1280	C – C stretching (Major)
8	1331	CF_2 asymmetric stretching (Major)
09	1103	CF_2 symmetric stretching (Major)
10	907	CF_3 deformation and amorphous PTFE
11	730	CF_2 scissoring (wagging)
12	660	CF deformation
13	627	CF_2 deformation
14	618	CF_2 bending
15	547	CF_2 twisting

Small peaks ranging from 547 – 627 cm^{-1} belong to CF_2 twisting, bending and deformation, along with an additional CF deformation shift at 730 cm^{-1}. Minor wagging of CF_2 results in a peak positioned at 730 cm^{-1}. CF_3 deformation and amorphous PTFE contribute towards a decline in polymerisation extent during PVD deposition. The chemical band demonstrating these shifts is represented by the coloured region under the peak 10 in the spectrum. The greater the area under this peak, the lower the degree of polymerisation since the CF_3 groups appear at the end of polymer chains. Therefore, excess of CF_3 groups relate to higher crosslinking and more monomers within the structure.

A set of strong peaks belonging to CF_x (x = 1, 2) appear in the wave number range of 1012 – 1547 cm^{-1}. The area under these peaks equates the polymerised content of PTFE. CF_x represents CF_2 groups mainly with some presence of CF. An idea about the amount of CF can be perceived by comparing the peak area in CF_x region to the peak area under peak 10. The area under peak 10 increases with an increase

in branching. Higher branching contains more CF bonds within the structure. The CF bonds also appear around C = C, which are the small fragments having lack of polymerisation. C = C peaks appear at 1665 cm^{-1} in the spectrum. The greater peak area under C = C peak also accounts for a higher number of CF bonds. The higher CF_2:CF produces smooth PTFE thin films [87]. This is because of less crosslinking within the structure. The cross-linking within the thin films increases the surface roughness of PTFE.

The strong peaks forming within CFx region of 1012 – 1564 cm^{-1} include major C – C stretch at 1280 cm^{-1}, CF_2 asymmetrical stretch at 1331 cm^{-1} and CF_2 symmetrical stretch at 1103 cm^{-1}. The major CF_x peak at 1315 cm^{-1} overlay the C- C and C – F vibrations due to their existence in the same chemical band. The spectrum shown in Figure 124 also represents minor deformation and stretching peaks of hydrocarbons at 1597 cm^{-1} and 2385 cm^{-1} respectively. C = CF_2 vibrations produce a chemical shift at 1813 cm^{-1}, which are responsible for the graphitic surface of PTFE thin films. Presence of oxygen within PVD sputtered thin films have been previously observed by Drabik et al. [14], when argon is used as working gas. This produces the characteristic peaks of CF_2CO_2. The higher amount of oxygen trapped within the film structure produces stronger CF_2CO_2 peak, shown at 1698 cm^{-1} in Figure 124. OH stretching vibration peaks between 3000 cm^{-1} to 3500 cm^{-1} do not appear, which specifies for the purity of PTFE coating. [14]

The polymerization ratio in the deposited fluorocarbon film is determined by areas under the peaks, which indicates 2% CF_3 in a polymer chain structure, representing the proportion of CF_x (x: 1, 2) and CF_3 to be 50:1. CF_3 peaks intensity is low due to growth of chain cross-linking and reduction in CF_3 assemblies after sputtering. CF and CF_3 within the polymer show tertiary carbon structures and branching within chains and around carbon skeleton of the chain.

6.5.1 Selection of PTFE target material

The PTFE thin films produced by the targets sourced from different suppliers gave different polymerisation ratio, hydrophobicity and morphology. This is due to all suppliers using different processing methods that affect the growth of chain lengths, which in turn, produced thin films having different surface energies and polymerisation ratios. To make the results reliable and reproducible, a study was conducted to find out if six different target materials have the same chemistry. This also provided some findings of surface properties of the resulting thin films, which were obtained by the deposition from those targets. Figure 125 shows that all the target materials give similar peaks representing the same chemical structure of all materials. The only difference is the % reflectivity. This is due to different grain size and morphology of the target. The surface of 'target material a' is much rougher than the rest of the materials due to larger grain size and larger polymer chains within the structure.

To verify the chemical structure, and to ensure that the % reflectivity is the only varying factor, a new set of spectra was obtained where the 'target materials e and f' are reflected at 45°, while the reflectance angle of 'target material a' was increased to 75°, as shown in Figure 129. The chemical composition of films remains the same, but the peaks show significant changes in areas under the peaks between 400 cm^{-1} and 1500 cm^{-1}; hence, this region represents the most relevant part of the spectrum. Overall, results of this study can be concluded as given below. All samples give similar peaks due to having the same chemical structure of the material. The percentage reflectance (%R) of all materials changes due to different grain size, morphology and optical properties of the target materials. The surface of 'target a' was the roughest because of its larger grain size and larger polymer chains within the structure so it would give a different polymerisation ratio, hydrophobicity and morphology. This was due to the use of different processing methods, providing a different growth structure, and resulting in dissimilar morphology and chain lengths. Disparities in film morphology and different area under the peaks indicate the need for selecting one target material as a reference. For this reason, the spectrum of 'target material e' was chosen as a standard reference to ensure same reference polymerisation ratio and microstructure. The chemical structure was compared to the standard spectrum every time, when a new target was installed in the sputter coater.

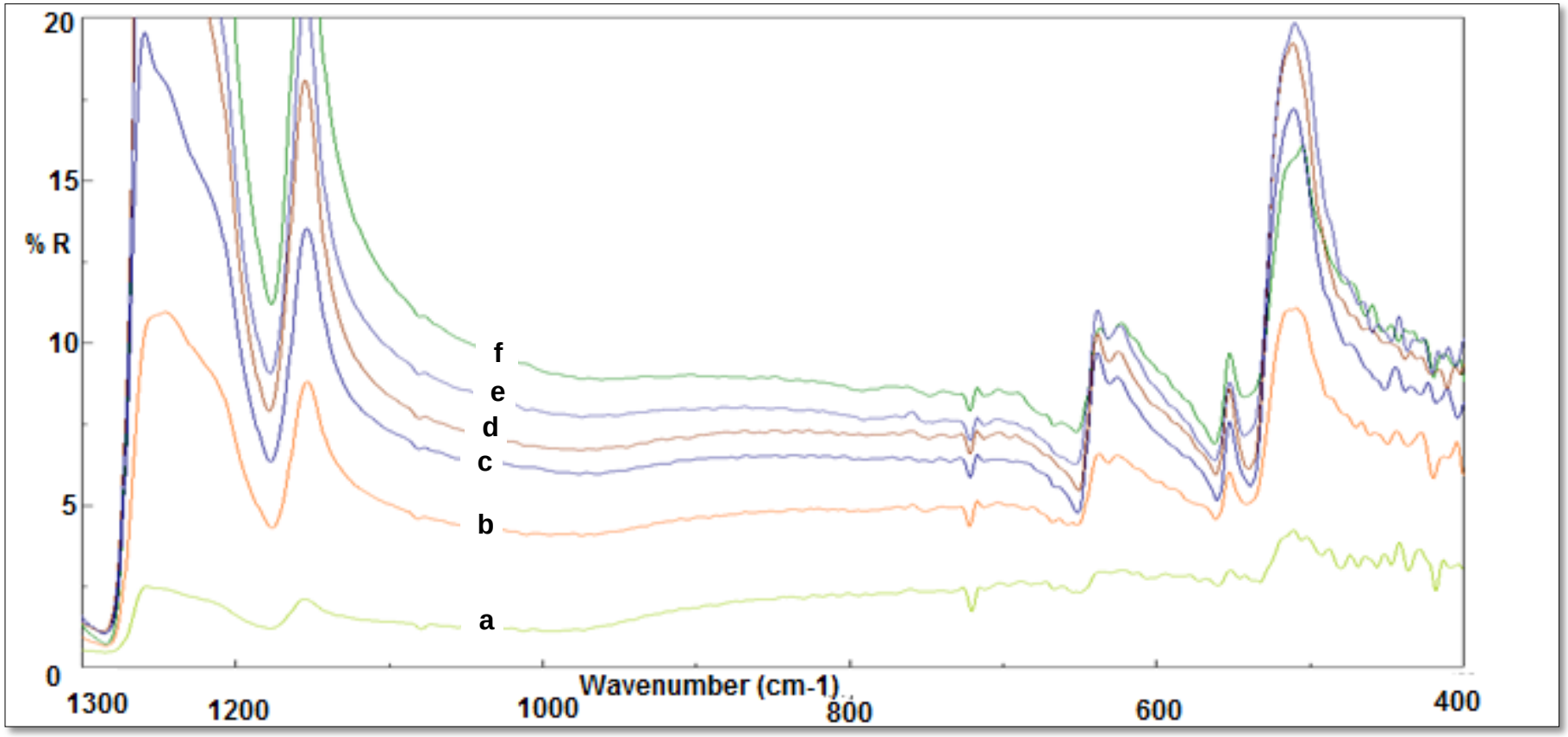

Figure 125: FTIR % reflectance spectrum of PTFE targets from various marker suppliers at a reflectance angle of 45°.

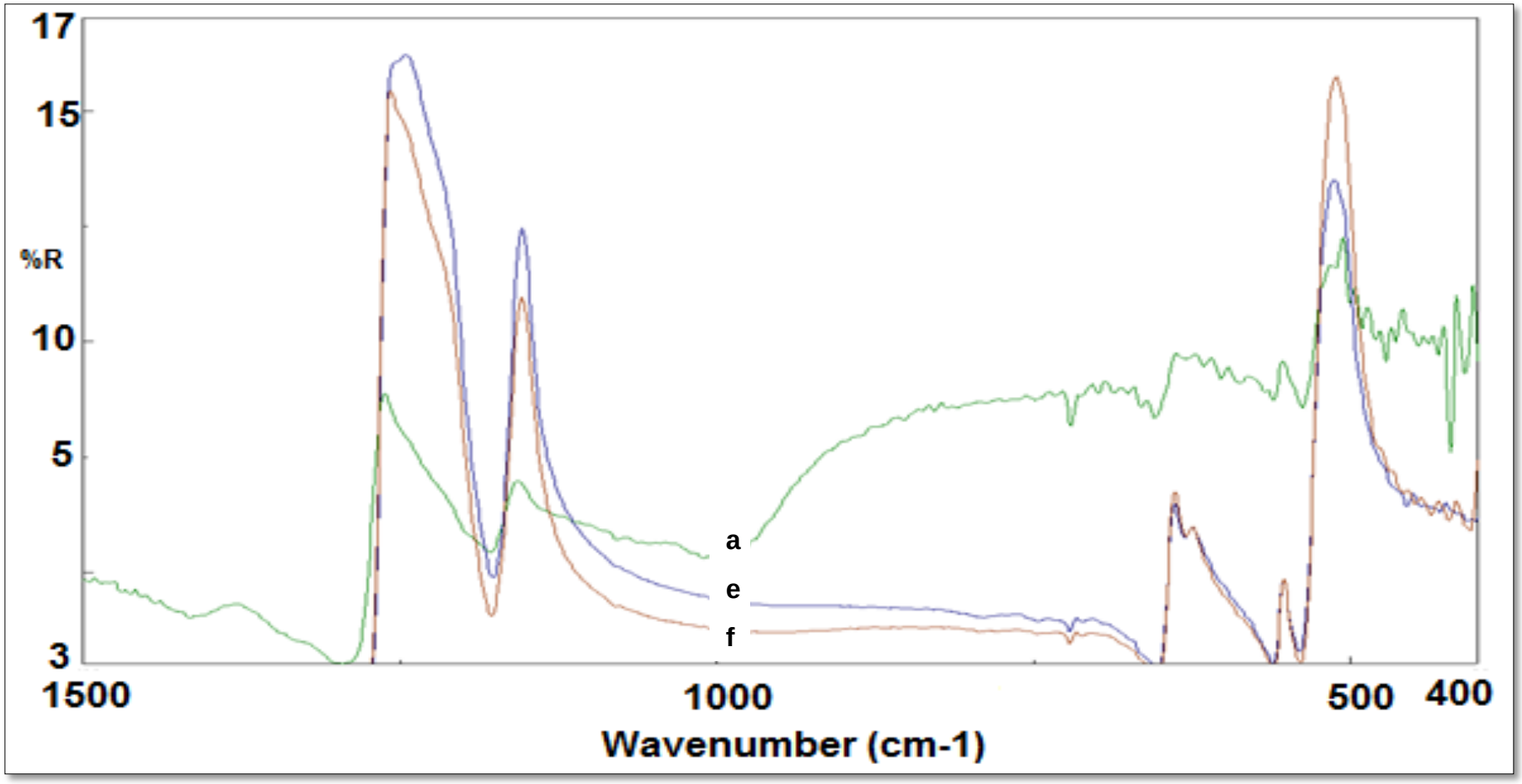

*Figure 126: FTIR % reflectance spectrum of PTFE at angle of 45° for 'target materials **e** and **f**', and 75° for 'target material **a**'.*

6.5.2 Effect of the polymerization ratio on hydrophobicity of PVD-PTFE

The polymerization ratio in the PTFE films deposited from the target materials provided by different suppliers (as discussed in section 6.5.1) yield different polymerization ratios, which was determined by areas under the peaks. Different polymerisation ratios indicate the percentage of CF_3 in the polymeric structure and represents the proportion of CF_x (x: 1, 2) and CF_3. CF and CF_3 within the polymer structure relate to tertiary carbon assemblies and indicate branching within the polymer chains, and present around carbon skeleton chain. FTIR absorbance spectra were obtained for PVD-PTFE thin films deposited at 125W RF, 20 x 10^{-3} mbar Ar pressure and 10 cm working distance. The thin films were analysed for hydrophobic behaviour by water contact angle (WCA) measurements. The results have been recorded in Table 25. The degree of polymerisation in the deposited films is determined by the calculation of polymerisation ratio followed by using areas under the peaks within spectrum. The percentage of CF_3 in PTFE thin film ranges from 2 to 7.5%.

Table 25: Polymerisation ratio and WCA of PTFE films.

Target material	**Polymerisation ratio (CF_2:CF_3)**	**CF_3/(CF_3+CF_2)**	**% of CF_3 in PTFE**	**WCA**
a	40.3	14.7	6.98	99
a	40:4	11.0	9.09	99
b	45:1	46.0	2.17	108
c	50:2	26.0	3.85	110
d	45:1	46.0	2.17	105
e	50:1	51.0	1.96	112
f	45:1	46.0	2.17	107

Deposited films from ‘target material a’ provide distinctively different and lower WCA that associate with different morphological surface having higher CF_3/(CF_3+CF_2) ratio. This disparity arises because of different chain lengths in the PTFE target materials as discussed in section 6.5.1. According to Table 25, there is a relationship

between polymerisation extent ($CF_3/(CF_3+CF_2)$) and WCA determines that the higher the polymerisation ratio within the polymer chain, the more hydrophobic the film becomes. The amount of $CF_3/(CF_3+CF_2)$ may approximate half the chain length. The findings of Table 25 are presented in Figure *127* below.

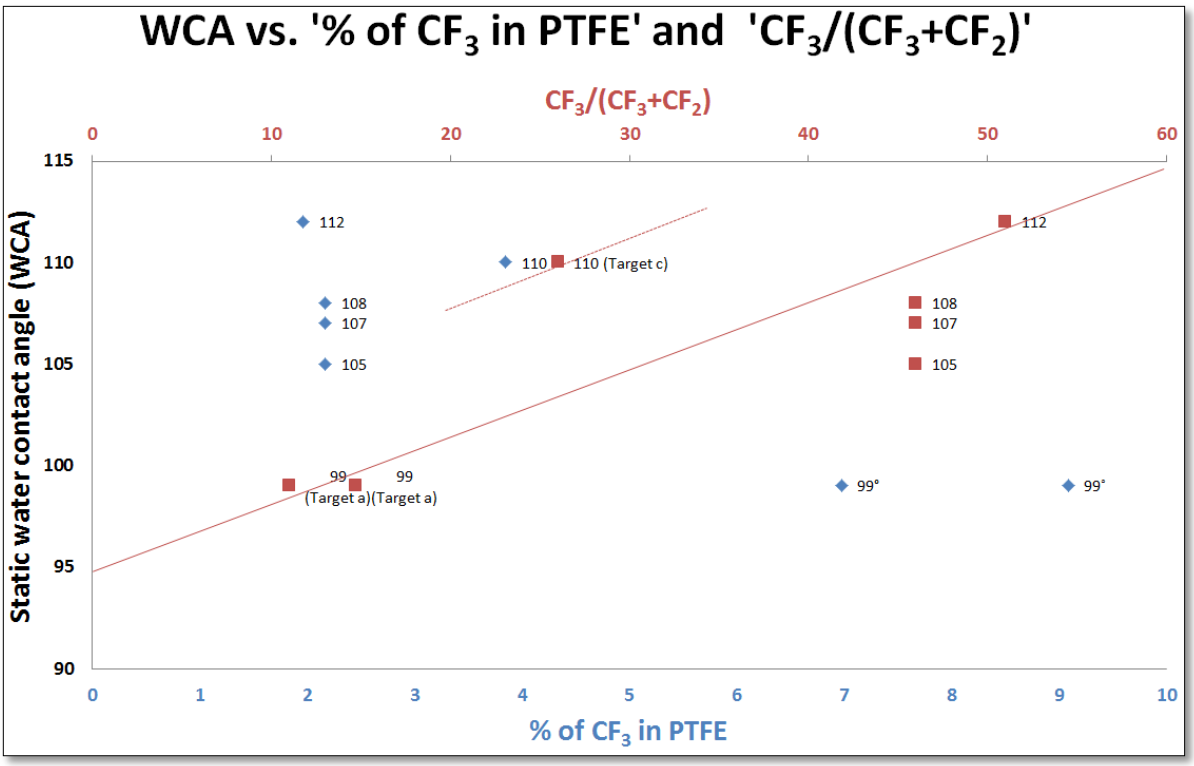

Figure 127: WCA against % of CF_3 in PTFE and 'CF_3 / (CF_3+CF_2)' for PTFE films from different target materials as listed in Table 25.

PTFE thin film continues to form successfully after PVD sputtering from various PTFE targets. The main peaks of the chemical structure of all PTFE thin films remain identical to Figure 124. OH stretching vibration peak remains absent indicating the purity of the thin films. There is a relationship between polymerisation extent ($CF_3/(CF_3+CF_2)$) and WCA, and the hydrophobicity increases with higher polymerisation extent within the polymer chain, the more hydrophobic he film. Thin films from 'target material a' has a different morphology as compared to other thin films, along with much higher $CF_3/(CF_3+CF_2)$. Thus, the deposited films from 'target material a' provide distinctively different and lower WCA. This indicates that the sputtering process was more destructive for 'target material a' breaking the polymer chains to shorter fragments, resulting in lowest sputtering yield. Although the rougher polymer surfaces have high hydrophobicity, but the thin films forming from the 'target

material a’ did not repolymerize thoroughly after sputtering. Higher percentages of CF_3 (chain ends) were found indicating lack of polymerization and excess of crosslinking. This increases the surface energy due to unreacted monomers present in the structure; accordingly, WCA decreases resulting in less hydrophobic surface. For a given degree of polymerization, target c gave a higher water contact angle. This is because a dependence on the degree of polymerization was observed for all targets evaluated with WCA depending on the $CF_3/(CF_3+CF_2)$ ratio, a measure of polymer chain length.

6.5.3 Effect of deposition parameters on polymerisation PVD-PTFE

A detailed FTIR study was carried out at various deposition powers and process pressures to investigate the influence of process conditions on the chemical properties of PVD-PTFE thin films. Ar pressure and RF power are the most influencing deposition parameters for PVD sputtered thin film characteristics.

Figure 128a shows a set of three FTIR spectra of PTFE thin films deposited on glass at 150W and at process pressures ranging from 5 to 15 x 10^{-3} mbar for 2 hours. The FTIR spectra of PTFE deposited on a glass substrate were presented after subtracting glass constituents from the spectra. The characteristic peaks of all three spectra are the same as previously discussed the spectrum shown in Figure 124. To understand the influence of process pressure on the polymerisation of post-sputtered PTFE thin films, the spectra shown in Figure 128a are divided into three regions labelled as A, B and C. The spectral bands in region A belong to CF_x / CF_2 symmetrical and asymmetrical stretching and C – C stretching peaks, which directly relate to the polymerised content within the material. Region B mostly consists of CF_3 deformation and amorphous PTFE, resulting from branching, crosslinks and lack of polymerisation. The peaks in region C are CF_2 deformation, bending and twisting peaks along with CF deformation and CF_2 scissoring (wagging). These peaks mainly influence the surface morphology and the film thickness.

To observe the peak absorbance at various process pressures, the major peak of CF_2 absorbance was plotted against the deposition pressure, as shown in Figure 128b. The absorbance of CF_x stretching increases with increasing process pressure from 5 x 10^{-3} to 15 x 10^{-3} mbar, confirming an increase in polymerisation extent. Increasing the pressure further to 25 x 10^{-3} mbar decreases the absorbance by polymerised content of the thin film. These results are similar to those presented in Biederman et al. [74] study, which investigated the increase in CF_2 absorbance followed by a decrease when it is plotted as a function of argon pressure (Figure 28).

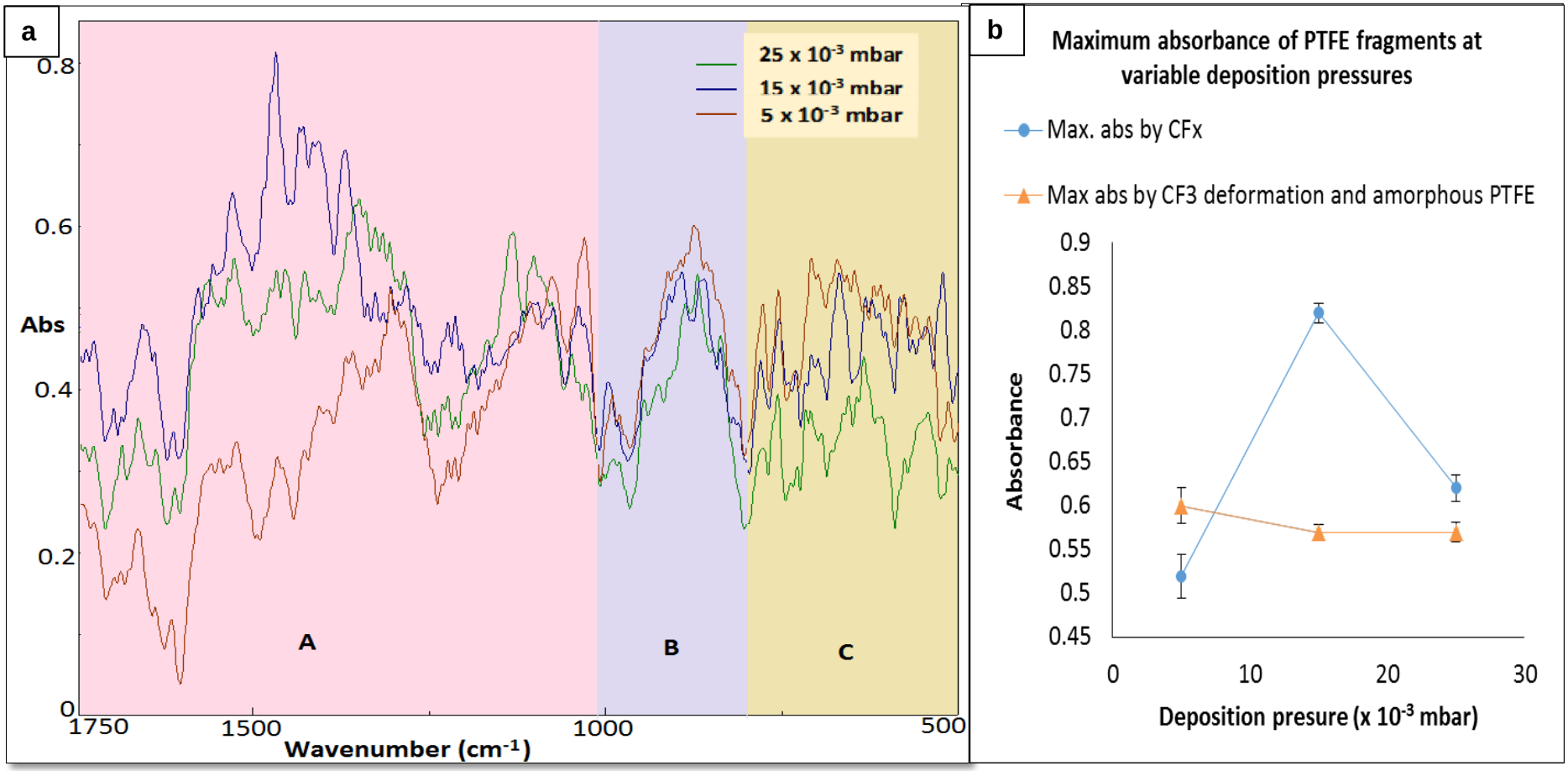

Figure 128: (a) Three FTIR spectra of PVD sputtered thin films of PTFE, deposited 2 hours at 150W and RF ranging from 5 x 10^{-3} to 25 x 10^{-3} mbar. (b) The relationship between maximum absorption peaks of CF_x and RF; and maximum peak absorbance of CF_3 and amorphous PTFE against process pressure.

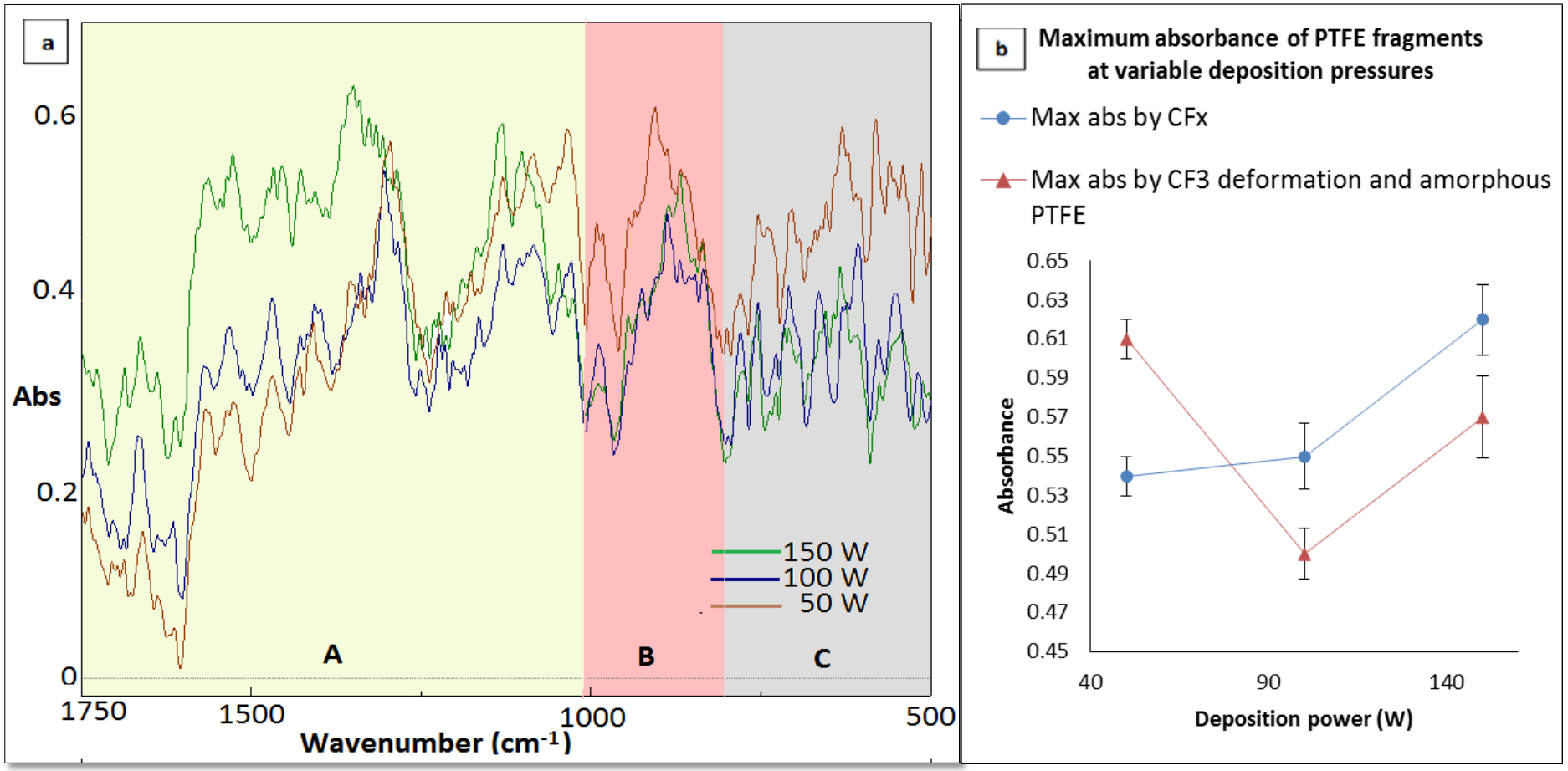

Figure 129: (a) Three FTIR spectra of PVD sputtered thin films of PTFE, deposited 2 hours at 25 x 10^{-3} mbar and RF ranging from 50 to 150 W. (b) The relationship between maximum absorption peaks of CF_x and RF; and maximum peak absorbance of CF_3 and amorphous PTFE against RF.

Figure 128b also shows the variance in maximum absorbance by CF_3 deformation and amorphous PTFE, which relate to the lack of polymerisation in PTFE thin films. CF_3 deformation and amorphous absorbance are higher than maximum absorbance by CF_x at 5 x 10^{-3} mbar. This establishes that 5 x 10^{-3} mbar is an inapt pressure to deposit a polymer by PVD sputtering. At 5 x 10^{-3} mbar, the polymerised PTFE content is less than amorphous material consisting of highly branched fragments with excessive crosslinking and a high proportion of unreacted monomers. 15 x 10^{-3} mbar was the most suitable process pressure due to a large difference between the two peaks. With the increase in deposition pressure from 5 x 10^{-3} mbar, the CF_x absorbance increased, and CF_3 absorbance decreased resulting in significantly high degree of polymerisation.

Further increase in process pressure from 15 x 10^{-3} to 25 x 10^{-3} mbar lowers the absorbance peak relating to amorphous PTFE and CF_3 stretching but the CF_x peak absorbance only lowers slightly. This phenomenon refers to the film thickness. Figure 107 shows that the deposition rate at 150W and 25 x 10^{-3} mbar is significantly low; for this reason, the film thickness at these process parameters is very small resulting in relatively transparent thin film. Higher film transparency relates to high percentage transmittance. Hence, low absorbance was observed for both types of chemical shifts (CF_x and CF_3-amorphous PTFE) at 25 x 10^{-3} mbar. Similarly, low absorption is found for the region C of the spectrum relating to the film deposited at 25 x 10^{-3} mbar. The lack of polymerisation in the thin film deposited at 5 x 10^{-3} mbar also provides a greater area under CF deformation peak at 638 cm^{-1}. $CF:CF_2$ also influences the film morphology and a higher $CF: CF_2$ results in rougher thin films [87].

Figure 129a presents a set of three FTIR spectra of PTFE thin films deposited on glass for 2 hours at 25 x 10^{-3} mbar and RF power ranging from 50 to 150W. The FTIR spectra of PTFE deposited on glass were presented after subtracting glass constituents from the spectra. The characteristic peaks of all three spectra are same as the previously discussed spectrum shown in Figure 124. The spectra shown in Figure 129a are divided into three regions labelled as A, B and C for understanding the influence of process power on the polymerisation of post-sputtered PTFE thin

films. The description of the spectral bands in each region in Figure 129a is same as Figure 128.

CF_2 major peak absorbance was plotted against the RF power to observe the peak absorbance at various RF powers as shown in Figure 129b. The absorbance of CF_x stretching increases with increasing the powers from 50 to 150 W, confirming an increase in polymerisation extent. There is a sharper increase in absorbance, when the deposition power was increased from 100W to 150W. Figure 129b also shows the variance in maximum absorbance by CF_3 deformation and amorphous PTFE, which relate to the lack of polymerisation in PTFE thin films. CF_3 deformation and amorphous absorbance are higher than maximum absorbance by CF_x at 50W. This suggests that 50W is an unsuitable power to deposit a polymer by PVD sputtering. At 50W, the polymerised PTFE content is less than in an amorphous material consisting of highly branched fragments with excessive crosslinking and a high proportion of unreacted monomers.

CF_x absorbance increases with an increase in deposition pressure from 100W to 150W, and CF_3 absorbance decreased resulting in significantly high degree of polymerisation. Therefore, these are the suitable process parameters for PTFE sputtering. The absorbance trend-lines between 100W and 150W RF for both types of functional groups are parallel to each other. The difference in the degree of absorbance at each deposition power corresponds to the film transparency because the deposition rate varies with changing RF resulting in dissimilar film thickness in same deposition time. Therefore, the film absorbs more when deposited at high deposition power and less transmission occurs, resulting in a decrease in film transparency. The film deposited at 50W appears to have the least transparency with most deposition thickness due to higher deposition rate. This follows the deposition trends described previously in the discussion relating to Figure 107 and Figure 108, which state that the deposition rate increases with a decrease RF at 25 x 10^{-3} mbar. Increasing the RF to 100W and 150W, decrease the deposition rate, which in turn decreases the film thickness results in low absorbance and high transmittance. Absorption in the region C of the spectrum is highest for the film deposited at 50W. The lack of polymerisation in the thin film deposited at 50W also provides a greater area under CF deformation peak at 632 cm^{-1}.

The above results relate well to the previous studies by Mandale et al. and Li et al., who described the effect of varying the PVD deposition power on the FTIR spectra of PTFE, (Figure 23). The results of the both studies establish that the deposition powers of PTFE thin films alter the film transparency without changing the functional groups and chemical structure of PTFE thin films [85; 86]. FTIR spectra found in both of those previous studies illustrate that the increase in deposition power decreases the extent of polymerisation, which differs from the results extracted from Figure 129a. This difference relates to the fact that the deposition rates against power have dissimilar trends at various process pressures. The deposition rates relate to the film thickness while the film thickness has a direct influence on peak absorbance and transmittance, and ultimately on the chemical properties of PVD sputtered PTFE. Similarly, there was a difference found between the spectra of the two studies in the trend of percentage in the transmittance at various deposition powers. With increasing RF, the transmittance of the PVD films is observed to be decreasing in Figure 23A while it increases in Figure 23B. The deposition time for the both deposition processes is 60 and 5 minutes respectively. The change in transmittance behaviour was related to film thickness [85; 86]. The thicker the coating, the less the transmittance it demonstrates. Therefore, to understand the above differences, a good understanding of the trend in the deposition rates against RF was needed, which was lacking in the existing literature and this deficiency has been fulfilled in Figure 107 and for current study.

6.5.4 Summary

The above discussion establishes that PTFE has successfully formed as a thin film polymer after PVD sputtering from a PTFE target. The resulting chemical characteristics matched well to all IR peaks provided in Table 6. A rough surfaced ‘target material a’ having larger grain size and larger polymer chains resulted in the lowest polymerisation ratio and hydrophobicity. In ‘target material a’ higher percentage of CF_3 (chain ends) was found indicating lack of polymerization and excess of crosslinking. The spectrum of ‘target material e’ with good polymerisation extent and hydrophobicity in thin films was selected as a standard reference, and it was compared to a new target’s film every time when the target was changed in the sputter coater. A dependence on the degree of polymerization was observed for all targets evaluated with WCA depending on the $CF_3/(CF_3+CF_2)$ ratio, a measure of polymer chain length. For a given degree of polymerization, target c gave a higher water contact angle.

For PTFE thin films deposited at 150W, the highest extent of polymerized peaks was obtained at 15 x 10^{-3} mbar, which decreased with increasing pressure to 25 x 10^{-3} mbar as well as by decreasing the pressure of 5 x 10^{-3} mbar. For the PTFE thin films sputtered at 25 x 10^{-3} mbar, the polymerization was most successful at 100 and 150 W, which decreased with decreasing RF to 50W. Thus, the extent of polymerization was limited to 50W and 5 x 10^{-3} mbar process parameters resulting in highly branched fragments with excessive crosslinking, a greater proportion of unreacted monomers the production of rougher thin films. The peak absorbance and transmittance of PTFE thin films directly relate to the deposition rate meaning the film thickness.

6.6 Surface analysis of PTFE and NiTi thin films

Surface analysis of PTFE and NiTi thin films was undertaken by SEM, AFM and wetting angle measurements. High-resolution scanning electron microscopy was performed using an FEI XL30 SFEG analytical SEM, and images of all PTFE and NiTi samples were taken at four different magnifications (x500, x2000, x5000 and x15000).

6.6.1 Surface analysis of PVD sputtered PTFE thin films

Two sets of SEM images(x5000 and x15000) are selected to report the morphology of PVD-PTFE thin films as shown in Figure 130 and Figure 132. Additional SEM images of PTFE films prepared at various process conditions are presented in the appendices. A Veeco Dimension^{TM} 3100 AFM was also used to study the surface topography of PTFE thin films. AFM images presenting the topographical features of PTFE films are presented in Figure 131 and Figure 133. In AFM images, the coatings appear on left-hand step-edge of the Si substrate.

Figure 130 and Figure 131 were assembled to investigate the influence of varying RF on the morphology of PVD-PTFE. SEM images in Figure 130 reports about the impact of changing power on the surface of the coatings prepared at 25 x 10^{-3} mbar. It is evident from Figure 130 that the smoother films are deposited at the lower powers. There are grains apparent in the image of the film deposited at 150W, and the film seems to have relatively lopsided surface with small clusters forming on the surface. The surface still looks uneven after decreasing the power to 100W, but the clusters start to merge and coalesce. The film deposited at 75W is significantly flat, and an even surface was observed at a magnification of x15000. Slight folds on the surface can be found in a parallel direction to the substrate. The AFM images in Figure 131 also show the effect of variance in RF on PTFE surface when the films were deposited at 5 x 10^{-3} mbar. The AFM images in Figure 131 report that a rough surface is acquired at 150W, which becomes relatively smoother by decreasing the power to 125 and 100 W. This change in surface roughness elaborates that a higher RF produces rougher thin films having wider columns, and clusters emerging on the surface. SEM studies carried out by Qi et al. [34] also demonstrate that segregated

grains of PTFE film become uniform, fine, round and closer because of the increasing power (energy) and the critical size declines.

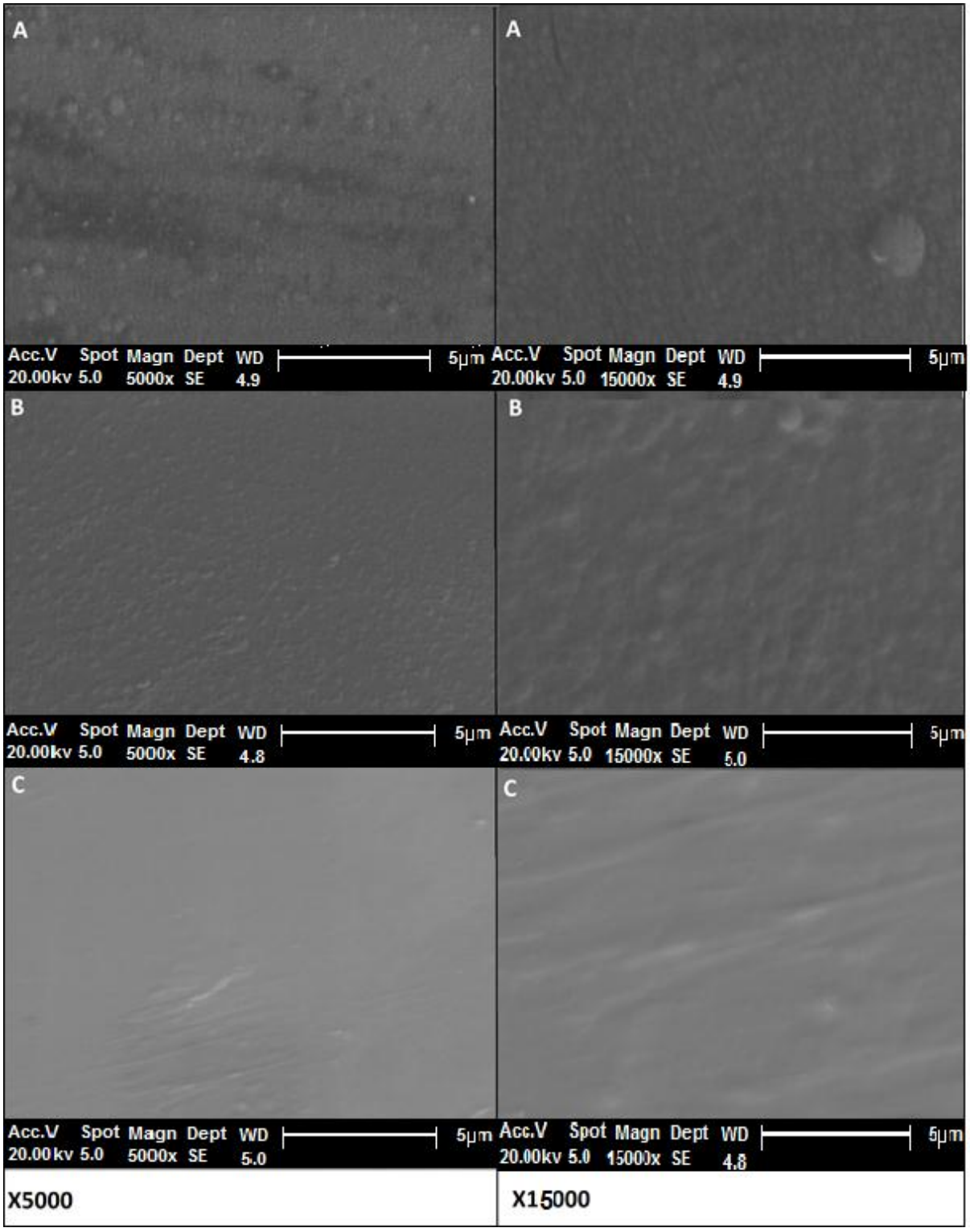

Figure 130: SEM images (x5000 and x15000) for PTFE deposited on glass substrate for 2 hours at 25 x 10-3 mbar process pressures (a) 150W, (b) 100W, and (c) 75W.

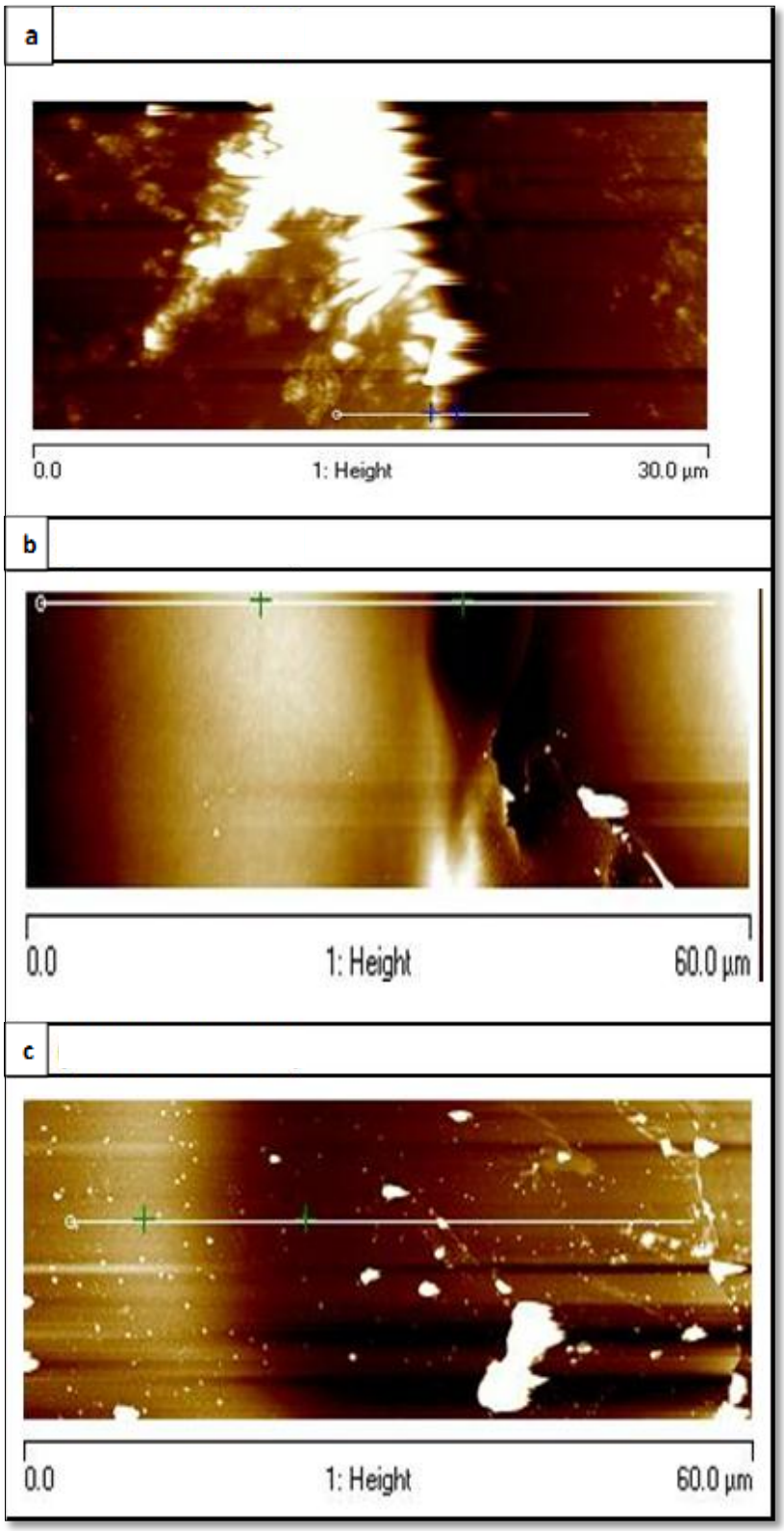

Figure 131: AFM topographic images for PTFE deposited on Si substrate for 2 hours at 5 x 10^{-3} mbar process pressures (a) 150W (b) 125W (c) 100W. The coatings appear on the left side of step-edge on the Si substrate.

The above SEM and AFM observations relate to the deposition rate vs. process conditions result that are reported previously in Figure 107 and Figure 108. Figure 107 and Figure 108 indicated that decreasing the RF from 150W to 75W at 25 x 10^{-3} mbar increased the deposition rate. This allows one to determine that the thin films deposited at 75W have the greatest deposition thickness. Therefore the thin films deposited at 25 x 10^{-3} mbar along with high RF result in Volmer-Weber's 3D island growth, which describes the film surface as 2D separate islands forming on the substrate surface, as shown in Table 4. Volmer-Weber's 3D island growth results in greater interaction between the film particles compared to that of the interaction between adjacent film and substrate particles. Thus, the amorphous films appear as the clusters assemblies deposited on the substrate surface (Figure 130a and Figure 130b). Decreasing the power to 75W increases the deposition rate; hence, the deposition thickness also increases, resulting in Stranski-Krastanov's layer plus island growth mode. In the Stranski-Krastanov's layer plus island mode, the formations of islands lead to the formation of one or two monolayers. Surface energy is high for the thicker films and a layer on the top of the substrate is strained to fit the substrate, which can be observed by folds of the layer in Figure 130c and Figure 131b.

The SEM image of PVD-PTFE thin film, shown in Figure 130c is similar to that of the SEM image presented by Biederman et al. [74; 87] in Figure 19. They describe the clusters in layers as dense fibres appearing in the perpendicular direction to the substrate, which is due to the central C – C chain growing perpendicular to the substrate along with C – F bonding appearing parallel to the substrate. PTFE thin films have also been reported previously as a three-dimensional network having columnar structures along with a 3D island growth mode, containing semi-continuous silkworm like islands connecting to each other. The sub-layers cover the initial layer by 50-70% and then the growth of sub-layer stops. This results in Volmer-Weber's 3D island growth changing to Stranski-Krastanov's layer-plus-island growth mode with increasing deposition thickness.[34; 74; 87]

Figure 132 and Figure 133 were assembled to investigate the influence of changing process pressure on the surface of PVD sputtered PTFE. SEM images in Figure 132 presented the impact of deposition pressure on the film morphology when the RF was maintained at 100W, and the pressure was varied from 25 x 10^{-3} mbar to 10 x 10^{-3} mbar. AFM images in Figure 133 provide further understanding about the effect of variance of pressure on the surface of thin films deposited under the same process conditions. According to the Figure 132, all films deposited at 100W are granular. The grain size decreases with decreasing process pressure, and the film appears to be relatively smoother. Figure 133 also explains that the surface roughness decreases with the decreasing deposition pressure, and the coatings become smoother.

Biederman et al. [74] conducted another study at a higher range of process pressures (10 x 10^{-2} – 70 x 10^{-2} mbar). Their study reported lower surface roughness of approximately 3 nm for the thin film deposited at pressure values in the range of 10 x 10^{-2} – 50 x 10^{-2} mbar and 200W in an Ar flux of 26 sccm (Figure 26). If the pressure is increased to 70 x 10^{-2} mbar, the surface roughness increases to 40 nm with flakes-like structures appearing on the film surface. Thus, the deposition pressure decreases the surface roughness of PVD-PTFE thin films to some extent at a small range deposition pressures. However, at further low process pressure of 5 x 10^{-3} mbar, the film becomes more crystalline and fragmented, which can be seen in AFM image provided in Figure 131a.

The above explanation correlates to the trend of deposition rate against process pressure provided in Figure 108, which reports that the deposition rate rises with increasing process pressure. Deposition rate directly relates to the film thickness, meaning that the thicker films are smoother. The cluster shapes of PTFE thin films are relatively more defined and granular at higher deposition pressures and mostly amorphous films deposit at low pressures. The reason is a decrease in the degree of polymerisation with decreasing process pressure, as reported in Figure 128a. The extent of polymerization is limited at low process pressures because of the unreacted monomers, short PTFE fragments, and amorphous PTFE accumulating within the film structure during the plasma polymerisation process.

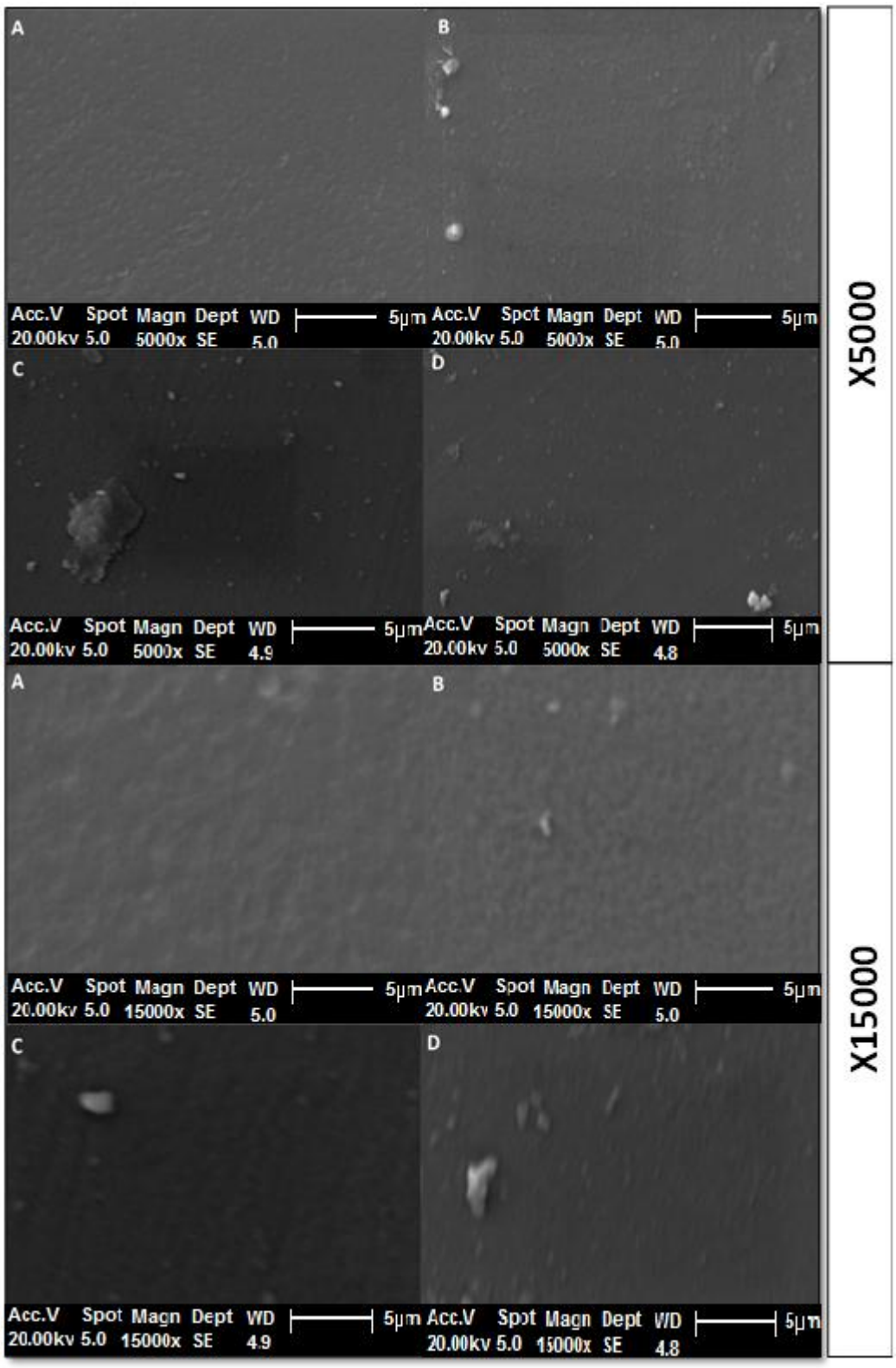

Figure 132: SEM images (x5000 and x15000) for PTFE deposited for 2 hours on glass substrate at 100W (a) 25 x 10^{-3} mbar, (b) 20 x 10^{-3} mbar, (c) 10 x 10^{-3} mbar, and (d) 5 x 10^{-3} mbar.

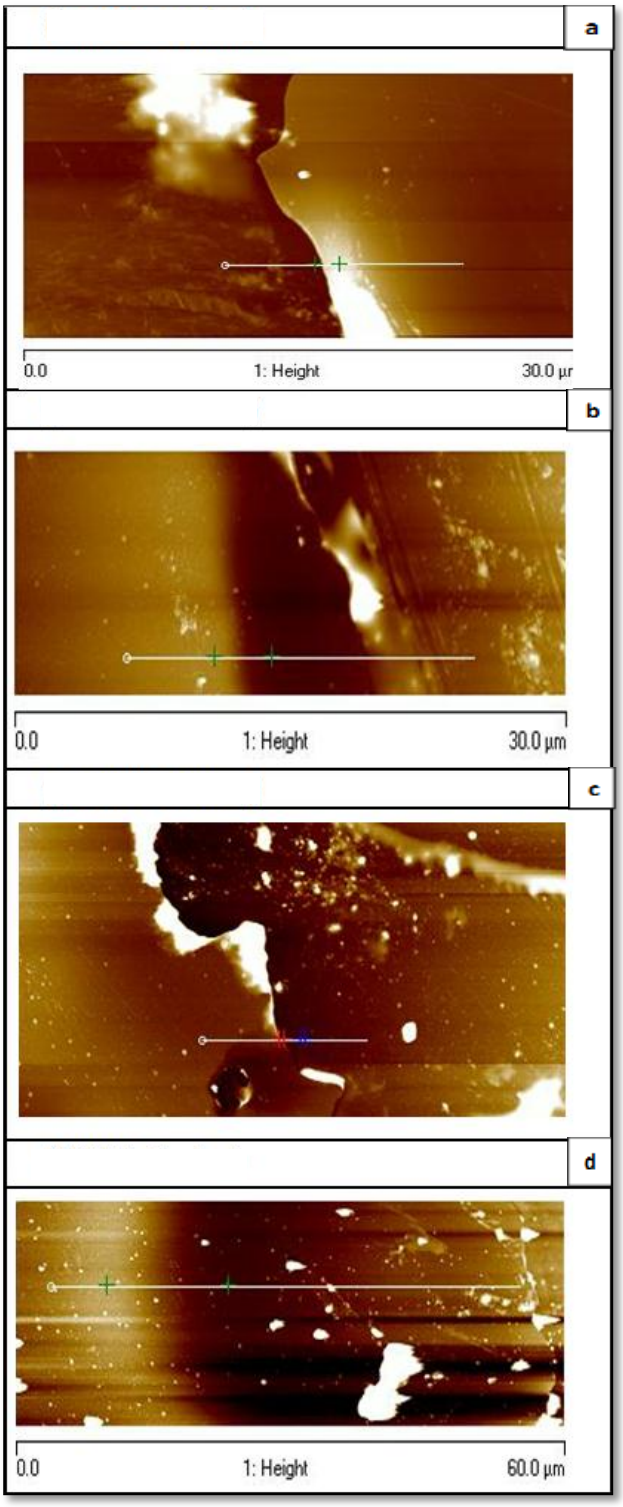

Figure 133: AFM topographic images of PTFE deposited for two hours on Si substrate at 100W (a) 20 x 10^{-3} mbar, (b) 15 x 10^{-3} mbar, (c) 10 x 10^{-3} mbar, and (d) 5 x 10^{-3} mbar. The coatings appear on the left-hand side of step-edge on the Si substrate.

6.6.2 Surface analysis of PVD sputtered NiTi thin films

Two sets of images are selected to study the morphology of PVD-NiTi thin films, as shown in Figure 134 and Figure 136. More SEM images for NiTi films prepared at various process conditions are presented in the appendices. AFM images show the surface topography of the thin films in Figure 135, where the coatings appear on the left-hand step-edge on the Si substrate. The coatings are marked with a double-headed arrow underneath. Section 6.4 provides the detail of heat treatment and annealing procedure of NiTi thin films and reports about the crystal structures involved in phase changes during transformations. It has also been previously discussed in section 6.4.2 that the as-deposited thin films are amorphous with few B2 crystals shaping up for a broad peak positioned at 2Θ = 42.7° (110). The absence of any texture in the XRD profile reflects the lack of any lattices within the material. For that reason, the SEM and AFM images presented in Figure 134 – Figure 136 are mainly of amorphous NiTi but having some austenite crystals within the film structure. The SEM and AFM images selected for Figure 134 – Figure 136 are for $Ni_{52}Ti_{48}$ thin films deposited for 2 hours, with variance of +/- 0.6 at.% in the film composition.

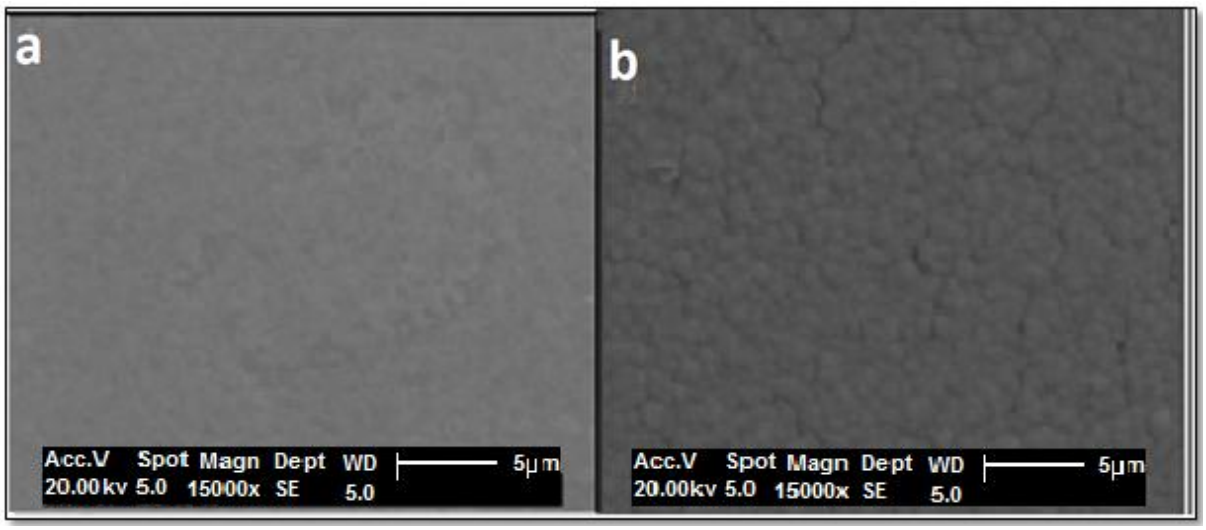

Figure 134: SEM images (x15000) for NiTi deposited for two hours on the glass substrate at 10 x 10^{-3} mbar (a) 100W (b) 50W.

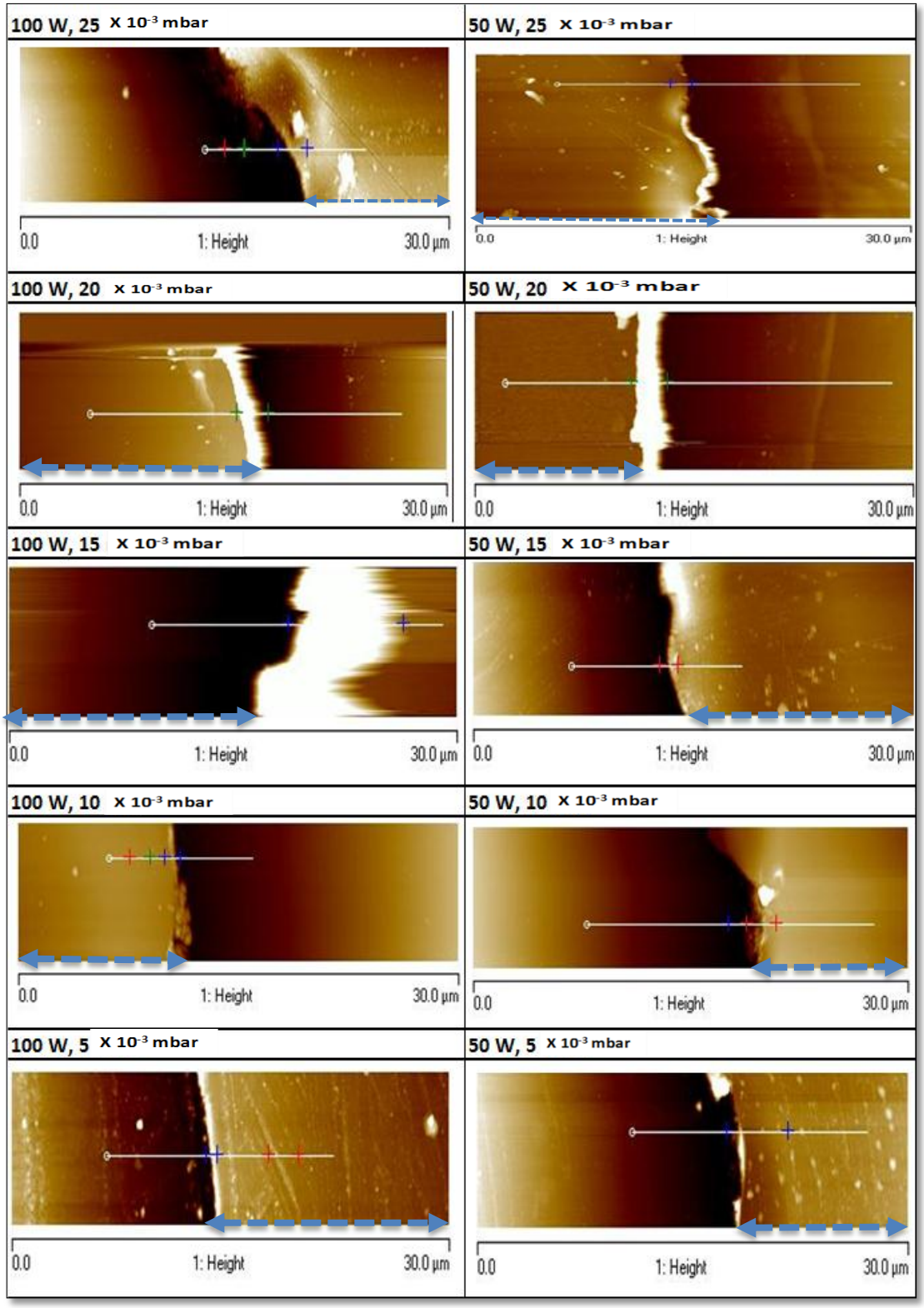

Figure 135: AFM topographic images of NiTi deposited on Si substrate at 50 and 100W at process pressures ranging from 5 x 10^{-3} to 25 x 10^{-3} mbar. The coatings marked with a double-headed arrow underneath, appear with a step-edge on the Si substrate.

The SEM and AFM images in Figure 134 and Figure 135 were compiled to investigate the influence of changing power on the surface morphology of PVD sputtered NiTi. SEM images in Figure 134 present the significance of changing power from 100 and 50W, when the films were deposited at 20 x 10^{-3} mbar. The AFM images in Figure 135 allow further examination of the surface for the variance in deposition power from 100 to 50 W at a range of process pressures.

The thin films have defect-free surface with grains having some crystals emerging from the grain boundaries of the granular clusters. The size of the clusters increases with decreasing the deposition pressure and relatively more defined grain boundaries appear in Figure 134B. Larger grain size and wider columns account for a slightly rougher surface of the film deposited at 50W compared to the film deposited at 100W, while the pressure (20 x 10^{-3} mbar) was the same for both depositions (Figure 135). This relates to the fact that the deposition of NiTi at higher power delivers more energy for the plasma and higher sputtering rate results in thicker thin films having a smoother surface.

The appearance of furrows around each columnar grain accounts for the parent austenite phase developing along with precipitates due to Ni-rich film composition. The film deposited at 100W has a densely packed columnar microstructure matching to zone T of the Thornton diagram and growth pattern resembles Stranski-Krastanov's layer plus island growth mode. In the Stranski-Krastanov's layer plus island mode, the formation of islands is accompanied by the development of sub-layers. Surface energy is higher for the thicker films and a layer on the top of the substrate is strained to fit the substrate, which can be seen for both of the images presented in Figure 134 where cracks have started to form at column boundaries. Decreasing the deposition power to 50W changes the microstructure of NiTi thin films by increasing the grain size and corresponds to zone 2 of the Thronton zone model.

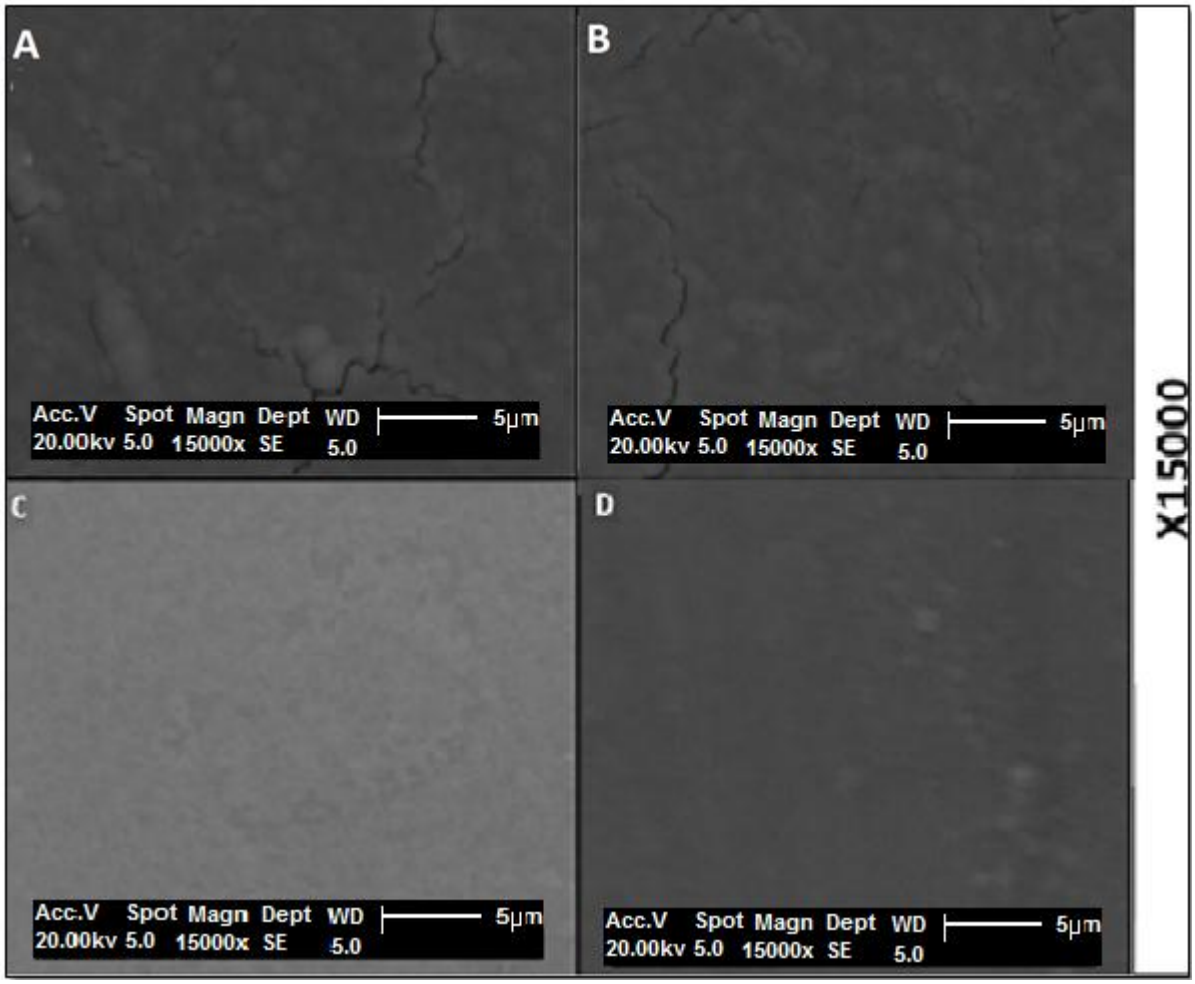

Figure 136: SEM images (x15000) for NiTi samples deposited at 100W (a) 25 mbar (b) 20 x 10^{-3} mbar (c) 10 x 10^{-3} mbar (d) 5 x 10^{-3} mbar.

Figure 135 and Figure 136 present the effect of varying the process pressure on the morphology of PVD sputtered NiTi. SEM images in Figure 136 show the influence of varying the process pressure in the range of 25 x 10^{-3} to 5 x 10^{-3} mbar, when the films were deposited at 100W. The AFM images in Figure 135 show the topographical surface of NiTi films, which were deposited at 100 and 50 W. A detailed analysis of the SEM and AFM images is given below.

Figure 136 shows all thin films having a defect-free surface with crystalline austenite phase incipient on the amorphous grain boundaries of the granular clusters. The size of the clusters decreases with decreasing the deposition pressure, and relatively more defined grain boundaries appear in Figure 136A and Figure 136B. The larger grain size and wider columns in the SEM of NiTi shown in Figure 136A and Figure 136B account for the increasing surface roughness at 100W along with higher

process pressures. Figure 136C and Figure 136D demonstrate a densely packed surface at lower pressures matching to zone T of the Thornton zone model. Thornton et al. added zone T between zones 1 and 2 of the thin film models to explain the influence of process pressures on the microstructures. The microstructure in zone T consists of a dense array of poorly defined fibrous grains, and the surface of films is relatively smoother and the deposition rates are higher than the films having microstructure matching to other Thornton zones [49]. This region typically contains densely packed fibrous grains as shown in the Thornton structure-zone diagram (Figure 11), which relates well to the surface images shown in Figure 135 and Figure 136, and the trend of deposition rates provided in Figure 109 and Figure 110. A decrease in sputtering gas pressure during deposition results in larger mean free paths of particles; therefore, the increased kinetic energy of the species impinges the particles on the substrate surface resulting in relatively dense microstructures [49].

The surface roughness decreases continuously by decreasing the process pressure from 25 x 10^{-3} to 5 x 10^{-3} mbar, which is associated with the fact that the deposition rates of NiTi increase with the increasing process pressure; consequently, the deposition thickness increases with increase un process pressure. Thus, increase in pressure makes the NiTi film smoother and defect-free due to increasing deposition thickness and packing density of granular clusters. NiTi thin films sputtered at higher process pressures deposit as a columnar microstructure matching to zone 2 of the Thornton diagram, which can be shown by the columnar cracks in the SEM images (Figure 136A and Figure 136B). The appearance of cracks around columnar grains relates to the B2 phase developing along with Ni_4Ti_3 precipitates. Similar cracks can also be seen in Figure 135B. These cracks appear due to tensile stress most at the interface of B2 phase and Ni_4Ti_3.

6.6.3 Wetting angles of PTFE and NiTi thin films

Alongside the control on microstructural and morphological properties of intercalated PTFE-NiTi nanocomposite, this project also proposed to investigate and characterise the functional responses of intercalation in the nanocomposite by wetting angle measurements. For this reason, it is very significant to examine the wetting angles of NiTi and PTFE, and to understand the influence of process parameters on the wettability of thin films. Figure 137 and Figure 138 show the effect of changing deposition power and process pressure respectively for PTFE thin films, whereas Figure 139 and Figure 140 display the influence of varying power and process pressure respectively for NiTi deposition.

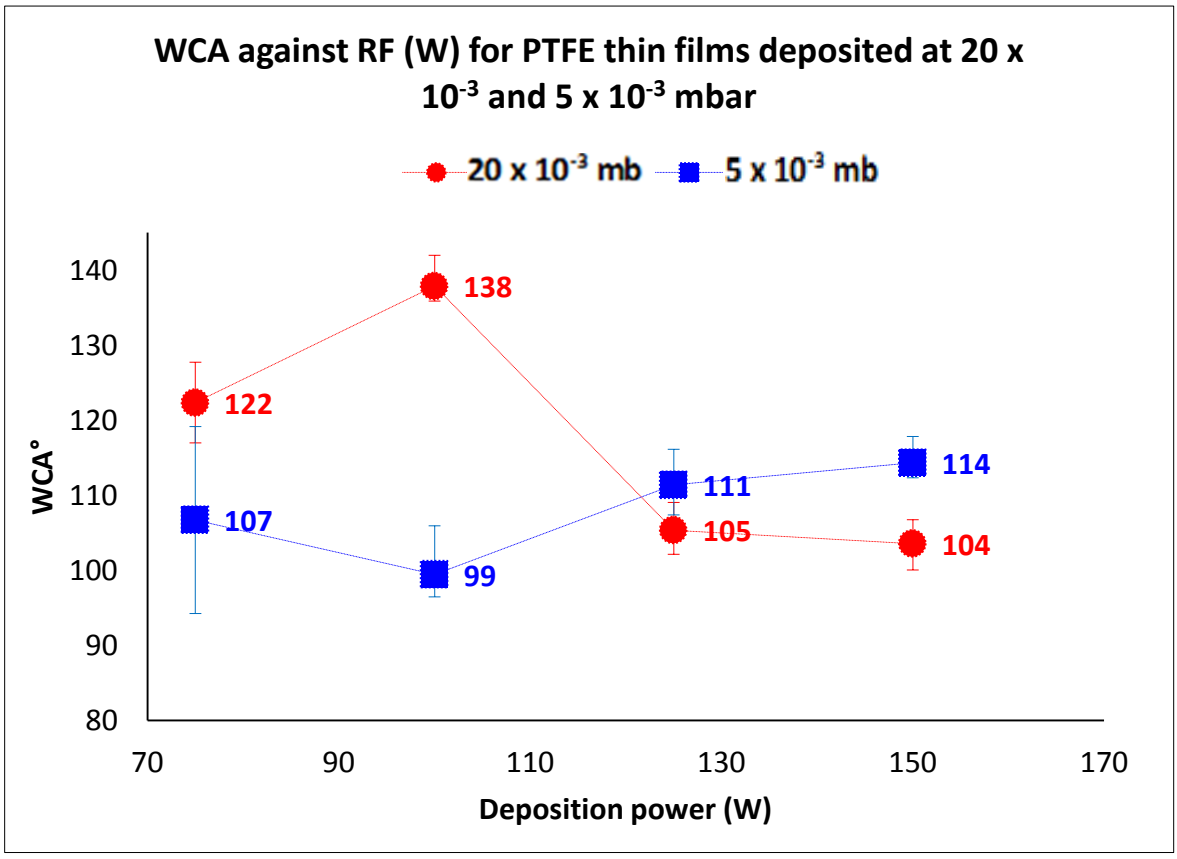

Figure 137: WCA against RF (W) for PTFE thin films deposited at 20 x 10^{-3} and 5 x 10^{-3} mbar.

Increasing the RF from 75 to 100 W, increases the WCA from 122° to 138°. Further increase in deposition power (150W) decreases the WCA to 103°. A similar trend was observed by Qi et al. [34] for depositing 250 nm thick PTFE film at 30 x 10^{-3} mbar in N_2, when the pressure varied from 25 to 200 W. This study shows that the

WCA increases with increasing deposition power up to 100W, whereas a constant decrease in WCA is observed on increasing the RF power above 100W. The explanation of the above trend can be found by considering the deposition rate vs. power pattern in Figure 107. Similar trend-lines as the above-discussed pattern can be seen in Figure 107 for deposition at 25 x 10^{-3} and 20 x 10^{-3} mbar. The trend-lines explain that the changes in wetting angles of PTFE are directly related to deposition rates, hence, the film thickness. The same result is experiential for WCA vs. power trend-line at 5 x 10^{-3} mbar in Figure 137, where the WCA slightly decreases followed by a slow and steady increase.

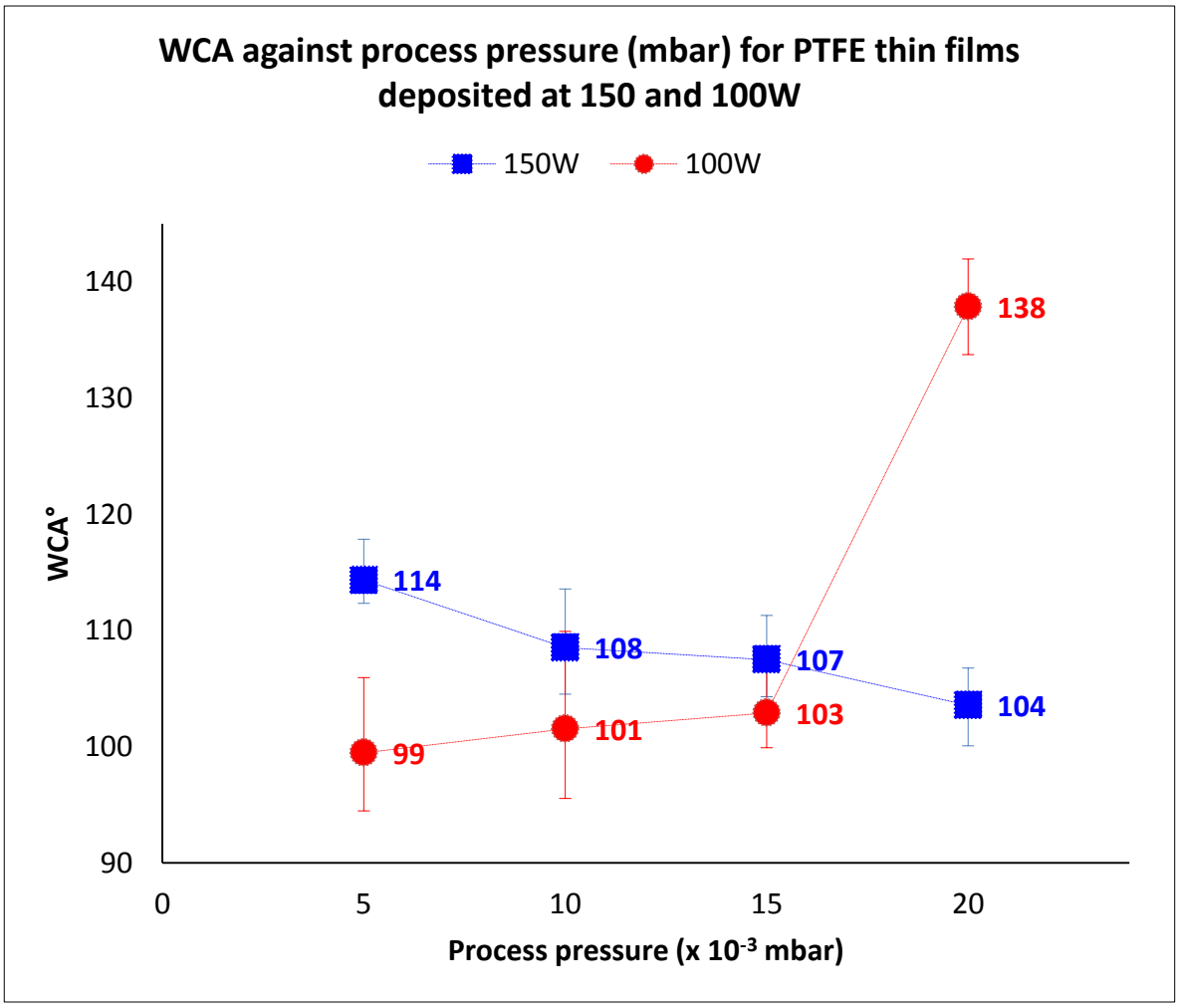

Figure 138: WCA against process pressure (x 10^{-3} mbar) for PTFE thin films deposited at 150 and 100 W.

Figure 138 shows that increasing the process pressure from 5 x 10^{-3} to 20 x 10^{-3} mbar reduces the WCA at high deposition power (150W), and the trend reverses at a lower deposition power of 100W. The most hydrophobic PTFE film was observed at 100W and 20 x 10^{-3} mbar, which relates to oxygen, entrapped within the polymer chains at high deposition pressures. The combined presence of oxygen and fluorine in the polymer structure intensifies the electronegativity resulting in the greater repellency to the water droplet on the thin film surface resulting in higher WCA.

A higher CF and CF_x incorporation at the film surface results in compact film with high hydrophobicity. The deposition rate and hydrophobicity decline with a simultaneous increase in process pressure and deposition power, because of excessive fragmentation and local target melting leading to less compact thin film surface with reduced film thickness. At low pressures, the deposition rate vs. deposition power becomes independent of the changes in deposition pressure, and higher deposition powers prevent excess fragmentation and reduce polymerization time resulting in thicker and more hydrophobic films.

Combining the WCA results with the explanation of Figure 130 and Figure 131 reveal that at high deposition pressures (20 x 10^{-3} – 25 x 10^{-3} mbar), increasing powers increase the surface roughness and hydrophobicity of PVD-PTFE thin films. Biederman et al. [74] and Drabik et al. [14] observed an increase in WCA by increasing process pressure for 200W RF deposited films (Figure 27), which is different to the trend seen in this study. The difference in trend is due to the much greater magnitude of RF power used and comparatively lower range of process pressures selected in their reports. At such high deposition power and lower process pressures, the sputtering yield is higher and more compact and thicker films are produced showing a rise in hydrophobicity.

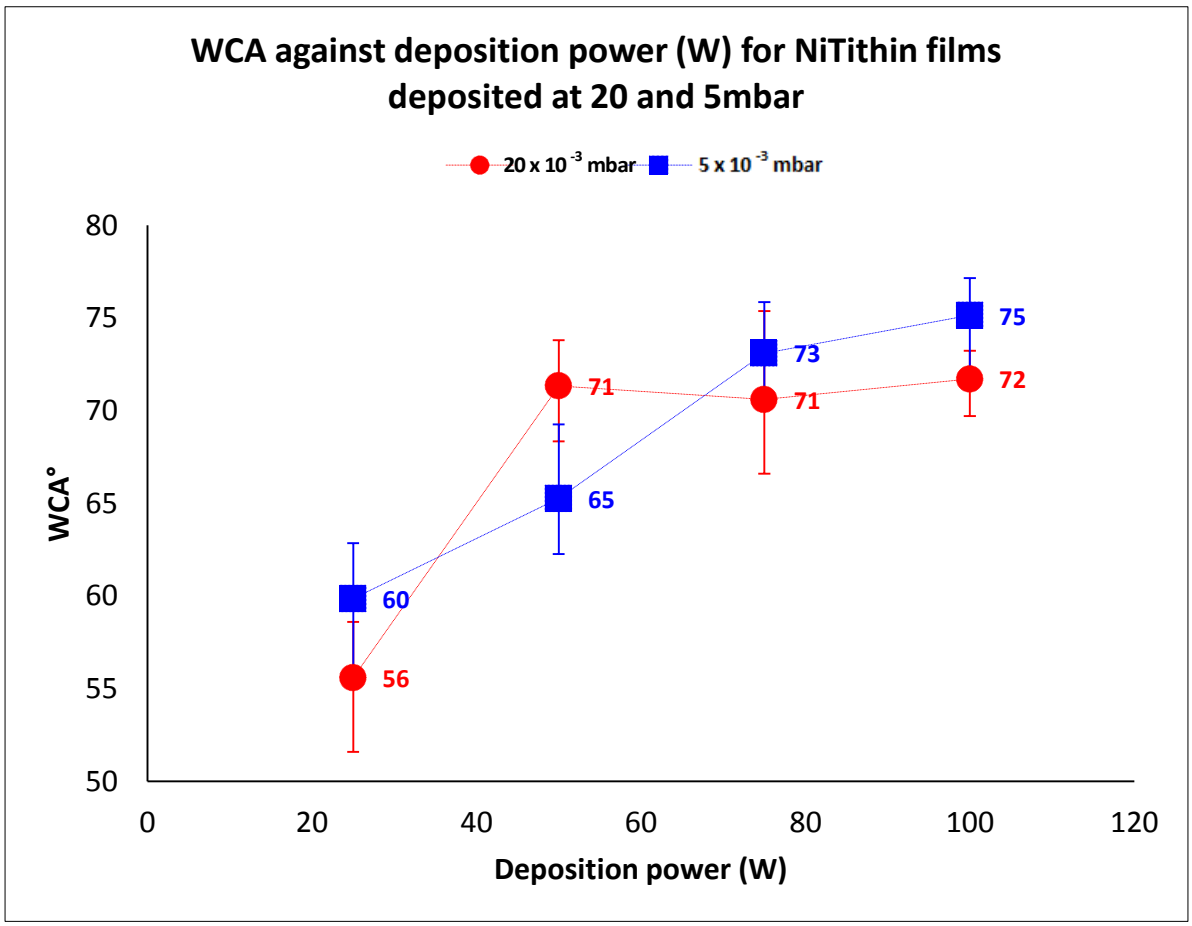

Figure 139: WCA against deposition power (W) for NiTi thin films deposited at 20 x 10^{-3} and 5 x 10^{-3} mbar.

Figure 139 show that the WCA of NiTi thin films increases with an increase in deposition power, which relates to the film thickness. To understand this relationship, the trend of WCA against deposition power is observed in conjunction with the results relating to Figure 109. Figure 109 shows that the deposition rate of NiTi thin films increases with increasing deposition power because of more energy available for sputtering. However, at high process pressure of 20 x 10^{-3} mbar, the WCA does not alter significantly with increasing power above 50W (Figure 139). This relates to the deposition thickness not changing at those process conditions (Figure 109). TiO_x formation at the high process pressures is associated with the increased deposition thickness at higher pressure is because a combination of high power and high process pressures favour TiO_x and atomic Ni deposition rather than NiTi deposition (sections 3.3 and 6.4), resulting in slight deviation in wetting angles at 25 x 10^{-3} mbar and 5 x 10^{-3} mbar process pressures.

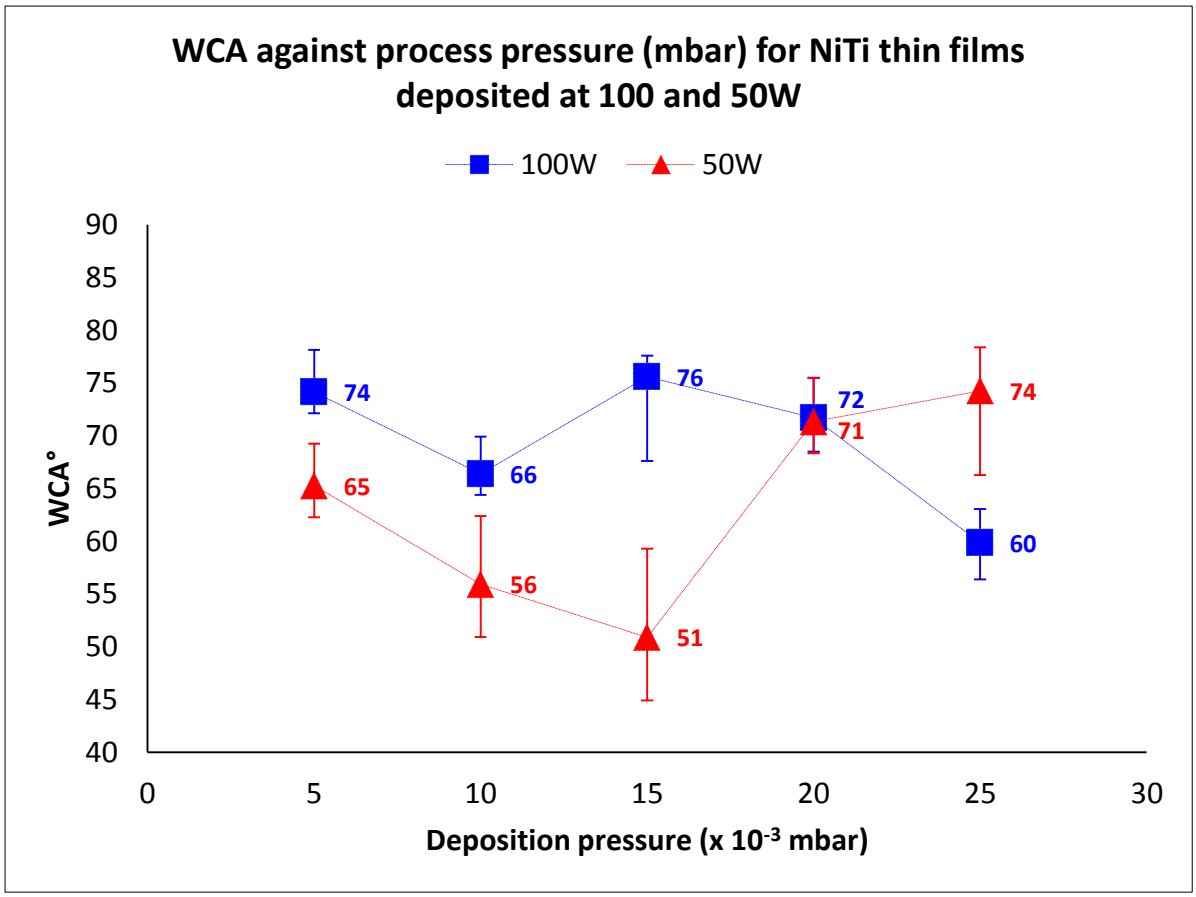

Figure 140: WCA against process pressure (mbar) for NiTi thin films deposited at 100 and 50W.

The WCA vs. process pressure trends presented in Figure 140 are for NiTi thin films deposited at 100 and 50 W. Similar to the results presented in Figure 139, the WCA changes with variance in deposition thickness; therefore, correlates well to Figure 110. At low process pressures, the WCA of NiTi thin films decreases with increasing process pressures and this pattern is similar at 100 and 50 W deposition. However, the high process pressure contributes to the deposition of TiO_x and atomic Ni on the surface of NiTi thin film, resulting in dissimilar WCA vs. deposition pressure trends at 100 and 50W.

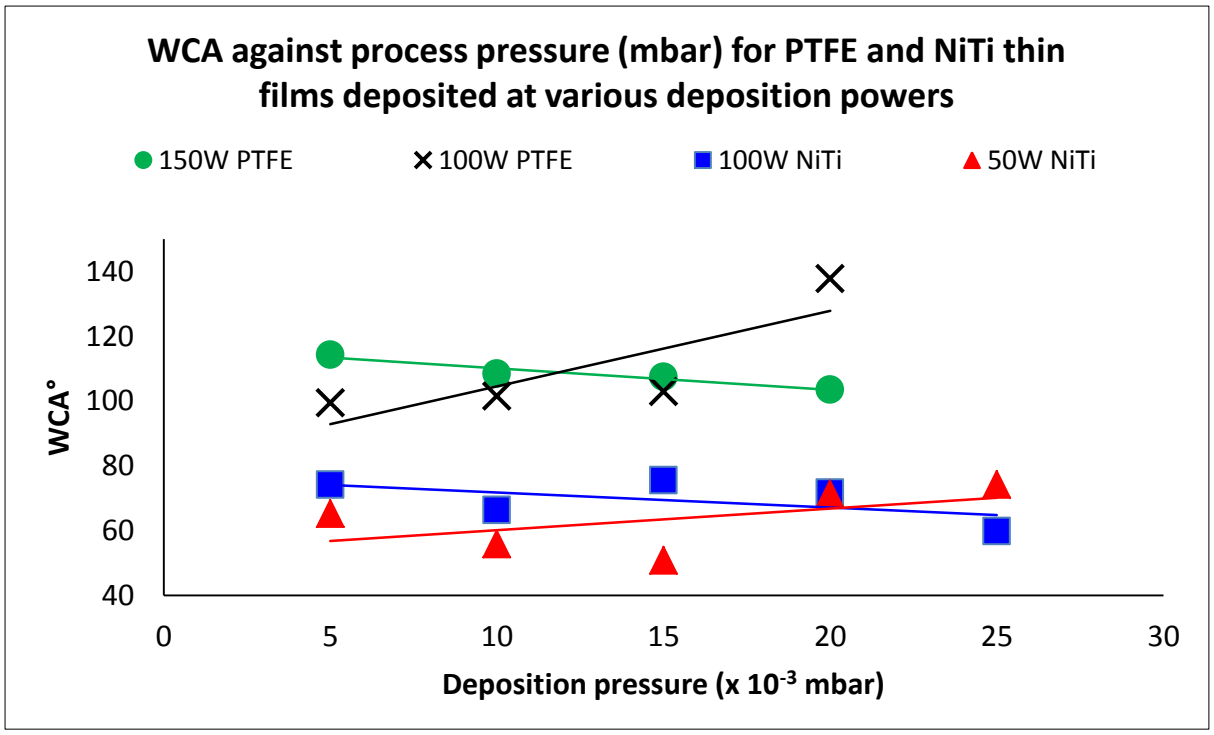

Figure 141: WCA against process pressure (mbar) for PTFE and NiTi thin films deposited at various deposition powers.

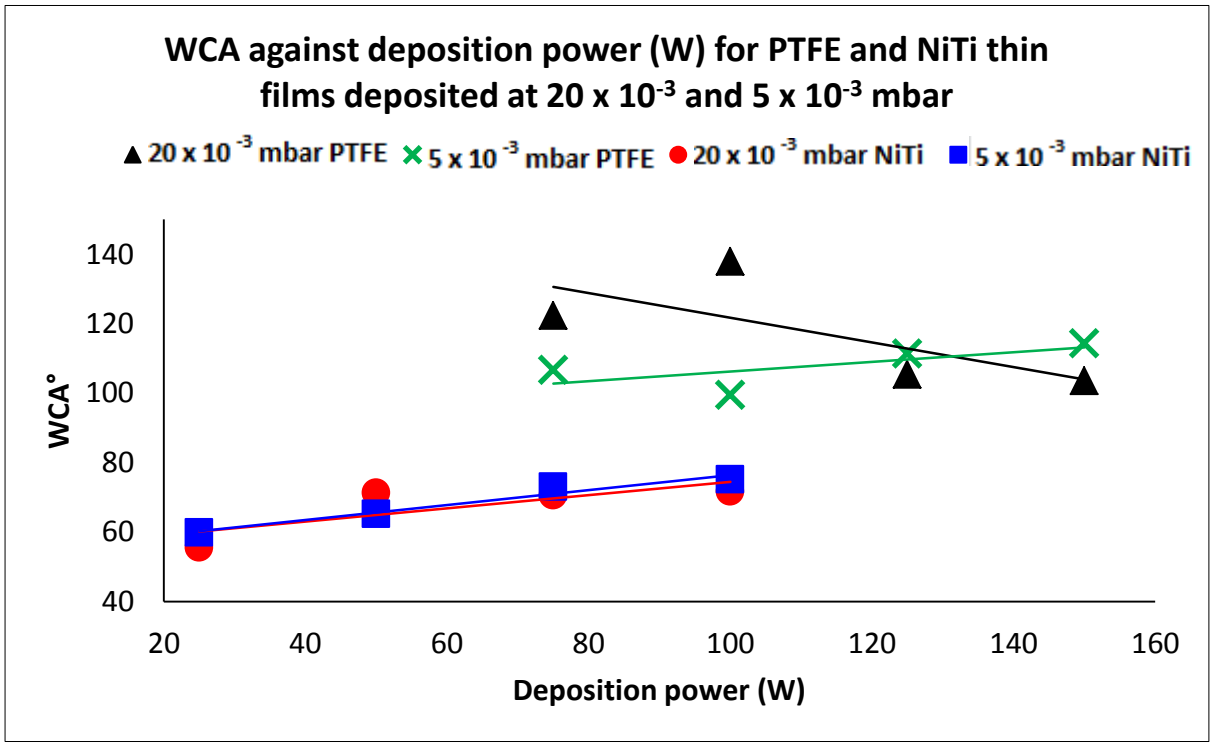

Figure 142: WCA against deposition power (W) for PTFE and NiTi thin films deposited at 20 x 10^{-3} and 5 x 10^{-3} mbar.

Figure 141 and Figure 142 combine and summarise the above-discussed results of WCA vs. process parameters for PTFE and NiTi thin films. PTFE is more hydrophobic than NiTi at all process conditions. However, the difference between the wetting angles for both materials changes with changing process parameters. The film structure and morphology of PTFE is more susceptible to changes in variance in deposition conditions, as compared to NiTi because of plasma fragmentation mechanism during sputtering. The changes in the film structure and morphology change the surface energy and roughness, and for that reason the WCA of PTFE thin films alters. The WCA of NiTi thin films is relatively unaffected by the changes in deposition parameters (Figure 142). The trend-lines presented for NiTi in Figure 141 are somewhat opposite to each other due a thermodynamic competition between TiO_x and Ti with changing process parameters. Increasing process pressure increases the amount of residual oxygen adsorbed into the system along with working gas while increase in power provides more energy for the thermodynamic reactions. TiO_x needs more energy for deposition as compared to Ti; thus, higher pressure and power combinations favour TiO_x deposition within the film.

6.6.4 Lubricity of PTFE and NiTi thin films

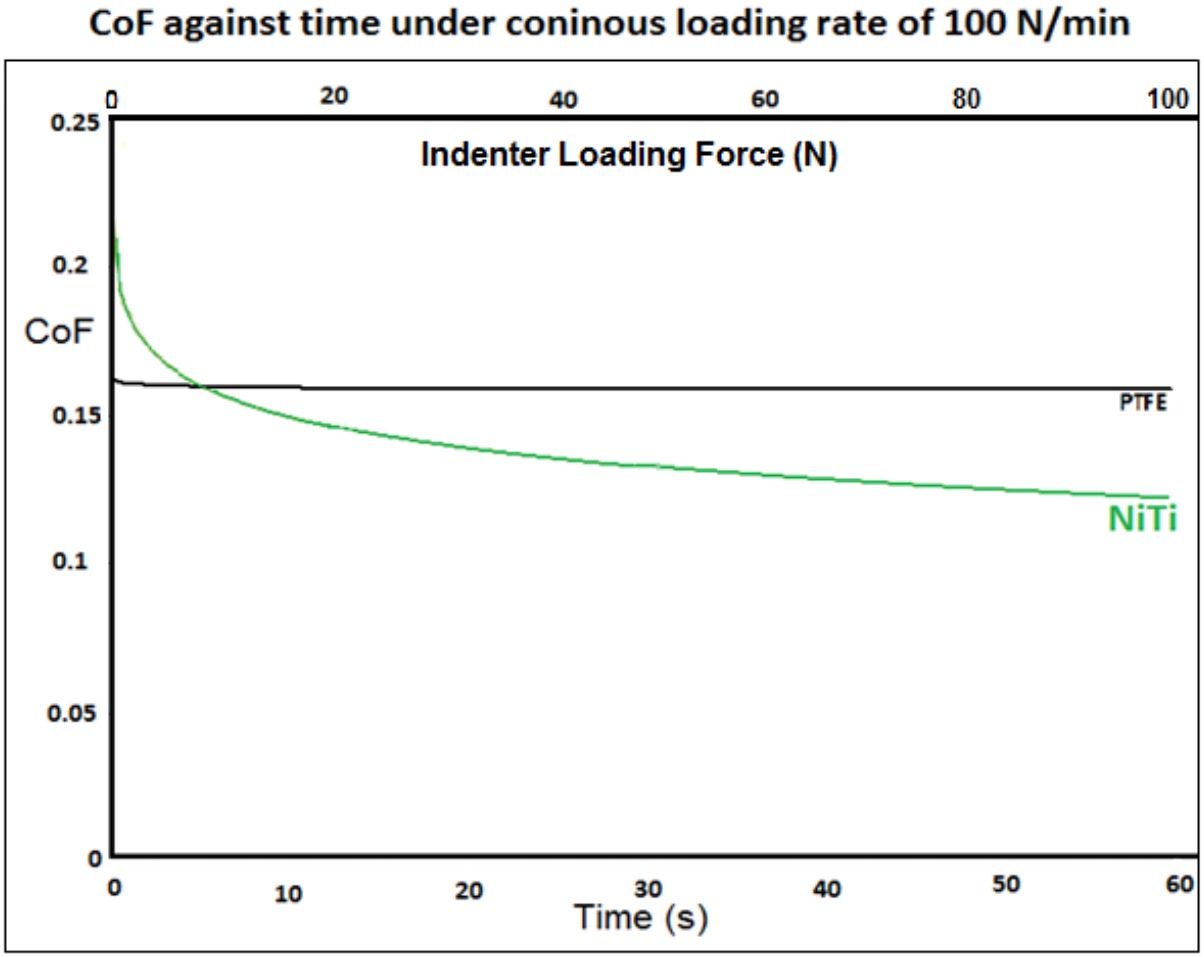

Figure 143: Coefficient against time under continuous loading rate of 100N/min for PTFE and NiTi thin films.

Single pass scratch tests were performed to analyse the lubricity of the PTFE and NiTi thin films, using a tungsten carbide ball indenter operating under continuous progressive loads, with forces ranging 1 – 100 N at loading rate of 100 N/min having maximum friction force of 50 N. The CoF as a function of time (logarithmic regression) was plotted for PTFE and NiTi thin films, shown in Figure 143. PTFE deposited in this study has a constant coefficient of friction of 0.17 for contact loads from 0 to 100 N. NiTi displays a drop in CoF from 0.22 to 0.13, with increasing load. PTFE maintains the friction coefficient at approximately 0.17 with increasing loads while NiTi is more lubricious than PTFE at higher loads.

6.6.5 Summary

All SEM images of PTFE deposited on glass show no irregularities, and suitably matches with other methods used to prepare nano-PTFE films. All images show smooth and continuous surface morphology with minimal defects. Similar observations were deduced from the AFM images. The deposition parameters alter the surface structure of thin films deposited for an equal amount of time. Thinner coatings grow in Volmer-Weber's 3D island growth mode and have a granular structure with discrete 2D islands. As the deposition thickness increases, the film grows in Stranski-Krastanov's layer plus island growth mode, leading to the formation of multiple sublayers covering dense clusters of C-C chains arising in a perpendicular direction to the substrate. This structure appears as folds on the surface of the thin films. The surface roughness of thin films increases with increasing deposition power and decreasing the process pressure. The smoothness of thin films at low deposition pressures relates to the lack of polymerization. The lack of polymerisation at low process pressure occurs as a consequence of the unreacted monomers, short PTFE fragments and amorphous PTFE assembling within the composition of the PTFE during PVD sputter deposition.

All SEM and AFM images of NiTi deposited on glass are defect-free and exhibit a continuous surface morphology. The growth mode for all NiTi films is Stranski-Krastanov's layer plus island. The appearance of furrows and channels around each columnar grain accounts for the parent austenite phase developing with some Ni-rich precipitates. The cluster size increases with decreasing deposition power and relatively more defined grain boundaries form. The cluster size decreases by decreasing the deposition pressure, demonstrating a densely packed smoother surface, due to increasing deposition thickness and packing density of the granular clusters. NiTi thin films sputtered at higher process pressures deposit with a columnar microstructure corresponding to the zone 2 of the Thornton diagram. Decreasing the deposition pressure decreases the grain size, which corresponds to the zone T of the Thronton zone model.

PTFE thin films are more hydrophobic (WCA range: 99° – 137°) than NiTi thin films. NiTi has the WCA ranging 55° to 75°. Both types of coatings were stable when exposed to continuous progressive loads, with forces ranging from 1 to 100N at

loading rate of 100 N/min. NiTi displays a drop in CoF from 0.22 to 0.13, with increasing load. PTFE maintains the friction coefficient at approximately 0.17 with increasing loads, so NiTi is more lubricious than PTFE at higher loads.

6.7 Selection of the process conditions for PTFE-NiTi

PVD sputtering is a nanoscale manufacturing method and the deposition of a nanocomposite by PVD sputtering requires a good control on the compositions and process conditions. For this reason, for both PTFE and NiTi, the process parameters, composition, structure, morphology, and the functional properties such as wetting angles and lubricity were studied in detail (Sections 6.1 – 6.5). This provided a comprehensive understanding of maximum factors that may influence the composition or performance of the intercalated PTFE-NiTi nanocomposite. The findings from the results reported in sections 6.1 – 6.5 and the information provided in the literature were considered to draw following directions for the fabrication of PTFE-NiTi nanocomposite.

Location of the substrate holder in the sputter coater

The substrate holder was placed at a constant location outside the magnetron ring (3 cm from the target centre) for depositing the layered nanocomposite, where it provided higher deposition rates as well. The vertical target-substrate distance was maintained at 10 cm for the fabrication of both layered and co-sputtered nanocomposites.

NiTi atomic composition

Heat treatment is not performed to crystallise NiTi deposited in nanocomposites because the melting temperature of PTFE (327°C) is below the crystallisation temperature of NiTi (497°C); consequently, NiTi in PTFE-NiTi is amorphous in this study. However, one of the objectives of this research is to select NiTi atomic composition that is suitable to perform the pseudoelastic transformations. The atomic composition is the most important factor affecting the phase transformations and crystal structures of PVD-NiTi thin films. Ni-rich $Ni_{53.5}Ti_{46.5}$ thin film composition is selected as for the production of PTFE-NiTi nanocomposite. Small Ni pieces are placed on racetrack of the target to get a desired atomic composition of NiTi.

Selection of PTFE target material

PTFE target material was selected after ensuring that the deposited thin films have excellent polymerisation extent and hydrophobicity.

Deposition power and process pressure

The deposition rates can be used to calculate the layer thickness and the content of each material deposited in the nanocomposite at a given time. Thus, the process parameters of power and pressure allow altering the deposition rate of PTFE and NiTi, and controlling the nanocomposite volume fraction. This approach enables adjusting the nanocomposite composition and the properties of the nanocomposites. High deposition rate of both PTFE and NiTi can be achieved by maintaining low-pressure and high power. At any specified process pressure and power, the deposition rate of NiTi is greater than that of PTFE. This difference is more significant at lower pressures but lesser at higher process pressures.

The process pressure is increased to obtain high deposition rates at small power values for PTFE. However, this is avoided in this project because of a higher Ti affinity of NiTi with oxygen to make TiO_x; hence, maintaining low pressures are essential to deposit NiTi in PTFE-NiTi production. A combination of relatively small magnitudes of base pressure, low process pressures and small magnitudes of deposition powers avoid the oxidation of NiTi thin films. The above results restrict the working parameters within the range of 5×10^{-3} to 10×10^{-3} mbar and DC power supply to 50 and 25 W for future NiTi depositions.

Polymerisation ratio of PTFE

PTFE deposition at 150W and 15×10^{-3} mbar results in highly polymerized content in PVD-PTFE films, whereas the polymerization decreased with increasing pressure to 25×10^{-3} mbar and decreasing the pressure to 5×10^{-3} mbar. For the PTFE thin films sputtered at 25×10^{-3} mbar, the more polymerization was successful at 100 and 150 W, which decreased with decreasing the RF to 50W. Thus, the polymerization was limited to 50W and 5×10^{-3} mbar process parameters resulting in highly branched fragments with an excessive crosslinking, and a high proportion of unreacted monomers producing rougher thin films. This further restricts the deposition pressure to 10×10^{-3} mbar and RF to 150W.

The preferable process parameters for PTFE-NiTi manufacturing are 10×10^{-3} mbar Ar pressure, 150W RF for PTFE and 50 or 25 W DC for NiTi deposition.

6.8 Co-sputtered PTFE-NiTi thin films

PVD magnetron sputter prepared, co-sputtered PTFE-NiTi thin film nanocomposites have variable volume fractions. The film thickness and the volume fractions of PTFE and NiTi were controlled by selecting various sputtering conditions (power and pressure). Figure 144 is a modified version of Figure 112, where the data-points representing the deposition parameters of different nanocomposites are enlarged and labelled. Desired volume fractions for all PTFE-NiTi nanocomposite specimens were obtained by sputtering the materials at the deposition conditions highlighted in Figure 144. Nanocomposites were characterised by SEM-EDS and WCA measurements. Co-sputtered films labelled as PNK1, PNA2, and PNF3 were manufactured by depositing from PTFE and NiTi targets simultaneously. Figure 145 shows the schematic plan of the thin films in which the depositions of PTFE and NiTi on the substrate are illustrated in pink and blue colours respectively. Table 26 presents the manufacturing parameters of the PVD co-sputtered films. PNK1, PNA2 and PNF3 were fabricated as NiTi-rich (35:65), nearly equal-composition (54:46), and PTFE-rich (60:40) nanocomposites respectively. The volume fractions of the nanocomposites were controlled by varying the deposition rate with respect to process parameters. The deposition of PNH4 and PNR5 films was attempted as well by single target source containing mainly PTFE target material with NiTi pieces added to the racetrack.

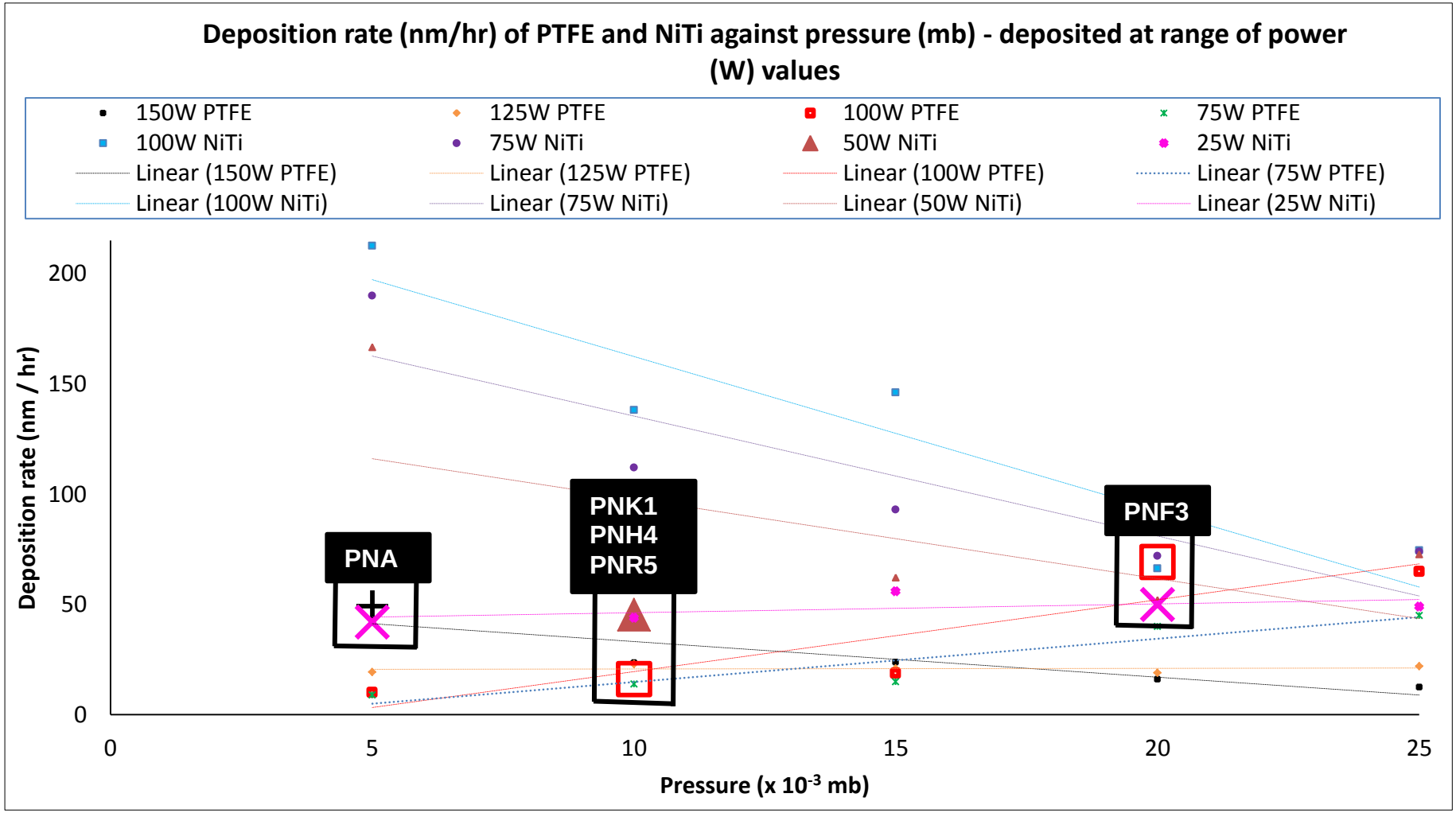

Figure 144: Deposition rate (nm/h) of PTFE and NiTi against power (W) - deposited at range of pressure values. The marked data - points represent the process parameters selected for the deposition of PTFE-NiTi nanocomposites.

Table 26: Manufacturing parameters for PVD co-sputtered PTFE-NiTi thin films. Cosputtering reduces the deposition rates by three times. The deposition rates mentioned in the table were measured in stationary mode PVD sputtering and provide the relative values only to obtain the desired volume fractions.

Specimen ID	**PNK1**	**PNA2**	**PNF3**	**PNH4**	**PNR5**
Volume fraction (PTFE:NiTi)	35:65	54:46	60:40		
Film thickness (µm)	0.5	0.5	0.5		
Pressure (x 10^{-3} mbar)	10	5	20	10	10
RF power - the PTFE deposition (W)	150	150	100	150	150
DC power - NiTi deposition (W)	50	25	25		
Deposition rate - PTFE (nm/h)	24	49	69		
Deposition rate - NiTi (nm/h)	45	42	52		
Deposition time (h)	30	30	30		
Intercalated nanocomposite	Yes	Yes	No	No	No

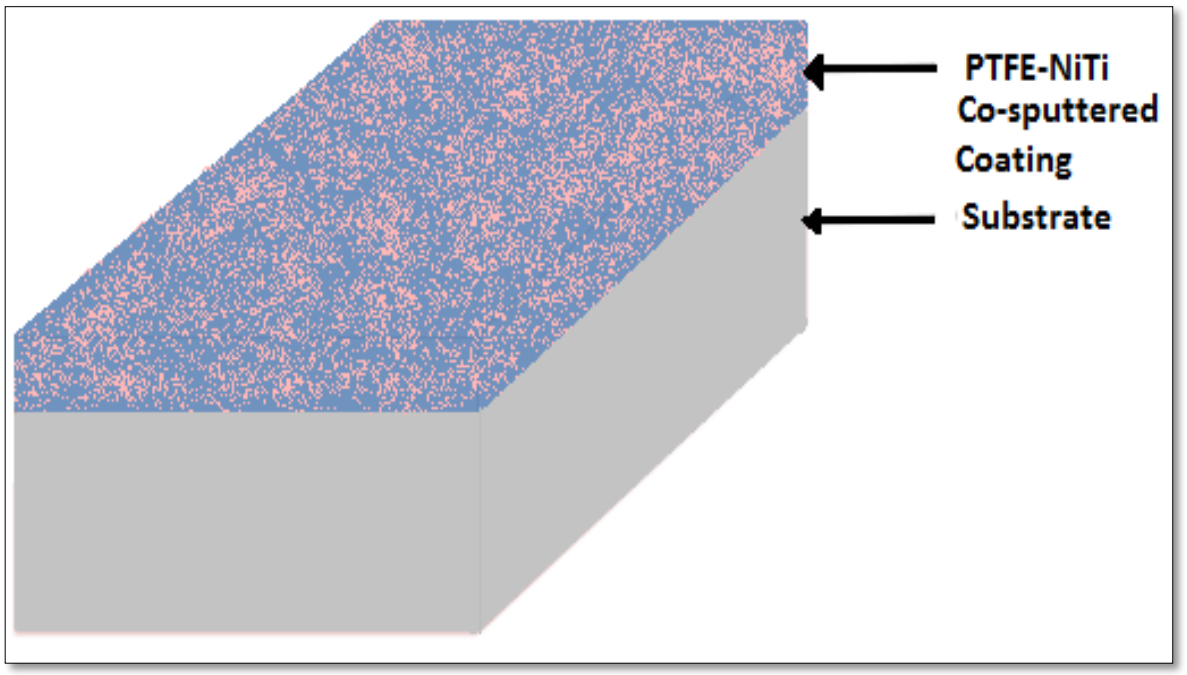

Figure 145: Schematic illustration for co-sputtered PTFE-NiTi thin films.

6.8.1 PTFE-NiTi – PNK1

The desired process parameters mentioned in section 6.6 were set to prepare a nanocomposite of 35:65 volume fraction of PTFE and NiTi. The selected process parameters are 10 x 10^{-3} mbar, 50W DC for NiTi deposition, and 150W RF for PTFE deposition, as highlighted in Figure 144.

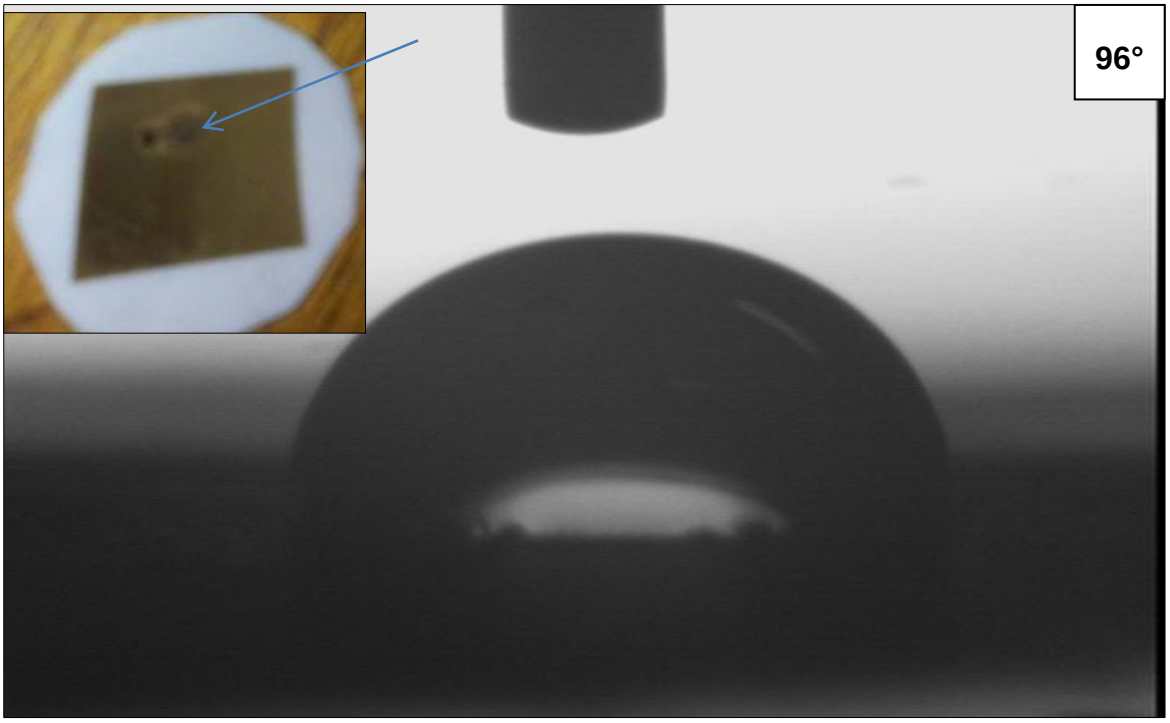

Figure 146: Image of an immediate WCA measurement on the surface of a PTFE-NiTi – PNK1 nanocomposite. The inset shows a picture of PNK1 film deposited on PTFE substrate.

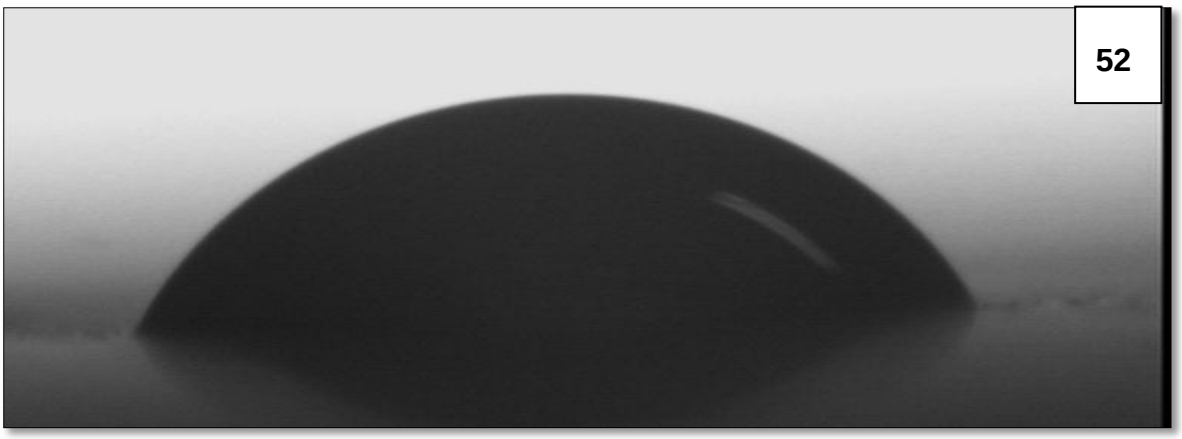

Figure 147: Water droplet on the surface of PTFE-NiTi – PNK1 after 10s.

PTFE-NiTi – PNK1 films are stable and adhesive to the substrate; however, WCA measurements demonstrated that the films have vacancies within the microstructure. The microstructural porosity was evident by absorbing of water droplets in the thin films during the WCA analysis, which lead to a drop in the WCA from 96° to 52° on the film surface in 10 seconds, as presented in Figure 146 and Figure 147. Water absorption can be verified by the leftover stain on the film surface indicating the area of water absorbance after the WCA measurements (Figure 146 inset). The amount of water absorbed by a 0.25 cm^2 area (volume: 0.05 mm^3) of 2 µm thick film was 0.017 µl. The quantity of water absorbed by a thin film was measured by dropping a small and known volume of water sessile drop on a specified area of the thin film by WCA equipment. Water was dropped until the water stopped diffusing into the nanocomposite structure, and any more water dropped by the WCA equipment stayed on the film surface. The absorbed water volume represents the vacant volume of the thin film, which is one-third of the total thin film volume. This indicates the presence of pores and vacancies within the film structure. The pores and vacancies forming within the nanocomposite structure might be forming because of the expanded interstitial gaps between PTFE and NiTi as a result of the intercalation. The co-sputtered nanocomposite was examined by EDS and SEM to investigate further about the possibility of an intercalated structure, and the results are presented in Figure 148 and Figure 149.

Figure 148 shows that the outcome of the EDS analysis reported the deposition of nearly equiatomic NiTi on the substrate, along with fluorocarbon. The double atomic percent of fluorine as compared to carbon indicates the chemical formula of PTFE monomer (- CF_2 -). Therefore, the empirical formula of the nanocomposite is [(- CF_2 -) – NiTi], where the stoichiometric ratio of carbon Ni and Ti is equal and a half of the fluorine. The EDS spectrum indicates a higher atomic percent of fluorine as compared to Ni and Ti, despite the lower volume fraction of the fluorocarbon, which can be described by a schematic illustration shown in Figure 150, which combines the EDS results with the surface morphology observed by SEM images.

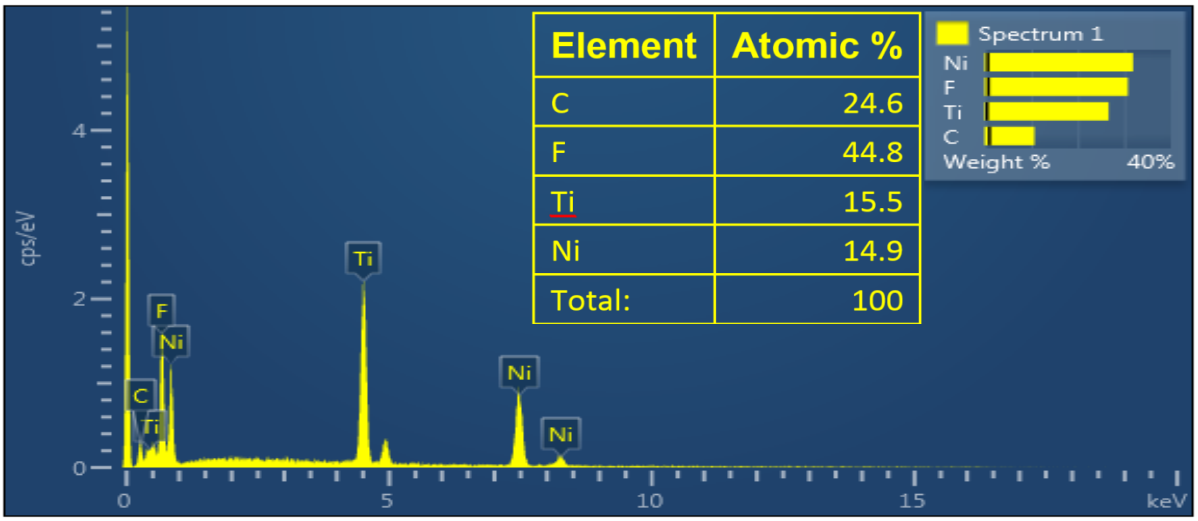

Figure 148: The EDS results for PTFE-NiTi – PNK1 nanocomposite.

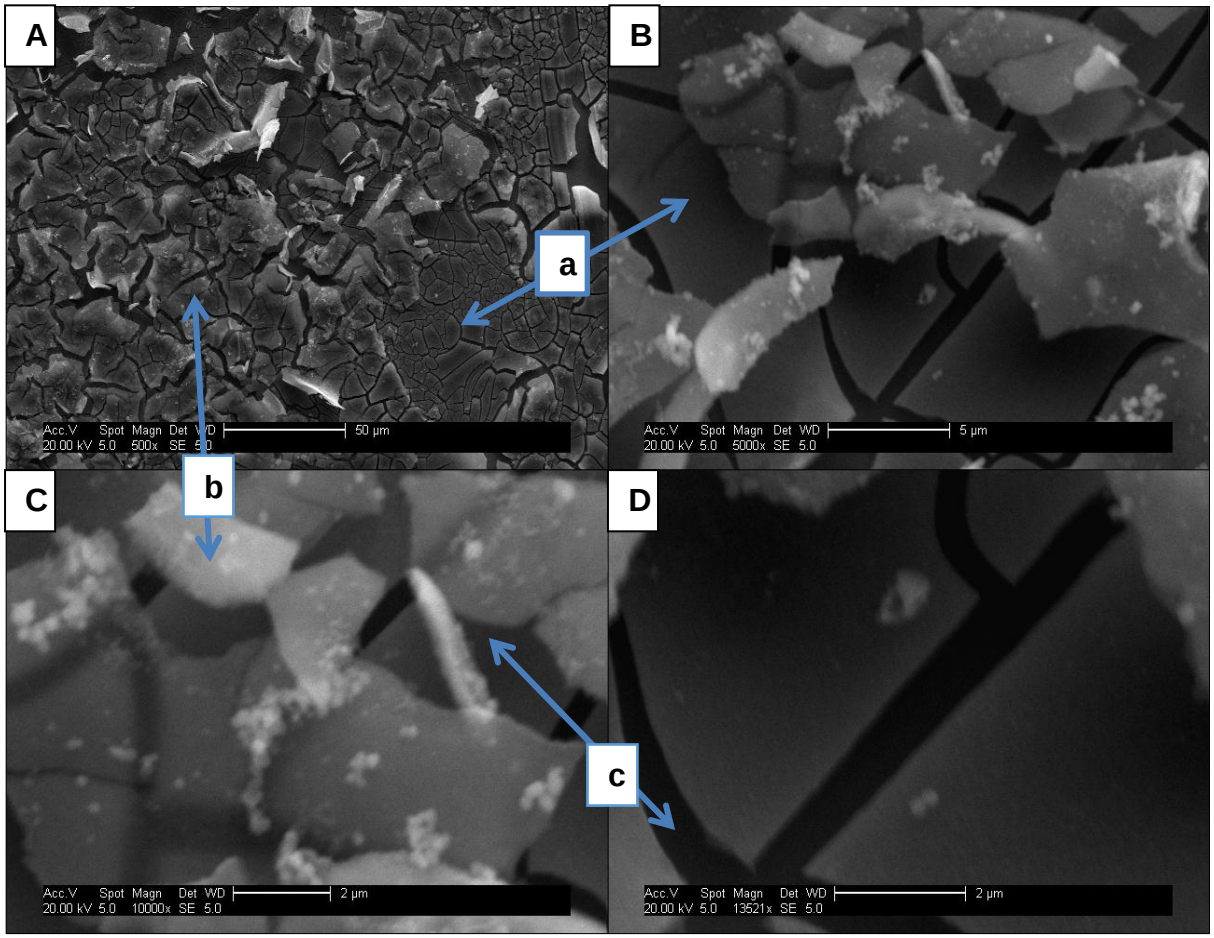

Figure 149: SEM images of PTFE-NiTi – PNK1 nanocomposite at magnifications of (A) x 500, (B) x 5000, (C) x 10, 000, and (D) x 20, 000. (a: PTFE, b: NiTi, c: inter-planar gaps between polymer chains and metallic lattice).

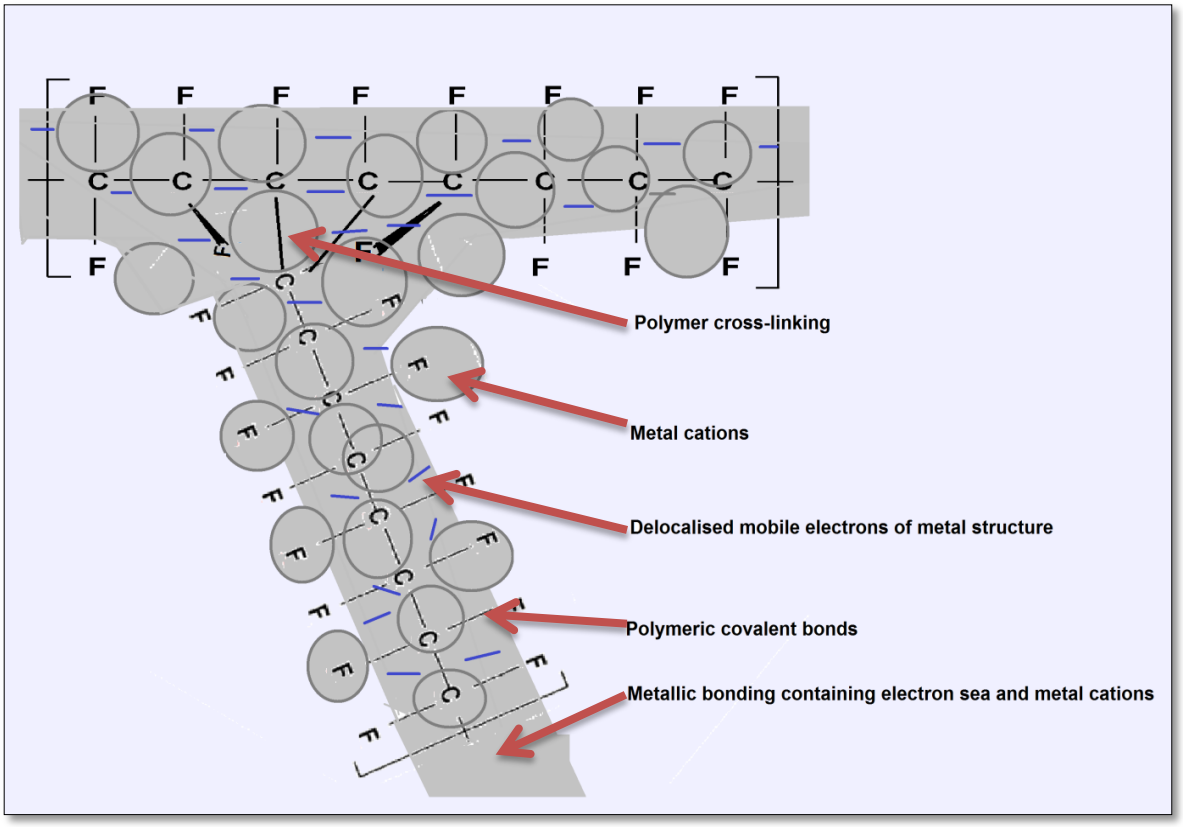

Figure 150: A schematic model of an intercalated PTFE-NiTi nanocomposite representing metallic structure of NiTi and covalent bonding in the PTFE, overlaying each other; while both materials reorient their atomic structure in order to accommodate the electrostatic repulsion between delocalized electrons of the metallic lattice and electronegative fluorine in polymer chain.

The schematic in Figure 150 illustrates the layout of a co-sputtered intercalated nanocomposite by PVD manufacturing. SEM images in Figure 149 show that PTFE and NiTi are present as discrete materials in the nanocomposite but retained within one microstructure framework. PTFE-NiTi nanocomposite contains metallic structure of NiTi and covalently bonded PTFE chains overlaying each other. The schematic illustration in Figure 150 displays that PTFE chains are somewhat continuous and cross-linked phenomena within and around the metallic lattice network. PVD-sputtered PTFE films contain cross-linked structure due to repolymerisation in the deposition plasma, as described in section 6.5. Both PTFE and NiTi in the nanocomposite formulate a matrix framework as explained below.

The metallic lattice and polymer chains reorient their atomic structure in order to accommodate the electrostatic repulsion between the delocalised electrons of

metallic lattice and electronegative fluorine in the polymer chain. The Van der Waal forces within hydrophobic and non-polar polymer chains and the electrostatic forces in the metallic lattice also contribute to realignment of the microstructure developing the interplanar gaps. Thus, the expansion of the overall microstructural nanocomposite lattice by secondary bonding (physical interactions and realignments) without causing changes to the primary structure and bonding, is called intercalation.

The electronegative nature of fluorine in the polymer chain keeps the fluorine atoms at the maximum possible distance from each other but within the chain geometry. The fluorine atoms that are covalently bonded around the carbon skeleton reorient themselves towards the outwards direction of the nanocomposite microstructure because of the repulsion from delocalised mobile electrons sea in the metallic lattice of the nanocomposite matrix. Outward reorientation of fluorine also explains the reason for EDS spectrum indicating higher atomic percent of fluorine as compared to Ni and Ti. The elemental detection spectroscopy is a surface analysis technique, and it mainly detects the elements at the top surface of the material. While aligning outward, fluorine also builds an affinity for positively charged metal ions of Ni and Ti. NiTi and Ti particles are firmly retained in the metallic lattice by electrostatic forces of attraction; thus do not leave the metallic lattice but incline slightly outwards because of the affinity for the electronegative fluorine atoms.

The WCA of the coatings was 96°, which is above NiTi WCA and below the WCA of PTFE deposited at specified power and pressure parameters (Table 26 and Figure 144). The WCA indicates interaction of NiTi with PTFE, as intercalated materials are expected to bond the two materials by internal physical interactions without any chemical reaction. Intercalation altered the wetting properties demonstrating changes in surface energy and morphology of the deposited materials. **The experimental results of nanocomposite PNK1 are the first to show fabrication of a PVD sputtered nanocomposite, which demonstrates intercalation between polymers and NiTi.**

6.8.2 PTFE-NiTi – PNA2

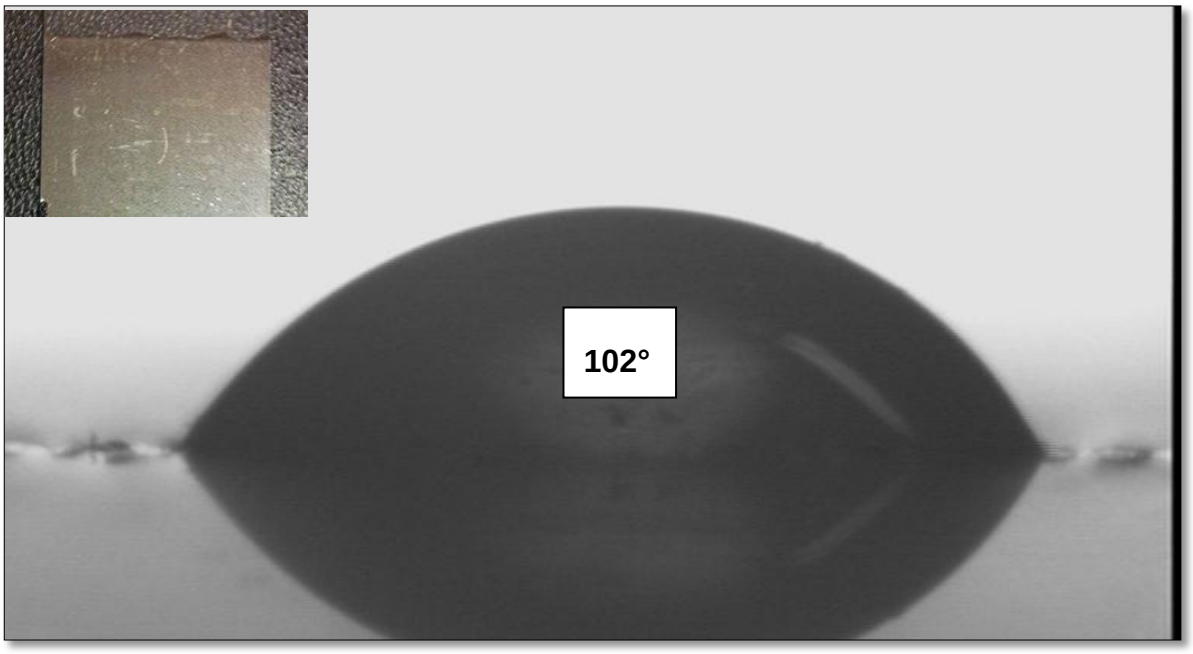

Figure 151: Image of an immediate measurement of WCA on the surface of a PTFE-NiTi – PNA2 nanocomposite. The inset shows a picture of PNA2 film deposited on the glass substrate.

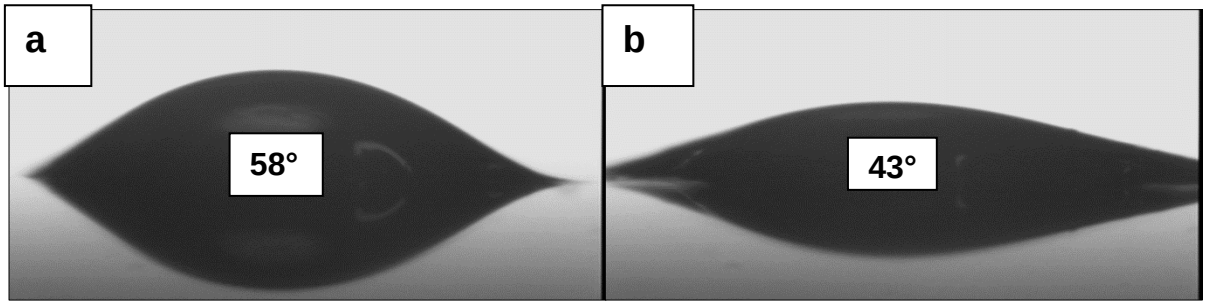

Figure 152: Water droplet on the surface of PTFE-NiTi – PNA2 nanocomposite after (a) 10s, and (b) 15s.

Ideally, a deposition pressure of 10 x 10^{-3} mbar should be maintained to ensure a high degree of polymerisation of PTFE (section 6.5.3), but PTFE always deposits at lower deposition rate than NiTi. Higher deposition rate of NiTi than PTFE trend has few exceptions, for example, PTFE and NiTi deposit at approximately same deposition rate (49.2 and 42 nm/h respectively) at low pressure and high RF combination. Therefore, the process conditions of 5 x 10^{-3} mbar Ar, 150W RF power for PTFE and 25W DC power for NiTi are a compromise in terms of deposition

pressure; hence, PTFE-NiTi nanocomposite (PNA2) is deposited with volume fraction of 54:46. The deposited films of the nanocomposite are well adherent to the substrate. The WCA of 102° indicates a strong intercalation between PTFE and NiTi within the microstructure of the nanocomposite (Figure 151). The WCA reduces to 58° and 43° after 10 and 15 seconds respectively, subsequent to the water drop from the WCA measuring equipment (Figure 152). Similar vacancies, cracks and pits are observed to those seen in PNK1 film.

The stoichiometric difference between PNK1 and PNA2 thin films can be described by EDS-SEM results provided in Figure 153 and Figure 156. Atomic percent by EDS show the deposition of Ni-rich NiTi, which is evident because of Ni having faster sputtering rate than titanium and additional Ni pieces added to the target racetrack in order to adjust the alloy transformation below the body temperature, as explained in section 6.4. The fluorocarbon content detected on the surface by EDS is also exceptionally high, despite equal volume fraction of PTFE and NiTi in the nanocomposite. The higher PTFE content in the microstructural surface as compared to NiTi also accompanies excessively higher fluorine.

PTFE and NiTi were identified by taking EDS scans on specific areas within the images. For example, the charged areas in the EDS-SEM images mainly contained PTFE while the grey coloured regions were NiTi-rich. However, the quantitative EDS results shown in Figure 153 belong to EDS scan over a larger area of the image. The white regions in the Figure 154 are due to charging up of the PTFE in SEM detection beam. In these areas, PTFE specks are formed due to shrinkage cracks. The cracks appear because of the weak bonding within the PTFE with the surrounding content. The weak bonding occurs due to the strong electronegative F bonds belonging to PTFE internal chain structure.

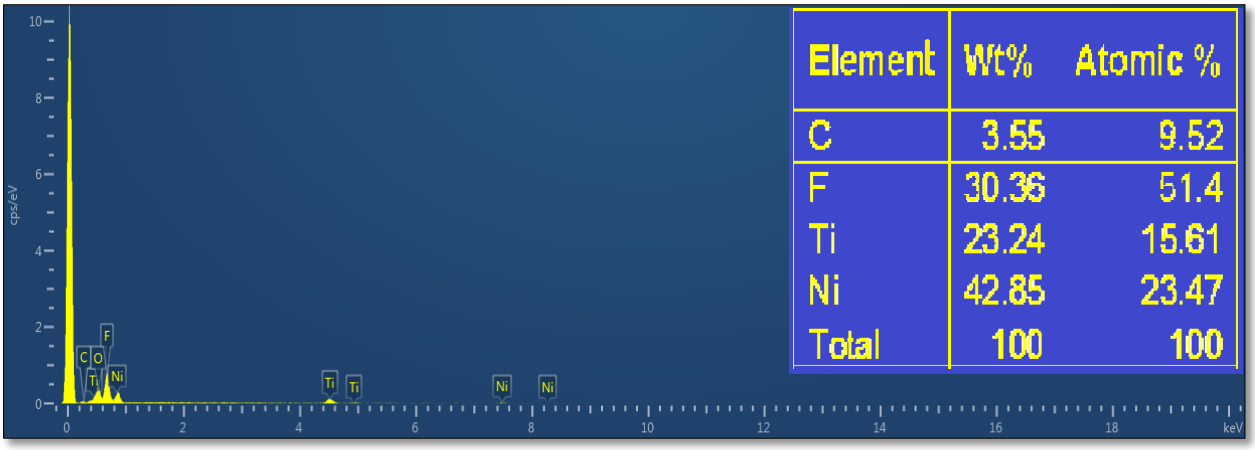

Figure 153: The EDS results for PTFE-NiTi – PNA2 nanocomposite.

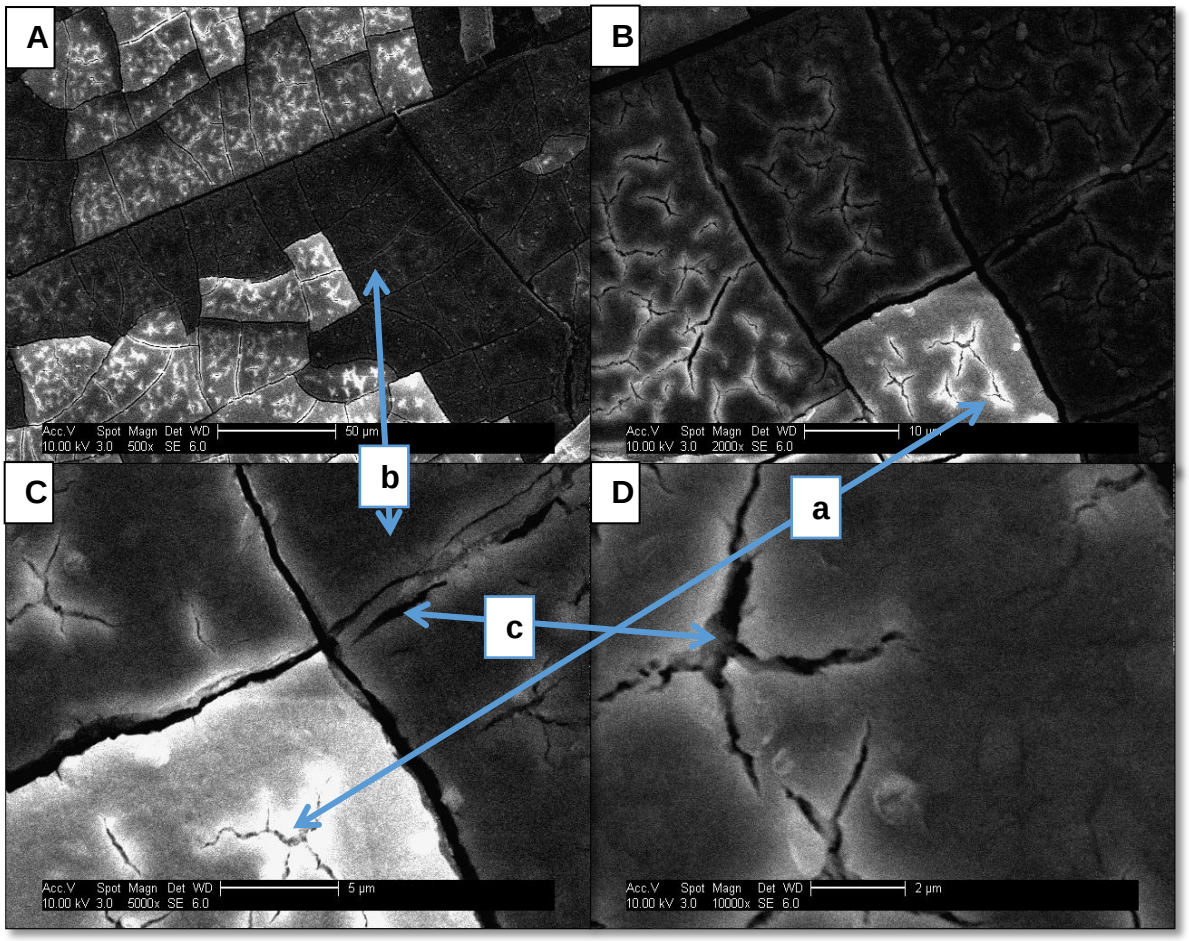

Figure 154: SEM images of PTFE-NiTi – PNA2 nanocomposite at magnifications of (A) x 500, (B) x 5000, (C) x 10, 000, and (D) x 20, 000. (a: PTFE, b: NiTi, c: inter-planar gaps between polymer chains and metallic lattice).

The water content that was absorbed into the nanocomposite (PNA2) was controlled and calculated in a similar way as described for PNK1 film. The wetting angle equipment was used to drop water droplet on a 0.25 cm^2 area of 1.6 µm thick film (volume: 0.04 mm^3). The volume of water absorbed in the thin film was 0.015 µl, which represents the unoccupied volume of the nanocomposite film. 0.015 µl is just above the one-third of total film volume.

The combination of WCA and EDS-SEM analysis reports a similar intercalated structure as described by the schematic illustration given in Figure 150. However, the fluorine content on the surface is greater than carbon and NiTi, and the polymer structure has more cross-linking in the nanocomposite PNA2 as compared to PNK1, as a result, a lower polymerisation ratio is obtained. The main reason for lack of polymerisation of PTFE at low pressure and high power process conditions is explained in detail in section 6.5.3, where it was established that the process conditions of 5 x 10^{-3} mbar and 150W RF power deposit PTFE with an excessively cross-linked and amorphous structure containing, monomers and fragmented chain patches.

6.8.3 PTFE-NiTi – PNF3

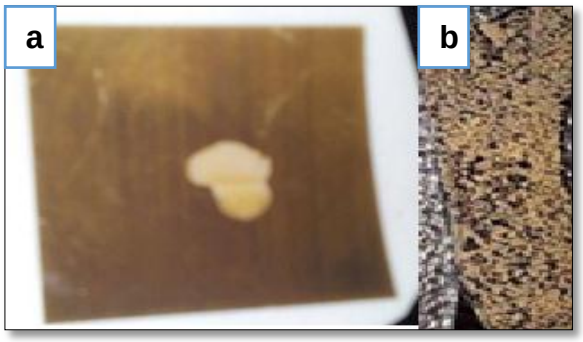

Figure 155: PTFE-NiTi – PNF3 deposited on (a) PTFE (b) Si substrates.

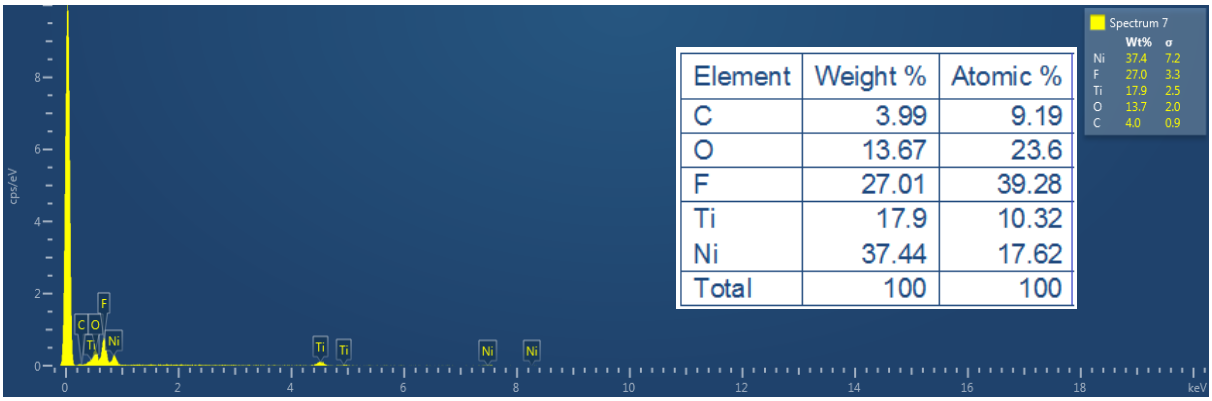

Element	Weight %	Atomic %
C	3.99	9.19
O	13.67	23.6
F	27.01	39.28
Ti	17.9	10.32
Ni	37.44	17.62
Total	100	100

Figure 156: The EDS results for PTFE-NiTi – PNF3 nanocomposite.

At low working gas pressure, PTFE does not deposit at higher rate than NiTi at any combination of process parameters (Figure 144). Thus, the process pressure for the sputtering process was a compromise, and the deposition was conducted at 20 x 10^{-3} mbar. PTFE was sputtered by RF at 100W power, whereas NiTi was deposited at 25W DC power. As a result, a PTFE-rich nanocomposite (PNF3) was prepared with a volume fraction of 60:40.

The resultant nanocomposite was highly oxidised, stressed and showed a lack of adhesion to the substrate (Figure 155). The composition was indicated by EDS results, shown in Figure 156, where Ni-rich NiTi was deposited with PTFE. The reason for the coating failure relates to excessive oxygen content in the nanocomposite. The PTFE was not fully polymerised in the nanocomposite because of the oxygen entrapping in the polymer chains. NiTi also oxidises to form TiO_x while Ni mostly remains in atomic form, as previously discussed in section 6.4.1.

Therefore, no intercalation was observed between PTFE and NiTi, and a nanocomposite was not formulated. The reason for more oxygen entrapping in this nanocomposite microstructural stoichiometry is that the PVD sputtering was conducted at 20 x 10^{-3} mbar. 20 x 10^{-3} was used as a compromise condition as described above, but the results indicate that the high-pressure deposition has turned out to be the wrong choice for the sputtering process and leads to a manufacturing failure, through oxidation of the NiTi target surface and the inclusion of oxygen in the PTFE film also.

6.8.4 PTFE-NiTi – PNH4 and PNR5

The rotatory table attached to the substrate holder in the sputter coater can be constantly rotated over two targets during co-sputtering resulting in three-time lower deposition rates than the stationary mode deposition; therefore, it takes longer to deposit a specified film thickness by co-sputtering as compared to layered thin films. The deposition of both materials from one target source was attempted to save time during co-sputtering of PTFE and NiTi. For this purpose, (0.5 x 0.5 cm^2) NiTi pieces were placed on the racetrack of PTFE target. It was not possible to do otherwise and place PTFE pieces on NiTi target because of low melting temperature of PTFE. The thicknesses of NiTi pieces were 0.05 and 0.5 cm for the production of PNH4 and PNR5 films respectively. The process parameters for the deposition were the same as those marked in Figure 144 and described in section 6.6.

Target cross-contamination was observed for both nanocomposite films (PNH4 and PNR5). For PNH4 film, the NiTi pieces were entirely coated with PTFE within first 15 minutes, and in an hour of deposition resulted in only PTFE deposition on the substrate. Thicker NiTi pieces placed on the PTFE target for the preparation of PNR8 films took slightly longer to be coated with PTFE (20 minutes). After that, no NiTi deposition was detected on the coating surface, and even PTFE deposited at substantially lower deposition rates than had been anticipated at the selected process conditions. The anticipated deposition rates were experimentally determined and previously reported in Figure 144. The lower deposition rates were detected because coated NiTi pieces now occupied the target racetrack area preventing the sputtering of NiTi from that area; thus, less PTFE from the target surface contributes to the plasma. Overall, PNH4 and PNR5 nanocomposites production was a futile manufacturing attempt, and no nanocomposite was formulated by using one target holder for depositing both PTFE and NiTi.

6.8.5 Summary

Intercalated PTFE-NiTi nanocomposites including PNK1 (NiTi-rich) and PNA2 (equi-composition) were fabricated by PVD co-sputtering. The nanocomposites contain cavities in the microstructure of two-phased material, which consume approximately one-third of the total thin film volume. SEM images observed the intercalated microstructure of co-sputtered PTFE-NiTi nanocomposites formed around these cavities and elemental detection spectroscopy found the elemental composition. WCA measurements provided the functional evidence of PTFE-NiTi interactions in the intercalated materials.

6.9 Layered PTFE-NiTi thin films

Layered PTFE-NiTi nanocomposite films have been deposited using PVD magnetron sputtering, prepared with various volume fractions of PTFE and NiTi. The film thickness, thickness of individual layers and volume fraction of PTFE and NiTi were controlled by selecting different sputtering conditions (power and pressure) from Figure 157. Figure 157 is a modified version of Figure 112, where the data-points representing the deposition parameters for nanocomposite production are enlarged and labelled. Thus, the desired volume fractions for PTFE-NiTi nanocomposites were obtained by sputtering the materials at marked deposition conditions in Figure 157.

Layered PTFE-NiTi nanocomposites were produced at 10 x 10^{-3} mbar Ar pressure, 150W RF power for PTFE and 50W DC power for NiTi. The selected deposition parameters are the same as those chosen in section 6.6. Figure 157 and Table 27 provides the detail of the selected process parameters and deposition rates to fabricate PTFE-NiTi nanocomposites. Equicomposition (PNS6: 50:50), PTFE-rich (PND7: 60:40) and NiTi-rich (PNL8: 25:75) nanocomposites were prepared. To prepare the layered nanocomposite films, the sample holder was placed at fixed positions above the PTFE and NiTi targets alternatively, and the power supply of only one target was switched on at a time during the deposition. Figure 158 shows the schematic plan of PTFE-NiTi films where the depositions of PTFE and NiTi on the substrate are illustrated in pink and blue colours respectively.

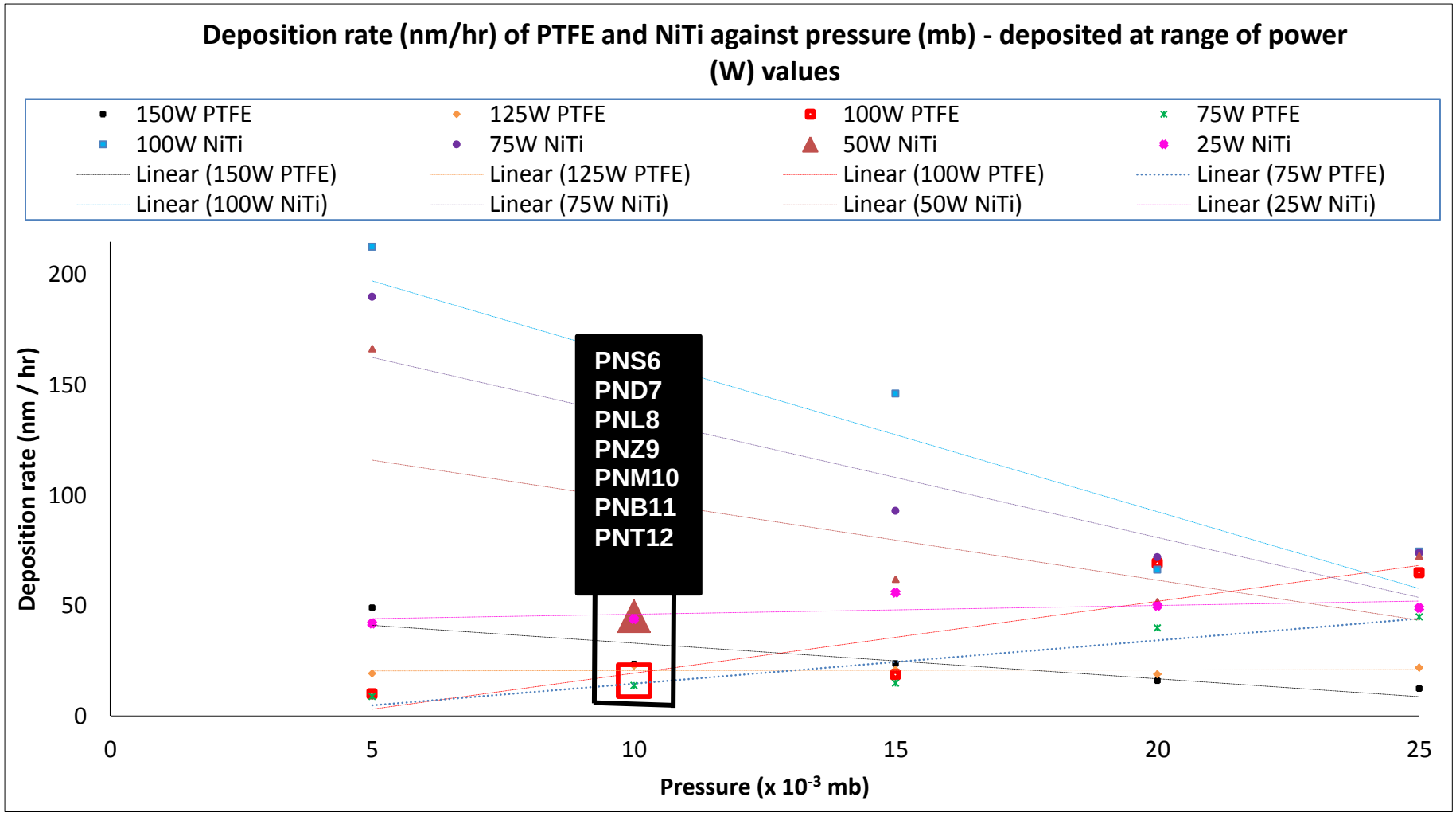

Figure 157: Deposition rate (nm/h) of PTFE and NiTi against power (W) - deposited at range of pressure values. The marked data - points represent the process parameters selected for the deposition of PTFE-NiTi nanocomposites.

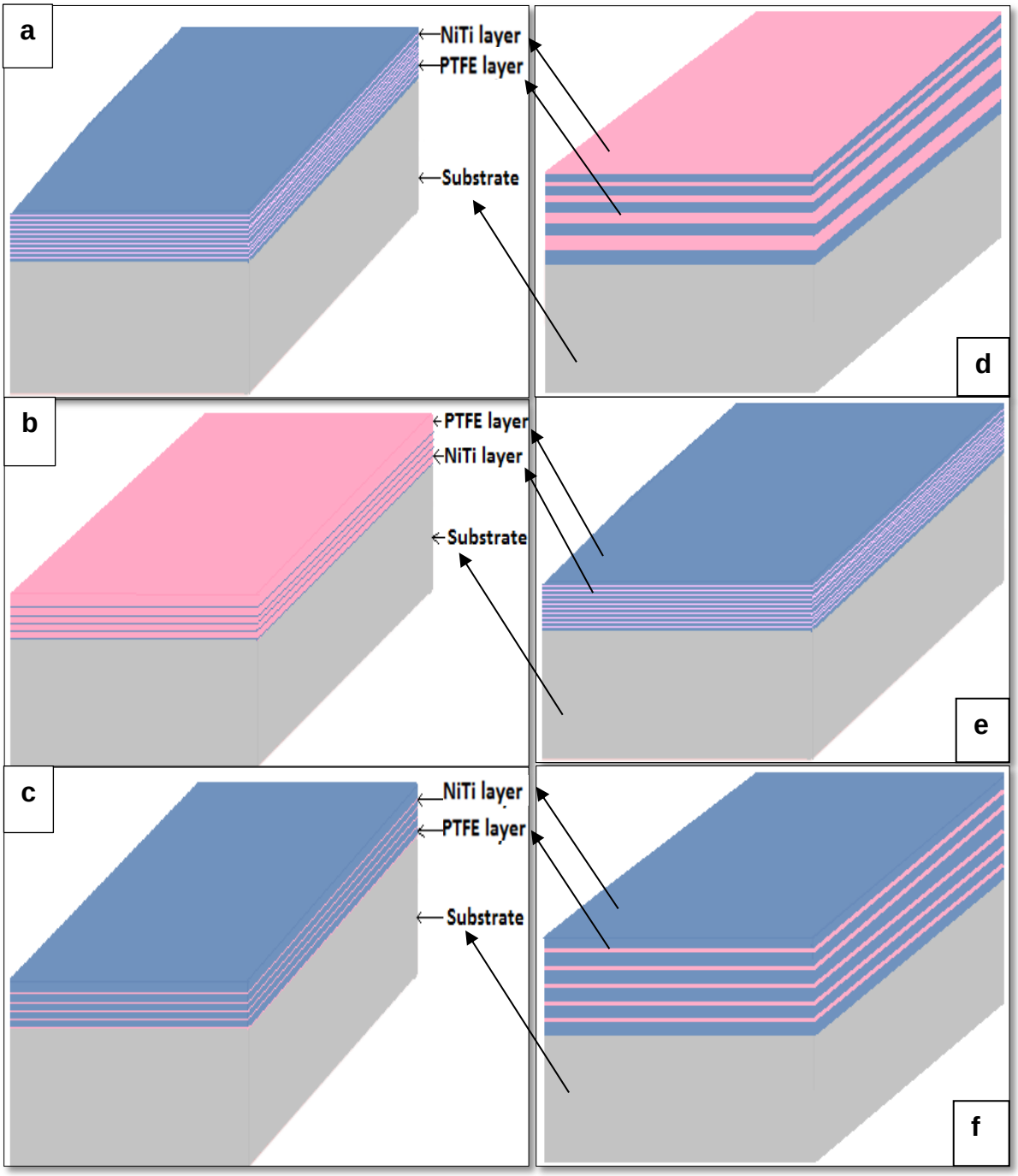

Figure 158: Schematic illustrations of layered PTFE-NiTi coatings: (a) PNS6, (b) PND7 (c) PNL8, , (d) PNZ9, (e) PNM10, and (f) PNB11.

Table 27: *Manufacturing parameters for PVD sputtered PTFE-NiTi thin films as Layered nanocomposites.*

Specimen ID	PNS6	PND7	PNL8	PNZ9	PNM10	PNB11	PNT12
Volume fraction (PTFE:NiTi)	50:50	75:25	25:75	30:70	50:50	10:90	10:90
Film thickness (µm)	1	0.75	0.75	1	0.5	2	3
Pressure (x 10^{-3} mbar)	10	10	10	10	10	10	10
RF (W) - for PTFE deposition	150	150	150	150	150	150	150
DC (W) - for NiTi deposition	50	50	50	50	50	50	50
PTFE deposition rate (nm/h)	24	24	24	24	24	24	24
NiTi deposition rate (nm/h)	45	45	45	45	45	45	45
Number of Layers	20	10	10	11	40	10	20
PTFE layer (nm)	50	100	25		25	20	15
NiTi layer (nm)	50	25	100		25	180	135
Deposition time for 1 PTFE layer (h)	2	4	1		1	0.75	1.2
Deposition time for 1 NiTi layer (h)	1	0.5	2		0.5	4.25	6
Intercalated nanocomposite	No	No	Yes	Yes	No	Yes	Yes

6.9.1 PTFE-NiTi – PNS6

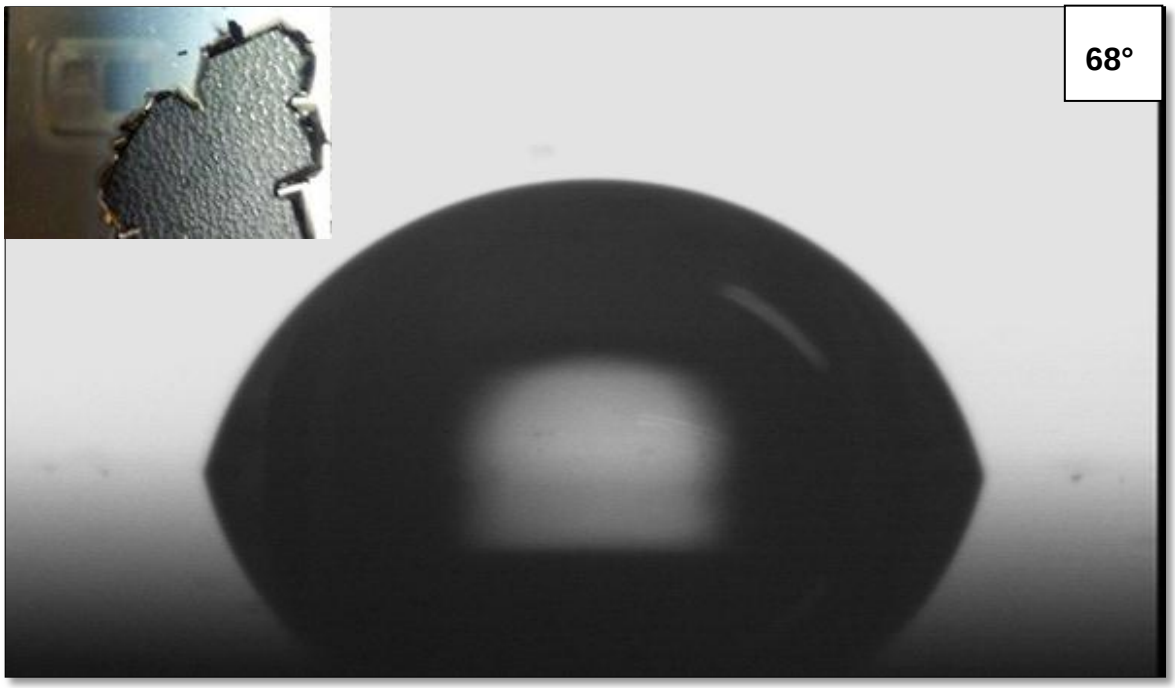

Figure 159: Water droplet on the surface of PTFE-NiTi nanocomposite PNS6. The inset shows a picture of PNS6 film deposited on the glass substrate.

PTFE-NiTi – PNS6 thin films were deposited with 50:50 volume fractions of PTFE and NiTi, where NiTi is the top layer. WCA of the coatings was 68°, which matches to NiTi WCA (Fig 137). The WCA indicates no interaction of NiTi (top layer) with PTFE deposited underneath. Intercalated material is anticipated to allow the formation of internal physical bonding between the two materials without any chemical reactions involved. Existence of intercalation phenomena is expected to alter the wetting properties of the top layer, demonstrating its interactions with a different material deposited underneath. Those interactions change the WCA because of the alterations in surface energy and morphology of the deposited materials.

PTFE-NiTi PNS6 thin films are not adherent to the substrate. The nanocomposite came off the substrate as a peeled and rolled up film, relating to the lack of cohesive forces between PTFE coating and the glass and the development of stress within the film. All pure PTFE thin films prepared in previous experiments showed an excellent adhesion to the glass. Therefore, NiTi was deposited above the PTFE layer at 10 x 10^{-3} mbar pressure and 50W power for preparing 50:50 volume fractions of

PTFE:NiTi nanocomposite, which leads to a failure of the film-substrate adhesion. This directly relates to the excessive intrinsic stress accumulating between PTFE-NiTi interface. The PTFE chains probably reorient themselves to reduce the stress intensity resulting in loss of film substrate adhesion, and consequently causing an adhesive failure. The stresses at the interfaces between the layers also lead to distorted PTFE-NiTi interactions at the interfaces, which cause a further failure of the structure to intercalate. The same was the reason for WCA measurements representing the top NiTi surface only.

Thus, no intercalation was perceived between PTFE and NiTi in the nanocomposite PNS6.

6.9.2 PTFE-NiTi – PND7

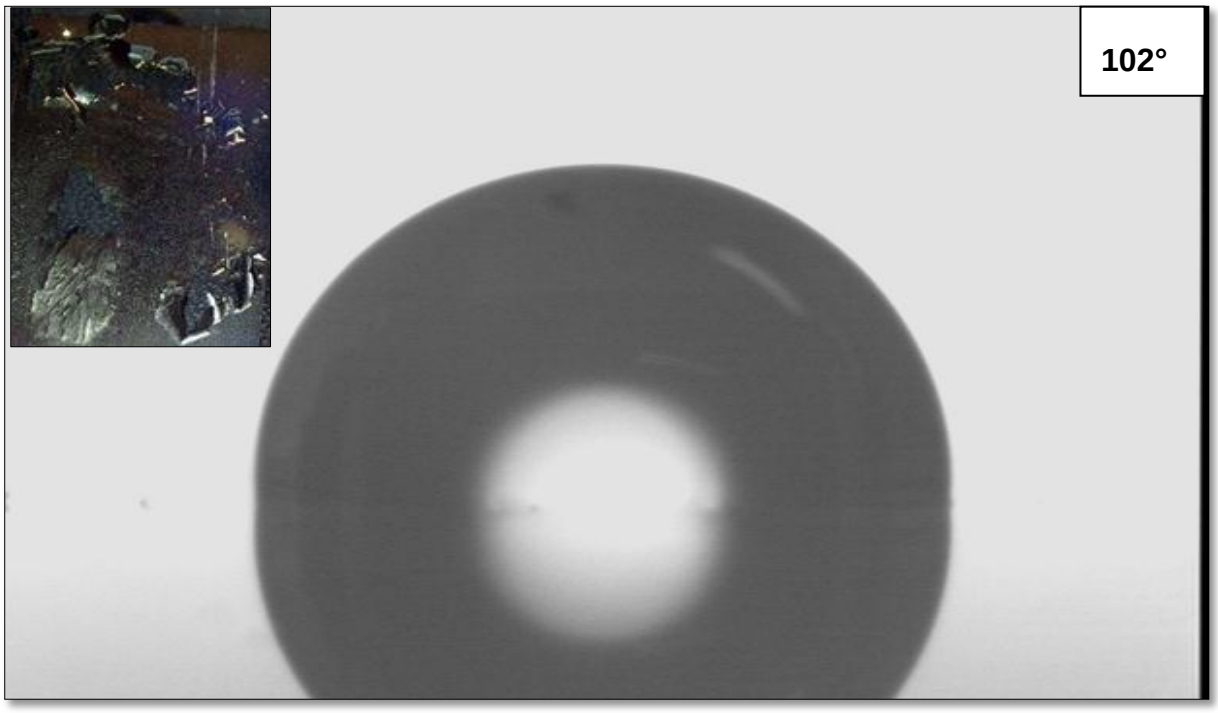

Figure 160: Water droplet on the surface of PTFE-NiTi – PND7 nanocomposite. The inset shows a picture of PND7 films.

PTFE-NiTi – PND7 thin films were deposited with 75:25 volume fractions of PTFE and NiTi respectively, where the top layer is NiTi. The WCA recorded on the film surface was 102°, which is near to the PTFE WCA deposited at specified process conditions (108°) earlier. Thus, WCA indicates no interaction of NiTi with PTFE layers deposited underneath the top layer of PTFE. Intercalation was anticipated to modify the wetting angle on the film surface demonstrating interactions between different materials deposited in the nanocomposite. PND7 films were not adhesive on the substrate as well, and the stress removes the film from the substrate in the form of broken flakes rather than rolled-up and peeled-off thin film removal. Removal of thin films by stress cracking into broken flasks indicates a cohesive failure. The nanocomposite composition contains more PTFE than NiTi forming the matrix of the nanocomposite. A polymeric network lacks sufficient strength to incorporate NiTi and to intercalate the nanocomposite in 75:25 or 50:50 volume fractions of PTFE and NiTi respectively. Thus, **No intercalation between PTFE and NiTi in the PND7 nanocomposite was observed.**

6.9.3 PTFE-NiTi – PNL8

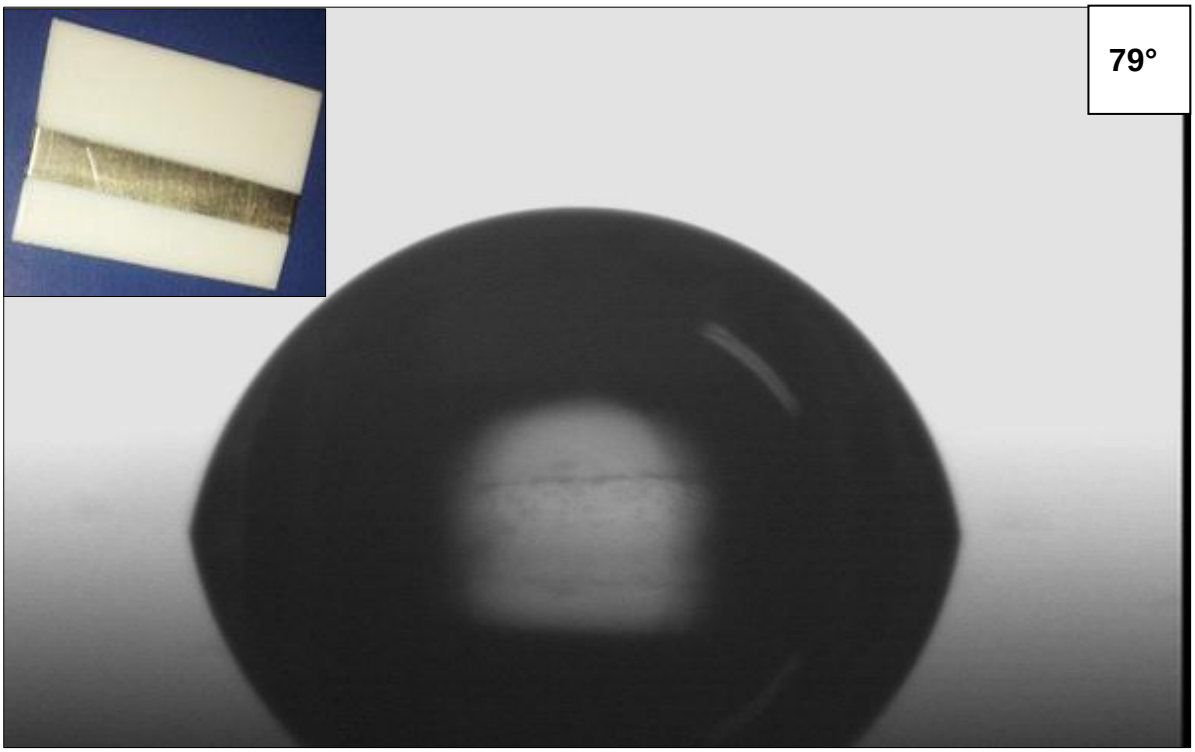

Figure 161: Water droplet on the surface of a PTFE-NiTi nanocomposite PNL8. The inset shows a picture of PNL8.

PTFE-NiTi – PNL8 thin films having volume 25:75 fractions of PTFE and NiTi were deposited as layered nanocomposite, where NiTi was deposited on the top of the film. PTFE-NiTi – PNL8 thin films deposited at volume 25:75 fractions of PTFE and NiTi form stable thin films, which display good adherence to the substrate as shown in the inset of the Figure 161. The above-mentioned results establish that it is possible to form a nanocomposite material by combining PTFE and NiTi by PVD sputtering route. The WCA was of the nanocomposite was 79°, which is above the WCA of NiTi and well below the WCA of PTFE. The WCA of pure NiTi films deposited at the same process conditions is 55° (Figure 141), which is well below the nanocomposite's wetting angle. The variation in WCA relates to the surface energy, internal nanocomposite structure and the film morphology. However, it is not known so far that if these interactions are stable and due to similar structural arrangement as that expected for an intercalated nanocomposite.

To verify this, PTFE-NiTi – PNL8 thin films are modified further with similar volume fractions and the modified films will be investigated by TEM analysis (section 6.9.4) and scratch testing (section 6.10). TEM analysis and scratch testing would provide microstructural and functional evidence of interaction in the thin films. The modification and further characterisation would also certify the reproducibility of the results.

Experimental results of 'PNL8 nanocomposite films' are the first to show fabrication of a PVD sputtered layered nanocomposite, which potentially exhibits intercalation between PTFE and NiTi.

6.9.4 PTFE-NiTi – PNZ9

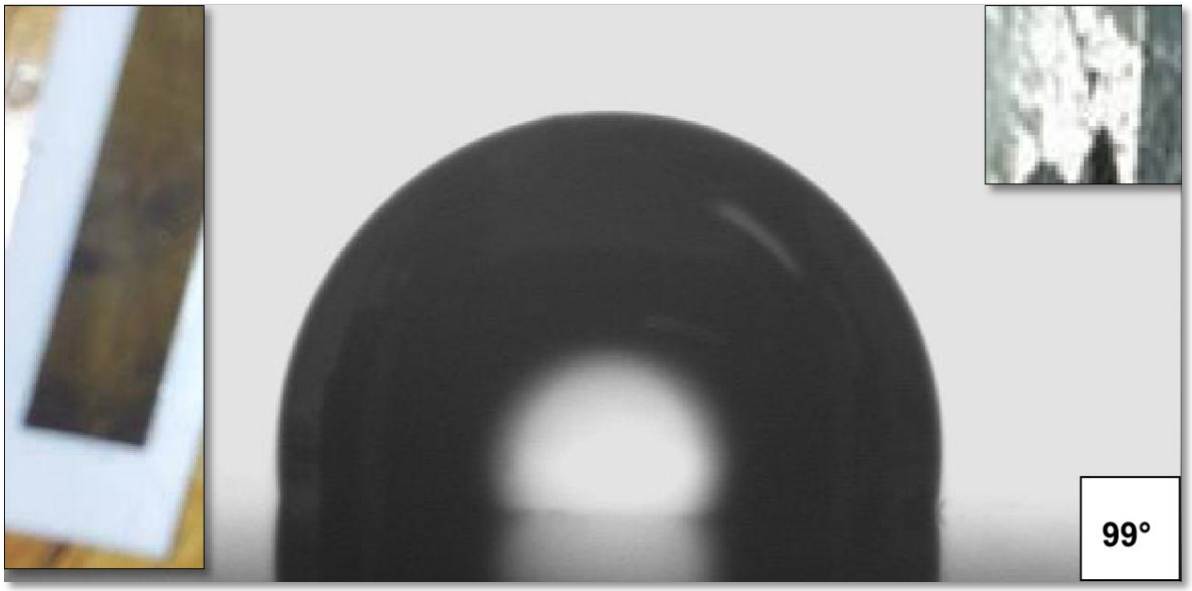

Figure 162: Water droplet on the surface of a PTFE-NiTi – PNZ9 nanocomposite. The insets show a picture of PNZ9 films on PTFE (left) and Si right) substrates.

Table 28: deposition time and individual layer thickness for PTFE-NiTi – PNZ9.

Layer	Material	Layer thickness (nm)	Deposition time (h)
1	PTFE	75	3.0
2	NiTi	225	5.0
3	PTFE	65	2.5
4	NiTi	125	2.5
5	PTFE	35	1.5
6	NiTi	100	2.2
7	PTFE	25	1.0
8	NiTi	75	1.6
9	PTFE	15	0.5
10	NiTi	50	1.1
11	PTFE and NiTi	150	7.0

After successful deposition of intercalated nanocomposites in layered (PNL8) and co-sputtered (PNK1 and PNA2) microstructural schemes, it was attempted to modify the nanocomposite by taking advantage of both layered and co-sputtering deposition methods. For this purpose, the nanocomposite was deposited in layers initially followed by co-sputtering of PTFE and NiTi. Thicknesses of the layers varied gradually form the first layer on the substrate to the top layer on the film surface. Ten alternate PTFE and NiTi layers were deposited on the substrate. The volume fraction of the PTFE-NiTi nanocomposite in each set of layers was maintained at 25:75. This volume fraction value was selected because of the previous success in depositing the NiTi-rich intercalated nanocomposites (PNK1, PNA2 and PNL8). Higher NiTi content provided additional strength to uphold the material framework. The individual thicknesses of all the layers in PNZ9 film are reported in Table 28. Following the layered deposition, PTFE and NiTi were co-sputtered to form an additional co-sputtered layer on the top of the coating surface.

The resulting PNZ9 film was adherent to PTFE substrate (Figure 162 inset on the left) but the PNZ9 films deposited on Si and glass seem to be under stress (Figure 162 inset on the right). Although the films do not come off the substrate by cohesive or adhesive failure; however, the poor adhesion to the substrate was observed because of the thick PTFE layers (75 and 65 nm) deposited initially. Thick PTFE layers were believed to be the reason for poor adhesion. This is because PNL8 nanocomposite containing only 25 nm thick well-adherent PTFE layers showed potential intercalation and was adherent, while PNS6 and PND7 thin films have thicker PTFE layers and they failed to form interacted nanocomposite as explained in sections 6.9.1 and 6.9.2. The reason for poor coating adhesion will be investigated further by attempting the fabrication of PNM10 in section 6.9.5. So far, it can be recognised that the modification of the nanocomposite by gradual change in layer thickness does not improve the film properties in terms of adhesion and stress contamination, and thin PTFE layers in the nanocomposite merely help formulate adhesive and unwavering intercalated PTFE-NiTi layers within the coatings (PNL8).

The co-sputtered layer of PTFE-NiTi on the coating surface was not adhesive at all to the top PTFE layer of the nanocomposite, and came off from the film surface as a completely amorphous dark-grey powder during initial manual handling after the manufacturing process. The manual handling of PNZ9 film involved removal of the

substrate holder from the sputter coater followed by separating the substrates coated by thin films from the substrate holder. Absence of the co-sputtered layer on the coating surface resulted in no water absorption by the coating during WCA analysis, which was previously observed by co-sputtered nanocomposite films (PNK1 and PNA2). WCA of nanocomposite PNZ9 is 99°, which is below the WCA of PTFE (108°) while above NiTi WCA (55°) stated in section 6.6.3 for the specified deposition conditions. The variance in WCA indicates an interaction between PTFE and NiTi within the nanocomposite microstructure. The WCA of PNZ9 is near to the PTFE WCA (108°); therefore, this variation in WCA is not as much as PNL8 films (79°) displayed after intercalating.

SEM was used as a characterisation technique for co-sputtered nanocomposite films, but the SEM show the microstructure of the film surface only; therefore, TEM analysis was undertaken for imaging the cross-sectional microstructure of the layered PTFE-NiTi nanocomposite after the sample preparation by FIB as described in section 5.3.8.

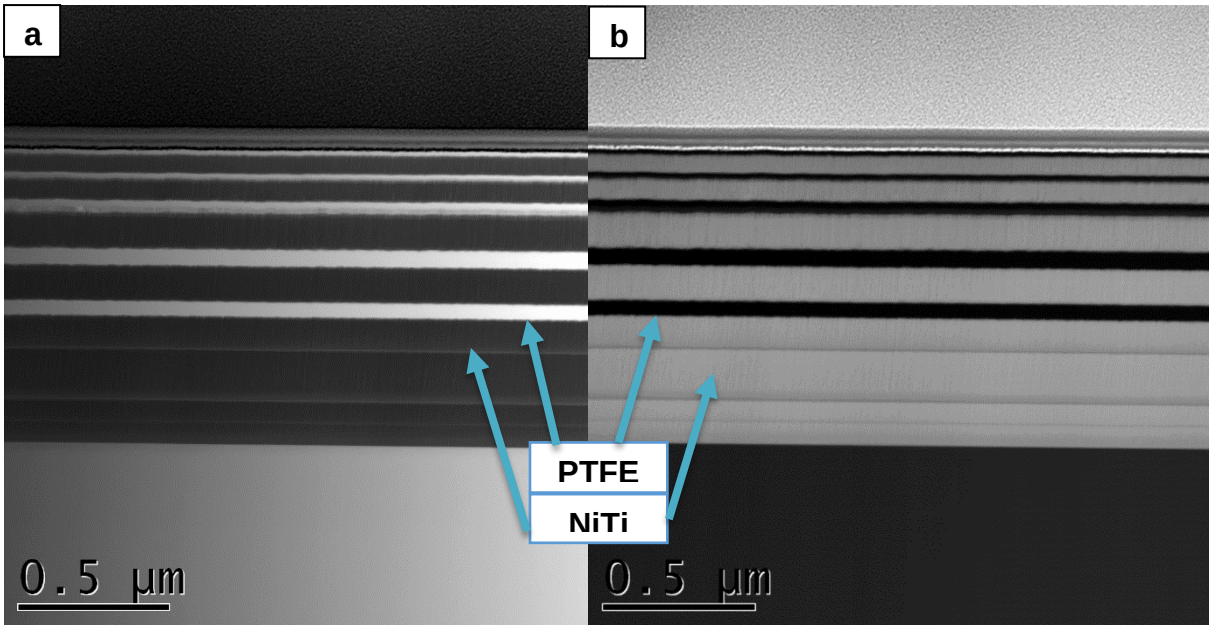

Figure 163: (a) A bright-field TEM image of PTFE-NiTi – PNZ9 presenting alternative layers of PTFE and NiTi. (b) A dark-field TEM image of PTFE-NiTi – PNZ9 presenting alternative layers of PTFE and NiTi.

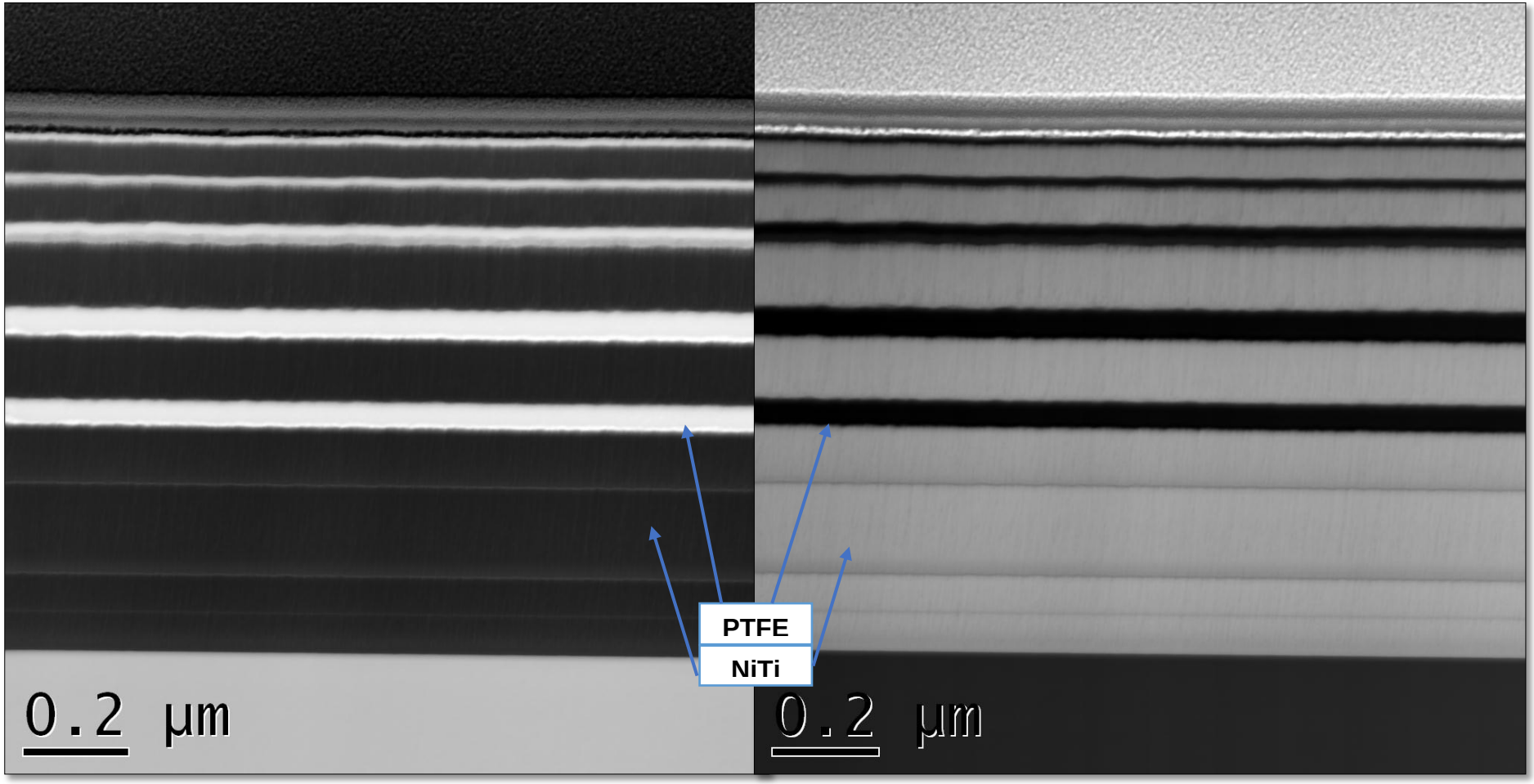

Figure 164: (a) A bright-field TEM image of PTFE-NiTi – PNZ9 presenting alternative layers of PTFE and NiTi. (b) A dark-field TEM image of PTFE-NiTi – PNZ9 presenting alternative layers of PTFE and NiTi.

Figure 163 – Figure 165 show bright-field and dark-field TEM images of PNZ9 nanocomposite having PTFE and NiTi alternative layers. TEM images provide additional evidence for the gradual variance in NiTi and PTFE layer thicknesses and the interfaces between the layers. Figure 163 additionally demonstrates that PTFE thin layers are stable and intact within the metallic thick layers of the nanocomposite.

Thin film zone models discussed in section 3.1.3 reported that metallic substances deposit as columnar microstructure by PVD sputtering (zone 1). Similar observations were obtained by SEM analysis conducted in this study for PVD-NiTi thin films (Section 6.6). However, the columnar grains are not porous as described by Movechan and Demchishin. Instead, the columnar fibres seem to be densely packed, and this property matches to zone T of the Thornton zone models. TEM images in Figure 163 – Figure 165 provide a further pictorial explanation of the same. As-sputtered NiTi is amorphous, and columnar grains appear as unidirectional elongated fibres between which are thin PTFE layers, which is displayed clearly in dark-field image of Figure 164. The dark-field TEM image in Figure 164 also show that the columnar fibres of NiTi deposit in a stratum arrangement resulting in grain boundaries forming between the stratum divisions as seen in firstly deposited 225 nm thick NiTi layer of PNZ9 film.

The polymer chains of PTFE stack between the NiTi columnar layers, as seen in bright-field TEM image of Figure 164. The central carbon chain skeleton of PTFE lies parallel to the substrate while the carbon-fluorine bonds along with fragments and chain ends of the crosslinks to align in the vertical direction of the substrate. Electronegative fluorine experience electrostatic repulsion to the electron sea of the metallic lattice at the boundary of NiTi layer (interface), resulting in the formation of minor fissures at the interface. Small interfacial fissures propagate parallel to the NiTi columnar fibres by PTFE chain extensions. Thus, solid-solid intercalations in PVD-nanocomposite films incorporate the PTFE fragments and chain extensions into the metallic (NiTi) columnar matrix because of the interfacial fissures created by following.

- Electrostatic repulsion between fluorine and delocalised electrons sea in the metallic lattice.
- Eelectrostatic attraction between fluorine and metal ions.

- Van der Waal forces within the polymer chains, which keep fluorine atoms at a maximum distance from each other in the polymer network and in the perpendicular direction to the carbon skeleton.

The thinner the PTFE layer the more interfacial fissures (intercalation) were observed, as seen in the thinner PTFE layers towards to the top of Figure 165.

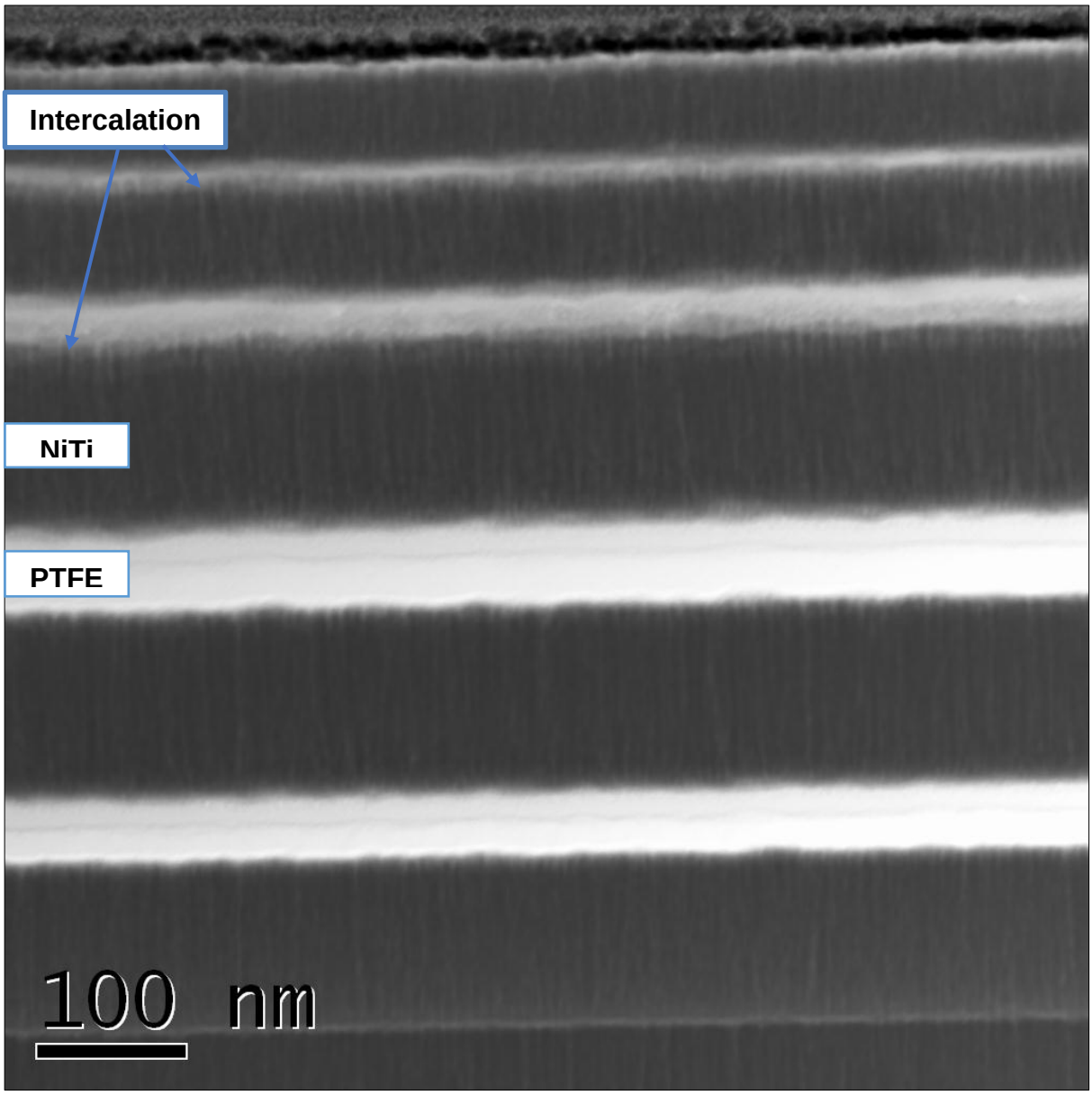

Figure 165: A bright-field TEM image of PTFE-NiTi – PNZ9 presenting alternative layers of PTFE and NiTi.

Intercalations physically interlock the two materials at the interface and allow the polymer fibres to run through the metallic lattice, which are observed in the film microstructure by TEM. Modifications in the internal microstructure due to intercalation also change the surface energy and other functional properties such as wetting angles.

PTFE-NiTi – PNZ9 nanocomposite films were characterised further by line scan EDS to evaluate the atomic composition across the cross-section of the layered film (not the top surface) as shown in the inset of Figure 166.

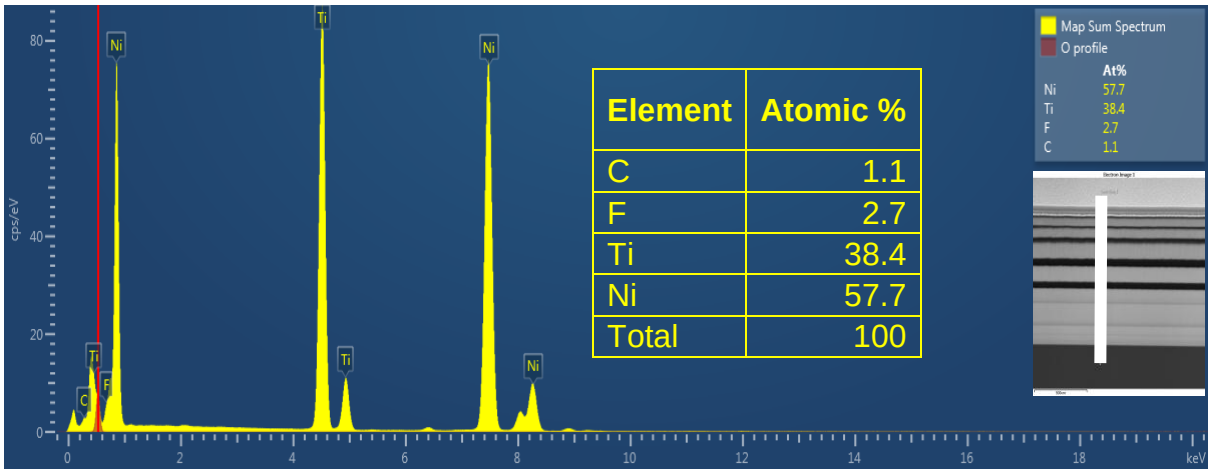

Element	Atomic %
C	1.1
F	2.7
Ti	38.4
Ni	57.7
Total	100

Figure 166: The line scan EDS results for PTFE-NiTi PNZ9 nanocomposite. The line scan was conducted sideways on the nanocomposite film cross-section prepared by FIB as shown in the inset.

The main findings of the line scan EDS analysis include a significantly high Ni content and small fluorocarbon amount. Small fluorocarbon amount was expected because of PTFE-NiTi volume fraction of 25: 75 in the nanocomposite; however, the fluorocarbon vs. NiTi ratio (5:95) obtained by line scan EDS is even smaller than the volume fraction stoichiometry. The smaller PTFE stoichiometry against NiTi content is explained by the orientation of fluorine atoms towards metallic lattice in a perpendicular direction to the substrate rather than sideways while the EDS scans the sideway cross-section of the film. Fluorine orientation towards metal ions was also observed in co-sputtered nanocomposite PNK1 and PNL2 films described by schematic illustration in Figure 145 (section 6.8.1). To put it differently, the fluorine atoms around the central carbon chain extend in the vertical direction towards the substrate forming polarised-electrostatic interactions with the metal ions. The line

scan conducted sideway (cross-section) on the nanocomposite only considers the polymer chain ends found of the layer-edge; thus, report even smaller volume fraction of PTFE in the thin films.

It is previously discussed in the literature review that Ti has exceptionally high affinity for oxygen, and it was experimentally investigated in detail in this study as well for which the results are reported and discussed in section 6.4. It is interesting to observe that Ni content is much higher than the deposited NiTi stoichiometric ratio of $Ni_{53.5}Ti_{46.5}$. It is proposed that the titanium ions bond with oxygen to form TiO_x (x: 1, 2) compounds leaving more atomic Ni^+ ions in the metallic lattice to interact with fluorine from PTFE and to develop NiTi SMA. Titanium ions find any residual oxygen in the sputtering chamber that are trapped in materials structures and produce titanium oxides, which are thermodynamically stable ionic compounds having strong electrostatic attraction between Ti and oxygen. It is already shown in Figure 145 that the metallic ions participating in intercalation with PTFE align outwards, which would shift titanium oxide inwards within the nanocomposite microstructure leaving the excess nickel on the outer lattice positions to interact with PTFE.

Oxygen was not auto-observed by EDS software, but it was witnessed in previous NiTi EDs analysis (section 6.4) that manually selecting the oxygen analysis along with Ni and Ti element detection declares substantial oxygen content. Therefore, the above explanation is verified by manually selecting oxygen in EDS software for obtaining EDS micrographs, when characterising the modified nanocomposite (PNT12). This explains the influence of oxygen on the nanocomposite microstructure, as reported in section 6.10 (Figure 177).

6.9.5 PTFE-NiTi – PNM10

Figure 167: PTFE –NiTi nanocomposite PNM10 deposited on the glass substrate. The stressed film comes off because of adhesive failure.

PTFE-NiTi – PNL8 has previously displayed a potential for intercalation in layered film, where PTFE and NiTi are deposited with 25:75 volume fraction. PTFE-rich (PNS6) and equi-compositional (PND7) nanocomposites were the failed attempts at the nanocomposite production because of stress accumulation. It was anticipated that thick PTFE layers in the nanocomposites (50 and 100 nm in PNS1 and PND3 respectively) might be the reason for the manufacturing failure, or a NiTi-rich might be the only way to gain intercalated ability in an adherent nanocomposite to the substrate. This anticipation was also supported by PTFE-NiTi – PNZ9 results discussed in section 6.9.4.

A nanocomposite PMN10 was prepared to find the exact reason for the manufacturing failure. The nanocomposite has a PTFE-NiTi volume fraction of 50:50, which was achieved by 25 nm thick alternative layers of PTFE and NiTi. In total 10 layers were deposited at the process conditions marked in Figure 157 and tabulated in Table 27. A 0.5 µm thick nanocomposite film lacked adhesion to the substrate and the intrinsic stress accumulating within thin film microstructure and at film–substrate interface lead to adhesive failure of the coating as shown in Figure 167. Hence, it can be concluded that thin PTFE-layers are not the only pre-requisite for intercalated thin film manufacturing, as established in section 6.9.4, but NiTi-rich stoichiometry of the nanocomposite is also essential. 50:50 or NiTi-rich nanocomposites did not exhibit intercalation and mostly adhesion failure occurs because of the lack of strength in polymer matrix; whereas, NiTi metallic lattice matrix provides the appropriate strength required to uphold the nanocomposite framework.

6.9.6 PTFE-NiTi – PNB11

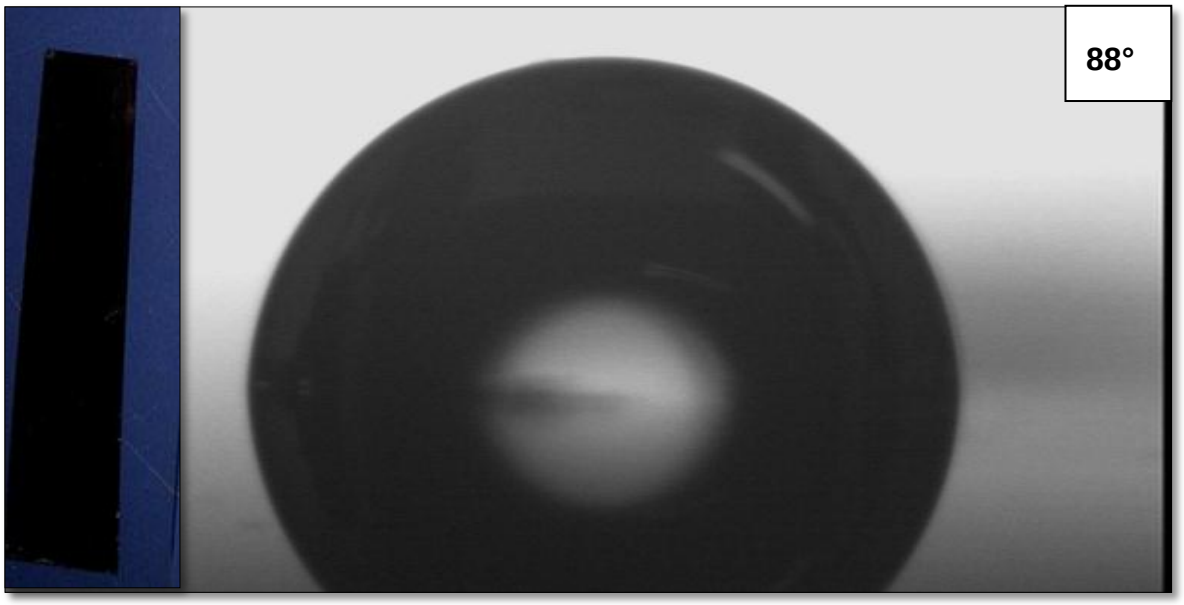

Figure 168: Water droplet on the surface of a PTFE-NiTi – PNB11 nanocomposite. The insets show a picture of PNB11 film on the glass substrate.

The results of the intercalated PNL8 (section 6.9.3) and PNZ9 (section 6.9.4) nanocomposite films, in combination to PNM10 (section 6.9.5) manufacturing failure reveal that NiTi-rich PTFE-NiTi and thin PTFE layers are the requisites for the fabrication of intercalated layered nanocomposites of PTFE-NiTi. Thus, PTFE-NiTi – PNB11 films were produced with layer thicknesses of 30 and 170 nm for PTFE and NiTi respectively, deposited on glass, Si and PTFE substrates. The deposition parameters employed for PVD manufacturing of the PTFE-NiTi nanocomposite are highlighted in Figure 157 and tabulated in Table 27, which are same as those selected in section 6.6. Following modifications were attempted in PNB11 films to improve the intercalation and adhesion of the nanocomposite films.

- PTFE-NiTi volume fraction of 10:90 was chosen to devise more NiTi-rich thin films. PTFE thickness was sustained at 30 nm to endeavour thin polymer layers because thinner PTFE layers were more intercalated in PTFE-NiTi – PNZ9 films.
- Ten alternating layers of PTFE and NiTi were deposited to produce 1-µm thick films, where all layers have constant PTFE and NiTi thickness throughout. This is because gradual variation in thin films resulted in stress accumulation

at the film-substrate interface (PNZ9), while thin layers containing constant volume fraction throughout produced thin films relatively less stressed films.

The fabrication of the nanocomposite with the above-mentioned modifications produced the intercalated films with WCA of 88°, which is below the WCA of PTFE (108°) and above NiTi WCA (55°) reported in section 6.6.3 for the stated deposition settings in Figure 157. PNB11 shows more alteration in WCA of the top layer (NiTi) than the previously observed intercalated nanocomposite films such as WCA of PNL8 film was 79° when the top layer was NiTi, and PNZ9 had a WCA of 99° when the top layer was PTFE. The alteration in WCA is a signpost for the interaction between PTFE and NiTi within the nanocomposite microstructure due to intercalation.

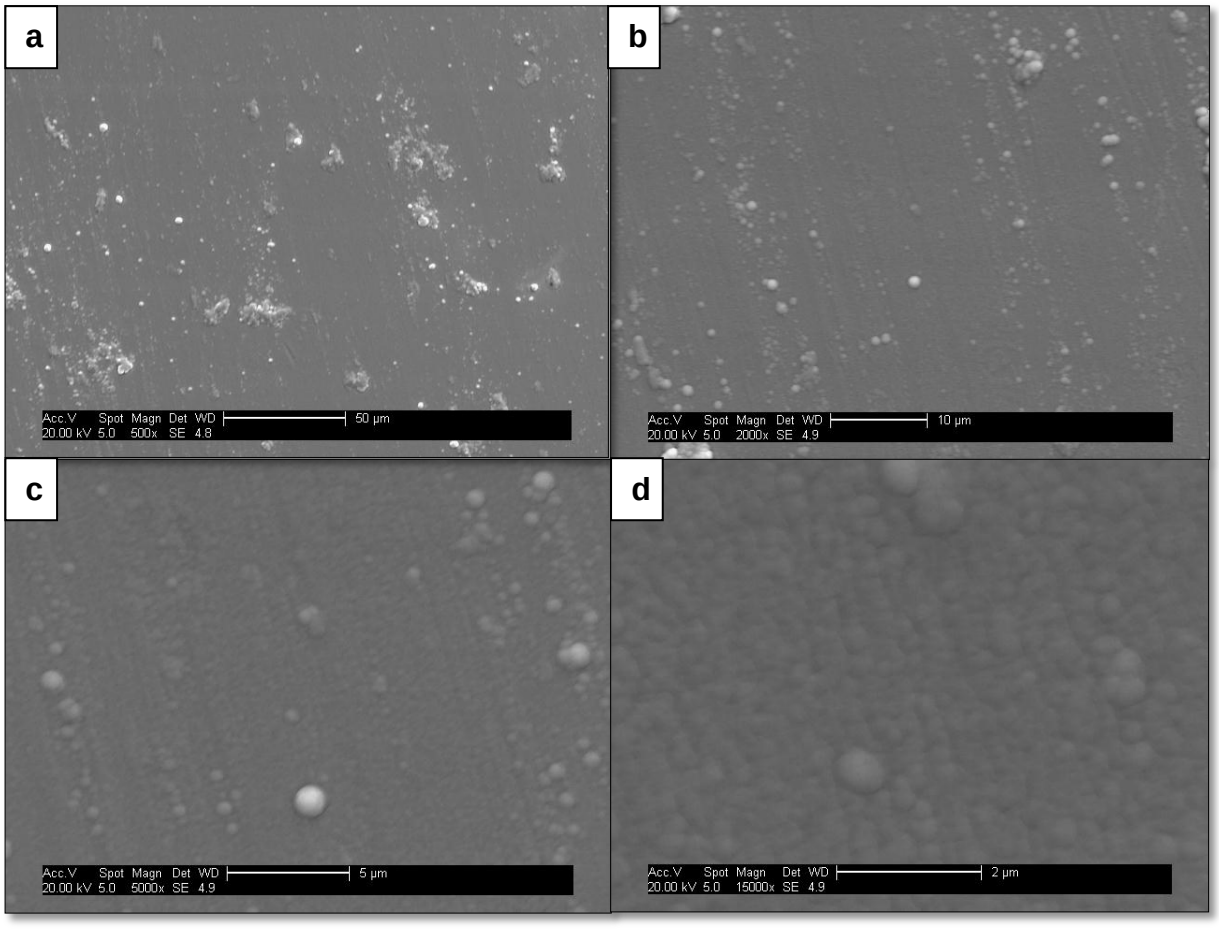

Figure 169: SEM images of PTFE-NiTi PNB11 nanocomposite at magnifications of (a) x 500, (b) x 2000, (c) x 5000, and (d) x 15, 000.

The modifications above also resulted in better adhesion and stable coatings with smoother film surface. The surface of the modified nanocomposites was characterised by SEM, and the acquired images are shown in Figure 169. PTFE-NiTi – PNB11 films show no irregularities and endure a smooth and continuous surface morphology with minimal defects. The surface is composed of dense array of columnar grains, which are more prominent at x15, 000 magnifications. SEM results of PNB11 films verify the TEM results for similar layered nanocomposite settings in PNZ9 films (section 6.9.4). The additional globular edifices on the film surface belong to PTFE-rich regions intercalating through the holes in the NiTi columnar fibres.

Better adhesion and improved intercalation in modified nanocomposite PNB11 confirmed that NiTi-rich films having thin PTFE layers is the strategy for manufacturing of the novel intercalated polymer-NiTi nanocomposites. The same approach was followed to prepare a final model of intercalated nanocomposite (PNT12), in which the layer thicknesses are half those in PNB11 films, but same volume fraction (10:90) of PTFE-NiTi is maintained.

6.9.7 Summary

PNS6 (equi-composition) and PND7 (PTFE-rich) nanocomposites did not fabricate stable intercalated PTFE-NiTi nanocomposites; however, PNL8 and PNZ9 (NiTi-rich) nanocomposite provided a functional evidence of PTFE and NiTi interactions in the intercalated materials by WCA measurements. TEM and SEM images observed the intercalated microstructure of layered PTFE-NiTi nanocomposites and elemental detection spectroscopy found the elemental composition. NiTi-rich matrix and thinner PTFE layers displayed higher intercalation ability.

6.10 PTFE-NiTi – PNT12 – an intercalated nanocomposite

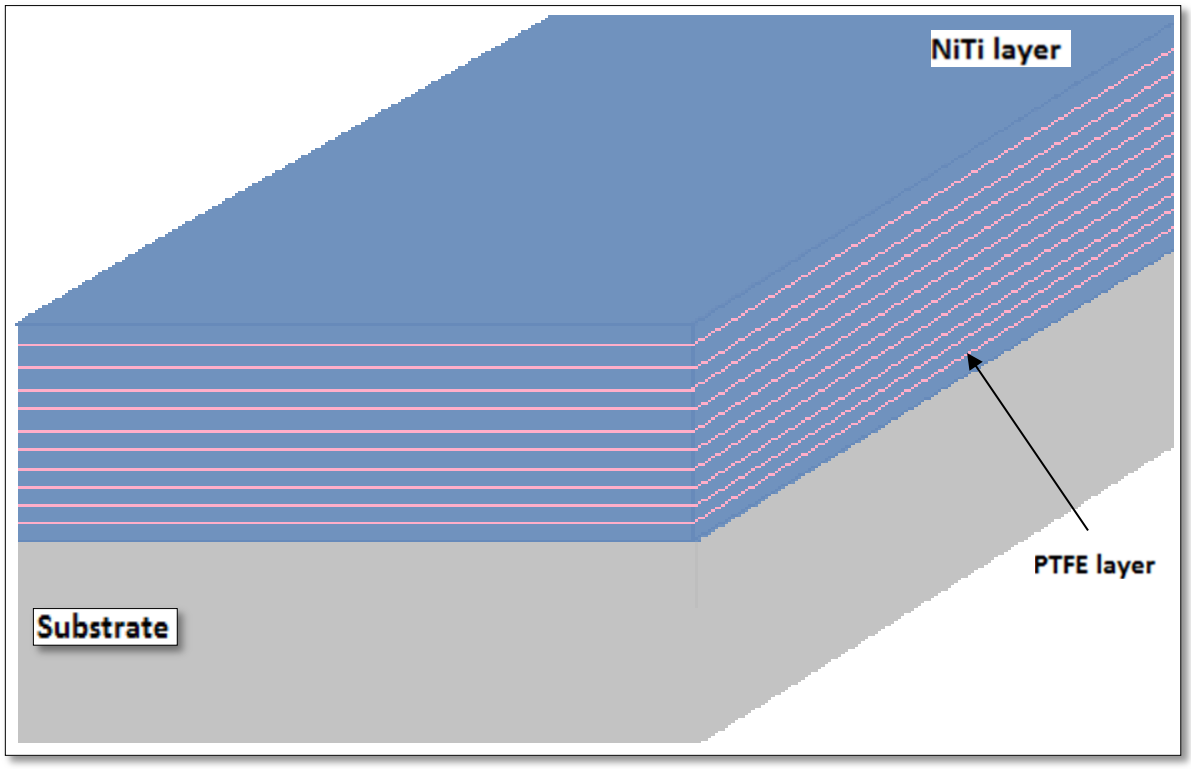

Figure 170: A schematic illustration of layered PTFE-NiTi thin film of PNT12.

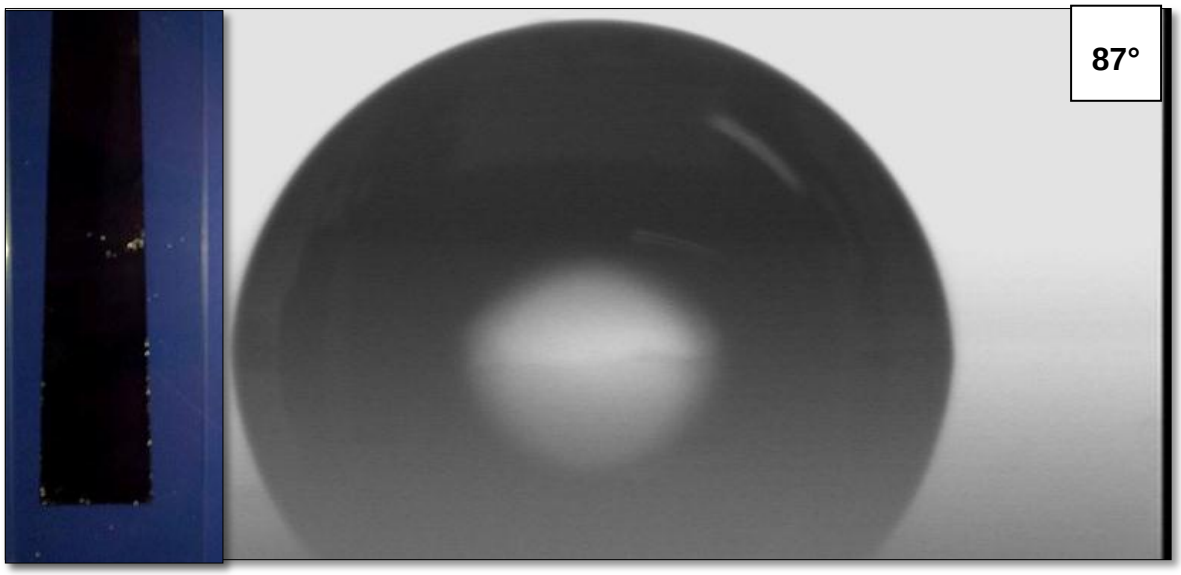

Figure 171: Water droplet on the surface of a PTFE-NiTi – PNT12 nanocomposite. The insets show a picture of PNT12 film deposited on the glass substrate.

Intercalated nanocomposite PTFE-NiTi – PNT12 films having layered microstructure were prepared by PVD magnetron sputtering on glass, Si and PTFE substrates. The sample holder was placed in fixed positions above PTFE and NiTi alternately, and the power supply of only one target was switched on at a time during the deposition. NiTi-rich nanocomposites with twenty alternative PTFE and NiTi layers were manufactured with a volume fraction of 10:90 in all sets of the deposited layers. The film thickness, thickness of individual layers and volume fraction of PTFE and NiTi were controlled by deposition rates and adjusted according to marked sputtering conditions (power and pressure) in Figure 157. Figure 157 presents that the process conditions for desired deposition rates are 10 x 10^{-3} mbar pressure, 150W RF for PTFE and 50W DC power for NiTi deposition as tabulated in Table 27. Figure 170 shows the schematic plan of PTFE-NiTi films where the depositions of PTFE and NiTi on the substrate are illustrated in pink and blue colours respectively. PNT12 thin films of PTFE-NiTi displayed an excellent adhesion on all substrate types, and no stress was visibly observed (Figure 171 inset).

Modifications in the internal microstructure due to intercalation also change the surface energy and other functional properties such as wetting angles. The WCA on pristine NiTi films deposited using the process conditions mentioned above is 55°, as previously investigated in Section 6.6.3 – Fig 137. PTFE-NiTi – PNZ12 films have NiTi as the top layer; however, the WCA on the nanocomposite surface was measured at 87° (Figure 171), which is much higher than the WCA of NiTi. The WCA of the coatings was 87° and indicates an interaction between the NiTi (top layer) with PTFE deposited layers underneath. Intercalation in the PNT12 films created minor fissures and interstitial gaps in the microstructure of the nanocomposite by altering the internal physical interactions between PTFE and NiTi, and without involving any chemical reactions. The above changes in the film microstructure altered the wetting properties of the top layer demonstrating interactions, along with modifying the surface energy and morphology as well.

SEM and TEM analysis were employed as microstructure analysis techniques. SEM allow studying the morphology of the film surface (Figure 175). Contrastingly, TEM was selected for imaging the cross-sectional microstructure of the layered PTFE-NiTi nanocomposite after sample preparation by FIB as described in section 5.3.8. Figure

172 - Figure 174 display the bright-field and dark-field TEM images of PNT12 nanocomposite having PTFE (15 nm) and NiTi (135 nm) alternative layers.

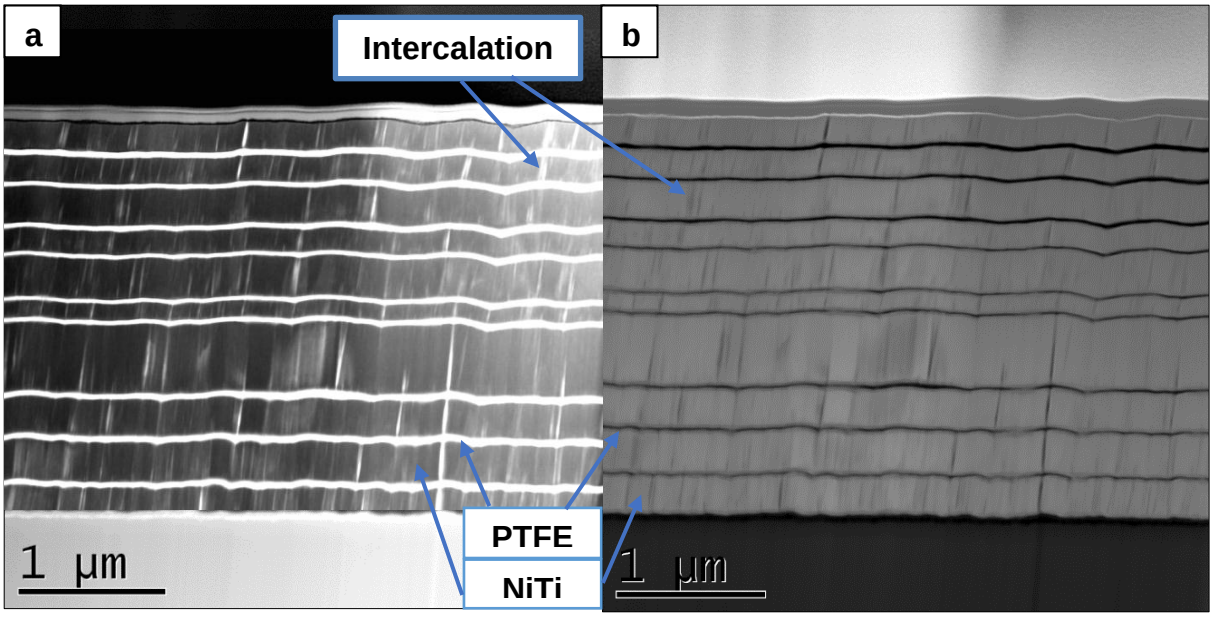

Figure 172: (a) A bright-field TEM image of PTFE-NiTi – PNT12 presenting alternative layers of PTFE and NiTi. (b) A dark-field TEM image of PTFE-NiTi – PNT12 presenting alternative layers of PTFE and NiTi.

TEM images in Figure 172 - Figure 174 provide an advanced pictographic elucidation of the fact that as-sputtered NiTi is amorphous and columnar grains appear as unidirectional elongated fibres between thin PTFE layers, and this is clearly displayed in dark-field image of Figure 173. TEM images demonstrate that the PTFE thin layers are stable and intact within the thicker metallic layers of the nanocomposite. 225 nm thick NiTi layer in PNZ9 film displayed stratum formation in the dark-field TEM image in Figure 164, which introduced interfaces within a single NiTi layers in a parallel direction to the substrate associated with fluctuations in deposition power. However, stratum formation is absent in PNT12 films because of the depositing thinner NiTi layers of 135 nm which now progress at a constant rate. Fine grains of NiTi extend perpendicular to the substrate and the grain shape matches to zone 1 of Thornton zone model, but contains a non-porous microstructure with densely packed columnar fibres represent zone T of the PVD sputtered thin films. Thus, NiTi has an interstitial zone alignment on Thornton zone model of PVD sputtered thin films, associated with the boundary between zone 1 and zone T.

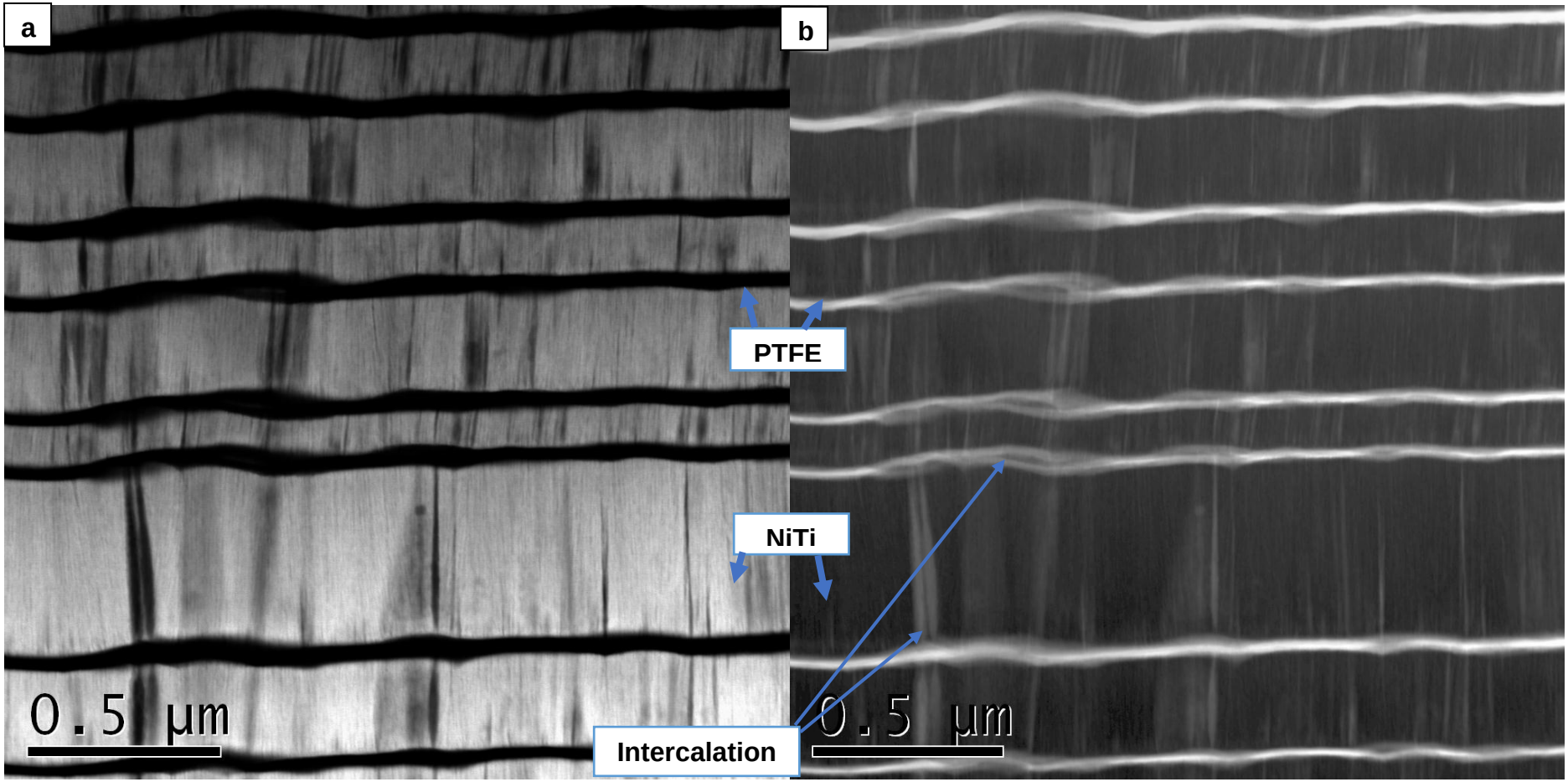

Figure 173: (a) A Dark-field TEM image of PTFE-NiTi – PNT12 presenting alternative layers of PTFE and NiTi. (b) A bright-field TEM image of PTFE-NiTi – PN12 presenting alternative layers of PTFE and NiTi.

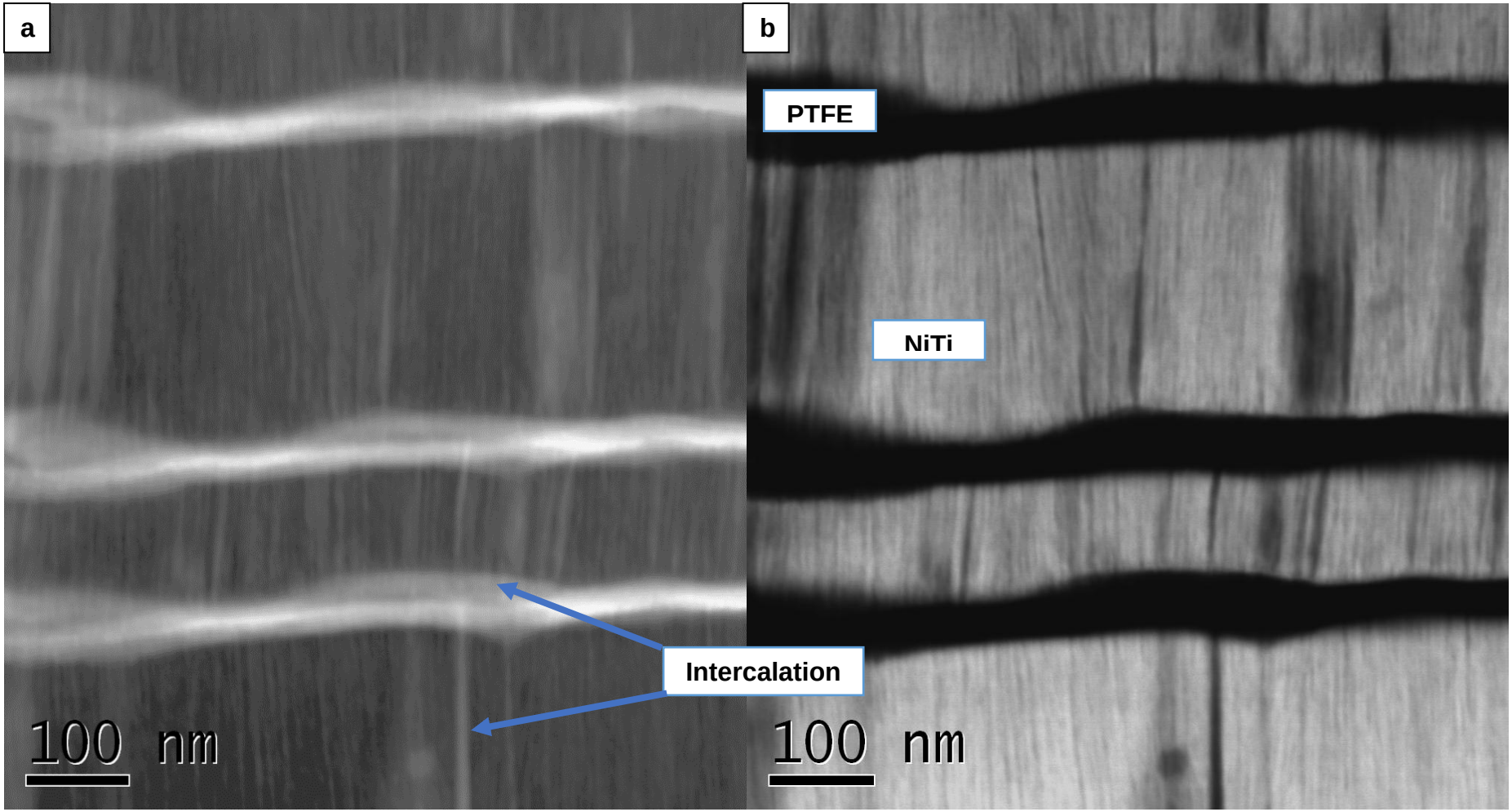

Figure 174: (a) A bright-field TEM image of PTFE-NiTi – PNT12 presenting alternative layers of PTFE and NiTi. (b) A dark-field TEM image of PTFE-NiTi – PNT12 presenting alternative layers of PTFE and NiTi.

The bright-field image in Figure 173 shows that the polymer chains of PTFE stack between the NiTi columnar layers. The carbon chain central skeleton aligns parallel to the substrate while the carbon-fluorine bonds along with fragments and chain ends of the crosslinks align in the vertical direction of the substrate. This solid-solid intercalation was introduced into the nanocomposites by sputtering interlocked PTFE and NiTi at the layer interfaces allowing the polymer material to stretch into metal structure through minor fissures and minute pores. The fissures and pores originate from the layer interfaces and extend into the metallic matrix, and here they formulate the repulsive-interaction of electronegative fluorine in the polymer with the electron sea of the metallic lattice, resulting in the formation of minor fissures at the interface. Small interfacial fissures propagate parallel to the NiTi columnar fibres by PTFE chain extensions. The thinner the PTFE layer the more interfacial fissures (intercalation) were observed, because more intercalation can be seen in the TEM images of PNT12 films (Figure 173) as compared to PNZ9 nanocomposite reported previously (Figure 165), which contained thicker PTFE layers.

Electrostatic attraction and Van der Waal forces are additional forces present in the nanocomposite microstructure that occur in addition to the primary bonding in the polymer (covalent) and metal (metallic). Apart from aforementioned fissures, the electrostatic forces also attract the polar-fluorine, the metal ions; whereas, the Van der Waal forces within the polymer chains keep fluorine atoms at maximum distance from each other in the polymer network, in the perpendicular direction to the carbon skeleton. The metallic lattice develops those fissures while the polymer chains reorient themselves to accommodate the above-mentioned repulsion. The electrostatic attraction between the metal ions and polar fluorine, and the Van der Waal forces direct the alignments of the intercalated spring-like PTFE into the NiTi matrix. It is easier for the thinner PTFE layers to extend into the vacancies within the metallic lattice and to reorientate forming the spring-like intercalated structures (Figure 174a) at the layer interfaces, which is named as solid-solid intercalation in PVD sputtering in this study.

Similar intercalation mechanism was found for co-sputtered PTFE-NiTi nanocomposites and layered nanocomposites prepared by PVD magnetron sputtering as shown in schematic illustration provided in Figure 145; however, the main difference is that the co-sputtered films (PNK1 and PNA2) contained nearly one-third vacant volume within the deposited films but layered nanocomposites only enclosed minor fissures. The difference between co-sputtered and layered intercalated nanocomposites is thought to be because of the higher polymer crosslinking and reduced packing density of the nanocomposite in co-sputtered films. During co-sputtering, the metal and polymer species are sputter deposited simultaneously on the substrate. Heavier metal ions hinder the growth in the polymer chains resulting in crosslinks and fragmented polymers interlocking within the metallic network, which leave more unoccupied spaces in the microstructure. Cross-linked polymers chains occupy more film volume as compared to the linear chains. Linear polymer chains in the layered arrangements have an option to extend in a parallel direction to the substrate on the metallic layer because of no metallic ions simultaneously deterring the plasma polymerisation.

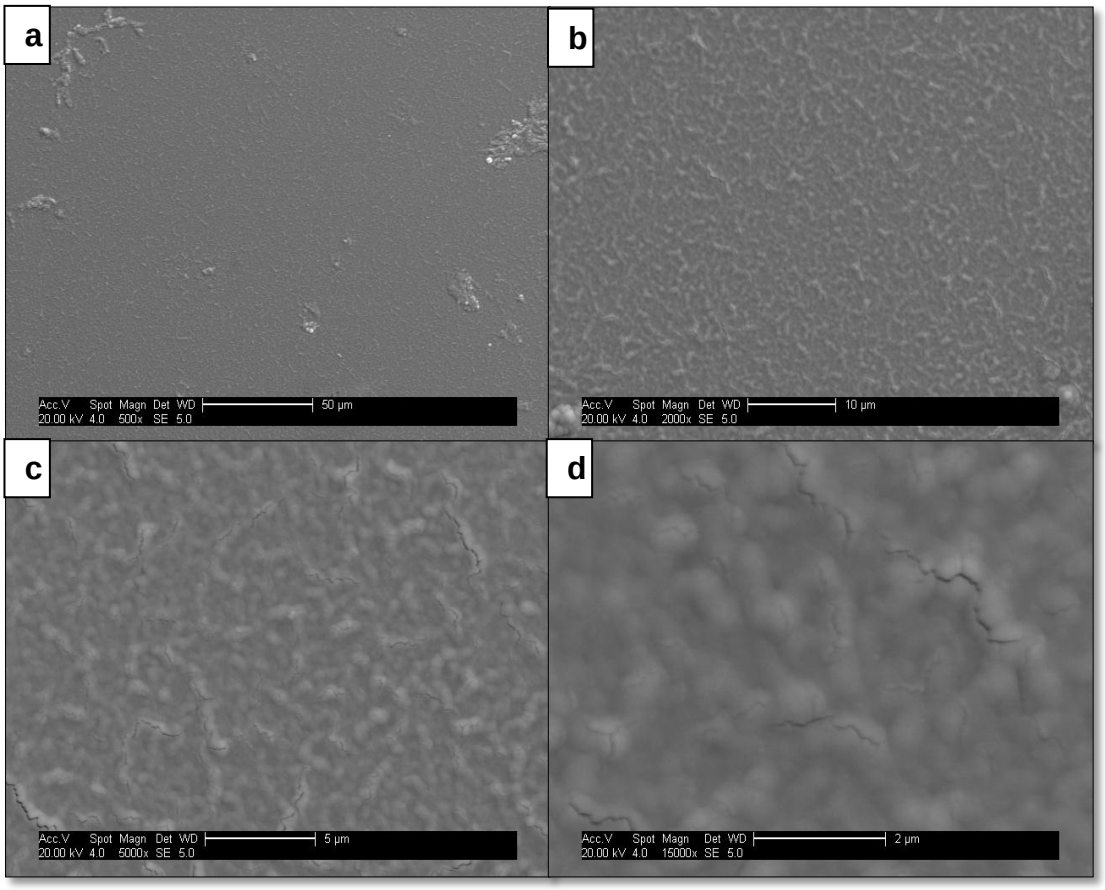

Figure 175: SEM images of PTFE-NiTi – PNB12 nanocomposite at magnifications of (a) x 500, (b) x 2000, (c) x 5000, and (d) x 15, 000.

The surface morphology of the modified PNT12 nanocomposite was characterised by SEM for which the images are shown in Figure 175. PTFE-NiTi – PNT12 films show no irregularities and endure a smooth and continuous surface with minimal imperfections. The columnar grains of NiTi seem to be merging, coalescing, and forming the grain boundaries around the fissures and pits observed by TEM. SEM results verify the TEM results about PTFE extension through the NiTi columnar fibres, and the intercalated PTFE at these fiber boundaries belonging to the layer underneath NiTi layer seen as emerging on the film surface through the holes within the microstructure.

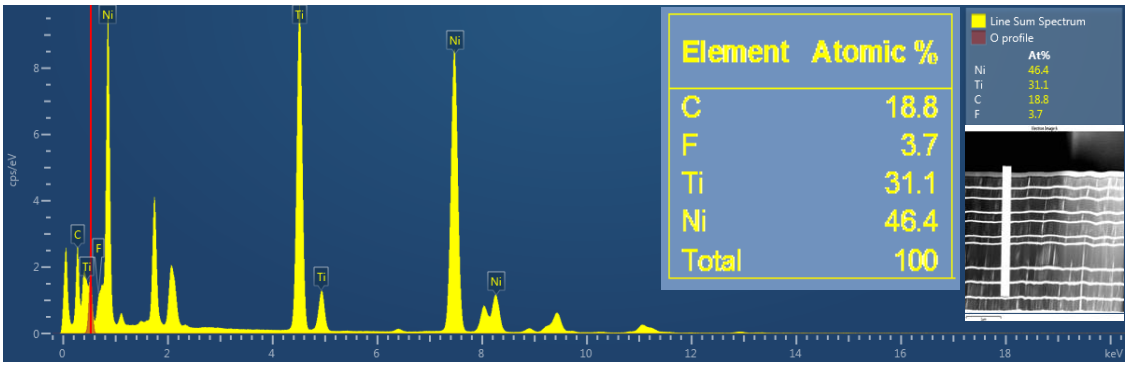

Figure 176: The line scan EDS results for PTFE-NiTi – PNT12 nanocomposite. The line scan was conducted sideways on the nanocomposite film cross-section prepared by FIB as shown in the inset.

PTFE-NiTi – PNT12 nanocomposite films were further analysed by line scan EDS to estimate the atomic composition across the cross-section of the layered film (not the top surface) as shown in the inset of Figure 176. The leading outcomes of the line scan EDS include considerably high Ni and small fluorocarbon atomic percent. The stoichiometric ratio of Ni and Ti suggests the formation of NiTi along with Ni_2Ti, both of which are SMAs having different positions in the NiTi phase diagrams. The fluorocarbon content relates to the fluorine atomic percent, not carbon. Excess carbon in the EDS results accounts for the carbon-based thin coating added to the specimen under investigation during the sample preparation by FIB. The reasons for the detection of the smaller fluorocarbon content as compared to NiTi and the reasons for higher Ni content than Ti are same as those explained previously for the EDS analysis of PNZ9 films (section 6.9.4).

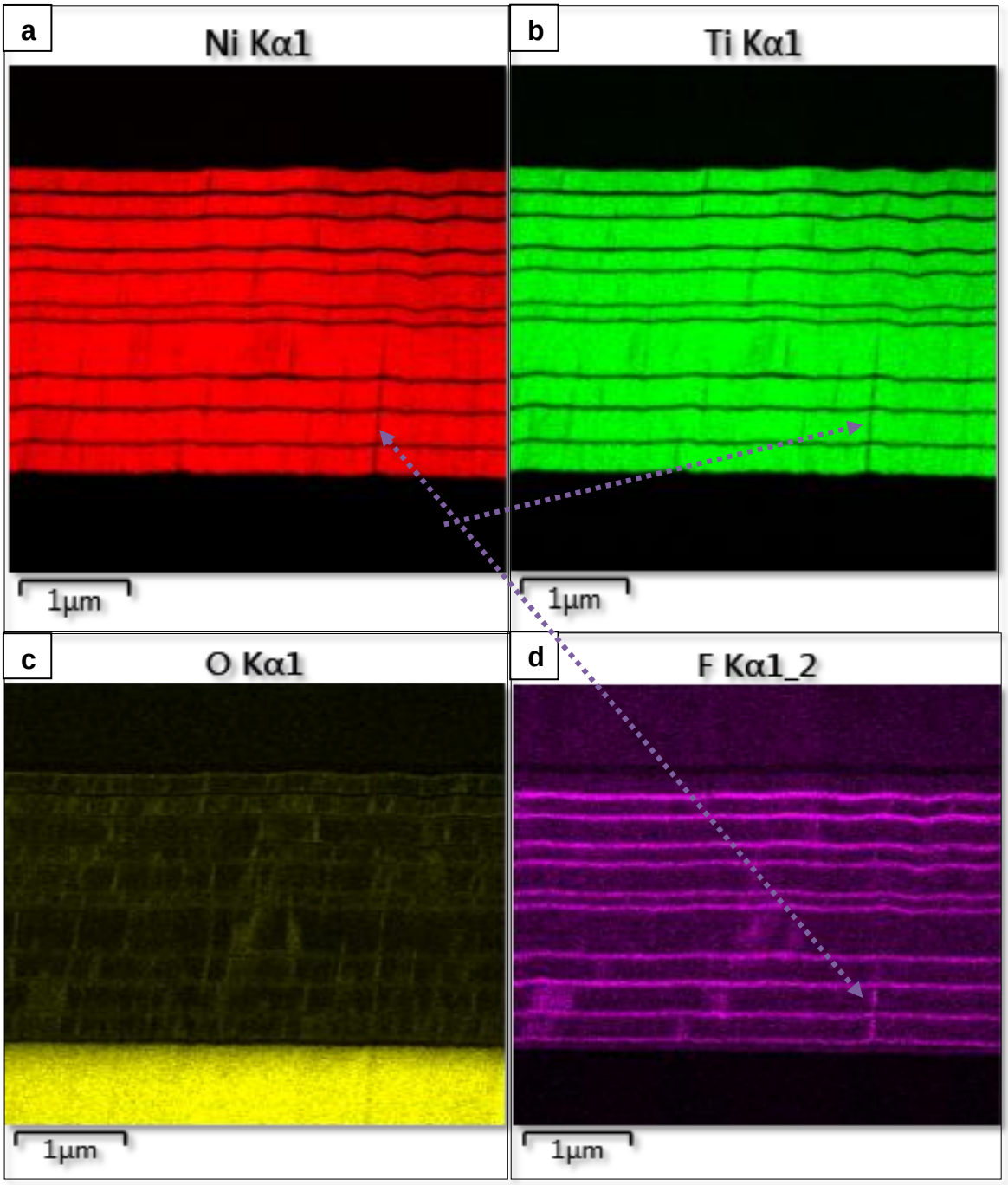

Figure 177: The EDS micrographs for PTFE-NiTi – PNT12 nanocomposite presenting various elements in the film microstructure.

EDS micrographs presented in Figure 177 were obtained by characterising the PTFE-NiTi – PNT12 nanocomposite films. The micrographs demonstrate the elemental composition of various elements including titanium, nickel, fluorine and oxygen in the film cross-section. FIB prepared the cross-sectional samples of the nanocomposite film. The colour intensities in the micrographs specifically relate to the elements concentration at that site of the film microstructure.

NiTi depositions are found as columnar fibres packed in between thin PTFE layers, which verify the previous discussion. Fluorine was mainly shown in intense colour at its primary location of the thin deposited layers, between NiTi layers; however, low colour intensity of fluorine is dispersed throughout the nanocomposite microstructure at NiTi fibre boundaries. Fluorine scatters through the film microstructure because of intercalation by extending its chains into the minor fissures and pits within the NiTi columnar fibres. Another fact that endorses the above explanation is the absence of Ni and Ti at those intercalated fissures, and an arrow on Figure 175 marks this. Contrastingly, no NiTi was found at the high colour intensity regions representing fluorine, which means NiTi does not outspread into the PTFE layers while PTFE disperses through the entire nanocomposite microstructure as a consequence of intercalation.

Ti has exceptionally high affinity for oxygen and titanium ions find any residual oxygen found in the sputtering chamber or oxygen that may be trapped in materials for producing titanium oxides, which are thermodynamically stable ionic compounds. The titanium ions bond with oxygen to form TiO_x (x: 1, 2) compounds leaving more atomic Ni^+ ions in the metallic lattice to interact with fluorine from PTFE and to form NiTi SMA. Excess oxygen in the nanocomposite can also lead to the nanocomposite manufacturing failure as previously observed for PNF3 films in section 6.8.3. For the above-stated reasons, it was crucial to determine the oxygen presence and ensure minimal oxygen content in the nanocomposites. Oxygen was not auto-detected by EDS software and had to be manually selected to obtain the EDS micrographs shown in Figure 177 in order to explain the influence of oxygen on PNT12 nanocomposite microstructure.

A higher oxygen concentration is perceived for the initially deposited layers because Ti would have immediately scavenged any residual oxygen or oxygen atoms trapped in the target or substrate materials. Later, some more oxygen impurities were added to the system along with the working gas supply, which was experienced in previous experiments and reported in sections 6.3 and 6.4. Figure 177 also show that oxygen is not only present in the metallic phase in the form of $TiO_{x,}$ but relatively higher oxygen was observed at intercalated fissures in some regions. The presence of oxygen, fluorine and carbon in the intercalated fissures follows because of their smaller atomic size as compared to Ni and Ti.

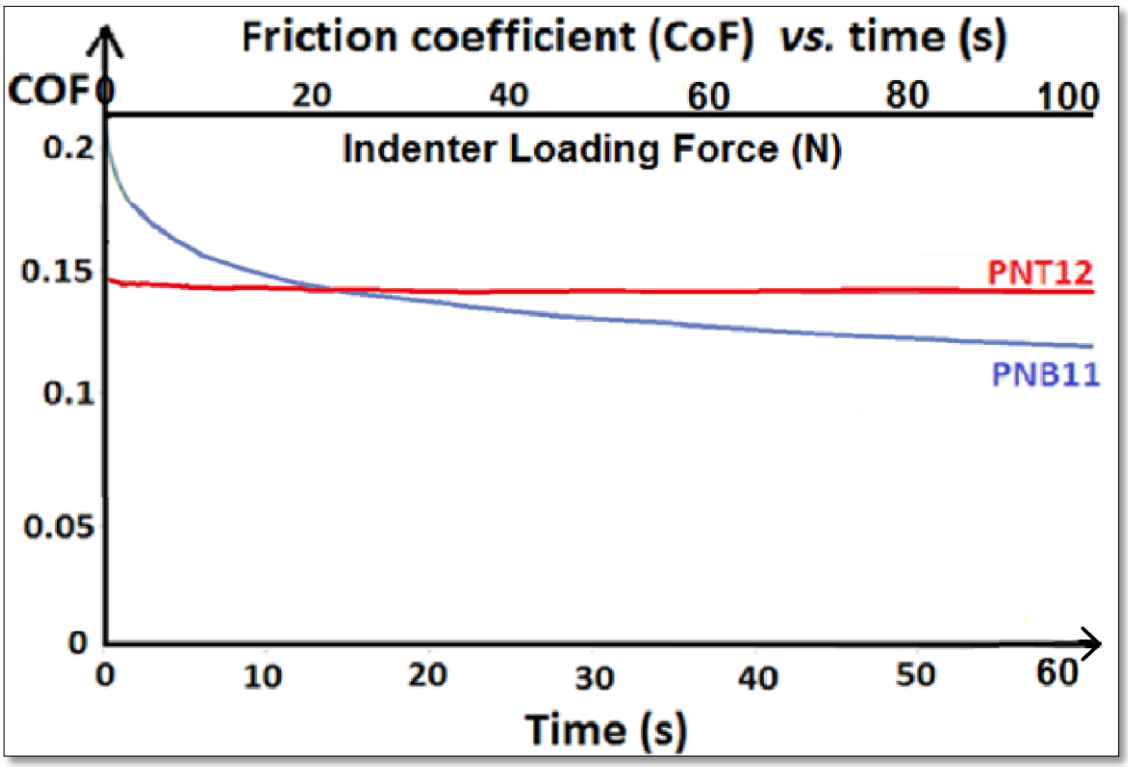

Figure 178: Coefficient of friction vs. time graph (trend / regression type: logarithmic) for PTFE-NiTi nanocomposites (PNB11 and PNT12) (measured by scratch testing using WC indenter under continuous progressive load (1 – 100 N), loading rate 100 N/min.

Functional characteristics of intercalated nanocomposite films were studied further by evaluating the lubricity. For this purpose, the PTFE-NiTi – PNB11 and PNB12 were selected, and scratch testing was used to estimate their surface lubricity. The scratch tester was equipped with a WC ball indenter, which performed the scratch test under a continuous progressive load (1 – 100 N), with a loading rate of 100 N/min (the maximum function force was set at 50N). The data obtained after scratch testing was processed to plot a friction coefficient vs. time graph (trend / regression type: logarithmic) for PTFE-NiTi nanocomposites (PNB11 and PNT12). The scratch testing at above-prescribed conditions did not cause coating failure, indicating an excellent adhesion to the substrate and stable microstructure of the thin films. Both PTFE-NiTi nanocomposites (PNB11 and PNT12) have the CoF values ranging from 0.1 to 0.2 as shown in Figure 178.

PNB11 nanocomposite was a 2 µm thick film containing 10 alternative layers of PTFE and NiTi with 20 and 180 nm respective layer thicknesses; whereas, PNT12 was a 3 µm thick film comprising 20 alternative layers of PTFE and NiTi with 15 and 135 nm respective layer thicknesses. The nanocomposite PNT12 retained a continuously low CoF throughout the test at 0.14 and did not display a significant discrepancy in CoF with the increasing load over time. Although PTFE was not deposited as the top-most layer, it is apparent that PTFE influenced the surface properties of the nanocomposite due to its dispersal in the microstructure by intercalation. This verifies the observation previously reported for the wetting angle measurements. PTFE-NiTi – PNB11 nanocomposite has an overall lower CoF as compared to PNT12 film. The pattern of CoF against increasing loading rate for nanocomposite PNB11 changes over time because NiTi provided the matrix strength to manufacture a load bearing thin film. Thicker NiTi layers within the microstructure resulted in the lack of much influence by PTFE deposited underneath the NiTi layers. Thus, the CoF vs. time trend of PNB11 varies from that of PNT12, which contains thinner NiTi layers and has more intercalated PTFE within the microstructure.

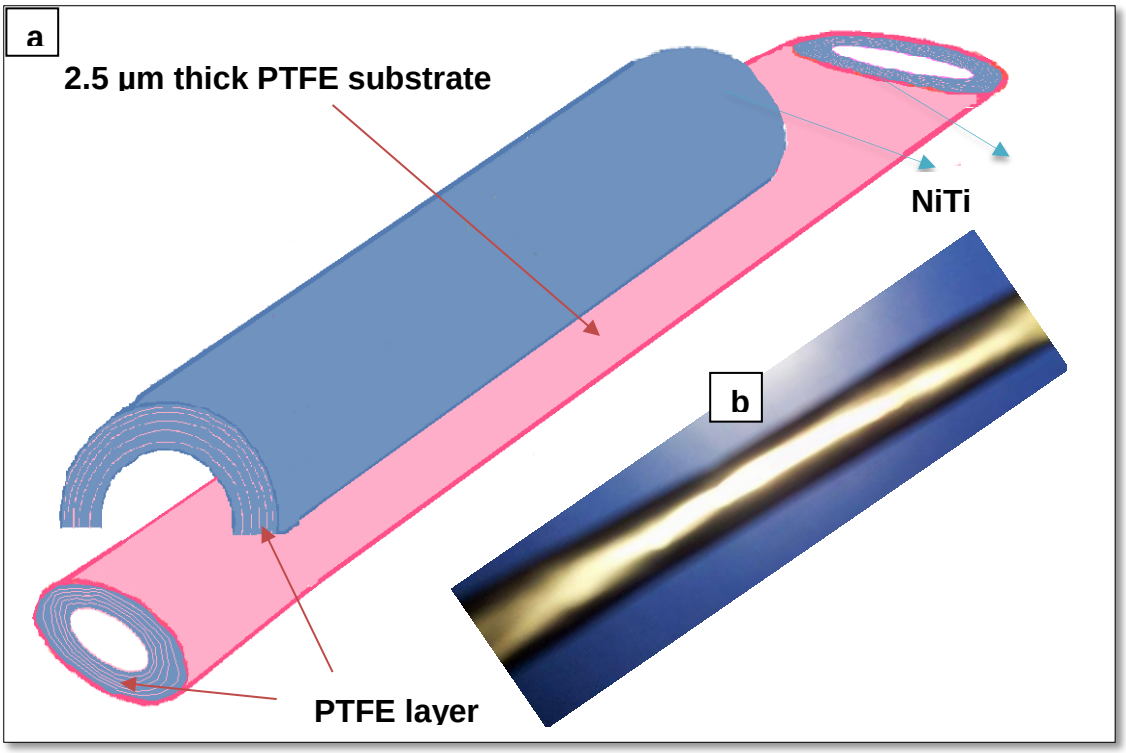

Figure 179: (a) The schematic for a urethral-model of layered PTFE-NiTi – PNT12 thin film, illustrating the mimicking of the structural order of urethral tissue that performs micturition, (b) A layered PTFE-NiTi – PNT12 thin film nanocomposite prepared by PVD sputtering as a biomimicked material.

PTFE-NiTi nanocomposites including the co-sputtered (PNK1) films and layered (PNT12) coatings were processed to fabricate urethral-models as illustrated in Figure 179a. An exceptionally thin PTFE substrate (2.5 µm) was used to prepare the nanocomposite model. PTFE is one of the deposited materials in the coating, and the thin substrate can be considered as a thick middle layer in the nanocomposite layout. The use of 2.5 µm thin PTFE substrate excludes the need for coating removal from the substrate after deposition. 5 µm thick nanocomposite films were fabricated for both co-sputtered and layered samples, which means 1.25 µm sputtering deposition was required on either side of 2.5 µm PTFE substrate as shown in the schematic illustration (Figure 179a). All deposition conditions used to manufacture the co-sputtered and layered nanocomposites were the same as previously described for PNK1 (section 6.8.1) and PNT12 (section 6.10) respectively.

The resultant co-sputtered specimen was adherent but stressed; thus, the films could not be rolled into a tubular shape after deposition. However, the layered PTFE-NiTi nanocomposite was adhesive to the substrate and maintained its stress-free microstructure in a tubular shape as well, as shown in Figure 179b. A needle was used to roll up the thin film, and small pieces of Kempton tape were used to secure the upper and lower ends of the rolled thin film. The surface of this tubular shape - PNT12 nanocomposite was found to have a WCA of 88°, which verified the intercalation. It was a significant landmark to be able to process the intercalated thin film into a tubular shape without damaging and still measuring its intercalated wetting response. The scope for the manufacturing of the optimised nanocomposite as a urethral-model is discussed below.

Natural tissue has a combination of hard and soft tissue, which varies their combining ratio depending on the function performed by that tissue. Soft elastomers and tough fibres both contain collagen in their structure, but the compositional ratio of the soft and hard matter changes depending on the requirements. This study provided an opportunity to tune the film microstructure and material properties by intercalation of a polymer and metallic substances. The microstructure and properties of the thin films can be modified further by altering the compositional ratio of the materials, and more interestingly, it is possible to change the extent of intercalation by altering the individual layer thicknesses of the two materials. Thus, introduction of solid-solid intercalation phenomena in PVD sputtered nanocomposites reveals the prospect to fine-tune the microstructure and properties such as surface energy, hydrophobicity, mechanical strength and lubricity depending on the applications of the thin films.

Urethra is a tubular structure that performs micturition involving liquid flow. Natural tissues involving fluid flow have WCA values matching to the requirement of the functional requirements. Wetting angles below 90° favour autonomous capillary action and keep the surface wet by providing excess fluids. Contrastingly, the WCA above 90° deter the hydrophilic substances and maintain a contamination free surface for longer. The urinary flow is mainly controlled by sphincter muscles working in response to the nervous

system. However, this study does not mimic the role of the nervous system to control the micturition, but the ultimate micturition function is mimicked by controlling the liquid flow. Thus, the aim of this study to combine a control on microstructure, wetting angles and lubricity by intercalation has been achieved. Solid-solid intercalation in PVD sputtered thin films without involving chemical reactions is a novel phenomenon in thin film engineering. An ability to include the pseudoelastic feature into the nanocomposite is an opportunity for future research, which is discussed further in section 10. A combination of the above four properties in one system would grant a flow control in a similar way to micturition.

7 INTERCALATION IMPACT ON MICROSTRUCTURE AND FUNCTION OF NANOMATERIALS

The PTFE-NiTi nanocomposites, having good adhesion to substrate and intercalated interactions within the microstructure, were deposited at process pressure of 10 x 10^{-3} mbar Ar and working vertical distance of 1 cm when the substrate holder was placed at horizontal distance of 3 cm from the magnetron centre. PTFE was deposited at 150W RF power, and NiTi was deposited at 50W DC power. All deposition conditions were carefully selected after a detailed investigation of the relationship between process conditions and the film properties, for which the results are reported in sections 6.1 to 6.6. The volume fraction of PTFE and NiTi in the nanocomposites was controlled by varying the deposition rates of PTFE and NiTi at a particular set of process conditions. The results for intercalated microstructure and film properties of all the nanocomposites samples endeavoured in this research are provided in Section 6.8 to 6.10. A comparative summary of the microstructural and functional properties (wetting and lubricity) of PTFE, NiTi and intercalated PTFE-NiTi nanocomposites (co-sputtered or layered) is provided in this section in relation to the schematic presented in Figure 150, which illustrates the novel solid-solid intercalation mechanism in PVD sputtered metal-polymer nanocomposites.

The manufacturing of intercalated PTFE-NiTi was only successful when the NiTi was present as more than half of the volume fraction of the nanocomposite. The higher the NiTi fraction in the film was, the more wetting angle alteration due to intercalation was observed. PTFE-NiTi nanocomposites contain metallic NiTi and PTFE chains, having covalent bonding. The two types of materials overlay each other because of cross-linking of PTFE into and around the NiTi metallic matrix-lattice. PVD-sputtered PTFE films contain a cross-linked structure due to polymerisation in the deposition plasma, as described in section 6.5. The mechanism of intercalation has been summarised earlier in this study, which appraises the previous discussion on the mechanism of intercalation for co-sputtered and

layered nanocomposites. To aid the understanding, during this re-appraisal, the schematic provided in Figure 150 is reproduced in this section.

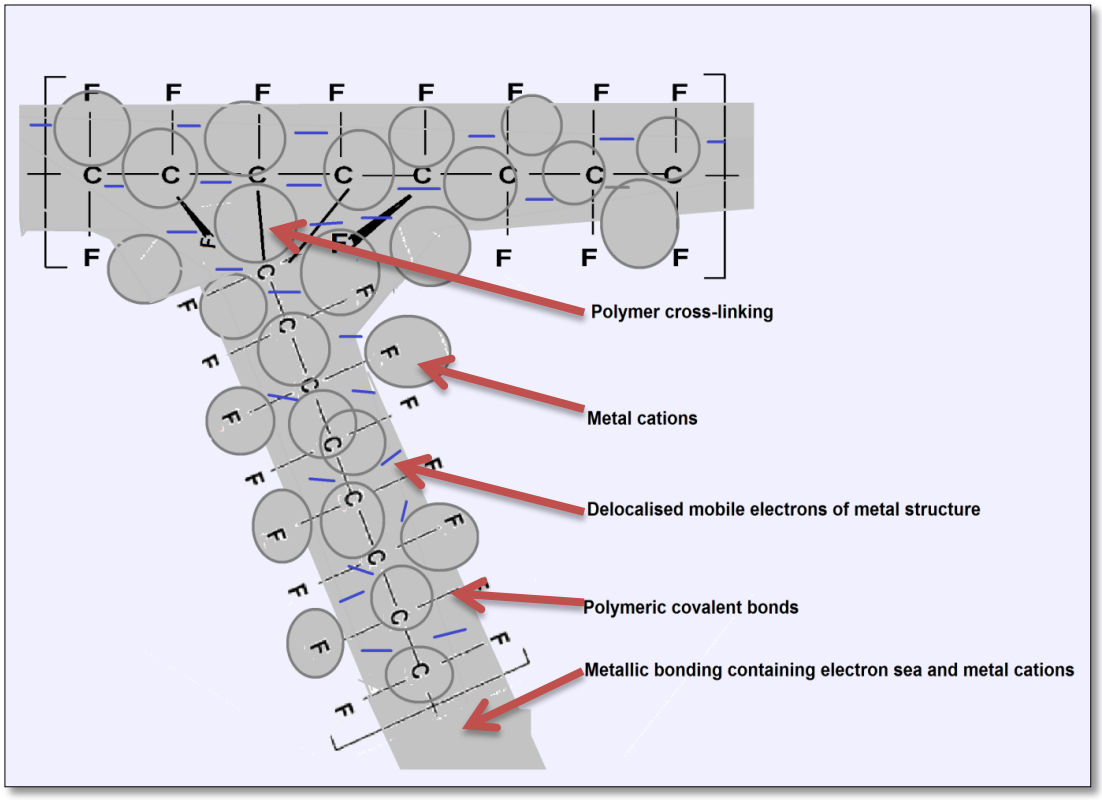

Figure 180: A schematic model of an intercalated PTFE-NiTi nanocomposite representing metallic structure of NiTi and covalent bonding in the PTFE overlaying each other; while both materials reorient their atomic structure in order to accommodate the electrostatic repulsion between delocalized electrons of the metallic lattice and electronegative fluorine in polymer chain.

The electronegative nature of fluorine in the polymer chain keeps the fluorine atoms at the maximum possible distance from each other but within the chain geometry. The fluorine atoms are covalently bonded around carbon skeleton resulting in a non-polar structure. The metallic lattice and polymer chains reorient their atomic structure in order to accommodate the electrostatic repulsion between the delocalised electrons of metallic lattice and electronegative fluorine in the polymer chain. Van der Waal forces within the polymer chains keep fluorine atoms at a maximum distance from each other in the polymer network and in a perpendicular direction to the carbon skeleton. Van der Waal forces within the hydrophobic and non-polar polymer chains

and electrostatic forces in the metallic lattice also contribute to the realignment of the microstructure developing the intercalated gaps.

Intercalation is the expansion of the overall microstructural lattice of the nanocomposite by secondary bonding (physical interactions and realignment), without causing changes to the primary structure and bonding. The fluorine atoms reorient themselves towards the outwards direction of the nanocomposite microstructure because of the repulsion from the delocalised mobile electron sea in the metallic lattice of the nanocomposite matrix. While aligning outwards, fluorine also builds an affinity for positively charged metal ions of Ni and Ti. Ni and Ti particles are firmly retained in the metallic lattice by electrostatic forces of attraction; thus, do not leave the metallic lattice but incline slightly outwards because of the affinity of electronegative fluorine.

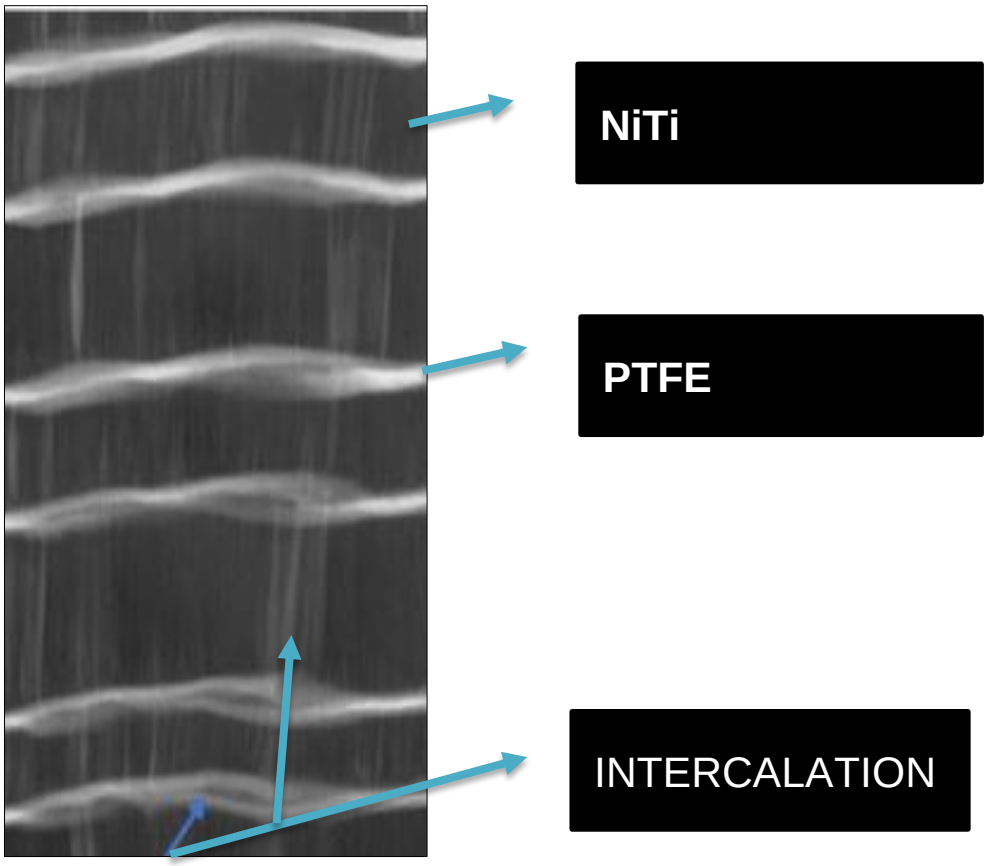

Figure 181: A supplement from Figure 174, to highlight the intercalation in layered nanocomposites. Figure 174 is a bright-field TEM image of PTFE-NiTi – PNT12 presenting alternative layers of PTFE and NiTi.

To aid the above solid-solid PVD-intercalated phenomena, the EDS-TEM results of the layered intercalated nanocomposites are taken into account. As-sputtered amorphous NiTi deposits as unidirectional elongated fibres between thin PTFE layers, both materials contain columnar grains in the microstructure. Fine grains of NiTi extend perpendicular to the substrate, and the grain shape matches to zone 1 of Thornton zone model but lack of porosity. The densely packed nature of the columnar fibres, which is a property expected from zone T. The polymer chains of PTFE stack between the NiTi columnar layers. The carbon chain central skeleton aligns parallel to the substrate while the carbon-fluorine bonds along with fragments and chain ends of the crosslinks align in the vertical direction of the substrate. The solid-solid intercalation introduced into the nanocomposites by sputtering interlocks the PTFE at the NiTi layered interfaces allowing the polymer material to stretch into the metal structure through minute fissures formation. The fissures originate from the layer interfaces and extend into the metallic matrix, and they formulate the repulsive-interaction of electronegative fluorine in polymer and the electron sea of the metallic lattice, resulting in the formation of minor fissures at the interface. Small interfacial fissures propagate parallel to the NiTi columnar fibres by PTFE chain extensions. The thinner the PTFE layer the more interfacial fissures (intercalation) were observed.

Oxygen also plays a significant role in determining the intercalated microstructure. Titanium's high affinity for oxygen thermodynamically favours the TiO_x (x: 1, 2) formation, which are stable ionic compounds having strong electrostatic attraction between Ti and oxygen. The titanium-oxygen bonding leaves more atomic Ni^+ ions in the metallic lattice to interact with fluorine from PTFE and to form NiTi SMA. Oxygen is not only present in the metallic phase in the form of $TiO_{x,}$ but the oxygen was located by EDS at intercalated fissures as well. Oxygen, fluorine and carbon in the intercalated fissures account for their smaller atomic size when compared to Ni and Ti atoms.

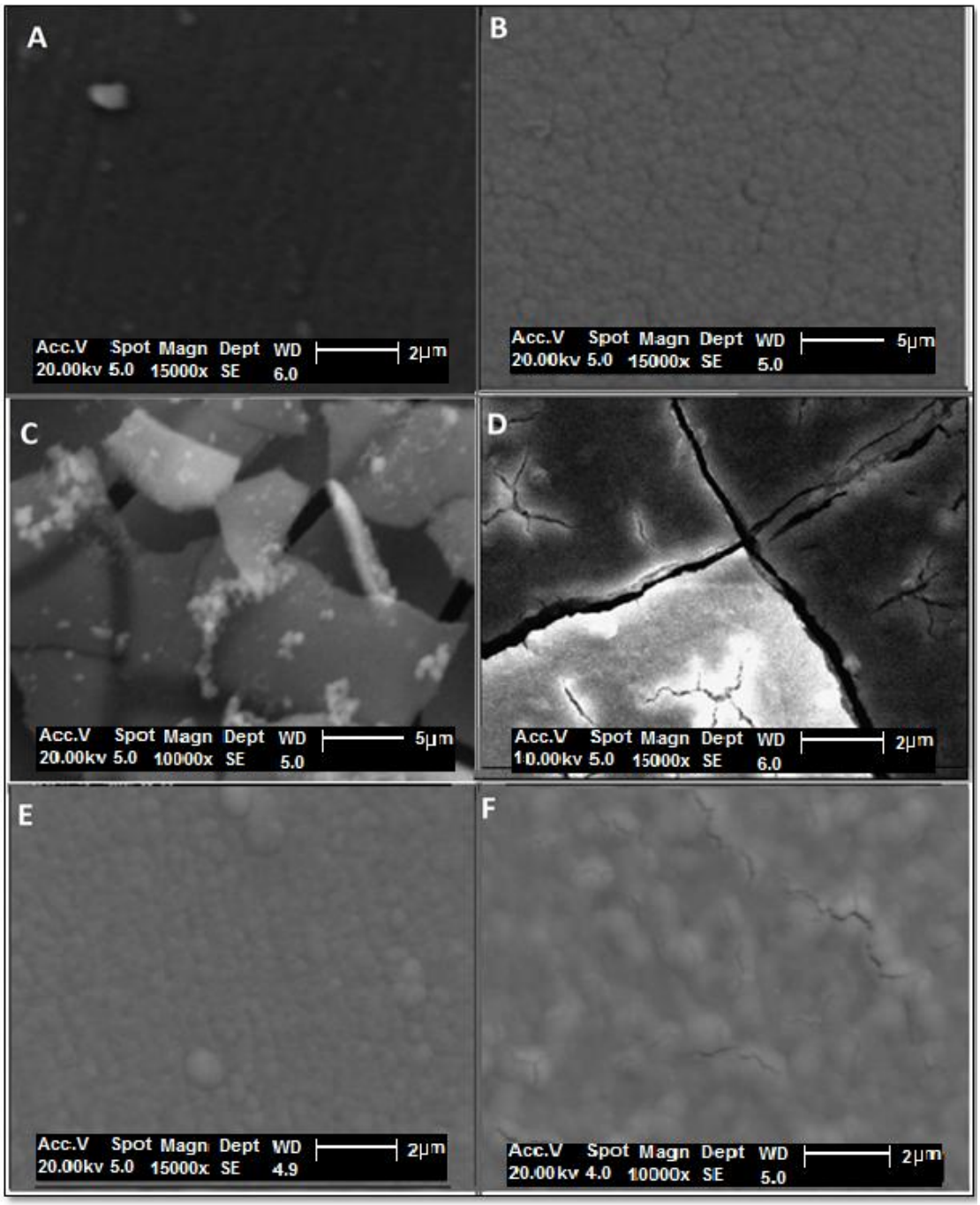

Figure 182: SEM images for PVD-deposited thin films of (a) PTFE (x15000), (b) NiTi - (x15000), (c) Co-sputtered NiTi rich nanocomposite of PTFE-NiTi – PNK1 (x10, 000), (d) Co-sputtered equi-composition nanocomposite of PTFE-NiTi – PNA2 (x5000), (e) Layered NiTi-rich nanocomposite of PTFE-NiTi – PNB11 (x15000), and (f) Layerd NiTi-rich nanocomposite of PTFE-NiTi – PNT12 (x15000).

Following a re-evaluation of the comprehensive review on intercalation provided above, the present section compares the morphology of the intercalated nanocomposites with pristine PTFE and NiTi thin films deposited under the same process conditions. For this purpose, previously discussed SEM images of PTFE, NiTi, co-sputtered nanocomposites (PNK1 and PNA2), and layered nanocomposites (PNB11 and PNT12) are presented again in Figure 182. All thin films represented in the SEM images in Figure 182 revealed an excellent adhesion to the substrate.

Figure 182A shows that PVD-PTFE deposited as smooth defect-free thin film having minuscule granular clusters; however, the cluster assemblies lack defined shapes in some areas indicating that the polymer chains are not linear and fully polymerised. Figure 182B presents NiTi deposits as regular coatings without any significant imperfections on the surface. The granular columns have some furrows surrounding them indicating the presence of few B2 crystals and boundaries. This was verified by XRD results in section 6.4.2. NiTi deposits mainly as an amorphous film; however, the XRD had one broad peak, the cube plane of the B2 lattice. The grains of PTFE match to zone T of structural zone model whereas NiTi grains are similar to those in zone 2, when both films were deposited at same process conditions. The reason for the difference between PTFE and NiTi microstructural zone relates to the fact that at specific process conditions polymer has a lower sputtering yield, and the microstructure is more sensitive to changing process pressure. Lower process pressure influences the polymerization of PTFE, and the defined cluster shape is lost. The influence of process pressure of the polymerization of PTFE is discussed in detail in section 6.5.3.

The morphology of co-sputtered PTFE-NiTi films demonstrates that the films have voids and vacancies in their microstructure, which was verified by water absorption in the nanocomposites (Figure 182C). It was previously reported in section 6.8.1 that, approximately one-third of the volume of the film microstructure is vacant. [(- CF_2 -) – NiTi] is the empirical formula of equi-compositional PTFE-NiTi – PNK1 nanocomposite, as reported by the EDS results study. PTFE and NiTi are physically discrete in the thin films, but intercalation retains them within one microstructural framework.

Layered PTFE-NiTi films show no irregularities and provide a surface morphology with minimal imperfections (Figure 182E and Figure 182F). The surface of PNB11 film (Figure 182E) was less granular than the surface morphology observed for PNT12 film, which account for the layer thickness of the respective nanocomposites. The PNB11 films contained 10 alternating PTFE and NiTi layers while PNT12 film contained 20 alternating layers of PTFE and NiTi having less deposition thickness of each of the individual layers. Therefore, the columnar grains of the NiTi seem to be merging, coalescing, and forming the grain boundaries around the fissures and pits in PTFE-NiTi – PNT12 films. The grain boundaries in this context are NiTi grains within intercalated PTFE that are surrounded by PTFE at boundaries as well. PTFE exudes through the NiTi columnar fibres and the PTFE specks from the layer underneath the NiTi top layer are seen as emerging from the film surface through the intercalated pits and fissures.

It is hard to determine the microstructural zones for NiTi and PTFE in the co-sputtered thin films because of the voids and 3D flakes within the microstructure observed by SEM. However, the microstructural zones in layered nanocomposite can be compared to PTFE and NiTi Thornton zones directly. At specified deposition conditions, NiTi was found to have a microstructure matching to zone 2 with well-defined and broad columnar grains as shown in Figure 182B; however, this changed to a structure expected in zone 1 and T interface when observed in the intercalated nanocomposite settings. The change in the microstructural zones relates to the realignment of the NiTi metallic lattice to accommodate the thin PTFE layers within the intercalated channels. In the process of doing so, the metallic adatoms consume some of the K.E from the sputtering process resulting in elastic collisions to become more sensitive to the deposition pressure, and have reduced time to deposit in defined granular columns. The microstructural zones for PTFE in the layered nanocomposite could not be observed by SEM or TEM due to its smaller volume fraction and thin-deposited layers, but it is anticipated that PTFE retains its T-zone microstructure because of compaction intensity of plasma polymerisation with deposition pressure, increased cross-linking and fragmentation by intercalation. More crosslinking

and the fragmented structure of PTFE is observed in co-sputtered thin films. The interfacial gaps due to intercalation are greater for co-sputtered thin films (Figure 182) while the functional control of wetting angles and lubricity was still witnessed without losing the film texture. Along with those features, maintaining a stress-free surface was also possible for layered and co-sputtered nanocomposites having intercalation. The changes in microstructure due to intercalation significantly alter the lubricity and wetting angles of the thin films, depending on the volume fractions and the layer thickness. The results of CoF and WCA are summarised below to evaluate the changes in the functional performance of the nanocomposites with respect to PTFE and NiTi thin film thickness.

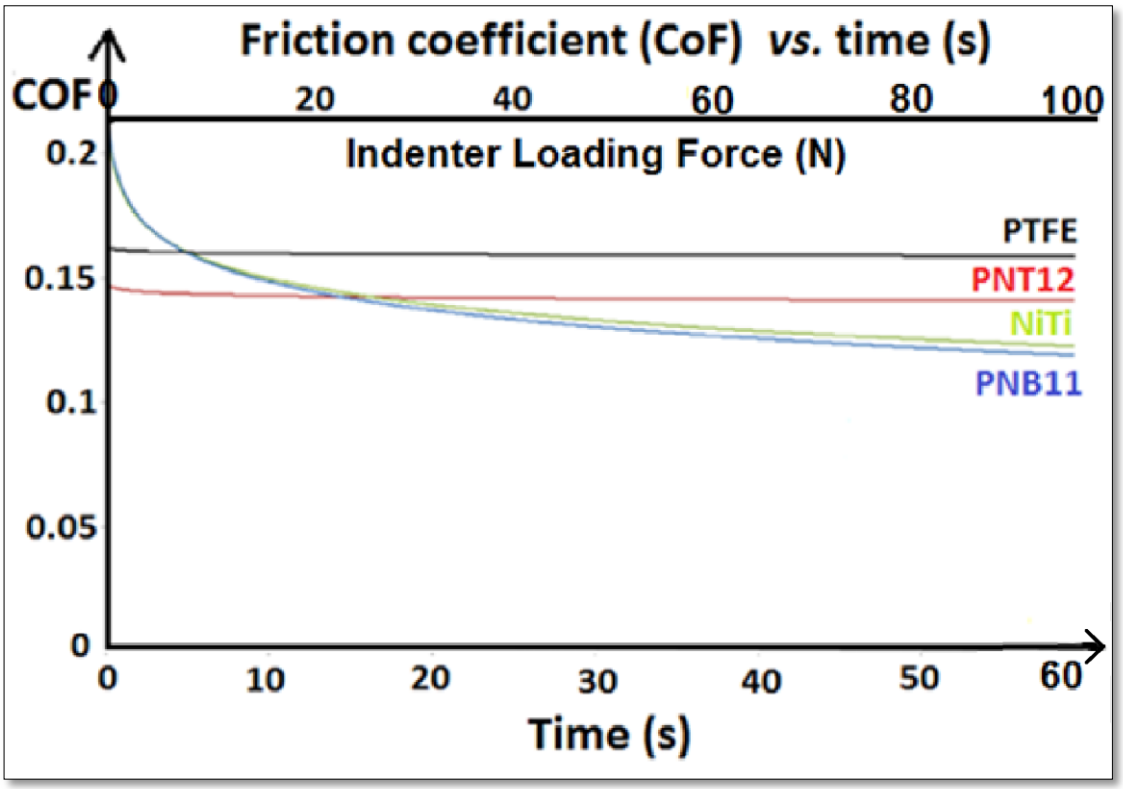

Figure 183: Coefficient of friction vs. time graph (trend / regression type: logarithmic) measured by scratch testing using WC indenter under continuous progressive load (1 – 100 N), loading rate 100 (N/min).

Small friction coefficient thin films offer lengthier lifetime and outstanding tribological characteristics [216]. The friction coefficients (CoF) of PTFE and NiTi were investigated previously, and the results reported in section 6.6.4

designated PTFE and NiTi films as low friction and lubricious coatings. Friction coefficient analysis by scratch testing for intercalated nanocomposite films (PNB11 and PNT12) was also discussed in section 6.10. The CoF vs. time trends of the nanocomposites, PVD-PTFE and PVD-NiTi films have been compared as shown in Figure 183. Figure 183 demonstrates that the scratch testing did not introduce the wear in the coatings and all thin films including PTFE, NiTi and PTFE-NiTi (PNB11 and PNT12) have CoF values ranging from 0.1 to 0.2. The coefficients of friction for all four samples are comparable to those of commercially available lubrication materials. For example, DLC (CoF: 0.2,) diamond (CoF: 0.5 – 0.1), tungsten carbide (CoF: 0.12) and Teflon sheets (CoF: 0.04 – 0.1), are commercially available lubricious materials having similar range of CoF.

PNT12 nanocomposite contains 20 layers alternative layers having thicknesses of 135 and 15 nm for NiTi and PTFE respectively. PTFE and nanocomposite PNT12 retained a low CoF in a similar fashion and did not display significant discrepancy in CoF with an increasing load over time. Although PTFE was not deposited as the top-most layer, PTFE obviously influenced the surface properties of the nanocomposite due to dispersal in the microstructure by intercalation. Similar observation was observed for the wetting angle measurements. PTFE-NiTi – PNB11 nanocomposite contains 10 layers alternative layers NiTi and PTFE with respective thicknesses of 180 and 20 nm, has the lowest CoF, and for this reason exhibits the most lubricity. The pattern of CoF against increasing loading rate over time for nanocomposite PNB11 and NiTi is alike. The nanocomposite has thicker NiTi layers at the film surface resulting in a lack of the influence of PTFE deposited underneath, resulting in NiTi-like lubricity pattern. The CoF decreases with increasing load over time; this deposition indicating the deposition of a load bearing coating resulting in the matrix strength provided by NiTi. NiTi is a shape memory and energy absorbing material and loading by scratch testing introduced stress, which may have led to some of the B2 crystals present in the amorphous NiTi layer transforming to martensitic phase resulting in a resistance to wear and an increase in lubricity.

Table 29: A summary table representing the static WCAs of pristine PTFE, pristine NiTi, and PTFE-NiTi nanocomposite films.

Thin film	WCA	
PTFE	108°	**PTFE and NiTi intercalate resulting in modifications in microstructure and functional properties. For example, WCA and lubricity of the film surface alter.**
NiTi	55°	
Layered PTFE-NiTi – PNT12	87°	
Co-sputtered PTFE-NiTi – PNK1	96°	

Modifications in thin films internal microstructure owing to intercalation altered the surface energy and the associated functional properties such as wetting angles. The optimised urethral-model of the layered nanocomposite (PTFE-NiTi – PNZ12) has NiTi coated as a surface layer. The WCA on the nanocomposite surface was measured at 87° (SD: 0.1), which is much higher than the WCA of NiTi (Figure 171). The WCA of pristine NiTi films deposited at process specified conditions is 55° (section 6.6.4 – Fig 137). The WCA of 87° results as an intercalated-interaction between the NiTi (surface layer) and thin PTFE layers deposited underneath. The WCA of the co-sputtered nanocomposite (96°) was measured to be above pristine NiTi WCA and below pristine PTFE WCA. However, the WCA dropped to 52° in 10 seconds, as presented before in Figure 146 and Figure 147. Water absorbance was explored by the amount of water absorbed by 0.25 cm^2 area (volume: 0.05 mm^3) of 0.2 µm thick film was 0.017 µl. Subtraction of absorbed water from the volume of thin film show a 0.006 mm^3 vacant volume of the thin film, which is one-third of the deposited film volume. This indicates the presence of fissures and vacancies within the film structure, owing to the intercalation.

8 RESEARCH APPRAISAL

The priliminary objectives of this project were to deposit and characterise PTFE and NiTi thin films by PVD magnetron sputtering. PTFE and NiTi coatings were characterised and compared to the existing literature for establishing the standard data. Analytical techniques including SEM, AFM, EDS, WCA, and scratch testing were employed to characterise the thin films. This followed the investigation of deposition rates, structure, composition, surface properties and hydrophobicity of PTFE and NiTi thin films for a range of deposition parameters including pressure, power and coating thicknesses. The control of working conditions was crucial because the effect PVD film properties are critically dependent upon the deposition conditions. RF PVD sputtered PTFE thin films reformed as intact polymer chains, like their bulk form, which was then characterised by FTIR spectroscopy for chemical structure and polymerised content within the coatings. NiTi films were deposited by DC magnetron sputtering, followed by DSC heat treatment. The cryatal microstructure of NiTi was studied by XRD.

Accomplishment of the above objectives was achieved, tailored for the deposition of intercalated nanocomposites manufacturing.

For PVD manufacturing of nanocomposites, the substrate holder was placed at a constant location over the magnetron ring, 3 cm from the target centre, where it provided the highest deposition rate as well. The vertical target substrate distance was maintained at 10 cm for both layered and co-sputtered deposition. PTFE target material was selected after ensuring that the deposited thin films have excellent polymerisation extent and hydrophobicity. The deposition rate database was obtained for PTFE and NiTi deposition at various process conditions. The process parameters of power and pressure allowed altering the deposition rate of PTFE and NiTi, and controlling the nanocomposite volume fraction. This approach enabled adjusting the nanocomposite composition and the properties of the nanocomposites by the

process parameters. High deposition rate of PTFE was achieved by maintaining a low pressure, and high RF power applied to the PTFE target. Higher deposition rate for NiTi was also obtained by sputtering at high power, but now DC power was used rather than RF, and small process pressures were maintained. At any specified process pressure and power, the deposition rate of NiTi was greater than that of PTFE. This difference was more significant at lower pressures but reduced at higher process pressures.

Preferred working parameters for NiTi were within the range of 5 x 10^{-3} to 10 x 10^{-3} mbar and DC power supply between 25W - 50W; these conditions were used for future depositions of NiTi to obtain NiTi thin films with little oxygen contamination. PTFE deposition at 150W and 15 x 10^{-3} mbar; this resulted in the highest polymerization content in PVD-PTFE films. For the PTFE thin films sputtered at 25 x 10^{-3} mbar, the polymerization was most successful at 100 and 150 W, which decreased with decreasing RF power to 50W. Thus, the polymerization was limited to 50W and 5 x 10^{-3} mbar process parameters resulting in highly branched fragments with an excessive crosslinking, high proportion of unreacted monomers, and rougher thin films were produced. This further limited the preferred deposition conditions to a pressure of 10 x 10^{-3} mbar and RF power of 150W for the PTFE deposition.

The aim of this study was to combine a control on microstructure, wetting angles and lubricity by intercalation. The microstructure was mimicked by combining hard and soft materials. The changes in layer thicknesses and volume fractions of PTFE and NiTi were used to adjust the intercalation in the microstructure in a similar way as would be expected in natural tissues; mimicked the variation in the amount of hard and soft collagen fibres for adjusting the load bearing and flexibility of the coating by way of comparison. Solid-solid intercalation in PVD sputtered thin films, without involving any electrochemical reactions, is researched for the first time in this study. The resulting nanocomposites reveal the prospect to modify the microstructure and the associated properties such as surface energy, hydrophobicity, lubricity and load bearing ability depending on the application. Intercalation was defined as inclusions of one type of material within the interplanar voids

of another material's lamellar layers forming a hybrid network. In this project, PTFE-NiTi nanocomposite is manufactured by inclusion of PTFE into NiTi. This correlates to the accomplishment of the objectives 5 and 6 of this project as restated below.

> The preparation of PTFE-NiTi nanocomposite coatings followed AFM, SEM, EDS, WCA, scratch testing and TEM analysis. Finally, an intercalated PTFE-NiTi nanocomposite device is manufactured by modifying the sputtering conditions, layer thicknesses and the material's composition. Controlled wetting is intended to be perceived by alterations in the wetting angles while maintaining the lubricity of the thin films.

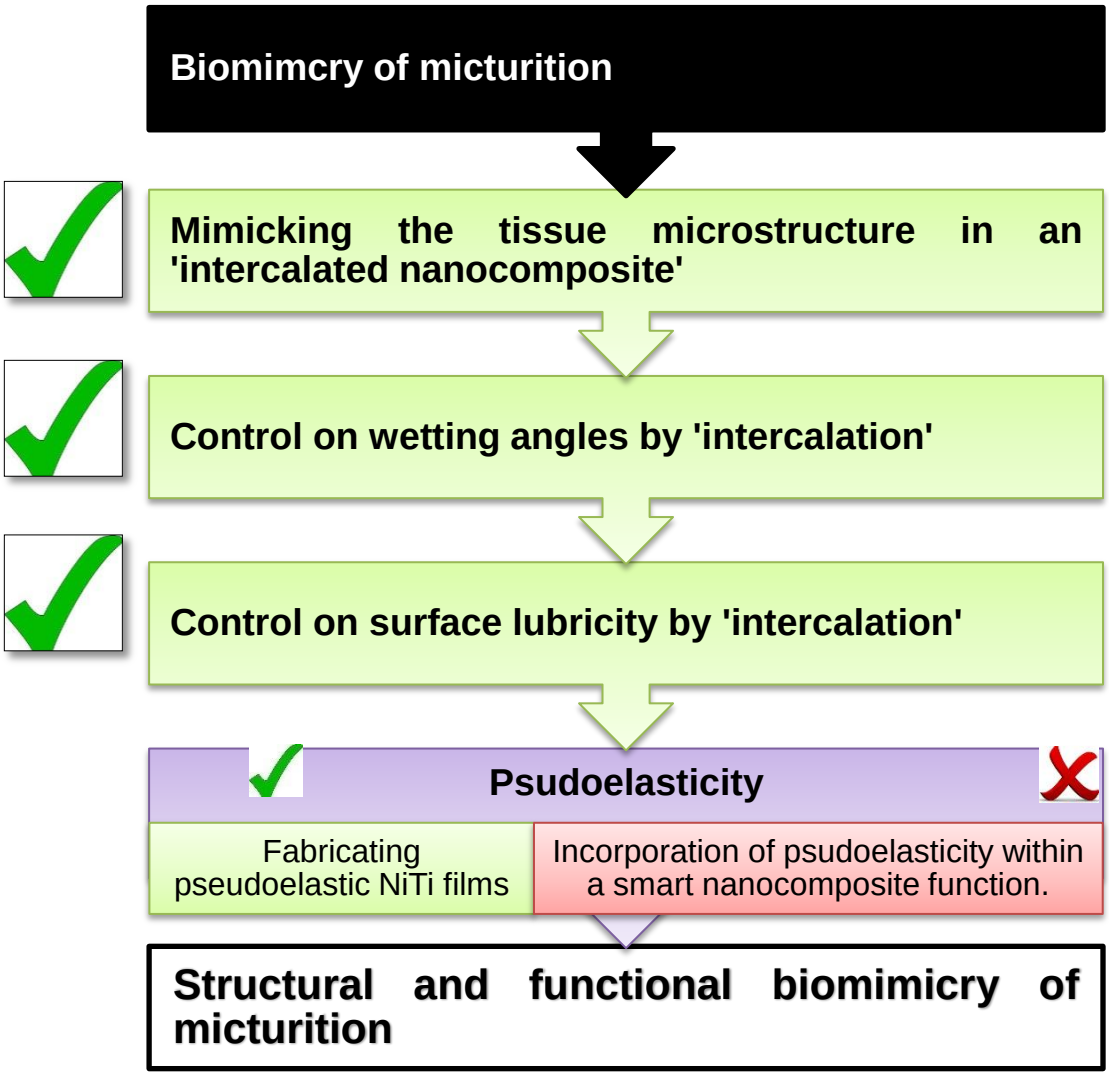

Figure 184: Steps of mimicking micturition.

Figure 184 summarises the contribution of this project towards mimicking the urethral structural order and function of the micturition. This project has met the objective of mimicking the urethral structural order; however, the NiTi can provide an additional feature by mimicking the sphincter muscles function involved in micturition. An additional ability to include the pseudoelasticity into the intercalated nanocomposite is an opportunity for future research to allow mimicking the micturition function as well. A combination of the above four properties in one system would grant a flow control in a similar way as micturition.

The difficulty in using the pseudoelastic feature along with intercalation for PTFE-NiTi nanocomposites was an absence of any crystallinity in the as-deposited NiTi. Crystallinity in NiTi can be attained by heat treatment during the manufacturing process or by post-sputter heat treatment. In either case, it requires a temperature above the melting point of PTFE, making it difficult to accommodate this additional functionality. Therefore, the scope of the project was limited to intercalation. Nevertheless, the some initial research were conducted (Section 6.4) to explore an opportunity to accommodate shape memory effect (particularly pseudoelasticity) intercalated PTFE-NiTi nanocomposite. For this purpose, a detailed study was undertaken on NiTi thin films to investigate the influence of stoichiometric composition and oxygen contamination, along with adjusting the transformation temperature of NiTi below the body temperature for allowing the stress-induced transformations on introducing the fluid loads. The study conducted to meet the objective 4 of this project was to modify the transformation temperatures of NiTi; which is restated below followed by a brief summary of the findings.

Tailoring the NiTi composition to attain the SMA's tranformations (transition temperatures) related to pseudoelasticity at the body temperature. NiTi thin films are analysed by DSC (phase transformations and associated enthalpies), XRD (crystal structure and composition).

The composition of Ni-rich $Ni_{53.5}Ti_{46.5}$ having the A_p of -19.24°C was chosen for PTFE-NiTi nanocomposite production. The desired Ni-rich atomic composition of NiTi thin films was achieved by the addition of small Ni pieces on the racetrack of the target. Heat treatment and annealing is vital for PVD sputtered NiTi thin films because the as-sputtered NiTi was amorphous as verified by the absence of any phase transformations in DSC thermogram, and lack of crystalline peaks in the XRD patterns. Excess oxidation within the SMA, during the heat treatment, resulted in the absence of any noticeable phase changes. The procedure of thermal treatment within the DSC chamber was modified to minimise the effects of oxidation. The transformation temperatures and the enthalpies for the phase transformations of the Ni-rich samples alter more by changes in NiTi stoichiometric ratio, as compared to the equiatomic and Ti-rich thin films. The transformation peaks of NiTi decrease with an increase in Ni content, which was carried out to obtain the austenite finish temperature below the body temperature for acquiring a pseudoelastic material. The Ni-rich NiTi accrued a high concentration of Ni-rich precipitates (Ni_4Ti_3) assembling on the crystal boundaries, deforming the martensitic NiTi lattices and resisting the phase transformations, resulting in small enthalpy values and low intensity of XRD peaks.

Table 30 provides a summary of the risks and obstacles that were addressed within this project along with the strategy adopted to overcome those problems.

Table 30: Risk and obstacles evaluation.

Risk / Obstacle	Consequences	Strategy to overcome	Outcome
May not intercalate at optimum working conditions.	Intercalated nanocomposite fabrication would fail to satisfy the aim of the study.	Systematic study of the known volume fractions and process parameters.	NiTi-rich nanocomposites are intercalated where PTFE is deposited as thin layers.
May not find a wetting and lubricity control by intercalation.	Intercalated nanocomposite manufacturing would fail to satisfy the aim of the study in terms of functionality.	Systematic study of varying the layer thicknesses and volume fractions to understand the mechanism of intercalation.	A Fine-tuned mechanism for controlling the WCA on the film surface was produced for lubricous nanocomposites.
NiTi transformations might not correspond to 37˚C.	Pseudoelasticity will not be perceived at body temperature.	Alterations in Ni and Ti ratios and heat treatment were used to control transformations.	Transformations temperatures were found below the body temperatures.
Complexity of polymer	No baseline data to know the complexity of a polymer reforming from a plasma.	The baseline data was obtained for PTFE sputtered films at various process conditions.	Examined the complexity before and after sputtering showing that PTFE reforms after deposition.
Residual oxygen in the chamber	Composite may not have desired properties due to oxygen in thin films.	Restrict oxygen supply by significantly low pressure and minimum Ar gas.	Oxygen supply was minimised, and the conditions were found where NiTi SMA forms and transforms.

The most significant risk was an inability to form an intercalate microstructure between the metal and the polymer, and it was experienced at the start of the project when the equi-compositional and PTFE-rich thin films failed to show any intercalated responses. This problem also accompanied the risk that the nanocomposites may not achieve intercalation at optimum working conditions found for PVD sputtering of PTFE and NiTi. A systematic study was conducted to investigate the reasons for failure and a way to attain the anticipated intercalated feature, where the volume fractions and the process parameters were altered methodically. The systematic study identified the NiTi-rich approach to be the right one to attain the desired results. It was also found that thin PTFE layers showed a better response for intercalation.

There was an additional risk that despite an intercalated microstructure, the intercalated nanocomposites may not respond to wetting and lubricity. This would fail to find the proposed functional response by intercalated nanocomposites. An orderly study was conducted by varying the layer thicknesses and volume fractions to understand the mechanism of intercalation and the factors that enhance the wetting responses. A fine-tuned mechanism ultimately evolved for controlling the WCA on the film surface of the lubricous nanocomposites; according to which the thinner films deposited within thick NiTi columnar fibres resulting in the efficient wetting and lubricity responses.

An objective of this study was to find the NiTi transformation below the body temperature as a biomimicking approach. The transformation temperatures in the initial studies were experienced above 100°C. Inability to find the right deposition temperature would prevent from taking an advantage from shape memory at 37˚C. Alterations in Ni and Ti ratios, removal of oxygen from the system and heat treatment were used as an approach to control transformations. Transformations temperatures were found to be below the body temperatures in Ni-rich thin films.

Complexity of the polymer was a primary concern because sputtering is an energetic process, which dissociates the polymer chains into short fragments and monomers. No baseline data was found in existing literature to explain

the complexity of a polymer and percentage polymerisation from plasma. To solve this problem, the baseline data was established at various process conditions and the percentage polymerisation at those conditions is evaluated. PTFE complexity was also examined before and after sputtering, which has shown that PTFE forms after deposition with a polymerisation ratio of above 90%.

Titanium has a substantially high thermodynamic affinity for oxygen, and it promptly forms oxides with any residual oxygen found in the chamber. This may lead to a decline nanocomposite performance, and the desired properties may not be achieved in thin films. To solve this problem the oxygen supply was further restricted by having substantially low working gas pressure, exceptionally high vacuum, addition of a getter and using minimum argon gas from one gas line rather than the multiple gas lines.

9 CONCLUSIONS

PVD sputtering has been useful to form intercalated PTFE-NiTi thin films on glass, Si and PTFE substrates. To acquire a high sputtering rate, the substrate holder was placed at a constant location above the magnetron ring, at 3 cm from the target centre. The process parameters for PTFE-NiTi nanocomposite manufacturing were 10 x 10^{-3} mbar Ar pressure, 150W RF for PTFE and 50W DC for NiTi deposition.

The process parameters of power and pressure allow altering the deposition rate of PTFE and NiTi. The highest deposition rate of PTFE was attained at low process pressure (5 x 10^{-3} mbar) and high deposition power (150W). At any specified pressure and power, the deposition rate of NiTi is greater than that of PTFE. This difference is greatest at lower pressures. The deposition rates at specific process conditions were used to calculate the volume fractions of each material in a PTFE-NiTi nanocomposite.

PVD-NiTi thin films are amorphous with few B2 NiTi crystals shaping up with a broad peak positioned at 2Θ = 42.7° (110) suggesting the early stage of nanocrystallite formation. The film compositions, the heat treatment conditions and the annealing temperatures significantly influenced the phase transformations and the associated enthalpies. Wider hysteresis and the higher enthalpies of the upper range heating-cooling cycle represent greater amount of material undergoing the phase transformations, as compared to the phase changes in lower range heating and cooling cycles. Equiatomic NiTi was precipitation-free while Ti_2Ni and Ni_4Ti_3 precipitates were mainly observed in Ti-rich and Ni-rich thin films respectively. Relatively small magnitudes of base pressure, low working gas pressures, small magnitudes of deposition power, and modified heat treatment method were employed as methodologies to avoid the oxidation of NiTi thin films.

PTFE has successfully formed as a thin film polymer after PVD sputtering. Reference data is established for a range of PTFE target material, and It is further verified that the some materials give a higher polymerization ratio. PTFE deposited at high power, and low pressure was highly polymerized with

a higher polymerization ratio within the coatings. An ability to modify the WCA, related to the polymerization content, was also established.

SEM images demonstrated that it was possible to form PTFE and NiTi with stable layers with smooth and continuous morphology containing minimal defects. The grains of PTFE matched to zone T of the Thronton diagram while NiTi grains are similar to those in zone 2 of Thronton zone growth model when both films were deposited at chosen process conditions.

Co-sputtering fabricated the NiTi-rich and equi-compositional intercalated PTFE-NiTi nanocomposites. The nanocomposites contained cavities in the microstructure of the two-phased material, which consumed approximately one-third of the total volume. SEM was used to observe the intercalated microstructure of co-sputtered PTFE-NiTi nanocomposites and TEM and SEM techniques were used to observe the intercalated microstructure of layered PTFE-NiTi nanocomposites. EDS found the elemental compositions. NiTi-rich matrix and thinner PTFE layers displayed higher intercalation ability for the layered nanocomposite films, which presented spring–like intercalated PTFE chains fissuring into the NiTi fibrous columns. WCA was used to examine the functional evidence of PTFE-NiTi interactions in all intercalated materials. All films including PTFE, NiTi and intercalated nanocomposites were exceptionally lubricious with low CoF within the range of 0.1 to 0.2. CoF vs. loading time pattern for the PTFE-NiTi films varied with changes in the intercalated microstructure.

10 POTENTIAL APPLICATIONS AND FUTURE STUDIES

Mimicking micturition fabricated the intercalated-nanocomposite films that allowed taking the advantages of individual material characteristics in combination, along with added benefit of their assemblage in intercalated settings would allow control of microfluidic flow. The intercalated films enable influencing the wetting capacity of the coating surface. The microstructural, physical and morphological properties of the nanocomposites vary by changing the deposition parameters, which make them the multifunctional, adjustable and advantageous candidate for the additional uses as thin films such as energy-absorbing nanomaterials. The metal-doped fluoropolymer and other polymer-based applications are commonly used for thermal stability of various devices [12]. PTFE-metal thin films can be a sustainable substitute for some of these uses.

Introduction of the novel nanocomposite uncovers innovative grounds for the multidisciplinary research of thin film active surfaces and offers potential for fluid flow applications, controlled by stress-induced contraction. PTFE-NiTi coatings are the first example to intercalate polymers and SMAs within a nanocomposite, suggesting a potential for stress-induced contraction and relaxation. As a result, this should be the first prospective step to take this study further. Above the body temperature, the nanocomposite would be responsive to the stress induction of fluid loads by expanding and relaxing the intercalated lattices. NiTi SMA allows stress-induced shape memory transitions and has a low wetting angle (hydrophilic). As a result, the fluid flow on NiTi film surface would be a self-driven phenomenon in a smart intercalated PTFE-NiTi. Thus, intercalated PTFE-NiTi nanocomposite has a potential to modify further as a device displaying a controlled flow by mimicking the sphincter muscle function, leading to micturition-like microfluidics applications. Some other research opportunities and potential applications of this study are also proposed below.

NiTi SMAs are used in various biomedical applications due to pseudoelasticity and shape memory effect. The concerns for NiTi in biological applications

include its inflammatory response in soft tissues because of the activation of monocytes, and the release of Ni ions and the hydrophilic nature of NiTi in some applications [86; 217]. Ni ions may cause allergy, toxicity or carcinogenetic reactions within the body [86]. Some surface modification treatments can control the nickel release and inflammatory response; a surrounding the outer layer of PTFE within a PTFE-NiTi nanocomposite is one example from this research.

Factors such as wasted target material and machine downtime, while replacing the target would reduce the profit. Better target utilisation and uniform thickness are oppositely related to each other, so both aspects had to be compromised to some extent. In this project, the target utilisation was not one of the main concerns as it was focused on the fabrication of intercalated nanocomposites. In industrial applications of such materials, the target utilisation will have a prime importance due to the cost-effectiveness being an important concern. For this reason, the deposition rates and target utilisations during the manufacturing process should be further modified in the future for the industrial applications.

Lubricious films are also advantageous for microfluidity. The nanoscale liquid flow varies significantly with small changes in film lubricity. The idea of controlling the lubricity by varying the intercalation and layer thicknesses in layered nanocomposites can have potential benefits for microfluidic applications. The formation of grooves and channels in the co-sputtered nanocomposites can produce fluid absorbing and deabsorbing actuators in which the stress induction is loaded by fluid interactions at the nanoscale. It was also experimented that the nanocomposite film (PNT12) became more lubricious on increasing the progressive load over time. The layered nanocomposites enduring the CoF within the range of 0.1 to 0.2 are the potential candidates for self-lubricating, load bearings and energy absorbing coatings.

The active characteristic responses to various fluids are beneficial for many applications. For example, multi-layered assemblies of blood vessels made of type I collagen in connective tissue are the most diverse specialised tissue in

the body, and they require different properties and structures according to tissue requirements [218]. Within those assemblies, 5 to 10 μm capillaries provide a network within the body to supply the fluids and constituents selectively. These fluids can be potentially controlled by smart nanocomposite material to allow opening and closing of the channels according to the temperature change. An ability to adjust the wetting angles by altering the microstructure opens the doorways for many microfluidic applications for PTFE-NiTi intercalated nanocomposites.

11 REFERENCES

[1] Whittingham, M. S. (1978), "Chemistry of intercalation compounds: metal guests in chalcogenide hosts", *Progress in Solid State Chemistry,* vol. 12, no. 1, pp. 41-99.

[2] Pande, G., Sravanthi, R. and Kapoor, R. (2011), "Bioinspired and Biomimetic Functional Hybrids as Tools for Regeneration of Orthopedic Interfaces", in Advances in Biomimetics, Anne George (Ed.) (ed.) *Advances in biomemetics,* InTech, Rijeka.

[3] Lehn, J., Benyus, J. and Swiegers, G. (2012), *Bioinspiration and Biomimicry in Chemistry: Reverse-engineering Nature,* John Wiley & Sons.

[4] T. Liskiewicz, A. Morina and A. Neville (2011), "Friction in nature", *International Journal of Design Engineering,* vol. 4, no. 1, pp. 71-84.

[5] Lloyd, A. W. (2002), "Interfacial Bioengineering to Enhance Surface Biocompatibility", *Medical device technology,* vol. 13, no. 1, pp. 18.

[6] *, Musco-skeletal support, Human biological science.*(2012), available at: http://tle.westone.wa.gov.au/content/file/969144ed-0d3b-fa04-2e88-8b23de2a630c/1/human_bio_science_3b.zip/content/003_musculo_skeletal_support/page_06.htm (accessed 02/2012).

[7] The MicGraw Hill Companies *, Spongy bone structure*, available at: http://mandevillehigh.stpsb.org/teachersites/laura_decker/spongy_bone_struct.bmp (accessed 08/2013).

[8] Snyder, T. E. *, The Global Library of Women's Medicine*, available at: http://www.glowm.com/section_view/heading/The%20Overactive%20Bladder/item/63 (accessed 10/13).

[9] Mybladder *, My bladder - The urinary system.*, available at: http://www.mybladder.com.sg/parts-of-the-urinary-system.aspx (accessed 10/13).

[10] Williams, D. F. and European Society for Biomaterials. (1987), "Definitions in biomaterials : proceedings of a consensus conference of the European Society for Biomaterials, Chester, England, March 3-5, 1986", Elsevier, Amsterdam; New York, .

[11] Duerig, T., Pelton, A. and Stöckel, D. (1999), "An overview of nitinol medical applications", *Materials Science and Engineering A,* vol. 273-275, pp. 149-160.

[12] Roy, R. A., Messier, R. and Krishnaswamy, S. V. (1983), "Preparation and properties of r.f.-sputtered polymer-metal thin films", *Thin Solid Films,* vol. 109, no. 1, pp. 27-35.

[13] Kholodkov, I., Biederman, H., Choukourov, A., Stelmashuk, V. and Slavinska, D. "
Hydrocarbon plasma polymer films prepared by Rf sputtering of polyethylene ", .

[14] Drábik, M., Polonskyi, O., Kylián, O., ?echvala, J., Artemenko, A., Gordeev, I., Choukourov, A., Slavínská, D., Matolínová, I. and Biederman, H. (2010), "Super-Hydrophobic Coatings Prepared by RF Magnetron Sputtering of PTFE", *Plasma Processes and Polymers,* vol. 7, no. 7, pp. 544-551.

[15] Liu, C., Gibbons, A. R., Arnell, R. D., Tong, J. and Ren, L. (2001), "Reactive deposition of aluminium oxide coatings on PTFE substrate", *Surface and Coatings Technology,* vol. 139, no. 2–3, pp. 111-117.

[16] He, J., Li, W., Wang, L., Wang, J. and Li, H. (1998), "Deposition of PTFE thin films by ion beam sputtering and a study of the ion bombardment effect", *Nuclear Instruments and Methods in Physics Research Section B: Beam Interactions with Materials and Atoms,* vol. 135, no. 1, pp. 512-516.

[17] Bártolo, P. and Bidanda, B. (2008)*, Bio-materials and prototyping applications in medicine*.

[18] Nair, L. S. and Laurencin, C. T. (2007), "Biodegradable polymers as biomaterials", *Progress in Polymer Science,* vol. 32, no. 8–9, pp. 762-798.

[19] Piskin, E. (1995), "Biodegradable polymers as biomaterials", *Journal of Biomaterials Science, Polymer Edition,* vol. 6, no. 9, pp. 775-795.

[20] H, B. (2000), "RF sputtering of polymers and its potential application", *Vacuum,* vol. 59, no. 2-3, pp. 594-599.

[21] Van Humbeeck, J. (1999), "Non-medical applications of shape memory alloys", *Materials Science and Engineering: A,* vol. 273–275, no. 0, pp. 134-148.

[22] Noebe, R., Biles, T. and and Padula, S. A. (2007), "Chapter 7. NiTi-Based High-Temperature Shape-Memory Alloys
Properties, Prospects, and Potential Applications", in Wole¬¥ Soboyejo and T . S . Srivatsan (ed.) *Advanced structural materials : properties, design optimization, and applications,* CRC Press, Boca Raton, FL, pp. 145-186.

[23] Sanjabi, S., Sadrnezhaad, S. K., Yates, K. A. and Barber, Z. H. (2005), "Growth and characterization of TixNi1−x shape memory thin films using

simultaneous sputter deposition from separate elemental targets", *Thin Solid Films,* vol. 491, no. 1–2, pp. 190-196.

[24] Cho, H., Kim, H. Y. and Miyazaki, S. (2006), "Alloying process of sputter-deposited Ti/Ni multilayer thin films", *Materials Science and Engineering: A,* vol. 438–440, no. 0, pp. 699-702.

[25] Winzek, B., Schmitz, S., Rumpf, H., Sterzl, T., Hassdorf, R., Thienhaus, S., Feydt, J., Moske, M. and Quandt, E. (2004), "Recent developments in shape memory thin film technology", *Materials Science and Engineering: A,* vol. 378, no. 1–2, pp. 40-46.

[26] Krulevitch, P., Lee, A. P., Ramsey, P. B., Trevino, J. C., Hamilton, J. and Northrup, M. A. (1996), "Thin film shape memory alloy microactuators", *Journal of Microelectromechanical Systems,* vol. 5, no. 4, pp. 270-282.

[27] E Wibowo and, C. Y. K. (2006), "Fabrication and characterization of sputtered NiTi shape memory thin films", *Journal of Micromechanics and Microengineering,* vol. 16, no. 1, pp. 101.

[28] Olson, G. B. and Hartman, H. (1982), "MARTENSITE AND LIFE : DISPLACIVE TRANSFORMATIONS AS BIOLOGICAL PROCESSES", *J.Phys.Colloques,* vol. 43, no. C4, pp. 4-855-4-865.

[29] Pond, R. C., Chai, Y. W. and Celotto, S. (2004), "Martensitic transformations in 'unfamiliar' systems", *Materials Science and Engineering A,* vol. 378, no. 1-2 SPEC. ISS., pp. 47-51.

[30] Frick, C. P., Lang, T. W., Spark, K. and Gall, K. (2006), "Stress-induced martensitic transformations and shape memory at nanometer scales", *Acta Materialia,* vol. 54, no. 8, pp. 2223-2234.

[31] Mohanty, A. K., Misra, M. and Drzal, L. T. (2005), *Natural fibers, biopolymers, and biocomposites,* Taylor & Francis, Boca Raton, FL.

[32] Zaporojtchenko, V., Chakravadhanula, V., Faupel, F., Tamulevičius, S., Andrulevičius, M., Tamulevičienė, A. and Augulis, L. (2010), "Residual stress in polytetrafluoroethylene-metal nanocomposite films prepared by magnetron sputtering", *Thin Solid Films,* vol. 518, no. 21, pp. 5944-5949.

[33] Mattox, D. M. (2010), "Chapter 10 - Atomistic Film Growth and Some Growth-Related Film Properties", in Mattox, D. M. (ed.) *Handbook of Physical Vapor Deposition (PVD) Processing (Second Edition),* William Andrew Publishing, Boston, pp. 333-398.

[34] Qi, H. J., Fu, Y. B., Wang, D., Yang, X. X., Sui, K. Y. and Ma, Z. L. (2000), "SEM study of fluorocarbon films by R.F. sputtering PTFE targets on PET substrates", *Surface and Coatings Technology,* vol. 131, no. 1–3, pp. 177-180.

[35] Biederman, H., Kylian, O., Drabik, M., Choukourov, A., Polonskyi, O. and Solar, P. (2012), "Nanocomposite and nanostructured films with plasma polymer matrix", *Surface and Coatings Technology,* vol. 211, pp. 127-137.

[36] Messier, R. (2008), "The nano-world of thin films", *Journal of Nanophotonics,* vol. 2, no. 1, pp. 021995-021995-21.

[37] Silva, M. F. V. and Nicholls, J. R. (2001), "A model for calculating the thickness profile of TiB2 and Al multilayer coatings produced by planar magnetron sputtering", *Surface and Coatings Technology,* vol. 142–144, no. 0, pp. 934-938.

[38] Kumar, A., Singh, D. and Kaur, D. (2009), "Grain size effect on structural, electrical and mechanical properties of NiTi thin films deposited by magnetron co-sputtering", *Surface and Coatings Technology,* vol. 203, no. 12, pp. 1596-1603.

[39] Campbell, S. A. (1996), *The science and engineering of microelectronic fabrication,* Oxford University Press, New York.

[40] Arnell, R. D. and Kelly, P. J. (1999), "Recent advances in magnetron sputtering", *Surface and Coatings Technology,* vol. 112, no. 1–3, pp. 170-176.

[41] Bunshah, R. F. (2001), "Handbook of hard coatings", .

[42] Biederman, H. (2011), "Nanocomposites and nanostructures based on plasma polymers", *Surface and Coatings Technology,* vol. 205, no. SUPPL. 2, pp. S10-S14.

[43] Faupel, F., Zaporojtchenko, V., Strunskus, T. and Elbahri, M. (2010), "Metal-Polymer Nanocomposites for Functional Applications", *Advanced Engineering Materials,* vol. 12, no. 12, pp. 1177-1190.

[44] Liu, C., Fairhurst, R., Ren, L., Green, S., Tong, J. and Arnell, R. (2002), "Co-deposition of titanium/polytetrafluoroethylene films by unbalanced magnetron sputtering", *Surface and Coatings Technology,* vol. 149, no. 2, pp. 143-150.

[45] Kumomi, H. and G. Shi, F. (2002), "Chapter 6 - Fundamentals for the formation and structure control of thin films: Nucleation, growth, solid-state transformations", in Nalwa, H. S. (ed.) *Handbook of Thin Films,* Academic Press, Burlington, pp. 319-373.

[46] Peraldo Bicelli, L. and Kozlov, V. M. (2002), "Chapter 5 - Electrochemical formation of thin films of binary III-V compounds", in Nalwa, H. S. (ed.) *Handbook of Thin Films,* Academic Press, Burlington, pp. 261-318.

[47] Huang, Z., Donohue, P. P., Zhang, Q., Williams, D., Anthony, C. J., Todd, M. A. and Whatmore, R. W. (2002), "Comparative Studies of PST Thin Films as Prepared by Sol-Gel, LDCVD and Sputtering Techniques", *Integrated Ferroelectrics,* vol. 45, no. 1, pp. 79-87.

[48] Bunshah, R. F. (1994), *Handbook of deposition technologies for films and coatings: science, technology, and applications,* William Andrew.

[49] Pauleau, Y. (2002), "Chapter 9 - Residual stresses in physically vapor-deposited thin films", in Nalwa, H. S. (ed.) *Handbook of Thin Films,* Academic Press, Burlington, pp. 455-522.

[50] Bhushan, B., and Gupta, B. K. (1991), *Handbook of tribology : materials, coatings, and surface treatments,* McGraw-Hill, New York.

[51] Sigma-Aldrich (2014), *Physical Vapor Deposition (PVD)*, available at: http://www.sigmaaldrich.com/materials-science/material-science-products.html?TablePage=108832720 (accessed 10/13).

[52] Schulz, U., Fritscher, K. and Peters, M. (1996), "EB-PVD Y< sub> 2</sub> O< sub> 3</sub>-and CeO2Y2O3-stabilized zirconia thermal barrier coatings—crystal habit and phase composition", *Surface and Coatings Technology,* vol. 82, no. 3, pp. 259-269.

[53] Gröning, P. (2002), "Chapter 4 - Cold plasma processes in surface science and technology", in Nalwa, H. S. (ed.) *Handbook of Thin Films,* Academic Press, Burlington, pp. 219-260.

[54] Kusumoto, Y. and Iwata, K. (2004), "Numerical study of the characteristics of erosion in magnetron sputtering", *Vacuum,* vol. 74, no. 3–4, pp. 359-365.

[55] Marcus, R. K. and Broekaert, J. A. (2003), *Glow discharge plasmas in analytical spectroscopy,* John Wiley & Sons.

[56] Oya, T. and Kusano, E. (2008), "Characterization of organic polymer thin films deposited by rf magnetron sputtering", *Vacuum,* vol. 83, no. 3, pp. 564-568.

[57] Chen, C., Richter, A. and Thomson, R. (2010), "Investigation of mechanical properties of intermetallic phases in multi-component Al–Si alloys using hot-stage nanoindentation", *Intermetallics,* vol. 18, no. 4, pp. 499-508.

[58] Miyazaki, S. and Kohl, M. (1998), "Recent development in TiNi-based shape memory alloys", in Wuttig M (ed.), *Smart Structures and Materials 1998 SMart Materials Technologies,* Vol. 3324, 4 March 1998 through 5 March 1998, San Diego, CA, pp. 2.

[59] Kelly, P. J., Abu-Zeid, O. A., Arnell, R. D. and Tong, J. (1996), "The deposition of aluminium oxide coatings by reactive unbalanced magnetron sputtering", *Surface and Coatings Technology,* vol. 86–87, Part 1, no. 0, pp. 28-32.

[60] Rao (*), J., Roberts, T., Lawson, K. and Nicholls, J. (2010), "Nickel titanium and nickel titanium hafnium shape memory alloy thin films", *Surface & Coatings Technology,* vol. 204, pp. 2331-2336.

[61] Kaiser, N. (2002), "Review of the fundamentals of thin-film growth", *Applied Optics,* vol. 41, no. 16, pp. 3053-3060.

[62] Kashchiev, D. (2000), *Nucleation,* Butterworth-Heinemann.

[63] Kaune, G., Ruderer, M. A., Metwalli, E., Wang, W., Couet, S., Schlage, K., RÃ¶hlsberger, R., Roth, S. V. and MÃ¼ller-Buschbaum, P. (2009), "In Situ GISAXS Study of Gold Film Growth on Conducting Polymer Films", *ACS Applied Materials & Interfaces,* vol. 1, no. 2, pp. 353-360.

[64] Li, N. and Zinke-Allmang, M. (2002), "Chapter 1 - Classification of cluster morphologies", in Nalwa, H. S. (ed.) *Handbook of Thin Films,* Academic Press, Burlington, pp. 1-59.

[65] Polop, C., Rosiepen, C., Bleikamp, S., Drese, R., Mayer, J., Dimyati, A. and Michely, T. (2007), "The STM view of the initial stages of polycrystalline Ag film formation", *New Journal of Physics,* vol. 9, no. 3, pp. 74.

[66] Spencer, D. R. (2002), *Alacrites consultancy ltd. Thin film growth independant film expertiese.*, available at: http://www.alacritas-consulting.com/advice/thin-film-growth/ (accessed 08/11).

[67] Zhang, S. and Ali, N. (2007), *Nanocomposite thin films and coatings: processing, properties and performance,* World Scientific.

[68] Phuku, P., Bertrand, P. and De Puydt, Y. (1991), "Adhesion, microstructure and composition of thermally evaporated aluminium thin layers on polyethylene terephthalate films", *Thin Solid Films,* vol. 200, no. 2, pp. 263-274.

[69] Vestel, M. J. and Grummon, D. S. (2004), "Precipitates and lamellar microstructures in NiTi films", *Materials Science and Engineering: A,* vol. 378, no. 1–2, pp. 437-442.

[70] Thornton, J. A. (1977), "High Rate Thick Film Growth", *Annual Review of Materials Science,* vol. 7, no. 1, pp. 239-260.

[71] Sark, W. G. J. H. M. v. (2002), "Chapter 1 - Methods of deposition of hydrogenated amorphous silicon for device applications", in Nalwa, H. S. (ed.) *Handbook of Thin Films,* Academic Press, Burlington, pp. 1-102.

[72] Movachan, B. and Demchishin, A. (1969), "Study of the Structure and Properties of Thick Vacuum Condensates of Nickel, Titanium, Tungsten, Aluminum Oxide and Zirconium Dioxide Fiz", *Met.Metall,* vol. 28, no. 4, pp. 83-90.

[73] Musil, J. (1998), "Recent advances in magnetron sputtering technology", *Surface and Coatings Technology,* vol. 100–101, no. 0, pp. 280-286.

[74] Stelmashuk, V., Biederman, H., Slavínská, D., Zemek, J. and Trchová, M. (2005), "Plasma polymer films rf sputtered from PTFE under various argon pressures", *Vacuum,* vol. 77, no. 2, pp. 131-137.

[75] Thornton, J. A. and Hoffman, D. (1989), "Stress-related effects in thin films", *Thin Solid Films,* vol. 171, no. 1, pp. 5-31.

[76] Vencl, A., Arostegui, S., Favaro, G., Zivic, F., Mrdak, M., Mitrović, S. and Popovic, V. (2011), "Evaluation of adhesion/cohesion bond strength of the thick plasma spray coatings by scratch testing on coatings cross-sections", *Tribology International,* vol. 44, no. 11, pp. 1281-1288.

[77] Moura e Silva, Carlos W, Alves, E., Ramos, A., Sandu, C. S. and Cavaleiro, A. (2009), "Adhesion failures on hard coatings induced by interface anomalies", *Vacuum,* vol. 83, no. 10, pp. 1213-1217.

[78] Biederman, H., Stelmashuk, V., Kholodkov, I., Choukourov, A. and SlavÄ±´nskÃ¡, D. (2003), "RF sputtering of hydrocarbon polymers and their derivatives", *Surface and Coatings Technology,* vol. 174-175, no. 0, pp. 27-32.

[79] Lehmann, H., Frick, K., Widmer, R., Vossen, J. and James, E. (1978), "Reactive sputtering of PTFE films in argon-CF< sub> 4</sub> mixtures", *Thin Solid Films,* vol. 52, no. 2, pp. 231-235.

[80] Kitoh, M. and Honda, Y. (1995), "Preparation and tribological properties of sputtered polyimide film", *Thin Solid Films,* vol. 271, no. 1-2, pp. 92-95.

[81] Biederman, H., Stelmashuk, V., Kholodkov, I., Choukourov, A. and SlavÄ±´nskÃ¡, D. (2003), "RF sputtering of hydrocarbon polymers and their derivatives", *Surface and Coatings Technology,* vol. 174–175, no. 0, pp. 27-32.

[82] Lawson, K. and Nicholls, J. (2002), "Ultrathin PTFE, PVDF, and FEP coatings deposited using plasma-assisted physical vapor deposition", in *Fluoropolymers 1: Synthesis,* Springer, , pp. 313-320.

[83] Mihály, J., Sterkel, S., Ortner, H. M., Kocsis, L., Hajba, L., Furdyga, É. and Mink, J. (2006), "FTIR and FT-Raman spectroscopic study on

polymer based high pressure digestion vessels", *Croatica Chemica Acta,* vol. 79, no. 3, pp. 497-501.

[84] Yamada, Y., Tanaka, K. and Saito, K. (1990), "Friction and damage of coatings formed by sputtering polytetrafluoroethylene and polyimide", *Surface and Coatings Technology,* vol. 43-44, Part 2, no. 0, pp. 618-628.

[85] Bodas, D. S., Mandale, A. B. and Gangal, S. A. (2005), "Deposition of PTFE thin films by RF plasma sputtering on 〈1 0 0〉 silicon substrates", *Applied Surface Science,* vol. 245, no. 1–4, pp. 202-207.

[86] Li, L., Zi, F. T. and Zheng, Y. F. (2008), "The characterization of fluorocarbon films on NiTi alloy by magnetron sputtering", *Applied Surface Science,* vol. 255, no. 2, pp. 432-434.

[87] Biederman, H., Bílková, P., Ježek, J., Hlídek, P. and Slavínská, D. (1997), "RF magnetron sputtering of polymers", *Journal of Non-Crystalline Solids,* vol. 218, no. 0, pp. 44-49.

[88] Liu, D., Gu, J., Feng, Z., Li, D., Niu, J. and Benstetter, G. (2010), "Comparison of fluorocarbon film deposition by pulsed/continuous wave and downstream radio frequency plasmas", *Vacuum,* vol. 85, no. 2, pp. 253-262.

[89] Biederman, H., Zeuner, M., Zalman, J., Bílková, P., Slavínská, D., Stelmasuk, V. and Boldyreva, A. (2001), "Rf magnetron sputtering of polytetrafluoroethylene under various conditions", *Thin Solid Films,* vol. 392, no. 2, pp. 208-213.

[90] Liu, C., Gibbons, A. R., Arnell, R. D., Tong, J. and Ren, L. (2001), "Reactive depositon of aluminium oxide coatings on PTFE substrate", *Surface and Coatings Technology,* vol. 139, no. 2-3, pp. 111-117.

[91] Harrop, R. and Harrop, P. (1969), "Friction of sputtered PTFE films", *Thin Solid Films,* vol. 3, no. 2, pp. 109-117.

[92] ROBINSON, A. L. (1976), "Metallurgy: Extraordinary Alloys That Remember Their Past", *Science,* vol. 191, no. 4230, pp. 934-936.

[93] KAUFFMAN, G.,B. and MAYO, ,I.S.A.A.C. (1997), "The Story of Nitinol: The Serendipitous Discovery of the Memory Metal and Its Applications", *The Chemical Educator,* , no. 2, pp. 1-21.

[94] Frick, C. P., Ortega, A. M., Tyber, J., Maksound, A. E. M., Maier, H. J., Liu, Y. and Gall, K. (2005), "Thermal processing of polycrystalline NiTi shape memory alloys", *Materials Science and Engineering A,* vol. 405, no. 1-2, pp. 34-49.

[95] Gust, L. K. .

[96] Images SI Inc. (2012), *Images Scientific instruments*, available at: http://www.imagesco.com/nitinol/nitinol-index.html (accessed 08/10).

[97] Uchil, J., Mohanchandra, K. P., Kumara, K. G. and Mahesh, K. K. (1998), "Study of critical dependence of stable phases in Nitinol on heat treatment using electrical resistivity probe", *Materials Science and Engineering A,* vol. 251, no. 1-2, pp. 58-63.

[98] Uchil, J., Kumara, K.G. and Mahesh, K.K., (2002), *Effect of thermal cycling on R-phase stability in a NiTi shape memory alloy*.

[99] Antonucci, V., Faiella, G., Giordano, M., Mennella, F. and Nicolais, L. (2007), "Electrical resistivity study and characterization during NiTi phase transformations", *Thermochimica Acta,* vol. 462, no. 1–2, pp. 64-69.

[100] Huang, X. and Liu, Y. (2001), "Effect of annealing on the transformation behavior and superelasticity of NiTi shape memory alloy", *Scripta Materialia,* vol. 45, no. 2, pp. 153-160.

[101] Tillmann, W. and Momeni, S. (2015), "In-situ annealing of NiTi thin films at different temperatures", *Sensors and Actuators A: Physical,* vol. 221, no. 0, pp. 9-14.

[102] Surbled, P., Clerc, C., Le Pioufle, B., Ataka, M. and Fujita, H. (2001), "Effect of the composition and thermal annealing on the transformation temperatures of sputtered TiNi shape memory alloy thin films", *Thin Solid Films,* vol. 401, no. 1–2, pp. 52-59.

[103] Botterill, N. W. and Grant, D. M. (2004), "Novel micro-thermal characterisation of thin film NiTi shape memory alloys", *Materials Science and Engineering: A,* vol. 378, no. 1–2, pp. 424-428.

[104] Tillmann, W. and Momeni, S., (2014), *Deposition of superelastic composite NiTi based films*.

[105] Schiedeck, F. and Morita, T. (2012), "Ultrasonic-assisted hydrothermal deposition of ferroelectric PbZrO3 thin film on NiTi-based superelastic shape memory alloys", *Journal of Electroceramics,* vol. 28, no. 1, pp. 45-52.

[106] Grummon, D. S. (2003), "Thin-film shape-memory materials for high-temperature applications", *JOM,* vol. 55, no. 12, pp. 24-32.

[107] Chen, K. C. (2003), "NiTi-Magic or Phase Transformation?", *Proceedings of the ASEE Annual Conference & Exposition: Nashville, TN,* .

[108] Elahinia, M. H., Hashemi, M., Tabesh, M. and Bhaduri, S. B. (2012), "Manufacturing and processing of NiTi implants: A review", *Progress in Materials Science,* vol. 57, no. 5, pp. 911-946.

[109] Rumpf, H., Winzek, B., Zamponi, C., Siegert, W., Neuking, K. and Quandt, E. (2004), "Sputter deposition of NiTi to investigate the Ti loss rate as a function of composition from cast melted targets", *Materials Science and Engineering A,* vol. 378, no. 1-2 SPEC. ISS., pp. 429-433.

[110] Zhang, J. X., Sato, M. and Ishida, A. (2003), "On the Ti2Ni precipitates and Guinier–Preston zones in Ti-rich Ti–Ni thin films", *Acta Materialia,* vol. 51, no. 11, pp. 3121-3130.

[111] Zhang, J., Botterill, N. W., Roberts, C. J. and Grant, D. M. (2003), "Micro-thermal analysis of NiTi shape memory alloy thin films", *Thermochimica acta,* vol. 401, no. 2, pp. 111-119.

[112] Vestel, M. J., Grummon, D. S., Gronsky, R. and Pisano, A. P. (2003), "Effect of temperature on the devitrification kinetics of NiTi films", *Acta Materialia,* vol. 51, no. 18, pp. 5309-5318.

[113] Yang, Y. Q., Jia, H. S., Zhang, Z. F., Shen, H. M., Hu, A. and Wang, Y. N. (1995), "Transformations in sputter-deposited thin films of NiTi shape memory alloy", *Materials Letters,* vol. 22, no. 3–4, pp. 137-140.

[114] Nomura, K., Miyazaki, S. and Ishida, A. (1995), "Effect of plastic strain on shape memory characteristics in sputter-deposited Ti-Ni thin films", *Journal de physique.IV,* vol. 5, no. 8, pp. C8. 695-C8. 700.

[115] Wang, F., Huang, P., Chen, W. and Xu, K. (2010), "Size effects of superelasticity in nanocrystalline NiTi shape memory alloy", *2010 3rd International Nanoelectronics Conference, INEC 2010,* 3 January 2010 through 8 January 2010, Hongkong, pp. 989.

[116] Kumar, A., Sharma, S. K., Bysakh, S., Kamat, S. V. and Mohan, S. (2010), "Effect of Substrate and Annealing Temperatures on Mechanical Properties of Ti-rich NiTi Films", *Journal of Materials Science & Technology,* vol. 26, no. 11, pp. 961-966.

[117] Liu, K. T. and Duh, J. G. (2008), "Hardness evolution of NiTi and NiTiAl thin films under various annealing temperatures", *Surface and Coatings Technology,* vol. 202, no. 12, pp. 2737-2742.

[118] Rumpf, H., Walther, T., Zamponi, C. and Quandt, E. (2006), "High ultimate tensile stress in nano-grained superelastic NiTi thin films", *Materials Science and Engineering: A,* vol. 415, no. 1–2, pp. 304-308.

[119] Povoden-Karadeniz, E., Cirstea, D. C., Lang, P., Wojcik, T. and Kozeschnik, E. (2013), "Thermodynamics of Ti–Ni shape memory alloys", *Calphad,* vol. 41, no. 0, pp. 128-139.

[120] Gong, F. F., Shen, H. M. and Wang, Y. N. (1995), "Fabrication and characterization of sputtered Ni-rich NiTi thin films", *Materials Letters,* vol. 25, no. 1-2, pp. 13-16.

[121] Zhang, J. X., Sato, M. and Ishida, A. (2001), "Structure of martensite in sputter-deposited Ti–Ni thin films containing Guinier–Preston zones", *Acta Materialia,* vol. 49, no. 15, pp. 3001-3010.

[122] Otsuka, K. (1999), *Shape memory materials,* Cambridge Univ. Press, Cambridge.

[123] Porter, G., Liaw, P., Tiegs, T. and Wu, K. (2000), "Particle size reduction of NiTi shape-memory alloy powders", *Scripta Materialia,* vol. 43, no. 12, pp. 1111-1117.

[124] Takeuchi, S. and Shimoyama, I. (2000), "A three-dimensional shape memory alloy microelectrode with clipping structure for insect neural recording", *Microelectromechanical Systems, Journal of,* vol. 9, no. 1, pp. 24-31.

[125] Hou, L. and Grummon, D. S. (1995), "Transformational superelasticity in sputtered titanium-nickel thin films", *Scripta Metallurgica et Materiala,* vol. 33, no. 6, pp. 989-995.

[126] Zamponi, C., Rumpf, H., Schmutz, C. and Quandt, E. (2008), "Structuring of sputtered superelastic NiTi thin films by photolithography and etching", *Materials Science and Engineering: A,* vol. 481–482, no. 0, pp. 623-625.

[127] Gill, J. J., Chang, D. T., Momoda, L. A. and Carman, G. P. (2001), "Manufacturing issues of thin film NiTi microwrapper", *Sensors and Actuators A: Physical,* vol. 93, no. 2, pp. 148-156.

[128] Ishida, A. and Sato, M. (2003), "Thickness effect on SMA NiTi thin film", *Acta Materialia,* , pp. 5571-5578.

[129] Lexecllent, C., Moyne, S., Ishida, A. and Miyazaki, S. (1998), "Deformation behaviour of NiTi SMA thernodynamic modelling.", *Thin Solid Films,* vol. 324, pp. 184-189.

[130] Kohl, M., Dittmann, D., Quandt, E. and Winzek, B. (2000), "Thin film shape memory microvalves with adjustable operation temperature", *Sensors and Actuators A: Physical,* vol. 83, no. 1, pp. 214-219.

[131] Moyne, S., Poilane, C., Kitamura, K., Miyazaki, S., Dellobelle, P. and Lexecellent, C. (1999), "Thermomechanical behaviour of NiTi using nanoindentation", *Materials Science and Engineering A,* , pp. 273-275, 727-7232.

[132] Zhang, Y., Cheng, Y. and Grummom, D. S. (2007), "Novel tribological systems using shape memory alloys and thin films", *Surface and Coatings Technology,* vol. 202, no. 4–7, pp. 998-1002.

[133] Zhang, J. X., Sato, M. and Ishida, A. (2006), "Deformation mechanism of martensite in Ti-rich Ti–Ni shape memory alloy thin films", *Acta Materialia,* vol. 54, no. 4, pp. 1185-1198.

[134] Otsuka, K. and Kakeshita, T. (2002), "Science and Technology of Shape-Memory Alloys: New Developments", *MRS Bulletin,* vol. 27, no. 02, pp. 91.

[135] Kong, M. C., Axinte, D. and Voice, W. (2011), "Challenges in using waterjet machining of NiTi shape memory alloys: An analysis of controlled-depth milling", *Journal of Materials Processing Technology,* vol. 211, no. 6, pp. 959-971.

[136] Duerig, T. W. and Melton, K. N. (1989), "Designing with the shape memory effect", *MRS International Meeting on Advanced Materials,* vol. 9, pp. 581-597.

[137] Kwong, H. Y., Wong, M. H., Wong, Y. W. and Wong, K. H. (2007), "Superhydrophobicity of polytetrafluoroethylene thin film fabricated by pulsed laser deposition", *Applied Surface Science,* vol. 253, no. 22, pp. 8841-8845.

[138] Ishida, A., Sato, M., Takei, A. and Miyazaki, S. (1995), "Effect of heat treatment on shape memory behavior of Ti-rich Ti-Ni thin films", *Materials Transactions, JIM,* vol. 36, no. 11, pp. 1349-1355.

[139] Saburi, T., Yoshida, M. and Nenno, S. (1984), "Deformation behavior of shape memory TiNi alloy crystals", *Scripta Metallurgica,* vol. 18, no. 4, pp. 363-366.

[140] Habijan, T., De Miranda, R. L., Zamponi, C., Quandt, E., Greulich, C., Schildhauer, T. A. and Köller, M. (2012), "The biocompatibility and mechanical properties of cylindrical NiTi thin films produced by magnetron sputtering", *Materials Science and Engineering: C,* vol. 32, no. 8, pp. 2523-2528.

[141] Gong, F. F., Shen, H. M. and Wang, Y. N. (1996), "Structures and defects induced during annealing of sputtered near-equiatomic NiTi shape memory thin films", *Applied Physics Letters,* vol. 69, no. 18, pp. 2656-2658.

[142] Ju, X. and Dong, H. (2006), "Plasma surface modification of NiTi shape memory alloy", *Surface and Coatings Technology,* vol. 201, no. 3, pp. 1542-1547.

[143] BATALU, D., GUOQIU, H., ALOMAN, A., COŞMELEAŢĂ, G., XIAOSHAN, L. and ZHIHUA, Z. "A review on TiNi shape memory alloys (SMA) used for medical applications. Recycling aspects", .

[144] Chan, C. -., Trigwell, S. and Duerig, T. (1990), "Oxidation of an NiTi alloy", *Surface and Interface Analysis,* vol. 15, no. 6, pp. 349-354.

[145] Mao, S., Li, H., Liu, Y., Deng, Q., Wang, L., Zhang, Y., Zhang, Z. and Han, X. (2013), "Stress-induced martensitic transformation in nanometric NiTi shape memory alloy strips: an in situ TEM study of the thickness/size effect", *Journal of Alloys and Compounds,* vol. 579, pp. 100-111.

[146] Kajiwara, S., Kikuchi, T., Ogawa, K., Matsunaga, T. and Miyazaki, S. (1996), "Strengthening of Ti-Ni shape-memory films by coherent subnanometric plate precipitates", *Philosophical Magazine Letters,* vol. 74, no. 3, pp. 137-144.

[147] Busch, J. D., Johnson, A. D., Lee, C. H. and Stevenson, D. A. (1990), "Shape-memory properties in Ni-Ti sputter-deposited film", *Journal of Applied Physics,* vol. 68, no. 12, pp. 6224-6228.

[148] Fischer-Cripps, A. C., (2002), "Nanoindentation", in *Mechanical Engineering Series,* Springer, New York, pp. 101-2.

[149] Brantley, W. (1973), "Calculated elastic constants for stress problems associated with semiconductor devices", *Journal of Applied Physics,* vol. 44, pp. 534.

[150] Bishara, S. E., Barrett, R. D. and Selim, M. I. (1993), "Biodegradation of orthodontic appliances. Part II. Changes in the blood level of nickel", *American Journal of Orthodontics and Dentofacial Orthopedics,* vol. 103, no. 2, pp. 115-119.

[151] Barrett, R. D., Bishara, S. E. and Quinn, J. K. (1993), "Biodegradation of orthodontic appliances. Part I. Biodegradation of nickel and chromium in vitro", *American Journal of Orthodontics and Dentofacial Orthopedics,* vol. 103, no. 1, pp. 8-14.

[152] Faupel, F., Zaporojtchenko, V., Greve, H., Schürmann, U., Chakravadhanula, V. S. K., Hanisch, C., Kulkarni, A., Gerber, A., Quandt, E. and Podschun, R. (2007), "Deposition of Nanocomposites by Plasmas", *Contributions to Plasma Physics,* vol. 47, no. 7, pp. 537-544.

[153] Brabec, C. J. (2003), *Organic photovoltaics: concepts and realization,* Springer.

[154] Fusaro, R. L. (1990), "Self-lubricating polymer composites and polymer transfer film lubrication for space applications", *Tribology International,* vol. 23, no. 2, pp. 105-122.

[155] Farooq, M. and Lee, Z. (2002), "Optimization of the sputtering process for depositing composite thin films", .

[156] Murasawa, G., Tohgo, K. and Ishii, H. (2004), "Deformation Behavior of NiTi/Polymer Shape Memory Alloy Composites - Experimental Verifications", *Journal of Composite Materials,* vol. 38, no. 5, pp. 399-416.

[157] Neuking, K., Abu-Zarifa, A. and Eggeler, G. (2008), "Surface engineering of shape memory alloy/polymer-composites: Improvement of the adhesion between polymers and pseudoelastic shape memory alloys", *Materials Science and Engineering: A,* vol. 481, pp. 606-611.

[158] Tahiri, V. -., Patoor, E. and Eberhardt, A. (2004), "An analysis of the thermomechanical behaviour of a shape memory alloy/elastomer composite", in Lexcellent C. and Patoor E. (eds.), *EUROMECH-MECAMAT'2003: 7th European Mechanics of Materials Conference on Adaptive Systems and Materials: Constitutive Materials and Hybrid Structures,* Vol. 115, 18 May 2003 through 23 May 2003, Frejus, pp. 195.

[159] Winzek, B., Sterzl, T., Rumpf, H. and Quandt, E. (2003), "Composites of different shape memory alloys and polymers for complex actuator motions", in Pietikainen J. and Soderberg, E. O. (eds.), *International Conference on Martensitic Transformations,* Vol. 112 II, 10 June 2002 through 14 June 2002, Espoo, pp. 1163.

[160] Neuking, K., Abu-Zarifa, A., Youcheu-Kemtchou, S. and Eggeler, G. (2005), "Polymer/NiTi-composites: Fundamental Aspects, Processing and Properties", *Advanced Engineering Materials,* vol. 7, no. 11, pp. 1014-1023.

[161] Smith, N., Antoun, G., Ellis, A. and Crone, W. (2004), "Improved adhesion between nickel–titanium shape memory alloy and a polymer matrix via silane coupling agents", *Composites Part A: Applied Science and Manufacturing,* vol. 35, no. 11, pp. 1307-1312.

[162] Schürmann, U., Takele, H., Zaporojtchenko, V. and Faupel, F. (2006), "Optical and electrical properties of polymer metal nanocomposites prepared by magnetron co-sputtering", *Thin Solid Films,* vol. 515, no. 2, pp. 801-804.

[163] Schürmann, U., Hartung, W., Takele, H., Zaporojtchenko, V. and Faupel, F. (2005), "Controlled syntheses of Ag–polytetrafluoroethylene nanocomposite thin films by co-sputtering from two magnetron sources", *Nanotechnology,* vol. 16, no. 8, pp. 1078.

[164] Siegel, J., Polívková, M., Kasálková, N. S., Kolská, Z. and Švorčík, V. (2013), "Properties of silver nanostructure-coated PTFE and its biocompatibility", *Nanoscale research letters,* vol. 8, no. 1, pp. 1-10.

[165] Zhang, Y. and Qi, H. (2008), "Composite fluorocarbon/ZnO films prepared by R.F. magnetron sputtering of Zn and PTFE", *Surface and Coatings Technology,* vol. 202, no. 12, pp. 2612-2615.

[166] Greve, H., Pochstein, C., Takele, H., Zaporojtchenko, V., Faupel, F., Gerber, A., Frommberger, M. and Quandt, E. (2006), "Nanostructured magnetic Fe–Ni–Co/Teflon multilayers for high-frequency applications in the gigahertz range", *Applied Physics Letters,* vol. 89, no. 24, pp. 242501-242501-3.

[167] Zaporojtchenko, V., Podschun, R., Schürmann, U., Kulkarni, A. and Faupel, F. (2006), "Physico-chemical and antimicrobial properties of co-sputtered Ag–Au/PTFE nanocomposite coatings", *Nanotechnology,* vol. 17, no. 19, pp. 4904.

[168] Alissawi, N., Zaporojtchenko, V., Strunskus, T., Hrkac, T., Kocabas, I., Erkartal, B., Chakravadhanula, V., Kienle, L., Grundmeier, G. and Garbe-Schönberg, D. (2012), "Tuning of the ion release properties of silver nanoparticles buried under a hydrophobic polymer barrier", *Journal of Nanoparticle Research,* vol. 14, no. 7, pp. 1-12.

[169] Folarin, O. M., Sadiku, E. R. and Maity, A. (2011), "Polymer-noble metal nanocomposites: review", .

[170] Shelemin, A., Choukourov, A., Kylian, O., Hanus, J., Kousal, J., Slavinska, D. and Biederman, H. "Nanocomposite Films with Plasma Polymer Matrix Prepared Using a Gas Aggregation Cluster Source", .

[171] Miyake, S. and Shindo, T. (2013), "Deposition and tribological properties of multilayer and mixed films composed of gold and polytetrafluoroethylene", *Thin Solid Films,* vol. 527, no. 0, pp. 210-221.

[172] Kamegawa, T., Shimizu, Y. and Yamashita, H. (2012), "Superhydrophobic Surfaces with Photocatalytic Self-Cleaning Properties by Nanocomposite Coating of TiO2 and Polytetrafluoroethylene", *Advanced Materials,* vol. 24, no. 27, pp. 3697-3700.

[173] Ouvrard, G. and Guyomard, D. (1996), "Intercalation chemistry", *Current Opinion in Solid State and Materials Science,* vol. 1, no. 2, pp. 260-267.

[174] Schöllhorn, R. (1980), "Intercalation chemistry", *Physica B+C,* vol. 99, no. 1–4, pp. 89-99.

[175] LeBaron, P. C., Wang, Z. and Pinnavaia, T. J. (1999), "Polymer-layered silicate nanocomposites: an overview", *Applied Clay Science,* vol. 15, no. 1, pp. 11-29.

[176] Byrne, M. T. and Gun'ko, Y. K. (2010), "Recent Advances in Research on Carbon Nanotube?Polymer Composites", *Advanced Materials,* vol. 22, no. 15, pp. 1672-1688.

[177] Coleman, J. ?., Cadek, M., Blake, R., Nicolosi, V., Ryan, K. ?., Belton, C., Fonseca, A., Nagy, J. ?., Gun'ko, Y. ?. and Blau, W. ?. (2004), "High

Performance Nanotube-Reinforced Plastics: Understanding the Mechanism of Strength Increase", *Advanced Functional Materials,* vol. 14, no. 8, pp. 791-798.

[178] Liao, C., Wu, M., Yen, J., Leu, I. and Fung, K. (2006), "Preparation of RF-sputtered lithium cobalt oxide nanorods by using porous anodic alumina (PAA) template", *Journal of Alloys and Compounds,* vol. 414, no. 1, pp. 302-309.

[179] Figueroa, R., Kleinke, M., Cruz, T. G. and Gorenstein, A. (2006), "Influence of the microstructure on the electrochemical performance of thin film WO< sub> 3</sub> cathode", *Journal of Power Sources,* vol. 162, no. 2, pp. 1351-1356.

[180] Brousse, T., Fragnaud, P., Marchand, R. and Schleich, D. (1996), "Characterization of sprayed and sputtered thin films for lithium ion microbatteries", *Ionics,* vol. 2, no. 5-6, pp. 398-404.

[181] Miyazaki, H., Sakamura, H., Kamei, M. and Yasui, I. (1999), "Electrochemical evaluation of oriented vanadium oxide films deposited by reactive rf magnetron sputtering", *Solid State Ionics,* vol. 122, no. 1, pp. 223-229.

[182] Thißen, A., Ensling, D., Liberatore, M., Wu, Q., Madrigal, F. F., Bhuvaneswari, M., Hunger, R. and Jaegermann, W. (2009), "Experimental routes to in situ characterization of the electronic structure and chemical composition of cathode materials for lithium ion batteries during lithium intercalation and deintercalation using photoelectron spectroscopy and related techniques", *Ionics,* vol. 15, no. 4, pp. 393-403.

[183] Punitha, K., Sivakumar, R. and Sanjeeviraja, C. (2014), "Enhanced Colouration Efficiency of Pulsed DC Magnetron Sputtered WO 3 Films Cycled in H 2 SO 4 Electrolyte Solution", *Smart Materials Research,* vol. 2014.

[184] Selinder, T., Sjöstrand, M., Nordin, M., Larsson, M., Östlund, Å. and Hogmark, S. (1998), "Performance of PVD TiN/TaN and TiN/NbN superlattice coated cemented carbide tools in stainless steel machining", *Surface and coatings technology,* vol. 105, no. 1, pp. 51-55.

[185] Sanchez, C., Arribart, H. and Guille, M. M. G. (2005), "Biomimetism and bioinspiration as tools for the design of innovative materials and systems", *Nature materials,* vol. 4, no. 4, pp. 277-288.

[186] Dan Guo and Guoxin Xie and,Jianbin Luo (2014), "Mechanical properties of nanoparticles: basics and applications", *Journal of Physics D: Applied Physics,* vol. 47, no. 1, pp. 013001.

[187] Cai, W., Meng, X. L. and Zhao, L. C. (2005), "Recent development of TiNi-based shape memory alloys", *Current Opinion in Solid State and Materials Science,* vol. 9, no. 6, pp. 296-302.

[188] Leite, F. and Herrmann, P. (2005), "Application of atomic force spectroscopy (AFS) to studies of adhesion phenomena: a review", *Journal of Adhesion Science and Technology,* vol. 19, no. 3-5, pp. 365-405.

[189] *, FTIR Spectroscopy.*, available at: http://www.fc.up.pt/pessoas/peter.eaton/tutorial/sld011.htm (accessed 08/14).

[190] Griffiths, P. R. and De Haseth, J. A. (2007), *Fourier transform infrared spectrometry,* John Wiley & Sons.

[191] *Introduction to Fourier Transform Infrared Spectrometry,* (2001), , Thermo Nicolet corporation, Madison, U.S.A.

[192] Gill, P., Moghadam, T. T. and Ranjbar, B. (2010), "Differential scanning calorimetry techniques: applications in biology and nanoscience", *Journal of biomolecular techniques : JBT,* vol. 21, no. 4, pp. 167-193.

[193] *, Hitachi High-Tech Science Corporation, DSC.*(2014), available at: http://www.hitachi-hitec-science.com/en/products/thermal/tec_descriptions/dsc.html (accessed 08/14).

[194] Haynie, D. T. (2008), *Biological Thermodynamics.*Cambridge University Press.

[195] *, USGS, Coastal and marine geology pragram.* ***A Laboratory Manual for X-Ray Powder Diffraction***, available at: http://pubs.usgs.gov/of/2001/of01-041/htmldocs/xrpd.htm (accessed 08/11).

[196] Holmberg, K., Laukkanen, A., Ronkainen, H., Wallin, K., Varjus, S. and Koskinen, J. (2006), "Tribological contact analysis of a rigid ball sliding on a hard coated surface: Part I: Modelling stresses and strains", *Surface and Coatings Technology,* vol. 200, no. 12, pp. 3793-3809.

[197] Sander, T., Tremmel, S. and Wartzack, S. (2011), "A modified scratch test for the mechanical characterization of scratch resistance and adhesion of thin hard coatings on soft substrates", *Surface and Coatings Technology,* vol. 206, no. 7, pp. 1873-1878.

[198] Petit, F., Ott, C. and Cambier, F. (2009), "Multiple scratch tests and surface-related fatigue properties of monolithic ceramics and soda lime glass", *Journal of the European Ceramic Society,* vol. 29, no. 8, pp. 1299-1307.

[199] Lin, J. and Zhou, Y. (2013), "Can scratch tests give fracture toughness?", *Engineering Fracture Mechanics,* vol. 109, pp. 161-168.

[200] Akono, A. and Ulm, F. (2011), "Scratch test model for the determination of fracture toughness", *Engineering Fracture Mechanics,* vol. 78, no. 2, pp. 334-342.

[201] Wong, M., Lim, G., Moyse, A., Reddy, J. and Sue, H. (2004), "A new test methodology for evaluating scratch resistance of polymers", *Wear,* vol. 256, no. 11, pp. 1214-1227.

[202] *, CSM Instruments, A company of Anton Paar; INDENTATION*, available at: http://www.csm-instruments.com/de/taxonomy/term/61?page=2 (accessed 08/16).

[203] Paladines, A., Aperador, W. and Sequeda, F. "Evaluación de las propiedades tribológicas y corrosión del Sistema CrN/Cr depositado sobre acero AISI 304, 4140, 1075 por la técnica Magnetron Sputtering Reactivo DC", .

[204] *, PVD coatings, welcome to the future, scratch tester.*(2014), available at: http://www.pvd-coatings.co.uk/pvd-coating-technology/testing-equipment/scratch-tester/ (accessed 08/17).

[205] Borrero-López, O., Hoffman, M., Bendavid, A. and Martin, P. J. (2010), "The use of the scratch test to measure the fracture strength of brittle thin films", *Thin Solid Films,* vol. 518, no. 17, pp. 4911-4917.

[206] *, Scanning Electron Microscope, Radiological and Environmental Management, Purdue University*(2014), available at: http://www.purdue.edu/ehps/rem/rs/sem.htm (accessed 08/11).

[207] *, Atomic World, Principal of TEM.*, available at: http://www.hk-phy.org/atomic_world/tem/tem02_e.html (accessed 08/12).

[208] Friedrich, H., de Jongh, P. E., Verkleij, A. J. and de Jong, K. P. (2009), "Electron tomography for heterogeneous catalysts and related nanostructured materials", *Chemical reviews,* vol. 109, no. 5, pp. 1613-1629.

[209] *, DSC - A biggeners guide.*, available at: http://www.perkinelmer.co.uk/CMSResources/Images/44-74542GDE_DSCBeginnersGuide.pdf (accessed 08/14).

[210] Zhao, A. and Chao, A. (2007)*, Microscopes: How it Works (and Images) Group 2*, available at: http://isbbio1.pbworks.com/w/page/9205985/How%20it%20Works%20(and%20Images)%20Group%202 (accessed 08/11).

[211] Saucedo, S. (2013), *The Zen of STEM -Scanning Electron Microscopy.*, available at: http://zenofstem.com/project/using-the-sem/ (accessed 08/11).

[212] Khursheed, A. (2011), *Scanning electron microscope optics and spectrometers,* World Scientific.

[213] *, McSwiggen & Associates, Technical notes WDS vs EDS.*(2005), available at: http://www.mcswiggen.com/TechNotes/WDSvsEDS.htm (accessed 08/12).

[214] Kim, H. Y., Ikehara, Y., Kim, J. I., Hosoda, H. and Miyazaki, S. (2006), "Martensitic transformation, shape memory effect and superelasticity of Ti–Nb binary alloys", *Acta Materialia,* vol. 54, no. 9, pp. 2419-2429.

[215] Rao, J., Cruz, R., Lawson, K. J. and Nicholls, J. R. (2005), "Sputtered DLC-TiB2 multilayer films for tribological applications", *Diamond and Related Materials,* vol. 14, no. 11–12, pp. 1805-1809.

[216] Rao, J., Cruz, R., Lawson, K. J. and Nicholls, J. R. (2005), "Sputtered DLC-TiB2 multilayer films for tribological applications", *Diamond and Related Materials,* vol. 14, no. 11-12, pp. 1805-1809.

[217] Sun, T., Wang, M. and Lee, W. (2011), "Surface characteristics, properties and in vitro biological assessment of a NiTi shape memory alloy after high temperature heat treatment or surface H2O2-oxidation: A comparative study", *Materials Chemistry and Physics,* vol. 130, no. 1–2, pp. 45-58.

[218] Fratzl, P., Elbaum, R. and Burgert, I. (2008), "Cellulose fibrils direct plant organ movements", *Faraday discussions,* vol. 139, pp. 275-282.

12 APPENDICES

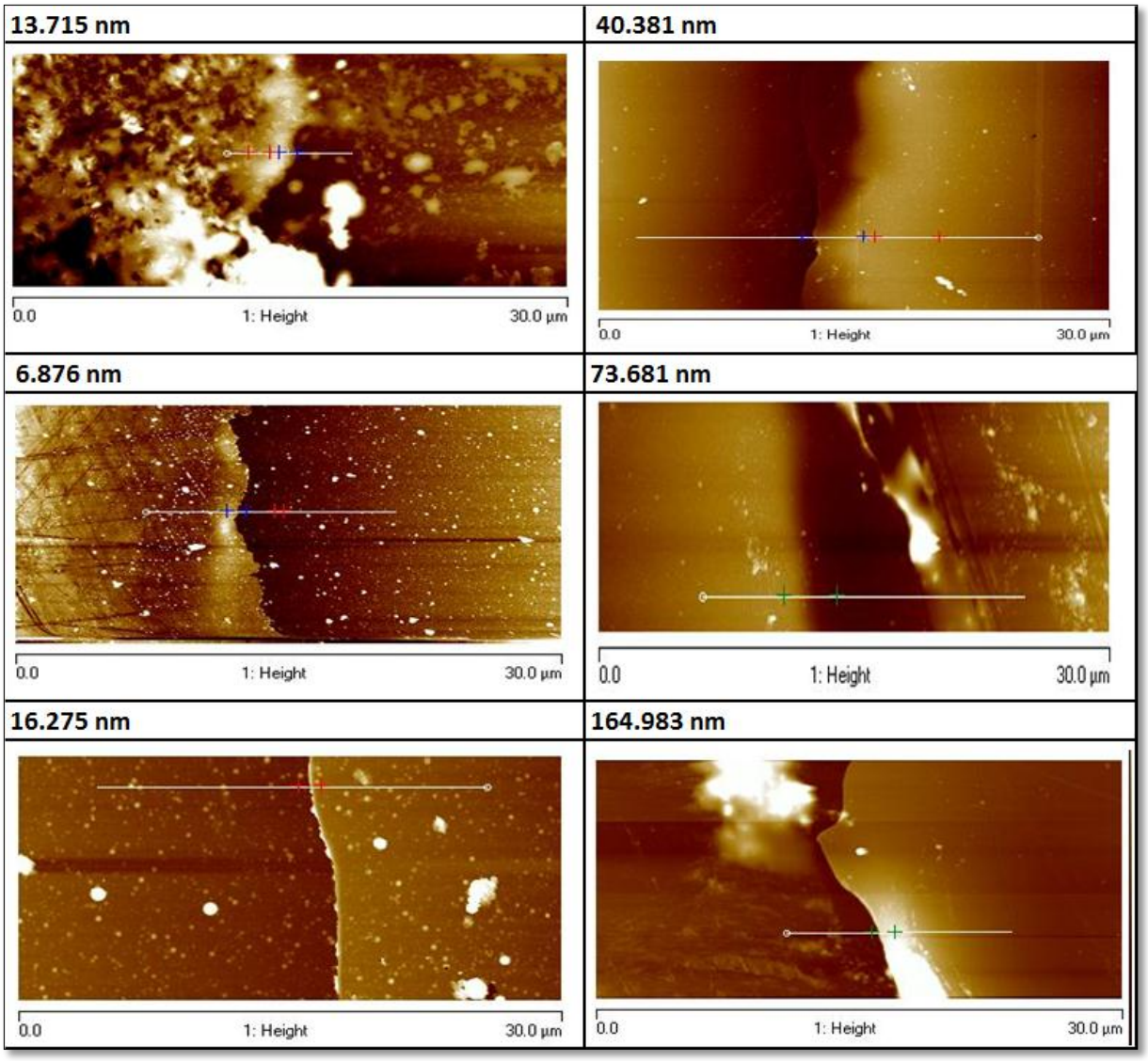

Figure 185: PTFE thin film morphology according to the coating thickness.

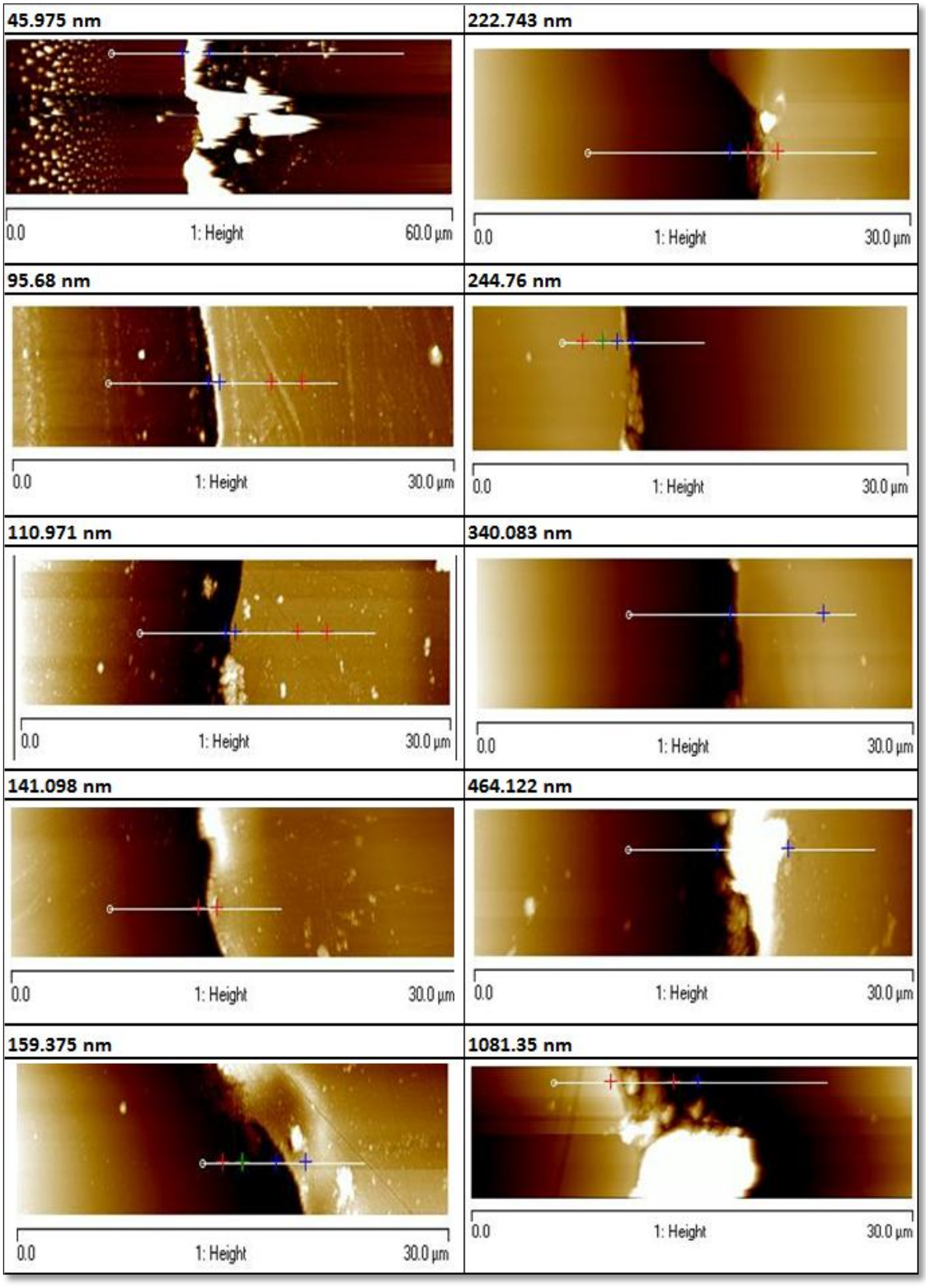

Figure 186: PTFE thin film topography according to the coating thickness.

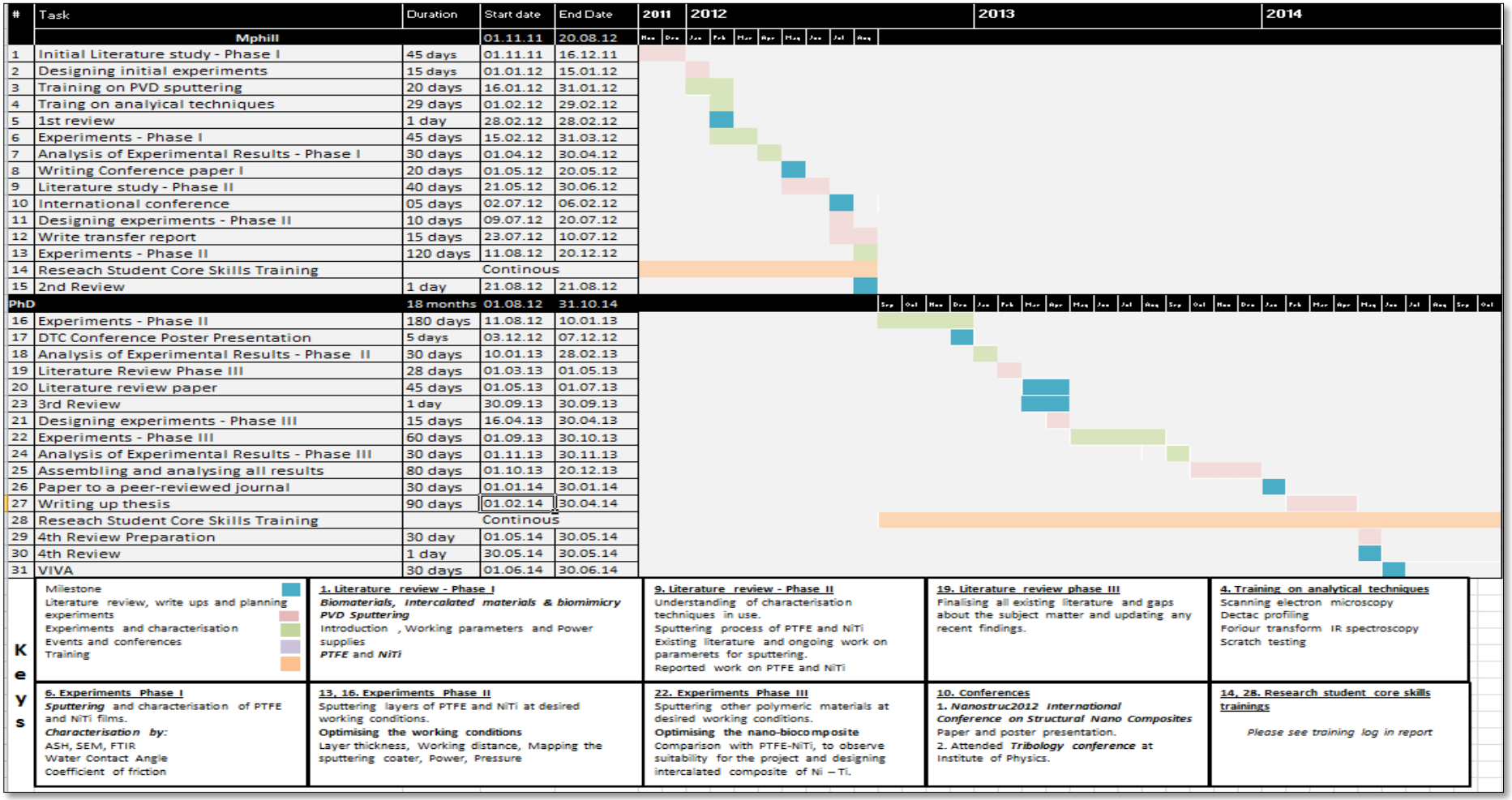

#	Task	Duration	Start date	End Date
	Mphill		01.11.11	20.08.12
1	Initial Literature study - Phase I	45 days	01.11.11	16.12.11
2	Designing initial experiments	15 days	01.01.12	15.01.12
3	Training on PVD sputtering	20 days	16.01.12	31.01.12
4	Traing on analyical techniques	29 days	01.02.12	29.02.12
5	1st review	1 day	28.02.12	28.02.12
6	Experiments - Phase I	45 days	15.02.12	31.03.12
7	Analysis of Experimental Results - Phase I	30 days	01.04.12	30.04.12
8	Writing Conference paper I	20 days	01.05.12	20.05.12
9	Literature study - Phase II	40 days	21.05.12	30.06.12
10	International conference	05 days	02.07.12	06.02.12
11	Designing experiments - Phase II	10 days	09.07.12	20.07.12
12	Write transfer report	15 days	23.07.12	10.07.12
13	Experiments - Phase II	120 days	11.08.12	20.12.12
14	Reseach Student Core Skills Training		Continous	
15	2nd Review	1 day	21.08.12	21.08.12
PhD		18 months	01.08.12	31.10.14
16	Experiments - Phase II	180 days	11.08.12	10.01.13
17	DTC Conference Poster Presentation	5 days	03.12.12	07.12.12
18	Analysis of Experimental Results - Phase II	30 days	10.01.13	28.02.13
19	Literature Review Phase III	28 days	01.03.13	01.05.13
20	Literature review paper	45 days	01.05.13	01.07.13
23	3rd Review	1 day	30.09.13	30.09.13
21	Designing experiments - Phase III	15 days	16.04.13	30.04.13
22	Experiments - Phase III	60 days	01.09.13	30.10.13
24	Analysis of Experimental Results - Phase III	30 days	01.11.13	30.11.13
25	Assembling and analysing all results	80 days	01.10.13	20.12.13
26	Paper to a peer-reviewed journal	30 days	01.01.14	30.01.14
27	Writing up thesis	90 days	01.02.14	30.04.14
28	Reseach Student Core Skills Training		Continous	
29	4th Review Preparation	30 day	01.05.14	30.05.14
30	4th Review	1 day	30.05.14	30.05.14
31	VIVA	30 days	01.06.14	30.06.14

Keys

Milestone
Literature review, write ups and planning
experiments
Experiments and characterisation
Events and conferences
Training

1. Literature review - Phase I
Biomaterials, Intercalated materials & biomimicry
PVD Sputtering
Introduction , Working parameters and Power supplies
PTFE and ***NiTi***

9. Literature review - Phase II
Understanding of characterisation techniques in use.
Sputtering process of PTFE and NiTi
Existing literature and ongoing work on paramerets for sputtering.
Reported work on PTFE and NiTi

19. Literature review phase III
Finalising all existing literature and gaps about the subject matter and updating any recent findings.

4. Training on analytical techniques
Scanning electron microscopy
Dectac profiling
Foriour transform IR spectroscopy
Scratch testing

6. Experiments Phase I
Sputtering and characterisation of PTFE and NiTi films.
Characterisation by:
ASH, SEM, FTIR
Water Contact Angle
Coefficient of friction

13, 16. Experiments Phase II
Sputtering layers of PTFE and NiTi at desired working conditions.
Optimising the working conditions
Layer thickness, Working distance, Mapping the sputtering coater, Power, Pressure

22. Experiments Phase III
Sputtering other polymeric materials at desired working conditions.
Optimising the nano-biocomposite
Comparison with PTFE-NiTi, to observe suitability for the project and designing intercalated composite of Ni – Ti.

10. Conferences
1. ***Nanostruc2012 International Conference on Structural Nano Composites***
Paper and poster presentation.
2. Attended ***Tribology conference*** at Institute of Physics.

14, 28. Research student core skills trainings
Please see training log in report

Figure 187: Gantt chart.

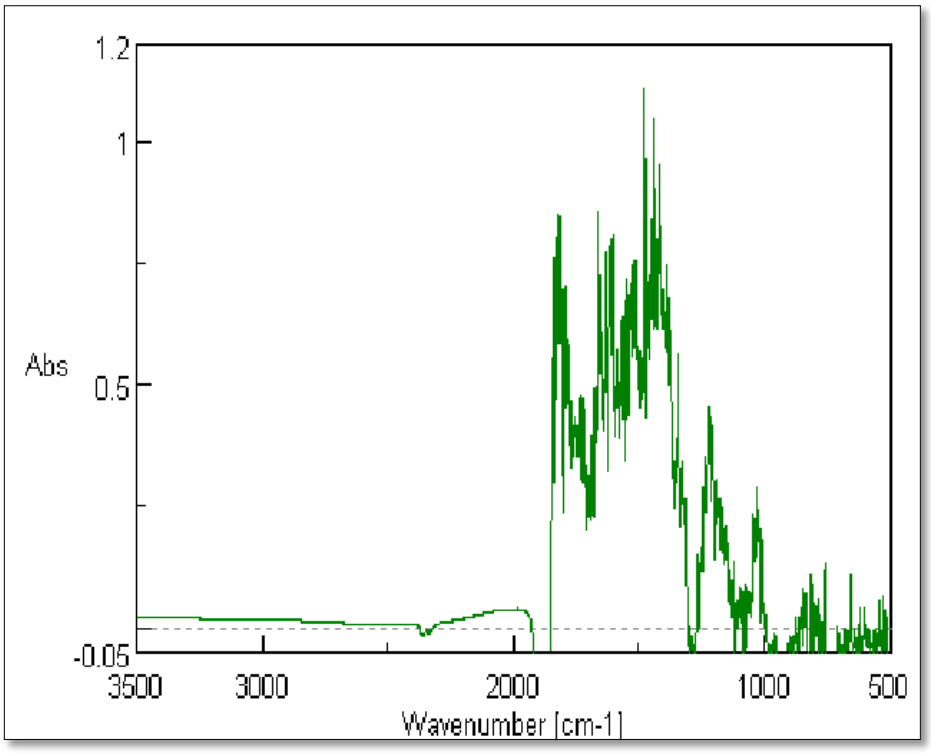

Figure 188: FTIR spectrum of PTFE after subtracting glass spectrum.

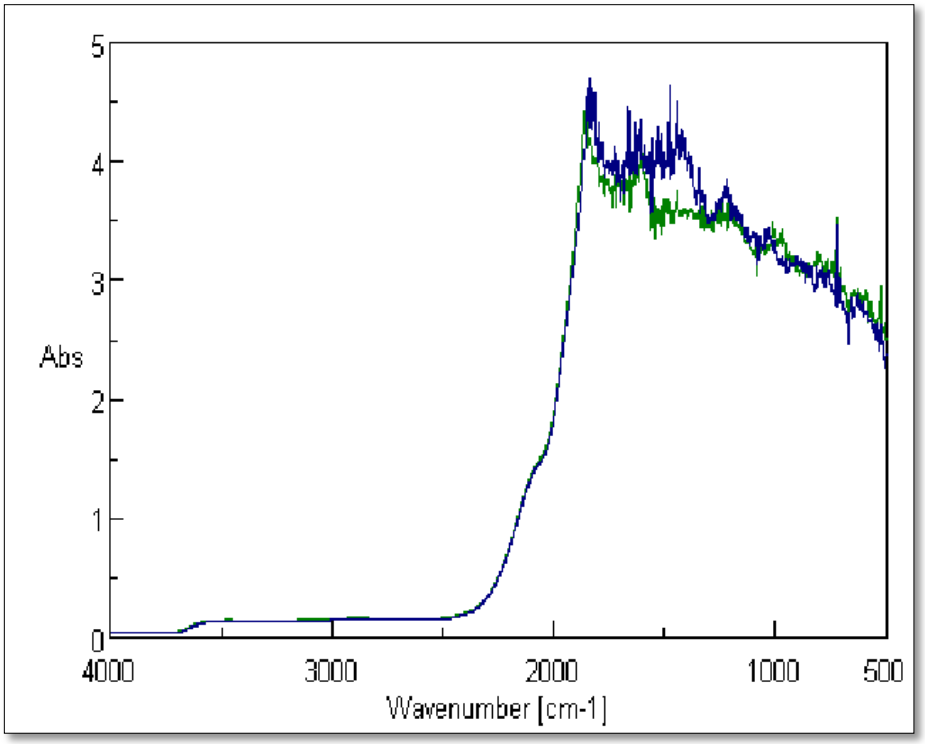

Figure 189: FTIR spectra of PTFE deposited at 100 and 150 W before subtracting from the glass.

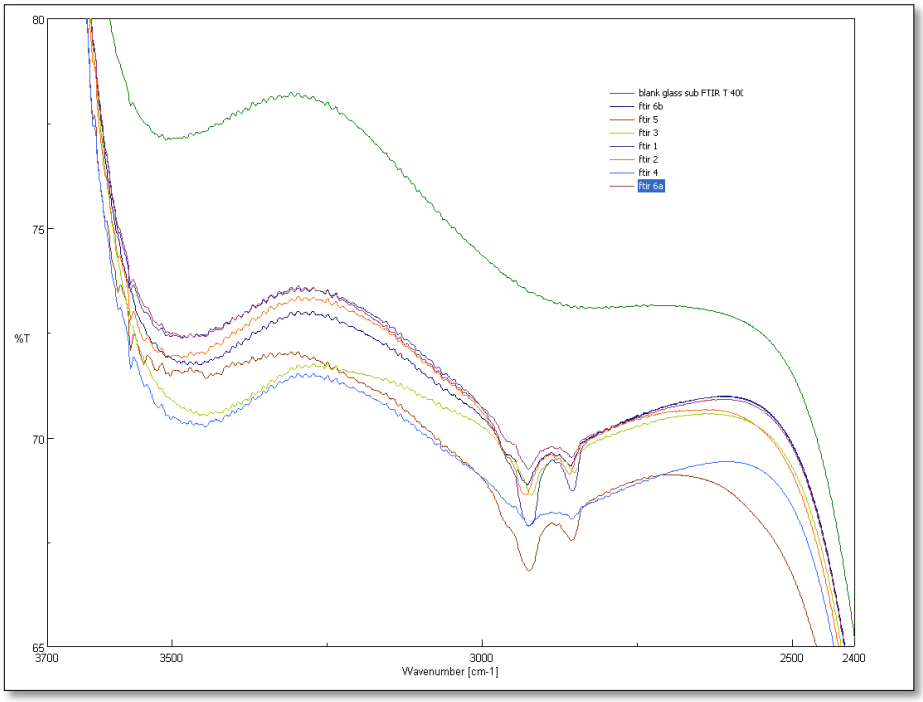

Figure 190: % transmittance FTIR spectra of various PTFE and glass substrate without processing to subtract and amplify.

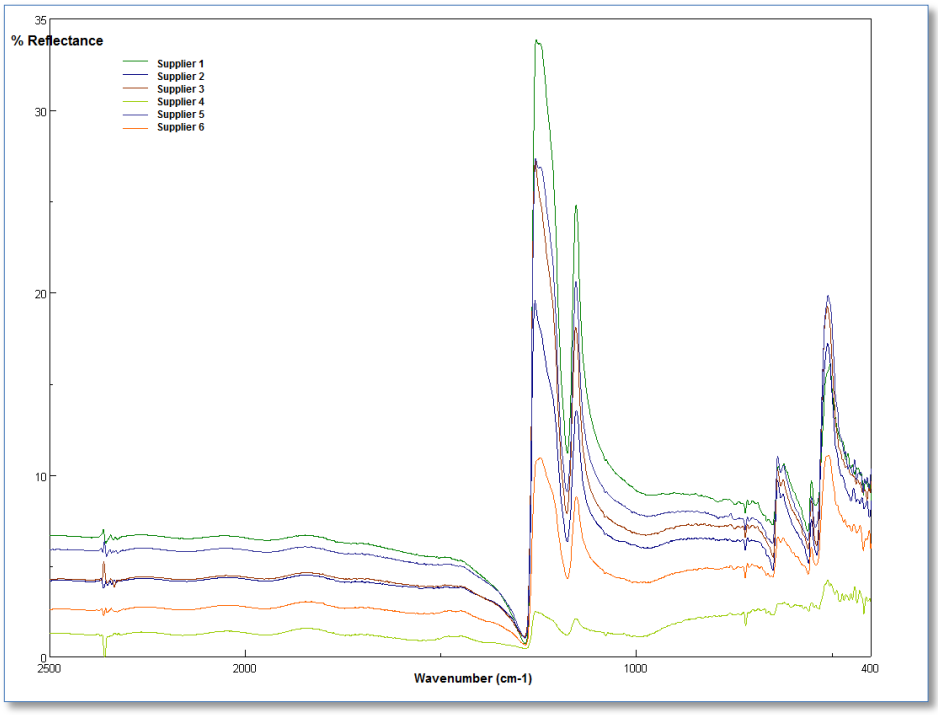

Figure 191: FTIR spectra for various target materials used to deposit PTFE.

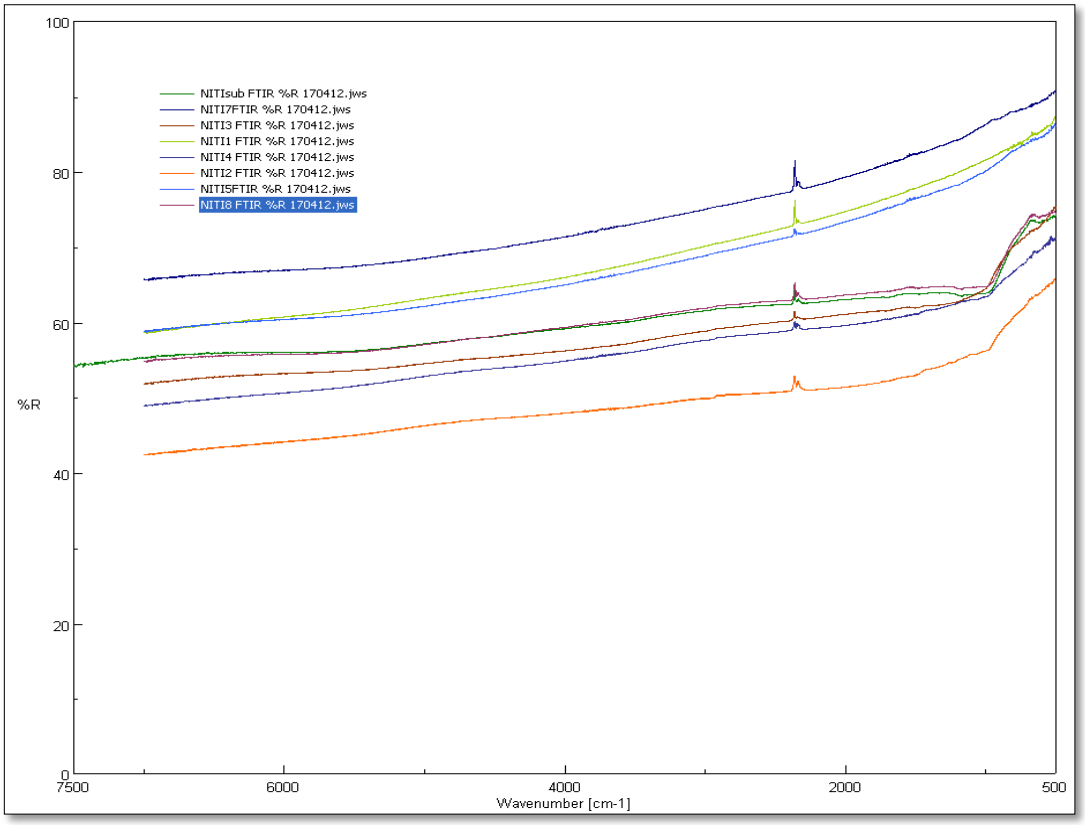

Figure 192: FTIR spectra for NiTi deposited at 50W and process pressure ranging 5 x 10^{-3} – 25 x 10^{-3} mbar.

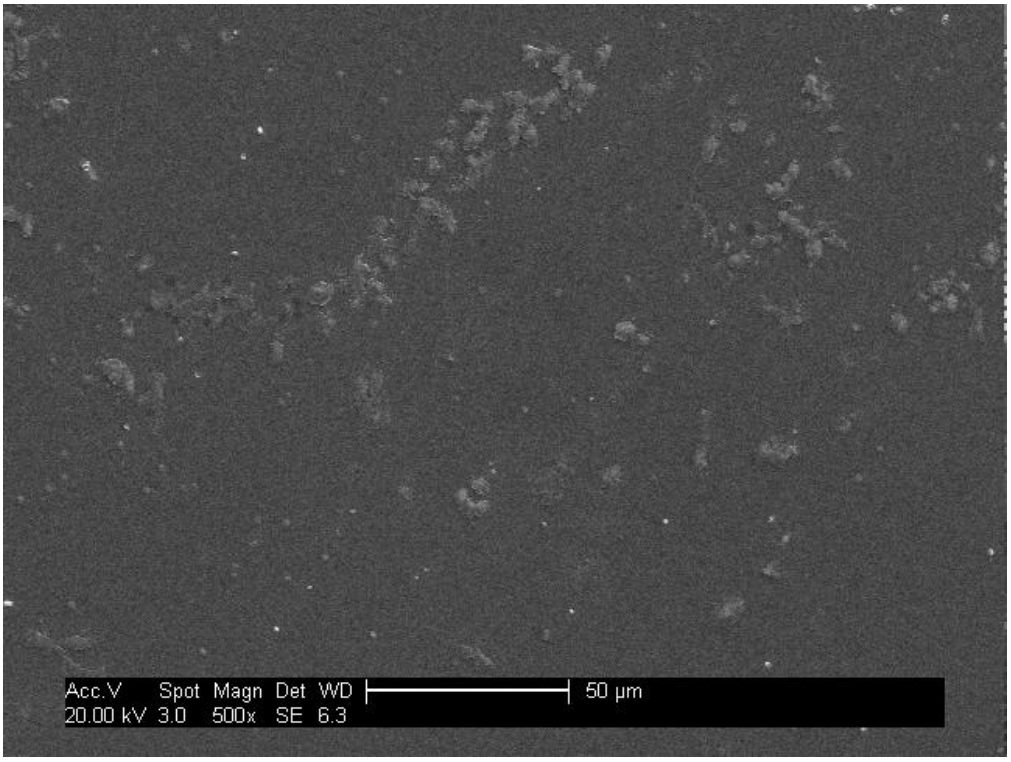

Figure 193: SEM image (x500) for PTFE deposited at 125W and 15 x 10^{-3} mbar.

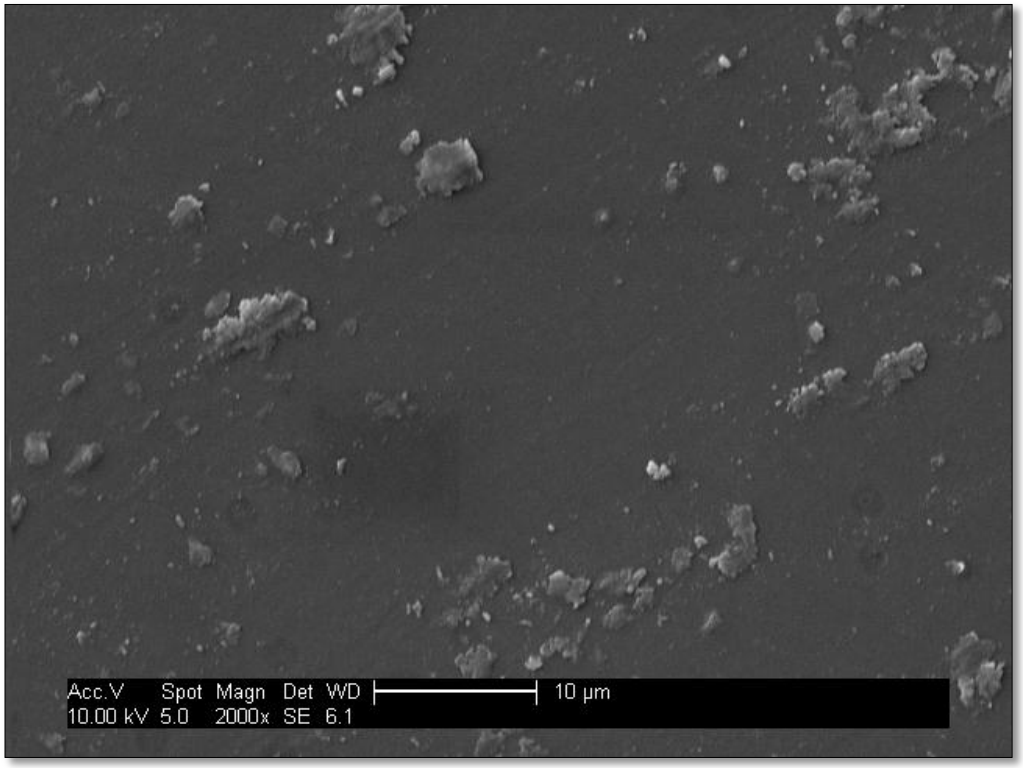

Figure 194: SEM image (x2000) for PTFE deposited at 125W and 15 x 10^{-3} mbar.

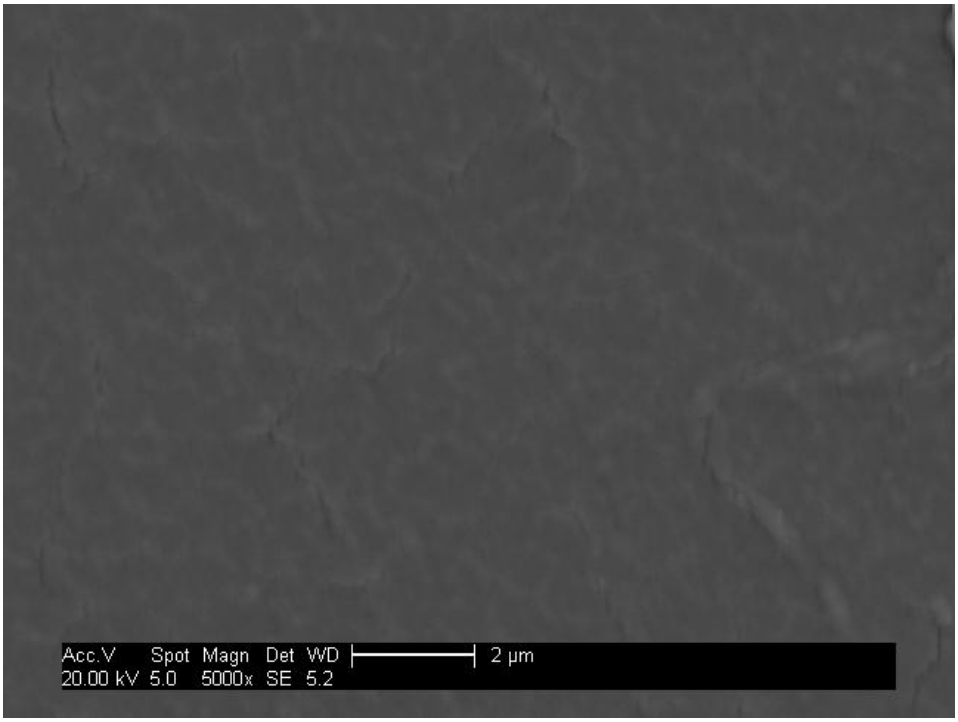

Figure 195: SEM image (x5000) for NiTi deposited at 75W and 25 x 10^{-3} mbar.

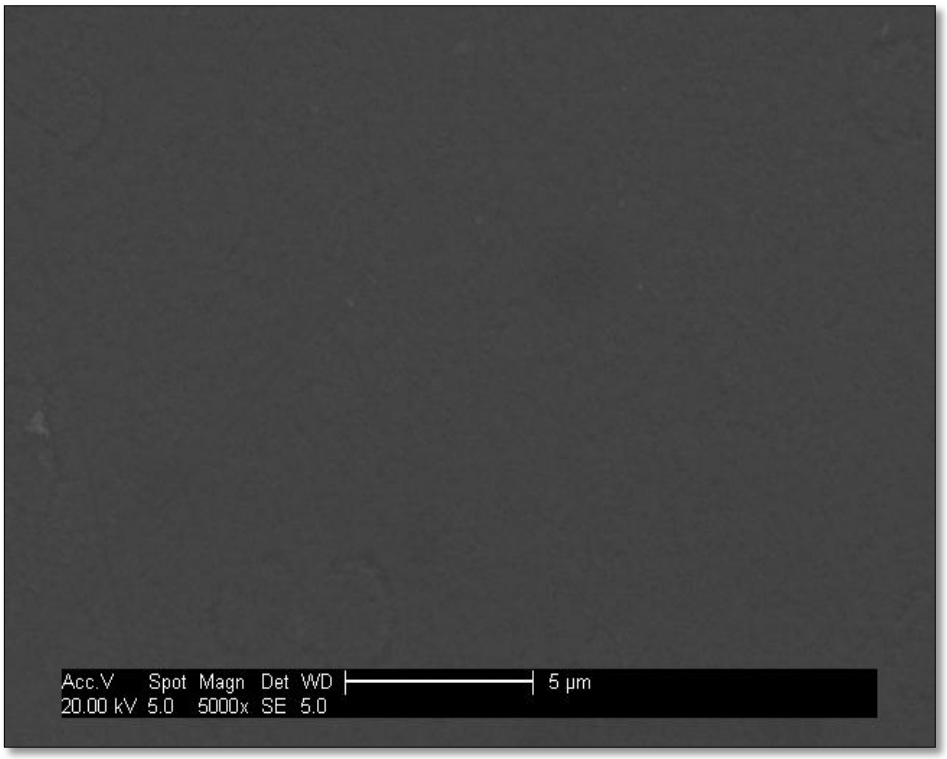

Figure 196: SEM image (x5000) for NiTi deposited at 75W and 5 x 10^{-3} mbar.

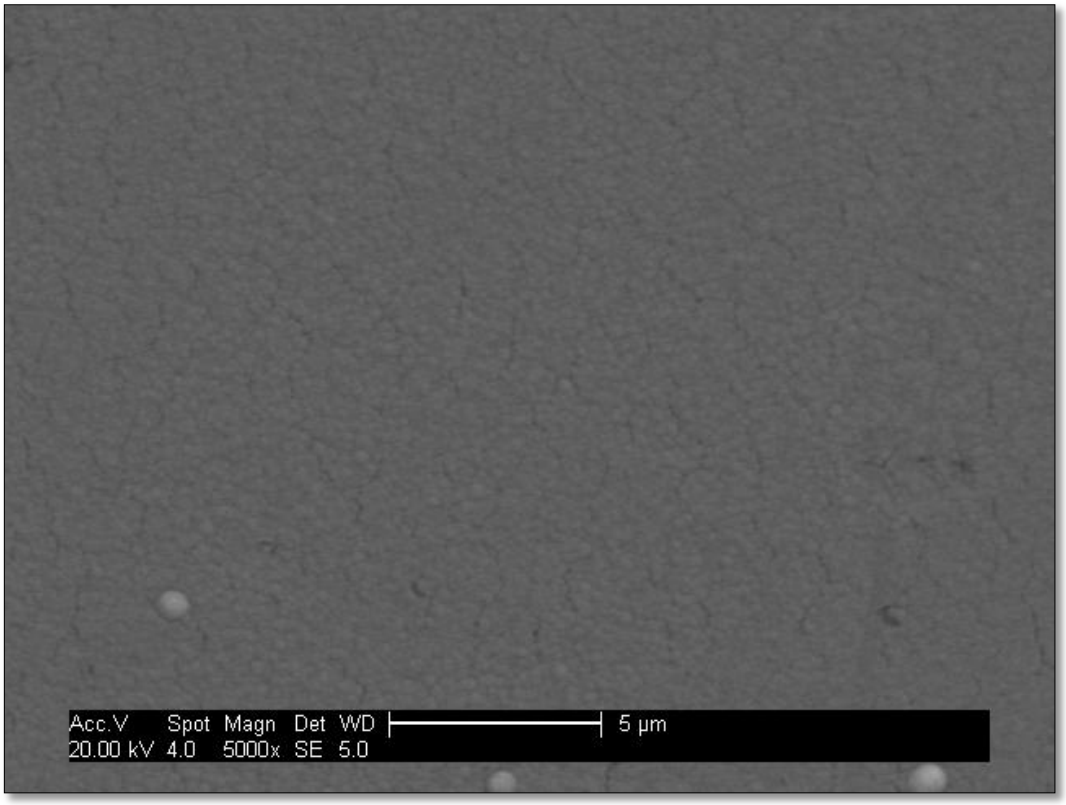

Figure 197: SEM image (x5000) for NiTi deposited at 50W and 10 x 10^{-3} mbar.

Figure 198: EDS – SEM image of PTFE-NiTi – PNA2

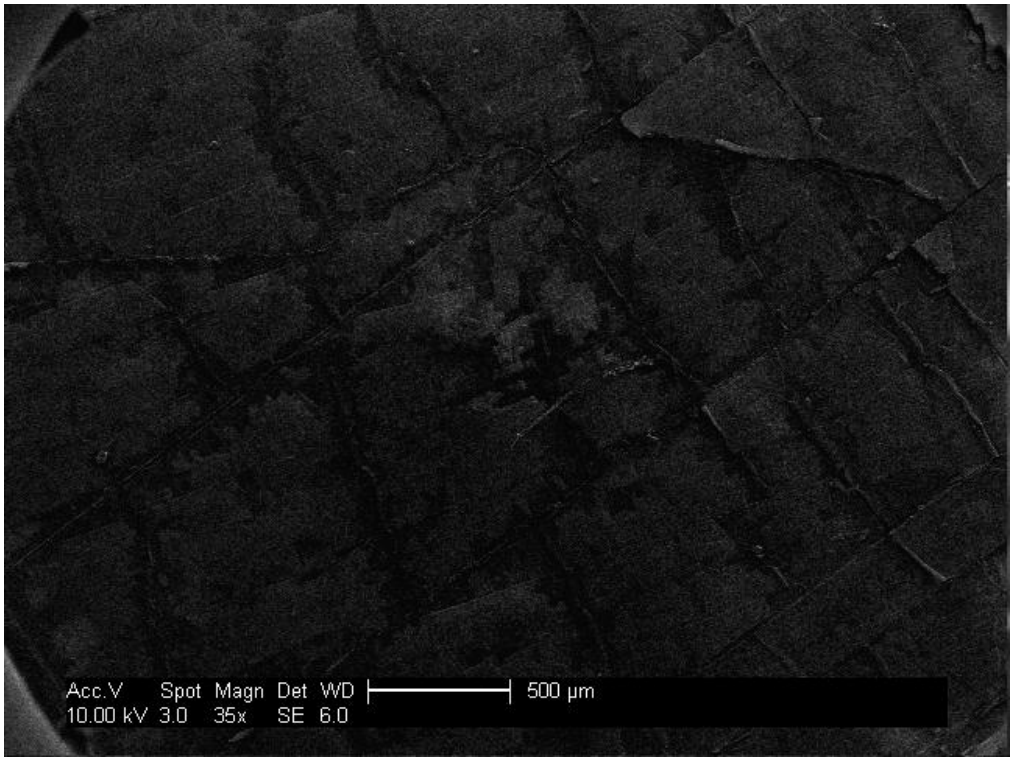

Figure 199: EDS – SEM image of PTFE-NiTi – PNA2

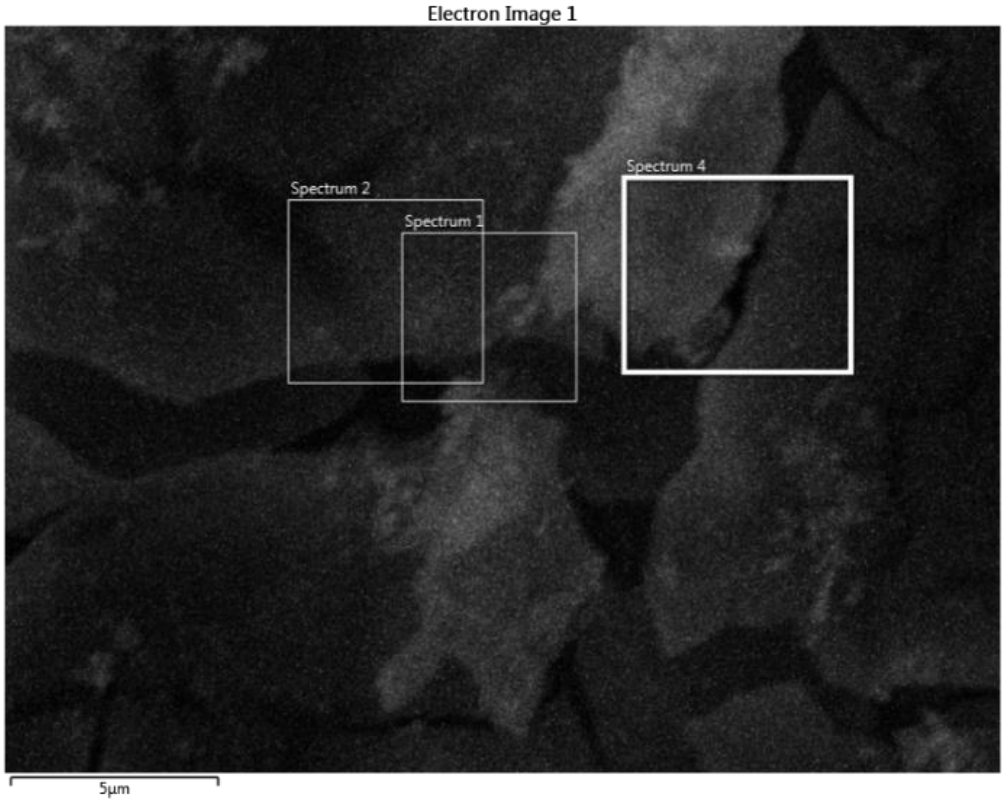

Figure 200: EDS – SEM image of PTFE-NiTi – PNK1.

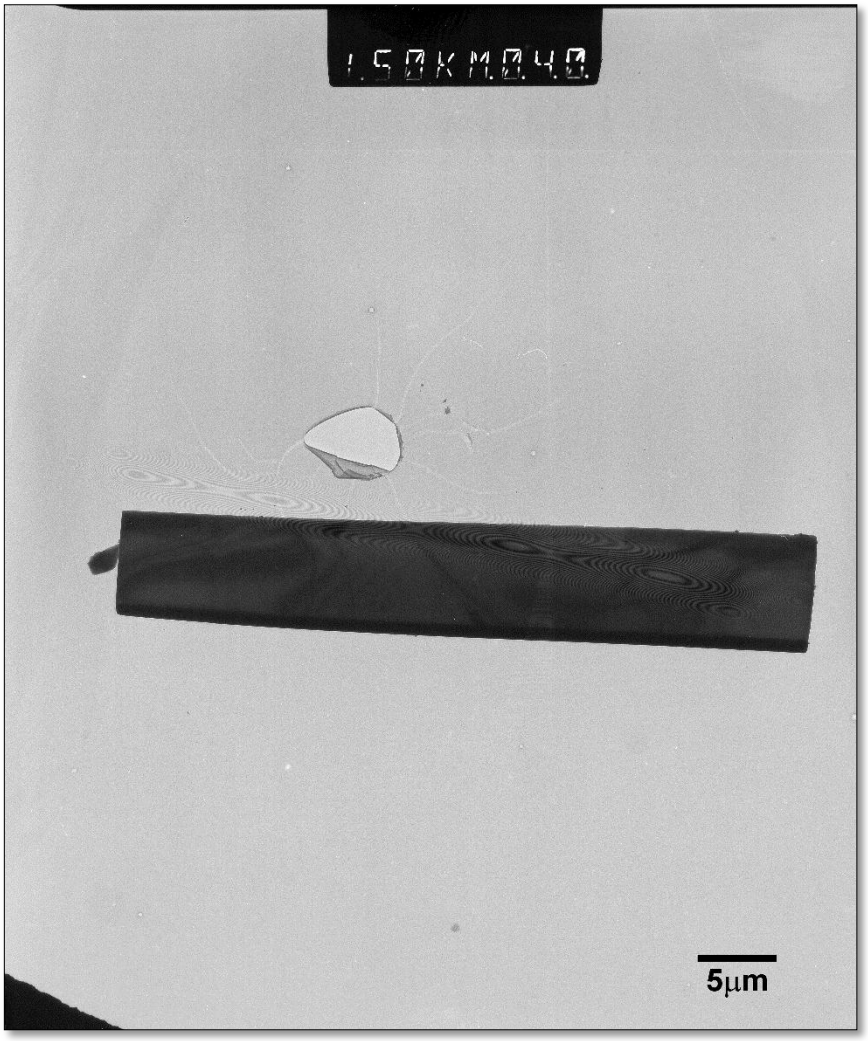

Figure 201: PTFE-NiTi – PNT12 sample prepared by FIB for TEM analysis.

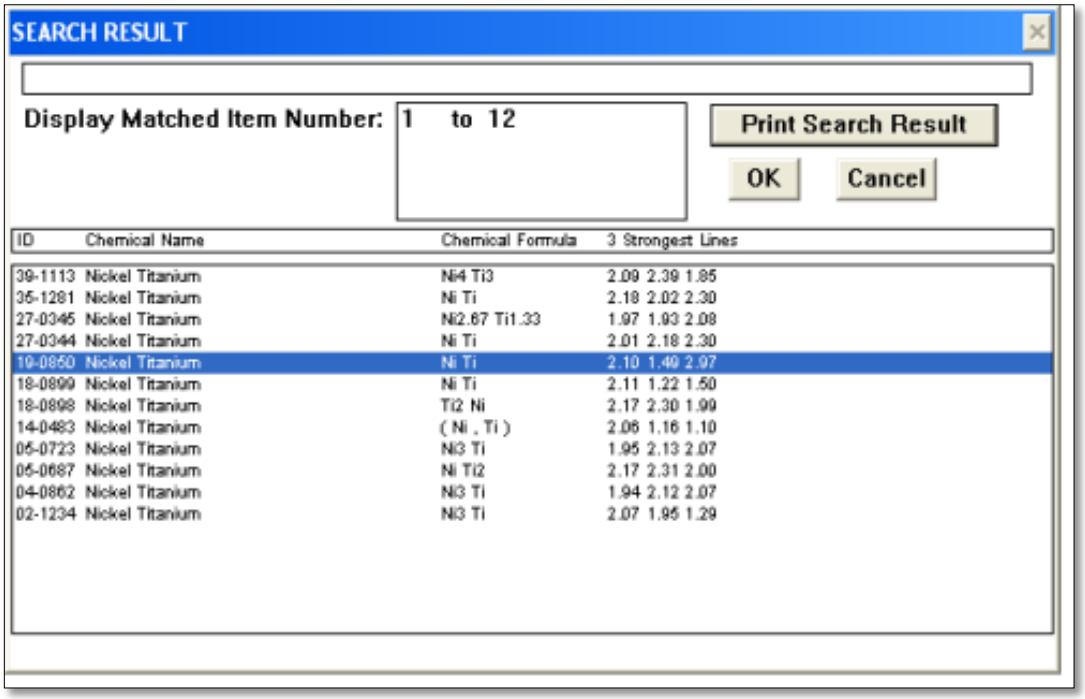

Figure 202: XRD peak position search from the database to identify NiTi and associated precipitates.

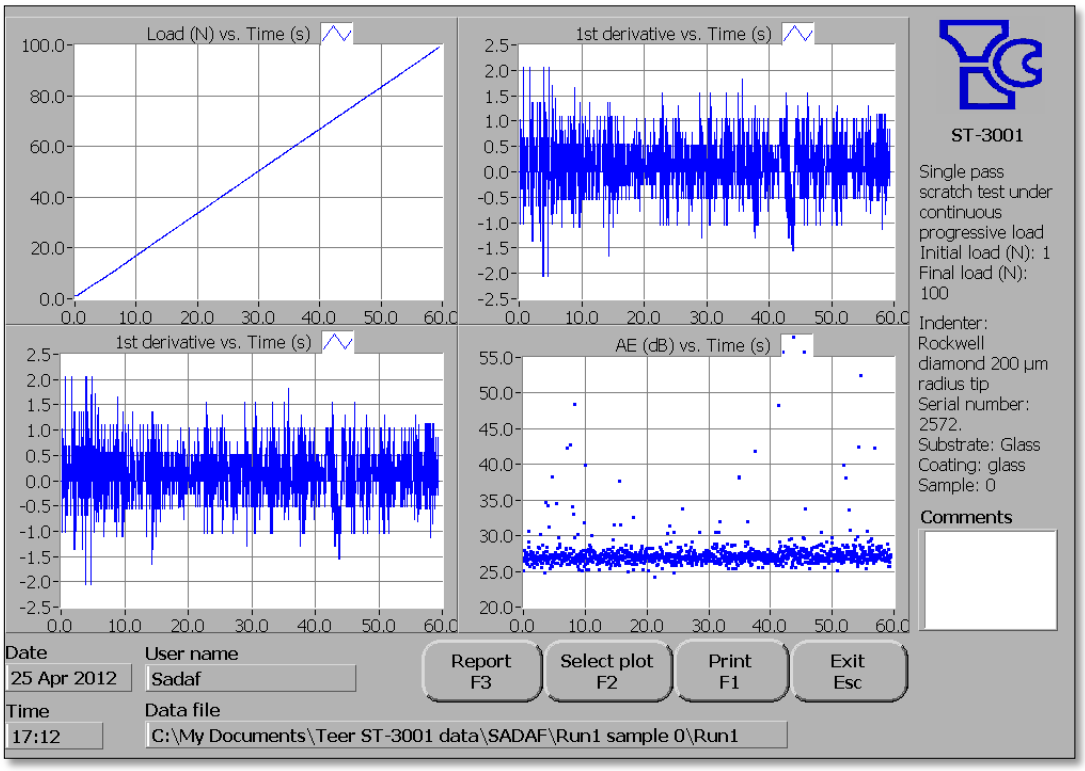

Figure 203: Single pass scratch test results screen under progressive loads.

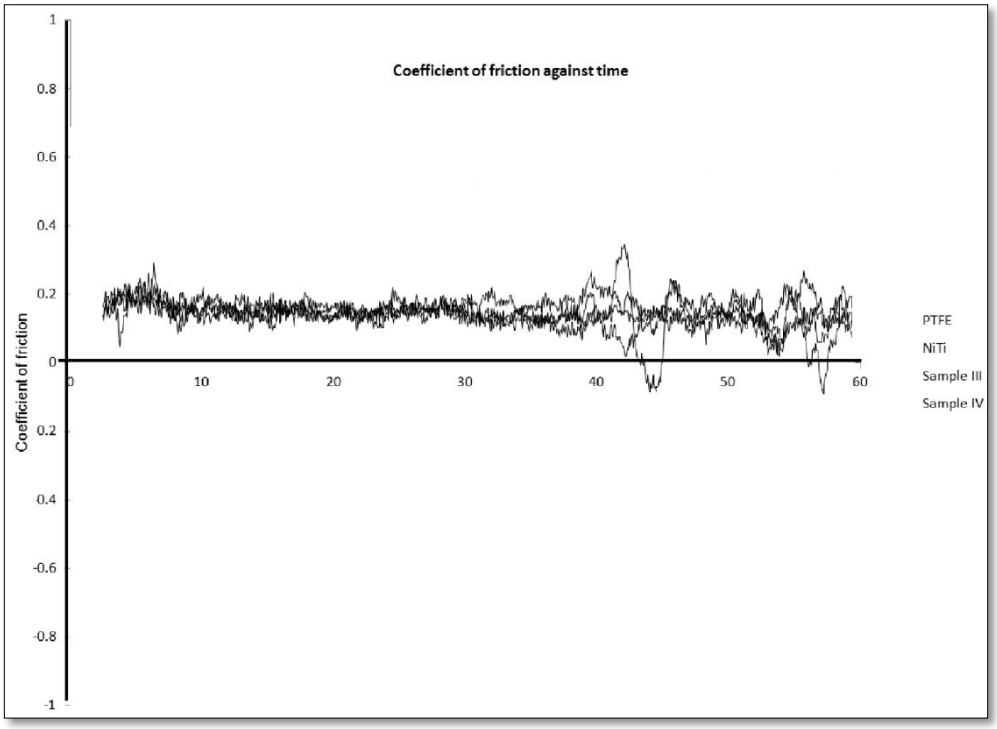

Figure 204: CoF vs. time results for PTFE, NiTi and nanocomposite (PNB11 and PNT12) without processing the results to convert into log_{10} values.

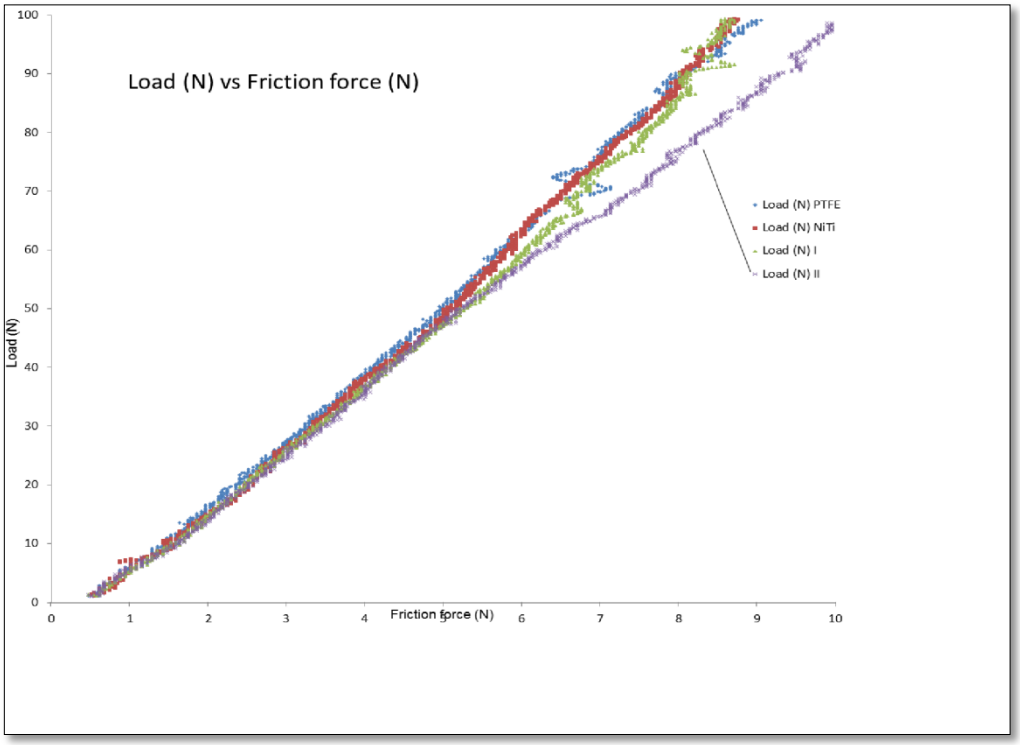

Figure 205: Load vs. frictional force results for PTFE, NiTi and nanocomposite (PNB11 and PNT12).